

LA-13977

Approved for public release;
distribution is unlimited.

TYBO/BENHAM:

**Model Analysis of Groundwater Flow
and Radionuclide Migration
from Underground Nuclear Tests
in Southwestern Pahute Mesa, Nevada**

This work was supported by the U.S. Department of Energy,
National Nuclear Security Administration, Nevada Operations Office.

Los Alamos National Laboratory, an affirmative action/
equal opportunity employer, is operated by the University
of California for the United States Department of Energy
under contract W-7405-ENG-36.



This report was prepared as an account of work sponsored by an agency of the United States Government. Neither the Regents of the University of California, the United States Government nor any agency thereof, nor any of their employees make any warranty, express or implied, or assume any legal liability or responsibility for the accuracy, completeness, or usefulness of any information, apparatus, product, or process disclosed, or represent that its use would not infringe privately owned rights. Reference herein to any specific commercial product, process, or service by trade name, trademark, manufacturer, or otherwise does not necessarily constitute or imply its endorsement, recommendation, or favoring by the Regents of the University of California, the United States Government, or any agency thereof. The views and opinions of authors expressed herein do not necessarily state or reflect those of the Regents of the University of California, the United States Government, or any agency thereof. Los Alamos National Laboratory strongly supports academic freedom and a researcher's right to publish; as an institution, however, the Laboratory does not endorse the viewpoint of a publication or guarantee its technical correctness.

LA-13977
Issued: September 2002

TYBO/BENHAM:
**Model Analysis of Groundwater Flow
and Radionuclide Migration
from Underground Nuclear Tests
in Southwestern Pahute Mesa, Nevada**

Andrew Wolfsberg

Lee Glascoe

Guoping Lu

Alyssa Olson

Peter Lichtner

Maureen McGraw

Terry Cherry

Guy Roemer

Document Revision History

Revision Number	Date	Comments
Rev 0.0a	5-9-2001	<ul style="list-style-type: none">• First printing.• Draft predecisional U.S. Department of Energy document that is not releasable to the public.
Rev 0.0b	5-2-2002	<ul style="list-style-type: none">• Incorporates comments from DOE and internal reviews.• Draft predecisional U.S. Department of Energy document that is not releasable to the public.
Rev 0.0c	5-17-2002	<ul style="list-style-type: none">• Minor edits to Rev 0.0b• Draft predecisional U.S. Department of Energy document that is not releasable to the public.
Rev 0.0	9-1-2002	<ul style="list-style-type: none">• Incorporates comments from DOE Office of Public Affairs and Information review• Official LA-13977 report number

Abstract

Recent field studies have led to the discovery of trace quantities of plutonium originating from the BENHAM underground nuclear test in two groundwater observation wells on Pahute Mesa at the Nevada Test Site. These observation wells are located 1.3 km from the BENHAM underground nuclear test and approximately 300 m from the TYBO underground nuclear test. In addition to plutonium, several other conservative (e.g. tritium) and reactive (e.g. cesium) radionuclides were found in both observation wells. The highest radionuclide concentrations were found in a well sampling a welded tuff aquifer more than 500 m above the BENHAM emplacement depth. These measurements have prompted additional investigations to ascertain the mechanisms, processes, and conditions affecting subsurface radionuclide transport in Pahute Mesa groundwater.

This report describes an integrated modeling approach used to simulate groundwater flow, radionuclide source release, and radionuclide transport near the BENHAM and TYBO underground nuclear tests on Pahute Mesa. The components of the model include a flow model at a scale large enough to encompass many wells for calibration, a source-term model capable of predicting radionuclide releases to aquifers following complex processes associated with non-isothermal flow and glass dissolution, and site-scale transport models that consider migration of solutes and colloids in fractured volcanic rock. Although multiple modeling components contribute to the methodology presented in this report, they are coupled and yield results consistent with laboratory and field observations. Additionally, sensitivity analyses are conducted to provide insight into the relative importance of uncertainty ranges in the transport parameters.

Acknowledgements

This modeling study would not be possible without the field and laboratory data collected by many individuals on and off of the NTS-UGTA project. We are particularly grateful to Paul Reimus, Ning Ping Lu, Doug Ware, Chris Benedict, Inez Triay, Rick Warren, Lance Prothro, Sig Drellack, Annie Kersting, and Dave Smith for their efforts and interactions in helping us integrate their relevant data. We are also grateful to Mavrik Zavarin for his surface complexation data base, Carl Gable for his guidance with grid generation activities, Bruce Robinson and George Zyvoloski for assistance with the FEHM code, and Jennifer Boryta for assistance with the final document production. Internal DOE reviews provided by Andy Tompson, Dave Prudic, Greg Pohl, Rick Waddell, Vefa Yucel, Carol Bruton, Roger Jacobson, Janet Wille, Mike Sully, and Robert Bangerter were insightful and of great benefit to this study.

Nomenclature

ANOVA	Analysis of Variation
BFCU	Bull Frog Confining Unit
CAU	Corrective Action Unit
CHZCM	Calico Hills Zeolitic Composit Unit
DOE	U.S. Department of Energy
DRI	Desert Research Institute
FEHM	Finite Element Heat and Mass transfer code
GDPM	Generalized Dual-Porosity Model
HSU	Hydrostratigraphic Unit
IT	International Technology Corporation
LANL	Los Alamos National Laboratory
LLNL	Lawrence Livermore National Laboratory
MG	Melt Glass
NTS	Nevada Test Site
PEST	Parameter Estimation SofTware
RN	Radionuclide
RTTF	Residence Time Transfer Function particle tracking
SPTR	Streamline Particle Tracking
THC	Thermal-Hydrologic-Chemical
TSA	Topopah Spring Aquifer
UGTA	Underground Test Area
USGS	U.S. Geological Survey
WPM	Western Pahute Mesa

Note: Additional hydrostratigraphic nomenclature in Table 2-1 and radionuclide nomenclature in Table 1-1.

Table of Contents

	EXECUTIVE SUMMARY	1
Chapter 1:	Introduction	1-1
	1.1 Introduction	1-1
	1.2 Study Objectives	1-2
	1.3 Model Components: A Road Map Through the Document	1-3
	1.3.1 Sub-CAU Flow Model	1-4
	1.3.2 Site-Scale Flow Model	1-4
	1.3.3 Source-Term Model	1-6
	1.3.4 Site-Scale Transport Model	1-6
	1.4 Computer Codes Used In This Study	1-7
	1.4.1 Finite-Element Heat and Mass Transfer Code (FEHM)	1-7
	1.4.2 FloTran	1-7
	1.5 Review of Sampling and Analysis at the ER-20-5 wells	1-8
	1.6 Other Relevant Studies in Western Pahute Mesa	1-9
	1.6.1 The CHESHIRE Study	1-9
	1.6.2 Pahute Mesa Hydrostratigraphic Model	1-12
	1.7 Summary	1-13
Chapter 2:	Stratigraphy and Model Domain Definitions	2-1
	2.1 Introduction	2-1
	2.2 Geologic Cross Sections Through the Model	2-1
	2.3 Model Domains	2-9
	2.4 Hydrostratigraphy of the Sub-CAU Domain	2-13
Chapter 3:	Sub-CAU Flow Model Components	3-1
	3.1 Introduction	3-1
	3.2 Components of the Sub-CAU Flow Model	3-1
	3.2.1 Boundary Conditions	3-2
	3.2.2 Head Observations	3-3
	3.2.3 Water Table	3-7
	3.2.4 Faults	3-7
	3.2.5 Permeability	3-8
	3.2.6 Perched Water	3-9
	3.2.7 Recharge	3-10
	3.2.8 Thermal Gradients	3-10
	3.2.9 Thermal Effects on Hydraulic Conductivity	3-10
	3.3 Data Quality Issues	3-11
	3.3.1 Hydrostratigraphic Model	3-11
	3.3.2 Head Observations	3-11
	3.3.3 Flux Estimates	3-18
	3.3.4 Recharge Estimates	3-18
	3.3.5 Boundary Condition Assumptions	3-19
	3.3.6 Thermal Data Quality	3-19

Chapter 4:	Sub-CAU Flow Model Calibration	4-1
	4.1 Calibration Objectives	4-1
	4.2 Calibration Process with PEST2000	4-1
	4.3 Calibration Results	4-5
	4.3.1 Calibration Features	4-9
	4.3.2 Calibration Guidelines: Where Does this Study Fit in?	4-11
	4.3.3 Calibration Sensitivity to Boundary Conditions	4-20
	4.3.4 Calibration Sensitivity to Internal Assumptions	4-26
	4.4 Summary	4-34
Chapter 5:	Site-Scale Flow Model	5-1
	5.1 Introduction	5-1
	5.2 Deterministic HSUs	5-1
	5.3 Heterogeneous Attribute Maps	5-1
	5.3.1 Background	5-1
	5.3.2 Approach	5-3
	5.3.3 Assigning Fracture Characteristics: Creating Two New Classes	5-7
	5.3.4 Limitations of Heterogeneous Attribute Maps	5-10
	5.4 Boundary Conditions	5-11
	5.5 Effective Block Permeability	5-11
	5.6 Deterministic Site-Scale Flow-Model Results	5-16
	5.7 Geostatistical Site-Scale Flow-Model Results	5-19
	5.8 TYBO Effects on Paths from BENHAM	5-19
	5.9 Transport Parameters: Preliminary Considerations	5-28
Chapter 6:	Source-Term Model	6-1
	6.1 Introduction	6-1
	6.1.1 Overview	6-1
	6.1.2 Source-Term Model Goal	6-2
	6.1.3 The BENHAM Test	6-2
	6.1.4 The TYBO Test	6-3
	6.2 Flow and Transport Model	6-5
	6.2.1 Mass and Heat Flow Model	6-5
	6.2.2 Particle-Tracking Transport Model	6-7
	6.3 Model Domain, Boundary Conditions, and Initial Conditions	6-8
	6.4 Rayleigh-Number Analysis	6-9
	6.4.1 Relative Rayleigh Numbers	6-9
	6.4.2 Solute Retardation and Rayleigh Numbers	6-10
	6.5 Model Parameters	6-11
	6.5.1 Physical and Thermal Parameters	6-11
	6.5.2 Radionuclide Source Parameters	6-12
	6.5.3 Glass Dissolution Estimation	6-16
	6.5.4 Transient Particle Release in the Melt Glass	6-17
	6.6 Melt Glass Release: Conservative Radionuclide Example	6-24
	6.6.1 Comparison with THC Model	6-26
	6.6.2 BASE CASE Simulation Results (CASE 1)	6-27
	6.6.3 CASE 2 Simulations: Variable Chimney Permeabilities	6-30

6.6.4	CASE 3 Simulations: Absence of Residual Heat	6-37
6.6.5	CASE 4 Simulations: Lower Melt Glass Temperature.	6-42
6.6.6	CASE 5 Simulations: Different Initial Melt Glass Volume or Properties	6-45
6.6.7	CASE 6 Simulations: LAVA Permeability Variation	6-50
6.7	Melt-Glass Release: Sorptive Plutonium Example	6-50
6.8	Source Term for all 16 Radionuclides	6-56
6.8.1	Initial Mass Source: Exchange-Volume and Melt-Glass Distribution	6-57
6.8.2	Mass Flux Curves	6-60
6.8.3	Cumulative Mass Curves	6-65
6.9	Summary and Conclusions	6-69
Chapter 7:	Site-Scale Particle-Tracking Transport Model	7-1
7.1	Introduction	7-1
7.2	Chapter Road Map	7-1
7.3	Convolution Integral Approach	7-2
7.4	Source Term	7-4
7.5	Parameter Distributions	7-5
7.6	Justification For Particle-Tracking Model	7-10
7.6.1	Review of the Reactive Transport Model Approach	7-10
7.6.2	Review of the Particle-Tracking Model Approach.	7-10
7.6.3	Comparison of the Two Different Approaches.	7-10
7.7	Transport Using the Deterministic HSU Model	7-11
7.7.1	Introduction.	7-11
7.7.2	Base-Case Results.	7-12
7.7.3	Estimated Radionuclide Concentrations in Groundwater at the ER-20-5 Wells	7-13
7.7.4	Parameter Sensitivity: Downstream Mass Flux Curves	7-24
7.7.5	Summary of Transport Simulations on Deterministic Flow Field . .	7-37
7.8	Heterogeneous Flow Fields	7-38
7.8.1	Source Terms	7-39
7.8.2	Site-Scale Breakthrough Curves.	7-39
7.8.3	Transport on Geostatistical Flow Realization #3 with Base-Case Parameters	7-45
7.8.4	Estimation of Groundwater Pu-Colloid Concentrations at ER-20-5 Wells and the NTS Boundary	7-49
7.9	Geostatistical Sensitivity Study	7-52
7.9.1	Parameter Sensitivity I: BASE-CASE Source.	7-52
7.9.2	Parameter Sensitivity II: Impact Ratios	7-58
7.9.3	Parameter Sensitivity III: Analysis of Variation (ANOVA).	7-63
7.9.4	Summary of Transport Simulations on Heterogeneous Flow Fields	7-73
7.10	Summary and Conclusions	7-74
Chapter 8:	Summary and Recommendations	8-1
8.1	Review of the Integrated Model	8-1
8.1.1	Sub-CAU Flow Model	8-1

8.1.2	Source-Term Models	8-1
8.1.3	Site-Scale Transport Models: Descriptions	8-2
8.1.4	Site-Scale Transport Models: Results	8-3
8.1.5	Integrating Heterogeneous Attribute Maps	8-5
8.1.6	Confidence in Results	8-5
8.2	Other Plausible Explanations	8-6
8.3	Recommendations	8-6
8.3.1	Assessment of Transport Processes	8-6
8.3.2	Modeling Methods	8-7
Chapter 9:	References	9-1
Appendix A:	Sub-CAU Flow Model Grid Generation	A-1
A.1	Introduction	A-1
A.1.1	Grid Generation Tools and Software	A-1
A.2	Details of Method	A-1
A.2.1	Create Quadrilateral Surfaces Grids	A-2
A.2.2	Create Boundary and Refinement Surfaces	A-3
A.2.3	Stack Surfaces into the 3-D Sub-CAU Hexahedral Mesh	A-4
A.2.4	Embed a High-Resolution Site-Scale Mesh in the Sub-CAU Mesh	A-4
A.2.5	Optimize Sub-CAU and Embedded Mesh for Computations	A-5
A.2.6	Assign Fault and Unit Material Identification Values	A-6
A.2.7	Compute and Output Volume and Area Matrix Coefficients	A-7
A.2.8	Define Node Sets for Setting Initial Conditions, Boundary Conditions and Material Properties	A-8
A.2.9	Perform Mesh Quality Checks	A-8
A.2.10	Summary	A-9
A.3	References	A-9
Appendix B:	Coupled Thermal-Hydrologic-Chemical (THC) Source Term Model	B-1
B.1	Introduction	B-1
B.2	THC-Coupled Processes	B-2
B.2.1	Mass and Heat Conservation Equations	B-4
B.2.2	Reactive Transport Equations	B-5
B.3	Applications to the BENHAM Underground Nuclear Test	B-9
B.3.1	Melt Glass Source Term: Composition and Dissolution Rate	B-9
B.3.2	Rate Controlling Step	B-13
B.3.3	Geologic Model	B-15
B.3.4	Initial and Boundary Conditions	B-19
B.3.5	THC-Modeling Results	B-22
B.4	Discussion	B-23
B.5	Conclusions	B-23
Appendix C:	Field-Scale Transport in Fractured Rock: Reactive Dual-Porosity Particle Tracking	C-1
C.1	Introduction	C-1
C.2	Advective and Dispersive Components	C-2

C.3	Dual-Porosity Reactive Streamline Particle Tracking in FEHM	C-2
C.4	References.	C-4
Appendix D: Reactive, Colloid-Facilitated Plutonium Transport Model: Development and Testing D-1		
D.1	Overview.	D-1
D.2	Background for Dual-Porosity Fracture Transport Model	D-1
D.3	Mathematical Model	D-2
D.3.1	Introduction	D-2
D.3.2	Chemical Speciation Network	D-2
D.3.3	Plutonium-Colloid Reactions	D-4
D.3.4	Colloid Filtration	D-7
D.3.5	Surface Complexation of Plutonium with Fracture and Matrix Minerals.	D-8
D.4	Pu-Colloid Transport in Fractured Column Experiments	D-12
D.4.1	Overview of Column Experiments	D-12
D.4.2	Column Simulations	D-13
D.4.3	Sensitivity Analysis	D-14
D.5	Pu Speciation Reactions	D-20
D.6	Summary	D-24
D.7	References.	D-25
Appendix E: Field-Scale Transport in Fractured Rock: The Generalized Dual-Porosity Model (GDPM) E-1		
E.1	Generalized Dual-Porosity Model Description.	E-1
E.2	Verifying GDPM	E-2
E.2.1	One-Dimensional Tests: Diffusion and Reactive Transport	E-2
E.2.2	Applying GDPM Along Streamtubes in Three-Dimensional Flow Fields	E-3
E.3	References.	E-9
Appendix F: Site-Scale Transport Model - Reactive Transport Along Streamlines F-1		
F.1	Introduction	F-1
F.2	Reactive Transport in Fractured Rock	F-2
F.2.1	Generalized Dual-Porosity Model	F-2
F.2.2	Solutes of Interest and Reactive Processes	F-2
F.3	Transport Parameters for Site-Scale Calculations	F-3
F.3.1	Data Sources	F-3
F.3.2	Process Model Parameter Road Map	F-3
F.3.3	Transport Parameters in Heterogeneous Domains	F-5
F.3.4	Aqueous System Chemistry: Carbonate Speciation	F-5
F.3.5	Sorption in Fractures.	F-13
F.3.6	Additional Fracture K_e^{lump} Uncertainty	F-24
F.3.7	Matrix Sorption.	F-25
F.3.8	Matrix Diffusion	F-28
F.3.9	Fracture Properties d , b , ϕ_f	F-29
F.3.10	Plutonium-Colloid Reactions	F-31

F.4	Reactive Transport Along Heterogeneous Pathlines	F-33
F.5	Site-Scale Application	F-34
	F.5.1 Overview.....	F-34
	F.5.2 Source Term	F-35
	F.5.3 Plutonium Base, Minimum, and Maximum Cases	F-35
	F.5.4 Uranium, Neptunium and Strontium.....	F-40
	F.5.5 Colloid Transport of Other Radionuclides	F-40
F.6	Non-reactive Class I Species	F-40
F.7	Sensitivity Analysis	F-44
F.8	Summary	F-53
F.9	References	F-55
Appendix G: Personal Communication Regarding Development of Geostatistical Attribute		
	Maps at DRI	G-1
G.1	Introduction.....	G-1
G.2	Background Information.....	G-2
	G.2.1 Approaches to Modeling	G-3
	G.2.2 Deterministic Zonation	G-4
	G.2.3 Geostatistical Fields	G-5
G.3	Methods/Approach	G-7
	G.3.1 Zoned Geostatistical Simulations	G-7
	G.3.2 Approach	G-9
G.4	Results and Discussion	G-19
G.5	Conclusions.....	G-25
G.6	Recomendations	G-25
G.7	References.....	G-27

List of Figures

Figure 1-1. The Nevada Test Site (NTS) and the specific locations of the BENHAM and TYBO tests.	1-1
Figure 1-2. Cross-section along Transect A-A' in Figure 1-1 showing possible migration paths of plutonium away from BENHAM.	1-3
Figure 1-3. Models used in this study	1-5
Figure 2-1. Stratigraphic surface of the top of the Belted Range Aquifer under Areas 19 and 20 from Drellack and Prothro (1997). Similar surfaces exist for all 22 units. Blue dots show wells used to calibrate sub-CAU-scale flow model. Red dots show BENHAM and TYBO. Red lines in upper plot show mapped faults in Areas 19 and 20.	2-2
Figure 2-2. Plan view of BENHAM vicinity showing cross-section transects, well names, and faults.	2-4
Figure 2-3. Stratigraphic units along A-A' transect. Note, the plutonium from BENHAM was found in ER-20-5 observation wells sampling the TSA and a lava formation embedded within the CHZCM. Transect and wells are identified in Figure 2-2.	2-5
Figure 2-4. Stratigraphic units along B-B' transect which are identified in Figure 2-2.	2-6
Figure 2-5. View of three-dimensional geologic model from the northwest. Transects and wells are identified in Figure 2-2.	2-7
Figure 2-6. View of three-dimensional geologic model from the southwest. Transects and wells are identified in Figure 2-2.	2-8
Figure 2-7. Plan view of the sub-CAU and site-scale domains relative to Area 20 in Western Pahute Mesa.	2-11
Figure 2-8. Hydrostratigraphy of Western Pahute Mesa showing downdrop between the Purse Fault and the West Greeley Fault.	2-12
Figure 3-1. Sub-CAU flow model domain. Dashed yellow lines indicate boundaries where heads are fixed in the flow model.	3-1
Figure 3-2. View of fixed boundary heads, in meters, on the northeast corner of the sub-CAU model domain.	3-3
Figure 3-3. HSUs as viewed from the northeast. The Boxcar and West Boxcar Faults are shown in dark blue. Colors indicate different HSUs.	3-4
Figure 3-4. Interpolation of measured heads (m) between wells in the sub-CAU domain. Data for this figure are derived from Table 3-1 and only those wells labeled on the figure are used (because they have head data in the upper HSUs close to the water table). When multiple intervals exist, data from the highest elevation are used. This map is only semi-quantitative because the data contoured are measured at various elevations in the different wells. However, this simple contouring demonstrates an apparent gradient at the West Boxcar Fault.	3-8

Figure 3-5. Head with depth in UE-20f, as reported by Blankennagel and Wier (1973).	3-12
Figure 3-6. Water levels at UE-20f after the BENHAM test (after Fenelon, 2000).	3-15
Figure 3-7. Plan view of the sub-CAU domain. Black circles represent wells with hydrologic data and red circles indicate wells that were used for underground nuclear testing. Red circles are sized relative to the unclassified announced yield or maximum of the unclassified announced range in yields of the tests. For example, the BENHAM test conducted in well U-20c had the largest announced yield. Indicated in red is the year that the test was conducted.	3-16
Figure 4-1. Plan view of the sub-CAU model domain showing the contours of the best-fit calibration at an elevation of 1185 m. The apparent water mounding over the faults is an artifact of low fault-zone permeabilities and uniform recharge at all locations. If the vadose zone were modeled, then the recharge in the fault zones would be diverted. This error could be corrected in future models by neglecting recharge in fault zones and, possibly, increasing it appropriately in neighboring zones.	4-6
Figure 4-2. Plan view of the sub-CAU model domain showing the contours of the best-fit calibration at an elevation of 820 m.	4-7
Figure 4-3. Vertical slice along easting 545000. Note the high pressure in the deep units preserved by low permeability units overlying the BRAQ HSU. This model also captures the shallow downward vertical gradients.	4-8
Figure 4-4. Head observations at wells ER-20-5 #1, ER-20-5 #3, BENHAM (U-20c), and ER-20-1. Note the horizontal gradient of a little over a meter between BENHAM and ER-20-5 #3 and vertical gradient of almost 3 m through the LPCU. Data at ER-20-5 wells indicate almost no vertical gradient through the upper CHZCM.	4-10
Figure 4-5. Weighted residuals plotted by observation group.	4-17
Figure 4-6. Plot of group 1 weighted residuals.	4-18
Figure 4-7. Contours in the sub-CAU model domain drawn at an elevation of 1185 m. The high gradient between the Boxcar and the West Boxcar Fault on the northern boundary has been eliminated. The West Boxcar Fault continues to be a barrier to flow. Heads on the northern boundary are based on four observations in UE-20f. Overall, the head has been reduced 5 m west of the Boxcar Faults, and the shape of the flow field west of the West Boxcar Fault has been changed.	4-22
Figure 4-8. Contours in the sub-CAU model domain drawn at an elevation of 820 m. The high gradient between the Boxcar and the West Boxcar Fault on the northern boundary has been eliminated. The West Boxcar Fault still is a barrier to flow. Heads on northern boundary based on four observations in UE-20f. Overall the head has been reduced 5 m west of the Boxcar Faults, and the shape of the flow field West of the West Boxcar Fault has been changed.	4-23

Figure 4-9. Plan view of the sub-CAU model domain. Contours are drawn at an elevation of 820 m. The northern boundary condition is based on only two observations at UE-20f and the flow gradient is set at the West Boxcar Fault. Overall, the head has been reduced 5 m west of the Boxcar Faults and the shape of the flow field has been altered.	4-24
Figure 4-10. Contours in the sub-CAU model domain at 1185 m for the case with no internal faults. The northern boundary condition is based on four observations at UE-20f and a gradient at the West Boxcar Fault. Note the remarkable change in the flow field, with heads west of the Boxcar Faults rising by 30 m in some locations.	4-30
Figure 4-11. Contours in the sub-CAU model domain at 820 m for the case with no internal faults. The northern boundary condition is based on four observations at UE-20f and a gradient at the West Boxcar Fault. Note the remarkable change in the flow field, with heads west of the Boxcar Faults rising by 30 m in some locations.	4-31
Figure 4-12. Plan view of the sub-CAU domain showing the contours at 820 m for double the recharge of the best-fit model.	4-32
Figure 4-13. Plan view of the sub-CAU domain showing the contours at 1185 m for double the recharge of the best-fit model.	4-33
Figure 5-1. Site-scale model domain within the sub-CAU domain in Area 20.	5-2
Figure 5-2. HSUs in the deterministic site-scale model. Note, the lava formation mapped by Prothro and Warren (2001) sandwiched within the CHZCM above BENHAM and sampled by ER-20-5 #3 is not part of the CAU-scale HSU models of Drellack and Prothro (1997) or Bechtel (2002).	5-3
Figure 5-3. The deterministic HSU model shown with (a) north-south, east-west transects and (b) with transects through the boreholes.	5-5
Figure 5-4. Four geostatistical realizations of lithologic attributes (classes).	5-6
Figure 5-5. Rendition of 2 geostatistical class maps showing only welded tuff in blue. Note that the welded tuff is not a continuous class through the domain where the TSA is mapped, as in Figure 5-3.	5-7
Figure 5-6. Observed natural log of hydraulic conductivity (m/d) plotted against the normal score for each of the five classes.	5-8
Figure 5-7. Simulated permeabilities in the same fields for which classes are shown in Figure 5-4.	5-9
Figure 5-8. The boundary conditions for the site-scale domain are extracted from the sub-CAU domain. The slices are drawn through the sub-CAU domain and the site-scale domain is shown as a solid cube. Heads are contoured in meters.	5-12
Figure 5-9. Site-scale domain head boundary conditions calculated from the sub-CAU scale model. View from southeast with head contours in meters.	5-13
Figure 5-10. Geostatistical fields colored by their permeability's order of magnitude. The slice is drawn at the BENHAM easting and the view is looking from the west.	5-14

Figure 5-11. Time-of-flight particle paths with BENHAM releases in the TSA and LAVA without transport chemistry.	5-17
Figure 5-12. Time-of-flight particle paths with TYBO releases in the TSA without transport chemistry or dispersion.	5-18
Figure 5-13. Time-of-flight particle paths with TYBO releases in the TSA with dispersion (10/3/0.01) but without transport chemistry.	5-18
Figure 5-14. Head contour variations within geostatistical fields 3, 10, 15, and 30.	5-20
Figure 5-15. Time-of-flight paths for unretarded particles released from BENHAM in the TSA in flow fields 3, 10, 15, and 30.	5-21
Figure 5-16. Time-of-flight paths for unretarded particles released from BENHAM in the LAVA in flow fields 3, 10, 15, and 30.	5-22
Figure 5-17. Flight paths of particles colored according to travel in different geologic material zones (zone numbers, as identified by different colors, defined in Table 5-1). Particles are released from BENHAM at an elevation consistent with the TSA. Note how little welded tuff (Zone 3) these particles travel through.	5-23
Figure 5-18. Flight Paths of Particles colored according to travel in different geologic material zones (zone numbers, as identified by different colors, defined in Table 5-1). Particles released from BENHAM at an elevation consistent with the LAVA.	5-24
Figure 5-19. Time-of-flight paths for unretarded particles released from TYBO in flow fields 3, 10, 15, and 30.	5-25
Figure 5-20. Flight paths of particles colored according to travel in different geologic material zones (zone numbers, as identified by different colors, defined in Table 5-1). Particles are released from TYBO at the elevation of the TSA.	5-26
Figure 5-21. Response curves for reduced and increased pressure following the TYBO test. Simulations are conducted with site-scale flow model and material storativity of $2.4e-5$ m ⁻¹ . Time-history data are recorded at the center of each anomaly.	5-28
Figure 6-1. The natural, pre-detonation geology of the modeled BENHAM system has the following stratigraphy: Topopah Spring Aquifer (TSA), Calico Hills Zeolitic Composite Unit (CHZM), Lava Aquifer (LAVA), and Inlet Aquifer (IA). The working point (detonation point) for BENHAM was at 512 m above sea level, approximately 1.4 km below the surface. Transect A-A' is shown in Figure 1-1.	6-4
Figure 6-2. Cavity and chimney formation after underground detonation: (a) the rock is vaporized immediately after detonation; (b) after radial fracturing away from the cavity the vaporized rock condenses and begins to form the melt glass (MG); (c) the top of the cavity becomes unstable and begins to collapse into the cavity void and MG; (d) chimney collapse is completed into the cavity void (after Pawloski, 1999, Figure 2).	6-5

Figure 6-3. The post-detonation geology of the modeled system. A 100-m-radius spherical cavity (outlined by the dashed red line) and cylindrical chimney are added to the natural stratigraphy. The cavity consists of the melt glass (MG) pooled at the cavity bottom with the remaining cavity volume termed the exchange volume (EV). Transect A-A' is shown in Figure 1-1.	6-6
Figure 6-4. System and local H for Rayleigh number calculations in Equation 6-5.	6-10
Figure 6-5. Vertical temperature profiles at the center of the cavity/chimney system for the BASE CASE simulation.	6-20
Figure 6-6. Simulated MG temperature history from the BASE CASE simulation and the Arrhenius factor for an activation energy of 83.74 kJ/mol. Plot A is the temperature history in the middle of the MG, plot B is the Pu release history from Equation 6-10, and plot C is the particle-release history based on Equation 6-10 and 385 000 particles/mole Pu.	6-21
Figure 6-7. Two-dimensional FLOTRAN simulations of MG/Pu dissolution (see Appendix B). Note that the maximum glass dissolution of $3.85\text{e-}13$ moles glass/cc/sec is the equivalent of $8.5\text{e-}22$ moles Pu/cc/sec (compared with $3.9\text{e-}22$ moles Pu/cc/sec estimated for the BASE CASE at 20 years).	6-22
Figure 6-8. Simulated MG temperature history from the higher permeability MG simulation (CASE 5B) and the Arrhenius factor for an activation energy of 83.74 kJ/mol. Plot A is the temperature history in the middle of the MG, plot B is the Pu release history from Equation 6-10, and plot C is the particle-release history based on Equation 6-10 and 385 000 particles/mole Pu.	6-23
Figure 6-9. Comparison of simulated particle release to the TSA and LAVA with fully coupled THC results from Appendix B. Using the properties described in Appendix B, a two-dimensional particle-tracking model was constructed to compare with the two-dimensional THC model. Solid lines represent particle model, dashed lines represent THC model.	6-27
Figure 6-10. BASE CASE temperature contours after 20 years of simulation.	6-28
Figure 6-11. Three representative 1000-year particle pathways in the x-z domain for the BASE CASE simulation. Entrance times to the TSA and LAVA aquifers are noted next to each particle.	6-29
Figure 6-12. Lower chimney permeability case (CASE 2A) temperature contours after 20 years of simulation.	6-31
Figure 6-13. Lower chimney permeability (CASE 2A) 1000-year particle pathways projected on an x-z plane. Entrance times to the TSA and LAVA aquifers are noted next to each particle.	6-32
Figure 6-14. Medium chimney permeability case (CASE 2B) temperature contours after 20 years of simulation.	6-33

Figure 6-15. Medium chimney permeability (CASE 2B) 1000-year particle pathways projected on an x-z plane. Entrance times to the TSA and LAVA aquifers are noted next to each particle.	6-34
Figure 6-16. High chimney permeability (CASE 2C) temperature contours after 20 years of simulation.	6-35
Figure 6-17. High chimney permeability (CASE 2C) 1000-year particle pathways projected on an x-z plane. Entrance times to the TSA and LAVA aquifers are noted next to each particle.	6-36
Figure 6-18. Temperature contours after 20 years of simulation under the influence of a geothermal gradient only (CASE 3A).	6-38
Figure 6-19. 1000-year particle pathways (projected on an x-z plane) under the influence of a geothermal gradient only (CASE 3A). Particles do not enter TSA or LAVA aquifers in 1000 years of simulation.	6-39
Figure 6-20. Temperature contours after 20 years of simulation under the influence of a geothermal gradient only and in the presence of high chimney permeability (CASE 3B).	6-40
Figure 6-21. 1000-year particle pathways (projected on an x-z plane) under the influence of a geothermal gradient only and in the presence of high chimney permeability (CASE 3B). Particles do not enter TSA or LAVA aquifers in 1000 years of simulation.	6-41
Figure 6-22. Temperature contours after 20 years of simulation for a lower MG temperature (CASE 4).	6-43
Figure 6-23. 1000-year particle pathways projected on an x-z plane for a lower MG temperature (CASE 4). Entrance times to the TSA and LAVA aquifers are noted next to each particle.	6-44
Figure 6-24. Larger MG volume case (CASE 5A) temperature contours after 20 years.	6-46
Figure 6-25. MG volume increased by 2x (CASE 5A). 1000-year particle pathways projected on an x-z plane. Entrance times to the TSA and LAVA aquifers are noted next to each particle.	6-47
Figure 6-26. High MG permeability case (CASE 5B) temperature contours after 20 years. ..	6-48
Figure 6-27. High MG permeability case (CASE 5B) with 1000-year particle pathways projected on an x-z plane. Entrance times to the TSA and LAVA aquifers are noted next to each particle.	6-49
Figure 6-28. Relative Raleigh numbers vs. the breakthrough time 300 m downstream from the chimney in the TSA and LAVA for 0.01% of total mass present. Closed symbols represent non-sorbing species with a Kd of 0.0, open circles represent sorbing species with a Kd of 0.1. All flow scenarios in Cases 1 through 4 are plotted.	6-53

Figure 6-29. Sorptive Rayleigh numbers vs. the breakthrough time 300 m downstream from the chimney in the TSA and LAVA for 0.01% of total mass present. BASE CASE and CASE 2C scenarios are identified with multiple K_d s (cc/g) identified in this figure as k_d	6-54
Figure 6-30. Unretarded (dotted lines) and retarded ($K_d = 0.1$ cc/g, solid lines) particle pathways for the BASE CASE. The travel times of retarded particles to the upper TSA aquifer are faster than expected (for $K_d=0.1$ cc/g, $R = 2.04$). This is due to a shorter path followed by the retarded particle (fewer and weaker convection cells at later times). Conversely, the travel time to the LAVA is longer than expected. This is due to a decrease in buoyancy at later times resulting in slower vertical transport within the cavity.	6-55
Figure 6-31. ^{99}Tc breakthrough mass fluxes to the TSA and LAVA from the MG and the EV.	6-58
Figure 6-32. ^{239}Pu breakthrough mass fluxes to the TSA and LAVA from the MG and the EV.	6-59
Figure 6-33. SOURCE 1 (BASE CASE $R\hat{a}_{\text{sys}}$) mass flux of conservative RNs (Class I and VI) entering the TSA and the LAVA from the cavity/chimney.	6-62
Figure 6-34. SOURCE 1A (BASE CASE $R\hat{a}_{\text{sys}}$) mass flux of Class II through VI RNs modeled without chimney sorption, entering the TSA and the LAVA from the cavity/chimney.	6-62
Figure 6-35. SOURCE 1B (BASE CASE $R\hat{a}_{\text{sys}}$) mass flux of Class II through VI RNs modeled with chimney sorption, entering the TSA and the LAVA from the cavity/chimney.	6-62
Figure 6-36. SOURCE 2 (med. $R\hat{a}_{\text{sys}}$) mass flux of conservative RNs (Class I and VI) entering the TSA and the LAVA from the cavity/chimney.	6-63
Figure 6-37. SOURCE 2A (med. $R\hat{a}_{\text{sys}}$) mass flux of Class II through VI RNs modeled without chimney sorption, entering the TSA and the LAVA from the cavity/chimney.	6-63
Figure 6-38. SOURCE 2B (med. $R\hat{a}_{\text{sys}}$) mass flux of remaining RNs modeled with chimney sorption, entering the TSA and the LAVA from the cavity/chimney.	6-63
Figure 6-39. SOURCE 3 (low $R\hat{a}_{\text{sys}}$) mass flux of conservative RNs entering the TSA and the LAVA from the cavity/chimney.	6-64
Figure 6-40. SOURCE 3A (low $R\hat{a}_{\text{sys}}$) mass flux of Class II through VI RNs modeled without chimney sorption, entering the TSA and the LAVA from the cavity/chimney.	6-64
Figure 6-41. SOURCE 3B (low $R\hat{a}_{\text{sys}}$) mass flux of remaining RNs modeled with chimney sorption, entering the TSA and the LAVA from the cavity/chimney.	6-64
Figure 6-42. SOURCE 1 (BASE CASE $R\hat{a}_{\text{sys}}$) cumulative mass of conservative RNs (Class I and VI) entering the TSA and the LAVA from the cavity/chimney.	6-66

Figure 6-43. SOURCE 1A (BASE CASE $R\hat{a}_{sys}$) cumulative mass of Class II through VI RNs modeled without chimney sorption, entering the TSA and the LAVA.	6-66
Figure 6-44. SOURCE 1B (BASE CASE $R\hat{a}_{sys}$) cumulative mass of Class II through VI RNs modeled with chimney sorption, entering the TSA and the LAVA.	6-66
Figure 6-45. SOURCE 2 (med. $R\hat{a}_{sys}$) cumulative mass of conservative RNs (Class I and VI) entering the TSA and the LAVA from the cavity/chimney.	6-67
Figure 6-46. SOURCE 2A (med. $R\hat{a}_{sys}$) cumulative mass of Class II through VI RNs modeled without chimney sorption, entering the TSA and the LAVA from the cavity/chimney.	6-67
Figure 6-47. SOURCE 2B (Medium $R\hat{a}_{sys}$) cumulative mass of Class II through VI RNs modeled with chimney sorption, entering the TSA and the LAVA from the cavity/chimney.	6-67
Figure 6-48. SOURCE 3 (low $R\hat{a}_{sys}$) cumulative mass of conservative RNs (Class I and VI) entering the TSA and the LAVA from the cavity/chimney.	6-68
Figure 6-49. SOURCE 3A (low $R\hat{a}_{sys}$) cumulative mass of Class II through VI RNs modeled without chimney sorption, entering the TSA and the LAVA from the cavity/chimney.	6-68
Figure 6-50. SOURCE 3B (low $R\hat{a}_{sys}$) cumulative mass of Class II through VI RNs modeled with chimney sorption, entering the TSA and the LAVA from the cavity/chimney. ...	6-68
Figure 7-1. The convolution operation of the source-mass fluxes (top plot), in conjunction with the unit-source breakthrough curves (middle plot), are used to obtain downstream mass fluxes adjusted for decay (bottom plot). This illustration shows convolution for rapidly decaying, unretarded species (A) and a slow decaying, retarded species (B).	7-3
Figure 7-2. Downstream breakthrough curves for different BENHAM particle releases (625, 2500, and 10 000) for a non-retarded species (A) and a retarded species (B).	7-4
Figure 7-3. Comparison of reactive transport model with particle-tracking model. Curves show uranium breakthrough at NTS boundary using the two different approaches. Slightly more dispersion is seen in the finite-element reactive transport model as expected, but the results are extremely similar.	7-11
Figure 7-4. Unit breakthrough curves at the ER-20-5 wells (well #1 is in the TSA, #3 is in the LAVA) for the deterministic flow field and unit releases at BENHAM in the two aquifers. Note Class IV arrives at the wells after 50 years.	7-12
Figure 7-5. Simulated and observed Pu-colloid concentrations at ER-20-5 wells. The simulations use the BASE-CASE BENHAM source described in Chapter 6. Retardation factors for colloids in fractures are listed in parentheses. Note that no Pu arrives at the wells as an aqueous species in these simulations.	7-14

Figure 7-6. Structure of plumes originating from TYBO in the deterministic flow model. The upper plot shows plume shape for case of no dispersion. The lower plot shows same simulation, but with a lateral dispersivity of 3 m. Capture zone radii of 50 m and 150 m for ER-20-5 #1 are also shown.	7-15
Figure 7-7. Simulated and observed Pu-colloid concentrations at ER-20-5 wells. The simulations use the BASE-CASE BENHAM and TYBO sources described in Chapter 6. Transport from TYBO is subject to dispersivity and capture-zone size constraints discussed in this report. Retardation factors for colloids in fractures are listed in parentheses.	7-16
Figure 7-8. Simulated and observed tritium concentrations at ER-20-5 wells for BASE-CASE source and transport parameters.	7-17
Figure 7-9. Simulated and observed chlorine-36 concentrations at ER-20-5 wells for BASE-CASE source and transport parameters.	7-18
Figure 7-10. Simulated and observed carbon-14 concentrations at ER-20-5 wells for BASE-CASE source and transport parameters.	7-18
Figure 7-11. Simulated and observed technetium-99 concentrations at ER-20-5 wells for BASE-CASE source and transport parameters.	7-19
Figure 7-12. Simulated and observed iodine-129 concentrations at ER-20-5 wells for BASE-CASE source and transport parameters. Note, data for ER-20-5 #1 from Table 1-1 is below the detection limit for that measurement. It is plotted here to show date of non-zero detect.	7-20
Figure 7-13. Simulated and observed aqueous cesium-137 concentrations at ER-20-5 wells for BASE-CASE source and transport parameters. No arrivals from BENHAM simulated.	7-22
Figure 7-14. Simulated and observed colloidal cesium-137 concentrations at ER-20-5 wells for BASE-CASE source and transport parameters (source reduction factor 1e-5).	7-22
Figure 7-15. Simulated and observed colloidal europium concentrations at ER-20-5 wells for BASE-CASE source and transport parameters (source reduction factor 1e-4).	7-23
Figure 7-16. Simulated and observed colloidal americium-241 concentrations at ER-20-5 wells for BASE-CASE source and transport parameters (source reduction factor 1e-5).	7-23
Figure 7-17. Chlorine-36 mass breakthrough at the NTS boundary for the BASE-CASE TSA source release.	7-25
Figure 7-18. Chlorine-36 mass breakthrough at the NTS boundary for the BASE-CASE LAVA source release.	7-26
Figure 7-19. Total chlorine-36 mass breakthrough at the NTS boundary for the BASE-CASE TSA and LAVA source releases.	7-26
Figure 7-20. Total tritium mass breakthrough at the NTS boundary for the BASE-CASE TSA and LAVA source releases.	7-27

Figure 7-21. Total carbon-14 mass breakthrough at the NTS boundary for the BASE-CASE TSA and LAVA source releases.	7-27
Figure 7-22. Total chlorine-36 mass breakthrough at the NTS boundary for the medium Rayleigh number TSA and LAVA source releases (Table 6-9: Case 2B).	7-28
Figure 7-23. Total chlorine-36 mass breakthrough at the NTS boundary for the low Rayleigh number TSA and LAVA source releases (Table 6-9: Case 3A).	7-28
Figure 7-24. Uranium mass breakthrough at the NTS boundary for the TSA source release involving no chimney sorption and high R_{asys} (Case 1, no sorption; Table 6-9).	7-30
Figure 7-25. Uranium mass breakthrough at the NTS boundary for the LAVA source release involving no chimney sorption and high R_{asys} (Source 1a, no sorption; Table 6-9).	7-31
Figure 7-26. Total uranium mass breakthrough at the NTS boundary for the combined TSA and LAVA source release involving no chimney sorption and high R_{asys} (Source 1a, no sorption; Table 6-9).	7-31
Figure 7-27. Total neptunium mass breakthrough at the NTS boundary for the combined TSA and LAVA source release involving no chimney sorption and high R_{asys} (Source 1a, no sorption; Table 6-9).	7-32
Figure 7-28. Total uranium mass breakthrough at the NTS boundary for the combined TSA and LAVA source release involving no chimney sorption and medium R_{asys} (Source 2a, no sorption; Table 6-9).	7-32
Figure 7-29. Total uranium mass breakthrough at the NTS boundary for the combined TSA and LAVA source release involving no chimney sorption and low R_{asys} (Source 3a, no sorption; Table 6-9).	7-33
Figure 7-30. Total uranium mass breakthrough at the NTS boundary for the combined TSA and LAVA source release involving chimney sorption and high R_{asys} (Source 1b, with sorption; Table 6-9).	7-33
Figure 7-31. Total uranium mass breakthrough at the NTS boundary for the combined TSA and LAVA source release involving chimney sorption and medium R_{asys} (Source 2b, with sorption; Table 6-9).	7-34
Figure 7-32. Total uranium mass breakthrough at the NTS boundary for the combined TSA and LAVA source release involving chimney sorption and low R_{asys} (Source 3b, with sorption; Table 6-9).	7-34
Figure 7-33. Total Pu-colloid mass breakthrough at the NTS boundary for the combined TSA and LAVA source release involving no chimney sorption and high R_{asys} (Source 1A, no sorption; Table 6-9). Note that the mobile mass of Pu-colloid is assumed to be 1/10 000 of aqueous Pu released from melt glass.	7-35
Figure 7-34. Total Pu-colloid mass breakthrough at the NTS boundary for the combined TSA and LAVA source release involving no chimney sorption and medium R_{asys} (Source 2A, no sorption; Table 6-9). Note that the mobile mass of Pu-colloid is assumed to be 1/10 000 of aqueous Pu released from melt glass.	7-36

- Figure 7-35. Total Pu-colloid mass breakthrough at the NTS boundary for the combined TSA and LAVA source release involving no chimney sorption and low Rasys (Source 3A, no sorption; Table 6-9). Note that the mobile mass of Pu-colloid is assumed to be 1/10 000 of aqueous Pu released from melt glass. 7-36
- Figure 7-36. Unit breakthrough curves at ER-20-5 #1 of unretarded colloid species originating at BENHAM chimney in TSA. All 30 realizations are shown. Nontrivial breakthrough within 30 years occurs in about half of the realizations. For diffusing solutes, even fewer realizations yield arrivals within 30 years. 7-38
- Figure 7-37. Time of flight for particles released from the TSA source location at BENHAM. Base-case transport parameters are assigned to each of the different radionuclide classes. 7-41
- Figure 7-38. Time of flight for particles released from the LAVA source location at BENHAM. Base-case transport parameters are assigned to each of the different radionuclide classes. 7-42
- Figure 7-39. Breakthrough curves at the ER-20-5 wells for source releases in the TSA and LAVA at BENHAM using flow-field realization #3. LAVA breakthrough corresponds with ER-20-5 #3 and TSA breakthrough corresponds with ER-20-5 #1. Note that Class II, III and V never break through. Also note that some Class VI particles do arrive at well ER-20-5 #1, unlike the results using the coupled reactive transport model in Appendix F. 7-43
- Figure 7-40. Breakthrough curves at the NTS boundary for source releases in the TSA and LAVA at BENHAM using flow-field realization #3. Note that Class II, III, and V never break through. 7-44
- Figure 7-41. CLASS I mass flux in flow-field realization #3 with BASE-CASE source conditions and base-case transport properties. The top plot illustrates the combined TSA and LAVA source curves for Class I radionuclides ^3H and ^{36}Cl . The bottom plot illustrates the downstream mass flux curves at the ER-20-5 wells and at the NTS boundary. 7-46
- Figure 7-42. CLASS IV mass flux in flow-field realization #3 with BASE-CASE source conditions and base-case transport properties. The top plot illustrates the combined TSA and LAVA source curves for Class IV radionuclide U (reported as total U, or the sum of ^{238}U and ^{234}U). The bottom plot illustrates the downstream mass flux curves at the ER-20-5 wells and at the NTS boundary. 7-47
- Figure 7-43. CLASS V and VI mass flux in flow-field realization #3 with BASE-CASE source conditions and base-case transport properties. The top plot illustrates the combined TSA and LAVA source curves for Class V radionuclide Pu (reported as the sum of ^{239}Pu and ^{240}Pu) and Class VI Pu-colloid (reported as 1/10 000 of total Pu source). The bottom plot illustrates the downstream mass flux curves at the ER-20-5 wells and at the NTS boundary. Note that only Pu-colloid breaks through to the wells and NTS boundary. 7-48

Figure 7-44. Cumulative mass at the ER-20-5 wells for flow-field realization, BASE-CASE source (Source 1a) function, and base-case transport parameters. For Pu-colloid results, it is assumed that 1/10 000 of total Pu is transported with colloidal material.	7-50
Figure 7-45. Cumulative mass at the NTS boundary for flow-field realization #3, BASE-CASE source function (Source 1a), and base-case transport parameters. For Pu-colloid results, it is assumed that 1/10 000 of total Pu is transported with colloidal material.	7-51
Figure 7-46. Estimated Pu-colloid concentrations in groundwater at the ER-20-5 observation wells and at the NTS boundary for flow-field realization #3, Source 1a, and base-case transport parameters. Inset shows log scale of concentration to highlight low, but non-zero, simulated concentration at ER-20-5 #1 for this realization.	7-51
Figure 7-47. “Breakthrough bars” for 7 sensitivity cases for BASE-CASE source thermal conditions (Source 1A, Table 6-9). Each bar represents the average total amount of tritium crossing the NTS boundary after 30 years, 100 years, and 1000 years for all 30 flow-field realizations. Error bars represent one standard deviation for the 30 different flow fields.	7-53
Figure 7-48. “Breakthrough bars” for 7 sensitivity cases (using Source 1A, Table 6-9). Each bar represents the average total amount of ^{36}Cl crossing the NTS boundary after 30 years, 100 years, and 1000 years for all 30 flow-field realizations. Error bars represent one standard deviation for the 30 different flow fields.	7-54
Figure 7-49. “Breakthrough bars” for all 13 sensitivity cases (using Source 1A, Table 6-9). Each bar represents the average total amount of U crossing the NTS boundary after 30 years, 100 years, and 1000 years for all 30 flow-field realizations. Error bars represent one standard deviation for the 30 different flow fields.	7-55
Figure 7-50. “Breakthrough bars” for all 13 sensitivity cases (using Source 1A, Table 6-9). Each bar represents the average total amount of Np crossing the NTS boundary after 30 years, 100 years, and 1000 years for all 30 flow-field realizations. Error bars represent one standard deviation for the 30 different flow fields.	7-56
Figure 7-51. “Breakthrough bars” for all 13 sensitivity cases (using Source 1A, Table 6-9). Each bar represents the average total amount of Pu-Colloid crossing the NTS boundary after 30 years, 100 years, and 1000 years for all 30 flow-field realizations. Error bars represent one standard deviation for the 30 different flow fields. Note that the logarithmic scale makes standard deviation bars seem less significant. Also, $K_d(\text{fr})$ is the equilibrium parameter with which retardation due to filtration is approximated.	7-57
Figure 7-52. Impact ratios for tritium transport to the NTS boundary for simulations of 30 years.	7-59
Figure 7-53. Impact ratios for tritium transport to the NTS boundary for simulations of 100 years.	7-60

Figure 7-54. Impact ratios for chlorine-36 transport to the NTS boundary for simulations of 100 years.	7-60
Figure 7-55. Impact ratios for uranium transport to the NTS boundary for simulations of 1000 years.	7-61
Figure 7-56. Impact ratios for neptunium transport to the NTS boundary for simulations of 1000 years.	7-61
Figure 7-57. Impact ratios for Pu-colloid transport to the NTS boundary for simulations of 100 years.	7-62
Figure 7-58. Impact ratios for Pu-colloid transport to the NTS boundary for simulations of 1000 years.	7-62
Figure 7-59. The mass flux and cumulative mass curves of tritium for the deterministic simulations of low fracture porosity and high fracture porosity in the LAVA at the NTS boundary. The late-arriving high-porosity ^3H has less mass because more radioactive decay has occurred.	7-66
Figure 7-60. The mass flux and cumulative mass curves of ^{36}Cl for the deterministic simulations of low fracture porosity and high fracture porosity in the LAVA at the NTS boundary. The late-arriving high-porosity ^{36}Cl has comparable mass because little radioactive decay has occurred.	7-66

This Page Intentionally Left Blank

EXECUTIVE SUMMARY

Introduction

Recent field studies have led to the discovery of trace quantities of plutonium in two groundwater observation wells originating from the BENHAM underground nuclear test (Kersting et al., 1999). These wells are located 1.3 km from BENHAM and approximately 300 m from the TYBO underground nuclear test on Pahute Mesa at the Nevada Test Site. In addition to plutonium, several other conservative (e.g. tritium) and reactive (e.g. europium) radionuclides were found in both observation wells. The radionuclides were discovered in observation well ER-20-5 #3, which samples a lava formation at about the same elevation as the working point of BENHAM, and in observation well ER-20-5 #1, which samples a welded tuff aquifer more than 500 m above BENHAM's working point. The welded tuff aquifer sampled by well ER-20-5 #1 is also located just above TYBO's working point.

Because these field studies have indicated the mobility of radionuclides in Pahute Mesa groundwater systems, they have prompted additional investigations to ascertain the mechanisms, processes, and conditions affecting subsurface radionuclide transport. This study integrates field, laboratory, and other modeling data into a modeling process that captures the relevant mechanisms affecting plutonium and other radionuclide transport in Pahute Mesa groundwater. Specifically, this study has the following goals:

1. Present a modeling approach for studying radionuclide migration in Western Pahute Mesa groundwater.
2. Integrate field, laboratory and other modeling data into a framework for assessing processes and mechanisms associated with the observations of plutonium and other radionuclides found in the ER-20-5 observation wells southwest of TYBO.
3. Provide a methodology for evaluating parameter sensitivity in model predictions and the worth of new or existing data.

This executive summary describes briefly the integrated modeling approach used to simulate groundwater flow, radionuclide source release, and radionuclide transport near the BENHAM and TYBO underground nuclear tests on Pahute Mesa. A sub-CAU (Corrective Action Unit) model is employed to calibrate hydrologic parameters for the source and site-scale analyses of radionuclide transport at BENHAM. Source-term models are used to investigate vertical convection and dissolution of radionuclides from the melted rock referred to as melt glass (MG) in the chimney created after a nuclear explosion. The source-term models are then used as input to the site-scale models, which are used to evaluate the downstream migration of radionuclides to the observations wells and the Nevada Test Site (NTS) boundary. Although multiple modeling components contribute to the methodology, they are coupled and yield consistent results. This modeling approach achieves results consistent with laboratory and field observations. Discrepancies between model results and field observations are explained and recommendations for improvement are provided.

Along with a large number of data sets, different models are integrated in this study to provide a framework for evaluating process-level complexities. Process models are abstracted into application models, which can be broken down into three component groups:

- Sub-CAU flow model,
- Source term models, and
- TYBO/BENHAM site-scale transport models.

Combined, these components are used to consider (1) complex flow in layered, faulted, and fractured volcanic tuff; (2) thermal issues associated with radionuclide release from MG and cavity-chimney systems; and (3) radionuclide transport in fractured media, including fracture properties, diffusion, groundwater chemistry, colloids, fracture mineral exposure, and heterogeneity. In the latter two components, process models capture mechanistic complexities associated with the studied system. Based on the processes that most affect the system's response, a reduction in complexity is then invoked to enable efficient screening, sensitivity testing, and uncertainty analysis.

Because parameters used to model these three components are inherently uncertain, we conduct and analyze sensitivity simulations for each component. By using expected values (calibrated in the sub-CAU flow model component, culled from data sets and process models for the transport models), this modeling system predicts field observations of hydraulic head and radionuclide concentrations well. Thus, even amidst parameter uncertainty, the methods and results presented in this report provide a reliable framework that effectively addresses flow and transport processes. The sensitivity studies provide insight and guidance for CAU-scale modeling studies that may require confidence intervals on contaminant boundaries.

Sub-CAU Model Calibration

There are not enough wells in the immediate vicinity of TYBO and BENHAM to characterize adequately the hydrologic system for predictions of radionuclide transport away from BENHAM. Specifically, flow complications associated with large-scale vertical and horizontal gradients and the neighboring Boxcar Faults cannot be captured adequately without taking into consideration a region that extends well beyond the potential solute pathways away from these tests. Therefore, a sub-CAU domain was selected on which to calibrate material properties with the goals of preserving observed gradients and providing defensible boundary conditions for high-resolution, site-scale modeling.

The sub-CAU flow model calibration was conducted with the groundwater flow model FEHM (Finite-Element Heat and Mass transport; Zyvoloski et al., 1997) and the automatic parameter estimation software package PEST (Doherty, 2000). FEHM was modified to integrate into PEST thereby providing a straightforward calibration process. Calibrating the sub-CAU model begins with permeability estimates for each hydrostratigraphic unit (HSU), head interpolations along the boundaries, and flux estimates from other studies. Simulations with FEHM and PEST provide optimized HSU permeabilities that minimize the difference between observed and modeled heads in wells within the domain. Additionally, an assessment of the flow model's sensitivity to each calibrated permeability is provided with this method. Although the model matches observed heads very well, the sensitivity analysis indicates that the results are not unique due to data sparseness in the domain.

The calibrated model captures upward gradients from a deep aquifer with low permeability confining units. A small downward gradient in the thin upper volcanic units, also preserved by low permeability confining units, is affected by local recharge. A large gradient across a north-trending fault is preserved with reduced fault-zone permeabilities. However, no such gradient exists across the east-trending fault in the domain, and as a result calibration parameters for such fault-zones are

different. This specific difference between the north and east trending fault properties may be a meaningful indicator for larger-scale domains.

Source-Term Models

A fully coupled, two-dimensional thermal-hydrologic-chemical (THC) transport model and a three-dimensional source-term abstraction model complement each other in predicting source releases to the site-scale domain. Both models simulate transient convective cells that form and then decay due to initial heating and subsequent cooling within the cavity-chimney system. The THC model solves simultaneously the transient, heat-affected flow field, as well as the complex chemistry associated with melt-glass (MG) dissolution. In addition to predicting the evolution and decay of thermal convection cells, the THC model predicts a significant relationship between the effective MG-dissolution rate and the MG temperature. At higher temperatures, the dissolution rate is limited by the rate at which dissolved species diffuse away from the MG.

The relationships for MG-dissolution rate in the non-isothermal source region are applied to a particle release function for a three-dimensional source-term model. This model simulates the transient thermal flow and cooling processes in the cavity-chimney system and couples particle release in the MG to the temperature-dependent dissolution processes identified in the THC model. As the temperature of the MG cools during simulation, the particle-release rate from the MG decreases consistently with the more rigorously calculated MG-dissolution rate of the THC model. The efficiency of the three-dimensional source-term model allows for consideration of multiple sensitivity cases based on uncertainty in cavity-chimney hydrologic properties as well as uncertainty in initial thermal conditions. For each sensitivity simulation, mass fluxes of 14 radionuclides exiting the source region and entering the site-scale flow domain are computed. A particularly elegant component of the source term model is the development of a characteristic quantifier, the Rayleigh Number, that is used to assess the potential of a cavity-chimney system to support thermal convection cells and vertical transport of sorbing and non-sorbing solutes. Essentially, the Rayleigh Number provides a ratio of the forces that promote convection and vertical transport to those that dampen them. Thus, once thermal conditions and rock properties have been established (or chosen for sensitivity analysis), rough estimates can be provided before conducting any numerical simulation.

Site-Scale Transport Models

The site-scale domain of BENHAM and TYBO is approximately 3 km on a side and discretized at a much higher resolution than the sub-CAU flow model. Model subcomponents contributing to the assessment of radionuclide migration in the site-scale domain include the following:

- Development of a reactive, colloid-facilitated transport model for fractured rock,
- Verification of the model against laboratory experiments,
- Development of a methodology for considering fracture-matrix interactions in field-scale simulations,
- Extension of the model for other radionuclides,
- Site-scale application in heterogeneous material,
- Abstraction of the method to a highly efficient particle-tracking approach using convolution integration,

- Comparison of simulations with field observations of radionuclide concentrations, and
- Sensitivity analysis of uncertain transport parameters.

Site-scale modeling is performed with a field-scale reactive-process-level model and a field-scale particle-tracking model. Based on finite-volume continuity equations, the process model can simulate the complexities of rate limited reactions and interspecies reactions. The particle-tracking model captures the key processes with an efficient algorithm suitable for extensive sensitivity analysis.

Field-Scale GDPM Reactive Transport Process Model

The reactive transport process model used to match column studies of colloid-facilitated plutonium transport is extended to the field scale to provide insight and justification for simplifications in the field-scale particle-tracking model. The extension involves implementation of the Generalized Dual-Porosity Model (GDPM) which simulates coupled reactive transport with the fracture-matrix interactions along streamtubes in heterogeneous three-dimensional flow fields. Conclusions resulting from the site-scale process model simulations in a single heterogeneous flow field include the following:

- With base-case parameters, migration of plutonium and other radionuclides from BENHAM to observation well ER-20-5 #3 is feasible in less than 30 years only if kinetic reactions with colloids are considered. This result is conditioned by the fact that the lava formation sampled by well ER-20-5 #3 is maintained in the heterogeneous attribute map as a semi-intact lithologic unit between BENHAM and the observation well.
- The welded tuff aquifer sampled by well ER-20-5 #1 (where the highest level of plutonium was observed) is not maintained as a continuous unit between BENHAM and the observation well in all geostatistical simulations of heterogeneous attribute distributions (it is not continuous in the specific realization highlighted in this study). Most transport pathlines between BENHAM and well ER-20-5 #1, in any of the heterogeneous fields, are not exclusively in fractured media. Significant retardation occurs in unfractured material as a result of slow velocities and sorption to matrix minerals. Possible extensions of this work include: (1) conditioning the welded tuff so that it is continuous in the models (as was done for the LAVA) or (2) selecting and discarding realizations based upon their consistency in transport simulations with field observations of radionuclide at ER-20-5 #1.
- The most sensitive parameters are the groundwater's Eh, the colloid site concentration, and the available reactive surface area of fracture minerals.
- Uranium, neptunium, and strontium are the only reactive radionuclides that demonstrate mobility of more than a hundred meters the **absence** of colloids. Breakthrough of strontium at the NTS boundary in less than 1000 years could be simulated only with the most conservative (i.e., most conducive to supporting mobility in groundwater) set of transport parameters drawn from the ranges of uncertainty. However, for most parameter sets some uranium and neptunium are generally simulated to migrate more than a kilometer in less than 1000 years. Migration of these radionuclides is most sensitive to matrix Kd and fracture mineral reactive surface area. Variations in Eh were not considered for uranium and neptunium.
- The nonreactive radionuclides (^3H , ^{14}C , ^{36}Cl , ^{99}Tc , and ^{129}I) experience diffusion and radioactive decay in their otherwise unretarded migration from the source to the NTS boundary. Only ^3H shows significant reduction in mass due to its short half-life. Travel times of less than 50 years from BENHAM to the NTS boundary in the continuously fractured LAVA

are estimated. Total mass breakthrough for any of these non-reactive species is very small, but similar to the total mass entering the site-scale model from the source-term simulations.

Field-Scale Reactive Particle-Tracking Transport Model

Although the site-scale GDPM reactive transport model accounts explicitly for kinetic chemical reactions and competitive speciation reactions, it is also computationally intensive. After analyzing results from the reactive transport process model, we determined that the most significant processes could be simplified and modeled by using a highly efficient particle-tracking model. The particle-tracking model is based on two key components:

- Three-dimensional, reactive dual-porosity particle-tracking simulations of unit source (instantaneous pulse) transport within site-scale flow fields to obtain unit source breakthrough curves.
- Convolution of the unit source breakthrough curves at observation wells and at the NTS boundary with transient source functions from the source term model to create individual radionuclide breakthrough curves.

The site-scale particle-tracking model is used for both deterministic HSU and heterogeneous representations of material properties. On the deterministic property field, simulations closely match the observations of all radionuclides found at both ER-20-5 wells, considering that the source releases are based on unclassified average inventory values. Simulated arrival times and concentrations are consistent with field observations, considering that the source term is based upon unclassified inventories that are not specific to any specific test. The results support the assessment of Kersting et al. (1999) that the plutonium found in both wells originated at BENHAM. Further supporting this argument are transport simulations specifying BENHAM as the source of the other radionuclides found in the ER-20-5 wells. However, sensitivity analyses indicate the possibility of TYBO related radionuclides migrating to observation well ER-20-5 #1, but not to ER-20-5 #3. Thus, BENHAM is either the sole source for all radionuclides in both wells or it is the sole source for those found in ER-20-5 #3, with TYBO contributing some or completely to the observations in ER-20-5 #1. Because the plutonium found in both wells fingerprints only to BENHAM and because Kersting et al. (1999) argue that mixing of Pu originating at both BENHAM and TYBO is unlikely, we speculate that TYBO releases are not captured in any significant quantities at ER-20-5 #1. Rather, the plume from TYBO evolves east of the observation wells. Many of the simulations on heterogeneous attribute maps support the hypothesis that TYBO releases are not captured by ER-20-5 #1.

With the site-scale particle-tracking model, spatial attribute distributions, transport parameter uncertainty, and source term uncertainty are evaluated taking into consideration the following:

- Thirty heterogeneous flow fields.
- Two release locations, one in a lava formation and the other in a shallower welded tuff aquifer.
- Six radionuclide classes representing 14 radionuclides.
- Up to 11 transport parameter sensitivity combinations.
- Up to 6 source functions (3 for non reactive radionuclides).

These combinations represent more than 25 000 breakthrough curves for a set of analyses that identify the uncertain parameters to which the results are most sensitive. Summarizing the results, ma-

trix Kd dominates the sensitivity analysis for U and Np transport that results from the large range of uncertainty considered for this parameter. Transport results for U and Np are also sensitive to fracture aperture and fracture porosity, parameters that ultimately affect how much diffusion can occur. Only filtration and groundwater velocity, a function of fracture porosity, affect the migration rate of the solute-colloid species. Finally, the sensitivity study demonstrates that the transport predictions are sensitive to the source-term model results. Several different source term scenarios, within our range of uncertainty, are examined to evaluate their impact on mass flux at downstream locations. The results show a complex relationship between the cavity-chimney system properties and transport in the site-scale model. Specifically, processes that preclude vertical migration in the chimney sometimes enhance release rates to the lower aquifer. Thus, an important consideration is how the continuity of the aquifers is represented in the models.

Chapter 1: Introduction

1.1 Introduction

The Nevada Test Site (NTS) is the United States' continental nuclear weapons testing site. Between 1951 and 1992, 828 underground tests were conducted at the NTS (DOE, 2000). The larger underground tests were conducted at Pahute Mesa, where both the BENHAM and TYBO tests are located (Figure 1-1). The BENHAM underground nuclear test was detonated 1.4 km below the surface of Pahute Mesa on December 19, 1968; it had an officially announced 1.15-megaton yield. The TYBO test was executed May 14, 1975, at a depth of 765 m; its officially announced yield was between 200 to 1000 kt (DOE, 2000).

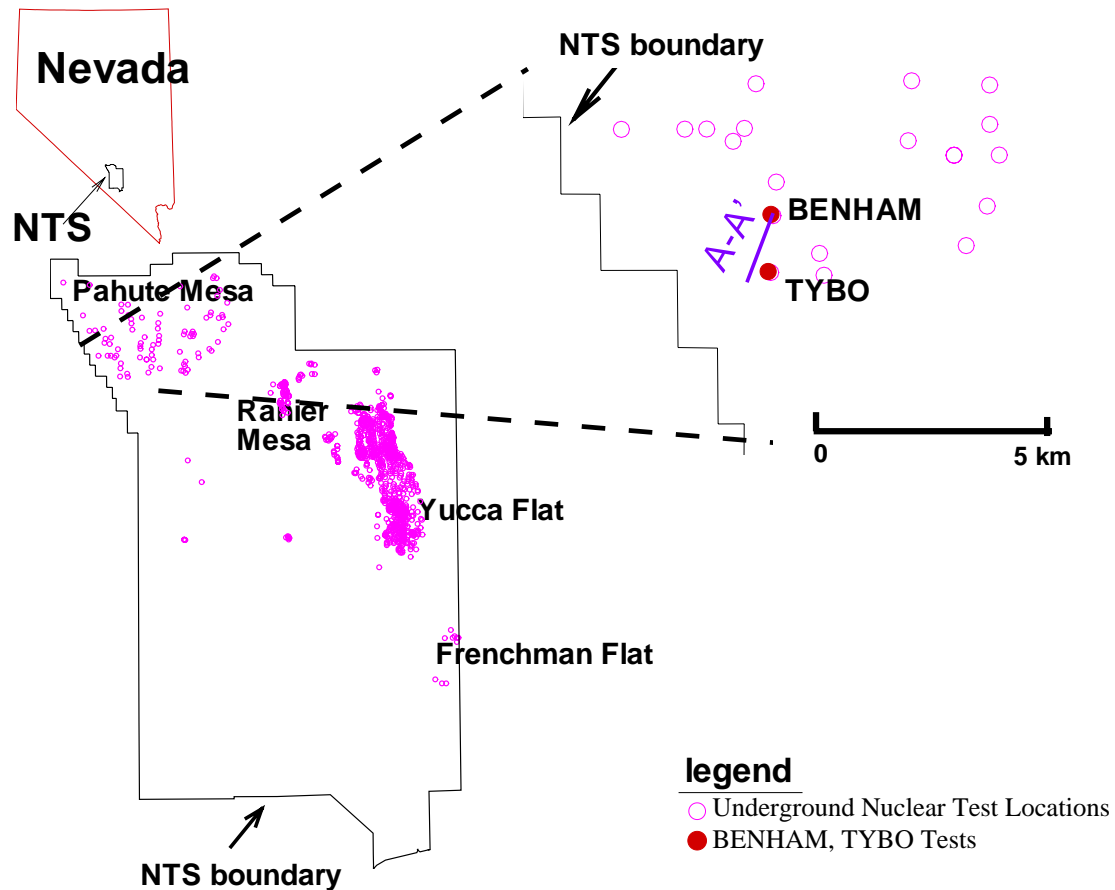


Figure 1-1. The Nevada Test Site (NTS) and the specific locations of the BENHAM and TYBO tests.

Observation wells ER-20-5 #1 and ER-20-5 #3 are approximately 300 m southwest of TYBO and were completed in 1995 and 1996, respectively (DOE, 1997a). ER-20-5 #1, drilled to

a depth of 860.5 m, samples the Topopah Spring welded tuff formation, the same formation in which the TYBO test was emplaced (Pawloski, 1999). ER-20-5 #3, drilled to a depth of 1267.2 m, samples a lava formation within the Calico Hills formation. This lava formation, mapped by Prothro and Warren (2001), is expected to be the same lava formation up to which the BENHAM cavity extends (Pawloski, 1999). Sampling of these observation wells between 1996 and 1998 indicates test-related levels of isotopes for hydrogen, carbon, chlorine, strontium, technetium, iodine, cesium, cobalt, europium, americium, and plutonium (see Tables 1-1 and 1-2).

Increased attention to these observation wells began with the analyses of Kersting et al. (1999), who focussed on the low levels of plutonium (Pu) found in the two observation wells. Pu was detected in ER-20-5 #3 at approximately the elevation of the BENHAM working point and in ER-20-5 #1, approximately 500 m above the lava (see Figure 1-2). The concentration of Pu measured in the welded tuff aquifer sampled by ER-20-5 #1 (0.63 pCi/L) is significantly higher than the concentration measured in the lava by ER-20-5 #3 (0.011 pCi/L). In both cases, the Pu was found associated with colloidal material.

Initially, the radionuclides found in the observation wells were assumed to have originated from the TYBO test because of its proximity to the observation wells. However, isotopic fingerprinting by Kersting et al. (1999) indicated that the Pu originated at BENHAM, not TYBO. This observation suggests that Pu, previously considered immobile, in fact migrated 500 m vertically and 1300 m horizontally. Possible mechanisms explaining these data findings are Pu migration via ground water transport and/or prompt injection. However, as Kersting et al. (1999) point out, it seems unlikely that Pu from BENHAM was blasted and deposited to the distances necessary for observation at the two separate ER-20-5 wells, thus diminishing the plausibility of prompt injection as the only migration mechanism. Further, because the Pu detected in the ER-20-5 wells was entirely associated with colloids, Pu migration via groundwater transport is implied. There are no diagnostic fingerprints to link any of the other radionuclides found in the observations wells to one source or another. Further, whereas colloid-facilitated transport of plutonium is implicated by its association with colloidal material, transport of several of the other radionuclides are governed by advection, dispersion, and matrix diffusion, not by reactions with mobile and immobile materials.

1.2 Study Objectives

The observations reported by Kersting et al. (1999) and the proximity of Area 19 tests to the NTS boundary accentuate the need to understand the transport of sorbing and nonsorbing radionuclides in Western Pahute Mesa groundwater systems. Therefore, the objectives of this study are as follows:

1. Present a modeling approach to study radionuclide migration in Western Pahute Mesa groundwater.
2. Integrate field, laboratory, and other modeling data into a framework to assess processes and mechanisms associated with the observations of Pu and other radionuclides found in the ER-20-5 observation wells southwest of TYBO.
3. Provide a methodology to evaluate parameter sensitivity in model predictions and the value of new or existing data.

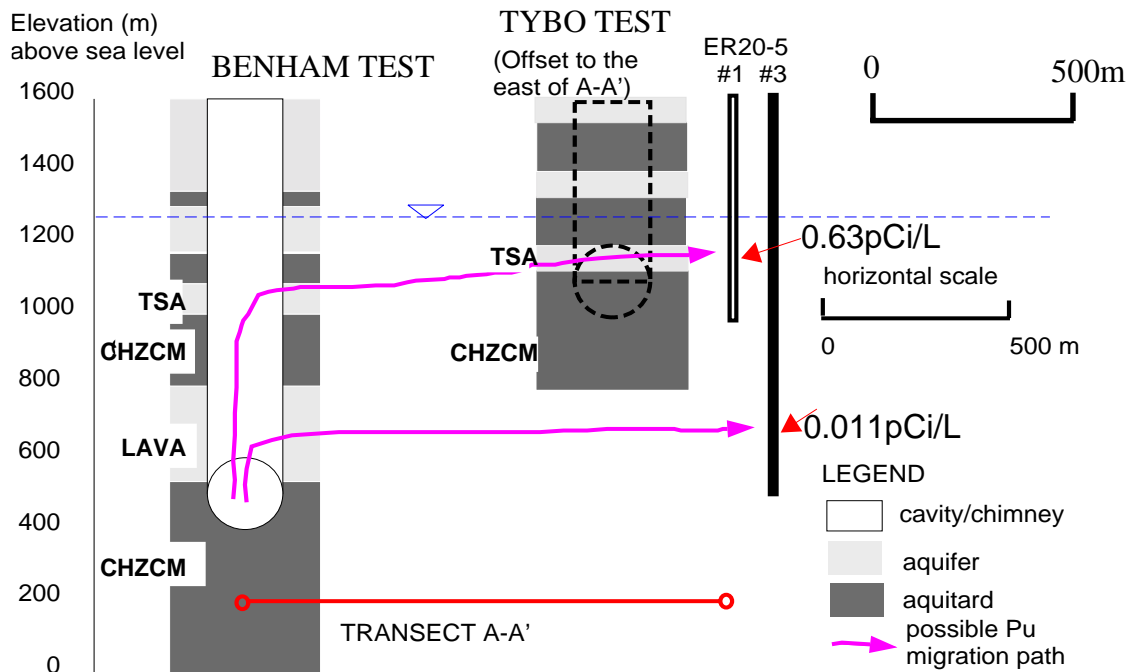


Figure 1-2. Cross-section along Transect A-A' in Figure 1-1 showing possible migration paths of plutonium away from BENHAM.

The motivation for this work involves understanding how Pu, previously considered immobile in groundwater, could migrate more than a kilometer from BENHAM to the ER-20-5 observation wells. However, one related issue addressed in the site-scale transport sections outlined below involves the potential for radionuclide migration from TYBO to the ER-20-5 observation wells. Kersting et al. (1999) show through isotopic fingerprinting that the Pu found in both ER-20-5 observation wells likely originated at BENHAM. The modeling presented in this report considers the broader context of all radionuclides (not fingerprinted as Pu was) and provides a framework for considering the importance of aquifer heterogeneity and how it is modeled and verified under sparse data conditions.

1.3 Model Components: A Road Map Through the Document

This study can be broken down into three primary components:

- sub-CAU (Corrective Action Unit) flow model calibration and site-scale flow model development,
- source term modeling
- TYBO/BENHAM site-scale transport modeling.

These components have the following relationships:

- The sub-CAU flow model provides boundary conditions for the higher resolution site-scale flow model.
- The source-term models provide transient radionuclide release functions into the site-scale domain.
- Site-scale transport models are used to simulate migration of radionuclides away from BENHAM and TYBO, with consideration to arrivals at the ER-20-5 wells and the NTS boundary. Site-scale flow and transport are conducted on hydrostratigraphic unit (HSU) stratigraphy and on heterogeneous realizations of material properties.

For both the source-term model and the site-scale transport models, the transport calculations are conducted predominantly with particle-tracking solutions. However, for both the source-term and the site-scale transport models, detailed mechanistic models considering processes more complicated than those allowed in the particle-tracking model are developed to provide an increased understanding of fundamental processes, as well as a basis for the simplifying assumptions invoked with the particle-tracking solver.

The efficiency of the particle-tracking models allows for multiple realizations that address model sensitivity and parameter uncertainty. Further, the source-term model represents a process that can be readily extended to other sources. In addition, the site-scale particle-tracking model is readily extendable to CAU-scale transport simulations. Figure 1-3 highlights the components for the various models used in this study. The next sections describe each model's purpose in greater detail.

1.3.1 Sub-CAU Flow Model

The sub-CAU flow model calibration ensures that the model reproduces field observations of head that are used to evaluate the role of faults in western Pahute Mesa. It is also used to constrain the hydrologic parameters employed in the transport simulations.

Chapter 2 provides an overview of the hydrostratigraphy on Pahute Mesa and defines the boundaries for the sub-CAU and site-scale model domains used in this study. The HSUs defined in this chapter are the units for which permeabilities are determined in the calibration exercise.

Chapter 3 introduces all of the components of the flow model, including boundary conditions, head observations, recharge, vertical gradients, thermal gradients, assumptions, and data quality issues. Sub-CAU flow modeling is performed on an unstructured finite-element grid, described in Appendix A, designed to capture the complex geometric shapes of the HSUs.

Chapter 4 describes the calibration calculations performed with the Finite Element Heat and Mass transport (FEHM) code (Zyvoloski et al., 1997) flow model and PEST parameter estimation software (Doherty, 2000). Results from this calibration provide the hydrologic control for the boundary conditions on the site-scale model used for transport calculations.

1.3.2 Site-Scale Flow Model

The site-scale domain is discretized at a much higher resolution than the sub-CAU domain to support spatial variability in heterogeneous attributes and to provide for more accurate transport calculations. Researchers at the Desert Research Institute (DRI) provided 30 maps of lithologic classes and the corresponding hydraulic conductivities.

FLOW MODELS

Site-Scale Flow Model - FEHM

Processes Modeled

- Steady-state flow in BENHAM and TYBO vicinity.

Characteristics:

- Boundary conditions from Sub-CAU flow model.
- CAU deterministic hydrostratigraphy.
- 30 geostatistical attribute fields.
- Structured high-resolution grid.

Sub-CAU Flow Model - FEHM

Processes Modeled

- Flow with depth-dependent thermal properties to provide boundary conditions for the site-scale model.

Characteristics

- HSU permeabilities calibrated.
- CAU deterministic hydrostratigraphy.
- Unstructured finite-element grid.
- Faults considered as discrete features.

BENHAM SOURCE-TERM MODELS

BENHAM 3-D Source Model - FEHM

Processes Modeled

- Coupled non-isothermal transient flow, glass dissolution, and particle transport in BENHAM cavity/chimney system.
- Flow- and temperature-dependent glass dissolution and particle release based on THC model results.
- Linear sorption in chimney.

Characteristics:

- Provides mass flux of sorbing and non-sorbing radionuclides into the TSA and LAVA aquifers.
- Considers multiple chimney material properties and thermal conditions for sensitivity analysis.
- No aqueous speciation (e.g., $\text{PuO}_2(\text{CO})_3$), rock-water reactions, or pH variations.

BENHAM 2-D Coupled THC Model - FLOTTRAN (Appendix B)

Processes Modeled

- Coupled non-isothermal transient flow, glass dissolution, and full reactive transport in BENHAM cavity/chimney system.

Characteristics:

- Sorption (complexation/ion exchange) of Pu to rubble not considered.
- Investigates role of changing geochemical conditions in complex transient system (such as changing pH, silica dependent dissolution rates, etc.).

TRANSPORT MODELS

Site-Scale Particle Transport Model - FEHM

Processes Modeled

- Reactive, dual-porosity transport in steady-state 3-D flow fields.

Characteristics:

- Highly efficient - multiple realizations considered for sensitivity of source term, flow field, and transport parameters.
- No speciation reactions (e.g., no Pu-colloid reactions).
- Equilibrium sorption reactions with fracture coatings and matrix material.
- Deterministic and 30 heterogeneous realizations considered.
- Simplification of speciation and sorption by assuming unchanging groundwater chemistry.
- Isothermal flow fields.
- Also used to investigate TYBO releases.

Site-Scale Reactive Transport Model - FEHM (Appendix F)

Processes Modeled

- Reactive, dual-porosity, solute, and colloid-facilitated Pu transport along steady-state streamtubes in a 3-D flow field.

Characteristics:

- Kinetic Pu-Colloid reactions.
- Equilibrium sorption reactions with fracture coatings and matrix material.
- Only one heterogeneous realization considered.
- Speciation and sorption (but simplified by assuming unchanging groundwater chemistry).
- Isothermal flow fields.
- Generalized Dual Porosity Model (GDPM) for fracture-matrix interactions.

Figure 1-3. Models used in this study

Chapter 5 describes the flow fields computed on the heterogeneous attribute maps and compares them with flow fields computed on the deterministic HSU stratigraphy. These flow fields provide the basis for all site-scale transport calculations performed throughout the remainder of the study. Appendix C describes the dual-porosity particle-tracking code used to (a) highlight flow paths in the flow fields, (b) create streamtubes for reactive transport calculations, and (c) serve as the transport module for the site-scale particle-tracking model.

1.3.3 Source-Term Model

Chapter 6 presents the three-dimensional source-term model that provides fluxes of radionuclides into the aquifers of the site-scale flow domain. The source-term model captures transient three-dimensional non-isothermal flow processes in the BENHAM cavity-chimney system. A highly efficient particle-tracking model simulates the dissolution of cavity melt glass, the mobilization of radionuclides in the melt glass, and the transport of solutes in this flow system. Used to conduct extensive parameter sensitivity studies and provide all of the source terms for the site-scale transport models, the particle-tracking model simplifies some of the coupled processes that likely occur in the source region. Therefore, Appendix B describes a fully coupled thermal-hydrologic-chemical (THC) model that solves simultaneously the transient heat-affected flow field, as well as the complex chemistry associated with melt-glass dissolution. This model provides a glass-dissolution rate relationship with temperature for the more efficient particle-tracking source-term model. Chapter 6 also describes the development and use of Rayleigh Numbers for assessing thermal convection potential in cavity-chimney systems.

1.3.4 Site-Scale Transport Model

Chapter 7 presents a field-scale transport simulator that is highly efficient and works in three-dimensions. Based on particle-tracking and convolution integrals, this model is used to estimate radionuclide concentrations at the ER-20-5 observation wells and to conduct an extensive parameter sensitivity analysis involving 30 heterogeneous flow fields, up to 6 different source functions, 11 transport parameter sensitivity variations, and 6 different classes of radionuclides. A statistical analysis of variation (ANOVA) performed on the substantial set of results helps identify parameters to which model simulations are most sensitive.

Mechanistic reactive transport process models in Appendix D and Appendix F provide support for simplifying assumptions in the particle-tracking transport model. Appendix D presents the reactive transport model derivation and describes simulations of colloid-facilitated plutonium transport in a laboratory column experiment. Appendix F extends the reactive transport model for site-scale simulations using the new Generalized Dual-Porosity Model (GDPM) described in Appendix E. In these appendices, data tables are compiled that present ranges of uncertainty for parameters affecting radionuclide transport in Western Pahute Mesa aquifers. Using source functions computed with the source-term model, the reactive transport model simulates radionuclide transport on a heterogeneous flow field. Reactive transport parameter sensitivity studies highlight parameters to which model simulations are most sensitive.

1.4 Computer Codes Used In This Study

1.4.1 Finite-Element Heat and Mass Transfer Code (FEHM)

The primary code used in this study is FEHM (Zyvoloski et al., 1997), a finite-element/finite-volume groundwater flow simulator with three different coupled transport options. FEHM is maintained at Los Alamos National Laboratory (LANL) in software configuration management with quality assurance, verification, and validation documentation (Dash et al., 1997; Dash, 2000, 2001).

Sub-CAU and Site-Scale Flow Models

For these flow model simulations, FEHM is used to simulate steady-state, single-phase groundwater systems. Although the coupled thermal solution capability in FEHM is not implemented, the code does correct groundwater viscosity as a function of temperature, specified according to a geothermal gradient. Aquifer materials are represented with a single continuum approach because fracture-matrix interactions (as they affect storage and release of water) are not relevant in steady-state flow calculations.

Source Term Model

For the source-term model in Chapter 6, FEHM is used to simulate non-isothermal transient flow coupled with particle-tracking solute transport. Particles are released from the melt glass as a function of glass dissolution (a function of flow and temperature). The particles move with the water, with those representing reactive solutes sorbing via linear Kd relationships.

Site-Scale Reactive Transport Model

Dual-porosity reactive transport is simulated along stream tubes in the three-dimensional site-scale flow model (Appendix F). For multiple radionuclides, the processes of aqueous speciation, sorption to fracture minerals, diffusion into matrix material, and sorption-to-matrix minerals are considered. Additionally, plutonium sorption to colloids is modeled. These simulations all assume constant temperature and constant groundwater chemical composition.

Site-Scale Particle-Tracking Transport Model

Dual-porosity particle tracking is used in Chapter 7 to simulate radionuclide transport in the three-dimensional site-scale flow model. Although this model does not consider interspecies reactions, it does take into account sorption to both fracture minerals and matrix minerals. These simulations all assume constant temperature and constant groundwater chemical composition.

1.4.2 FloTran

Coupled THC Source-Term Model

Appendix B describes a two-dimensional fully coupled thermal-hydrologic-chemical source-term model. Whereas the three-dimensional source-term model uses particle tracking for the solute transport calculations, this model includes consideration of changing chemical conditions in the transient flow field. For example, the evolution of pH is accounted for in this coupled model. The computer code FloTran was used for the calculations recorded in this appendix. It was developed by the researcher responsible for the work and has been cited in peer

reviewed publications and reports, where it was used for solving mechanistic reactive solute transport problems (Callahan et al., 2002; Lichtner, 2000, 2001).

1.5 Review of Sampling and Analysis at the ER-20-5 wells

A series of LANL and LLNL annual reports have documented the installation and subsequent groundwater sampling of the ER-20-5 observation wells (Thompson et al., 1996, 1999; Kersting et al., 1998a,b). ER-20-5 #1 was sampled on January 3, 1996 and June 3, 1996, with the pumping of 5000 gal. and 401 000 gal., respectively (Thompson et al., 1997). Analyses were conducted for ^3H , ^{137}Cs , ^{60}Co , and $^{152,154,155}\text{Eu}$. ^3H , ^{137}Cs , and ^{60}Co were found in both samples; these elements were expected because of the location of the observation well relative to a nuclear test cavity. ^3H moves unretarded with groundwater, ^{137}Cs has a gaseous precursor in ^{137}Xe , and ^{60}Co is abundant in device assembly and may be slightly more volatile than Eu or Pu. The Eu found in both samples was not expected and led to additional analyses for Pu.

In both the January and June ER-20-5 #1 samples, the concentrations of all 6 radionuclides cited above remained nearly constant, even though 80 times more water was pumped in June (Table 1-1). The deeper observation well, ER-20-5 #3, was sampled February 15, 1996 and July 31, 1996, with the pumping of 8000 gal. and 531 359 gal., respectively. ^3H , ^{137}Cs , and ^{60}Co were also detected in this well, although at lower concentrations than those in ER-20-5 #1 (Table 1-2). Eu isotopes were not detected in ER-20-5 #3.

Kersting et al. (1998a,b) summarize all sampling in both observation wells through September of 1997, including one additional set beyond those described above. This report includes the analyses for $^{239,240}\text{Pu}$ in the ER-20-5 groundwater samples and describes the filtering process that led to the conclusion that all detected Pu is on colloidal material. Additionally, Kersting et al. (1998a,b) document the isotopic fingerprinting of the Pu found in the ER-20-5 wells, linking it with the BENHAM test rather than the TYBO test. Several relevant conclusions drawn by Kersting et al. (1998a,b) are as follows:

- Co, Cs, Eu, and Pu radionuclides were associated with particulates and colloids in groundwater samples taken from ER-20-5 #1 and #3.
- The Pu isotopic ratios found in both ER-20-5 observation wells match the BENHAM test. They do not match the TYBO test. Mixing even a small amount of groundwater made up of the isotopic ratio of TYBO with groundwater that has BENHAM's isotopic composition will result in a ratio at the observation wells that is between TYBO and BENHAM values.
- The activities measured in ER-20-5 #1 (the upper well) are significantly greater than in ER-20-5 #3, even though ER-20-5 #1 is approximately 600 m stratigraphically above the BENHAM cavity.
- The measured radionuclide concentrations changed very little between sampling exercises in each observation well.

- The sampling and isotopic analysis indicate more southerly than southwest flow, and as a result the groundwater from BENHAM, but not TYBO, reaches the ER-20-5 observation wells.

Following these findings, LANL and LLNL conducted additional studies. Thompson et al. (1999) report a fourth set of samples and analyses in ER-20-5 #1 conducted in July 1998. The ^3H , ^{137}Cs , ^{60}Co , and $^{152,154,155}\text{Eu}$ concentrations were again approximately the same as those measured in the previous 3 sampling exercises. However, continuing analysis on a 1997 sample from ER-20-5 #1 revealed small concentrations of ^{241}Am . At $2.4\text{E-}14$ g/L, this small mass of ^{241}Am is 300 times less than that of Pu in the same sample.

Thompson et al. (1999) and Brachman and Kersting (2000) summarize results regarding composition, size distribution, and concentration of colloidal material in NTS groundwater. Thompson et al. (1999) show the differences in colloid counts in filtered and unfiltered water from ER-20-5 #1 then go on to present distributions for filtered water from ER-20-5 #1 and ER-20-5 #3. For both wells, the reported size distribution ranges between 50 (minimum detection limit) and 200 nm. The peak for both distributions is approximately 60 nm and only negligible counts are found for sizes greater than 120 nm. Brachman and Kersting (2000) also analyzed samples from the ER-20-5 wells. They found that the analyzed colloids generally mimic the host rock of the aquifer from which they were collected; the rocks are primarily clays and zeolites. The size distribution is monomodal, with particles ranging in size from approximately 80 nm and 150 nm, yielding an average of approximately 80 nm. The colloid concentration in ER-20-5 #1 well is approximately $3\text{E}10$ colloids/ml and $7.8\text{E}10$ colloids/ml in ER-20-5 #3.

Additionally, Rose et al. (1997) analyzed 1996 water samples from both observation wells for ^{36}Cl and ^{14}C (Tables 1-1 and 1-2). Concentrations for both of these isotopes indicate clear anthropogenic contributions from subsurface nuclear tests. The $^{36}\text{Cl}/^{35}\text{Cl}$ ratios of 173×10^{-13} in ER-20-5 #3 and $39\,400 \times 10^{-13}$ in ER-20-5 #1 are well above current precipitation ratios at the NTS of 5×10^{-13} . Similarly, the percent modern carbon measurements are 1450 and 28 169 in ER-20-5 #1 and #3, respectively. The signals for both ^{36}Cl and ^{14}C are significantly stronger in the upper well, indicating that either mixing with ambient water is greater in the lava aquifer sampled by ER-20-5 #3, that the source of these nuclides is stronger in the upper aquifer (possible contributions from both BENHAM and TYBO), or some combination of both.

1.6 Other Relevant Studies in Western Pahute Mesa

1.6.1 The CHESHIRE Study

During the development of this model for the BENHAM, TYBO, and ER-20-5 domain, LLNL conducted a concurrent effort to develop a hydrologic source-term model for the CHESHIRE underground nuclear test (Pawloski et al., 2001). The CHESHIRE test was carried out approximately 4.5 km northeast of BENHAM. Although both tests were performed in the regional hydrostratigraphic unit called the Calico Hills Zeolitic Composite Unit (CHZCM), the local

Table 1-1. Activity in pCi/L for ER-20-5 #1 Samples

Isotope	Element	Jan. 3, 1996 18.9 m ³ pumped	June 3, 1996 1520 m ³ pumped	April 22, 1997 223 m ³ pumped	July 9, 1998 110 m ³ pumped
³ H	Tritium (³ H)	6.6E07	6.81E07 6.58E07 7.2E07 7.38E07 (lab duplicate)	6.89E07 5.20E07 6.04E07	6.3E07 6.21E07
¹³⁷ Cs	Cesium (Cs)	1.19E01	1.55E01 1.18E01 2.26E01 (lab duplicate)	1.57E01 1.2E01	1.32E01 1.63E01
⁶⁰ Co	Cobalt (Co)	1.9E00	1.8E00	1.7E00	1.3E00
¹⁵² Eu	Europium (Eu)	1.6E00	1.5E00	1.4E00	1.3E00
¹⁵⁴ Eu	Europium (Eu)	1.88E00	1.7E00	1.6E00	1.4E00
¹⁵⁵ Eu	Europium (Eu)	4.7E-01	4.4E-01	3.1E-01	2.9E-01
^{239,240} Pu	Plutonium (Pu)	5.3E-01	2.6E-01 7.6E-01 6.3E-01 (lab duplicate)	6.3E-01 6.2E-01	
²⁴¹ Am	Americium (Am)			8.2E-02	
¹⁴ C	Carbon (C)		6.32E01	7.51E01 2.60E02	1.79E02 (<1530)
³⁶ Cl	Chlorine (Cl)		3.43E00	2.89E00	3.32E00
⁹⁹ Tc	Technetium (Tc)		1.57E00 (<2.26) 2.62E00 (lab duplicate)	7.9E-01	2.7E-01 (<1.88)
¹²⁹ I	Iodine (I)		4.87E-02 (<1.14) 4.97E-01 (<1.04) (lab duplicate)		(<570)
⁹⁰ Sr	Strontium (Sr)		5.0E-01 (<0.55)		
²¹⁴ Pb	Lead (Pb)		3.66E01	1.08E01	
Data obtained from NNSA/NV UGTA Program					
< - Indicates isotope detected at activity below the method detection limit					

distribution of facies and minerals are quite different. Whereas the focus of the present study is on migration of radionuclides over distances greater than a kilometer, the CHESHIRE study focusses on near field processes. Nevertheless, there still are some fundamental similarities between the two studies. For example, both studies have identified the need to simulate non-isothermal, transient flow and transport in the immediate vicinity of the source to predict releases of radionuclides to the aquifers. Specifically, there are a number of complex processes that affect these releases, such as the vertical convection in the collapse chimney associated with the test heat and release of radionuclides as the melt glass dissolves and cools. Ideally, these processes should be studied with a fully coupled flow and reactive transport model that captures the chemical and physical processes associated with melt glass dissolution and thermal convection cells. However, to date such models have not been developed for three-dimensional systems. Therefore, the CHESHIRE study, like the present one, invokes simplifications to simulate the complex cavity/chimney system.

The primary simulation method in both studies involves coupled flow and reactive particle-tracking models linked to functions representing melt-glass dissolution changes with time. These

Table 1-2. Activity in pCi/L for ER-20-5 #3 Samples

Isotope	Element	Feb. 15, 1996 30.3 m ³ pumped	July 31, 1996 2010 m ³ pumped	April 22, 1997 144 m ³ pumped	April 30, 1998 170 m ³ pumped
³ H	Tritium (³ H)	6.5E04	1.46E05 6.46E04 1.49E05 1.52E05 (lab duplicate) 1.46E05 (field duplicate)	1.42E05 1.06E05 2.91E05	5.05E05 1.56E05 1.42E05
¹³⁷ Cs	Cesium (Cs)	1.7E-01	1.4E-01 (<6.79) (<7.66) (lab duplicate) (<9.03) (field duplicate)	6.0E-02	(<1.39E01)
⁶⁰ Co	Cobalt (Co)	5.0E-02	9.0E-02	6.0E-02	
^{239,240} Pu	Plutonium (Pu)		8.0e-03 3.0E-02 1.7E-02 (lab duplicate) 1.4E-02 (field duplicate)	1.13E-02 8.5e-03 8.8E-02	
¹⁴ C	Carbon (C)		1.89E00	1.90E00	1.73E00
³⁶ Cl	Chlorine (Cl)		1.0E-02	9.0E-03	1.1E-02
⁹⁹ Tc	Technetium (Tc)		4.44E00 (<4.66) 1.63E00 (<4.69) (lab duplicate) 4.03E00 (<4.88) (field duplicate)		1.0E-02 (<5.17)
¹²⁹ I	Iodine (I)		4.77E-01 (<8.66E-01) (lab duplicate) 4.54E-02 (<9.78E-01) (field duplicate)		
⁹⁰ Sr	Strontium (Sr)		4.26E00 4.4E-01 (lab duplicate) 4.3E-01 (<0.46) (field duplicate)		
²¹⁴ Pb	Lead (Pb)		1.32E02 1.09E02 (lab duplicate) 1.27E02 (field duplicate)	9.0E00	
Data obtained from NNSA/NV UGTA Program					
< - Indicates isotope detected at activity below the method detection limit					

models, which are substantially more efficient than fully coupled flow and reactive transport models, capture the primary components of the systems under investigation. However, assumptions and simplifications are required because the particle-tracking models do not simulate processes such as speciation, rock-water interactions, kinetic effects, changes in groundwater chemistry, and competitive sorption. Some differences between the two studies are associated with the mechanistic detailed models used to support the particle-tracking models. In the present study, a fully coupled thermal-hydrologic-chemical (THC) model was developed and applied for a two-dimensional representation of the BENHAM test. This THC model provides insight into the melt glass dissolution process and informs the simplified three-dimensional model. The three-dimensional flow and particle-tracking model then uses flux and thermal changes in the melt glass

to estimate the dissolution rate at any time during the simulations. In the CHESHIRE study, reactive batch and one-dimensional calculations of the melt glass are used to develop the glass dissolution function for changing temperature, which is then applied to the three-dimensional flow and particle-tracking model. In addition, fully reactive transport simulations are conducted along streamlines, but only after 100 years, at which time the system has cooled and is nearly at steady state.

Compared to the present study, the CHESHIRE study considers far greater complexities in the geologic media immediately near the test. In the present study, only a layered representation of the geologic media is considered in the direct vicinity of the test and heterogeneous attributes are considered in the aquifers and aquitards away from the test. Both studies also include parameter sensitivity analyses.

Although the CHESHIRE and present study have similarities in how transport is modeled in the non-isothermal cavity/chimney system, the CHESHIRE study devotes more attention to the region near the CHIMNEY, whereas the present study focuses on transport in fractured rock away from the source region.

1.6.2 Pahute Mesa Hydrostratigraphic Model

During the development and completion of the present model, the following hydrostratigraphic model was also being developed:

A Hydrostratigraphic Model and Alternatives for the Groundwater Flow and Contaminant Transport Model of Corrective Action Units 101 and 102: Central and Western Pahute Mesa, Nye County, Nevada (Bechtel, 2002).

However, the portion of the hydrostratigraphic model associated with the domain considered in the present study had mostly been developed (Drellack and Prothro, 1997) and was available in digital format as necessary for this study. The Drellack and Prothro (1997) model covering the present study domain was incorporated completely into the Bechtel (2002) model, with the exception of the small portion of present study domain south of the Timber Mountain Moat Fault (See Chapter 2). New wells (e.g., ER-EC-6) installed since 1997 have led to improvements in the hydrostratigraphic representation south of the Timber Mountain Moat Fault. That region is a small part of the present study's flow model and it is not included at all in the present study's radionuclide transport simulations, which are focussed closer to BENHAM and TYBO, north of the Timber Mountain Moat Fault. Nevertheless, the present report notes, as appropriate, how new models may benefit from improved hydrostratigraphic representation associated with the new Bechtel (2002) model.

1.7 Summary

This study consists of three integrated major components that provide predictions of radionuclide migration in Pahute Mesa groundwater in the vicinity of BENHAM and TYBO. The simulations conducted in this study are motivated by the observations reported in the previous section. This study provides an integrated framework to address important questions raised by the field observations by developing a flow model at a scale large enough to encompass many wells for calibration, a source-term model capable of predicting radionuclide releases to aquifers following complex processes associated with non-isothermal flow and glass dissolution, and site-scale transport models that consider migration of solutes and colloids in fractured volcanic rock. Combined, the various components of this study lead to model results consistent with those field observations and additional insight into radionuclide migration in Pahute Mesa groundwater.

This Page Intentionally Left Blank

Chapter 2: Stratigraphy and Model Domain Definitions

2.1 Introduction

Drellack and Prothro (1997) developed a model representing the thickness, distribution, and geometric relationships of hydrostratigraphic units (HSUs) for Western and Central Pahute Mesa area. Section 1.6.2 describes the relationship of this model to the Hydrostratigraphic Model of the Pahute Mesa - Oasis Valley Area, Nye County, Nevada (currently in review). The Drellack and Prothro (1997) model provides contoured surfaces of the tops of 22 HSUs. The contoured surfaces were provided in digital format on a 300-m-spaced regular grid. These surfaces are read into either the StrataModel geologic model software (SGM, 1995) or the GEOMESH/LaGriT grid-generation software package (George, 1997), both of which can be used to visualize individual HSU surfaces and the spatial relationship between different surfaces. Figure 2-1 shows the domain of Drellack and Prothro and one of the 22 surfaces, as well as the names of faults and the locations of wells near BENHAM and TYBO.

The three-dimensional model was developed by stacking and connecting all of the contoured surfaces of the HSUs and populating the volume between the layers with HSU attributes (such as porosity, permeability, and transport parameters). Table 2-1 shows the names of the units identified by Drellack and Prothro and the ranges of hydraulic conductivity they estimate for each HSU. These ranges are used in Chapter 4 to bound the sub-CAU model flow calibration.

2.2 Geologic Cross Sections Through the Model

Cross sections through the stratigraphic model are constructed to display the dipping stratigraphy, pinchouts, fault zones, and well depths. Figure 2-2 shows the vicinity of BENHAM in plan view with four different cross-sectional transects. Figures 2-3 through 2-6 show the cross sections along the prescribed transects shown in Figure 2-2.

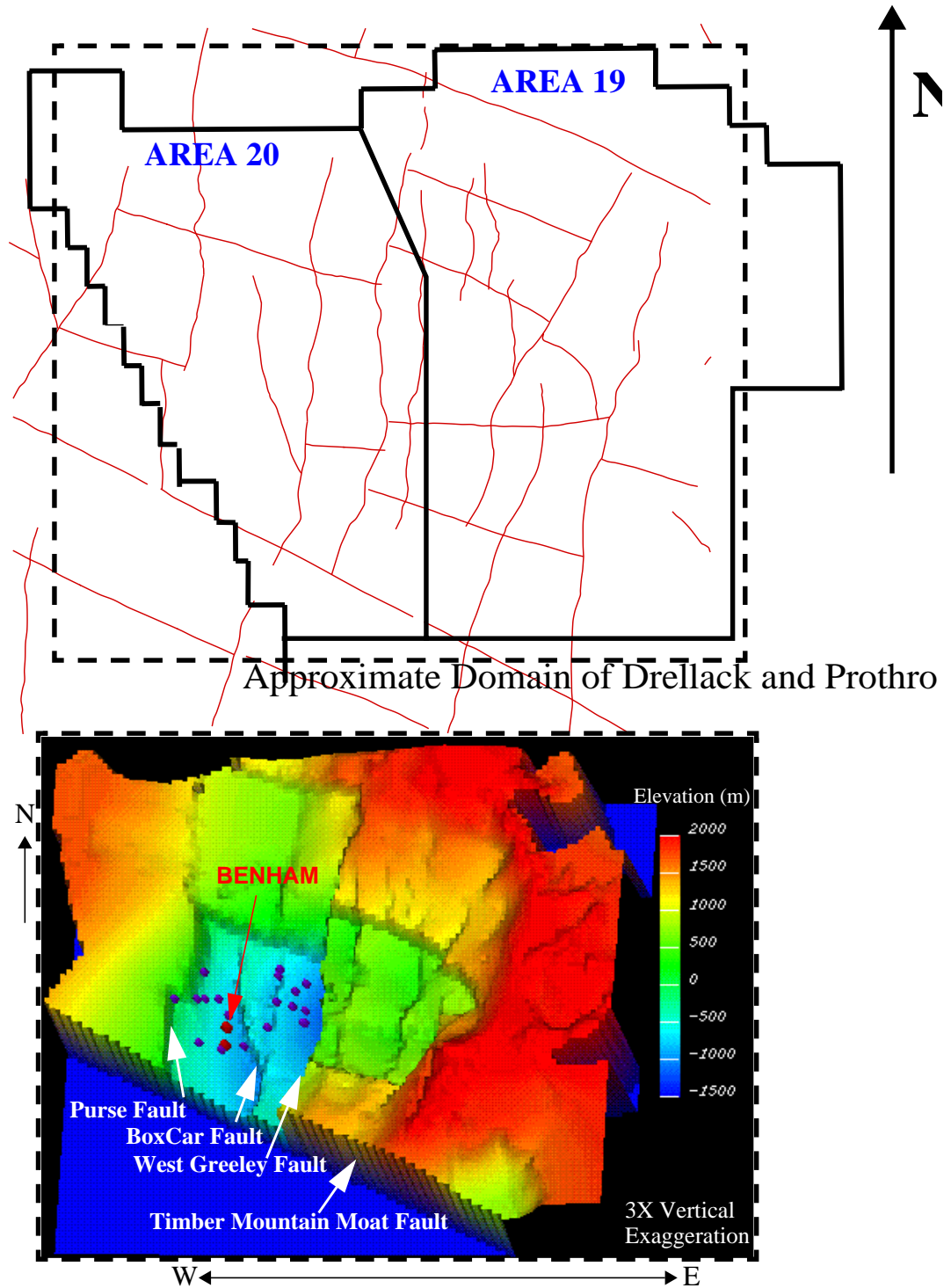


Figure 2-1. Stratigraphic surface of the top of the Belted Range Aquifer under Areas 19 and 20 from Drellack and Prothro (1997). Similar surfaces exist for all 22 units. Blue dots show wells used to calibrate sub-CAU-scale flow model. Red dots show BENHAM and TYBO. Red lines in upper plot show mapped faults in Areas 19 and 20.

Table 2-1. Names of HSUs and Estimated Hydraulic Conductivity Ranges (From Drellack and Prothro, 1997)

Hydrostratigraphic Unit	Nomenclature (Drellack and Prothro, 1997)	Hydraulic Conductivity (m/d)
Timber Mountain Aquifer	TMA	1 - 30
Timber Mountain Composite Unit	TMCM	0.001 - 0.5
Windy Wash Aquifer	WWA	1 - 20
Paintbrush Vitric Tuff Aquifer	PVTA	0.1 - 1
Benham Aquifer	BA	1 - 20
Upper Paintbrush Confining Unit	UPCU	0.001 - 0.5
Tiva Canyon Aquifer	TCA	0.5 - 1.0
Paintbrush Lava-Flow Aquifer	PLFA	1 - 20
Lower Paintbrush Confining Unit	LPCU	0.001 - 0.5
Topopah Spring Aquifer	TSA	5 - 30
Calico Hills Vitric Tuff Aquifer	CHVTA	0.1 - 1
Calico Hills Vitric Composite Unit	CHVCM	0.1 - 20
Calico Hills Zeolitized Composite Unit	CHZCM	0.001 - 15
Calico Hills Confining Unit	CHCU	0.001 - 0.5
Inlet Aquifer	IAQ	0.1 - 5
Crater Flat Composite Unit	CFCM	0.001 - 5
Crater Flat Confining Unit	CFCU	0.001 - 0.5
Kearsarge Aquifer	KA	0.1 - 5
Bullfrog Confining Unit	BFCU	0.001 - 0.5
Belted Range Aquifer	BRAQ	0.5 - 15
Pre-Belted Range Composite Unit	PBRCM	N/A
Pre-Tertiary	PreT	N/A

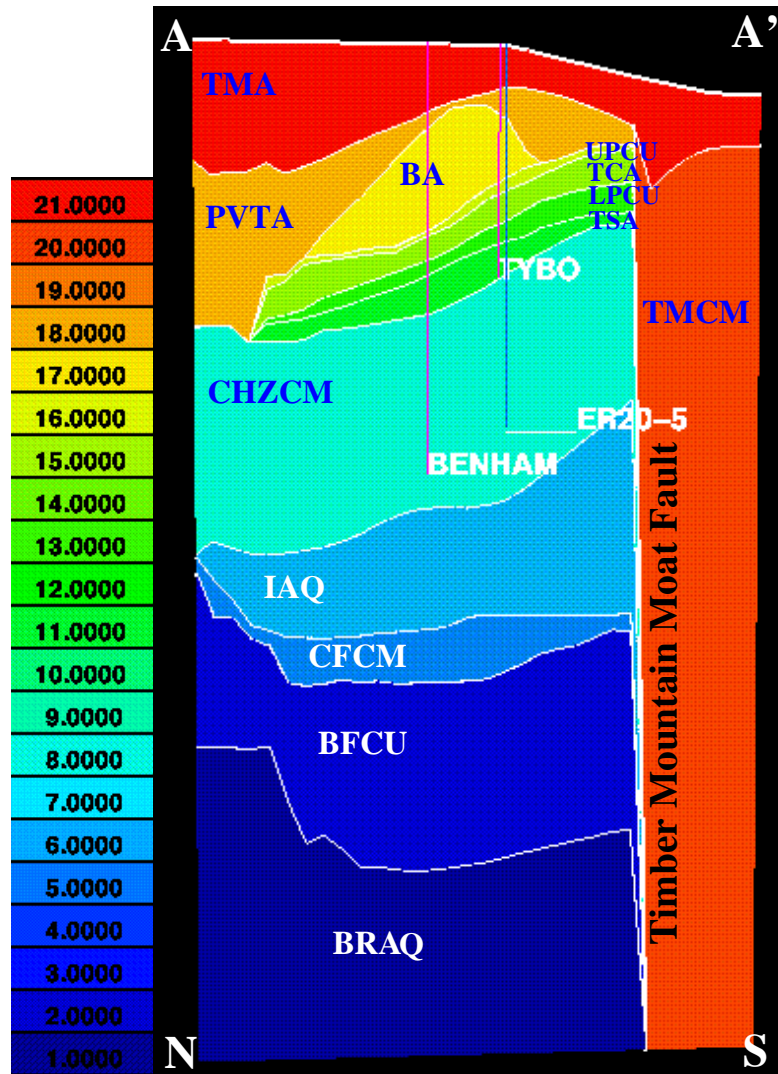


Figure 2-3. Stratigraphic units along A-A' transect. Note, the plutonium from BENHAM was found in ER-20-5 observation wells sampling the TSA and a lava formation embedded within the CHZCM. Transect and wells are identified in Figure 2-2.

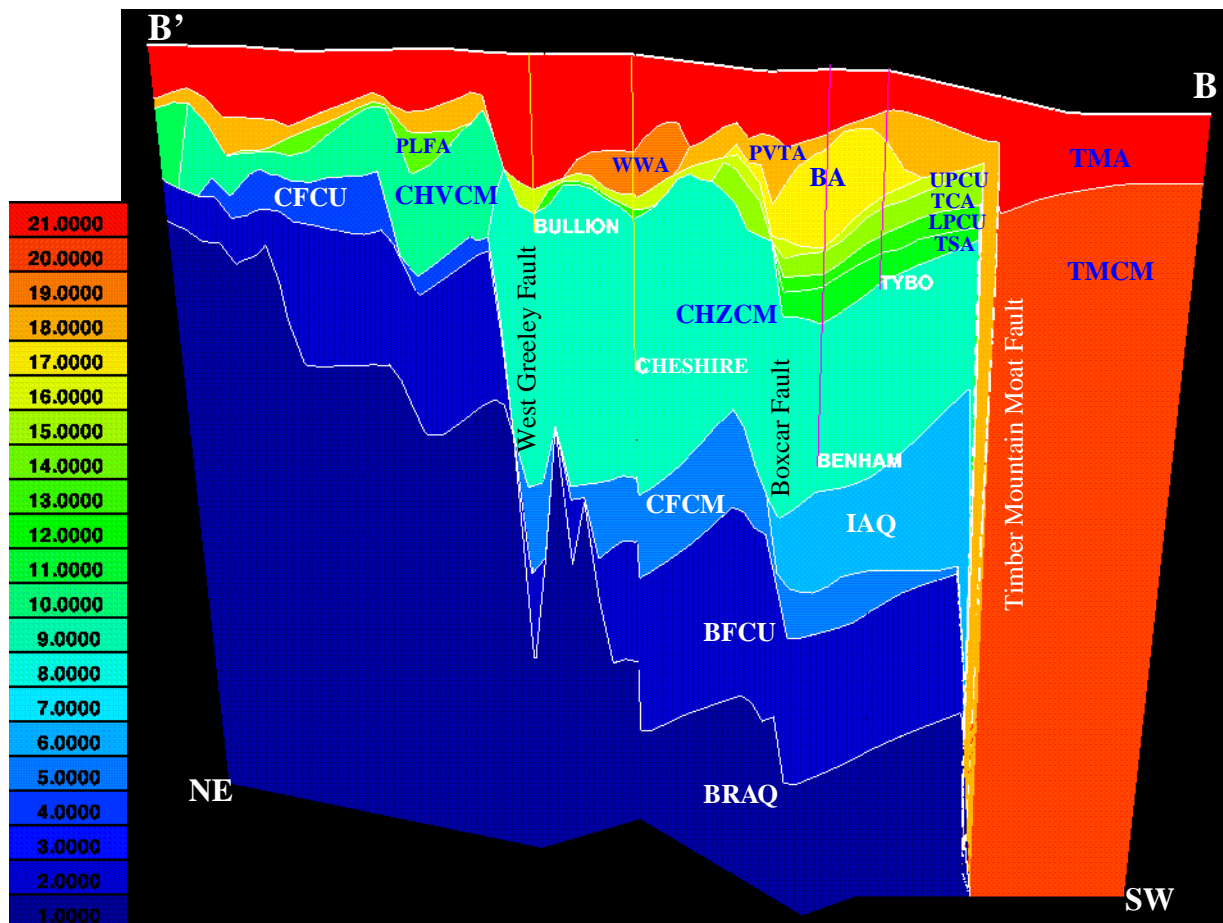


Figure 2-4. Stratigraphic units along B-B' transect which are identified in Figure 2-2.

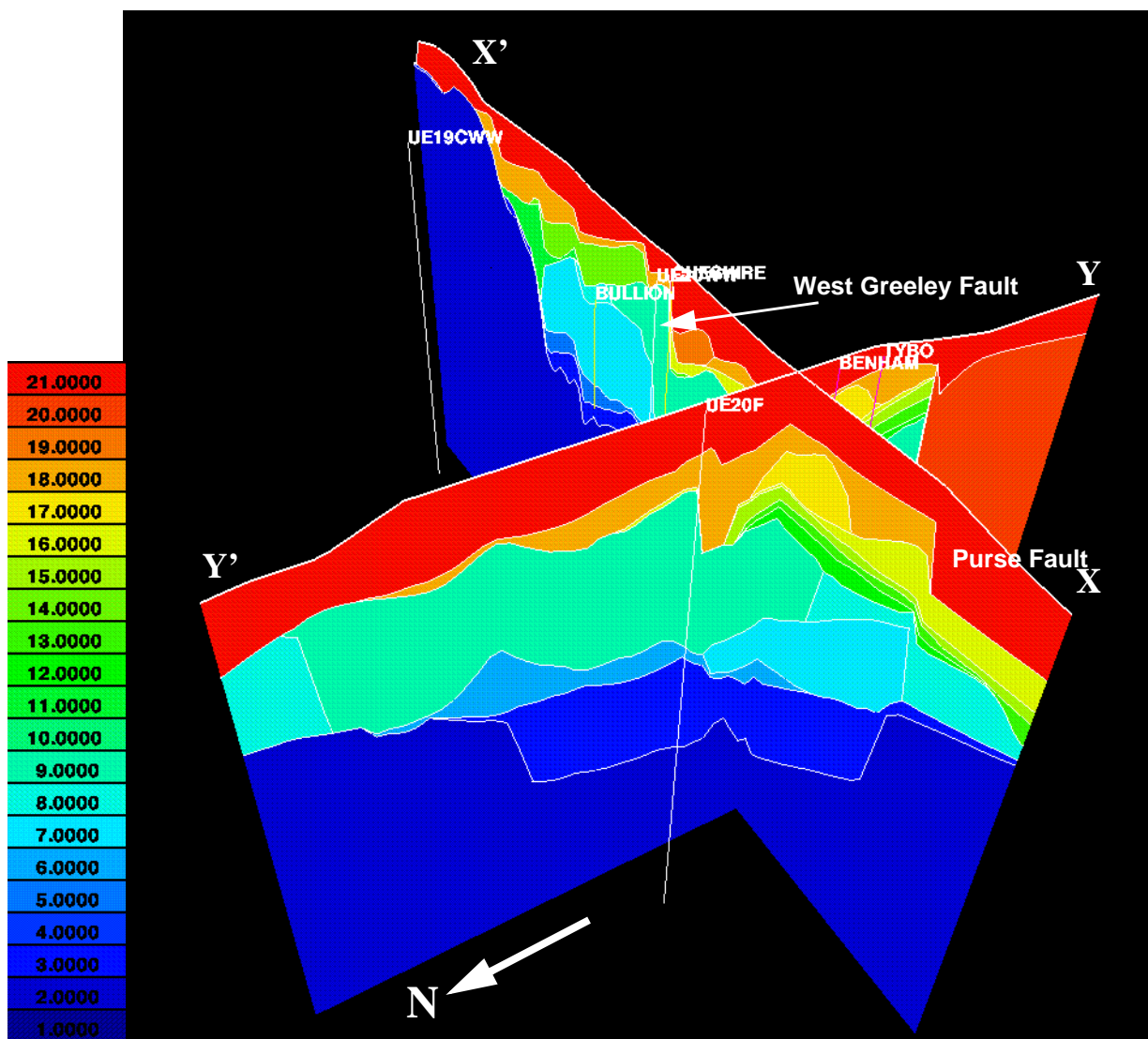


Figure 2-5. View of three-dimensional geologic model from the northwest. Transects and wells are identified in Figure 2-2.

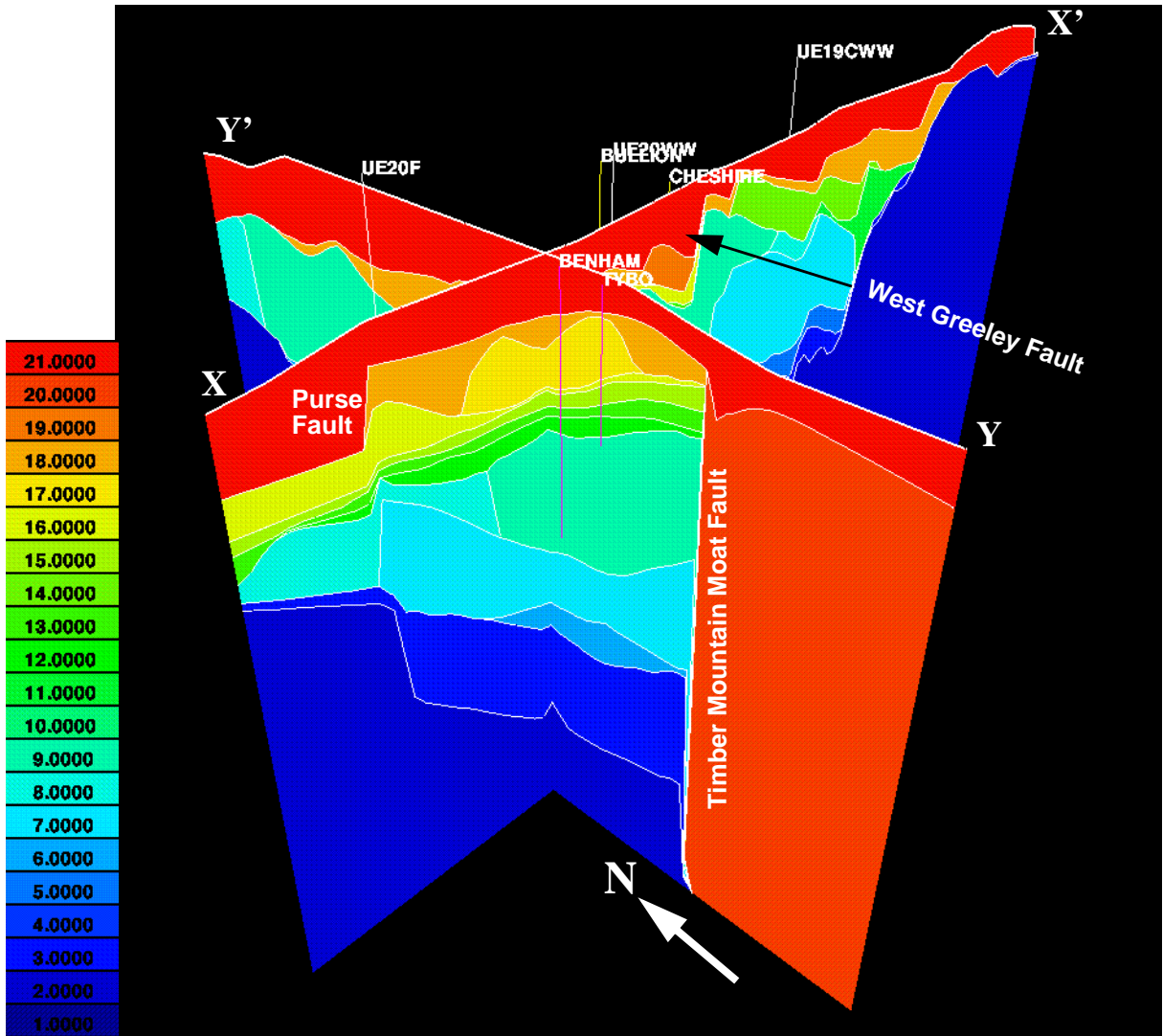


Figure 2-6. View of three-dimensional geologic model from the southwest. Transects and wells are identified in Figure 2-2.

The most important features, relative to this study, shown in the cross sections are as follows:

- The extensive Calico Hills Zeolitic Composite Unit, CHZCM, west of the West Greeley Fault.
- The major unit offset at the West Greeley Fault.
- The offset of units at the Boxcar Fault and the presence of the TSA south and west of it.
- The truncation of all units at the Timber Mountain Moat Fault and the single TMCM unit on the south side (primarily due to lack of data when model was constructed).
- The presence of the Bullfrog Confining Unit (BFCU) below the CHZCM as far north as well UE-20-f.
- The unit truncations at the Purse Fault.

2.3 Model Domains

This model was not designed to provide a flow solution for the entire Western Pahute Mesa CAU domain. Therefore, model domain boundaries were chosen to provide the minimum domain size in which sufficient information exists to specify adequate hydrogeologic control for prediction of flow and transport in the BENHAM and TYBO test region. Following the evaluation of Drellack and Prothro's model and hydrologic data from Western Pahute Mesa, a sub-CAU-scale and site-scale domain were chosen such that

- the sub-CAU model domain is extensive enough to include adequate hydrologic information to
- that provides a calibrated flow model using Drellack and Prothro's HSU definitions.
- the site-scale model domain is large enough to predict the migration of radionuclides away from BENHAM but small enough to support high-resolution attribute definitions.

Figure 2-7 shows the sub-CAU and site-scale domains selected based upon the above criteria. Section 3.2.1 provides more detail of the conditions along the boundaries described in this section. The sub-CAU domain is bounded to the north by the an east-west transect through wells UE-20f and UE-20h. Well UE-20f contains the deepest set of head observations in the region. In fact, it is the only well that penetrates and measures head below the Bullfrog Confining Unit (BFCU), an aquitard below the Calico Hills Zeolitic Composite Material (CHZCM), the hydrogeologic unit in which many (as well as the deepest) underground nuclear tests were conducted. The northern boundary of the sub-CAU domain is 3.6 km north of the TYBO/BENHAM site-scale domain on which transport calculations are performed.

The sub-CAU domain extends south of the Timber Mountain Moat Fault into the Timber Mountain Caldera Complex, where a detailed geologic model has not been completed. The current hydrostratigraphic model (Drellack and Prothro, 1997) provides only one composite unit south of the Timber Mountain Moat Fault, the Timber Mountain Composite Material (TMCM). Thus, gradients are expected to be uniform in that portion of the domain, with the head reasonably well defined by well ER-EC-6.

The sub-CAU model is bounded to the east and west by the West Greeley Fault and the Purse Fault, respectively. The hydrostratigraphic model of Drellack and Prothro (1997) shows that the lower units are down dropped between these two faults. Figure 2-8 provides an east-west cross section through Western Pahute Mesa showing the graben that defines the east and west boundaries of the sub-CAU model domain. Other figures showing the stratigraphy between these two faults are Figures 2-1 and 2-4.

There are three major faults within the interior of the sub-CAU model domain: the Boxcar Fault, the West Boxcar Fault, and the Moat Fault (Figure 2-7). The Moat Fault forms the boundary between the Silent Canyon Caldera and the Timber Mountain Caldera Complex. The Boxcar Fault trends north to south while the West Boxcar Fault trends to the northwest from its intersection with the Boxcar Fault.

The site-scale domain is chosen simply to include BENHAM, TYBO, and the ER-20-5 wells. It is situated such that it falls between the Boxcar Fault and the Moat Fault, so no fault properties within the site-scale domain need to be considered. The boundary conditions for the site-scale model are derived from the sub-CAU model, as described in Chapter 5.

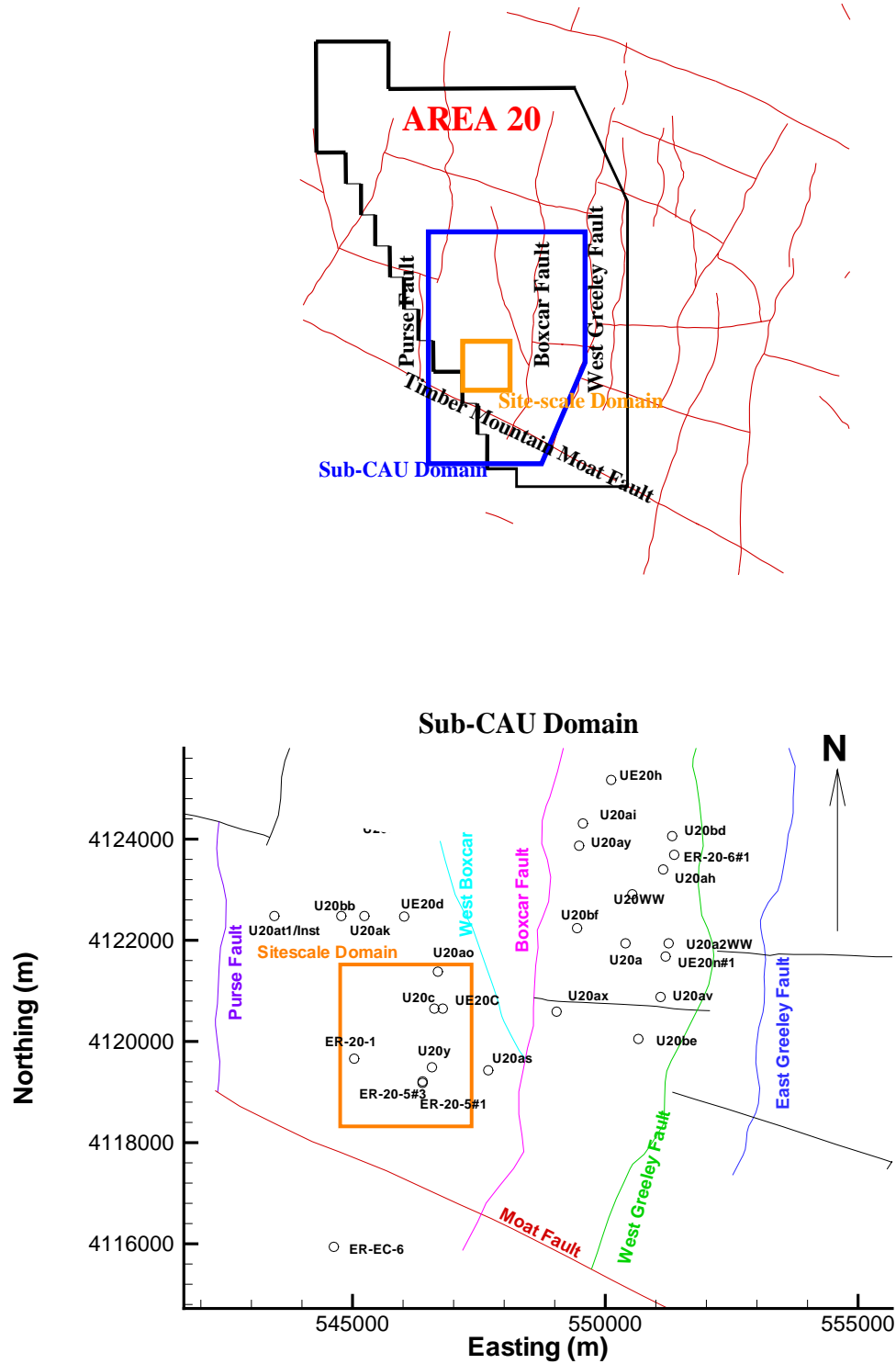


Figure 2-7. Plan view of the sub-CAU and site-scale domains relative to Area 20 in Western Pahute Mesa.

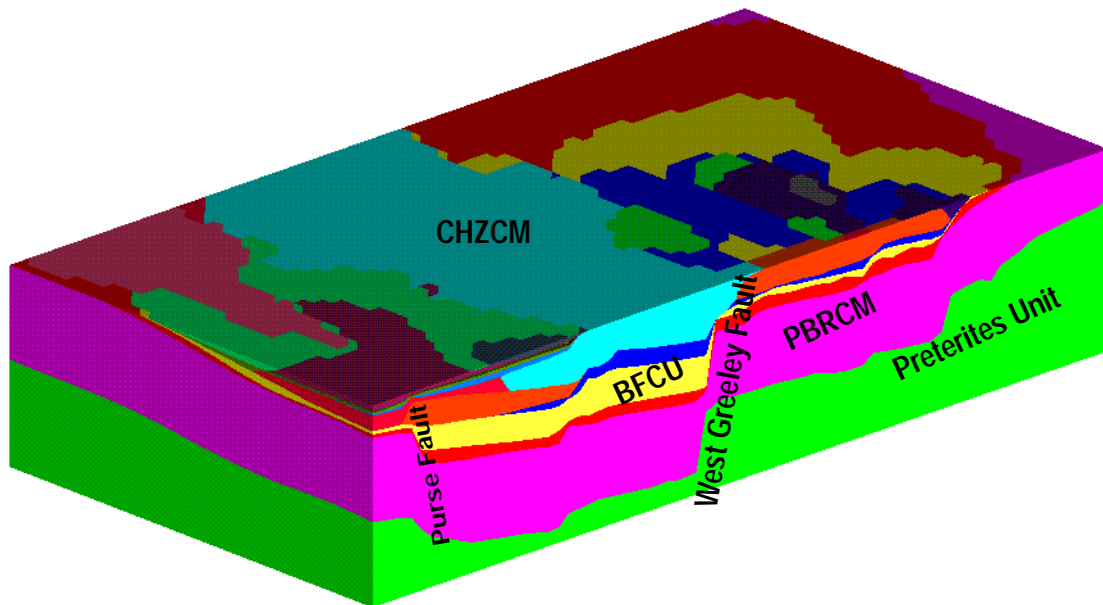


Figure 2-8. Hydrostratigraphy of Western Pahute Mesa showing downdrop between the Purse Fault and the West Greeley Fault.

2.4 Hydrostratigraphy of the Sub-CAU Domain

The sub-CAU domain consists of layered volcanic rocks. The rock types are primarily ash-flow or ash-fall tuffs and lava flows. Various hydrogeologic classification schemes have been suggested, but for the purposes of this work the scheme of Drellack and Prothro (1997) has been adopted (Table 2-2). Table 2-3 defines the individual HSUs present in the sub-CAU model domain.

The Silent Canyon Caldera was buried by the Timber Mountain Caldera Complex and buried again by the Thirsty Canyon ash-flows from the Black Mountain Caldera to the West (Laczniak et al., 1996). The regional basement rock is generally considered to be pre-Tertiary carbonates; however, there are no wells in the model domain that confirm the presence of these rocks. The depth of the volcanics exceeds 4171.5 m (13 686 ft.), which is the total depth of the deepest well in the area, UE-20f.

Table 2-2. Definitions of Hydrogeologic Grouping Structure from Drellack and Prothro (1997)

Hydrogeologic Unit	Definition
Vitric-Tuff Aquifer (VTA)	Bedded tuffs, ash-fall, and reworked tuffs; vitric
Welded-Tuff Aquifer (WTA)	Welded ash-flow tuff; vitric to devitrified
Tuff Confining Unit (TCU)	Zeolitized bedded tuff with interbedded, but less significant, zeolitized, nonwelded to partially welded ash-flow tuffs
Lava-Flow Aquifer (LFA)	Rhyolite lava flows; includes flow breccias and pumiceous zones

Table 2-3. Hydrogeologic Units Present in the Model Based on Drellack and Prothro (1997)

HSU Name with Abbreviation	Model Unit #	Hydrogeologic Unit Group	In this Study
Pre-belted Range Composite Material (PRBCM)	2	TCU, WTA, LFA	TCU
Belted Range Aquifer (BRAQ)	3	LFA, WTA	LFA
Bullfrog Confining Unit (BFCU)	4	TCU	TCU
Crater Flat Composite Material (CFCM)	7	LFA, TCU	LFA
Inlet Aquifer (IAQ)	8	LFA	LFA
Calico Hills Confining Unit (CHCU)	9	TCU, LFA	TCU
Calico Hills Zeolitized Composite Unit (CHZCM)	10	LFA, TCU	TCU
Topopah Spring Aquifer (TSA)	13	WTA	WTA
Lower Paintbrush Confining Unit (LPCU)	14	TCU	TCU
Tiva Canyon Aquifer (TPCA)	16	WTA	WTA
Upper Paintbrush Confining Unit (UPCU)	17	TCU	TCU
Benham Aquifer (BENA)	18	LFA	LFA
Paintbrush Vitric Tuff Aquifer (PVTA)	19	VTA	VTA
Timber Mountain Confining Unit (TMCM)	21	TCU, WTA, LFA	TCU

The highest permeability units in Table 2-3 tend to be generally unaltered and are either welded tuff, lava, or vitric tuff formations. The welded tuffs and lavas tend to fracture more easily than the vitric tuff, a significant issue when considering solute migration. The altered units comprise confining units and tend to have quite low permeabilities. They are also expected to provide substantial retardation to reactive solute migration due to their mineralogic composition. Studies on Yucca Mountain tuffs (CRWMS M&O, 2000 g) show that the retarding potential of altered tuffs for reactive radionuclides (e.g., uranium, neptunium, plutonium, americium, europium, samarium, etc.) is greater than that of unaltered tuffs.

The locations of the different units and their contrasting properties lead to a complex, three-dimensional flow system with more flow occurring in some units than others, as well as vertical gradients causing some upward and some downward flow patterns. The hydrologic properties are discussed in greater detail in Chapters 3 and 4; however, it is worthwhile to note the general characteristics here with respect to the unit locations.

Although the flow field will be affected by all units and structures (e.g., faults) in the domain, the transport of radionuclides will be most affected by the properties of the units in which they migrate. For releases from BENHAM, the units of greatest significance, as indicated in Figure 2-3, will be the CHZCM, the TSA (bound above by the LPCU), and the IAQ only if migration downward in the CHZCM can be supported.

Extensive fracturing in the TSA, in which Kersting et al. (1999) found the highest level of plutonium, should make it a high-velocity, large-flow aquifer. This unit has been studied in great detail by the Yucca Mountain Project because it is the unit in which the potential repository will reside, although it exists above the water table at Yucca Mountain. Investigators have identified the TSA as a fractured HSU that would promote rapid migration of non-reactive solutes (e.g., Wolfsberg et. al., 2000) and reactive solutes (e.g., Viswanathan et. al., 1998). Therefore, the primary issue associated with the TSA is the process by which radionuclides can get to it from the BENHAM test conducted hundreds of meters lower in the CHZCM. Chapter 6 and Appendix B investigate potential mechanisms.

The CHZCM is significantly more complex than the TSA, principally because of the huge range in hydraulic conductivities estimated by Drellack and Prothro (1997), as shown in Table 2-1. Because it is a composite unit, multiple different rock types are expected to be found in it. Prothro and Warren (2001) characterized a lava flow aquifer embedded within the CHZCM extending from BENHAM at least to the observation well ER-20-5 #3, where Kersting et al. (1999) also found plutonium from BENHAM. This lava flow aquifer is minor in extent relative to the other units in Table 2-1, but quite significant with respect to the vicinity of BENHAM and TYBO. Although the CHZCM, a zeolitized composite unit, would normally be characterized with low permeability and poor fracturing, the embedded lava could have high permeability and fracturing similar to the TSA, hence making it a fast-path aquifer for solute migration.

This issue regarding the scale of significance of HSU identification plays an important role in guiding alternative representations of hydrostratigraphy at small scales. One such alternative, presented in Chapter 5, is the implementation of geostatistical methods for prescribing hydrologic attributes at significantly higher resolution in local domains. Another approach not investigated here would be to increase the resolution of models such as Drellack and Prothro (1997) in small site-related domains to improve hydrologic and mineralogic representations. Descriptions such as those from Prothro and Warren (2001) could provide such input.

This Page Intentionally Left Blank

Chapter 3: Sub-CAU Flow Model Components

3.1 Introduction

The sub-CAU flow model provides hydrologic control for the site-scale flow and transport model domain, a region that is not sufficiently sampled to properly estimate its boundary heads and fluxes. This chapter describes the necessary components of the sub-CAU flow model, as well as the data quality issues associated with each of them. In the next chapter, we calibrate the hydrologic parameters associated with the sub-CAU model. Figure 3-1 provides a reference for well locations relative to the sub-CAU model domain.

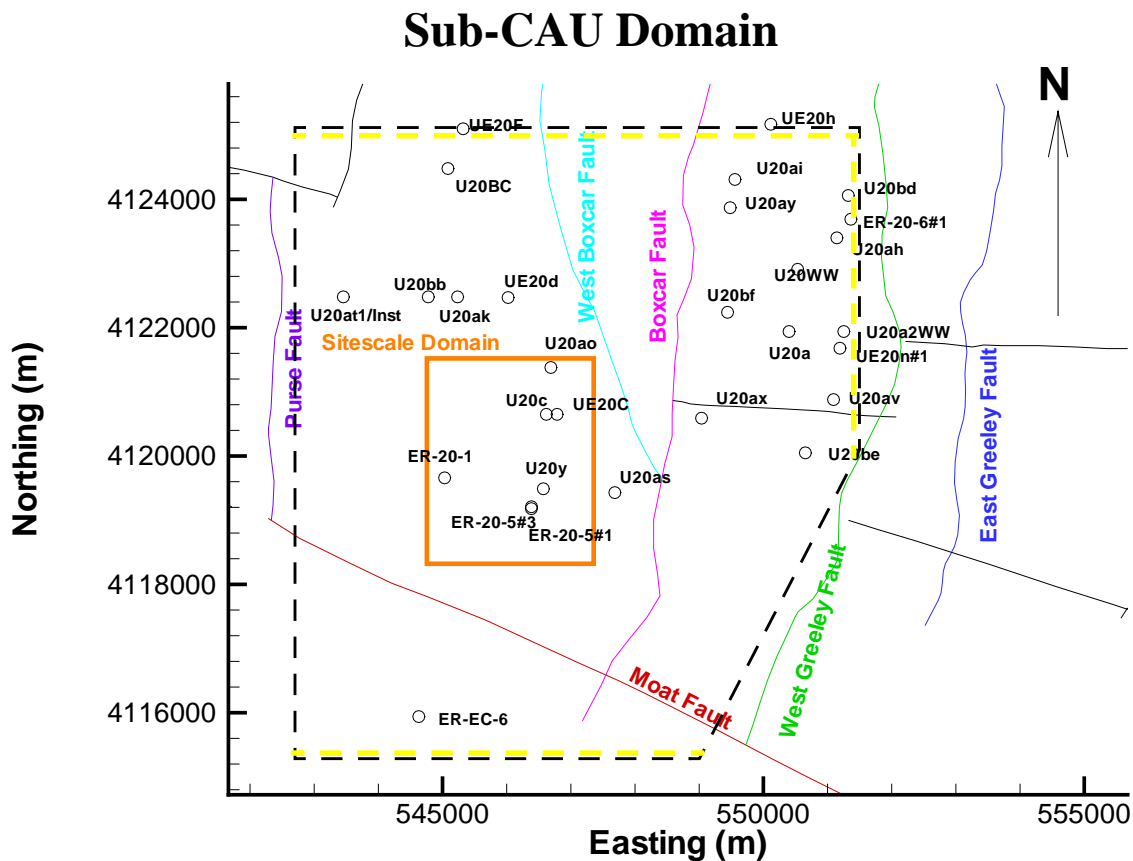


Figure 3-1. Sub-CAU flow model domain. Dashed yellow lines indicate boundaries where heads are fixed in the flow model.

3.2 Components of the Sub-CAU Flow Model

In this section, we describe the components of the steady-state sub-CAU flow model, including boundary conditions, head observations, permeability, faults, recharge, and thermal

gradients. Chapter 2 provides the cross sections and HSU names referenced in this chapter. The sub-CAU flow model is developed on the assumption that available data represent a steady-state situation. Due to the impacts of pumping and underground testing, the data actually represent a transient system. However, later in this chapter, the data used to calibrate the steady-state flow model are discussed and those with a greater likelihood of representing transient effects are weighted less than those with a greater likelihood of representing the steady-state system. Further, due to the geothermal gradient, groundwater temperatures change with depth. Although the flow model is not a fully-coupled thermal flow model, it does account for temperature effects on hydraulic conductivity (a function of both rock and fluid properties). As discussed in Section 3.2.9, thermal effects on fluid viscosity are included in the calibration of rock properties.

3.2.1 Boundary Conditions

Heads are fixed on the northern, southern, and northeastern boundaries, as shown with dashed yellow lines in Figure 3-1. The remaining two-side boundaries are treated with no-flow conditions, as is the bottom of the model that extends into the pre-Tertiary volcanics. The top boundary is specified with a recharge flux, as described later in this chapter.

Twenty-seven head observations, measured in 14 wells, are used to prescribe fixed heads on the northern and eastern boundaries. Five observations at different intervals in UE-20f, west of the Boxcar and West Boxcar Fault, and six observations in UE-20h are used to set the northern boundary. One measurement in UE-20f is the only observation, boundary or interior, in the deep Belted Range Aquifer (BRAQ). All six measurements in UE-20h are within the CHZCM HSU, thus providing less vertical gradient information on the eastern side of the Boxcar Fault.

Interpolation of head along these boundaries between the observation points is achieved by simulating steady-state heads in each boundary plane while maintaining hydrostratigraphic definitions. Resultant boundary heads on the northern and northeast boundary are shown in Figure 3-2. The HSUs present in the northern and eastern boundaries are shown in Figure 3-3. The BFCU separates the high heads in the lower units from the low heads in the upper units in the western part of the northern boundary, whereas the West Boxcar Fault separates the high heads to the east from the low heads to the west, above the BFCU. Model sensitivity to this process of specifying heads on the northern and northeastern boundaries is examined in Section 4.3.4.

The western side of the model domain coincides approximately with the Purse Fault and is modeled as a no-flow boundary. This fault and the area immediately to the west were declared a zone of hydrologic discontinuity by O'Hagan and Lacznik (1996). Their contours indicate little flow across the Purse Fault in the northern and central portion of the sub-CAU model's western boundary. Across the southern portion of the western boundary, the gradient determined by head observations in ER-20-5 and the new wells ER-EC-6 and ER-EC-1 indicate potential southwesterly flow. However, ER-EC-1 is outside the model domain, as is the west side of the southern projection of the Purse Fault. To incorporate its head measurement in an assessment of a possible specified head boundary condition on the southern portion of the western boundary, it would be necessary also to include the new geologic interpretations of that region (completed after this study). Therefore, in this study the southern portion of the western model domain is treated as a no-flow boundary, but its potential impact on pulling pathlines to the southwest is considered later in the transport simulations. Heads along the southern boundary in the Timber Mountain Caldera are set by subtracting 0.25 m of head from the observation at the ER-EC-6 well, consistent with the gradient from the ER-20-5 wells to ER-EC-6. The lower portions of the eastern domain

coincide with the West Greenly Fault and are modeled as a no-flow boundary, primarily because groundwater table contours are approximately normal to the fault in this region (O'Hagan and Lacznia, 1996).

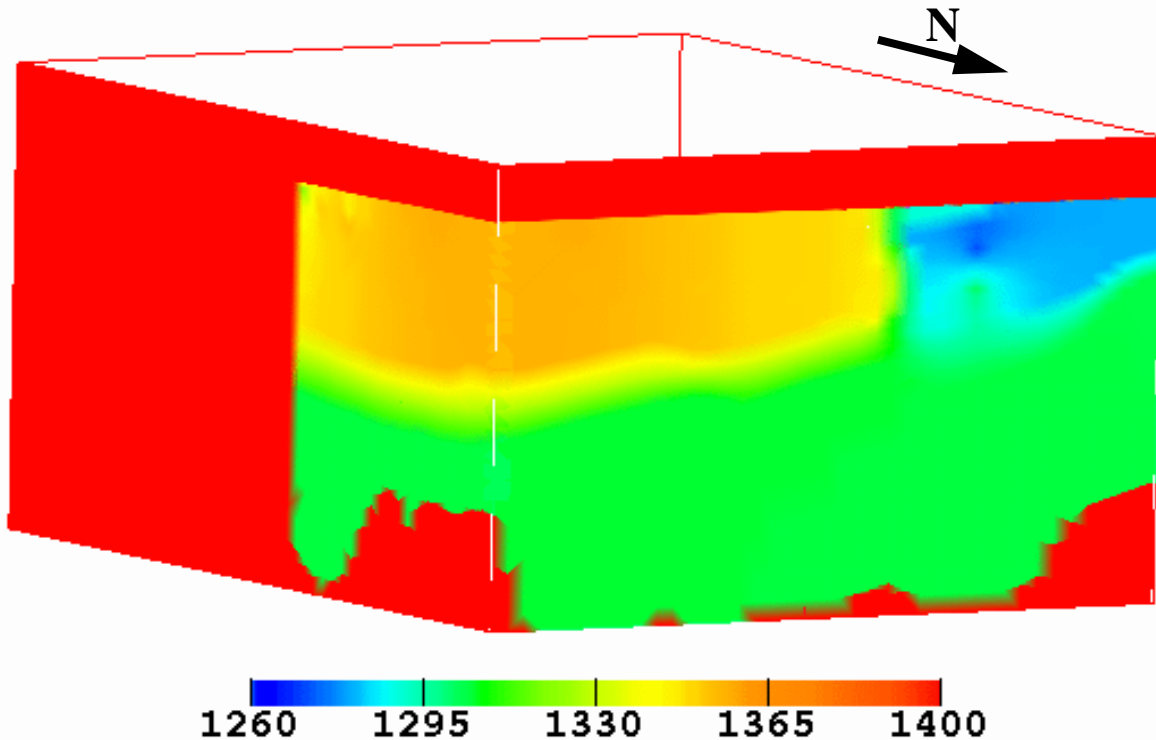


Figure 3-2. View of fixed boundary heads, in meters, on the northeast corner of the sub-CAU model domain.

3.2.2 Head Observations

Table 3-1 lists data for the wells used in the sub-CAU model calibration, including locations, observed head, HSU, and whether the observation was used in the model for specifying boundary conditions or for calibration (e.g., an interior well). Figure 3-1 provides a plan-view map of well locations.

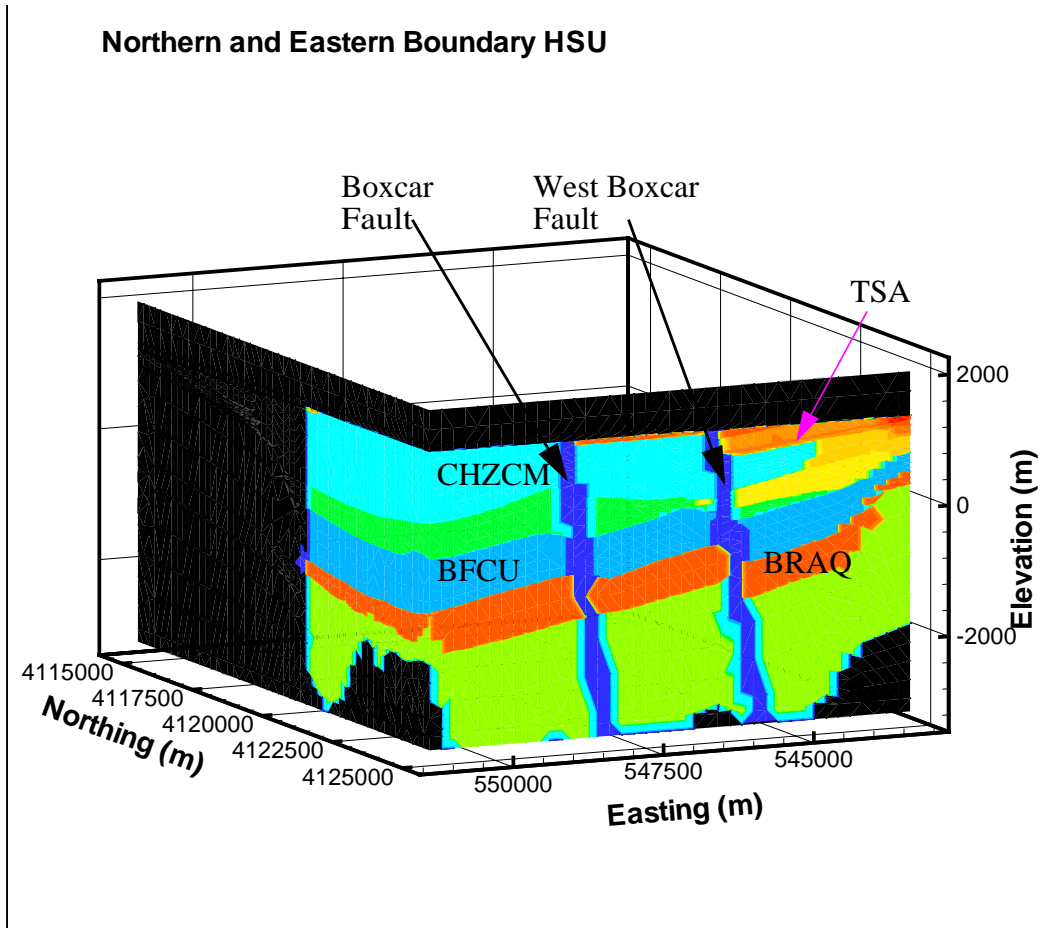


Figure 3-3. HSUs as viewed from the northeast. The Boxcar and West Boxcar Faults are shown in dark blue. Colors indicate different HSUs.

Table 3-1. Interior and Boundary Wells for Model Calibration

Well ID	Northing (m)	Easting (m)	Model Target Elevation (m) ¹	Head Observation (m)	HSU	Boundary or Interior Well
ER-20-1	4119473.7	545271.1	1274.9	1278.1	TPCA	Interior
ER-20-5 #1	4119208.3	546385.9	1163.25	1274.2	TSA	Interior
ER-20-5 #3	4119177	546384.7	809.65	1274.1	CHZCM/ LAVA	Interior
EREC-6	4115728.8	544674.1	1260.09	1273.6	TMCM	Interior
U-20a	4121751.5	550485.9	1326.15	1328.7	CHZCM	Interior
U-20ai	4124119.4	549634.2	1341.45	1356.2	CHZCM	Interior
U-20ak	4122276.7	545309.0	1269.75	1278.5	BENA	Interior
U-20ao	4121175.3	546768.7	1287.9	1317.3	BENA	Interior
U-20as	4119239.5	547765.3	1271.3	1284.5	UPCU	Interior
U-20at1	4122267.3	543535.2	1356.65	1284.4	UPCU	Interior
U-20ax	4120387.5	549114.1	1325.75	1329.7	CHZCM	Interior
U-20ay	4123673.25	549562.44	1355.6	1364	CHZCM	Interior
U-20bb1	4122274.3	544865.5	1211.55	1280.9	UPCU	Interior
U-20bc	4123970.9	545176.7	1284.8	1303.1	UPCU	Interior
U-20be	4119842.5	550743.8	1303.3	1303.8	CHZCM	Interior
U-20bf	4122054.0	549523.2	1328.1	1338.1	CHZCM	Interior
U-20c	4120466.1	546698.7	718.1	1275.36	CHZCM	Interior
U-20ww	4122707.7	550628.0	1253.3	1344.6	CHZCM	Interior
U-20y	4119294.9	546655.9	1190.45	1276.9	TSA	Interior
UE-20c	4120436.3	546871.4	1218.65	1267.0	TPCA	Interior
UE-20d1	4122281.0	543097.3	763.99	1359.74	CHZCM	Interior
UE-20d2	4122281.0	546097.3	1108.15	1272.53	TPCA	Interior
UE-20f	4124896.5	545393.3	-883.6	1301.54	BRAQ	Boundary

Table 3-1. Interior and Boundary Wells for Model Calibration (Continued)

Well ID	Northing (m)	Easting (m)	Model Target Elevation (m) ¹	Head Observation (m)	HSU	Boundary or Interior Well
UE-20f	4124896.5	545393.3	401.31	1298.19	IAQ	Boundary
UE-20f	4124896.5	545393.3	816.6	1268.62	CHZCM	Boundary
UE-20f	4124896.5	545393.3	904.41	1258.26	CHZCM	Boundary
UE-20f	4124896.5	545393.3	1052.45	1271.06	TPCA	Boundary
UE-20h ww	4124985.6	550195.5	732.36	1353.24	CHZCM	Boundary
UE-20h ww	4124985.6	550195.5	786.62	1353.54	CHZCM	Boundary
UE-20h ww	4124985.6	550195.5	843.61	1354.15	CHZCM	Boundary
UE-20h ww	4124985.6	550195.5	951.82	1355.07	CHZCM	Boundary
UE-20h ww	4124985.6	550195.5	1091.57	1353.54	CHZCM	Boundary
UE-20h ww	4124985.6	550195.5	1188.04	1355.07	CHZCM	Boundary
ER-20-6 #1	4123691.8	551362.8	1142.18	1355.4	CHZCM/ LAVA	Boundary
ER-20-6 #2	4123661.6	551328.05	1149.13	1355.2	CHZCM/ LAVA	Boundary
U-20a2 ww	4121756.8	551348.2	1258.26	1343.58	CHZCM	Boundary
U-20a2 ww	4121756.8	551348.2	1269.54	1344.19	CHZCM	Boundary
U-20a2 ww	4121756.8	551348.2	1021.13	1348.16	CHZCM	Boundary
U-20a2 ww	4121756.8	551348.2	981.2	1353.64	CHZCM	Boundary
U-20a2 ww	4121756.8	551348.2	1072.65	1343.7	CHZCM	Boundary

Table 3-1. Interior and Boundary Wells for Model Calibration (Continued)

Well ID	Northing (m)	Easting (m)	Model Target Elevation (m) ¹	Head Observation (m)	HSU	Boundary or Interior Well
U-20a2 ww	4121756.8	551348.2	1082.09	1350.9	CHZCM	Boundary
U-20a2 ww	4121756.8	551348.2	1196.85	1343.89	CHZCM	Boundary
U-20a2 ww	4121756.8	551348.2	1167.13	1344.19	CHZCM	Boundary
U-20ah	4123204.5	551240.9	1336.9	1354.0	CHZCM	Boundary
U-20av	4120677.2	551182.3	1345.3	1336.8	LPCU	Boundary
U-20bd1	4123864.5	551402.5	1295.4	1355.5	CHZCM	Boundary
U-20bd2	4123857.0	551437.3	1285.15	1375.3	CHZCM	Boundary
UE-20av	4120739.3	551255.9	1225.6	1319.5	CHZCM	Boundary
UE-20n1	4121479.0	551276.0	1220.23	1349.4	CHZCM	Boundary

1 - Model target elevations are either the midpoint of the open interval or within the highest permeability HSU when the open interval in the well crosses several HSUs.

3.2.3 Water Table

The steady-state saturated-zone model is simulated with a confined aquifer approximation. The top of the model is represented with an estimate of the water table, as shown in Figure 3-4. This interpolation is generated with heads as measured in the wells that do not penetrate below the upper volcanics below the water table. Thus, the top of the model is not flat, but it also does not change during the course of model calibration described in the next chapter. Minor changes in the calibrated permeability compensate for any errors associated with differences in aquifer thickness between the piezometric surface and the specified top of the saturated model in the uppermost units..

3.2.4 Faults

There currently are no hydrogeologic data from the fault structures in Western Pahute Mesa. Therefore, inferences about the hydrologic role of the faults must be drawn from a set of hydraulic head data measured away from the faults (e.g., Figure 3-4). First, heads in the northeast quadrant of the sub-CAU model, east of the Boxcar Fault, are higher than those to the west of the West Boxcar Fault. The sharp northeast-southwest gradient appears to occur through the Boxcar and West Boxcar Faults. Because no hydrologic data exist between these two faults, determining whether one or both control the gradient is currently impossible. Second, although the Boxcar Faults appear to be barriers to flow, creating a sharp gradient, the Timber Mountain Moat Fault appears to exert little or no control on the flow field. Head data from wells north of the Moat Fault and from the new ER-EC-6 well, south of the fault, indicate that there is not a strong gradient

through the fault. Note, however, that this hypothesis is based on an assumption of predominantly north-south trending flow through the Timber Mountain Moat Fault.

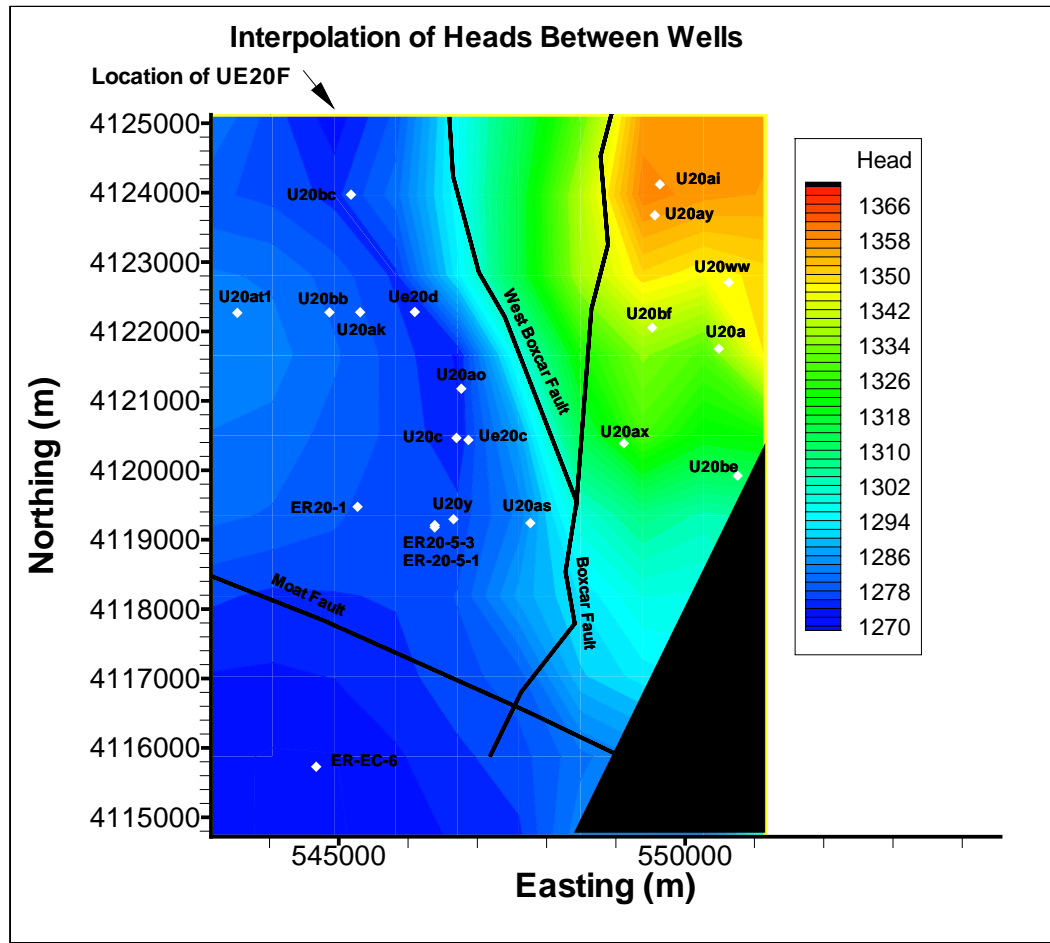


Figure 3-4. Interpolation of measured heads (m) between wells in the sub-CAU domain. Data for this figure are derived from Table 3-1 and only those wells labeled on the figure are used (because they have head data in the upper HSUs close to the water table). When multiple intervals exist, data from the highest elevation are used. This map is only semi-quantitative because the data contoured are measured at various elevations in the different wells. However, this simple contouring demonstrates an apparent gradient at the West Boxcar Fault.

3.2.5 Permeability

Permeability information for the Pahute Mesa area suggests a high degree of variability, even within the same unit. The lowest permeabilities have been generally associated with the zeolitized tuffs because fractures within this type of unit are generally resealed through mineral precipitation. Rhyolite lavas, rhyolite breccia, and vitrophyre were noted as yielding the most water to wells in the model area. However, some rhyolite lavas are also relatively impermeable (Blankennagel and Weir, 1973). Typically, the highest transmissivities are found in the upper 2000

feet of the saturated zone. Table 3-2 shows estimates of transmissivities given by Winograd and Thodarson (1975). Transmissivities at four well sites were calculated by Blankennagel and Weir (1973) from pump tests (Table 3-3). The ranges from the estimates and pump tests span four orders of magnitude.

Table 3-2. Transmissivity Ranges from Winograd and Thodarson (1975) with Equivalent SI Conversion.

Hydrologic Unit	Transmissivity (English)		Transmissivity (SI)	
	Minimum	Maximum	Minimum	Maximum
Welded Tuff Aquifer (WTA)	28 000 gpd/ft. (Jackass Flat) 200 gpd/ft. (Yucca Flat)	100 000 gpd/ft. (both Jackass and Yucca Flat)	347.2 m ² /day (Jackass Flat) 2.48 m ² /day (Yucca Flat)	1240.0 m ² /day (both Jackass and Yucca Flat)
Bedded Tuff Aquifer (VTA)	200 gpd/ft.	1000 gpd/ft.	2.48 m ² /day	12.40 m ² /day
Lava Flow Aquifer (LFA)	range not specified	28 000 gpd/ft.	range not specified	347.2 m ² /day
Tuff Aquitard (TCU)	100 gpd/ft.	200 gpd/ft.	1.24 m ² /day	2.48 m ² /day

Table 3-3. Calculated Transmissivities from Pump Tests Conducted by Blankennagel and Weir (1973)

Well	Transmissivity (gpd/ft.)	Transmissivity (m ² /day)
U-20a2	18000	223.6
UE-20d	44000	546.6
UE-20f	>1000	12.42
UE-20h	11000	136.6

3.2.6 Perched Water

Perched water is suspected to be common throughout Pahute Mesa. However, little work has been done to quantify the nature of these perched systems. One study using a lithium bromide

tracer on the eastern side of Pahute Mesa found very slow groundwater velocities (Hershey and Brikowski, 1995), suggesting that the perched water bodies are time-limited contributors to the groundwater flow patterns on Pahute Mesa. Although recharge is included in the sub-CAU flow model analysis, specific effects associated with perched water are not considered.

3.2.7 Recharge

A uniformly distributed value of 4 mm/yr, as estimated for this portion of the regional domain by DOE (1997b) using the modified Maxey-Eakin method, is applied in our calibration calculations. Sensitivity studies consider variations in this value.

3.2.8 Thermal Gradients

Thermal gradient information suggests that the gradients on Pahute Mesa are on the order of 0.020 to 0.025 °C/m (Sass et. al, 1982). However, extreme variability exists around this range. For example, the thermal log from U-20c (BENHAM) indicates that the thermal gradient is 0.011 °C/m (Potteroff et. al, 1987). Examples of measured geothermal gradients are in Table 3-4. However, note that these gradients are for borehole water. It is not clear, nor has it been demonstrated, how well these measurements represent *formation water* temperatures.

3.2.9 Thermal Effects on Hydraulic Conductivity

Temperature affects groundwater viscosity. For example, as temperature increases, water viscosity decreases and hydraulic conductivity increases. Measurements at UE-20f, the deepest well in the domain, show a geothermal gradient of 0.029 °C/m (Blankennagel and Wier, 1973). With this gradient, the temperature ranges from 28.6 °C at the top of our model to as high as 159.2 °C at the bottom of the PBRCM. With this range in groundwater temperature, hydraulic conductivities vary by a factor of 4.9. Because of the depth of UE-20f, its thermal gradient is used throughout the sub-CAU domain. Using this geothermal gradient and a reference temperature of 121 °C at 12 270 ft below the surface (Blankennagel and Wier, 1973), the temperature at every node within the model is calculated based on the elevation of that node. There is insufficient data to develop an accurate spatial distribution of geothermal gradients over the entire model domain, so this distribution is applied universally. If temperature variation with elevation is not included (assumed to be 25 °C), then groundwater viscosities are overestimated and intrinsic permeabilities of the HSUs will be incorrectly estimated.

Table 3-4. Thermal Gradient Data from the Wells in the Pahute Mesa Domain (Potteroff et al., 1987)

Well Id	Date Logged	Gradient ($^{\circ}\text{C}/\text{m}$)
U-20a2	2-17-64	.02067
UE-20-d	8-14-64	.02428
UE-20-f	6-25-64	.02887
UE-20-h	8-16-64	.01706
U-20c	4-5-65	.01100

3.3 Data Quality Issues

This section presents some of the key data-quality issues associated with calibrating this sub-CAU model. Although data from wells are used to demonstrate the issues in several instances, this section does not provide the basis for data use in the study.

3.3.1 Hydrostratigraphic Model

Although the HSUs are complex and heterogeneous, each layer or unit is modeled as a homogenous layer. One example of this simplification is the representation of the CHZCM by Drellack and Prothro (1997) as a single unit. A later study by Prothro and Warren (2001) identifies the existence of lava flows within the CHZCM unit in the vicinity of the BENHAM and TYBO underground nuclear tests. Further, the geology south of the Moat Fault is modeled as just one unit because of the current lack of information about the Timber Mountain Caldera. However, recent well logs (e.g. ER-EC-6) indicate substantially greater complexity. In another study, Keating et al. (2000) found that the variation in measurements of hydraulic conductivity within HSUs were greater than the variation in the means of such values between neighboring units, thus calling into question the validity of using HSUs as delineators. These and other examples demonstrate that the current hydrogeologic model used for this analysis may need improvement. A new improved model is currently under construction by NTS geologists and hydrogeologists. Nevertheless, the current model provides a reasonable and complex representation of the faulted, layered, and volcanic rock on Pahute Mesa.

3.3.2 Head Observations

Resolution of Hydrostratigraphy

Variations in head observations within HSUs indicate either greater complexity than can be captured with a single set of material properties or significant measurement errors. For example, a head change of more than 70 m between UE-20f and U-20d in the same HSU (Figure 3-1 and

Table 3-1) would be impossible to achieve with a model that also requires significantly smaller gradients within the same HSU. For the same reason, unreconcilable differences in head between U-20ay and U-20ai exist.

For the few wells that contain information about vertical head gradients, there are also some puzzling trends. Primarily, five different head measurements in five different zones are reported for UE-20f. Figure 3-5 shows the measurements as reported by Blankennagel and Weir (1973). These measurements indicate downward gradients in the upper units and upward gradients in the lower units. However, O'Hagan and Laczniaik (1996) only report two of the measurements in UE-20f, in their attempt to characterize the high pressure deep aquifer and a lower pressure upper set of aquifers. Other complexities in assessing vertical gradients include the 87-m difference between CHZCM and TPCA (providing an upward gradient) at UE-20d, as well as an 8-m difference between the CHZCM in U-20c and the TSA in nearby UE-20c.

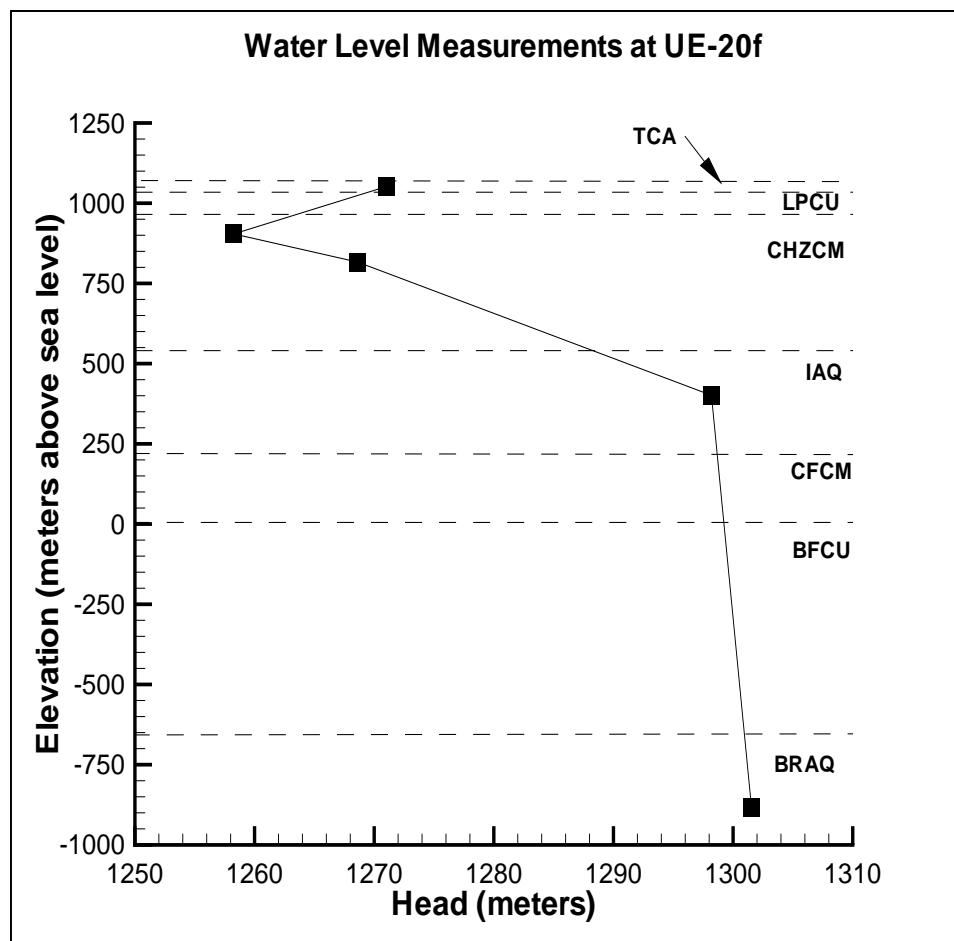


Figure 3-5. Head with depth in UE-20f, as reported by Blankennagel and Wier (1973).

HSUs Without Observations

Of 49 head observations, 35 are in the CHZCM (Table 3-5). There are several units in the model domain that lack any observations, such as the PRBCM, the BFCU, the IAQ, the CFCM, the CHCU, and the PVTA, thereby making calibration of these units speculative. Other units have

only one or two head measurements, which may also add to errors in calibration. These units include the BRAQ (the observation is used only for specifying boundary conditions), the TSA, the LPCU, the BENA, and the TMCM.

Table 3-5. Number of Head Observations for the Boundaries, Internal Domain, and Totals for Each Unit

Unit Name	Total Number of Observations	Boundary Number of Observations	Internal Number of Observations
Pre-Terts	0	0	0
PBRCM	0	0	0
BRAQ	1	1	0
BFCU	0	0	0
CFCM	0	0	0
IAQ	0	0	0
CHCU	0	0	0
CHZCM	35	25	10
TSA	2	0	2
LPCU	2	1	1
TPCA	3	0	3
UPCU	3	0	3
BENA	2	0	2
PVTA	0	0	0
TMCM	1	0	1
Sums	49	27	22

Perched Aquifer Measurements

There are several very shallow wells in the domain that encounter water that is suspected to be from perched aquifers (O'Hagan and Laczniak, 1996). Examples of these wells include U-20at1, U-20bc, and U-20ao. Because this model does not consider the vadose zone, perched systems are included. Data indication perched systems, or the possibility of perched systems, are noted primarily to indicate why they are either not used or weighted with low values for the saturated zone calculations.

Composite Aquifer Measurements

There are wells on Pahute Mesa that were drilled through multiple aquifer units. In deep emplacement wells and exploratory wells, water-level measurements may be composite representations of the several units penetrated. It is unclear what each unit contributes to the overall measurement. For the purposes of calibration, composite observations are assigned to the thickest aquifer unit specified by the well log. UE-20d and UE-20c are examples of wells that penetrate multiple aquifer units.

Construction Disturbances

Many wells, such as U-20ah, U-20at, U-20av, U-20bd1, U-20bd2, and U-20y(TYBO), do not have sufficiently long records to indicate whether the head in the well reached equilibrium after construction. For example, the head measurement at U-20y is reported nearly a month before the borehole was completed (Table 3-6), indicating the well may not have reached equilibrium with the surrounding geologic formation.

Correlation with Pumping Wells

A significant amount of water was pumped from the U-20ww water well from 1983 to 1992; after 1992, withdrawals dropped off dramatically. Water-level records show a 8.76-m decline from 1985 to 1995 and a 1.62-m rise in level from 1996 to 1998 (Fenelon, 2000). Water-level declines in observations at wells U-20be, U-20bf, and UE-20n-1 have been correlated to pumping activity at U-20ww (Fenelon, 2000). These are the only three wells in the model domain known to show a correlation with pumping.

Underground Nuclear Testing

Very few of the wells in the model domain have water-level records prior to the onset of underground testing on Pahute Mesa, making the detection of testing-induced water-level changes difficult, if not impossible. Well UE-20f, which in this calibration is used as a northern boundary well, clearly shows an increase in water levels after the BENHAM test in 1968 (Figure 3-6). A water-level increase of approximately 16 m had still not decayed to the baseline measurements by 1974. There were two other large tests within the vicinity of UE-20f that may have contributed to the sustained water-level increase at UE-20f (Fenelon, 2000). Fenelon also provides a list, including U-20bc, of wells with elevated water levels that are within 1 mile of underground nuclear tests. However, he also notes that many wells on Pahute Mesa are within 1 mile of an underground nuclear test and do not have elevated water levels. Figure 3-7 provides a relative perspective on the announced yields or yield ranges for the tests in the study domain.

Wells drilled after underground testing began may provide erroneous baseline water-level data because pre-testing water levels were not sampled. Without extensive groundwater monitoring on Pahute Mesa prior to the beginning of testing, it is practically impossible to determine which wells have elevated water-level measurements as a result of nuclear testing. However, some measurements are certainly old enough to be considered representative of the pre-testing steady-state condition, such as U-20c and U-20a, which were measured in 1965 and 1964, respectively. The BENHAM test was conducted in well U-20c on December 19, 1968, six years before the emplacement hole for the TYBO test was completed on March 19, 1975. The measurement at TYBO indicates a gradient from TYBO to BENHAM, contrary to the sub-CAU flow pattern described by O'Hagan and Laczniak (1996) and contrary to the gradient indicated by the observations in both ER-20-5 wells. Therefore, our conceptual model continues to assume

south the southwesterly flow. This result is supported by the calibration exercise described in the next chapter.

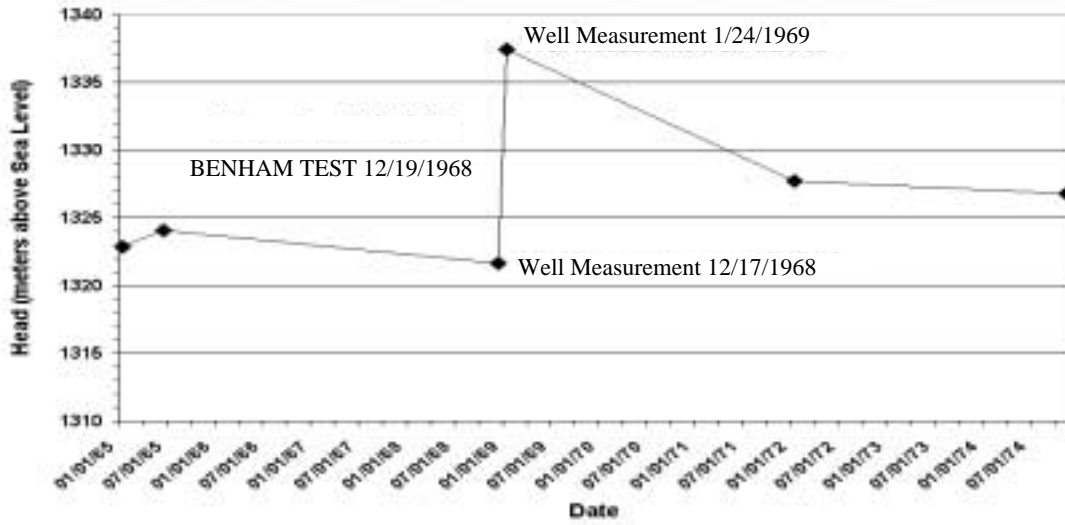


Figure 3-6. Water levels at UE-20f after the BENHAM test (after Fenelon, 2000).

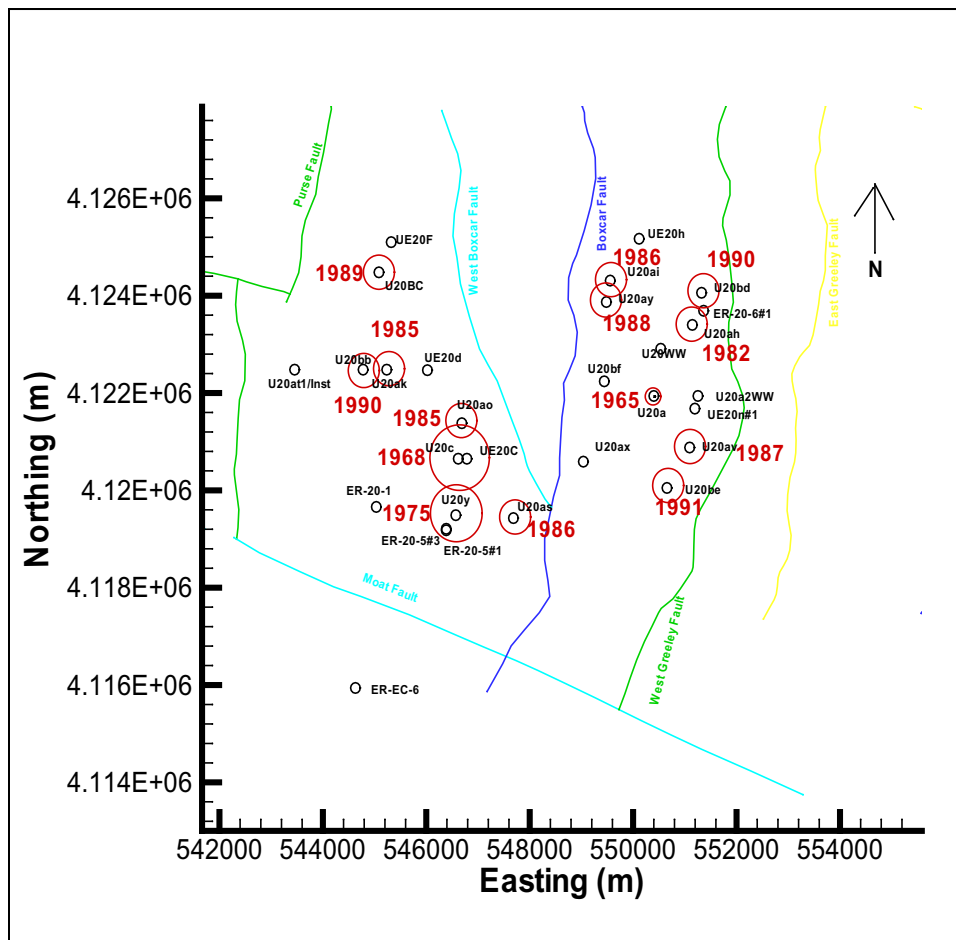


Figure 3-7. Plan view of the sub-CAU domain. Black circles represent wells with hydrologic data and red circles indicate wells that were used for underground nuclear testing. Red circles are sized relative to the unclassified announced yield or maximum of the unclassified announced range in yields of the tests. For example, the BENHAM test conducted in well U-20c had the largest announced yield. Indicated in red is the year that the test was conducted.

Table 3-6. Measurement Dates for Internal Observations

Well	Date of Well Completion	Date of Measurement	Date of Test
Internal Wells			
ER-EC-6	3/28/1999	3/2000	--
ER-20-5 #1	8/3/1993	10/26/1993	--
ER-20-5 #3	6/19/1990	11/3/1995	--
ER-20-1	9/8/1992	6/10/1996	--
U-20a	9/19/1965	2/13/1964	5/12/1965
U-20ai	8/26/1981	10/30/1985	4/22/1986
U-20ak	3/28/1982	2/12/1985	6/12/1985
U-20ao	3/9/1985	5/17/1985	12/28/1985
U-20as	4/16/1986	6/6/1986	10/16/1986
U-20at	8/29/1986	2/13/1987	4/18/1987
U-20ax	8/27/1987	3/31/1992	--
U-20ay	6/17/1987	1/11/1988	6/2/1988
U-20bb	6/11/1990	3/22/1990	10/12/1990
U-20bc	6/28/1988	8/2/1989	10/31/1989
U-20be	7/5/1989	6/5/1991	9/14/1991
U-20bf	10/4/1989	8/29/1990	4/16/1991
U-20c	5/13/1966	2/25/1965	12/19/1968
U-20ww	9/11/1982	2/28/1992	--
U-20y	3/19/1975	2/18/1975	5/14/1975
UE-20c	4/11/1964	2/28/1964	--
UE-20d	3/28/1967	1/14/1965	--

Table 3-6. Measurement Dates for Internal Observations (Continued)

Well	Date of Well Completion	Date of Measurement	Date of Test
Boundary Wells			
ER-20-6 #1			-
ER-20-6 #2			-
U-20a-2	1/13/1976	2/11/1965	-
U-20ah	6/5/1981	4/1/1981	4/25/1982
U-20av	7/28/1986	12/8/1986	4/30/1987
U-20bd	6/20/1989	--	6/13/1990
U-20bd1	--	--	--
U-20np2	--	--	--
UE-20av	3/21/1987	1/15/1987	--
UE-20n1	6/16/1987	11/16/1993	--
UE-20f	11/11/1975	--	--
UE-20h	2/5/1966	--	--

3.3.3 Flux Estimates

There are no direct flux measurements within the Pahute Mesa area. However, independent estimates from Blankennagel and Weir (1973) and DOE (1997b) have similar values. Therefore, these estimates are used directly in the calibration process to reduce uncertainty. Blankennagel and Weir's estimate of 560 AF/year-mile along an east-west cross section converts to approximately 114 kg/s through the 8-km-wide northern boundary of our domain; 80 kg/s is approximately what is derived from the DOE value. However, as discussed in the next chapter, even these estimates incur uncertainties in the modeling effort because the southern boundary is less than 8 km wide and inflow along the eastern boundary is permitted.

3.3.4 Recharge Estimates

Pahute Mesa is generally considered to be a recharge area, although there are no direct recharge measurements in the sub-CAU domain. Without direct measurements, values used during calibration are estimates with a high degree of uncertainty. The Yucca Mountain Project is currently developing a recharge map for the entire Death Valley basin that may help to reduce uncertainties on Pahute Mesa in future studies.

3.3.5 Boundary Condition Assumptions

Heads on the northern boundary are set by only two wells, UE-20h and UE-20f. UE-20h has observations in only one unit but controls the entire eastern portion of the northern boundary. UE-20f is the deepest well in the domain and the only source for deep head observations. This well sets the entire western section of the northern boundary and plays an important role in prescribing vertical gradients within the interior of the model.

The eastern boundary is divided into two sections, the northern and the southern. The northern section has quite a few observations, but there are none for the southern section. The southern section is set to a no-flow condition in the model (colored black in the head-contour figures). Head contours as mapped by O'Hagan and Laczniaik (1996) are nearly normal to this portion of the boundary, providing some justification for assuming no flow across the southern West Greeley Fault.

The southern boundary condition is essentially set by only one well. The flow out of the entire sub-CAU model is controlled by the head observation at ER-EC-6. Gradients between ER-EC-6 and wells north of the Moat Fault are similar to those between wells north of the Moat Fault, indicating that the fault does not cause any substantial gradients. Because there is only one HSU south of the Moat Fault, prescribing a single head value along the southern boundary induces no more error than the simplification of hydrostratigraphy in that region.

The western boundary corresponds with the Purse Fault. This area west of the Purse Fault has been characterized by O'Hagan and Laczniaik (1996) as a zone of discontinuity. However, approaching the Purse Fault from the east (within the model domain considered here), O'Hagan and Laczniaik (1996) show water-table contours nearly normal to the Purse Fault. The analysis follows that little flow occurs across the Purse Fault relative the north-south flow indicated by water levels measured in wells east of the fault. As noted in Section 3.2.1, water levels measured in wells ER-EC-6 (within the model domain) and ER-EC-1 (west of the model domain) indicate a southwesterly gradient. However, ER-EC-1 is outside of this model domain and to use it to specify a boundary condition other than no flow on the southern portion of the western boundary would require the inclusion of new geologic interpretations of that region (completed after this study) as well. Therefore, in this study the southern portion of the western model domain is treated as a no-flow boundary, but its potential impact on pulling pathlines to the southwest is considered later in the transport simulations.

Notably missing from the boundary condition are fluxes into and out of the domain across lateral boundaries. In this study, flux estimates from Blankennagel and Weir (1973) and DOE (1997b) are used as calibration targets rather than as fixed boundary conditions.

3.3.6 Thermal Data Quality

Thermal gradient data are available for several of the wells in the domain. However, because most of the wells at the Nevada Test Site were not completed with the intention of collecting thermal data, the quality of this data is speculative. Thus, for any thermal data from boreholes on Pahute Mesa, there is uncertainty regarding how well the data represent formation water temperatures.

This Page Intentionally Left Blank

Chapter 4: Sub-CAU Flow Model Calibration

4.1 Calibration Objectives

Using the hydrostratigraphy of Drellack and Prothro (1997) in the sub-CAU domain and boundary conditions estimated from available data, our goal with this calibration exercise is to develop a steady-state sub-CAU flow model that can be used to define boundary conditions for the site-scale flow model, which in turn will be used to run transport simulations. The calibration exercise has the following objectives:

- Minimize the residuals between observed and computed groundwater heads.
- Minimize the residuals between estimated and computed groundwater fluxes.
- Identify the hydrologic permeability of each HSU in the domain.
- Identify fault-zone properties.
- Provide boundary conditions for the site-scale transport domain.

4.2 Calibration Process with PEST2000

The calibration process was automated by using PEST2000 (Doherty, 2000), referred to from here on as PEST. PEST is a model-independent Parameter Estimation Software code that uses the Gauss-Marquardt-Levenberg algorithm to solve a non-linear problem by applying an iterative process. The robust algorithm searches for the minima of a multidimensional function and can be applied to a variety of problems. In this application, the multidimensional function is the sum of the square differences between the weighted observed heads and the simulated heads, as well as target fluxes (weighting based on data quality) and simulated fluxes in the flow model. PEST works with FEHM to match the weighted residuals by adjusting the permeabilities of HSUs in the domain. The observations are the head measurements at the interior wells and flux estimates along an east-west transect across the middle portion of the domain. PEST iteratively adjusts permeabilities until the fit to the weighted observations is within specified tolerances or no further improvement can be made. Each PEST model run produces a set of best-fit parameters and a set of statistics that indicate the quality of the parameters.

Using PEST to automate the calibration procedure greatly increases productivity during the calibration process. Automation allows for the addition of hypothesis testing during the calibration. For example, the role of the fault properties on the calibration can be evaluated in a variety of ways that serve to establish limits on the uncertainty associated with a lack of fault data. Because PEST runs in parallel mode by using multiple processors from as many computers on a given network as possible, it shortens the run time for each calibration. In the case of this work, the computer run time was shortened from one week to 8 hours per calibration. Hence, each calibration run could be conducted overnight.

Observation Weights and Flux Targets

The quality of the model calibration depends upon the quality of the data. To avoid strongly influencing the calibration with poor-quality data, the weights of poor-quality observations are lowered. Table 4-1 lists the weights of all interior wells and brief reasons for such weight reductions. Section 3.3 also describes data-quality issues. In this calibration exercise, four different weights are used, depending on our confidence in the data and the location of the observations relative to BENHAM and the ER-20-5 wells. All wells start out with a weight of 1, then some of the weights are reduced. Four of the wells have their weights reduced to 0.5 because their hydrographs do not represent a steady-state system. These four wells are on the east side of the Boxcar Faults; BENHAM and the ER-20-5 wells are on the west side of those faults. By deweighting these four wells, more emphasis is directed in the calibration to matching the heads in the region of greatest interest. Two additional wells are deweighted to 0.1. Well U-20a is east of the Boxcar Fault and has a head observation lower than any other wells around it. It would be required to be a sink in order for the model to match its head. Further, this well is an emplacement hole and therefore was not designed specifically for accurate measurement of groundwater head. UE-20c was the exploratory well prior to constructing BENHAM's emplacement hole, U-20c. The observation in UE-20c is more than 10 m lower than any boreholes in the vicinity. Therefore, it too is deweighted, assuming U-20c is a better measurement in approximately the same location. Finally, weights for four observations are set to zero, indicating zero confidence in the reported measurements as relevant for this sub-CAU calibration. The four weights used in this study are user specific and somewhat arbitrary. They indicate where we are most concerned and which observations apparently represent the steady-state system better than others. A more quantitative approach could be used, such as described by Hill (1998); however, such approaches do not account for the hydrogeologists' evaluation of the data. They only consider variation between multiple measurements from the same location. In this case, we have favored the hydrogeologists' assessment. In future studies, statistical data analysis should also be considered when determining observation weights for calibration.

Nonunique parameter estimates occur when only head boundary conditions are specified during the calibration of a flow model. In other words, the same head distribution could be simulated with greater or lower permeabilities, as long as the permeabilities in all units are scaled the same. The only difference would be the amount of water flowing through the system. Therefore, incorporating a flux target reduces the range of uncertainty in the estimation process. Although no measurements of flux exist for the domain of interest, independent estimates from Blankennagle and Weir (1973) and DOE (1997b) are similar (see Section 3.3.3). Therefore these estimates are used as a calibration target in addition to the head observations. Specified through an east-west cross section through the entire domain, the flux target is set a weight of 1.0.

Table 4-1. Weighting Assignments for Interior Wells in the Model Calibration. Weighting Scale from 0 to 1

Well ID	Head Observation	Weighting	Data-Quality Flags
ER-20-1	1278.1	1	-
ER-20-5 #1	1274.2	1	-
ER-20-5 #3	1274.4	1	-
ER-EC-6	1273.6	1	-
U-20a	1328.7	0.1	Located on east side of the Boxcar Fault, drilled less than 500 ft in saturated rock. ¹ Lowest reported head observation ¹ within ring of wells defined by U-20bf, U-20ah, U-20n, and U-20ax.
U-20ai	1356.2	0.5	Measurements over a period of four years do not show a steady state water level. ² Drilled less than 500 ft in saturated rock. ¹
U-20ak	1278.5	1	USGS ² data do not show steady-state well observations, over a period of three years. Drilled less than 500 ft in saturated rock. ¹
U-20ao	1317.3	0.0	Drilled less than 500 ft in saturated rock; flagged as anomalous by USGS. ¹
U-20as	1284.4	1	Drilled less than 500 ft in saturated rock. ¹
U-20at1	1284.4	1	Drilled less than 500 ft in saturated rock and flagged as anomalous by USGS. ¹
U-20ax	1329.7	0.5	Drilled less than 200 ft in saturated rock and flagged as an anomalously high value relative to the local groundwater system. ¹ May represent locally perched head above zeolite unit due to previous pluvial climate or underground testing effects. ¹
U-20ay	1364	0.0	Local groundwater mound that cannot be captured using current geologic model. Data point used is flagged as an anomaly by the USGS. ¹

Table 4-1. Weighting Assignments for Interior Wells in the Model Calibration. Weighting Scale from 0 to 1

Well ID	Head Observation	Weighting	Data-Quality Flags
U-20bb1	1280.9	1	Data collected by the USGS do not show a steady state water level for three months prior to underground test. ²
U-20bc	1303.1	0.0	Data are flagged as an anomalously high value relative to the local groundwater system and within 1 mile of large underground test. Shallow well drilled less than 500 ft in saturated rock.
U-20be	1303.8	0.0	Water level shows a correlation to the pumping activities at U-20ww.
U-20bf	1338.1	0.5	Water level shows a correlation to the pumping activities at U-20ww.
U-20c	1275.3	1	-
U-20ww	1344.6	0.5	Water-well data may be influenced by draw-down or recovery of well.
U-20y	1276.9	1	Measurement may not be representative of steady-state condition.
UE-20c	1267	0.1	Vertical Gradient between observation at U-20c and this well cannot be modeled with the current geological model.
UE-20d1	1359.74	--	Measurement implies a vertical gradient within the CHZCM that cannot be captured using the current geologic model. Removed from calibration.
UE-20d2	1272.53	1	-
1 - O'Hagan and Lazniack(1996) 2 - Fenelon (2000)			

4.3 Calibration Results

As part of this model's calibration, it is possible to adjust permeabilities in up to 60 unique zones. Such adjustment includes the 15 main HSUs and the fault-zone permeabilities of each HSU in the three different faults. However, because of the limited number of calibration targets (observations from boreholes), attempting to calibrate every possible variable would lead to an under-constrained problem. To reduce the number of adjustable parameters similar parameters must be grouped together. Each group has one main parameter, with the remaining parameters linked to it. When PEST adjusts the permeability of the main HSU, the permeability in the linked HSUs change by the same proportion. With each subsequent calibration run, the groups are modified and the permeabilities in insensitive HSUs are set to fixed values, thereby removing them from the calibration. Further, during the calibration processes, the significance of the thermal correction with elevation (see Sections 3.2.8, 3.3.6, and 3.2.9) was investigated.

The calibrated permeabilities that lead to the lowest residuals between model results and field observations are shown in Table 4-2, with comparisons to the ranges given by Drellack and Prothro (1997) and the calibrated model without a thermal correction. Contour plots drawn at elevations of 1185 and 820 m are shown for this calibration (Figures 4-1 and 4-2) and a north-south cross section near BENHAM is shown in Figure 4-3.

The primary calibration used a target of 80 kg/s across the northern boundary, based on north-south flux estimates of Blankennagle and Weir (1973) and DOE (1997b) (see Section 3.3.3). This target was weighted with 1.0 and was matched almost perfectly in the calibration. However, Section 4.3.4 discusses the impacts of uncertainty with respect to where this target is prescribed.

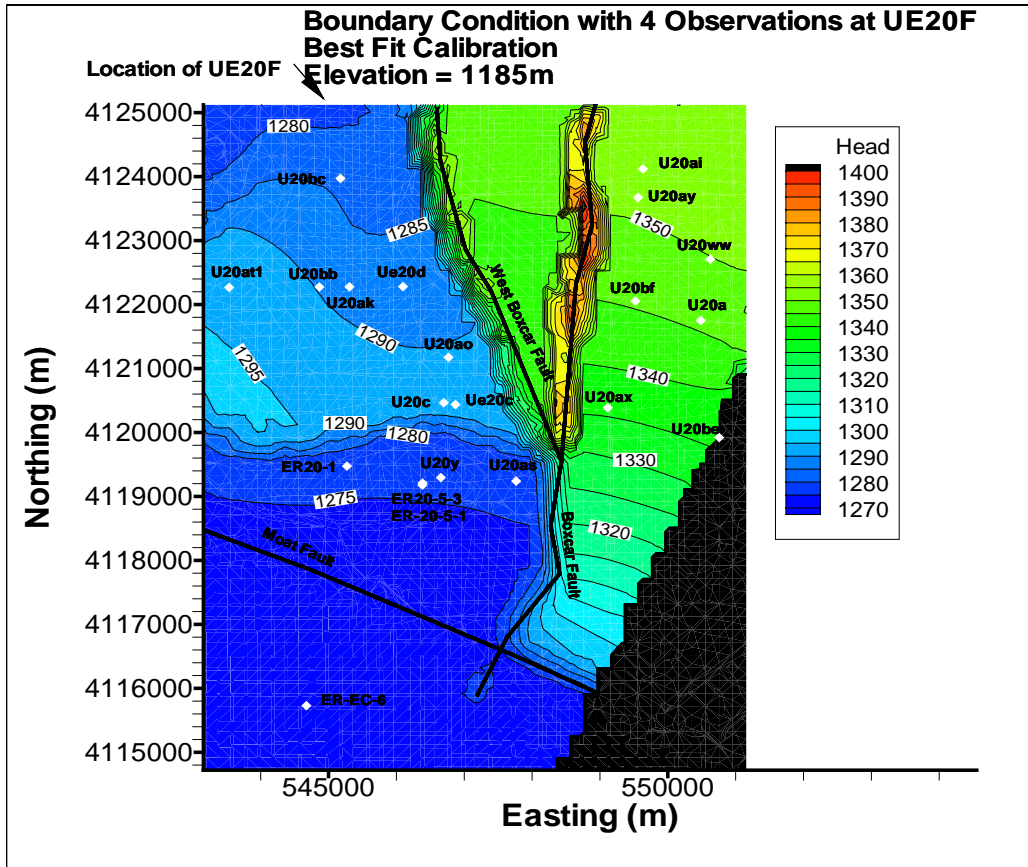


Figure 4-1. Plan view of the sub-CAU model domain showing the contours of the best-fit calibration at an elevation of 1185 m. The apparent water mounding over the faults is an artifact of low fault-zone permeabilities and uniform recharge at all locations. If the vadose zone were modeled, then the recharge in the fault zones would be diverted. This error could be corrected in future models by neglecting recharge in fault zones and, possibly, increasing it appropriately in neighboring zones.

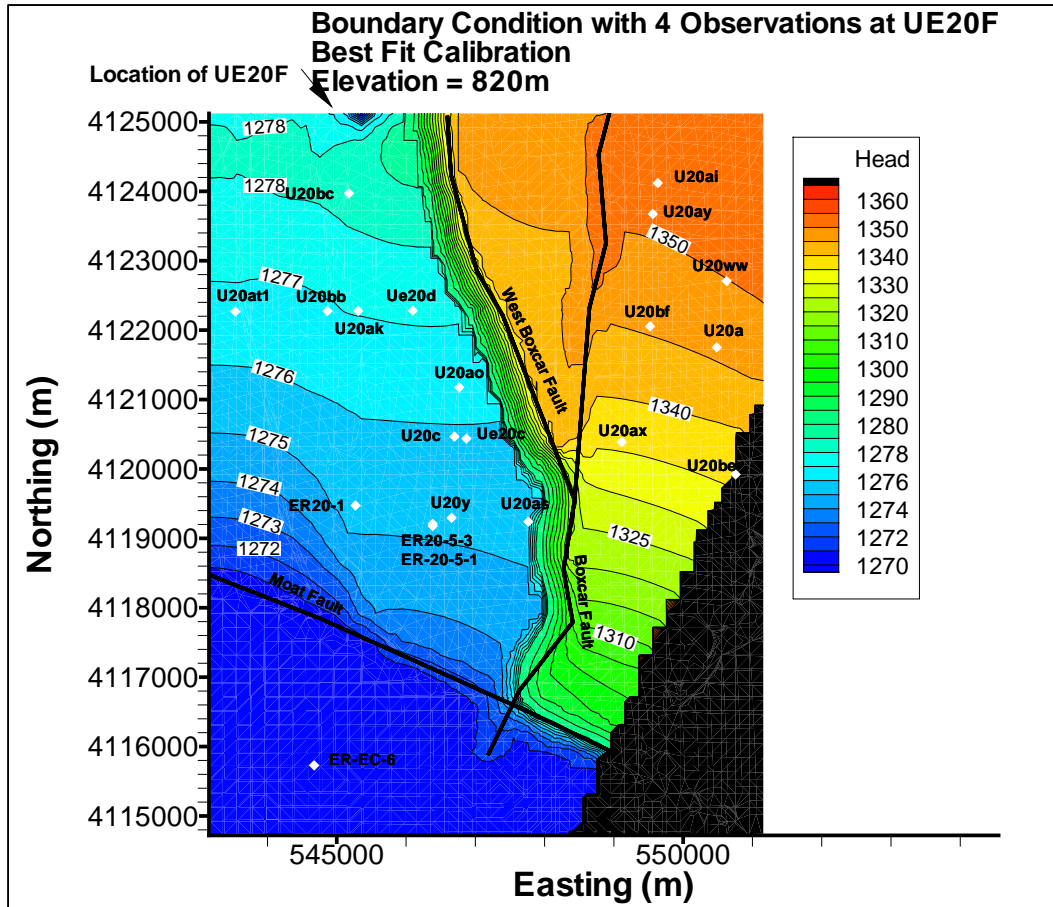


Figure 4-2. Plan view of the sub-CAU model domain showing the contours of the best-fit calibration at an elevation of 820 m.

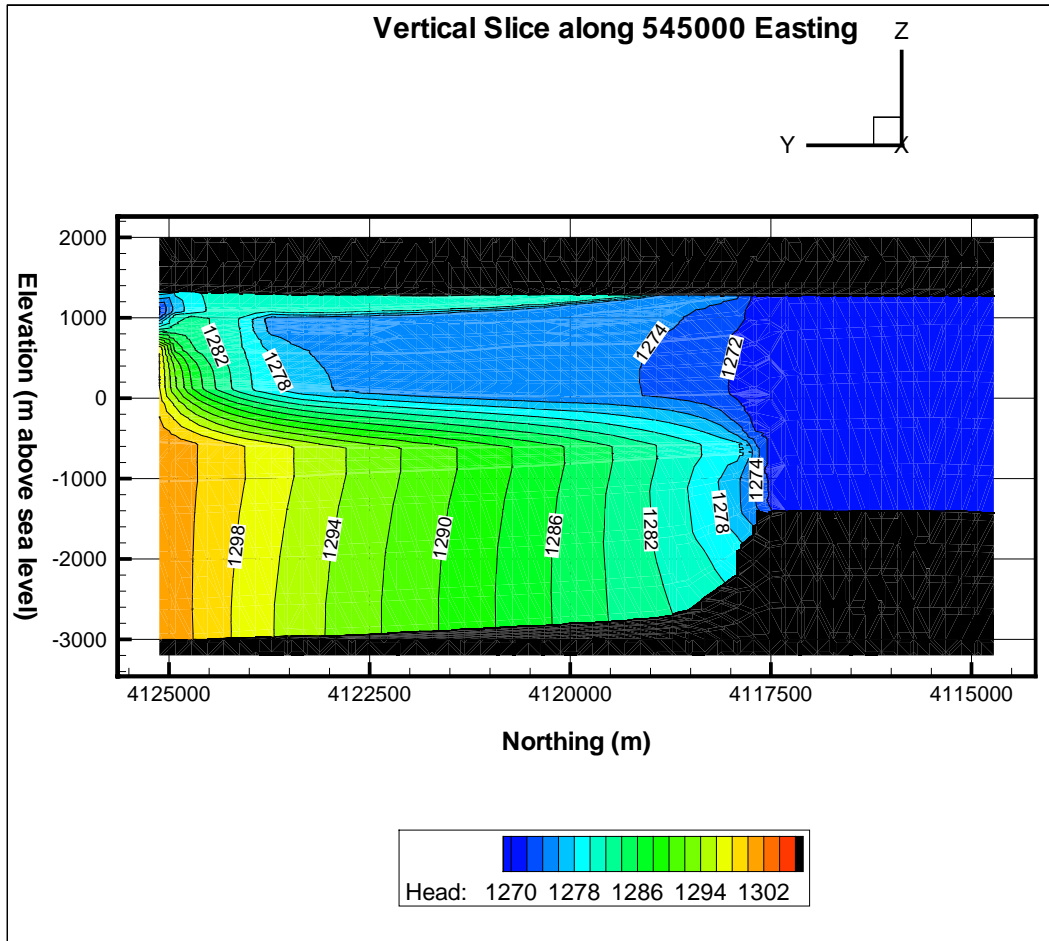


Figure 4-3. Vertical slice along easting 545000. Note the high pressure in the deep units preserved by low permeability units overlying the BRAQ HSU. This model also captures the shallow downward vertical gradients.

Table 4-2. Comparison of Calibrated Permeabilities Resulting from a Thermal Viscosity Correction. The Estimated Ranges from Drellack and Prothro (1997) are also Included for Comparison.

HSU	Drellack and Prothro (1997)		Calibrated Model Without Thermal Correction	Calibrated Model With Thermal Correction
	Minimum Permeability (m ²)	Maximum Permeability (m ²)	Permeability (m ²)	Permeability (m ²)
PRBCM	6.6e-15	6.6e-12	8.43e-15	8.43e-15
BRAQ	6.6e-13	2.0e-11	5.9e-14	3.11e-13
BFCU	1.3e-15	6.6e-13	1.07e-16	1.87e-16
CFCM	1.3e-15	6.6e-12	1.2e-15	5.93e-15
IAQ	1.3e-13	6.6e-12	1.65e-13	1.55e-13
CHCU	1.3e-15	6.6e-13	2.88e-15	2.88e-15
CHZCM	1.3e-15	2.0e-11	1.13e-13	1.41e-12
TSA	6.6e-12	4.0e-11	3.1e-11	1.0e-11
LPCU	1.3e-15	6.6e-13	5.0e-17	1.75e-17
TPCA	6.6e-13	1.3e-12	6.8e-14	2.199e-14
UPCU	1.3e-15	6.6e-13	4.04e-16	4.04e-15
BENA	1.3e-12	2.7e-11	1.35e-13	1.35e-13
PVTA	1.3e-13	1.3e-12	1.63e-13	1.63e-13
TMCM	1.3e-15	6.6e-13	3.5e-13	1.0e-11

4.3.1 Calibration Features

There were several important observations made during the calibration process. First, the data suggest that the Boxcar and West Boxcar Faults inhibit flow. The wells east of the Boxcar Faults have significantly higher heads than those to the west of the faults (there are no measurements between the Boxcar Faults). To match these head observations during calibration,

at least the West Boxcar and the southern portion of the Boxcar Fault must have a low permeability to preserve the gradient.

Captured in the calibration are vertical gradients in head between deep and shallow units. The northern boundary well, UE-20f, prescribes high heads in the lower portions of the domain that are not observed in the CHZCM wells. The gradient between the BRAQ and the IAQ is less than 4 m, whereas the gradient between the IAQ and the CHZCM is approximately 30 m. To restrict the upward flow of water, the CHZCM must have a permeability low enough to restrict upward flow and preserve the gradient. This high pressure at depth is set with the boundary condition, based on observations at well UE-20f, and is not confirmed by any other measurements interior to the model domain. Thus, there are no calibration targets for this high pressure either.

There are also downward vertical gradients in the very shallow units (Figure 4-4). The ER-20-1 well has a substantial observation record that suggests that the TPCA maintains a much higher head than some of the aquifer units below it. Therefore, the LPCU must be parameterized with low permeability to maintain the higher head in the shallow units above it.

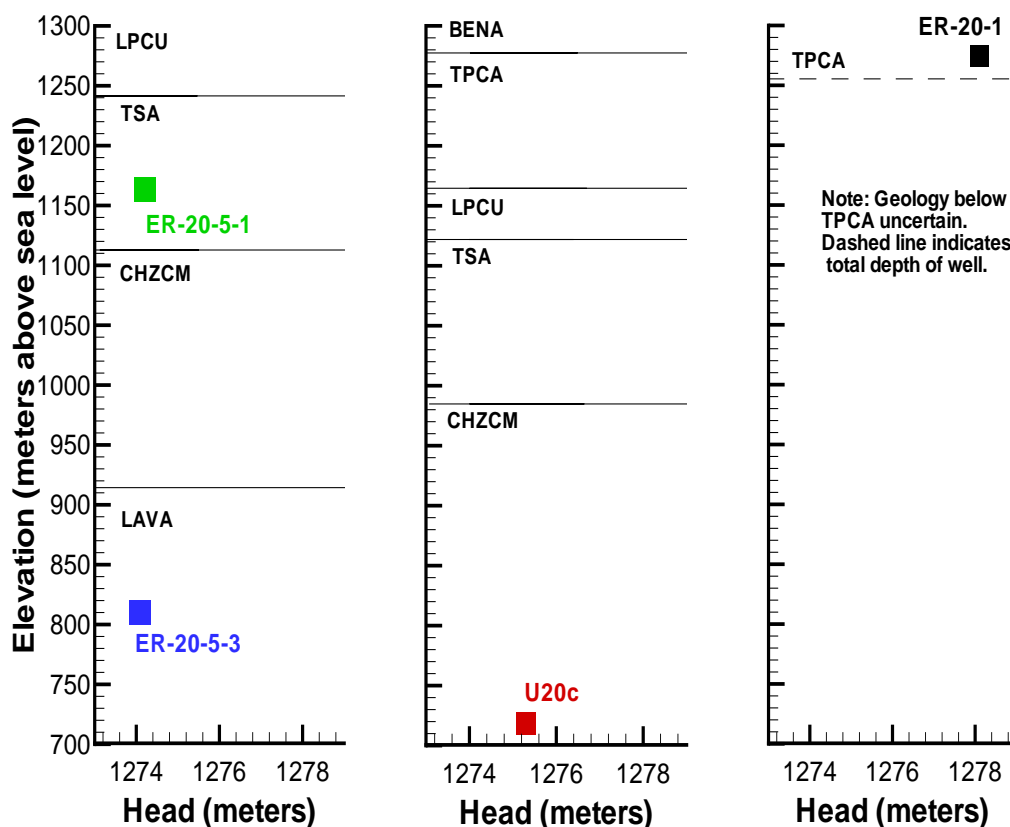


Figure 4-4. Head observations at wells ER-20-5 #1, ER-20-5 #3, BENHAM (U-20c), and ER-20-1. Note the horizontal gradient of a little over a meter between BENHAM and ER-20-5 #3 and vertical gradient of almost 3 m through the LPCU. Data at ER-20-5 wells indicate almost no vertical gradient through the upper CHZCM.

The calibration captures these relationships and closely matches the heads at the BENHAM and ER-20-5 wells. An interesting result of the calibration is that it yields a permeability for the CHZCM from the high end of the range. This is due to the composite nature of the unit. In addition to low-permeability zeolitic material, this unit also includes high-permeability lava flows (Prothro and Warren, 2001) that increase the overall permeability of the unit modeled here as a homogenous block. Although a substantial portion of the CHZCM may be low-permeability, altered, bedded tuff, the volume modeled must account for higher permeability contributions to the overall flow field.

4.3.2 Calibration Guidelines: Where Does this Study Fit in?

Hill (1998) suggests several diagnostic statistics to be considered during and after model calibration. These statistics also correspond to statistical information given in a PEST calibration and serve to assess the quality of the calibrated model as well as the assumptions about weights. Listed below are the statistics and a brief discussion relating the guideline to this calibration effort.

1. Observations and parameter sensitivities play an important role in prediction and model calibration. PEST computes composite sensitivities for each parameter and observation. The composite sensitivities for each parameter are related to the sensitivity of the other parameters with respect to all observations. The parameter composite sensitivity is defined in PEST as $s_i = (J^t Q J)_{ii}^{-1/2}$, where s_i is the composite sensitivity of parameter i , J is the jacobian matrix, and Q is a diagonal matrix of the square weights of the observations. In this case, the permeability parameters of the CHZCM, IAQ, LPCU, and TMCM have the largest importance in the calibration based on the large sensitivity value (Table 4-3). The Boxcar Fault has the lowest sensitivity and is the calibration's least important parameter. This is because we set the northern head boundary condition such that the steep gradient occurs through the West Boxcar Fault. The observation composite sensitivity is a measure of the sensitivity of that observation to all parameters involved in the parameter estimation process. The composite sensitivity of observation j is $s_j = [Q(JJ^T)]_{jj}^{-1/2}$. The sensitivity of an observation will be largely due to the assigned weight. Because of the large composite sensitivity value calculated for each of these observations, the important observations for this calibration are ER-20-1, ER-20-5 #1 and #3, U-20ak, U-20as, U-20at1, U-20bb1, U-20c, U-20y, UE-20d2, and the flux (Table 4-4). Each of these observations were given a higher weight because of their proximity to the site scale model domain used for subsequent transport calculations. This tool could be used to evaluate the value of proposed well locations and sampling intervals.

Table 4-3. Composite Sensitivities for Adjustable Parameters

Parameter name	Composite Sensitivity
IAQ	7.96
CHZCM	56.99
TSA	1.19
LPCU	29.94
TPCA	2.312
TMCM	19.11
Boxcar Fault	0.20
West Boxcar Fault	1.39
South Boxcar Fault	1.09

Table 4-4. Composite Sensitivities for Well Observations

Observation	Composite Sensitivity
ER-20-1	13.88
ER-20-5 #1	5.20
ER-20-5 #3	5.11
ER-EC-6	1.00
U-20a	4.75E-02
U-20ai	0.38
U-20ak	9.35
U-20ao	0
U-20as	19.94
U-20at1	15.35
U-20ax	0.84
U-20ay	0
U-20bb-1	10.25
U-20bc	0
U-20be	0
U-20bf	0.49
U-20c	5.19
U-20ww	0.22
U-20y	5.20
UE-20c	1.11
UE-20d2	5.21
flux	58.53

2. Standard error of weighted residuals indicates how well the model fits the data. The smaller the values, the better the fit. PEST calculates the standard error by finding the square root of the standard variance. The standard variance is calculated by dividing the sum of the squared weighted residuals by the system degrees of freedom. The system degrees of freedom is the number of observations with non-zero weight plus the number of prior information articles with non-zero weight minus the number of adjustable parameters. For each group, the variance is simply the contribution to the sum of the squared weighted residuals divided by the

number of observations with non-zero weight. For this calibration, the observations are divided into four groups, three groups for observations and one group for the flux. The groups are described in Table 4-5. Observation group 1 consists of wells considered critical to the calibration, such as the BENHAM and TYBO wells. Group 2 includes the observations on the east side of the Boxcar Fault and group 3 are poor-quality observations in and around the site scale domain and ER-EC-6 (not considered poor quality), which is south of the Moat Fault. Group 1 has 10 non-zero weighted residuals with a standard error of 1.55. Group 2 has 5 non-zero weighted residuals with a standard error of 3.78. Group 3 has 2 non-zero weighted residuals with a standard error of 1.10. Group 4, the flux through the domain targeted at estimates of Blankennagel and Weir (1973), has only one observation and a very small standard error. The calibration focused on a good model fit with the group 1 and three observations, so the low standard errors of 1.5 and 1.1 are a good indicator the model is successfully fitting these areas and that the weighting scheme is appropriate.

Table 4-5. Group Definitions for Well Observations

Observation	Group
ER-20-1	1
ER-20-5 #1	1
ER-20-5 #3	1
ER-EC-6	3
U-20a	2
U-20ai	2
U-20ak	1
U-20ao	3
U-20as	1
U-20at1	1
U-20ax	2
U-20ay	2
U-20bb-1	1
U-20bc	3
U-20be	2
U-20bf	2
U-20c	1
U-20ww	2
U-20y	1
UE-20c	3
UE-20d2	1
flux	flux_1

3. Weighted residuals should scatter randomly around zero. Minimum and maximum residuals should be fairly close together, with average weighted residuals equaling zero. All weighted residuals together from every group in the calibration appear to be skewed toward negative values. A quick tally of the residuals (Figure 4-5) reveals that 7 are positive and 14 are negative, confirming the interpretation of negatively skewed residuals. The majority of the residuals are fairly small, indicating that the weighting scheme is appropriate. However, one value

appears to have been assigned an improper weight: U-20ai has a weighted residual of -8.2. When evaluated together, all of the residuals are not randomly scattered around zero but have a negative skew. However, the negative skew is almost entirely due to group 2 observations. Table 4-6 shows minimum, maximum, and average weighted residuals. The weighted residuals from group 1 (Figure 4-6) have an average close to zero, a good indication of a proper weighting scheme in this group, as well as a good model fit in this area that is used for site-scale transport. Group 2 has a mean of -1.91 from 5 residuals of non-zero weight. This group is the most likely contributor of the overall negative skew of all the residuals. Group 3 has 2 residuals of non-zero weight and a mean close to zero.

Table 4-6. Basic Weighted Residual Statistics

Group	Minimum Weighted Residual	Maximum Weighted Residual	Average Weighted Residual
Group 1	-2.41 (U-20y)	2.20 (ER-20-1)	8.46E-02
Group 2	-8.21 (U-20ai)	1.16 (U-20a)	-1.91
Group 3	-0.72 (ER-EC-6)	1.38 (UE-20c)	0.33

- Parameter correlation coefficients indicate whether a parameter is likely to be unique. A value less than 0.95 is a good indication that the parameter is unique. The correlation coefficient matrix is calculated as $\rho_{ij} = \sigma_{ij} / \sqrt{\sigma_{ii} \sigma_{jj}}$, where σ_{ij} is the i'th row and j'th column of the covariance matrix. The correlation coefficient matrix in this case suggests that only one parameter relationship is not unique, the IAQ and the CHZCM (Table 4-8). The remaining parameters in this particular calibration are reasonable estimates based on this statistic. The IAQ and the CHZCM are most likely correlated because of their close proximity to each other and the overlapping unit properties. The CHZCM is a heterogeneous mix of low- and high-permeability material, which in this study is modeled as one homogenous unit. The IAQ should be a relatively high-permeability unit and the high correlation indicates that the model cannot clearly distinguish between the two units.

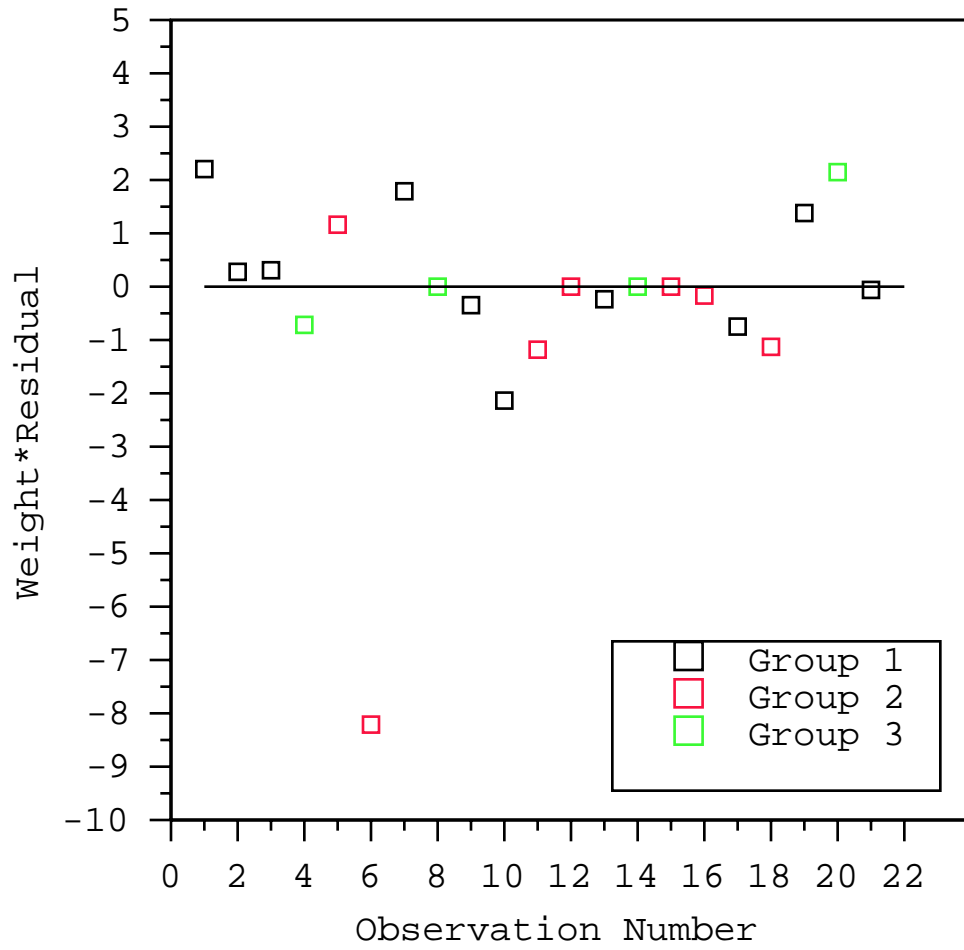


Figure 4-5. Weighted residuals plotted by observation group.

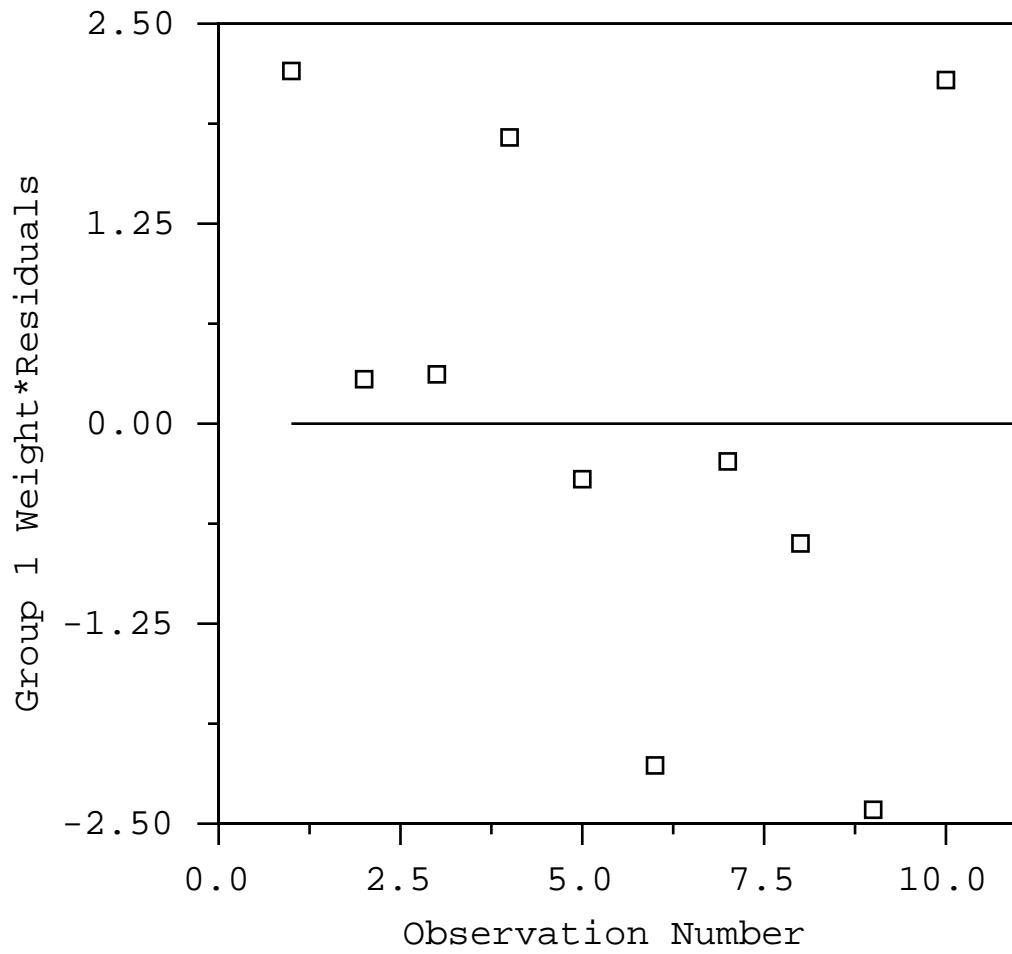


Figure 4-6. Plot of group 1 weighted residuals.

Table 4-7. Correlation Coefficient Matrix for Adjustable Parameters

Parameter name	IAQ	CHZCM	TSA	LPCU	TPCA	TMCM	Boxcar Fault	W. Boxcar Fault	S. Boxcar Fault
IAQ	1.0	-0.98	0.77	0.41	-0.081	0.83	-0.72	-0.0012	-0.095
CHZCM	-0.98	1.0	-0.77	-0.34	-0.08	-0.92	0.78	-0.19	-0.043
TSA	0.78	-0.77	1.0	0.33	-0.20	0.55	-0.50	0.083	-0.28
LPCU	0.41	-0.34	0.33	1.0	-0.55	0.16	-0.22	-0.33	0.0026
TPCA	-0.081	-0.08	-0.20	-0.55	1.0	0.40	-0.34	0.83	0.64
TMCM	0.84	-0.92	0.55	0.16	0.41	1.0	-0.83	0.48	0.35
Boxcar Fault	-0.72	0.78	-0.50	-0.22	-0.34	-0.83	1.0	-0.42	-0.32
W. Boxcar Fault	-0.001	-0.19	0.083	-0.33	0.83	0.48	-0.42	1.0	0.59
S. Boxcar Fault	-0.095	-0.043	-0.28	0.0026	0.64	0.35	-0.32	0.59	1.0

5. Confidence intervals indicate parameter uncertainty. PEST calculations of confidence intervals rely on a linearity assumption that may not extend into parameter space as far as the confidence interval (Doherty, 2000). Therefore, 95% confidence limits do not provide a meaningful range from which to select permeability values but rather suggest a degree of uncertainty around the optimized permeability. Extremely large confidence intervals from this calibration suggest that the LPCU is the only estimated permeability with a high level of certainty. The CHZCM has a large number of observations and the model fit is sensitive to changes in permeability. However, the confidence interval suggests that the unit's complexity is not well represented by the current stratigraphic representation and the estimated permeability. The large confidence intervals for the rest of the parameters suggest that the problem is not well constrained by the available information. However, we know that small changes in parameters with large confidence intervals actually lead to decreased calibration quality. This discrepancy is most likely associated with attempting to represent a complex system with very few data points that result from sampling some of the greatest complexities, such as the high pressure in the BRAQ. We expect that increasing the size of the domain toward a CAU-scale model to capture many more wells while increasing the number of HSUs by only a small amount will lead to tighter confidence limits on calibrated HSU permeabilities.

4.3.3 Calibration Sensitivity to Boundary Conditions

This section describes the impact of various boundary conditions on the model flow field and on calibration results. The development of the northern head boundary condition required determining the impact of the Boxcar and West Boxcar faults, how much information from well UE-20f to use, and the predetermining permeabilities of the units in the boundary condition. The following sections describe how altering these factors changes the flow field.

Fault Barriers

This sensitivity analysis compares the flow fields that result from two different northern boundary conditions, one in which the West Boxcar Fault controls the east-west gradient and the other in which the Boxcar Fault controls the gradient. There are no observations between the Boxcar and the West Boxcar Fault to indicate which fault actually controls the high gradient or if they both exert some control. Note that the calibrated model used to set site-scale mole boundary heads is based on a northern boundary condition with the gradient at the West Boxcar Fault.

With the gradient set at the Boxcar Fault, the heads decrease in the western portion of the domain. The gradient from the northern boundary to the Moat Fault also decreases. These decreases are especially apparent in the contour slice drawn at 820 m (Figure 4-8 compared with Figure 4-2). Additional comparisons can be made with the contour slices at 1185 m (Figure 4-7 and Figure 4-1). Direct comparisons of model differences with the final calibration are shown in Table 4-8. The heads at the ER-20-5 #1, -3, and U-20c have been lowered by one meter. A majority of the wells to the east of the fault do not change. Only the western portion of the domain is sensitive to the location of the high gradient on the boundary condition.

Table 4-8. Comparing Simulated and Observed Heads for Different Northern Boundary Conditions

Well ID	Observation (m)	Best Overall Calibration [with gradient set at W. Boxcar Fault] (m)	Boundary Condition Using Only 2 Observations at UE-20f (m)	Boundary Condition with Gradient Set at Boxcar Fault (m)
ER-20-1	1278.1	1294.4	1290.63	1291.72
ER-20-5 #1	1274.2	1275.12	1272.75	1273.75
ER-20-5 #3	1274.4	1275.09	1272.74	1273.73
ER-EC-6	1273.6	1273.46	1273.46	1273.42
U-20a	1328.7	1345.86	1345.86	1345.85
U-20ai	1356.2	1351.58	1351.50	1351.55
U-20ak	1278.5	1288.35	1283.89	1285.39
U-20ao	1317.3	1290.42	1286.21	1286.84
U-20as	1284.4	1291.65	1289.01	1289.49
U-20at	1284.4	1293.32	1288.77	1291.05
U-20ax	1329.7	1335.61	1335.61	1335.59
U-20ay	1364	1350.92	1350.88	1350.90
U-20bb	1280.9	1289.37	1284.91	1286.52
U-20bc	1303.1	1284.62	1279.64	1282.14
U-20be	1303.8	1336.49	1336.49	1336.47
U-20bf	1338.1	1335.87	1345.86	1345.85
U-20c	1275.3	1275.94	1273.09	1274.26
U-20ww	1344.6	1349.75	1349.74	1349.73
U-20y	1276.9	1275.26	1272.84	1273.85
UE-20c	1267	1291.39	1287.32	1287.75
UE-20d	1272.53	1287.68	1283.227	1284.55

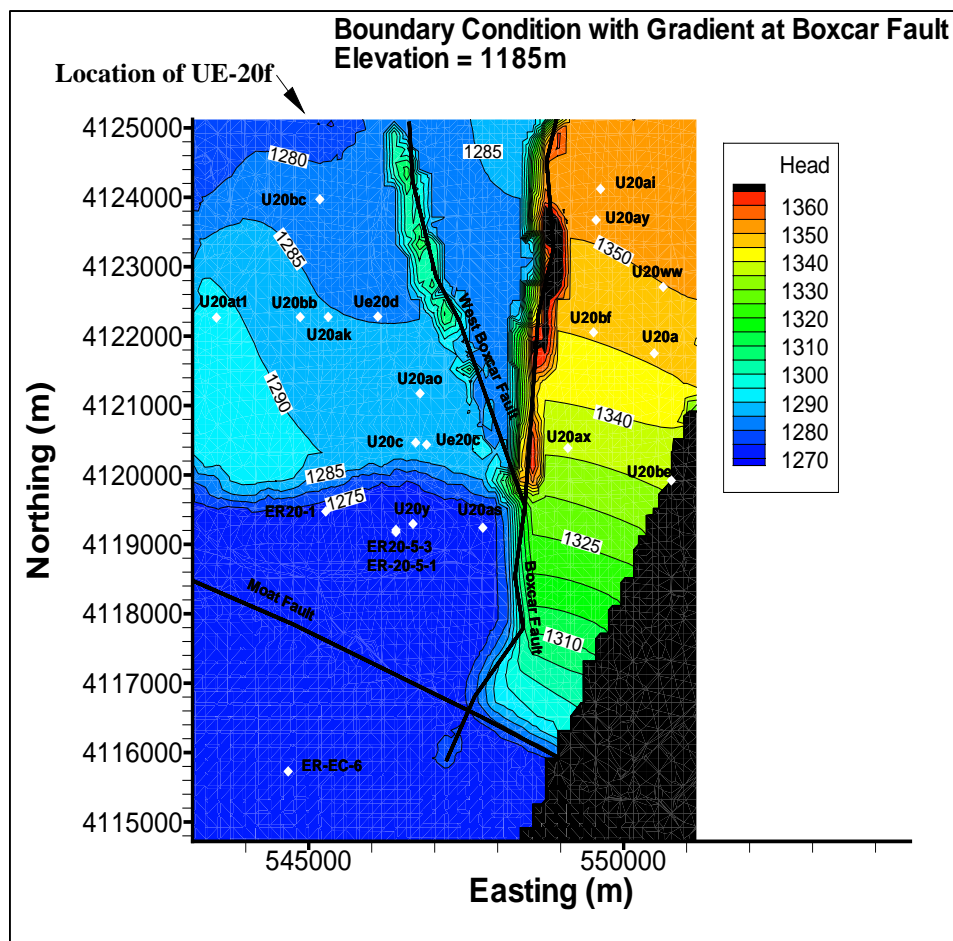


Figure 4-7. Contours in the sub-CAU model domain drawn at an elevation of 1185 m. The high gradient between the Boxcar and the West Boxcar Fault on the northern boundary has been eliminated. The West Boxcar Fault continues to be a barrier to flow. Heads on the northern boundary are based on four observations in UE-20f. Overall, the head has been reduced 5 m west of the Boxcar Faults, and the shape of the flow field west of the West Boxcar Fault has been changed.

UE-20f Influence on the Northern Boundary Condition

The well UE-20f presents some interesting challenges for calibrating the model. UE-20f is the deepest well in the sub-CAU model domain and it does not penetrate below the volcanics of the Silent Canyon Caldera. Observations from packer tests conducted at multiple intervals, isolating specific units, are reported by Blankennagel and Weir (1973). These data suggest that there are at least two changes in the direction of the vertical gradient in this well (Figure 3-5). Using all these data to establish a boundary condition forces flow in the upper unit toward the north, contrary to the regional flow field described by O'Hagan and Lasczniak (1996). Removing the lowest head observation eliminates much of this problem. However, O'Hagan and Lasczniak suggest that only two measurements should be used, the composite measurements for the original

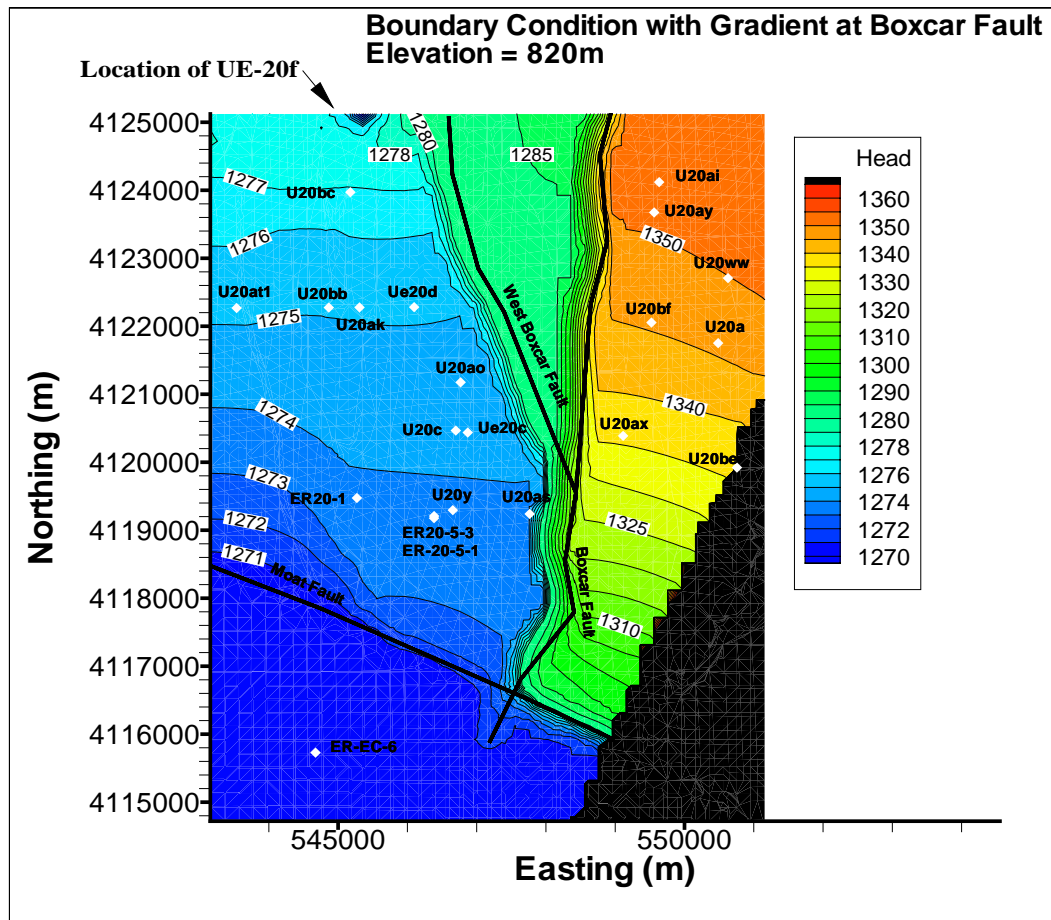


Figure 4-8. Contours in the sub-CAU model domain drawn at an elevation of 820 m. The high gradient between the Boxcar and the West Boxcar Fault on the northern boundary has been eliminated. The West Boxcar Fault still is a barrier to flow. Heads on northern boundary based on four observations in UE-20f. Overall the head has been reduced 5 m west of the Boxcar Faults, and the shape of the flow field West of the West Boxcar Fault has been changed.

shallow well and the newer deep well. Note that this well also shows a clear signal from underground nuclear testing.

Using four observations at UE-20f in our best calibration, our intention was to use as much information for the calibration as possible while preserving the regional flow direction. The sensitivity of this choice of boundary condition is evaluated by comparing changes in the flow field when the permeabilities from the final calibration are used with a different boundary condition that has only two observations at UE-20f. Contour slices drawn at 820 m can be compared with a slice drawn at the same elevation for the final calibration (Figure 4-9 and Figure 4-2). Table 4-8 lists the results at each well, indicating the impact of the reduced information on the boundary. The change in boundary condition at UE-20f lowers the heads by 2 to 6 m at the wells west of the Boxcar Fault depending upon the location.

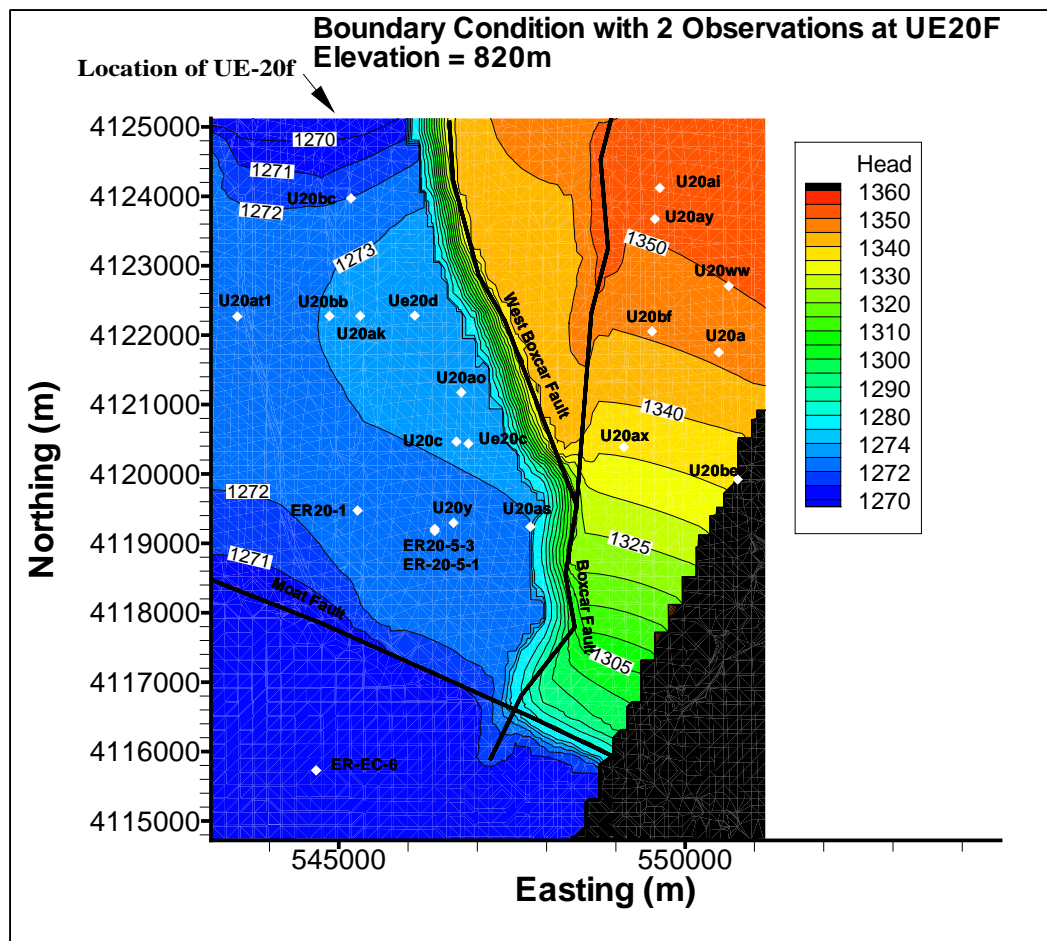


Figure 4-9. Plan view of the sub-CAU model domain. Contours are drawn at an elevation of 820 m. The northern boundary condition is based on only two observations at UE-20f and the flow gradient is set at the West Boxcar Fault. Overall, the head has been reduced 5 m west of the Boxcar Faults and the shape of the flow field has been altered.

Boundary Condition Permeabilities

During the simulations for prescribing heads on the northern and eastern boundaries, the permeabilities were specified prior to calibration with PEST. This is effectively a permeability-weighted interpolation scheme achieved with a flow simulation only along the boundary. Examining the sensitivity of the calibration to the boundary conditions led to the modification of selected permeabilities along the northern boundary. The boundary permeabilities used to compute the northern heads are listed in Table 4-9. Using the new boundary condition, the model was recalibrated with PEST. The alternative calibration resulted in lower permeabilities in the adjustable HSUs, with the exception of the LPCU and the TSA (Table 4-10).

Table 4-9. Comparing Permeabilities used in Computing Heads on the Northern and Eastern Boundary

HSU	Permeabilities used in the Original Northern and Eastern Boundaries	Permeabilities used in the New Northern and Eastern Boundaries
PRBCM	6.0e-15	6.0e-15
BRAQ	5.9e-12	5.9e-12
BFCU	1.18e-17	1.18e-17
CFCM	5.9e-15	5.9e-14
IAQ	1.18e-13	1.18e-12
CHCU	5.9e-14	1.18e-15
CHZCM	1.18e-13	1.18e-15
TSA	1.77e-12	1.77e-12
LPCU	5.9e-13	5.9e-13
TPCA	8.26e-13	8.26e-13
UPCU	1.18e-15	1.18e-15
BENA	1.18e-12	1.18e-12
PVTA	5.9e-13	5.9e-13
TMCM	1.18e-13	1.18e-13

Table 4-10. Comparing Calibrated Permeabilities with Different Boundary Conditions (Underlined HSUs were not Adjustable)

HSU	Original Northern Boundary Calibrated Permeabilities	Modified Northern Boundary Calibrated Permeabilities
<u>PRBCM</u>	8.43e-15	8.43e-15
<u>BRAQ</u>	3.11e-13	3.11e-13
<u>BFCU</u>	1.85e-16	1.85e-16
<u>CFCM</u>	5.93e-15	5.93e-15
IAQ	1.55e-13	1.33e-14
<u>CHCU</u>	2.88e-15	2.88e-15
CHZCM	1.41e-12	8.59e-14
TSA	1.00e-11	4.86e-11
LPCU	1.76e-17	7.98e-17
TPCA	2.20e-14	3.49e-15
<u>UPCU</u>	4.04e-15	4.04e-15
<u>BENA</u>	1.35e-13	1.35e-13
<u>PVTA</u>	1.63e-13	1.63e-13
TMCM	1.00e-11	5.09e-13

4.3.4 Calibration Sensitivity to Internal Assumptions

Flux Magnitude and Target Location

Underflow through Pahute Mesa is estimated to be 560 AF/yr-mile (Blankennagel and Weir, 1973). The sub-CAU domain is 8 km wide along the northern boundary, giving an estimated flux of 114 kg/s across that boundary. Another estimate of flux comes from the regional model (DOE, 1997b) as 80 kg/s for an 8-km-wide cross section. These estimates are in good agreement with each other. Calibrations for which the magnitude of the flux is varied between 114 kg/s and 80 kg/s did not produce substantially different permeabilities. Based on this result, the more conservative value of 80 kg/s along the northern boundary was used in the primary and other calibration-sensitivity simulations.

The use of flux as an observation target in PEST requires that a zone be defined across which the residual between simulated flux and target flux is minimized. In the case of this calibration, the location of the target zone is an important parameter. In previous calibration simulations, the target zone was specified as an east-west transect through the middle of the domain, just south of the flowing portion of the eastern boundary. Thus, the flux across the target zone is the same as the flux out of the model's southern boundary. In this sensitivity simulation, the target zone is changed to the model's northern boundary. The result is that approximately 4 times as much flow crosses the southern boundary as crosses the northern boundary; it enters through the northeastern boundary. Calibrating to this change increases the permeabilities of several HSUs to accommodate the flow increase, but it also decreases a few (Table 4-11).

Table 4-11. Comparing Calibrated Permeabilities with Change in Flux Target Location (Underlined HSUs were not Adjustable)

HSU	Calibrated Permeabilities with Flux Target on Northern Boundary	Calibrated Permeabilities with Flux Target in the Middle of the Domain
<u>PRBCM</u>	8.43e-15	8.43e-15
BRAQ	3.0e-13	3.11e-13
BFCU	1.09e-14	1.87e-16
<u>CFCM</u>	5.93e-15	5.93e-15
IAQ	1.59e-12	1.55E-13
<u>CHCU</u>	2.88e-15	2.88e-15
CHZCM	4.68e-12	1.41e-12
TSA	1.10e-11	1.0E-11
<u>LPCU</u>	1.20e-15	1.75e-17
<u>TPCA</u>	5.90e-13	2.20e-14
<u>UPCU</u>	4.04e-15	4.04e-15
BENA	5.00e-12	1.35e-13
PVTA	1.63e-13	1.63e-13
TMCM	1.77e-11	1.0e-11

Fault structures

The system seems to lend itself naturally to division by the Boxcar Fault. The observation wells to the east of the fault have noticeably higher heads than those observations to the west, suggesting a steep gradient across this fault system (Figure 3-4). This case looks at the extreme scenario of removing the faults from the simulation. Removing fault-specific properties dramatically changes the flow field, confirming that the faults play a major role in determining the structure of the flow field. The head is elevated by 30 m in some locations (Table 4-12, Figure 4-10, and Figure 4-11). Thus, closely matching the heads around the BENHAM test depends on the Boxcar Faults functioning as barriers.

Table 4-12. Comparing Head Values between the Best Overall Calibration with Two Evaluations of Internal Assumptions

Well ID	Head Observation (m)	Best Overall Calibration Head (m)	Removed Internal Fault Properties Head (m)	Doubled the Recharge Head (m)
ER-20-1	1278.1	1294.4	1320.89	1310.23
ER-20-5 #1	1274.2	1275.12	1295.74	1275.24
ER-20-5 #3	1274.4	1275.09	1295.67	1275.21
ER-EC-6	1273.6	1273.46	1273.88	1273.45
U-20a	1328.7	1345.86	1341.32	1345.88
U-20ai	1356.2	1351.58	1346.54	1351.59
U-20ak	1278.5	1288.35	1320.06	1297.14
U-20ao	1317.3	1290.42	1318.58	1300.60
U-20as	1284.4	1291.65	1309.54	1299.51
U-20at	1284.4	1293.32	1318.99	1308.13
U-20ax	1329.7	1335.61	1318.08	1335.65
U-20ay	1364	1350.92	1344.46	1350.93
U-20bb	1280.9	1289.37	1319.91	1299.35
U-20bc	1303.1	1284.62	1311.37	1289.68
U-20be	1303.8	1336.49	1324.88	1336.53
U-20bf	1338.1	1335.87	1335.50	1345.89
U-20c	1275.3	1275.94	1304.84	1276.05
U-20ww	1344.6	1349.75	1346.50	1349.75
U-20y	1276.9	1275.26	1297.75	1275.37
UE-20c	1267	1291.39	1317.38	1302.39
UE-20d	1272.53	1287.68	1320.48	1295.552

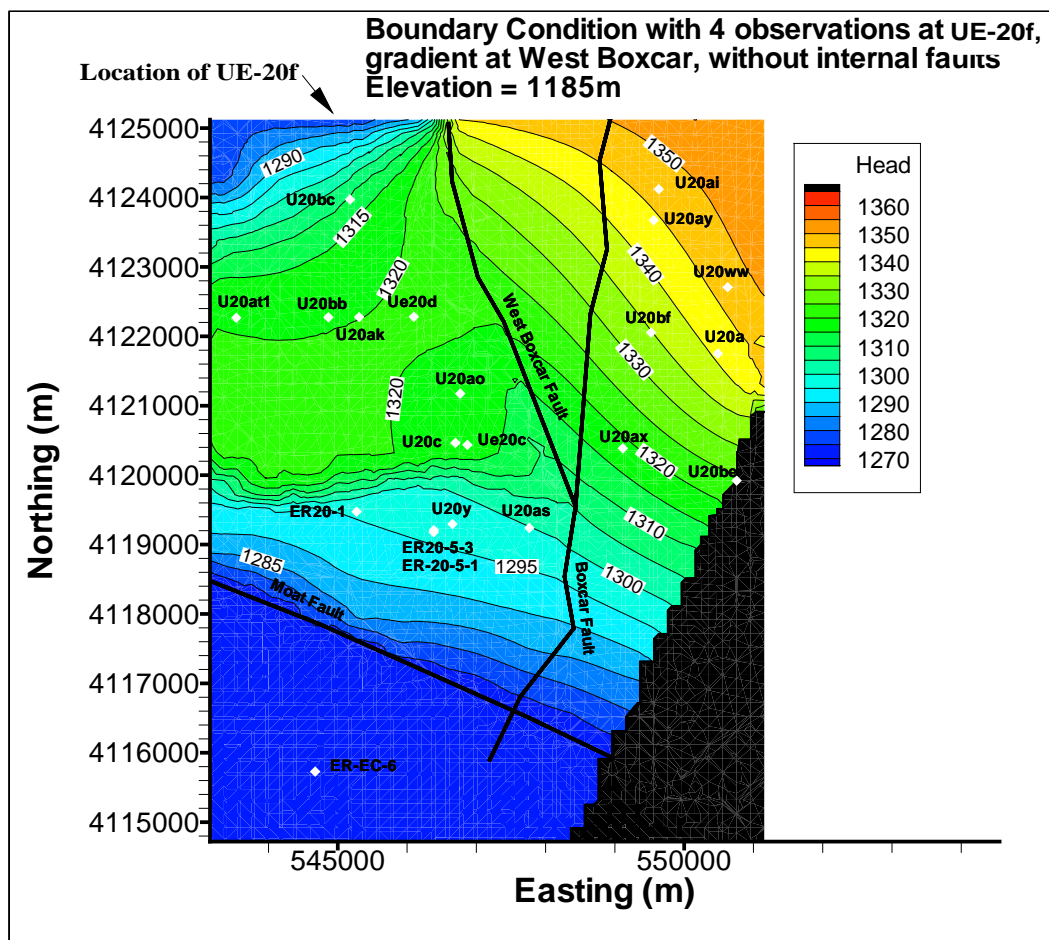


Figure 4-10. Contours in the sub-CAU model domain at 1185 m for the case with no internal faults. The northern boundary condition is based on four observations at UE-20f and a gradient at the West Boxcar Fault. Note the remarkable change in the flow field, with heads west of the Boxcar Faults rising by 30 m in some locations.

Recharge

Recharge for the Pahute Mesa model domain was estimated at 4 mm/yr based on Yucca Mountain information (DOE, 1997b). This value was used in the calibration with PEST, which in turn generated the final calibrated model. To examine the sensitivity of the recharge value we looked at changes in heads at locations within the domain by using final calibration parameters but doubling the recharge. The head is elevated by 10 m in the shallow wells U-20-1 and U-20bc, whereas deeper wells like the ER-20-5 wells only change by one tenth of a meter (Table 4-12, Figure 4-12, and Figure 4-13). To examine its sensitivity, recharge could be dealt with as a calibration parameter, or multiple calibrations could be performed with different recharge rates. This simulation simply shows that with parameters calibrated using 4 mm/yr recharge, a change leads to large differences in simulated heads. Such differences means that to match the heads with larger (and probably smaller) recharge values, significant changes in some HSUs' permeabilities

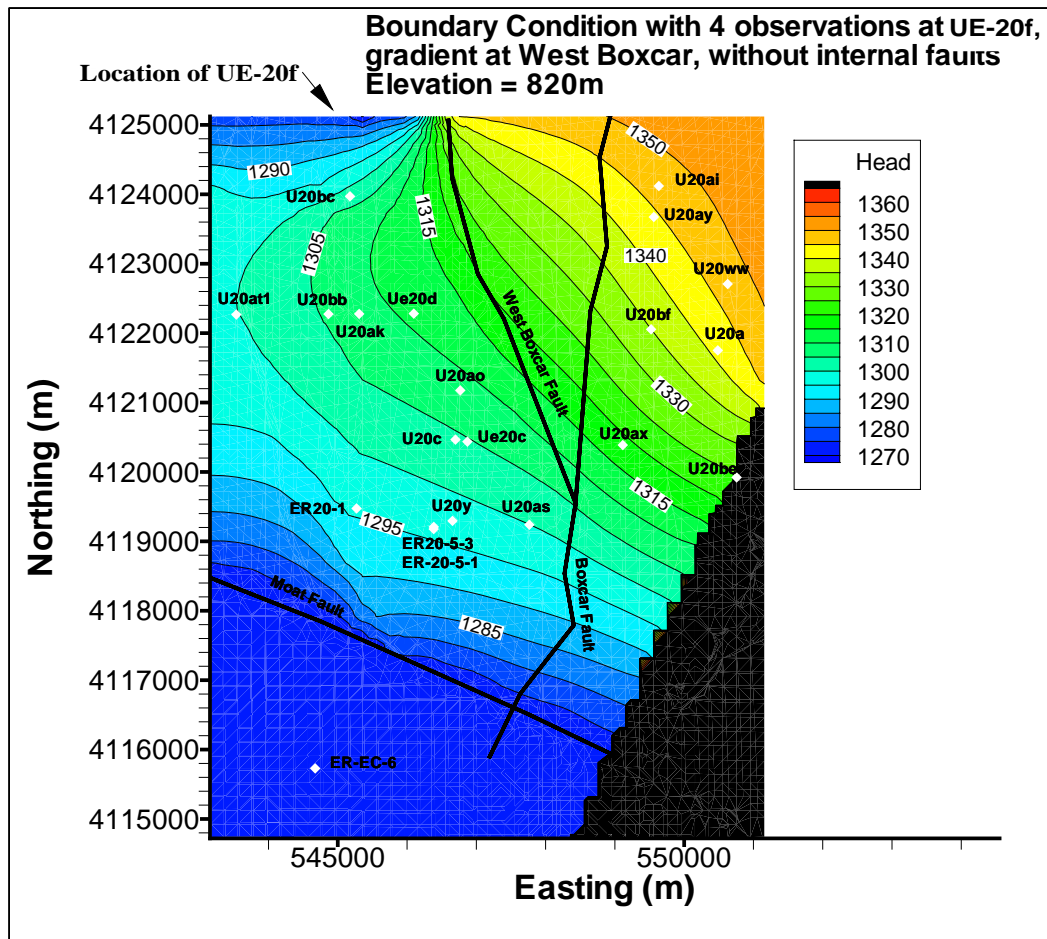


Figure 4-11. Contours in the sub-CAU model domain at 820 m for the case with no internal faults. The northern boundary condition is based on four observations at UE-20f and a gradient at the West Boxcar Fault. Note the remarkable change in the flow field, with heads west of the Boxcar Faults rising by 30 m in some locations.

will be required. Ongoing studies to characterize recharge in this region will contribute to future studies designed to reduce uncertainty.

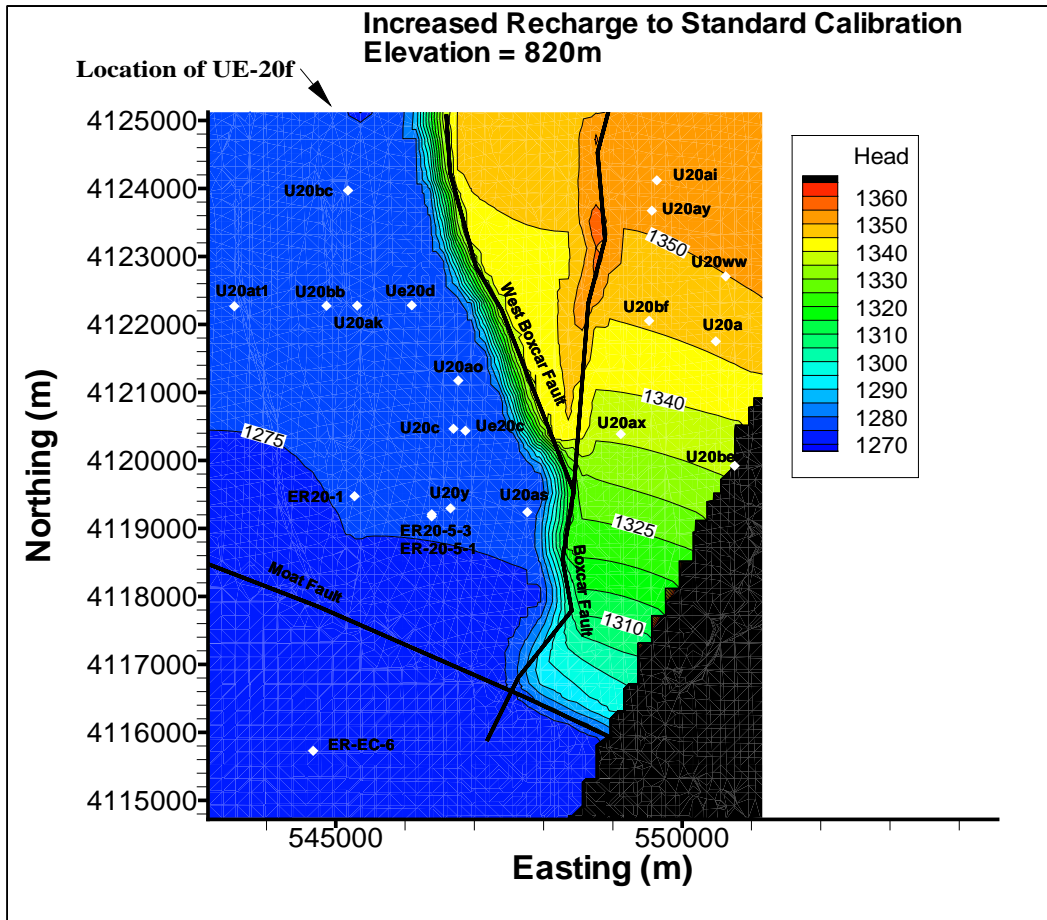


Figure 4-12. Plan view of the sub-CAU domain showing the contours at 820 m for double the recharge of the best-fit model.

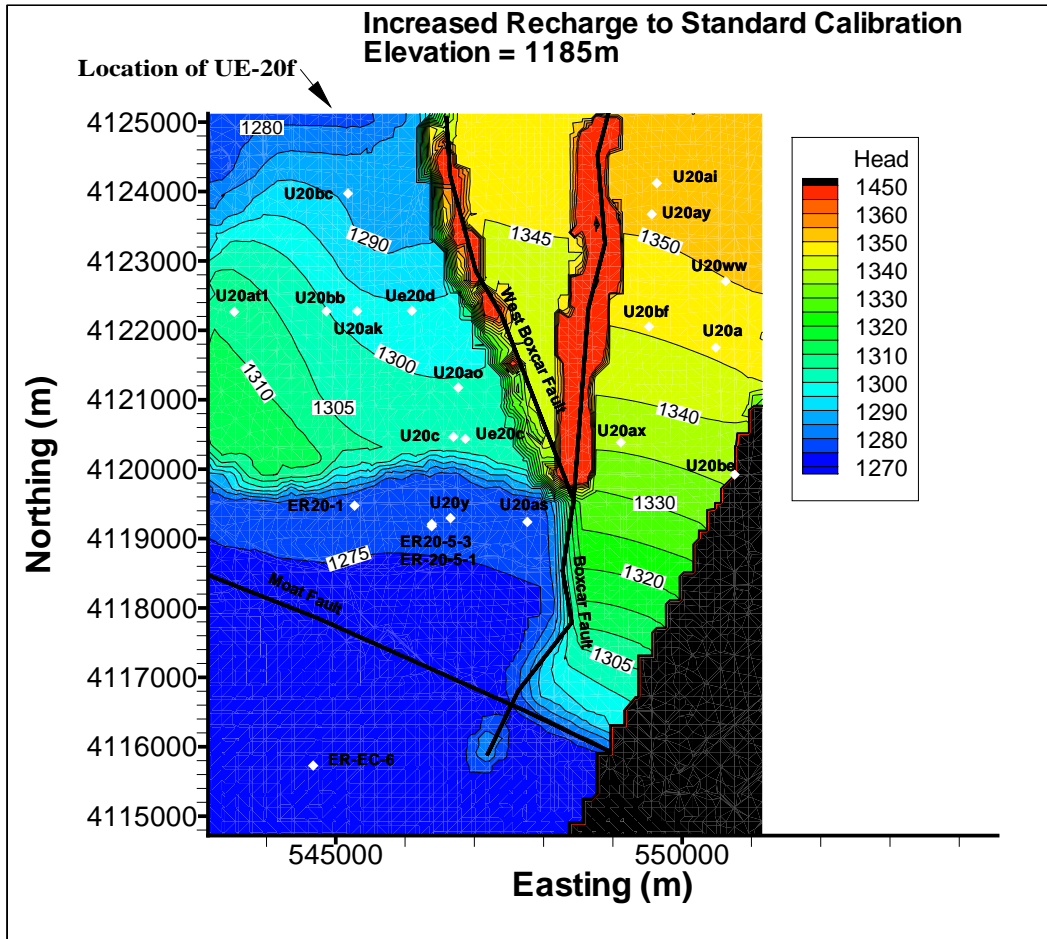


Figure 4-13. Plan view of the sub-CAU domain showing the contours at 1185 m for double the recharge of the best-fit model.

4.4 Summary

For the small domain considered, the calibrated flow model matches observed heads with acceptably low-weighted residuals. Expanding the domain size to include more observations in more HSUs, as will likely occur in CAU-scale models, will increase the calibration quality. However, by using automatic parameter estimation to compute HSU permeabilities, the calibration conducted on this sub-CAU scale model provides reasonable representation of the hydrologic system. Therefore, the heads derived from this model to specify site-scale boundary conditions are appropriately representative of the large-scale system in which the site-scale domain resides. They also represent an improvement over estimates that would be made in absence of the sub-CAU flow model.

The calibration is certainly not without uncertainty, as demonstrated in Sections 4.3.3 and 4.3.4, where sensitivity of the calibration was examined with respect to the following:

- how heads are distributed along the northern boundary due to the internal faults,
- the influence of how head measurements in UE-20f are used to specify the northern boundary head distribution,
- the underflow flux along the northern and northeastern boundaries,
- fault-zone properties, and
- recharge flux.

However, the base calibration presented prior to the sensitivity study yields the best estimates of heads in the model domain, relative to observed heads. This sensitivity study does not provide an analysis of model response to different assumptions about the boundary conditions along the West Greeley and Purse Faults. Much of the West Greeley Fault boundary and all of the Purse Fault boundary are specified as no-flow boundaries in this model. As described in Section 3.3.5, these properties are based on the best current hydrologic analyses of Western Pahute Mesa. Although it is possible to develop a sensitivity analysis to determine how such boundary conditions are specified, no such analysis was conducted for this project. As larger-scale analyses are conducted, it will be appropriate to examine whether the current thinking that little flow crosses those faults, where specified here too, should be reconsidered. Certainly, our best calibrated model shows little flow crossing the Boxcar and West Boxcar Faults, internal to our model domain, thus strengthening the assumption that little flow crosses the two closest faults (east and west) as well.

Chapter 5: Site-Scale Flow Model

5.1 Introduction

In this study, simulations of radionuclide migration are conducted on the site-scale model. The site-scale model domain extends 3.2 km northing, 2.6 km easting, and is 1330 m thick. Figure 5-1 shows the spatial location of the site-scale domain relative to the sub-CAU model domain, the NTS area boundaries, and the mapped faults in the region. The site-scale model is discretized uniformly with 50 m x 50 m x 10 m blocks, which provide a significantly higher resolution than the sub-CAU flow model (200 m x 200 m spatially, variable thickness). This resolution was chosen primarily to capture spatial variability in the physical and chemical attributes of the pathways along which solutes may migrate. Site-scale flow and transport calculations are conducted using the deterministic stratigraphy of Drellack and Prothro (1997), as well as heterogeneous attribute distributions developed by DRI researchers in support of this project (Appendix G). In this chapter, we first describe the distribution of attributes on the site-scale model. Second, we demonstrate the process for establishing boundary conditions on the site-scale domain. And third, we show the results of simulating steady-state flow on each flow field, which will be used in later chapters to simulate radionuclide migration.

5.2 Deterministic HSUs

The deterministic model uses the same HSUs that populated the sub-CAU flow model in Chapter 3. Figure 5-2 shows the layers in a north-south cross section through BENHAM and Figure 5-3 shows transects in the three-dimensional domain. With the addition of a lava unit embedded within the CHZCM mapped by Prothro and Warren (2001), this stratigraphy also provides the framework for the source-term modeling work described in Chapter 6 and Appendix B. Table 4-2 lists the the HSU permeabilities calibrated with the sub-CAU flow model.

5.3 Heterogeneous Attribute Maps

5.3.1 Background

Significant heterogeneities in attributes such as permeability exist at scales smaller than the HSU. In fact, the variability of permeability within an HSU may be greater than the variability in mean permeabilities between two adjacent HSUs. The implications of such heterogeneity for spreading solute plumes due to physical processes (such as channeling, focussed flow, and flow around low permeability zones) and chemical processes (such as uneven distribution of reactive minerals, bringing solutes into contact with, or keeping them away from certain minerals) are significant. Therefore, a portion of this study involves the use of heterogeneous attribute maps developed with geostatistical tools. These tools assimilate statistical information about the distribution of rock types and attributes within rock types and then simulate three-dimensional maps honoring the statistics. The data used in this process often indicate much greater attribute

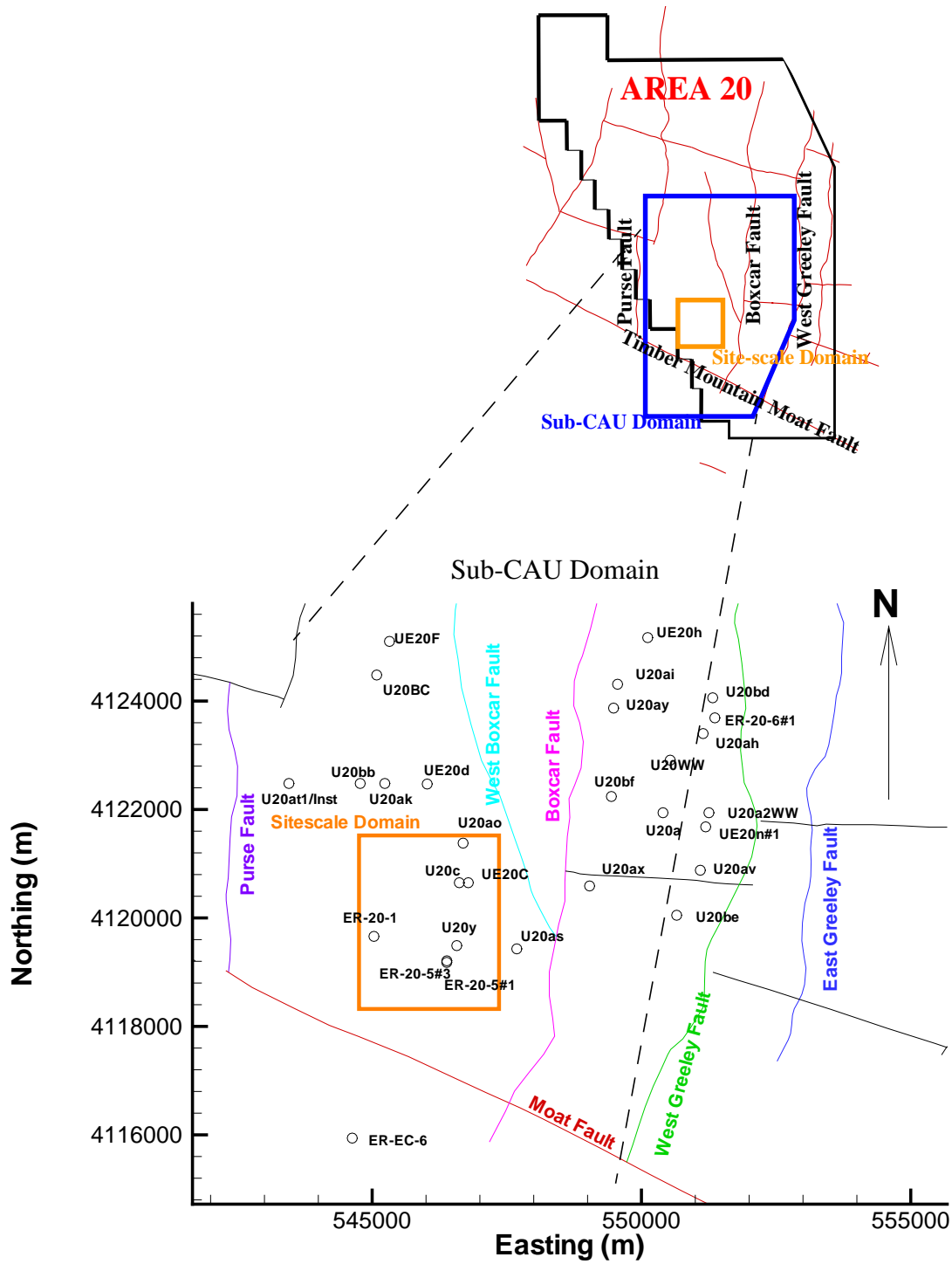


Figure 5-1. Site-scale model domain within the sub-CAU domain in Area 20.

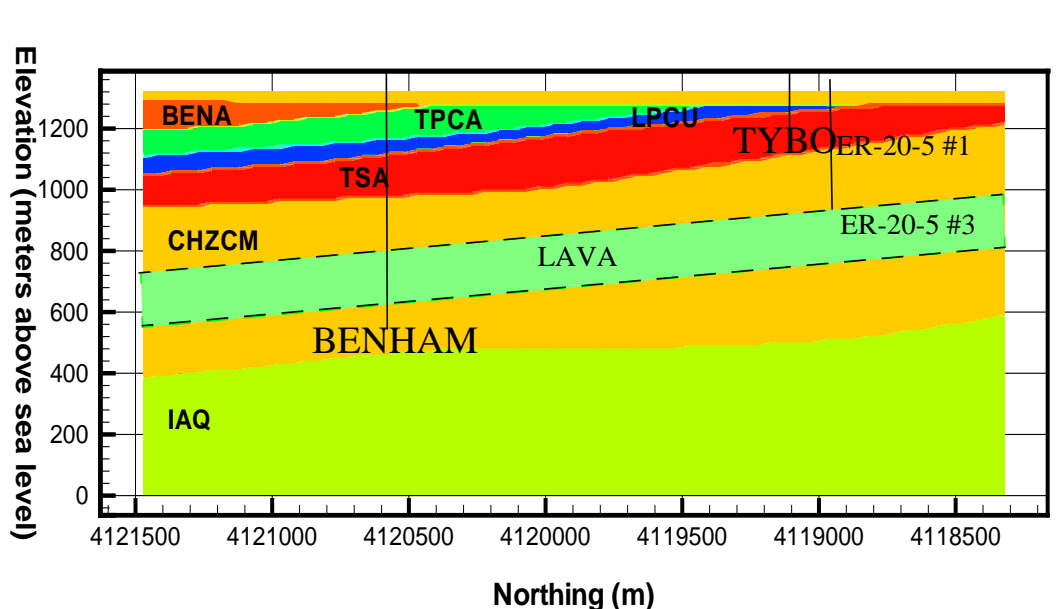


Figure 5-2. HSUs in the deterministic site-scale model. Note, the lava formation mapped by Prothro and Warren (2001) sandwiched within the CHZCM above BENHAM and sampled by ER-20-5 #3 is not part of the CAU-scale HSU models of Drellack and Prothro (1997) or Bechtel (2002).

variability than results from the averaging process of developing deterministic HSUs. For instance, the CHZCM is a large composite material that includes materials ranging from fractured lavas to zeolites. The treatment of this unit as one uniform hydrologic property in the deterministic single-permeability model does not accurately represent the heterogeneity most likely found in that location. Although a single representation of units in a deterministic model does not address the uncertainty associated with making simplifying assumptions about lithologic contacts, multiple realizations of heterogeneous attribute maps do provide a process for assessing the significance of uncertainty in spatial distributions of attributes.

In support of this project, researchers at DRI have analyzed borehole data and simulated heterogeneous attribute maps in the site-scale domain (Appendix G). The primary components of the DRI simulations used in this study are (a) 30 realizations of lithologic classes, (b) 30 corresponding realizations of permeability throughout the entire domain, and (c) simulations of matrix porosity.

5.3.2 Approach

Classes

During the first step, every node in each realization is assigned to one of 5 lithologic classes. The classes include (1) bedded tuff, (2) non-welded tuff, (3) welded tuff, (4) lava, and (5) altered material. A transitional probability simulation (Carle, 1999) generates a spatial distribution of the model classes. This method seeks to reproduce the juxtapositional tendencies

typically found in volcanic settings. Figures 5-3 and 5-4 show a comparison between the deterministic lithology in the site-scale domain with 4 of the geostatistical class maps.

One particularly important feature shown in geostatistical attribute maps is the semi-intact lava formation. This feature was preserved by researchers at DRI upon request following Prothro and Warren's (2001) mapping of a lava bed in the TYBO/BENHAM region, the same lava formation sampled by well ER-20-5 #3. Preserving some degree of continuity in this single class has tremendous impacts on transport simulations reported in later chapters. However, the region of the domain where the welded tuff TSA aquifer sits in the deterministic model was not preserved in the geostatistical simulation. Such a continuous pathway is not guaranteed in the heterogeneous class maps to the upper well ER-20-5 #1, even though Kersting et al. (1999) found indications of transport in both the TSA and LAVA aquifers (as identified in the deterministic model as well as the locations of the open intervals of the observation wells). Figure 5-5 demonstrates the lack of continuity in the welded tuff in the geostatistical simulations. The fact that the LAVA was preserved via user "intervention" and the TSA was not, creates a discrepancy, thereby making it difficult to use and interpret the geostatistical simulations. The design of future models must consider the implications (as highlighted later in the site-scale transport model results) associated with singling out individual HSUs for preservation in a model that does not normally preserve HSUs, as defined in the deterministic model.

During the second step, each class field receives spatially correlated attribute fields that depend upon means, variances, and correlation lengths. Once the classes have been determined in step 1, the attributes within the classes are treated as random variables. The attribute variability is simulated based on an assessment of spatial correlation within the class. Although only the attribute bulk permeability is needed for steady-state flow simulations, solute transport simulations for fractured rock require the attributes bulk permeability, matrix porosity, fracture porosity (the volume fraction of the bulk material associated with fractures), fracture apertures, and fracture density (note that knowing any two of the last three is sufficient). The spatial attribute fields simulated by DRI for this project include only bulk permeability and matrix porosity. Therefore, as discussed in Chapter 7 and Appendix F, the attributes for all fracture properties are estimated for each class, rather than for each location in the domain.

For matrix porosity and bulk permeability, the third step as described in Appendix G involves "construction of a composite attribute field by superpositioning attribute values from the various class specific fields according to the class designation at each grid location". For each attribute, data were analyzed, a population distribution was estimated, and the correlation lengths were estimated.

Permeability

Hydraulic conductivity data range in scale from sub-core plugs to aquifer tests. Each measurement technique has its own advantages and disadvantages in estimating representative hydraulic conductivities. The smaller-scale tests have the benefit of sampling only one lithologic unit but are disadvantaged by the tendency to represent the least conductive portion of the lithology. The larger-scale tests are more likely to encounter fractures and represent more of the unit but will tend to be more of an average of the location immediately surrounding the test. Based on the available information, the population distribution of hydraulic conductivity is biased toward the lower end of the measurements. Even field-scale, single-well tests may be biased toward smaller values. Figure 5-6 shows the range of permeability natural logs considered for the five

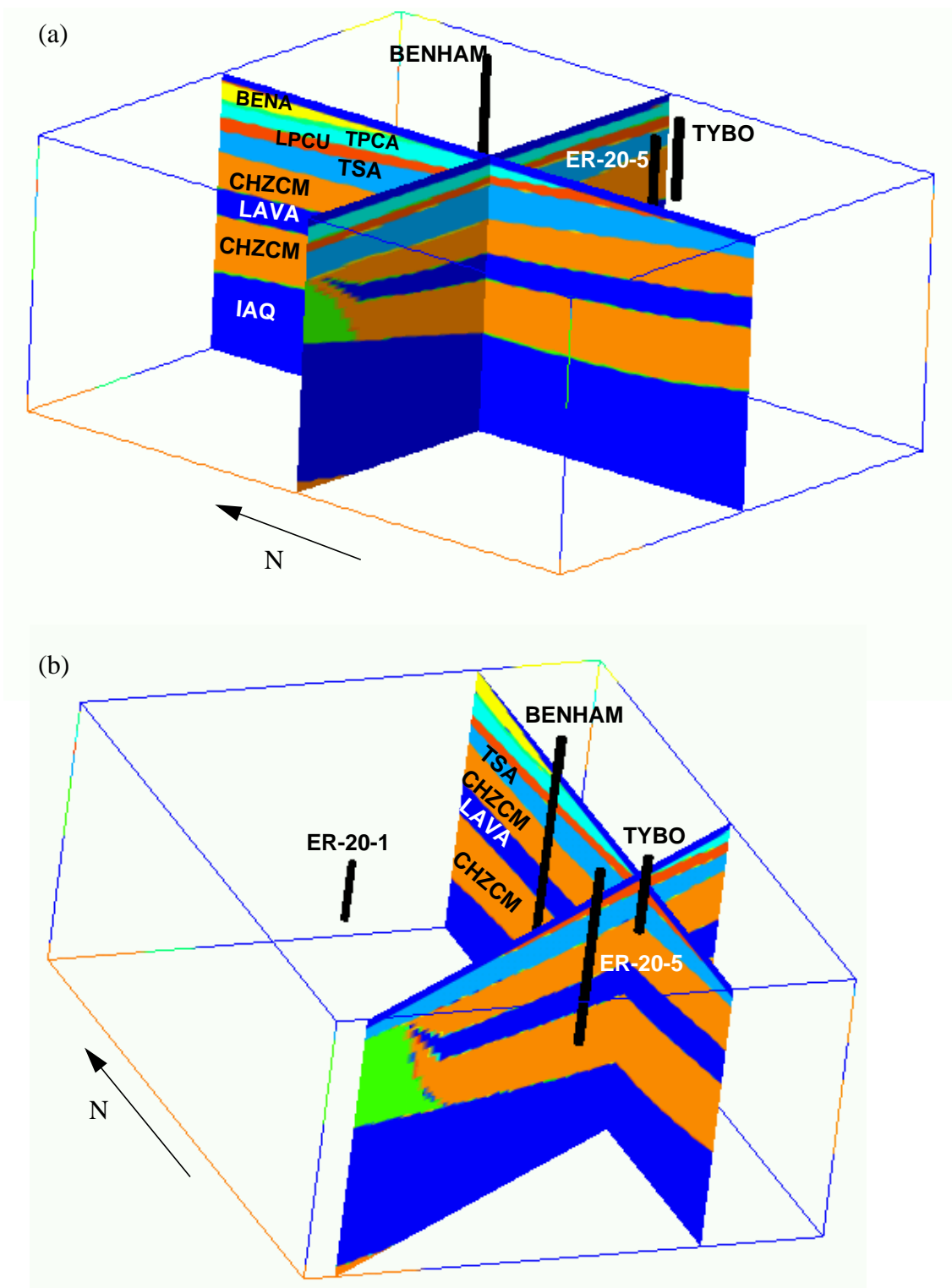


Figure 5-3. The deterministic HSU model shown with (a) north-south, east-west transects and (b) with transects through the boreholes.

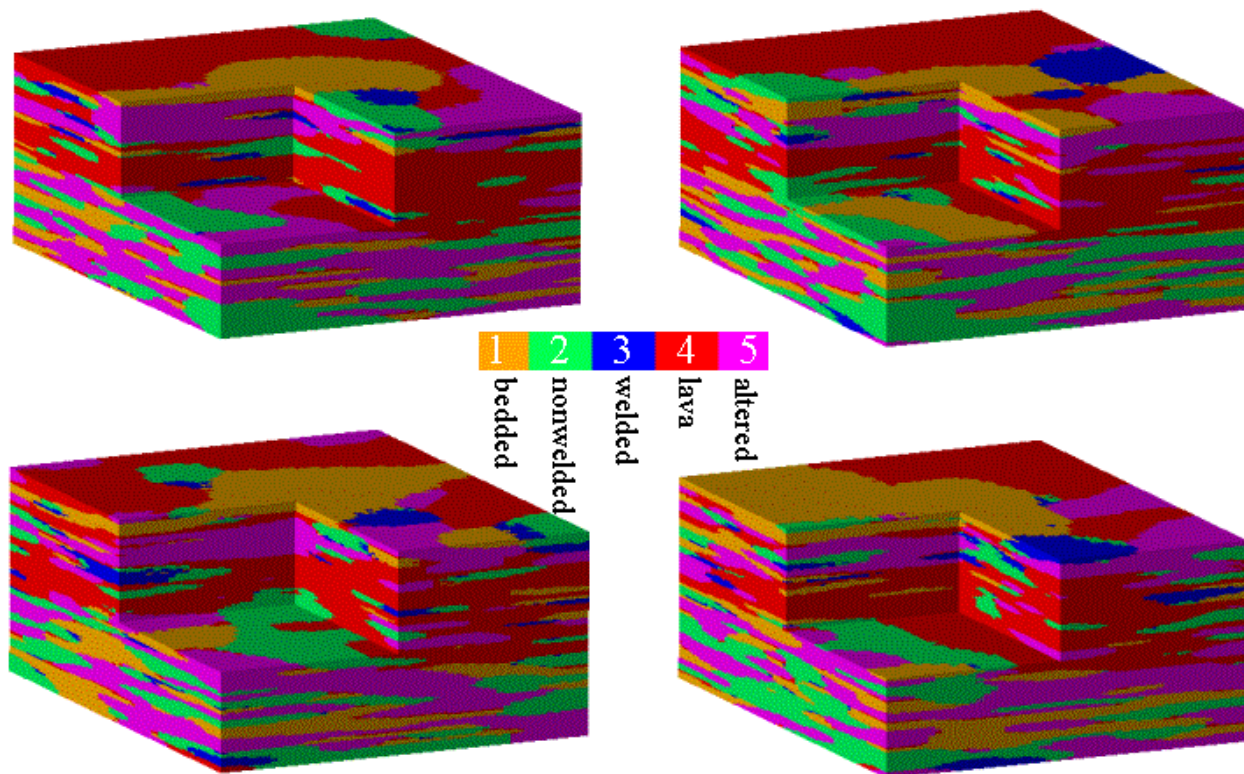


Figure 5-4. Four geostatistical realizations of lithologic attributes (classes).

lithologic classes. One of the most striking aspects of this plot is the similarity in permeability distributions for many of the classes. The similarity in these distributions indicates that these data do not really support the two-level geostatistical representation (hydrofacies and permeability) of the flow parameters used in this model (described in Appendix G). This observation plays a significant role in interpreting transport results in later chapters. Figure 5-7 shows the simulated hydraulic conductivities on the same realizations used in Figure 5-4. Thirteen orders of magnitude are spanned in the range of hydraulic conductivity. Because of the similarity in the distributions of the different hydrofacies (classes), it is very difficult to identify the class zones within the conductivity distributions and impossible to see the HSU definitions from the deterministic model. Thus, in addition to the lack of a fully connected fractured welded tuff in all realizations in which the TSA is mapped in the deterministic model, there also is not a clear zone of high permeability bounded by lower-permeability material. A significant implication of this characteristic of the geostatistical fields is that flow in the welded tuff class, where it exists, is not impeded from moving into other classes that may be less supportive of fracture-dominated transport.

Bulk Porosity

Bulk porosity distributions were estimated for the heterogeneous class maps (Appendix G). The data sources included core and sub-core samples, geophysical logs and calculated porosity from aquifer tests. In this study, uncertainty in bulk porosity is most likely not a significant component because rapid transport in fractured media is dominated by fracture porosities. Therefore, only average matrix porosity values for each of the lithologic classes are used. In

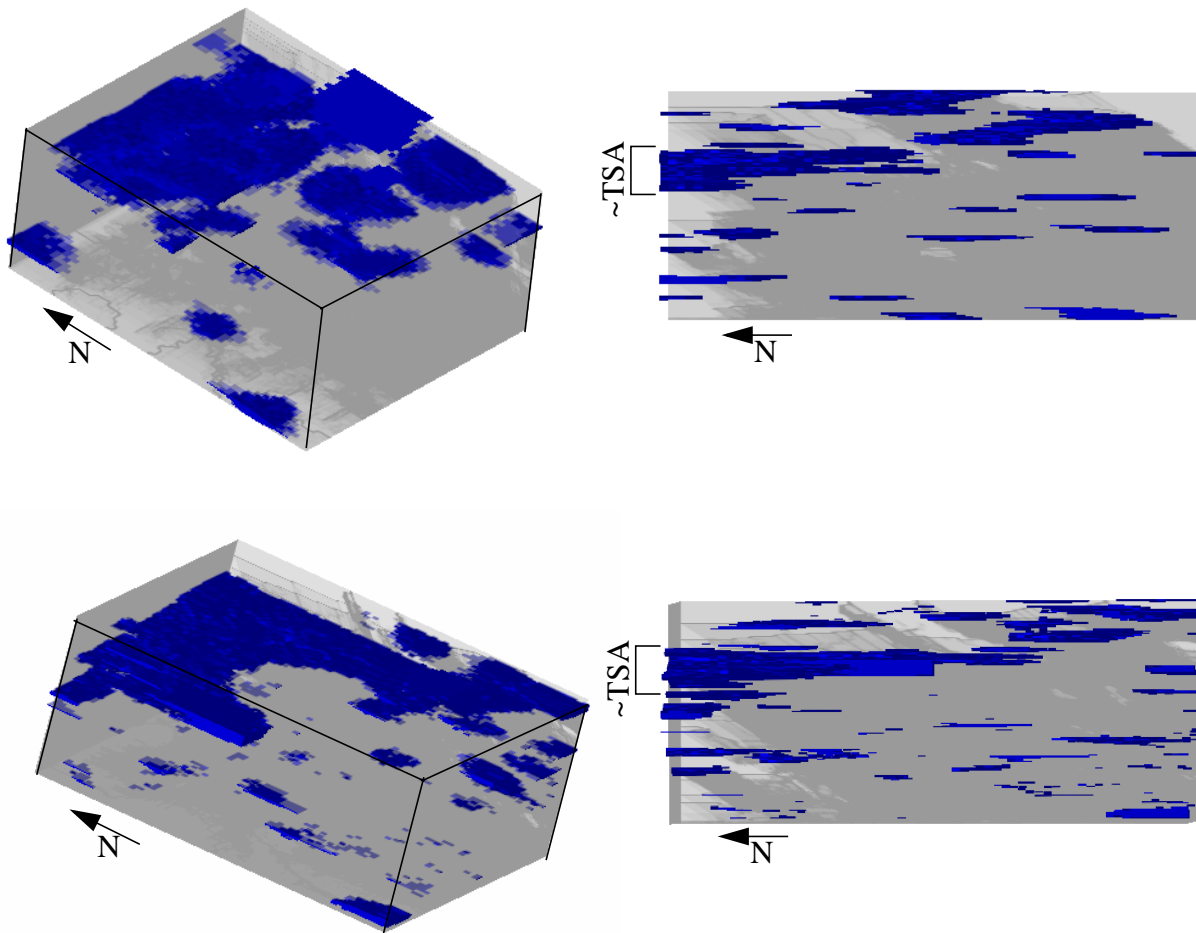


Figure 5-5. Rendition of 2 geostatistical class maps showing only welded tuff in blue. Note that the welded tuff is not a continuous class through the domain where the TSA is mapped, as in Figure 5-3.

Appendix F, geometric arguments are used to provide estimates of uncertainty ranges for fracture porosities.

5.3.3 Assigning Fracture Characteristics: Creating Two New Classes

We assign the lithologic classes used by DRI as either matrix flow only or fractured aquifers. Therefore, we first divide the non-welded tuff and altered classes into fracture and matrix-dominated components. All nodes in the non-welded tuff class with permeabilities greater than $1e-12 \text{ m}^2$ are reclassified as fractured non-welded tuff. All nodes in the altered class with permeabilities below $1e-15 \text{ m}^2$ are reclassified as nonfractured altered tuff. The basis for making this distinction is (a) attributes related to fracture properties are not provided with the simulations of class and permeability and (b) it is unlikely that unfractured components of classes could produce the high permeabilities in the distribution shown in Figure 5-6. Table 5-1 lists the units, their matrix properties, and the base-case fracture properties defined in later chapters.

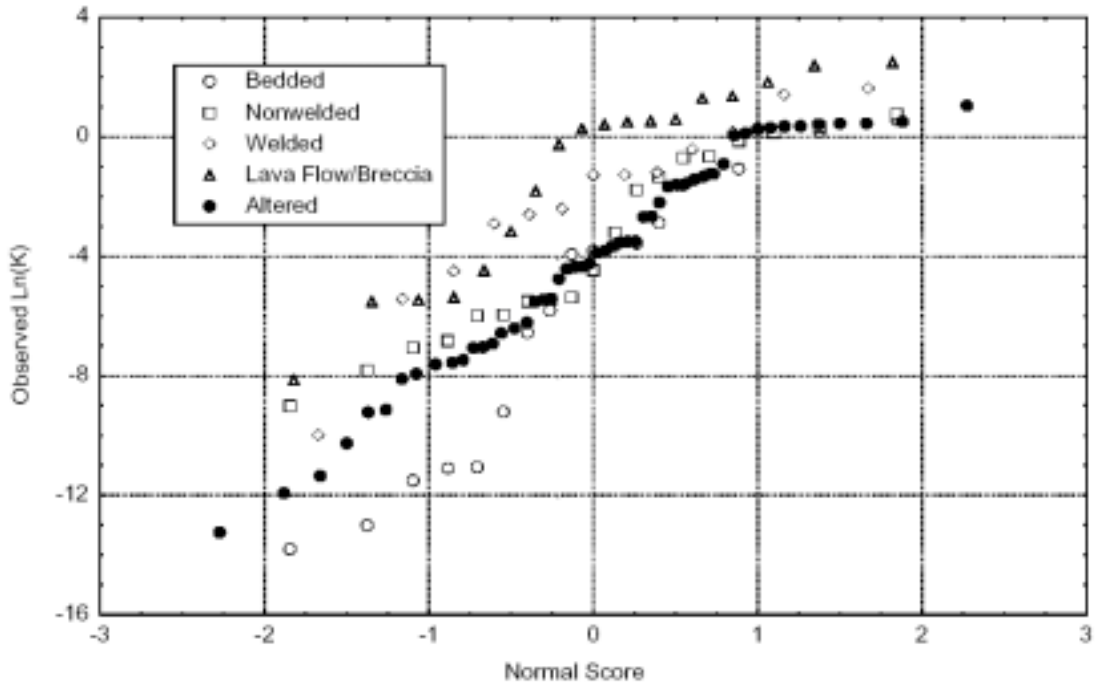


Figure 5-6. Observed natural log of hydraulic conductivity (m/d) plotted against the normal score for each of the five classes.

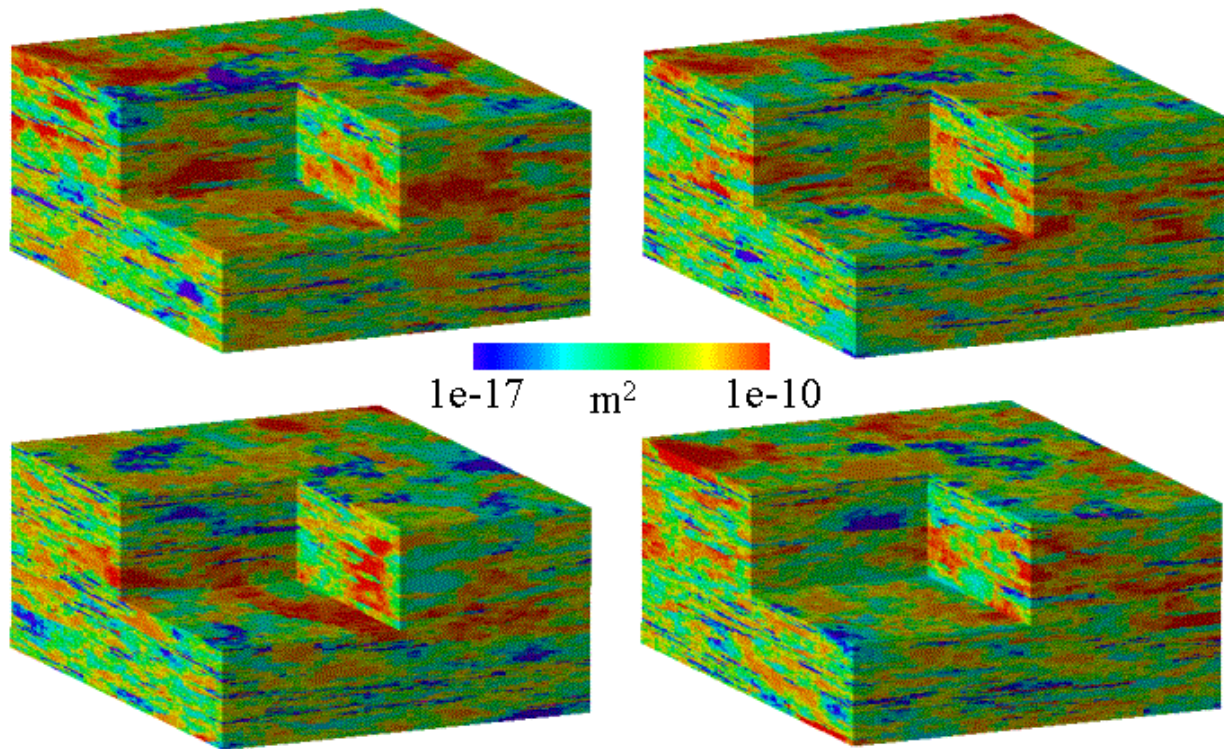


Figure 5-7. Simulated permeabilities in the same fields for which classes are shown in Figure 5-4.

Table 5-1. Matrix and Fracture Porosities for Deterministic and Geostatistical Zones

Deterministic Geologic Unit	Heterogeneous Zone Number	Geologic Type	Matrix Porosity ^a	Fracture Porosity ^b
	1	Bedded	0.4	-
	2	Non-welded	0.36	-
TSA	3	Welded	0.14	0.0005
	4	Lava	0.21	0.001
	5	Altered	0.28	0.0007
	6	Fractured non-welded	0.36	0.0005
CHZCM	7	Nonfractured - altered	0.28	-
LAVA ^c		Lava	0.35 ^c	0.005 - 0.018 ^c
<p>a-Mean of matrix porosities analyzed by DRI for heterogeneous zones. b-Base-case values estimated in Appendix F. c-Properties estimated in Bullion forced-gradient experiment (IT, 1998).</p>				

5.3.4 Limitations of Heterogeneous Attribute Maps

“A geologist familiar with the area should be able to conclude that any equiprobable class map is a reasonable approximation to reality” (Appendix G). Figure 5-4 clearly shows a continuous lava unit, forced by the design of these simulations. Would a geologist conclude that the welded-tuff distributions are a reasonable approximation to reality? Although there are nodes assigned to the welded-tuff class in the TSA, they are not continuous and their permeabilities are not unique relative to surrounding material so as to prevent flow from leaving the welded-tuff class. To a first approximation, a geologist would argue that the findings of Kersting et al. (1999) support the notion of substantial connectivity due to structure created in air fall and ash-flow tuffs. Such connectivity is not apparent in all realizations of welded tuff. Yet, all the realizations are designed to be equally probable representations of the system. An extension of this effort that would increase the utility of the attribute maps would be to discard attribute maps that do not support transport simulations consistent with the field observations at ER-20-5 #1, thereby adding another layer of conditioning to the process. Within the constraints of this project, we utilize the attribute maps that were provided and compare results with those generated from deterministic HSU domains.

5.4 Boundary Conditions

The boundary conditions for the site-scale flow model were extracted from the sub-CAU-scale flow model. Originally, we planned to conduct transport simulations on heterogeneous domains on the embedded grid within the sub-CAU flow model, described in Appendix A. However, we encountered discontinuities, numerical errors, and inaccurate flow fields caused by the sharp contrasts between geostatistical permeabilities and those calibrated in the sub-CAU model at nodes along the interface of the embedded model. Therefore, heads from the embedded domain in the calibrated sub-CAU model are mapped directly to nodes on all six sides of the site-scale domain. Figure 5-8 shows the heads on the site-scale model as mapped from the calibrated sub-CAU model and Figure 5-9 shows the boundary head distribution from the southeast with more resolution. The sharp head gradient in the upper units is caused by the LPCU. Therefore, the deterministic LPCU was added to each geostatistical attribute map to preserve this gradient. Figure 5-10 shows several geostatistical permeability maps with the LPCU properties superimposed on them. Preserving the calibrated gradient, this unit occurs well above source-release locations from the BENHAM chimney.

5.5 Effective Block Permeability

The effective permeabilities of the entire site-scale block for the geostatistically generated fields are generally one log unit lower than for the same block in the calibrated model. This feature may confirm that the measured permeabilities from single-well pump tests are biased toward lower values when compared to field-scale HSU permeabilities. It may also indicate that the correlation-length scales used in the geostatistical simulations were not large enough to preserve large high-conductivity units that would increase the effective block permeability of the entire model domain. The second explanation is consistent with the argument presented previously that the high-permeability welded tuff is not continuous enough to support rapid transport from BENHAM to ER-20-5 #1. Thus, an extension of this work (and certainly a guideline for future models of this or similar domains) would be to increase the horizontal correlation-length scales from those reported in Appendix G. An alternative approach is to scale the permeabilities of all nodes in the heterogeneous maps to ensure that the bulk permeability is equal to that of the calibrated model. Such an approach is based on the assumption that the measured permeabilities used in the distributions are biased toward low local values and are not representative of large-scale aquifer conditions in which connected fracture networks lead to increased overall permeability, but that the spatial distribution of the variability is still appropriate. Following this assumption, the permeabilities in each geostatistical realization were scaled such that the effective block permeability is equal to the same block in the calibrated sub-CAU model. A uniform gradient was applied to each realization and the resulting flux was then used to compute the effective permeability with Darcy's Law. The ratio of the effective permeabilities on the calibrated, deterministic model to each geostatistical field was calculated (Table 5-2) and used as a multiplier to scale the permeability of each node within each geostatistical field, leading to heterogeneous flow fields with consistent bulk permeabilities.

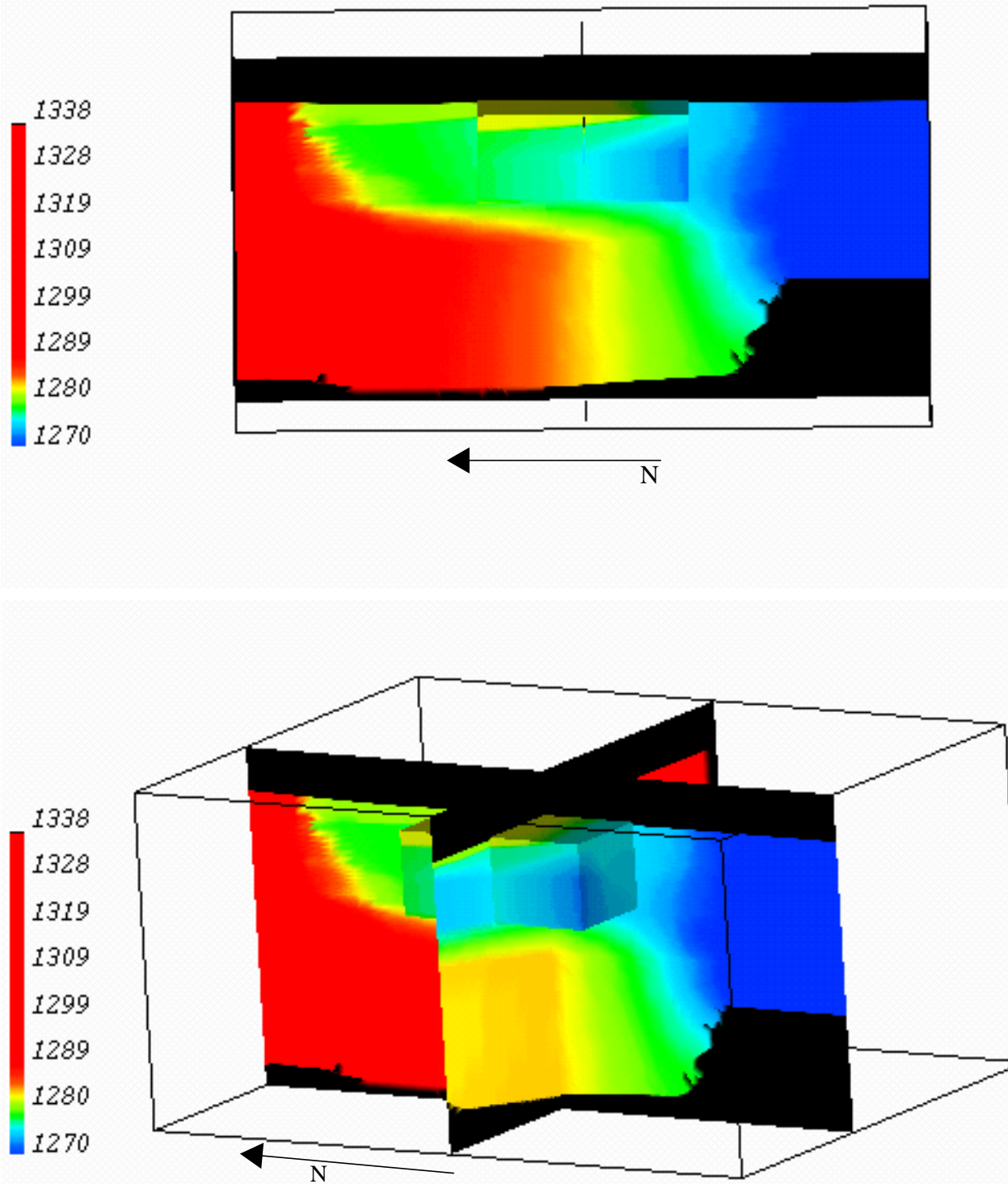


Figure 5-8. The boundary conditions for the site-scale domain are extracted from the sub-CAU domain. The slices are drawn through the sub-CAU domain and the site-scale domain is shown as a solid cube. Heads are contoured in meters.

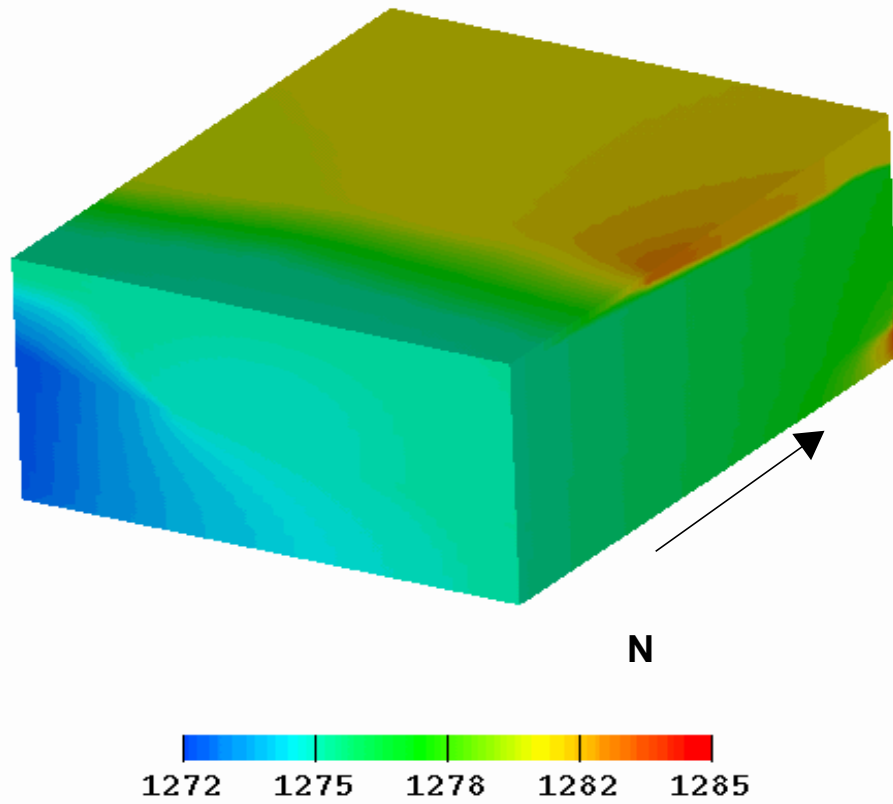


Figure 5-9. Site-scale domain head boundary conditions calculated from the sub-CAU scale model. View from southeast with head contours in meters.

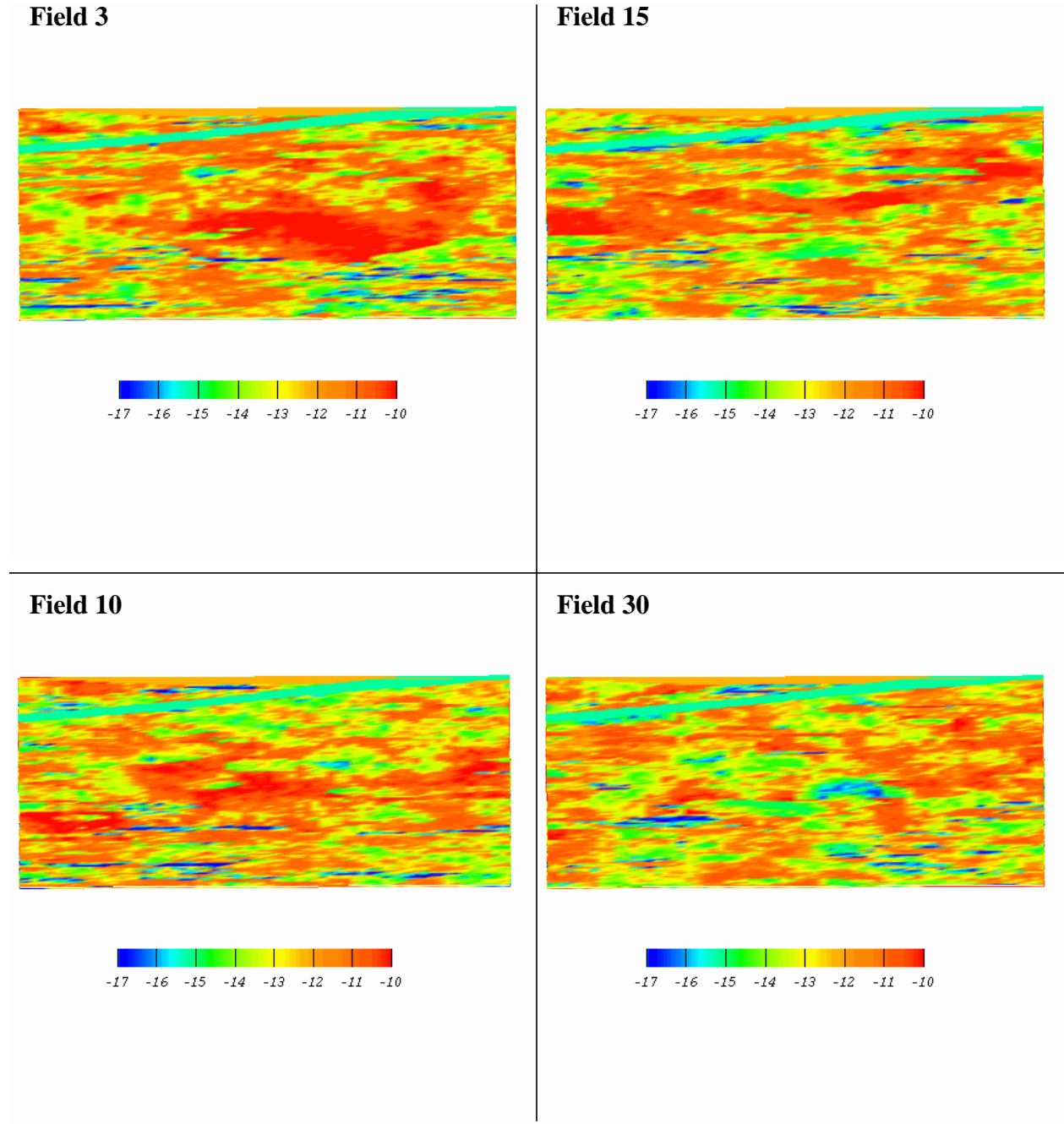


Figure 5-10. Geostatistical fields colored by their permeability’s order of magnitude. The slice is drawn at the BENHAM easting and the view is looking from the west.

Table 5-2. Calculated Permeability Multipliers for Each Geostatistical Field

Geostatistical Field	Permeability Multiplier
1	2.803
2	3.006
3	3.038
4	3.160
5	3.423
6	2.892
7	2.432
8	3.140
9	2.994
10	3.295
11	2.089
12	2.463
13	3.366
14	2.749
15	2.779
16	3.186
17	3.090
18	3.189
19	3.177
20	2.955
21	3.206
22	2.497
23	2.439
24	3.888
25	2.982
26	2.966
27	3.033
28	3.359
29	3.050
30	3.298

5.6 Deterministic Site-Scale Flow-Model Results

Conservative, non-diffusive, and non-reactive particle tracking is used to visualize the flow paths away from the BENHAM and TYBO tests. Appendix C provides a description of the particle-tracking algorithm in FEHM used for these simulations and for those involving diffusion and reactions, both of which are discussed later.

Figure 5-11 shows the flow paths away from BENHAM for TSA releases in the deterministic site-scale flow model. The particles travel south, away from BENHAM, but staying mostly within the TSA, with the exception of the lower particles that move into the CHZCM. Colored by time, the unretarded particles all leave the domain in less than 50 years. Figure 5-11 also shows the paths for particles released into the LAVA of the deterministic model. They travel slightly more westward than the TSA particles, indicating that gradients and flow paths are not identical at all depths in the model due to the different shapes of the aquifers and the three-dimensionality of the boundary conditions (see Figures 5-8 and 5-9). Like the TSA particles, they move fast and with little deviation from a straight pathline aligned with the flow.

The TYBO test was conducted near the interface of the TSA and CHZCM HSUs, with its cavity and chimney connecting the source to the TSA (Pawloski, 1999; also see Figure 1-2). Figure 5-12 shows the pathways and times of flight for particles released at the TYBO test. In the deterministic flow field, the flow paths away from TYBO are far to the east of the ER-20-5 #1, supporting the assertion of Kersting et al. (1999) that the contamination found in the ER-20-5 wells comes from BENHAM. The argument against TYBO contributing to samples at ER-20-5 #1 becomes less obvious if the following two factors are considered: (1) the dispersion of solutes in the plume leaving TYBO and (2) the effects of pumping ER-20-5 #1 during development and sampling. As a preview to transport simulations described later, Figure 5-13 shows the plume structure emanating from TYBO, simulated using a lateral dispersivity of 3 m (the dispersivity computed for the LAVA aquifer in the BULLION forced-gradient experiment; IT, 1998). The TYBO test is hundreds of meters above the LAVA aquifer and no particles released at TYBO in the deterministic flow fields reach the LAVA aquifer under any conditions considered.

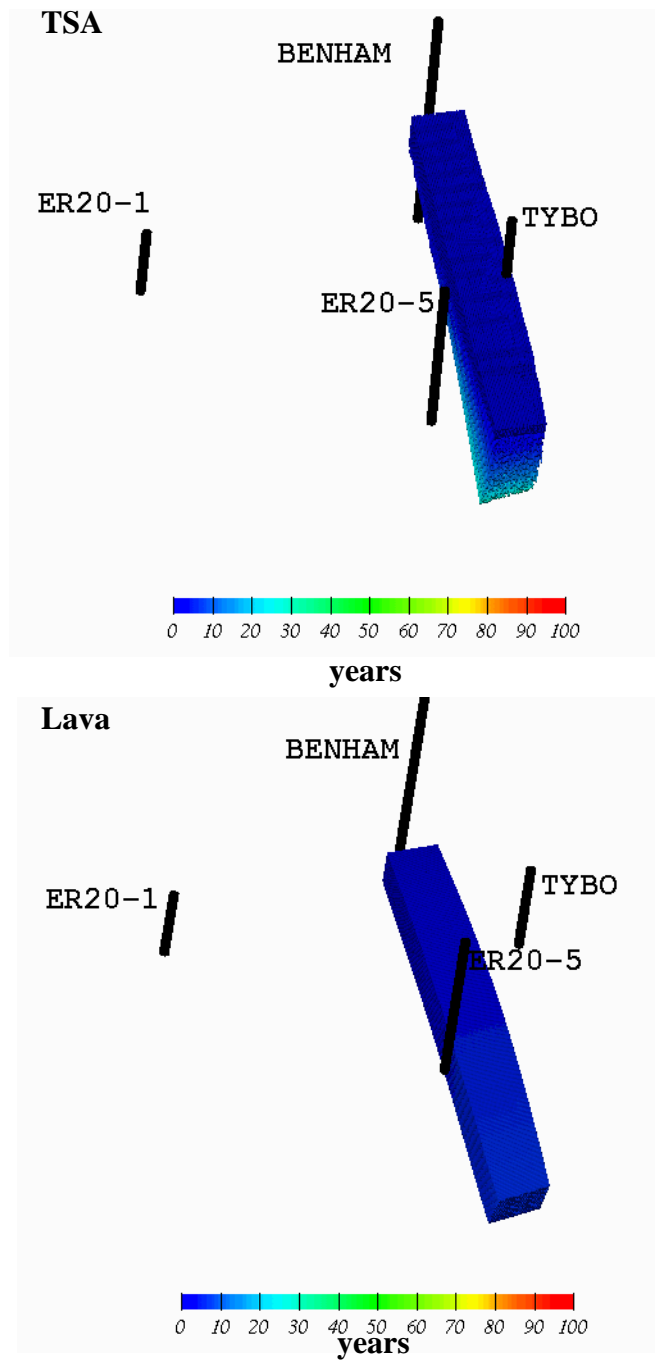


Figure 5-11. Time-of-flight particle paths with BENHAM releases in the TSA and LAVA without transport chemistry.

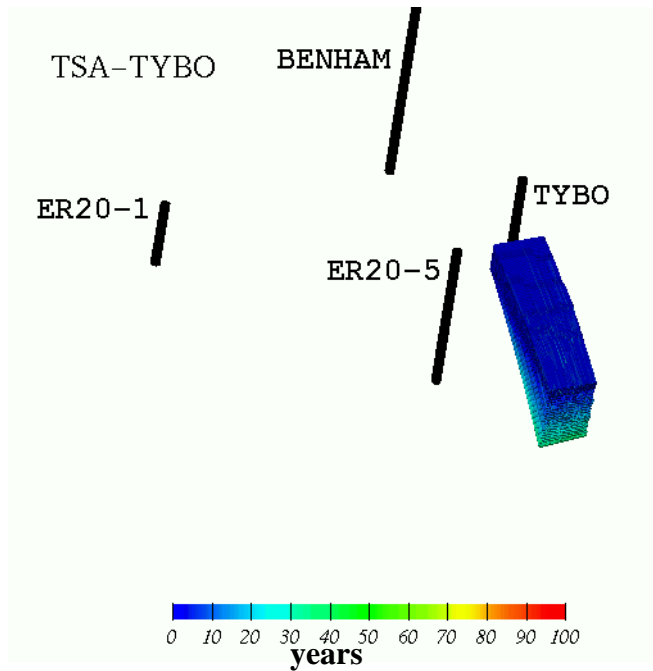


Figure 5-12. Time-of-flight particle paths with TYBO releases in the TSA without transport chemistry or dispersion.

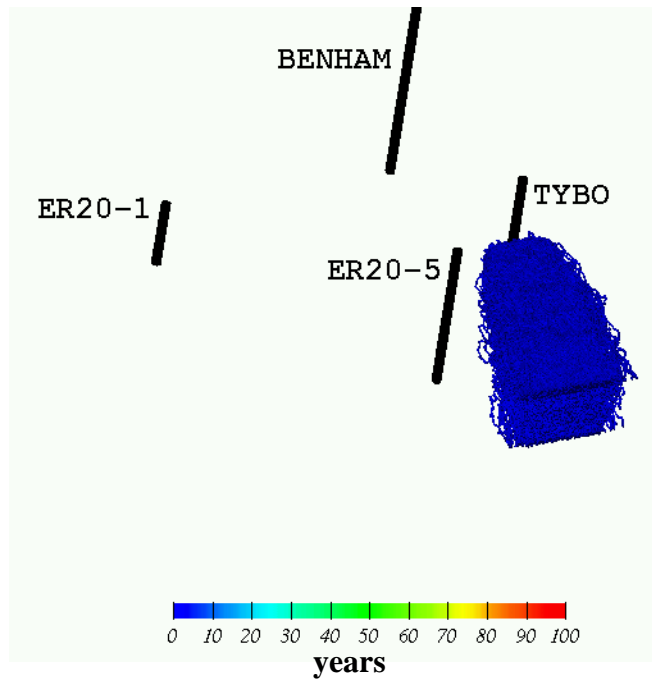


Figure 5-13. Time-of-flight particle paths with TYBO releases in the TSA with dispersion (10/3/0.01) but without transport chemistry.

5.7 Geostatistical Site-Scale Flow-Model Results

Steady-state flow fields using mapped boundary conditions are computed on each scaled geostatistical permeability realization. Figure 5-14 provides examples of head distributions on these steady-state flow fields. Conservative, non-diffusive, and non-reactive particles were released from BENHAM at elevations consistent with the TSA (Figure 5-15), LAVA (Figure 5-16), and from TYBO (at elevations consistent with the TSAAs shown in Figurea 5-19 and 5-20) in the geostatistical fields. The paths and the travel times are notably different from each other and from the paths computed in the deterministic flow field. Figure 5-17 and Figure 5-18 show the particle paths from BENHAM colored by attribute class. The particles released in the LAVA tend to stay in lava units whereas the particles released at the elevation of the TSA travel through several different material classes, including matrix-flow-dominated bedded tuffs. Such behavior highlights a very important difference between the deterministic and heterogeneous conceptual models of this system. Although layered stratigraphic processes lead us to conceptualize a continuous connected pathway in fractured tuff south and southwest of BENHAM, the statistics used to generate the heterogeneous attribute maps do not always preserve such a continuous pathway. Although forcing a LAVA class to reside in the region mapped by Prothro and Warren (2001), the range of variability in permeability for lava used in the simulations (Figure 5-6) yields a permeability map in which the LAVA often cannot be distinguished from other units. However, the key characteristic of the LAVA is that it is parameterized, as a class, as a fractured unit everywhere it exists. Thus, velocities are high in the LAVA and access to matrix material by solutes is achieved only by diffusion. The pathways from the TSA level releases at BENHAM and TYBO encounter welded tuff, non-welded tuff, bedded tuff, and so on. Because fracture properties were not simulated (Appendix G), we have assumed that flow is matrix-dominated in the bedded and non-welded tuffs. This assumption has a tremendous impact on (1) fluid residence times caused by the large difference in effective porosity between fractured units and non-fractured units and (2) material that reactive solutes come in contact with; matrix sorption is a direct retardation process in the matrix-flow units. These issues are addressed during a subsequent discussion on solute transport.

In the deterministic flow model, the flow paths from TYBO are well to the east of ER-20-5 #1, supporting the assertion of Kersting et al. (1999) that contaminants found in that observation well originate at BENHAM, not TYBO. In some of the heterogeneous realizations, some simulated flow paths from TYBO approach the ER-20-5 #1 observation well. This issue is further discussed in Chapter 7, where dispersivity and observation-well capture-zone size are considered.

5.8 TYBO Effects on Paths from BENHAM

This study does not explicitly address how underground nuclear testing impacts radionuclide migration in groundwater. However, groundwater anomalies following underground tests on Pahute Mesa have been documented (Fenelon, 2000). Although no specific anomalies are attributed to the TYBO test in that report, there are concerns about whether hydrologic perturbations following the TYBO test affect the migration of radionuclides from BENHAM to the

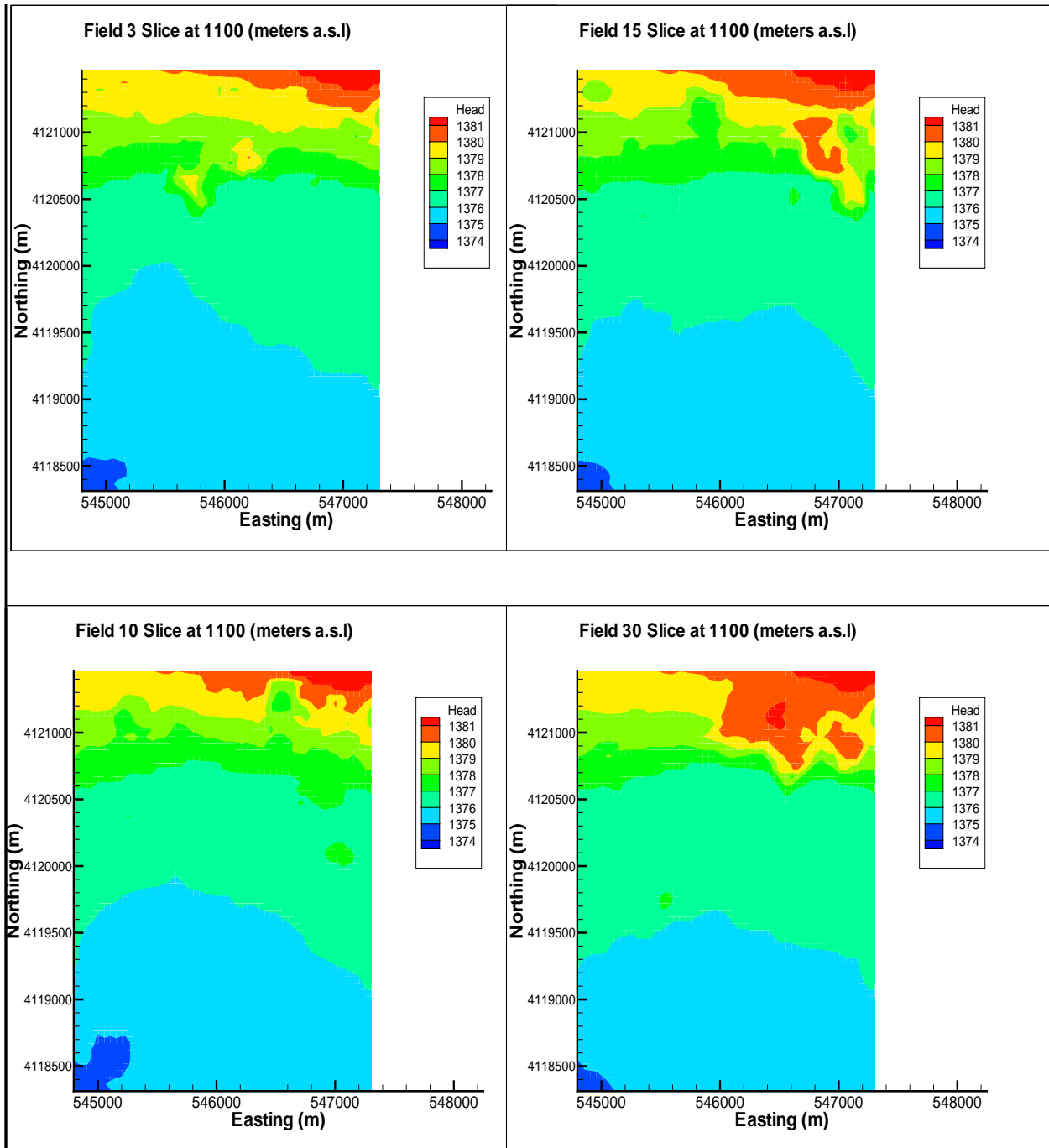


Figure 5-14. Head contour variations within geostatistical fields 3, 10, 15, and 30.

ER-20-5 wells. Therefore, the site-scale deterministic flow model is used to investigate possible TYBO test effects on transport pathlines originating at BENHAM. Two different scenarios are considered: (1) flow towards TYBO caused by a local decrease in head during infilling and (2) high pressure centered at TYBO caused by overpressure in neighboring material following the test. For both scenarios, simplifying assumptions are invoked. The multiphase environment following the

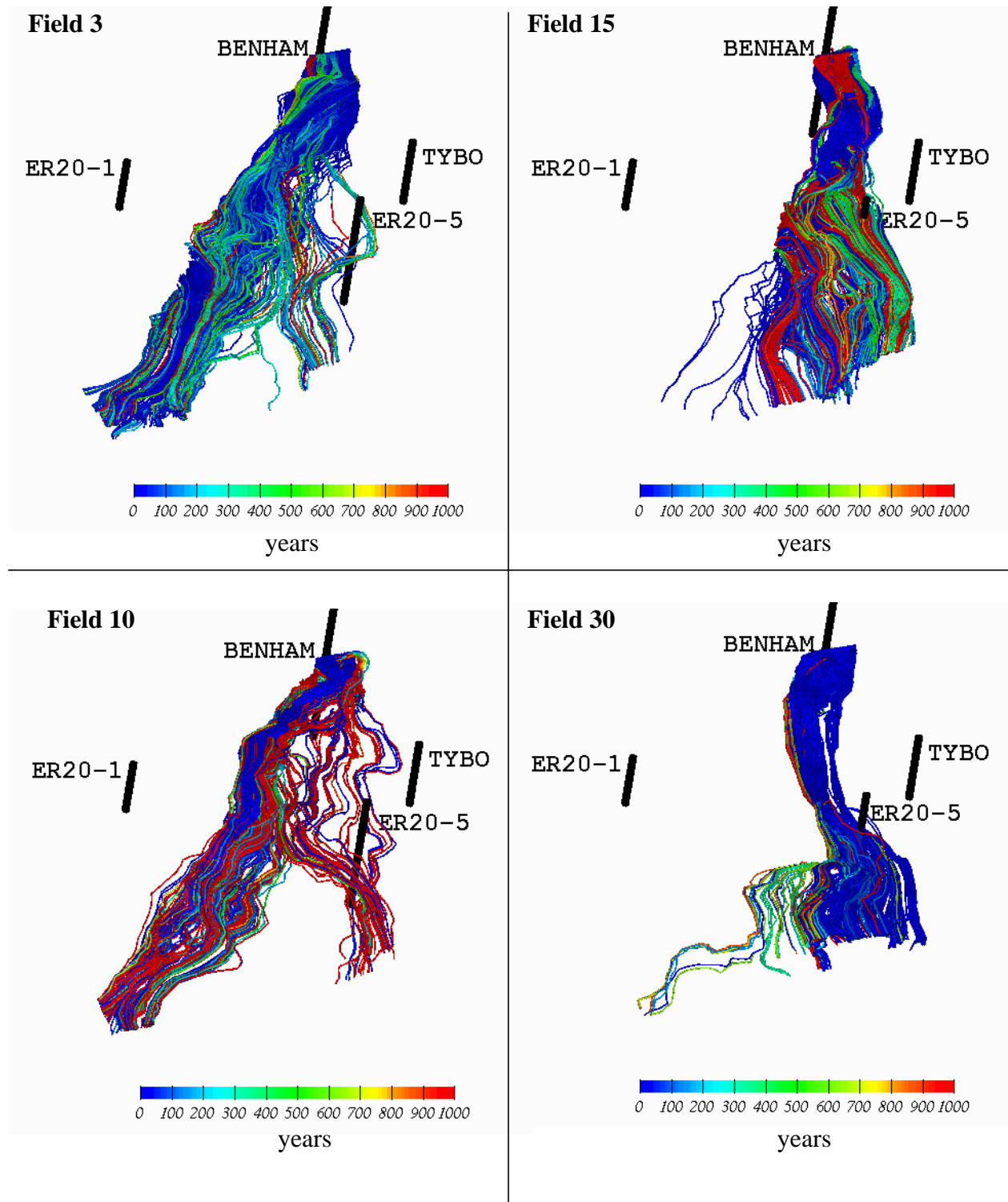


Figure 5-15. Time-of-flight paths for unretarded particles released from BENHAM in the TSA in flow fields 3, 10, 15, and 30.

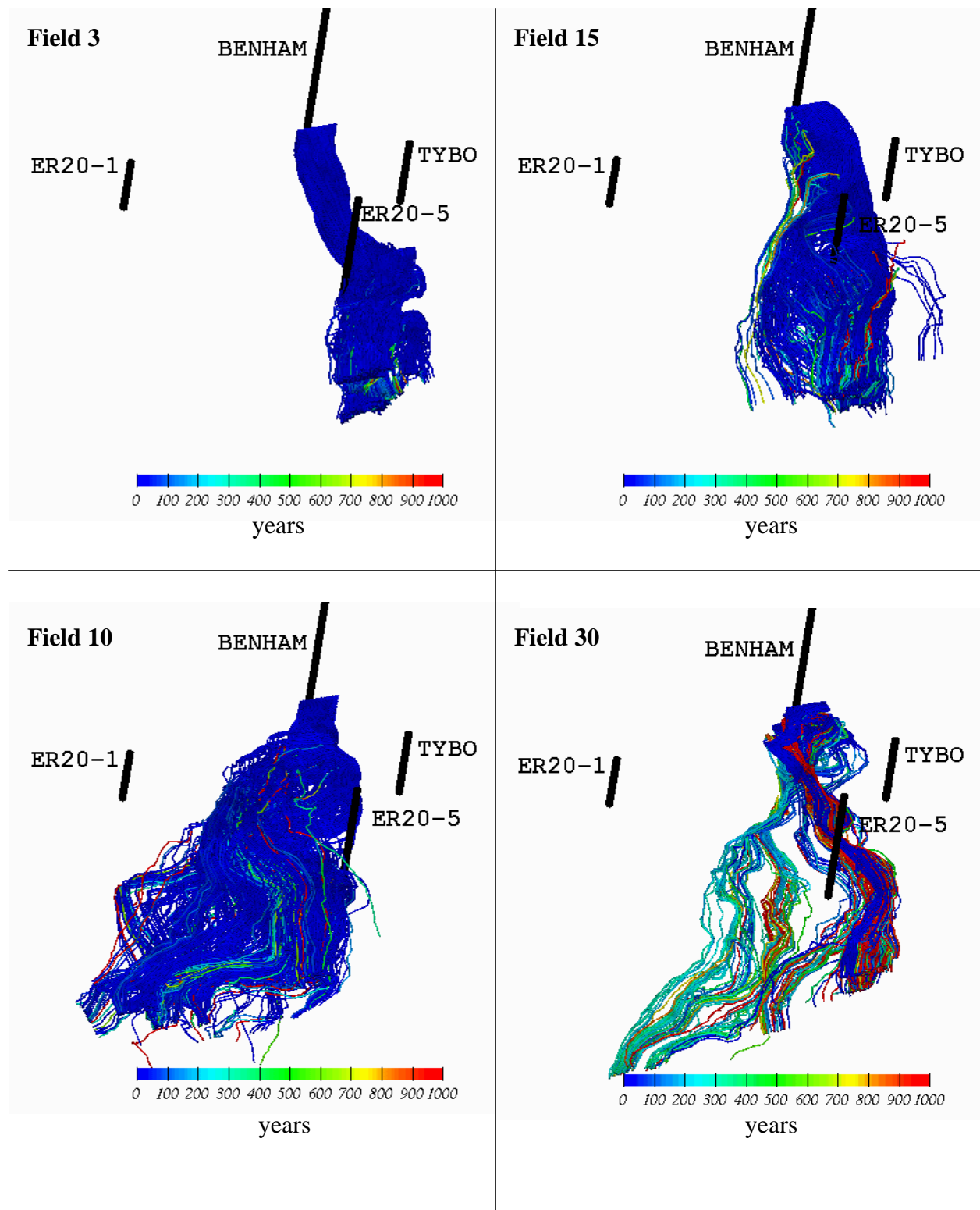


Figure 5-16. Time-of-flight paths for unretarded particles released from BENHAM in the LAVA in flow fields 3, 10, 15, and 30.

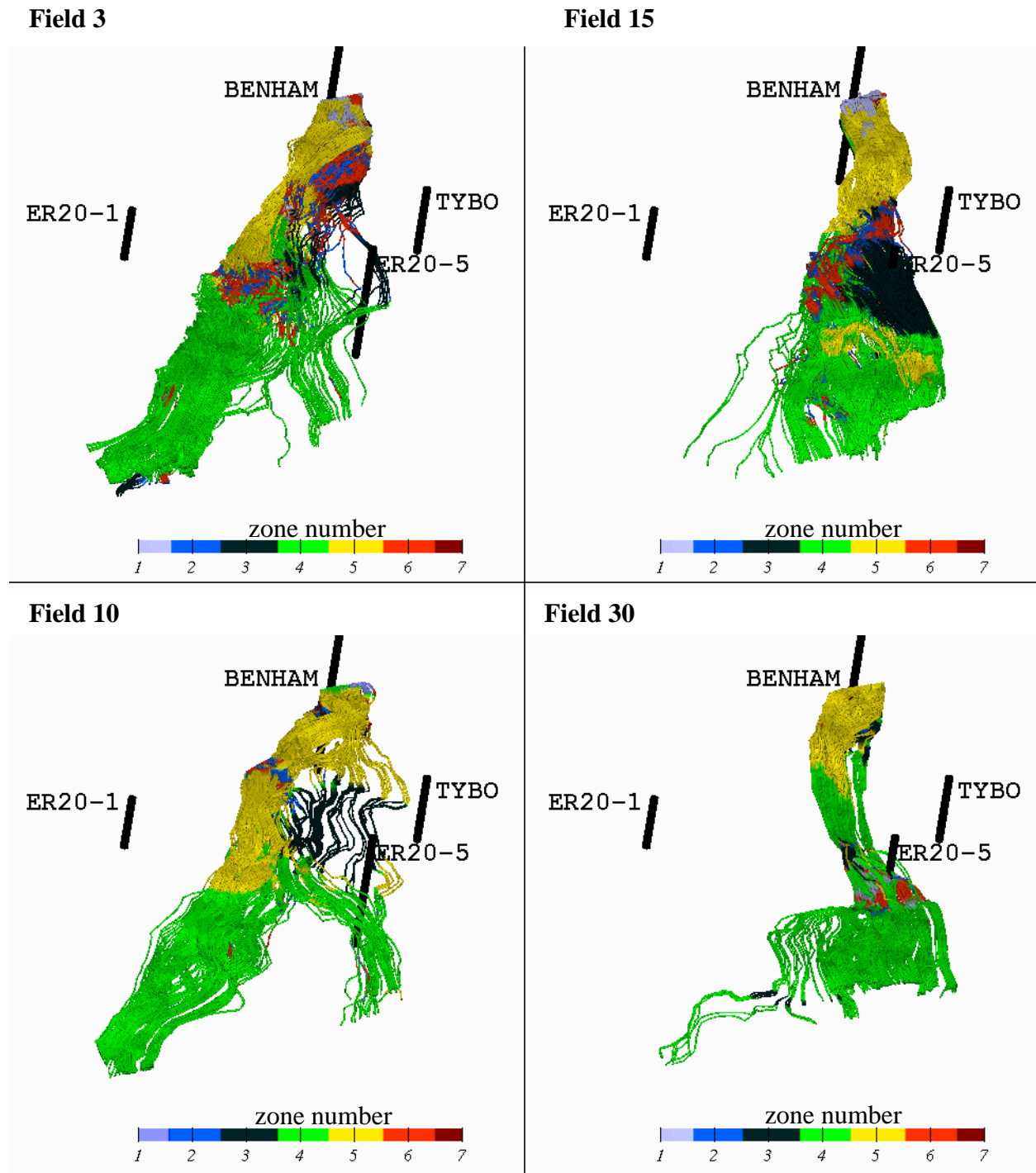


Figure 5-17. Flight paths of particles colored according to travel in different geologic material zones (zone numbers, as identified by different colors, defined in Table 5-1). Particles are released from BENHAM at an elevation consistent with the TSA. Note how little welded tuff (Zone 3) these particles travel through.

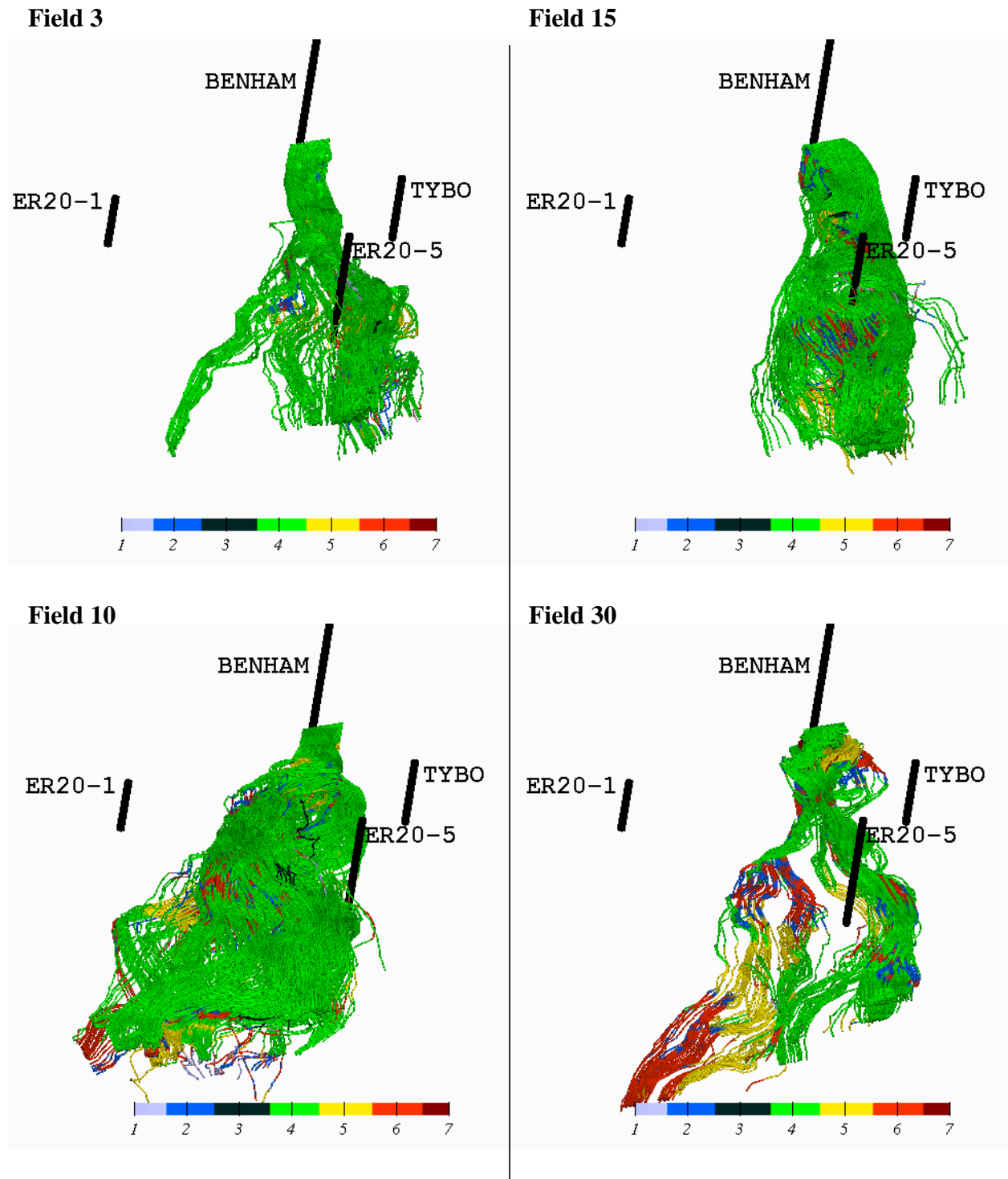


Figure 5-18. Flight Paths of Particles colored according to travel in different geologic material zones (zone numbers, as identified by different colors, defined in Table 5-1). Particles released from BENHAM at an elevation consistent with the LAVA.

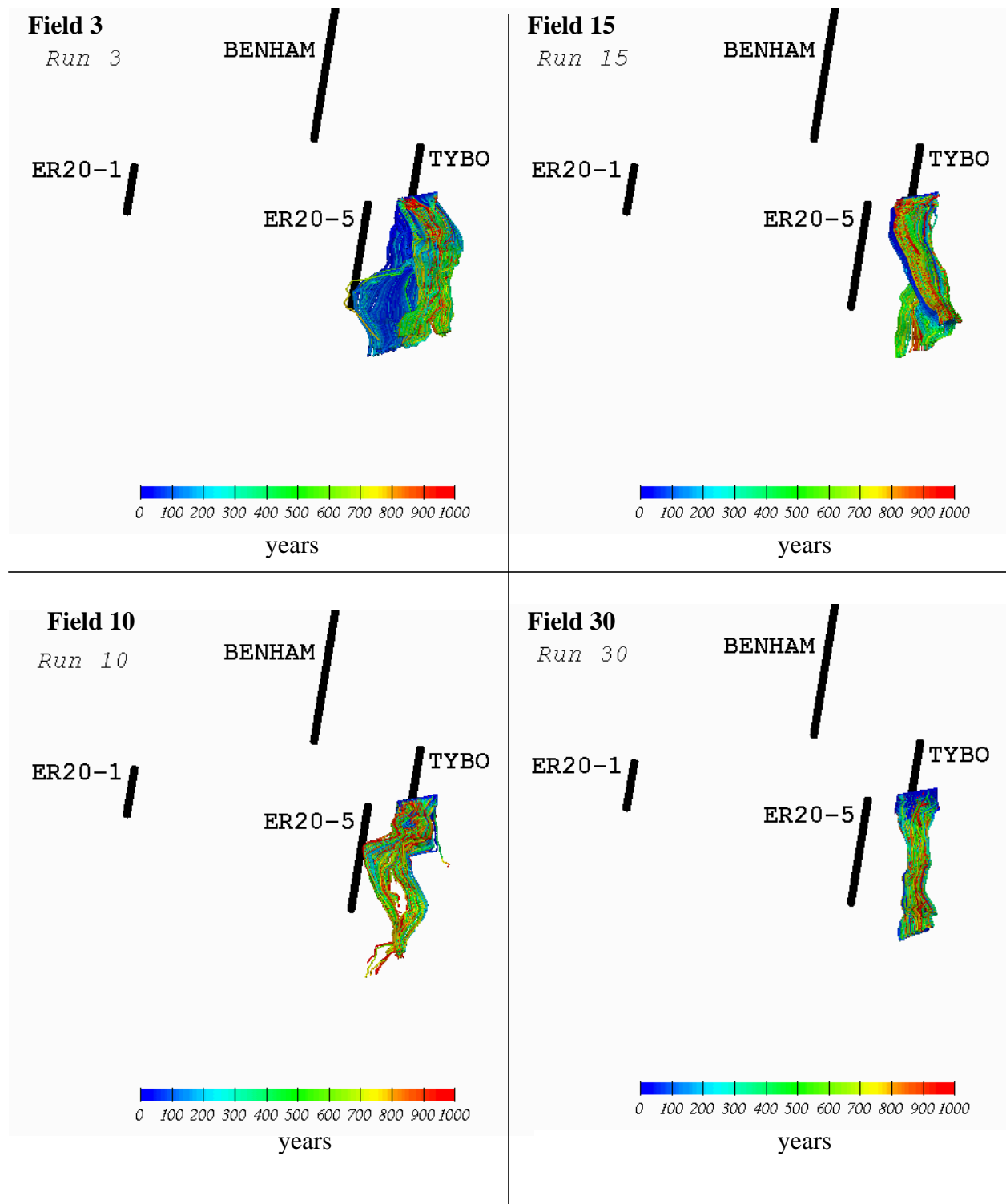


Figure 5-19. Time-of-flight paths for unretarded particles released from TYBO in flow fields 3, 10, 15, and 30.

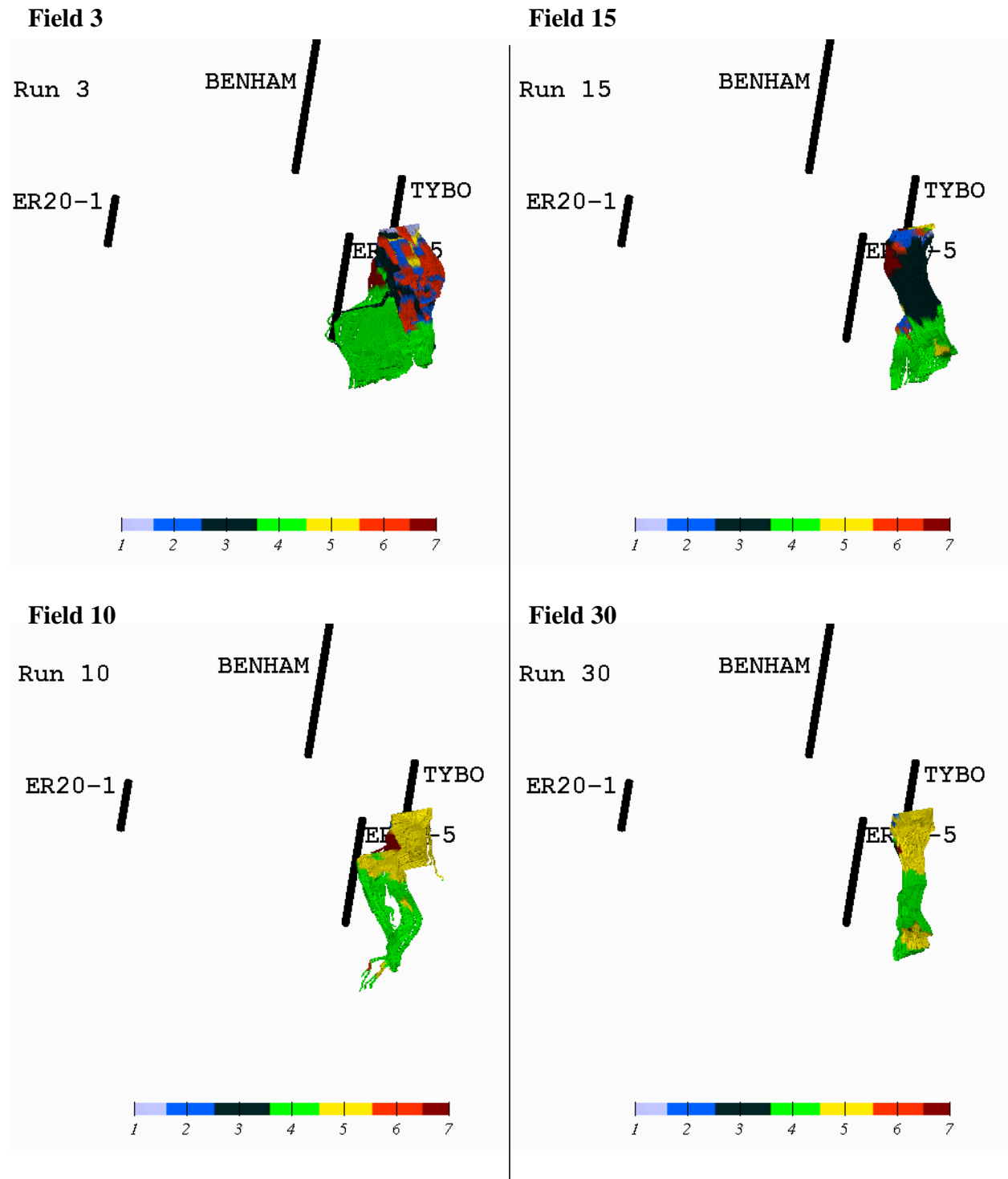


Figure 5-20. Flight paths of particles colored according to travel in different geologic material zones (zone numbers, as identified by different colors, defined in Table 5-1). Particles are released from TYBO at the elevation of the TSA.

TYBO test is not accounted for with this model. Thus, in addition to omitting the explosion phenomena, the simulations do not properly account for rewetting during infilling at TYBO. A primary difference between the model and the actual physical system is that the relative permeabilities and the seepage face associated with the locally unsaturated media are not captured with the model. Instead, the pressure is reduced, but the permeabilities remain set for fully saturated conditions. This feature likely leads to more rapid flow into the perturbed zone in the model. Another simplification is that the model does not account for the possible effects of the shock wave from TYBO on the hydrogeologic system. Thus, increased or decreased permeability caused by fractures opening or closing are not accounted for either.

Accounted for in these calculations is the specific storage of the aquifer. Thus, the aquifer's transient response in the model either to reduced pressure following dewatering of the cavity/chimney system or to increased pressure resulting from the test accounts for both compressibility of the fluid and the aquifer material. Specific storage coefficients (Freeze and Cherry, 1979) are estimated from the aquifer testing conducted in volcanic tuff by Geldon (1996). A representative value of specific storage in that study, $2.4\text{e-}5 \text{ m}^{-1}$, is used for these calculations.

The first scenario involves simulating reduced groundwater head in the TYBO cavity/chimney system following the test. This scenario is approximated with the model by starting with a steady-state flow field and then removing a volume of water equivalent to the TYBO cavity volume and setting the head 2 cavity radii lower in the entire cavity/chimney system. This procedure is done for the maximum estimated cavity radius, given the range of yields for the test (Pawloski, 1999). Immediately after this perturbation, the model is run in transient mode with very small time steps to monitor hydraulic response, as well as perturbations to particle paths originating at BENHAM seven years earlier.

The second scenario involves simulating increased groundwater head around the TYBO chimney following the test. Approximated with the model, this scenario begins with a steady-state flow field and by setting the head 2 cavity radii higher around cavity/chimney system. This, too, is done for the maximum estimated cavity radius, given the range of yields for the test (Pawloski, 1999). Immediately after this perturbation, the model is run in transient mode with very small time steps to monitor hydraulic response as well as perturbations to particle paths originating at BENHAM seven years earlier. In this scenario, flow from the perturbation is only away from the test because no pressure drop is considered in the cavity.

For both of these perturbations, virtually no impact on flow in the LAVA or TSA aquifers is observed in the simulations. The TSA permeability in this model is high enough that equilibration of heads in either scenario occurs over a very small time scale. Figure 5-21 shows the rapid pressure responses for both scenarios in the perturbed zones for both scenarios. The volume of water that flows toward the chimney for scenario 1 or away from the high pressure mound in scenario 2 is so small relative to the flux in the TSA that there is also virtually no impact on the travel paths or travel times of solutes originating at BENHAM.

The two scenarios considered in this section roughly approximate hydrologic perturbations that may have existed after the TYBO test. Simplifying assumption permitted these simulations to be conducted with the saturated-only site-scale flow model. The results indicate that the high permeability of the TSA aquifer leads to rapid equilibration of such perturbations and that their impact on transport paths from BENHAM may be negligible. However, this simple analysis for site-scale effects should not be mistaken for a local hydrologic analysis of post-test hydrologic

phenomena. Such a model should consider saturated/unsaturated conditions and preserve a mass balance for water displacement from the chimney to either increased water table location or compression and alteration of aquifer material into which the water is squeezed.

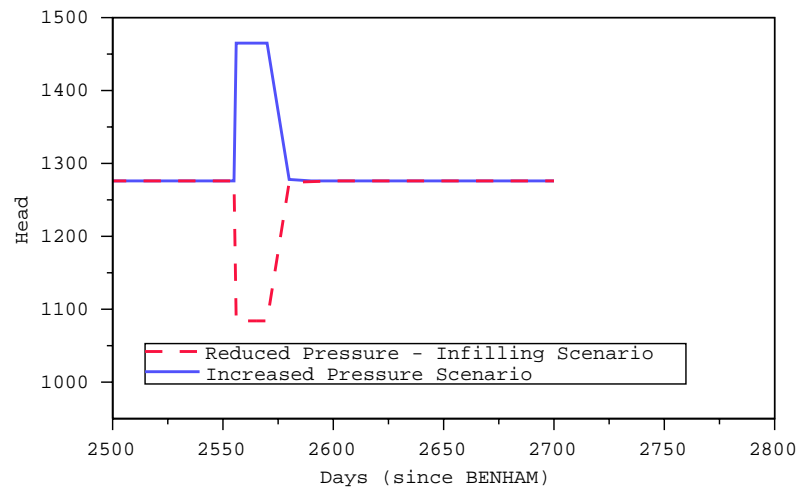


Figure 5-21. Response curves for reduced and increased pressure following the TYBO test. Simulations are conducted with site-scale flow model and material storativity of $2.4e-5 \text{ m}^{-1}$. Time-history data are recorded at the center of each anomaly.

5.9 Transport Parameters: Preliminary Considerations

The heterogeneous permeability maps (Appendix G) contain unique values for every cell in the model domain. The spatial distributions used to create the permeability maps do not exist for the transport parameters needed in this study (e.g., fracture spacing, fracture aperture, fracture coating thickness, fracture coating exposure to fluid, fracture porosity, matrix Kd , and solute diffusion coefficients). However, these parameters are often measured and correlated with lithologic classes (hydrofacies) such as welded tuff or lava. Therefore, the transport parameters in this study are distributed spatially according to the lithologic class assigned to each node in the domains. Thus, the transport parameter heterogeneity is at the scale shown in Figure 5-4. One of the primary distinguishing characteristics of a class is whether it is fractured. As will be demonstrated in later chapters, the conditioning exerted to maintain an intact LAVA unit consistent with the mapping of Prothro and Warren (2001) leads to significantly different transport behavior in the LAVA than occurs where the TSA welded tuff aquifer was mapped by Drellack and Prothro (1997). Specifically, solutes travelling in the LAVA tend to stay in the LAVA (e.g., Figure 5-18), but solutes traveling in welded tuff do not tend to stay in welded tuff. The transport parameters associated with the lithologies are developed and applied in Appendix F and Chapter 7, where the importance of the continuity of fractured aquifer material is highlighted.

Chapter 6: Source-Term Model

6.1 Introduction

6.1.1 Overview

A three-dimensional source-term model provides estimates of radionuclide (RN) releases from the BENHAM test to the LAVA and TSA aquifers (see Figures 1-2 and 5-2). This model captures the transient nature of non-isothermal groundwater flow in the cavity/chimney system after it fully resaturates following an underground nuclear explosion. It is a simplification because (a) it does not capture the processes associated with the explosion or immediately following the explosion when two-phase conditions exist and (b) it simplifies the complex chemistry associated with solute transport and rock-water interactions in the non-isothermal flow system. A specific source-term model for TYBO was not developed during this study; however, releases from TYBO to the TSA aquifer are estimated using the BENHAM source-term model. One of the key questions we seek to resolve in this study is how contaminants found in the TSA aquifer by Kersting et al. (1999) were transported to the TSA from the BENHAM source. The BENHAM source is located more than 500 m below the TSA, whereas the TYBO source is located within the TSA. Thus, the transport issues associated with a TYBO source focus on the feasibility of RN migration to ER-20-5 #1 and #3. These issues are addressed in the site-scale flow and transport model chapters, 5 and 7 respectively. For the purposes of this study, a BENHAM source-model was developed to predict RN releases to the TSA and LAVA aquifers. These releases are summed together to provide an approximate source function for TYBO in the site-scale transport simulations used to examine the potential for RNs observed at the ER-20-5 wells, which may have originated at TYBO.

The source-term model does not predict RN migration away from the test via “prompt injection,” a process that may enable small quantities of RNs to be transported while still in a vaporized phase immediately after detonation. Most, if not all, of the RNs released into the subsurface environment following an underground nuclear test are (1) distributed in the resolidified melted rock (termed the “melt glass” or MG), (2) distributed in the water in the disturbed zone (termed “exchange volume”), and (3) sorbed onto the rubblized material in the exchange volume. Pawloski et al. (2001) describe the initial RN distribution by using the average inventory of tests conducted near or below the water table in Western Pahute Mesa (developed by Smith, 2001). In their assessment, the only RNs that have initial distributions in the gas phase are ^{14}C , ^{39}Ar , ^{85}Kr , and to a lesser degree, ^3H . In this source-term model, as in the CHESHIRE source-term model described by Pawloski et al. (2001), we only consider mobilization and migration of RNs in the aqueous phase once the cavity and chimney that form following the test resaturate. Thus, we assume that significant flow and associated transport away from the test zone take place only after full resaturation. Therefore, errors incurred in this source-term model are associated with not accounting for the very early time processes before resaturation. Although the time for resaturation of the BENHAM test is not known, resaturation occurs in the days-to-months time scale, according to Pawloski et al. (2001).

Appendix B describes a detailed two-dimensional, fully coupled thermal-chemical-hydrological (THC) source-term model for BENHAM. The THC model simulates the chemical

reactions associated with MG dissolution, changes in groundwater chemistry, and the feedback such changes have on the dissolution rate. The results of the THC model study are used to help specify a time-varying, temperature-dependent MG dissolution rate, and as a result also specify the RN release rate in this three-dimensional source-term model.

6.1.2 Source-Term Model Goal

The source-term model's goal is to provide a relatively rapid method for evaluating multiple source conditions with variable chimney permeability, initial energy, and sorption properties for reactive RNs. Seventeen RNs with unique initial masses and distributions are considered in multiple source-term sensitivity simulations. The RN mass fluxes from BENHAM to the TSA and LAVA aquifers simulated with the source-term model are designed to provide input to the site-scale transport models described in and Appendix F and Chapter 7. The results from the BENHAM source-term model are abstracted to provide an approximate TYBO source term for simulations investigating the potential relationship between field observations and TYBO contributions.

6.1.3 The BENHAM Test

Described in Section 1.1 and in greater detail by Pawloski (1999), the BENHAM underground test disturbed the local, natural stratigraphy by producing a roughly spherical cavity with a radius of ~ 100 m. Rock vaporized during the explosion condensed and subsequently pooled as a puddle of MG at the bottom of the cavity (Figures 6-1 and 6-2). The remaining volume of cavity (i.e., the volumetric portion of the cavity not occupied by MG) is referred to here as the cavity-exchange volume (EV), as shown in Figure 6-3. Studies of other underground nuclear tests functioning as hydrologic source terms (e.g., Pawloski et al., 2001 and Tompson et al., 1999) include an additional volume of disturbed native rock beyond the EV's collapsed cavity region, extending approximately another half-cavity radius.

The MG mass produced by an underground test can be estimated as 700 metric tons for each kiloton of explosive (Smith, 1993). Hence, the BENHAM test, with an announced yield of 1.15 megatons (DOE, 2000), produced approximately 805 000 metric tons of MG, or between $322\ 000\ \text{m}^3$ and $375\ 000\ \text{m}^3$ by volume (for a rock density ranging between $2500\ \text{kg}/\text{m}^3$ and $2900\ \text{kg}/\text{m}^3$, and not including the void-space volume). This volume of MG is approximately 8 to 10 percent of the total cavity volume. During and following MG formation, the rock immediately above the cavity collapsed, thus creating a cylindrical chimney with a radius of ~ 100 m. Although chimney collapse events often reach to the ground surface, resulting in the formation of a surface crater, BENHAM's chimney collapse did not propagate to the ground surface (Grasso, 2001). Assuming that the void space created during cavity/chimney formation is uniformly distributed within the collapsed rubble, the chimney's porosity will be higher than the native rock. On the other hand, if the newly created void space is just translated to below a competent cap rock that prevented the chimney from extending to the ground surface, then the porosity in most of the chimney could be no greater or even less than the host rock. In this study, we assume uniformly increased porosity in the rubblized chimney, which is consistent with Pawloski et al. (2001). However, we do consider a smaller porosity in the MG than Pawloski et al., as described later in this chapter.

The properties of the collapsed chimney could have a significant impact on whether solutes or particles can migrate vertically from the BENHAM cavity source area to the TSA aquifer. A chimney formed by a rubblized collapse process is expected to have high permeability, whereas a

chimney formed by the collapse of large, intact blocks of rock may retain the original geological properties, including the low permeability of the CHZCM formation. Our conceptual model favors the former because post-test evaluations at the Nevada Test Site of rubblized vitric tuff and ashfall tuff formations indicate high-chimney permeabilities of $1.3\text{e-}11\text{ m}^2$ and $4\text{e-}12\text{ m}^2$, respectively (Snoeberger et al., 1971).

A residual heat source in the MG may drive convective currents and force flow up and into the chimney, if the chimney is of sufficiently high permeability. Under certain permeability and thermal conditions, flow within the cavity/chimney may transport particles and solutes up to the TSA, where horizontal transport (possibly colloid-facilitated) in fractured tuff to the ER-20-5 #1 observation well could occur. The geologic models of Drellack and Prothro (1997) and Prothro and Warren (2001) indicate that the aquitard separating the LAVA and the TSA will allow little hydrologic connection of these aquifers away from the collapsed chimney. Therefore, any fluid, solutes, or particles leaving BENHAM's cavity and reaching the TSA could likely travel vertically in the chimney without entering the LAVA formation. For this to occur, the upward forces acting on the fluid must be greater than the horizontal force associated with the flux in the LAVA. The key factors influencing the likelihood of this occurrence are the residual heat in the MG and the chimney permeability. A sensitivity study presented in this chapter attempts to bracket conditions that lead to vertical transport to the TSA and LAVA aquifers.

6.1.4 The TYBO Test

Rather than developing a full source-term model for TYBO, we used a simple summation of the BENHAM releases to the TSA and LAVA aquifers to approximate a source-term for the site-scale transport simulations that consider TYBO. A full model for assessing the potential for TYBO contributions to the TSA is not necessary because TYBO's cavity is in the TSA. Thus, the errors incurred by not developing a TYBO source model are associated with the total mass release and the rate of release. Although the announced yield for BENHAM is 1150 kt, a range between 200 and 1000 kt is anticipated for TYBO (DOE, 2000). Thus, as an unclassified source, there is substantial uncertainty in the MG's mass and volume, both of which are key components to estimating thermal energy and the release rate of RNs partitioned there initially. Considering the many uncertainties associated with source-term models (discussed later in this chapter and in Pawloski et al., 2001), the approximation for TYBO used in this study captures the essential components of an unclassified source term. The BENHAM model results include components of immediate releases to the aquifer, as well as time-dependent releases associated with MG dissolution. Therefore, our abstraction for the TYBO source is that all mass fluxes from TYBO to the TSA aquifer are equal to the sum of the mass fluxes from BENHAM both to the LAVA and TSA aquifers. At late time, once the initial heat dissipates, BENHAM releases are all to the LAVA, just as the TYBO releases will all be to the TSA, with both forming a reasonable surrogate. At early time, thermal convection brings some BENHAM source RNs to the TSA whereas others exit to the LAVA. No such thermal convection is expected for TYBO because the water table is just above the TSA. Thus, a rough surrogate for early time is to sum BENHAM's TSA and LAVA releases, accepting some error associated with residence times in the chimney (although there are early releases to the LAVA) and differences in flow rates between the LAVA and TSA.

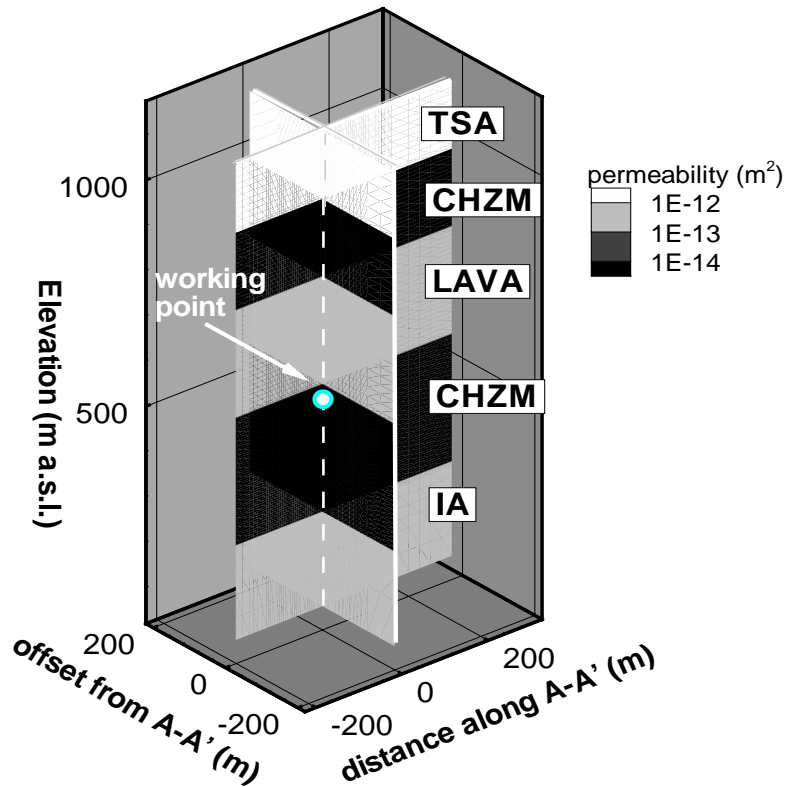


Figure 6-1. The natural, pre-detonation geology of the modeled BENHAM system has the following stratigraphy: Topopah Spring Aquifer (TSA), Calico Hills Zeolitic Composite Unit (CHZM), Lava Aquifer (LAVA), and Inlet Aquifer (IA). The working point (detonation point) for BENHAM was at 512 m above sea level, approximately 1.4 km below the surface. Transect A-A' is shown in Figure 1-1.

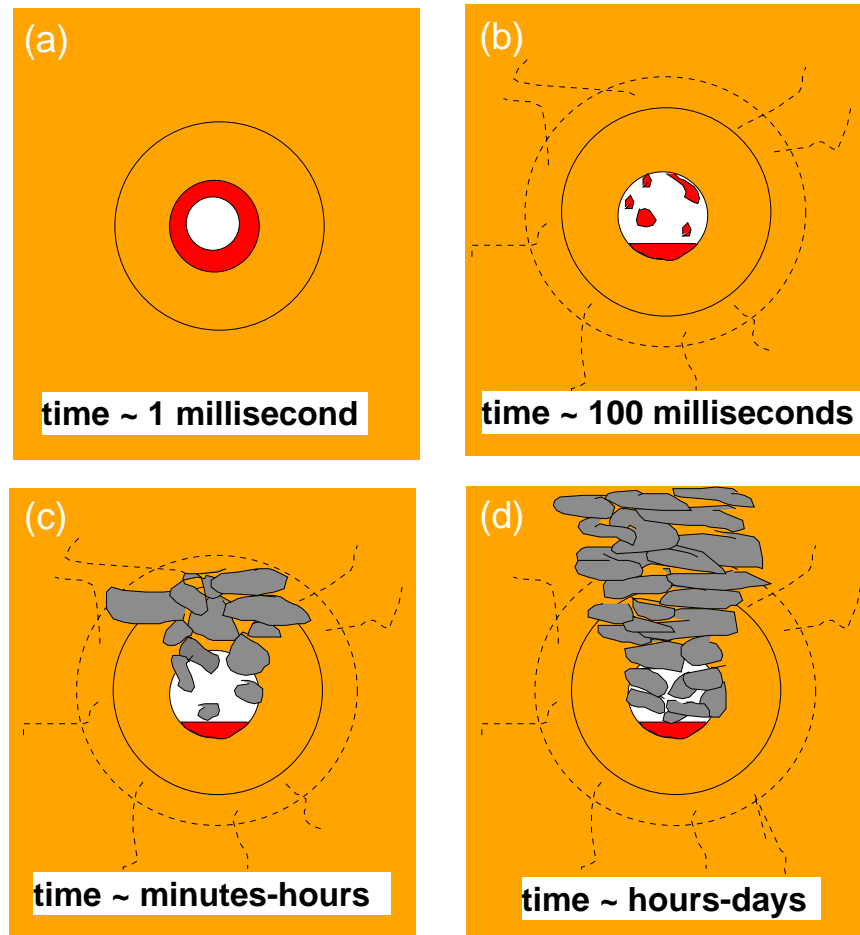


Figure 6-2. Cavity and chimney formation after underground detonation: (a) the rock is vaporized immediately after detonation; (b) after radial fracturing away from the cavity the vaporized rock condenses and begins to form the melt glass (MG); (c) the top of the cavity becomes unstable and begins to collapse into the cavity void and MG; (d) chimney collapse is completed into the cavity void (after Pawloski, 1999, Figure 2).

6.2 Flow and Transport Model

6.2.1 Mass and Heat Flow Model

Used for the sub-CAU flow model in Chapters 3 and 4 and the site-scale transport models in Appendix F and Chapter 7, the flow and transport model FEHM (Zyvoloski et al., 1997) is also used for these source-term simulations. Unique to the application in this chapter are the transient,

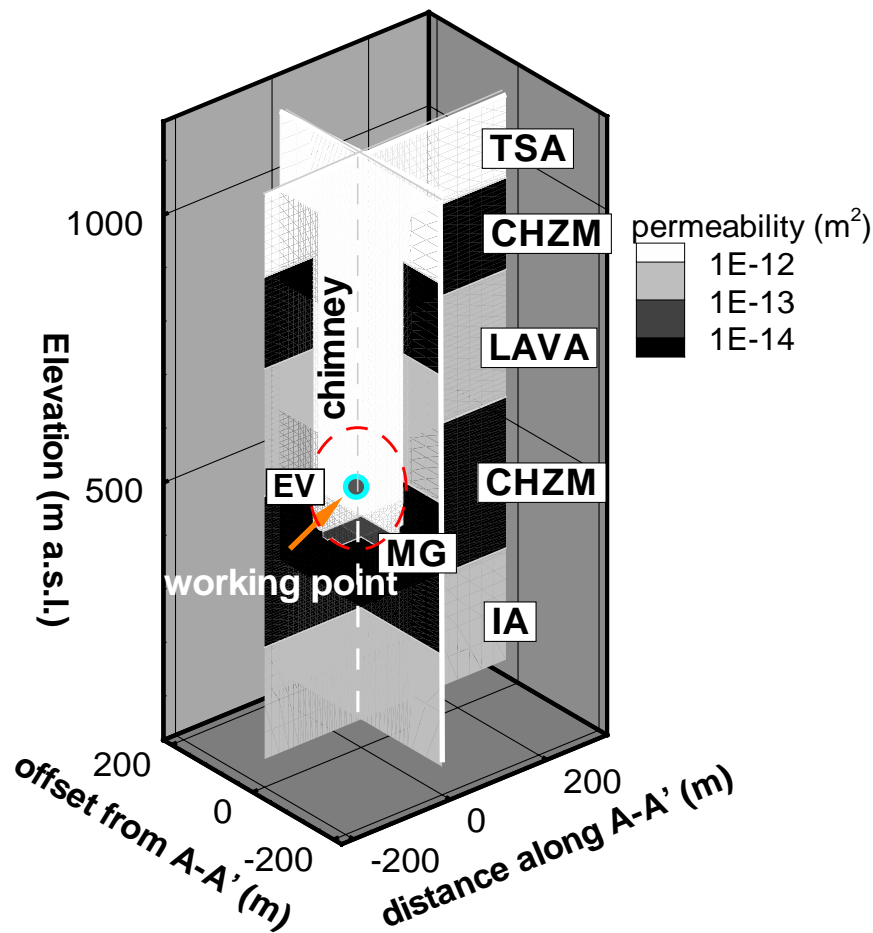


Figure 6-3. The post-detonation geology of the modeled system. A 100-m-radius spherical cavity (outlined by the dashed red line) and cylindrical chimney are added to the natural stratigraphy. The cavity consists of the melt glass (MG) pooled at the cavity bottom with the remaining cavity volume termed the exchange volume (EV). Transect A-A' is shown in Figure 1-1.

non-isothermal conditions associated with the evolution and dissipation of heat in the modeled system. The governing equations solved by FEHM for non-isothermal transient flow are a liquid water-balance equation for pressure and an enthalpy-balance equation for temperature. The flow of liquid water is solved by a conservation of water-mass equation:

$$\frac{\partial \phi S_w \rho_w}{\partial t} + \nabla(\phi S_w \rho_w v_w) = 0, \quad (\text{Eq. 6-1})$$

where ϕ is rock porosity, S_w is water saturation (1 in this case), ρ_w is water density as a function of pressure and temperature, and v_w is aqueous pore velocity as determined using Darcy's Law. The conservation of rock-liquid enthalpy is

$$\frac{\partial[(1-\phi)\rho_s c_{ps} + \phi S_w \rho_w c_{pw}]T}{\partial t} + \nabla(\phi S_w \rho_w h_w v_w - \lambda_m \nabla T) + q_e = 0, \quad (\text{Eq. 6-2})$$

where c_{ps} and c_{pw} are the specific heat capacities of the rock and water, T is the equilibrium temperature of the rock-water system, ρ_s is the grain density of the rock, h_w is the specific enthalpy of the liquid water, λ_m is the effective thermal conductivity of the rock-water system and q_e is an energy output.

FEHM solves the mass and enthalpy equations sequentially by employing the finite-volume computational method on a finite-element grid: this method ensures conservation of mass and energy for problems involving sharp temperature gradients (Zyvoloski et al., 1997). With the finite-volume method, node-based calculations are performed in which the volume surrounding each node is parameterized with the properties assigned to the node (e.g., permeability, porosity, and density).

6.2.2 Particle-Tracking Transport Model

FEHM simulates transport either by solving a reactive advection/dispersion equation (e.g., as in Appendix B and Appendix F) or by particle tracking. The latter method was chosen for this source analysis because of its computational efficiency in transient flow fields. Two particle-tracking transport methods are available in FEHM. The first is the “traditional” Streamline Particle TRacking method (SPTR), based on Pollock (1988) and similar to that of Tompson and Gelhar (1990), which requires accurate resolution of the velocity vector at each location of the modeling domain. The second method employs fluid mass fluxes from node to node as the basis for moving particles; it is modeled in FEHM by determining both the time that a particle spends in a given cell and the time when the particle leaves a given cell for an adjacent cell. This Residence-Time Transfer Function (RTTF) method determines the probabilistic residence time of a particle in a given cell by a transfer function (Zyvoloski et al., 1997). With sufficiently large numbers of particles, this method accurately represents transport in advection-dominated systems (Robinson et al., 2002; CRWMS M&O, 2000b).

As employed by FEHM, both SPTR and RTTF particle-tracking methods accommodate matrix diffusion in fractured media and retardation by adsorption both on fracture walls and within the matrix. Because mass flux quantities are known in finite-volume and finite-element calculations, the RTTF application is less computationally intensive. Therefore, when using RTTF, millions of particles can be tracked in a computationally efficient manner, whereas the SPTR method is slower because velocities must be computed at locations not coincident with grid nodes at every time step in the transient simulation. Therefore, RTTF particle tracking is used here to approximate efficiently the key governing processes associated with a more mechanistic fully-coupled reactive transport model (as described in Appendix B). Note that computational restrictions prevented the extension to three dimensions of the fully-coupled THC model in Appendix B.

6.3 Model Domain, Boundary Conditions, and Initial Conditions

The BENHAM source-term modeling effort focuses on the thermal and physical conditions necessary to induce vertical transport from the BENHAM cavity source to the LAVA and TSA aquifers. The model domain (Figure 6-3) is a plan area of 400 x 500 m centered on the working-point of the BENHAM test (4120466.1 m easting, 546698.7 m northing), and ranges in elevation between 72 m and 1122 m above sea level (a.s.l.), 1842 m and 792 m below the surface. The entire domain is saturated with water because the water table is at an elevation of 1274 m a.s.l. (640 m deep). The local stratigraphy (Figure 6-3), consists of four geologic zones (Drellack and Prothro, 1997; Prothro and Warren, 2001): (1) the welded tuff TSA; (2) the CHZCM; (3) the LAVA, which is embedded within the CHZCM; and (4) a deeper lava formation, the Inlet Aquifer, (IA).

A tetrahedron finite-element grid with 63 240 nodes is used with spacing of $10 \times 10 \times 10 \text{ m}^3$ in the refined area of the cavity/chimney coarsening to $50 \times 40 \times 28 \text{ m}^3$ on the upper-edged boundaries and to $50 \times 40 \times 100 \text{ m}^3$ on the lower-edged boundaries. Fixed boundary pressures are prescribed to both the upstream and downstream boundaries, thereby providing a head gradient of 2 m/km (based on the gradient between BENHAM and the ER-20-5 wells, which is consistent with the final calibrated model). All other boundaries have no flow conditions (i.e., $\nabla p = 0$). Temperatures are fixed at the surface and bottom boundaries to match the observed geothermal gradient with insulation conditions at all other boundaries (i.e., $\nabla T = 0$). The background geothermal gradient between 512 m and 1271 m a.s.l. is $0.01069^\circ\text{C}/\text{m}$, as calculated from thermal logs (Pottoroff et al, 1987). The upper boundary is set at an elevation of 1112 m a.s.l. because this is the approximate elevation of the upper confining unit above the TSA aquifer (Drellack and Prothro, 1997). The lower boundary is set at 62 m, within the inlet aquifer at an elevation deep enough below the working point to have little influence on the transient flow analysis. Similarly, the 400 m width of the plane perpendicular to the flow path and the 500 m length along the flow path are chosen because simulations show limited influence of boundaries at this distance on transient flow analysis within the cavity/chimney.

The entire system is saturated with water and the pressure within the cavity is approximately 8.0 MPa (~800 m of water). The boiling point for water at this pressure is 293°C (Cengel & Boles, 1989). For the initial condition, the detonation event itself is not simulated. Instead, a pre-detonation simulation is run to steady state on the undisturbed stratigraphy (Figure 6-1) to establish a steady flow and temperature field. This steady-state condition is then applied to the disturbed stratigraphy (Figure 6-3) as the initial temperatures and pressures for the post-detonation simulation. For simulations including residual heat from the test, a higher initial temperature in the MG is prescribed uniformly at the initial time. The initial condition is assumed to represent the system after the cessation of all rock collapse events and after the system has cooled to a single phase water continuum (i.e., after temperatures in the cavity have cooled to less than 293°C). The justification for this simplification is that only after the system becomes single phase can water flow away from rather than toward the cavity/chimney. And although there are concerns of prompt injection while the system is still two-phase, we are primarily concerned with a source release of the RNs in the MG and in the cavity/chimney system. It is only once the system

reaches single phase that significant water flow away from the cavity is expected, thereby beginning the onset of aqueous transport.

6.4 Rayleigh-Number Analysis

6.4.1 Relative Rayleigh Numbers

A Rayleigh-number analysis is employed to help characterize the conditions necessary for vertical convection in the cavity/chimney system. Rayleigh numbers (often referred to as Rayleigh-Darcy numbers) are used to determine the onset of vertical convection in a porous medium (Neild & Bejan, 1999). Bau & Torrance (1982) examined the nature of convective flow in a vertical cylinder heated from below with a permeable upper boundary. The heated open cylinder is not entirely applicable to the cavity/chimney system, which is not enclosed by an impervious horizontal boundary and does not exhibit over time a constant vertical temperature gradient within the chimney. However, an initial Rayleigh Number (at time = 0) can be used to gain insight into the nature of the physical and thermal conditions necessary to initiate vertical flow and transport from the cavity to the TSA and LAVA aquifers. The form of the Rayleigh number, Ra , used by Bau and Torrance for a vertical cylindrical system heated from below is

$$Ra = \frac{\rho_w^2 c_{pw} g \beta_w k_p H \Delta T}{\mu_w \lambda_m}, \quad (\text{Eq. 6-3})$$

where ρ_w is water density, c_{pw} is the specific heat capacity of the fluid, g is gravity, β_w is the thermal expansion coefficient of water, k_p is the intrinsic permeability, H is the height of the cylinder, ΔT is the temperature difference between the top and bottom of the cylinder, μ_w is the viscosity of water, and λ_m is the effective thermal conductivity of the porous medium.

A critical Rayleigh number is defined as the Rayleigh number at which convective instability develops. The critical Rayleigh number, Ra_c , for a vertical cylinder can be written as

$$Ra_c = 3.390 \frac{H^2}{r^2}, \quad (\text{Eq. 6-4})$$

where r is the radius of the cylinder (Neild & Bejan, 1999). As mentioned earlier, for the cavity/chimney system, the Ra analysis is further complicated due to the presence of the two transmissive aquifers (TSA and LAVA) intersecting the chimney. To evaluate the influence of these two aquifers, it is instructive to compare system and local Rayleigh numbers, Ra_{sys} and Ra_{loc} , to indicate conditions favorable for vertical transport up the chimney to the TSA. The key difference in these two Rayleigh numbers is cylinder height, H . As shown in Figure 6-4, this height is from the top of the MG to the bottom of the TSA (536 m) for Ra_{sys} , and is from the top of the MG to the bottom of the LAVA (126 m) for Ra_{loc} . To directly compare between system and local Rayleigh numbers, a relative Rayleigh number, defined as the ratio between the Rayleigh number and the critical Rayleigh number, is invoked, where i is either sys for system or loc for local Rayleigh numbers:

$$\hat{Ra}_i = \frac{Ra}{Ra_c} = \frac{\rho_w^2 c_{pw} g \beta_w k_p \Delta T r^2}{3.390 \mu_w \lambda_m H_i} \quad (\text{Eq. 6-5})$$

The relative Rayleigh number can be used for both system and local Rayleigh numbers, where ΔT is specified as the temperature difference between the MG and the bottom of the TSA, or between the MG and the top of the cavity, respectively (see Table 6-1). Note that $\hat{Ra}_{sys} = \hat{Ra}_{loc}$ is used for simulations of constant temperature gradient, whereas $\hat{Ra}_{sys} < \hat{Ra}_{loc}$ is used for simulations in which the temperature gradient is highest near the MG.

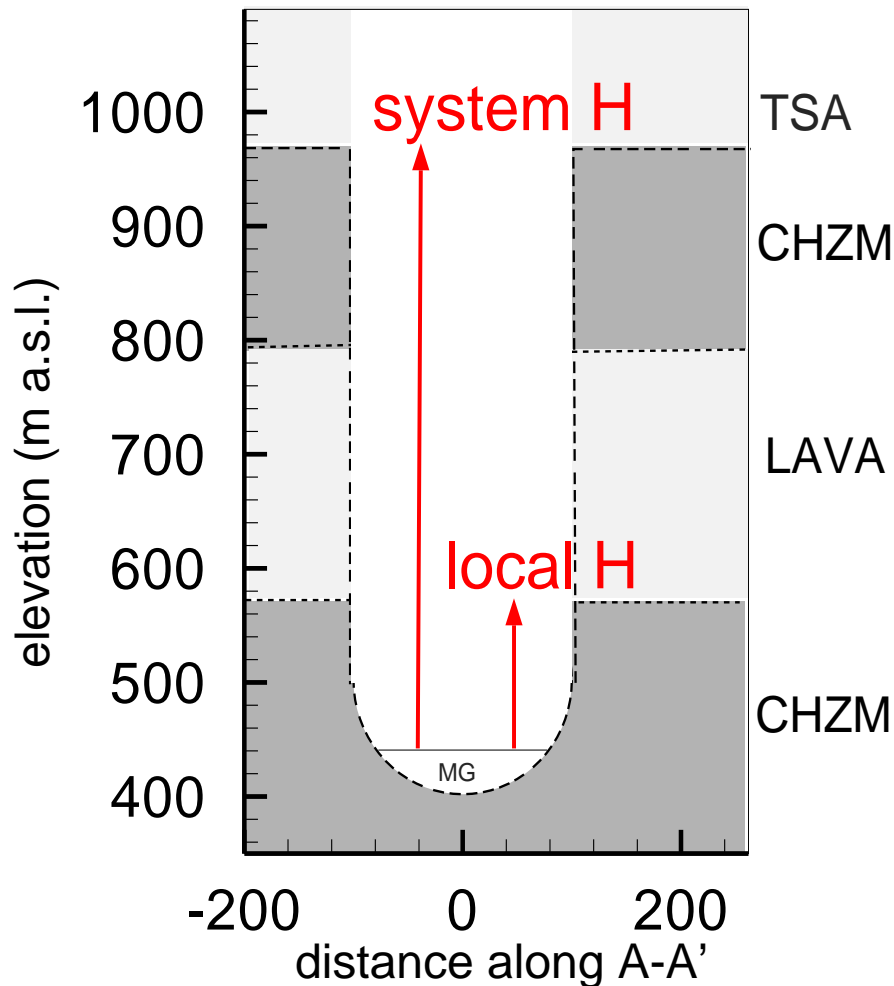


Figure 6-4. System and local H for Rayleigh number calculations in Equation 6-5.

6.4.2 Solute Retardation and Rayleigh Numbers

The Rayleigh number provides an assessment of convective potential within the chimney. Convection from the MG into the cavity/chimney drives the vertical flux in the system. However, retardation describes how much the advection of a non-conservative component is reduced relative to a conservative component. Therefore, a somewhat unconventional extension of Rayleigh

number analyses is to include sorption of solutes to immobile minerals in the Rayleigh number calculation. This inclusion helps to assess the reactive solute migration potential in the cavity-chimney system. In this case, the Rayleigh number, $R\hat{a}^{sorp}$, scaled for retarded transport, can be written as

$$Ra_i^{\hat{sorp}} = \frac{\hat{Ra}_i}{R} = \left(\frac{\rho_w^2 c_p w g \beta_w k_p \Delta T r^2}{3.390 \mu_w \lambda_m H_i} \right) \left(\frac{1}{1 + \frac{(1-\phi)\rho_s K_d}{\phi S_w}} \right) \quad (\text{Eq. 6-6})$$

where R is the retardation coefficient due to the adsorption of the transported solute. Hence, the sorptive Rayleigh number is a measure of the likelihood of vertical convection of a specific RN, taking into account the reduction in advective flux due to sorption. In this case, sorption is considered with a temperature invariant linear partitioning isotherm, K_d . We assume that using temperature invariant K_d s is acceptable for this semi-quantitative analysis, particularly because the variations in K_d s measured at laboratory temperature often span many order of magnitude.

6.5 Model Parameters

6.5.1 Physical and Thermal Parameters

The physical and thermal parameters used in the model are obtained from a variety of sources and the BASE-CASE values are summarized in Table 6-1. Uncertainty in these parameters leads to sensitivity analyses later in this chapter.

Aquifer permeabilities are based on preliminary sub-CAU model calibration results which are bounded by values in Drellack and Prothro (1997). The aquifer and aquitard permeabilities are not identical in the sub-CAU flow model and this source-term model because the models were developed concurrently. Exact transfer of permeabilities from the sub-CAU model to this source-term model would be impossible because (1) the sub-CAU flow model (Chapter 4) does not account for the LAVA unit separately (its effect is part of the composite CHZCM and (2) we are primarily interested in flow and transport in the rubblelized chimney of this source-term model, which is also not part of the sub-CAU flow model.

Density, porosity, heat capacity, and thermal conductivity estimates of the native rock are taken from Yucca Mountain studies (Rautman, 1995; Flint, 1998) and from general values listed in Landolt et al. (1982). The chimney permeability is estimated from measurements recorded by Snoeberger et al. (1971); these numbers are in agreement with the CHESHIRE calibration (Maxwell et al., 2000; Pawloski et al., 2001). The rock density and porosity of the cavity/chimney is estimated by a conservation of mass calculation, where the mass occupying the cavity/chimney region before detonation (M_1) is equal to the mass occupying the cavity/chimney after detonation plus the mass of the MG (M_2). MG permeability is obtained from a preliminary calibration for the CHESHIRE test (Maxwell et al., 2000). As noted in Table 6-1, we chose an MG porosity of 1%, a value appropriate for fractured glass. For the CHESHIRE test, a porosity of 20%, appropriate for vesicular material, was used by Maxwell et al. (2000) and Pawloski et al. (2001). The exact

structure of the MG is unknown, but 20% is considered in the sensitivity analysis. The MG porosity does not affect dissolution rate of glass in this model (Section 6.5.3 describes how the glass dissolution rate depends on temperature and groundwater flux in this model). It does serve to move released particles away from MG faster than if it were 20%, but the total impact is small because the chimney material into which the particles migrate has a high porosity and a substantially larger volume than the MG.

For these calculations, it is assumed that no additional mass is incorporated into the MG as a result of collapsed rock falling into the MG. Pawloski et al. (2001) make the same assumption in their CHESHIRE study due to lack of unclassified data with which to refine the estimate. Because the cavity/chimney is geometrically simplified to a cylinder atop a sphere, the initial mass, M_1 , and final mass, M_2 , can be calculated from the following relations:

$$M_1 = \pi r^2 \left(L_1 \rho_{b1} + \left[L_2 + L_4 + \frac{2}{3}r \right] \rho_{b2} + L_3 \rho_{b3} \right) \quad (\text{Eq. 6-7})$$

$$M_2 = \pi r^2 \left(\left[L_1 + L_2 + L_3 + L_4 + \frac{2}{3}r - \frac{4}{3}f_{MG}r \right] \rho_{bcc} + \frac{4}{3}f_{MG}r \rho_{MG} \right) \quad (\text{Eq. 6-8})$$

In these equations, L_j is the depth of a respective geologic unit ($j=1$ for TSA, 2 for CHZCM, 3 for LAVA, and 4 for CHZCM below the LAVA), ρ_{bj} is the bulk density of geologic unit j such that $\rho_{bj} = (1 - \phi_j) \rho_{sj}$ (where ρ_{sj} is the rock grain density), ρ_{MG} is the density of the MG, and f_{MG} is the volumetric fraction of MG in the cavity (8% for BENHAM). When Equations 6-7 and 6-8 are set equivalent, the bulk density of the cavity/chimney, ρ_{bcc} , can be calculated as

$$\rho_{bcc} = \left[\frac{M_1}{\pi r^2} - \frac{4}{3}f_{MG}r \rho_{MG} \right] \left[L_1 + L_2 + L_3 + L_4 + \frac{2}{3}r - \frac{4}{3}f_{MG}r \right]^{-1} \quad (\text{Eq. 6-9})$$

From this equation, assuming that rock grain density of the cavity/chimney, ρ_{scc} , is the volumetrically-weighted average of the host rock, the cavity/chimney porosity can be calculated by $\phi_{cc} = 1 - \rho_{bcc} / \rho_{scc}$. The resultant values are reported in Table 6-1.

The porosity and permeability of the chimney are assumed to be reasonably represented with a single continuum. In reality, it is possible that large blocks comprise the chimney and are not entirely available to flow. As data become available to parameterize such systems, dual continuum formulations for flow and transport (as used later in this report) may be appropriate.

6.5.2 Radionuclide Source Parameters

Table 6-3 lists 16 RNs associated with the Pahute Mesa source analysis. Pawloski et al. (2001) have expanded the list to 37 RNs, not including colloidal species. However, the original list provides a good representation of significant RNs with different source inventories and transport properties. It also includes all RNs found in the ER-20-5 observation wells, as listed in Tables 1-1 and 1-2. We have added a Pu-colloid pseudo-species and neglected ^{85}Kr , which is distributed primarily in the gas phase. Listed along with the RNs are estimated linear sorption coefficients, Kd , in the cavity/chimney, half-lives, and estimated post-test mass present in the MG and in the EV. In

Table 6-1. Physical Parameters Used in the BASE CASE Simulation

Unit	ϕ_s Matrix Porosity	ρ_s Rock Density (kg/m ³)	c_{ps} Specific Heat Capacity (kJ/kg/°C)	λ_s Thermal Conductivity (W/m/°C)	k_p Permeability (m ²)
TSA	0.161 (a)	2500 (c)	880 (c)	1.8 (b)	5.0e-11 (g)
CHZM	0.25 (a)	2350 (c)	1154 (c)	1.2 (b)	2.0e-14 (g)
LAVA	0.083 (a)	2270 (d)	1000 (d)	2.5 (d)	1.0e-12 (g)
IA	0.083 (a)	2270 (d)	1000 (d)	2.5 (d)	5.0e-13 (g)
Cavity/ chimney	0.185 (h)	2354 (h)	1043 (h)	1.8 (h)	1.0e-11 (e)
MG	0.01 ¹	2900 ²	1154 (d)	2.7 (d)	1.0e-14 (f)

References are (a) Pawloski, 1999; (b) Rautman, 1995; (c) Flint, 1998; (d) Landolt, 1982; (e) Snoeberger et al., 1971; (f) Maxwell et al., 2000; (g) see Table 6-2, and (h) from a mass-averaging of cavity/chimney rock.

¹The low BASE-CASE MG porosity used in this study reflects fractured glass. A larger value would be more appropriate for a vesicular material (note: Pawloski et al., 2001 use a porosity of 0.2 in their MG). 0.2 is considered in the sensitivity analysis (See Table 6-4). Note, the MG porosity does not affect the dissolution rate of glass in this model. It does serve to move released particles away from MG faster than if it were 0.20, but the total impact is small because the chimney material into which the particles migrate has a relatively high porosity and a substantially larger volume than MG.

²A density of 2900 kg/m³ was assumed for the MG in these calculations based on estimates associated with a particularly dense basalt. More recent analyses (Pawloski et al., 2001) indicate that an MG density of 2400 kg/m³ may be appropriate. The net impact of such a reduction would be to reduce the heat conduction by the MG by approximately 20%, a small impact considering that heat dissipation in this system is convection dominated.

this study, the EV is defined as the volume of the cavity, prior to collapse, not including the region occupied by MG (Note Pawloski et al., 2001 extend the EV to include about an additional 0.5 cavity radius). This source-term model conceptualizes the cavity/chimney as a single porous medium. Little data exist to develop a more complex representation. In a more detailed source-term study, focussing on the cavity/chimney system, Pawloski et al. (2001) also represent the material in the chimney as homogeneous porous media. In reality, it is possible that large blocks may make up the rubble, and if so then a dual continuum model may be more appropriate to represent mass transfer into the blocks when characterization data from chimneys are available.

The total number of moles of the RNs at the BENHAM test is estimated to be the average unclassified inventory for 76 Pahute Mesa nuclear tests below or within 100 m of the groundwater table (Smith, 2001). For example, in the case of plutonium (Pu) this average gives an estimated

Table 6-2. Comparison of Permeabilities in Various Studies (Units are m²)

HSU	DP _{min}	DP _{max}	This Chapter (Base Case)	THC Appendix B	Pawloski et al. (2001)	Calibration (Chapter 4)
TSA	6.65E-12	4.00E-11	5.00E-11	4.00E-11		3.10E-11
CHZM	1.33E-15	2.00E-11	2.00E-14	4.00E-15		
LAVA			1.00E-12*	5.00E-13		
IA	1.33E-13	6.65E-12	5.00E-13	6.15E-13		1.65E-13
Chimney			5.00E-11*	5.00E-11	5.00E-11	
MG			1.00E-14*	5.00E-13	4.00E-14	

Notes:

DP = Drellack and Prothro (1997).

*Parameters treated as uncertain in sensitivity analysis.

Much work on different source-term models was conducted concurrently or nearly concurrently on this and other studies. Generally, native material properties are drawn from the range of Drellack and Prothro (1997), although differences between exact values used in this chapter and Appendix B are due to refined understanding of the system during the progression of the study. For example, the LAVA aquifer permeability was initially set approximately the same as the IA in the THC model. It was increased in this chapter to take into account the high values measured at Bullion (and it is treated later as an uncertain parameter in the sensitivity study). Similarly, the CHZM permeabilities were increased slightly due to preliminary calibration results, although they are still so low that little significant flow occurs in the unit.

The CHZM includes the LAVA in the HSU model. Thus, the range presented for this unit includes high-permeability lava beds. Therefore, very low values are used in the source-term models for this part of the CHZM, excluding the LAVA.

MG permeability reduced in this chapter per Maxwell et al. (2000).

total post-detonation mass of 18.7 moles (17.1 moles of ²³⁹Pu; 1.5 moles of ²⁴⁰Pu; and 0.1 total combined moles of ²³⁸Pu, ²⁴¹Pu, and ²⁴²Pu). It is estimated that of the total 18.7 moles, 17.8 moles (95%) initially resides within the MG while the rest is distributed amongst the rubble and pore water of the cavity EV.

The RNs listed in Table 6-3 are grouped into five classes (I through V) with a sixth class (VI) used to represent a Pu-colloid pseudo-species. The classes are based on similar sorption properties, determined from Yucca Mountain sorption tests on crushed tuff (see Appendix F). RN Class I consists of conservative species present in the MG and EV, such as tritium (³H); RN Class II and III consist of highly sorbing species such as americium (Am); RN Class IV consists of neptunium (Np) and uranium (U); and RN Class V is Pu. The Pu sorption estimate is very conservative at 5 cc/g.

Table 6-3. Radionuclide Classes, Parameters, and Distribution

Radionuclide (RN Class)	Cavity/Chimney K_d (cc/g) ³ , Retardation factor in parentheses	Half-life (years) ¹	Total Estimated Mass Present (moles) ¹	% of Mass Estimated in MG ²	% of Mass Estimated in Cavity EV ²
³ H (I)	0 (1.0)	12.3	31.3	0	98
¹⁴ C (I)	0 (1.0)	5730	.117	0	20
³⁶ Cl (I)	0 (1.0)	3.01e5	2.37	50	50
⁹⁹ Tc (I)	0 (1.0)	2.13e5	2.41	80	20
¹²⁹ I (I)	0 (1.0)	1.57e7	.544	50	50
¹⁵¹ Sm (II)	100 (1041.)	90	.189	95	5
²⁴¹ Am (II)	100 (1041.)	433	.0743	95	5
¹⁵² Eu (II)	100 (1041.)	13.5	.0163	95	5
¹⁵⁴ Eu (II)	100 (1041.)	8.59	.0049	95	5
⁹⁰ Sr (III)	10 (105.)	29.1	1.28	40	60
¹³⁷ Cs (III)	10 (105.)	30.2	1.68	20	80
²³⁴ U (IV)	1 (11.4)	2.46e5	1	90	10
²³⁸ U (IV)	1 (11.4)	4.47e9	408	90	10
²³⁷ Np (IV) ⁶	.1 (2.04)	2.14e6	2.87	95	5
²³⁹ Pu (V)	5 (52.9)	2.41e4	17.1	95	5
²⁴⁰ Pu (V)	5 (52.9)	6560	1.5	95	5
Pu-colloid (VI) ⁵	0 (1.0)	2.41e4	1.86e-3 ⁴	95	5

¹Radioactive half-life and total estimated mass based on an average inventory of tests below or within 100 m of the water table on Pahute Mesa, decay corrected to 1994 from Smith (2001). Note: we do not decay correct Smith's unclassified inventory to the BENHAM test date in 1968 because this is an unclassified average. However, such correction would increase the initial mass of ³H, Eu, and Cs significantly (and is discussed in Chapter 7).

²Distribution of RNs between the MG and EV are based on Pawloski et al. (2001) which are derived from IAEE (1998)

³RN adsorption in the cavity/chimney is estimated from the Yucca Mountain Project data base (see Appendix F and Chapter 7). Values used here are taken from low ends of the ranges, anticipating reduced sorption under elevated temperature. (Analysis later in this chapter highlights sensitivity to whether any sorption is considered.) Under less simplifying assumptions, it is likely that the K_d varies with temperature. This is somewhat accounted for by specifying values from the low end of the range of measurements uniformly throughout the chimney where it is unlikely that such low values would exist everywhere at 25°C.

⁴The Pu associated with colloids is assumed to have a net mass 1/10000 of total Pu mass (see Section F.5.3).

⁵The association of nuclides other than Pu with colloids is considered in Chapter 7, with a source release function scaled to a fraction of the individual RN's inventory and unretarded transport in the chimney. Pu is the only nuclide for which an estimate of initial inventory could be computed based in sorption/desorption experiments.

⁶Np is generally considered to behave similarly to U in this report. However, the K_d for chimney sorption used for Np is smaller than that for U in the source-term study because (a) Np K_d values on Yucca Mountain tuffs are somewhat lower than U and (b) to demonstrate later in this chapter differences in release times to the aquifers when sorption is considered (the only reactive species to arrive at the TSA are Np and U).

6.5.3 Glass Dissolution Estimation

Appendix B describes the chemistry and controlling processes associated with MG dissolution under transient, non-isothermal conditions. Based on the details in Appendix B, we developed an approximation for the dissolution of MG and the associated release of RNs for our three-dimensional source-term model. The release of RNs from MG can be estimated through the dissolution of glass and the stoichiometric ratio of the RNs in the MG. The stoichiometry of a RN in MG can be estimated by relating the 8.0×10^8 kg of MG of molecular weight 100 g to each RN yielding, for example in the case of Pu, a stoichiometric ratio of 2.22×10^{-9} moles Pu/moles MG.

The fully-coupled THC reactive transport studies in Appendix B indicate that there are two dominant processes affecting the glass dissolution rate: (1) a surface controlled rate based on temperature and (2) a diffusion controlled rate (see Figure B-5). In this case, the first condition is enhanced by an Arrhenius function and the second by a transport/dissolution limitation. Considering both of these processes, the glass dissolution rate, $I_{diss-glass}$, is

$$I_{diss-glass} = \min(I_{temp-glass}, I_{flux-glass}), \quad (\text{Eq. 6-10})$$

where $I_{temp-glass}$ is the rate with Arrhenius enhancement and $I_{flux-glass}$ is the rate when limited by transport/dissolution. $I_{temp-glass}$ is approximated by a simplification of Equation B-27 as

$$I_{temp-glass} = k_{temp-glass} A, \quad (\text{Eq. 6-11})$$

where A is the specific surface area (10/cm in this case -- see Table B-5; Pawloski et al. (2001), use a similar value of 25/cm) and the rate constant $k_{temp-glass}$, which is written as

$$k_{temp-glass} = k_0 f_A(T), \quad (\text{Eq. 6-12})$$

where k_0 is the dissolution rate constant of the MG at 25°C neglecting pH and other water chemistry changes, estimated as 2.57×10^{-16} moles glass/cm²/sec (see k_0 in Appendix B). The Arrhenius factor, $f_A(T)$, empirically represents the positive relation between temperature and dissolution as a function of temperature (see Equation B-29). In this study, the specific surface area is not varied in the sensitivity analysis. However, Pawloski et al. (2001) examine the sensitivity to predicted melt glass dissolution associated with this uncertain parameter. The equation

$$f_A(T) = \exp\left(\frac{\Delta H}{R} \left(\frac{1}{T_0} - \frac{1}{T}\right)\right) \quad (\text{Eq. 6-13})$$

is of exponential form, where ΔH is the activation enthalpy, R is the gas constant, and T_0 is an absolute reference temperature (in Kelvin). For glass, the activation enthalpy is 83.74 kJ/mol. Therefore, Equation 6-13 can be rewritten for the dissolution of MG as

$$f_A(T) = \exp\left[10071.8 \left(\frac{1}{T_0} - \frac{1}{T}\right)\right] \quad (\text{Eq. 6-14})$$

The second temperature-dependent process factoring into Equation 6-10 is the transport/dissolution-limited release rate, where PuO₂ and other RN releases from the MG are related to the

dissolution and aqueous concentration of $\text{SiO}_2(\text{am})$. Dissolution-limited releases are approximated with the three-dimensional flow model, which considers silica-saturated water that flushes upward from the MG (at temperature T_1 , 5 m below the top of the MG) to the cavity/chimney region (not silica saturated at temperature $T_2 < T_1$, 5 m above the top of the MG). The vertical temperature gradient, $(\Delta T/\Delta z)_{12}$, and the absolute magnitude of the vertical flux, $q_{w,12}$, are dynamic and are recorded during transient, non-isothermal three-dimensional flow simulations. As the dissolved SiO_2 is flushed out of MG, it is assumed that MG dissolves at a rate to replace it. This is represented by

$$I_{flux-glass} = -S_{glass}q_{w,12}\frac{dC}{dT}\left(\frac{\Delta T}{\Delta z}\right)_{12}, \quad (\text{Eq. 6-15})$$

where S_{glass} is the stoichiometric ratio of MG to $\text{SiO}_2(\text{am})$, 1.307. The saturation concentration of $\text{SiO}_2(\text{am})$, C , is a function of temperature approximated from the EQ3/6 database as

$$\log_{10}(C) = c_1 + \frac{c_2}{T^2} + \frac{c_3}{T} + c_4\tau + c_5\ln(\tau), \quad (\text{Eq. 6-16})$$

where $\tau = T + 273.15^\circ\text{C}$ and c_1, c_2, c_3, c_4 and c_5 are coefficients fit to data ($c_1 = -167.471$, $c_2 = -648289$, $c_3 = 9434.79$, $c_4 = -0.0208465$, and $c_5 = 25.7021$). The derivative of C with respect to temperature, as needed in Equation 6-15, is

$$\frac{dC}{dT} = C\ln(10)\left(\frac{c_5}{T} + c_4 - \frac{c_3}{T^2} - \frac{2c_2}{T^3}\right) \quad (\text{Eq. 6-17})$$

This fairly simple approximation can capture a process that the more detailed THC model in Appendix B highlights as important, although the equation and implementation are quite a bit simpler in this case because the concentration of $\text{SiO}_2(\text{am})$ is a function of temperature but not of surface area. However, Equation 6-15 does account for rate changes as a function of both flow rate and temperature through the MG.

Equations 6-12 and 6-15 are used to estimate the glass dissolution rate in Equation 6-10. With this glass dissolution rate, the RN release rate from the MG is then determined from stoichiometry as

$$I_{RN} = S_{RN}I_{diss-glass} \quad (\text{Eq. 6-18})$$

where S_{RN} is the ratio of the RN in the MG (e.g., $2.22\text{e-}9$ for PuO_2). Thus, the simple case for 25°C , and assuming dissolution into water free of silica, yields a glass dissolution rate estimated from Equation 6-11 of $2.56\text{e-}15$ moles glass/cc/sec (for $A = 10/\text{cm}$). The Pu release rate, from Equation 6-18 is $5.7\text{e-}24$ mol Pu/cc/sec.

6.5.4 Transient Particle Release in the Melt Glass

The time-history of glass dissolution/RN release is simulated by releasing a large number of particles from the MG in temporal agreement with the dissolution limitation of Equation 6-10.

The glass dissolution rate is determined separately for each scenario, taking into consideration the three-dimensional models because each scenario has a different MG temperature history and a different vertical flux history, both of which are dependent on material properties and initial temperature. Particles are released uniformly according to Equations 6-10 and 6-18 over specified binning time periods at the average release rate for that time period. The time periods are shorter at first to capture the more transient nature of initial release. A 50-day binning period is used for the first 5 years; a 100-day binning period is used for years 5 through 10; and an ever-increasing binning period is used after year 10. Particles are released within each $10 \times 10 \times 10 \text{ m}^3$ grid block of the MG.

To demonstrate this method, two dissolution examples are briefly discussed: CASE 1 and CASE 5B, both of which are shown in Table 6-4. These two examples are transient-heat and mass-flow simulation scenarios; they are discussed in more detail in Section 6.6. First, dissolution and RN release for the BASE CASE simulation is considered ($R\hat{a}_{sys} = 84.6$, CASE 1, Table 6-4). For CASE 1, the temperature in the MG decreases from an initial 290°C to just under 150°C after 10 years and to 70°C after 35 years (Figure 6-5). Figure 6-6 illustrates the temperature history, the estimated Pu dissolution rate as predicted by Equation 6-10, and the particle-release history. The MG dissolution rate, and hence Pu release rate, is controlled by the dissolution rate adjusted by either the Arrhenius factor or the flux-solubility limitation, whichever is lowest. In this case, the dissolution rate is limited by the flux-solubility limitation at all times, as shown in Figure 6-6. The estimated particle equivalent of 385 800 particles/mole Pu was computed by equating a dissolution limitation of $1.266\text{e-}19$ moles Pu/cc/sec at $t = 0$ years, with 211 particles released from each MG node ($10 \times 10 \times 10 \text{ m}^3$) over the first 50 days. As estimated by Equation 6-10 at 20 years, the dissolution rate is very similar to the more mechanistic rate estimated by the complete THC modeling effort described in Appendix B. For example, after 20 years of simulation, the particle-release estimate of the Pu dissolution rate is $3.9\text{e-}22$ moles Pu/cc/sec, whereas the THC model predicts a maximum dissolution rate of $8.5\text{e-}22$ moles Pu/cc/sec (Figure 6-7). However, note in Figure 6-7 that the maximum rate in the THC model only occurs in a small portion of the MG. By applying the same rate everywhere in the MG in this three-dimensional model (also done in Pawloski et al., 2001), substantially more glass dissolves, leading to conservative approximations.

The second case considered from Table 6-4, CASE 5B ($R\hat{a}_{sys} = 84.6$), differs from CASE 1 in that the MG permeability is an order of magnitude larger, thus promoting greater flux through the MG. Figure 6-8 shows that the release rate of Pu from the MG is governed by the flux-solubility limitation only at early times ($t < 11$ years), after which the temperature dependence controls the rate. As with the CASE 1 example, the estimated particle equivalent of 385 800 particles/moles Pu was computed by equating a dissolution limitation of $1.266\text{e-}19$ moles Pu/cc/sec at $t = 0$ years, with 211 particles released from each MG node ($10 \times 10 \times 10 \text{ m}^3$) over the first 50 days.

Table 6-4. Parameters for Sensitivity Analysis

Simulation Scenario	$R\hat{a}_{sys}$	$R\hat{a}_{loc}$	$T_{0,MG}$	V_{MG} (1000 m ³)	ϕ_{MG}	$k_{p,cc}$ (m ²)	$k_{p,MG}$ (m ²)	$k_{p,LAVA}$ (m ²)
BASE CASE (CASE 1)	84.6	355	290	326	0.01	1e-11	1e-14	1e-12
CASE 2A	0.85	3.55	290	326	0.01	1e-13	1e-14	1e-12
CASE 2B	8.46	35.5	290	326	0.01	1e-12	1e-14	1e-12
CASE 2C	846.	3550.	290	326	0.01	1e-10	1e-14	1e-12
CASE 3A	1.89	1.89	40	326	0.01	1e-11	1e-14	1e-12
CASE 3B	18.9	18.9	40	326	0.01	1e-10	1e-14	1e-12
CASE 4	38.4	158.	150	326	0.01	1e-11	1e-14	1e-12
CASE 5A*	87.9	422.	290	756	0.01	1e-11	1e-14	1e-12
CASE 5B*	84.6	355.	290	326	0.01	1e-11	1e-13	1e-12
CASE 5C*	84.6	355.	290	326	0.2	1e-11	1e-14	1e-12
CASE 6A*	84.6	355.	290	326	0.01	1e-11	1e-14	1e-11
CASE 6B*	84.6	355.	290	326	0.01	1e-11	1e-14	1e-13

Twelve simulation scenarios were examined that had variations in initial MG temperatures (T_0), in MG volume (V_{MG}), in MG porosity (ϕ_{MG}), in cavity/chimney permeability ($k_{p,cc}$), in MG permeability ($k_{p,MG}$), and in LAVA permeability ($k_{p,LAVA}$). Note that the change from BASE CASE for each simulation scenario is in bold type. Cases followed by an asterisk (*) indicate scenarios that cannot be compared with the BASE CASE using a Rayleigh number analysis because the number does not account for changes in porosity or for differences in permeabilities outside of the chimney.

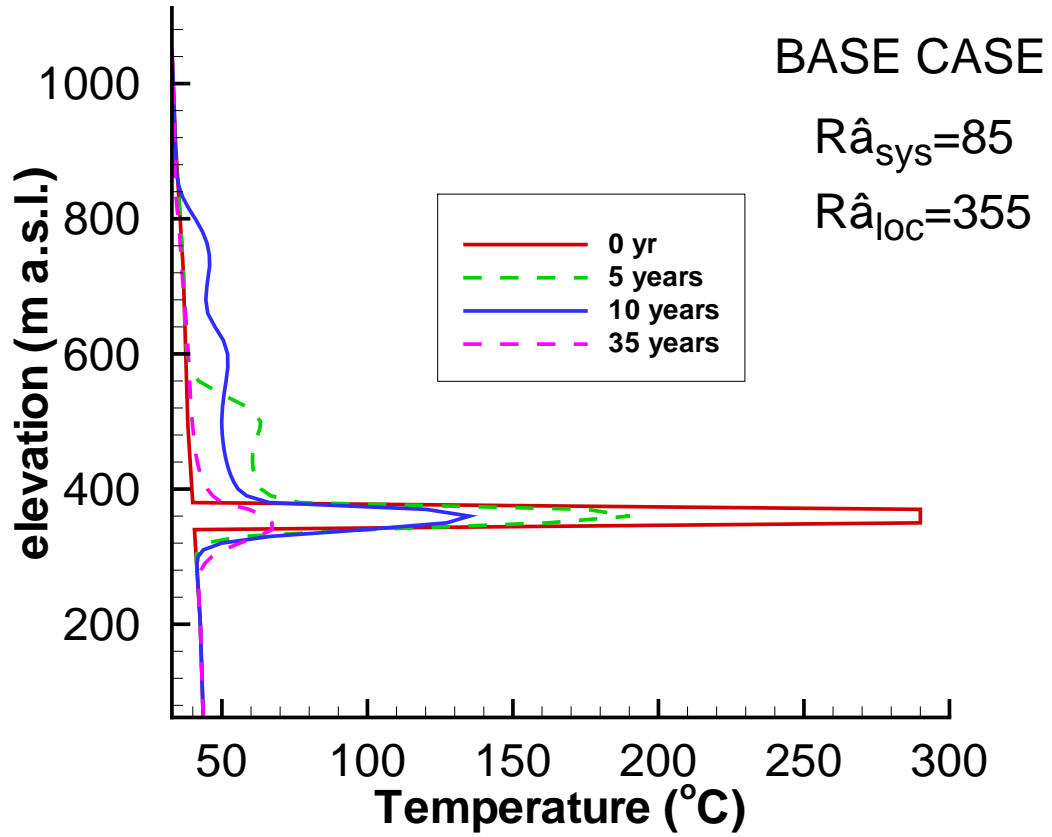


Figure 6-5. Vertical temperature profiles at the center of the cavity/chimney system for the BASE CASE simulation.

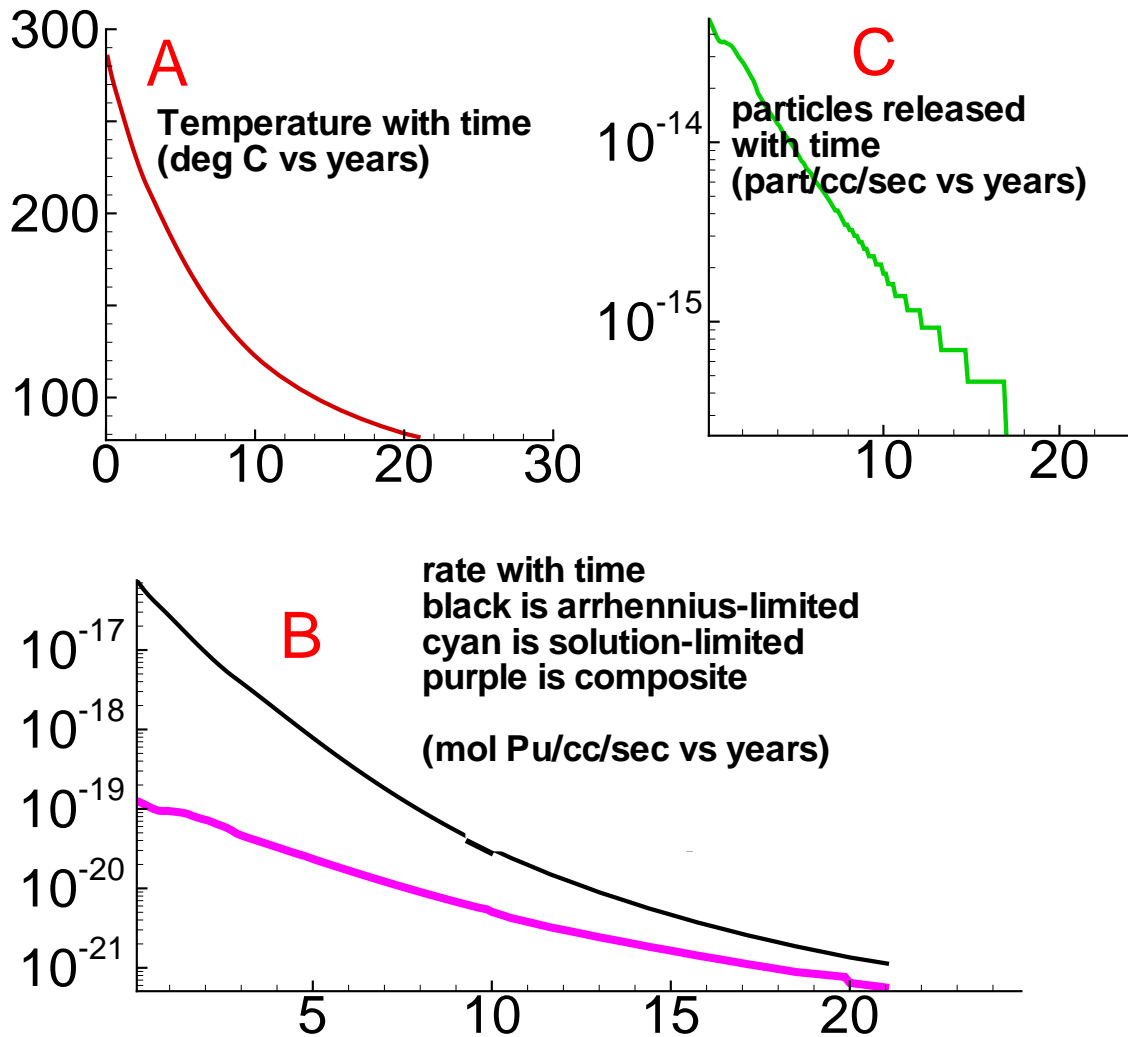


Figure 6-6. Simulated MG temperature history from the BASE CASE simulation and the Arrhenius factor for an activation energy of 83.74 kJ/mol. Plot A is the temperature history in the middle of the MG, plot B is the Pu release history from Equation 6-10, and plot C is the particle-release history based on Equation 6-10 and 385 000 particles/mole Pu.

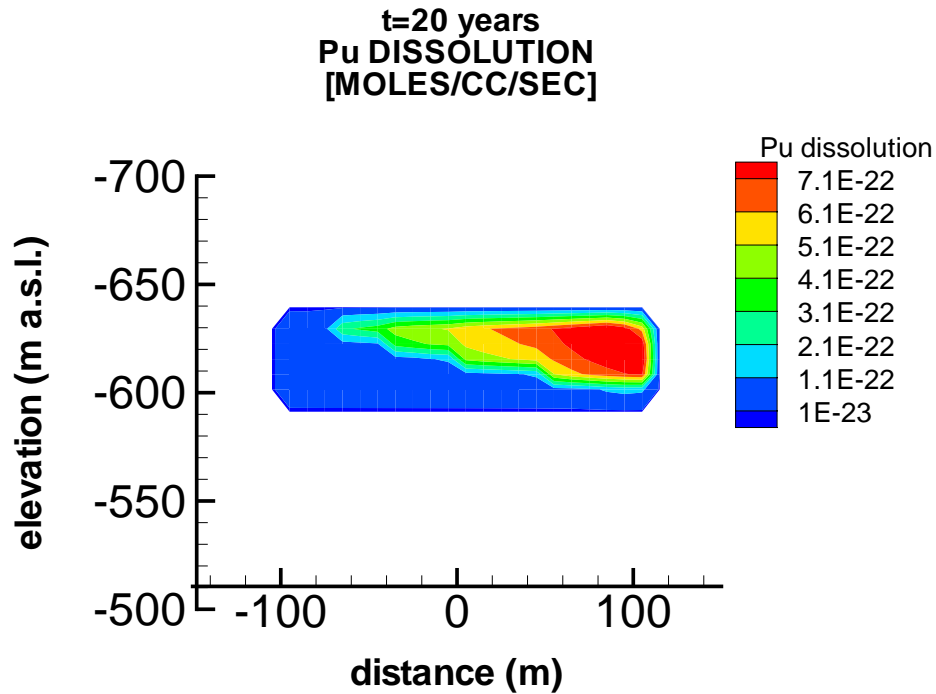


Figure 6-7. Two-dimensional FLOTRAN simulations of MG/Pu dissolution (see Appendix B). Note that the maximum glass dissolution of 3.85×10^{-13} moles glass/cc/sec is the equivalent of 8.5×10^{-22} moles Pu/cc/sec (compared with 3.9×10^{-22} moles Pu/cc/sec estimated for the BASE CASE at 20 years).

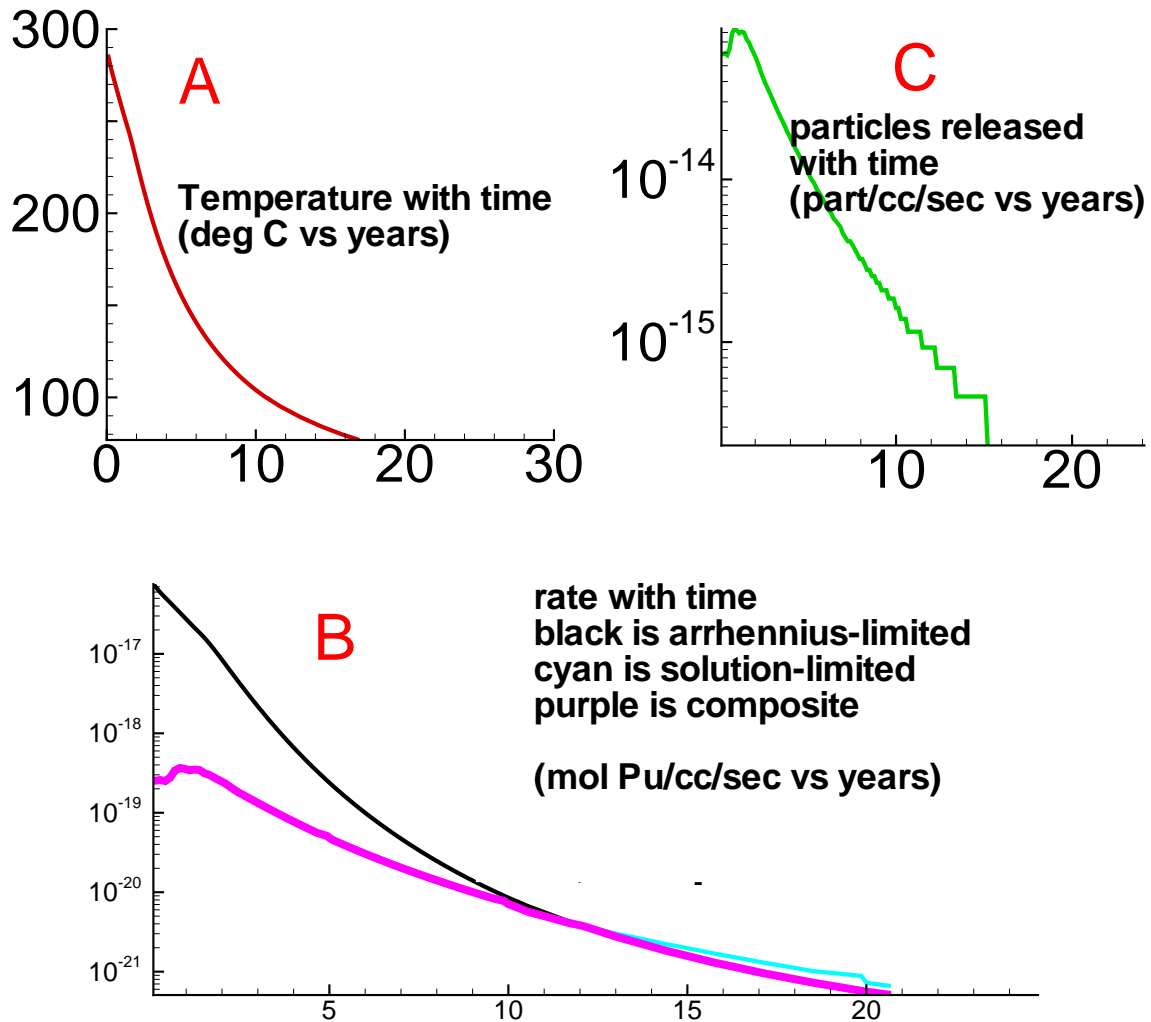


Figure 6-8. Simulated MG temperature history from the higher permeability MG simulation (CASE 5B) and the Arrhenius factor for an activation energy of 83.74 kJ/mol. Plot A is the temperature history in the middle of the MG, plot B is the Pu release history from Equation 6-10, and plot C is the particle-release history based on Equation 6-10 and 385 000 particles/mole Pu.

6.6 Melt Glass Release: Conservative Radionuclide Example

To assess the physical, chemical, and thermal conditions necessary for vertical migration of RNs in the BENHAM chimney, we conduct sensitivity simulations with varying permeabilities and initial conditions to bracket the conditions necessary for vertical convection and transport to the TSA and LAVA aquifers. The likelihood of vertical transport to these aquifers is judged against Rayleigh number calculations with the goal of using the initial Rayleigh number as a simple transport predictor for future analysis. As a demonstration of the release process, we first consider a conservative RN release from the MG only in this section; a combined release of MG and EV mass for each of the 17 RNs is addressed in Section 6.8.

The greatest parameter uncertainty in these simulations is associated with the nature of the MG (temperature and volume) and the physical properties of the collapsed chimney/cavity. To bracket the uncertainty of the modeling results, simulation cases for various chimney properties are investigated with and without residual heat in the MG. The BASE-CASE simulation investigates flow and transport over 1000 years using best estimates for MG temperature and chimney properties (see Table 6-1). As perturbations of the BASE CASE condition, the other simulations, listed in Table 6-4, often have different Rayleigh numbers than the BASE CASE due to variations in rock permeability or variations in initial MG temperature.

Approximately one million particles are released from the MG for each of the simulated cases. The particles are released in a time-varying manner according to the glass dissolution rate (see Section 6.5.3); for example, for the BASE CASE, dissolution drops from ~1500 particles/day over the whole MG at time = 0 to ~15 particles/day over the whole MG at time = 15 years. The exact number of particles released varies with each simulated scenario because of differences in dissolution-rate histories. Depending on the simulation scenario, particles may or may not reach the TSA or LAVA aquifers. For the analysis in this section, only conservative particles originating in the MG are considered. The estimated arrival time of the conservative RN to the aquifers occurs when 0.01% of the total mass present in the MG exits the chimney into the aquifer. Tables 6-5 and 6-6 register, for each simulation case, the arrival time estimates to the TSA and LAVA, respectively, along with the percentage of total MG-based RN mass entering the aquifer after a simulation of 1000 years.

Table 6-5. Mass Arrival to the TSA and $R\hat{a}_{sys}$

Simulation Scenario	$R\hat{a}_{sys}$	Arrival Time at TSA of 0.01% of MG-Source Solute (years)	% of Total Mass Entering TSA after 1000 yrs
BASE CASE (CASE 1)	84.6	11.35	13.83
CASE 2A(low chim. perm)	0.846	no arrival	0.00
CASE 2B(med. chim. perm.)	8.46	88.37	0.304
CASE 2C (high perm. chim.)	846.	2.383	21.11
CASE 3A (no residual heat)	1.89	no arrival	0.00
CASE 3B (no heat, high perm)	18.9	no arrival	3.95e-9
CASE 4 (low MG temp.)	38.4	27.24	0.2747
CASE 5A (high MG vol.)	87.9	8.435	45.91
CASE 5B (high MG perm.)	84.6	6.045	46.37
CASE 5C (high MG por.)	84.6	12.14	12.67
CASE 6A (low LAVA perm.)	84.6	12.06	22.51
CASE 6B (med LAVA perm.)	84.6	10.84	0.663
CASE 6C (high LAVA perm.)	84.6	10.83	0.655

Table 6-6. Mass Arrival to the LAVA and $R\hat{a}_{loc}$

Simulation Scenario	$R\hat{a}_{loc}$	Arrival Time at LAVA of 0.01% of MG-Source Solute (years)	% of Total Mass Entering LAVA after 1000 yrs
BASE CASE (CASE 1)	355	3.286	9.117
CASE 2A(low chim. perm)	3.55	48.82	12.00
CASE 2B(med. chim. perm.)	35.5	9.501	21.18
CASE 2C (high perm. chim.)	3550	1.471	0.8902
CASE 3A (no residual heat)	1.89	no arrival	3.118e-6
CASE 3B (no heat, high perm)	18.9	no arrival	3.531e-9
CASE 4 (low MG temp.)	158.	7.743	1.657
CASE 5A (high MG vol.)	422	2.521	7.233
CASE 5B (high MG perm.)	355	2.380	14.35
CASE 5C (high MG por.)	355	4.092	7.580
CASE 6A (low LAVA perm.)	355	5.992	0.7691
CASE 6B (med LAVA perm.)	355	2.038	21.52
CASE 6C (high LAVA perm.)	355	2.028	21.52

6.6.1 Comparison with THC Model

As modeled using FEHM with RTTF particles in this chapter, solute transport to the TSA and LAVA aquifers has been directly compared to the THC simulations described in Appendix B. When RTTF particles are released in a two-dimensional simulation in accordance with Equation 6-10, results compare well with THC modeling results illustrated in Figure B-12. For the comparison, a two-dimensional FEHM model was constructed with identical dimensions and parameters as those listed in Appendix B. The curves shown in Figure 6-9 show relative peaks and arrival times roughly in agreement with the THC model results. Although the comparison serves to validate the approach used in the three-dimensional source-term model, it must be noted that parameters were then changed in the three-dimensional model during the evolution of this project because subregional calibration was completed and other information became available.

These two-dimensional comparison results exhibit some important differences from the three-dimensional RTTF results, which are presented later in this chapter. It is important to note that the three-dimensional model results are generally shown as mass flux or cumulative mass curves exiting the cavity/chimney system into the TSA and LAVA aquifers. Figures B-12 and 6-9 show breakthrough concentration curves exiting the downstream modeled domain for a system in which porous media conditions are assumed for the LAVA (see Appendix B). Therefore, a key difference in these simulations and the simulations described later in this chapter is the timing of

RN entry to the LAVA aquifer. In Figures B-12 and 6-9, downstream breakthrough in the less permeable LAVA aquifer occurs after downstream breakthrough in the TSA. In the forthcoming figures illustrating three-dimensional results, RNs always enter the LAVA aquifer from the cavity/chimney before entering the TSA aquifer. A second difference between the breakthrough curves of Figure 6-9 and the forthcoming three-dimensional curves in this chapter is the time of arrival of the TSA pulse. In the two-dimensional simulations, this arrival occurs after approximately 5 years, whereas the three-dimensional simulations predict arrival times of 10 years or later. This discrepancy is explained by dimensional effects and the use of a higher chimney permeability ($5 \times 10^{-11} \text{ m}^2$) in the two-dimensional simulations.

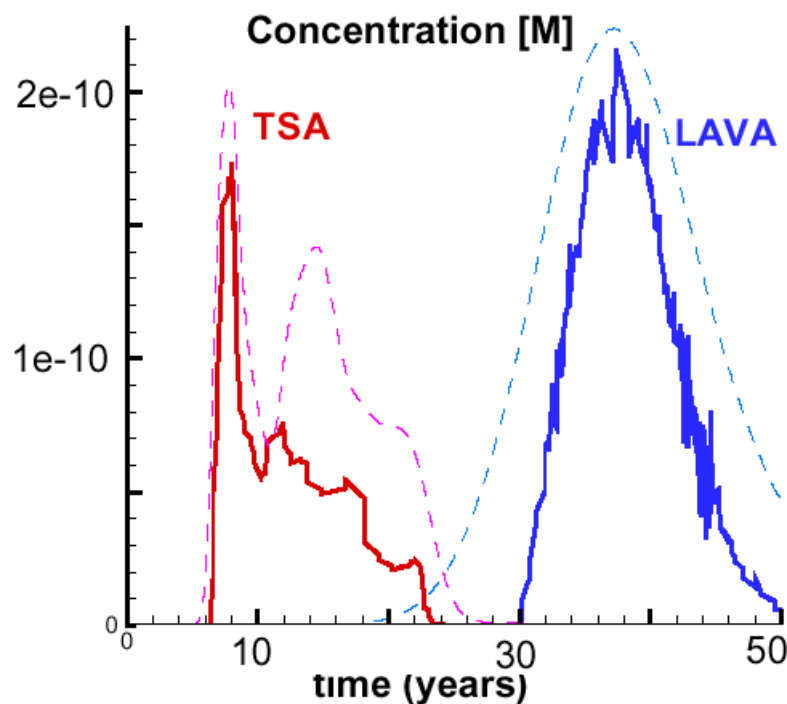


Figure 6-9. Comparison of simulated particle release to the TSA and LAVA with fully coupled THC results from Appendix B. Using the properties described in Appendix B, a two-dimensional particle-tracking model was constructed to compare with the two-dimensional THC model. Solid lines represent particle model, dashed lines represent THC model.

6.6.2 BASE CASE Simulation Results (CASE 1)

The MG undergoes a slow cooling process due to convection and conduction for BASE CASE conditions (Figures 6-5 and 6-6). The relative Rayleigh numbers for the BASE CASE are much greater than unity ($R\hat{a}_{sys}=84.6$, $R\hat{a}_{loc}=355$), indicating a high likelihood of vertical convection to both the TSA and LAVA aquifers. Figure 6-10 illustrates the convection of heat from the MG up the chimney after 20 years for the BASE CASE simulation. Figure 6-11 charts the pathways of three representative non-reactive SPTR particles that originate within the MG leaving

the cavity/chimney to both the TSA and the LAVA aquifers during a 1000-year transient simulation. Mass arrival times of particles and total mass entering in the aquifers are tabulated in Tables 6-5 and 6-6. The particle pathways indicate that, for the BASE CASE parameters, vertical convection from the MG source to the TSA and LAVA aquifers is both possible and likely. This result is in agreement with expectations because the relative Rayleigh numbers are both appreciably above unity.

1. BASE CASE

$$Ra_{sys}=85$$

$$Ra_{loc}=355$$

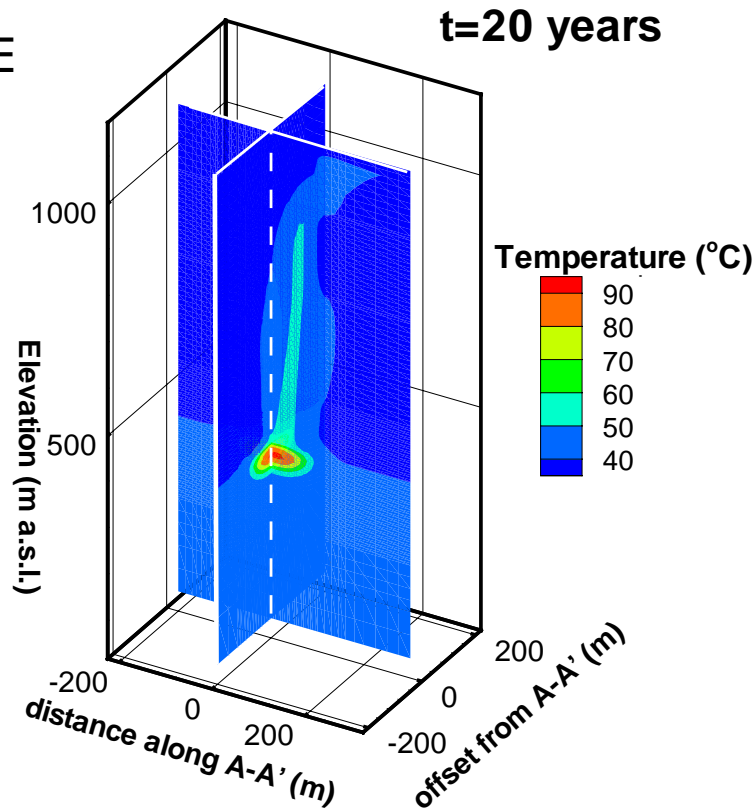


Figure 6-10. BASE CASE temperature contours after 20 years of simulation.

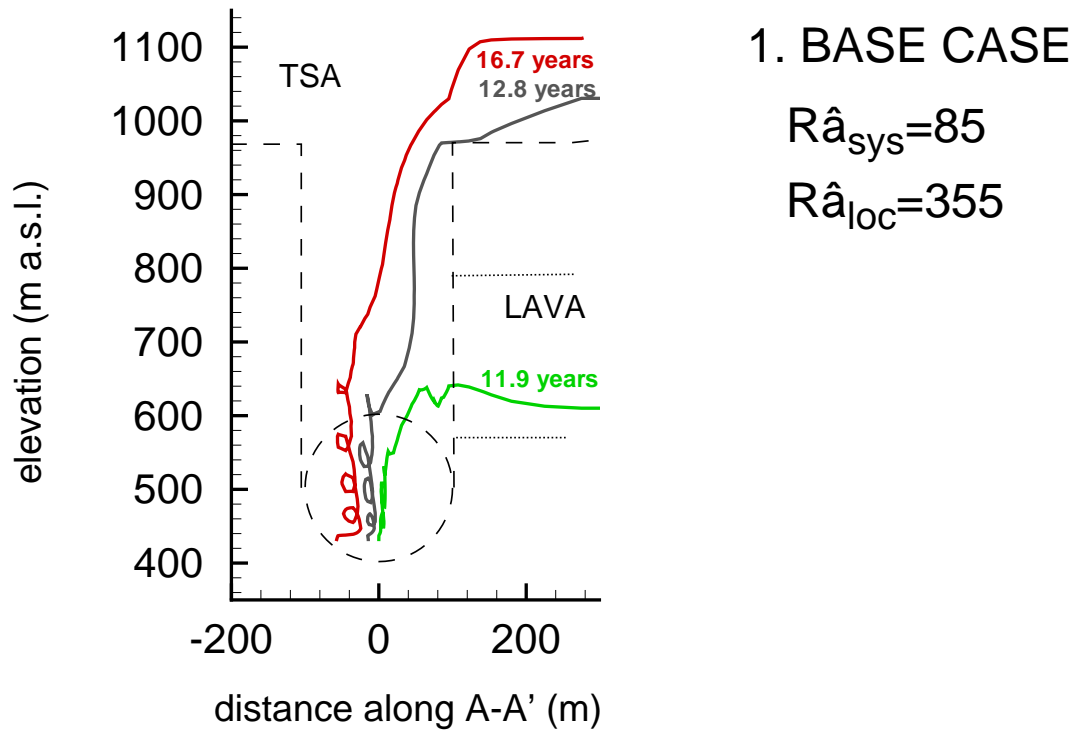


Figure 6-11. Three representative 1000-year particle pathways in the x-z domain for the BASE CASE simulation. Entrance times to the TSA and LAVA aquifers are noted next to each particle.

6.6.3 CASE 2 Simulations: Variable Chimney Permeabilities

Although estimates of chimney material permeability are high (e.g., Snoeberger et al., 1971), the true nature of collapse and its effect on permeability is largely unknown. Equation 6-5 shows that chimney permeability has a direct effect on Rayleigh number values, and, consequently, on the likelihood of vertical convection. Therefore, the three CASE 2 scenarios investigate variations in chimney permeability while keeping all other parameters the same as CASE 1 (see Table 6-4). The CASE 2A and 2B scenarios investigate lower cavity/chimney permeabilities that may occur if the post-detonation rubblelization described earlier is less complete, thereby preserving the lower permeability of the CHZCM, for instance. CASE 2C considers cavity/chimney permeability even higher than that of CASE 1.

For CASE 2A, vertical convection to the TSA is unlikely because $R\hat{a}_{sys}$ is less than unity. However, vertical convection to the LAVA is likely because $R\hat{a}_{loc}$ is above unity. The Rayleigh prediction is validated by numerical results; Figures 6-12 and 6-13 illustrate the lack of vertical convection of heat and particles to the TSA. In accordance with the higher local Rayleigh number, particles do convect to the nearer LAVA aquifer.

The medium permeability CASE 2B has both system and local Rayleigh numbers above unity, indicating likely vertical convection to the LAVA and, to a lesser degree, to the TSA. Figures 6-14 and 6-15 illustrate that again the Rayleigh number prediction is validated by numerical results; for CASE 2B, both heat and particles convect to the LAVA and, to a lesser degree, to the TSA. The Rayleigh Number and numerical analyses both imply a lack of convection to the TSA and decreased convection to the LAVA for permeabilities lower than $1e-13 \text{ m}^2$, when all other parameters are held constant at CASE 1 values.

Although simulations with lower chimney permeabilities illustrate slower or no breakthrough to the TSA and LAVA aquifers, simulations with higher chimney permeability and, hence, higher Rayleigh numbers should have faster breakthrough of particles to TSA and LAVA than the BASE CASE. CASE 2C investigates a condition of a high-permeability cavity/chimney with correspondingly high Rayleigh numbers (Table 6-4), thus predicting rapid convection to both TSA and LAVA aquifers. For this scenario, Figure 6-16 illustrates a cooler temperature profile at 20 years than the BASE CASE, indicating the heat has already dissipated due to increased water flux in the high-permeability chimney. Figure 6-17 follows the pathways of three SPTR particles originating in the MG. For this high cavity/chimney permeability, the three particles move quickly to the TSA. When RTTF particles are released throughout the entire MG for this scenario, a similar trend is observed, although some mass does enter the LAVA at times even earlier than the TSA arrivals (see Tables 6-5 and 6-6). This process implies that at high enough Rayleigh conditions the vertical thermal-driven transport gradient is much more dominant than the horizontal pressure-driven transport gradient in the LAVA, leading to preferential vertical convection of particles to the more permeable but more distant TSA rather than to the closer yet less permeable LAVA aquifer.

CASE 2A
Low Perm
Chimney

$$R\hat{a}_{\text{sys}}=0.8$$

$$R\hat{a}_{\text{loc}}=3.6$$

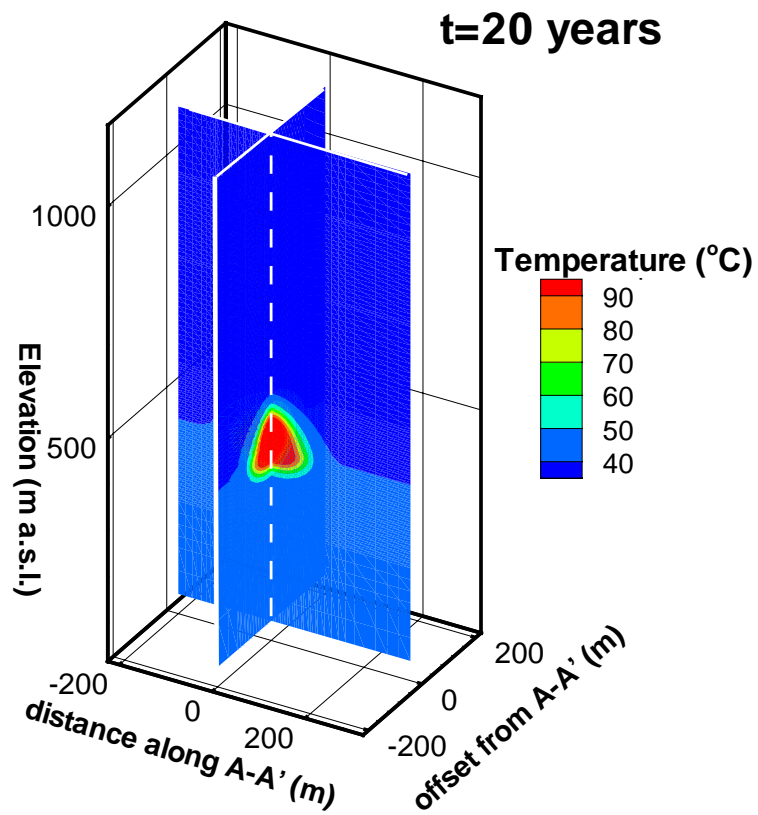


Figure 6-12. Lower chimney permeability case (CASE 2A) temperature contours after 20 years of simulation.

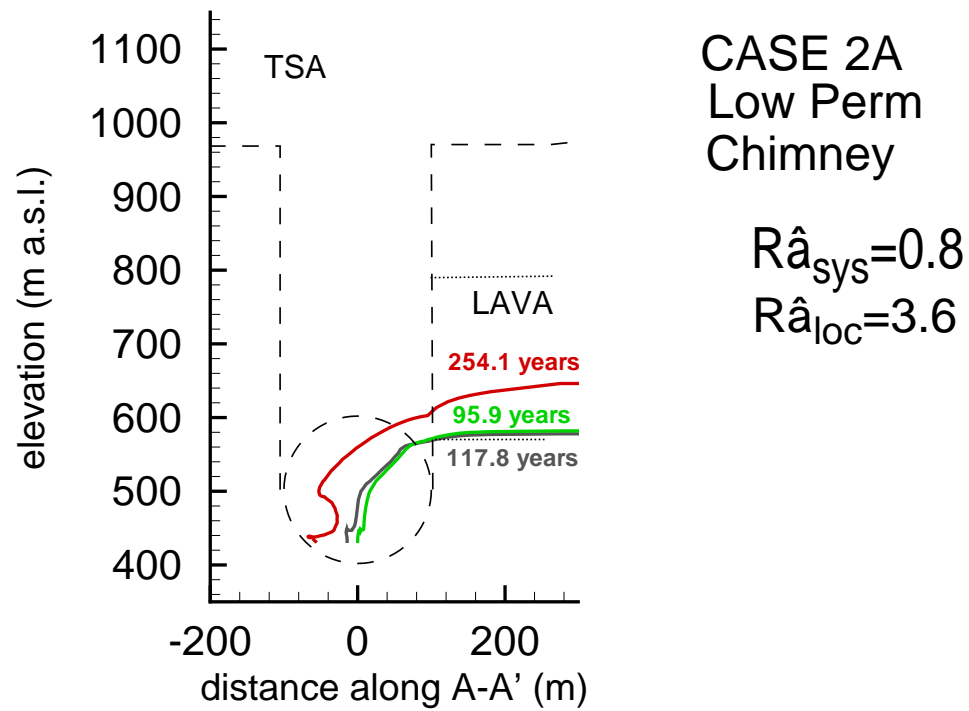


Figure 6-13. Lower chimney permeability (CASE 2A) 1000-year particle pathways projected on an x-z plane. Entrance times to the TSA and LAVA aquifers are noted next to each particle.

CASE 2B
Med Perm
Chimney

$$R\hat{a}_{\text{sys}}=8.5$$

$$R\hat{a}_{\text{loc}}=36$$

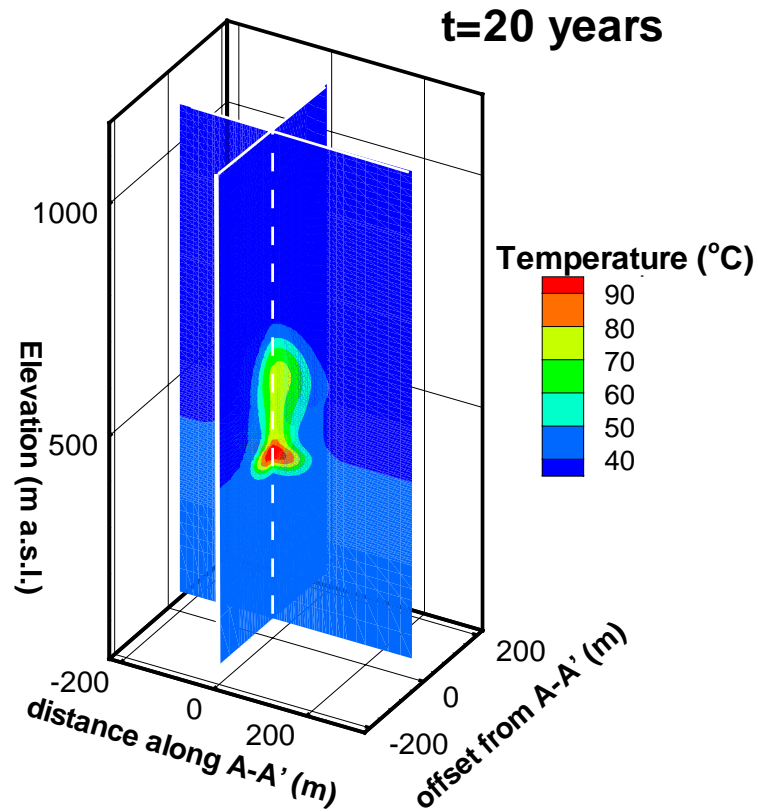


Figure 6-14. Medium chimney permeability case (CASE 2B) temperature contours after 20 years of simulation.

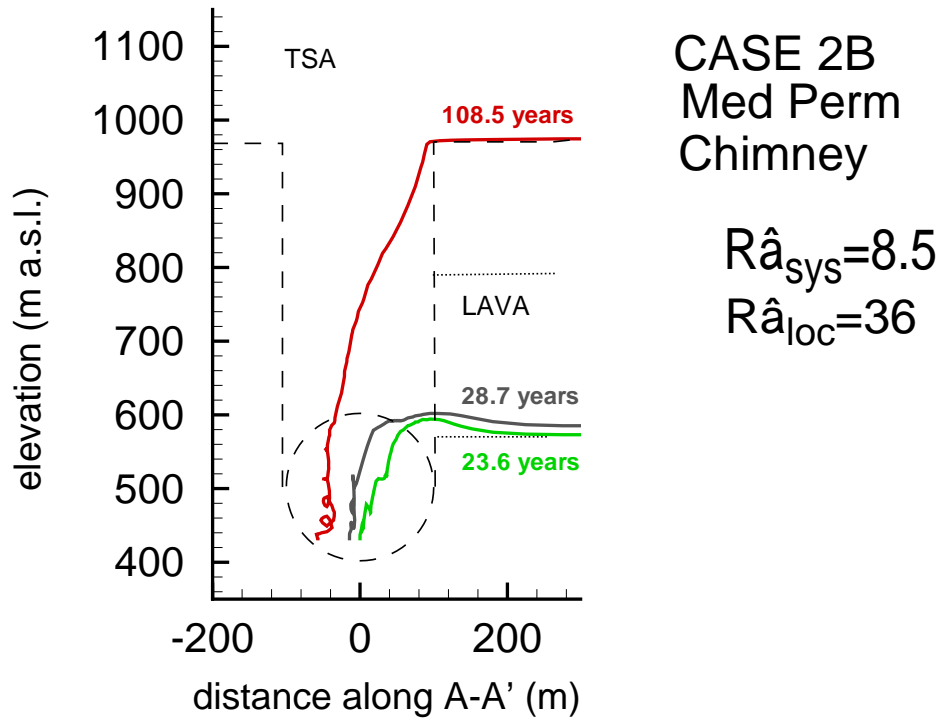


Figure 6-15. Medium chimney permeability (CASE 2B) 1000-year particle pathways projected on an x-z plane. Entrance times to the TSA and LAVA aquifers are noted next to each particle.

CASE 2C
High Perm
Chimney

$$R\hat{a}_{\text{sys}}=850$$

$$R\hat{a}_{\text{loc}}=3600$$

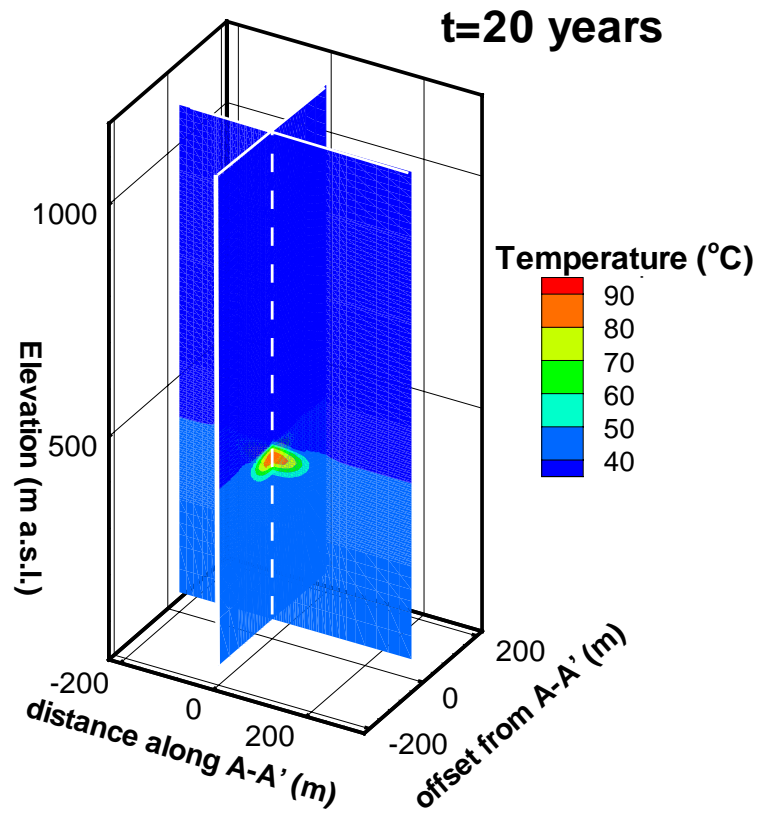


Figure 6-16. High chimney permeability (CASE 2C) temperature contours after 20 years of simulation.

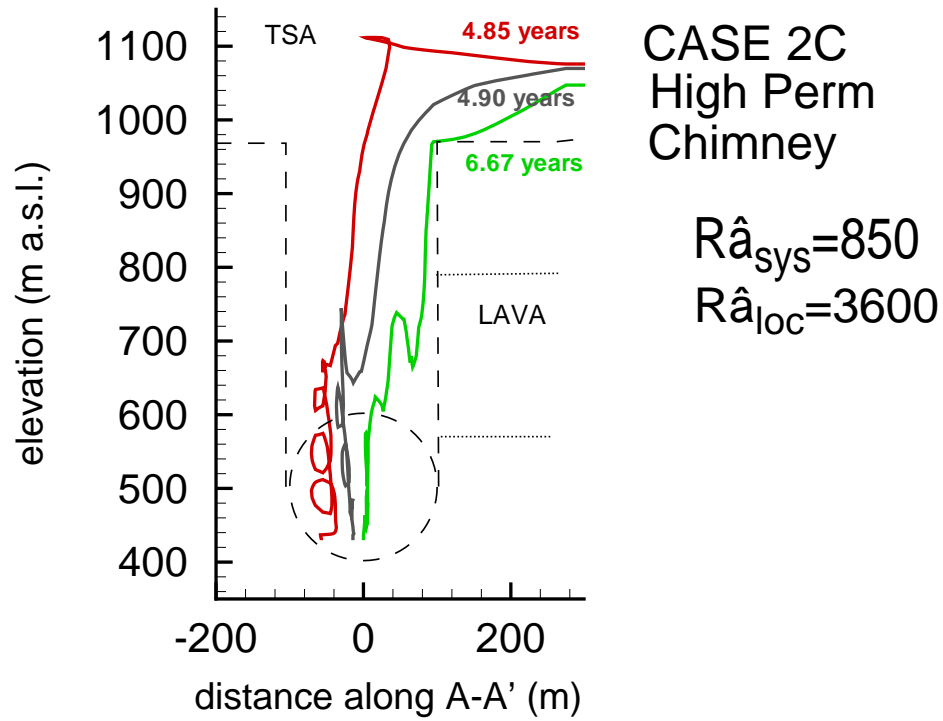


Figure 6-17. High chimney permeability (CASE 2C) 1000-year particle pathways projected on an x-z plane. Entrance times to the TSA and LAVA aquifers are noted next to each particle.

6.6.4 CASE 3 Simulations: Absence of Residual Heat

The CASE 3 scenarios investigate the likelihood of vertical convection in the absence of residual heat from an underground test. For the CASE 3 simulations, no special initial temperature is specified for the MG, leaving only the background geothermal gradient (Table 6-4). CASE 3A investigates the likelihood of convection for the BASE CASE cavity/chimney permeability ($k_{p,chim}=1e-11m^2$) in the absence residual heat, whereas CASE 3B investigates convection for a higher cavity/chimney permeability ($k_{p,chim}=1e-10 m^2$). The Rayleigh numbers for the lower-permeability CASE 3A simulation are barely above unity, $R\hat{a}_{sys} = R\hat{a}_{loc} = 1.9$. Illustrating 20-year temperature contours, Figure 6-18 shows a slight disruption in the geothermal gradient caused by the cavity/chimney disturbance. However, as anticipated from the Rayleigh number analysis, little vertical convection occurs; particles do not enter the TSA after 1000 years of simulation and only a small amount (less than the 0.01% detection cutoff) of mass enters the LAVA (Figure 6-19, Tables 6-5 and 6-6).

The very high cavity/chimney permeability CASE 3B is run to investigate the possibility of vertical convection in the absence of residual heat. In this case, higher Rayleigh numbers result, $R\hat{a}_{sys} = R\hat{a}_{loc} = 19$, predicting that vertical convection to both aquifers is likely. However, Figure 6-20 illustrates that because of the high permeability of the chimney, cool water from the TSA flows down into the cavity, largely precluding buoyant vertical convection. Figure 6-21 illustrates this phenomenon more clearly, tracking 3 representative SPTR particles and showing that none of them enter the LAVA or TSA. Note, however, that over 1000 years a very small amount of mass (below the 0.01% detection cutoff of Tables 6-5 and 6-6) does enter the TSA and LAVA. Hence, because of the increased down flow associated with the highly permeable TSA aquifer, vertical convection in the absence of residual heat is small even for higher Rayleigh numbers. These results are in agreement with the findings of Brikowski (1993), who demonstrated that a vertical hydraulic gradient was necessary for isothermal vertical flow in a cavity/chimney system.

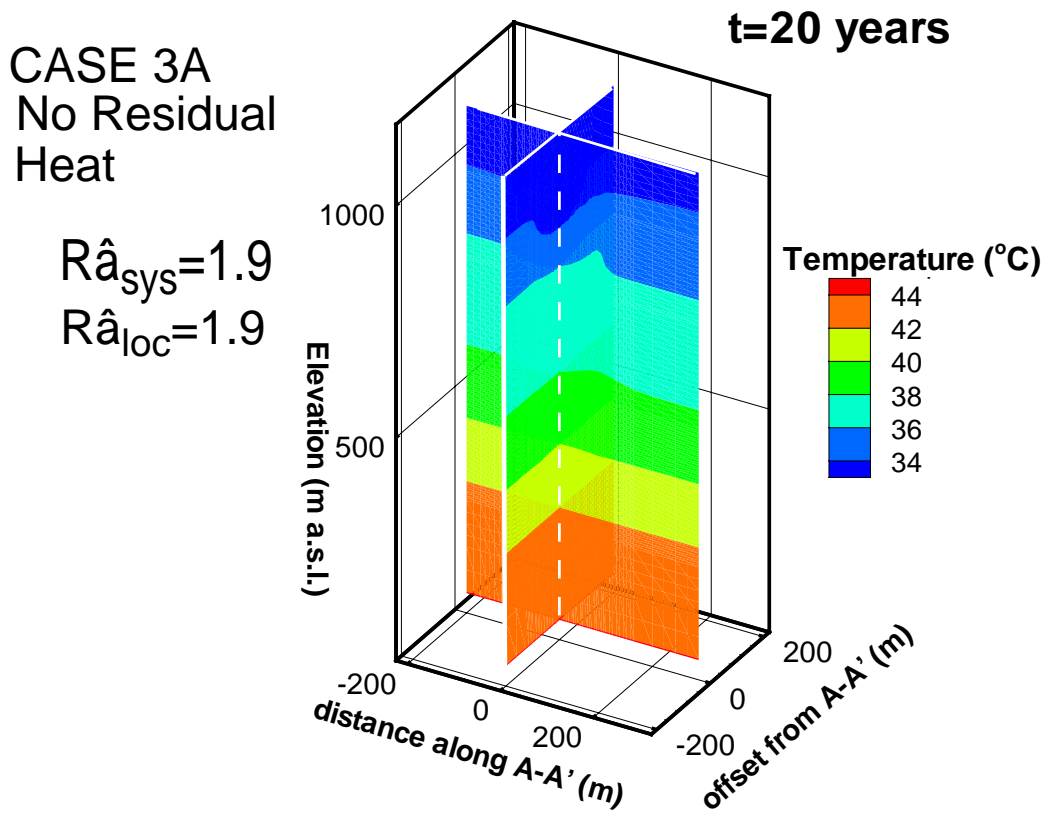


Figure 6-18. Temperature contours after 20 years of simulation under the influence of a geothermal gradient only (CASE 3A).

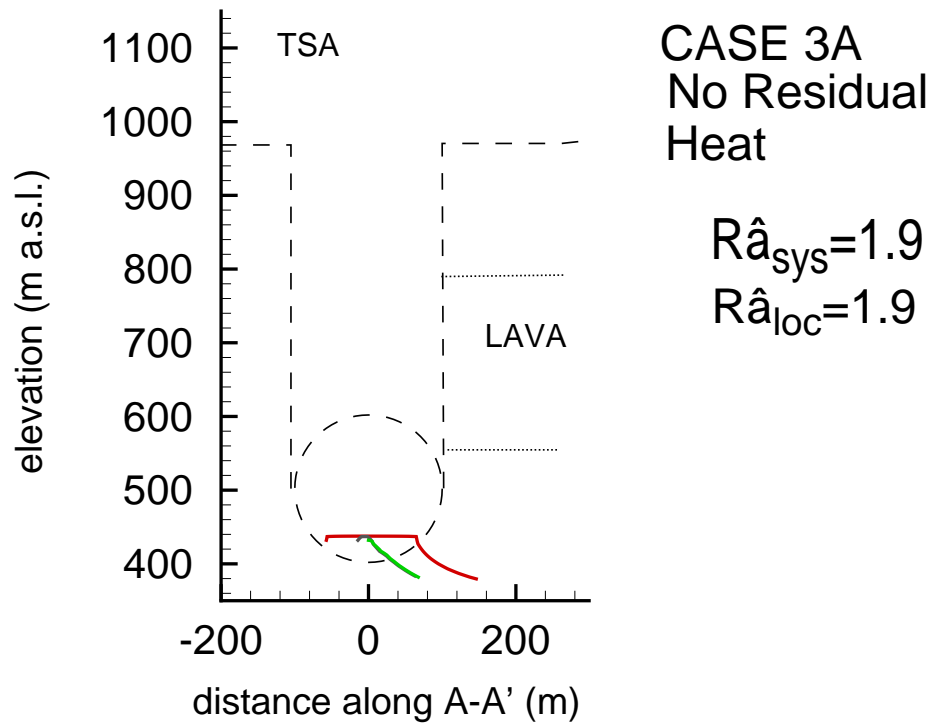


Figure 6-19. 1000-year particle pathways (projected on an x-z plane) under the influence of a geothermal gradient only (CASE 3A). Particles do not enter TSA or LAVA aquifers in 1000 years of simulation.

CASE 3B
No Residual
Heat, Hi Perm

$$\hat{R}_{\text{sys}}=19$$

$$\hat{R}_{\text{loc}}=19$$

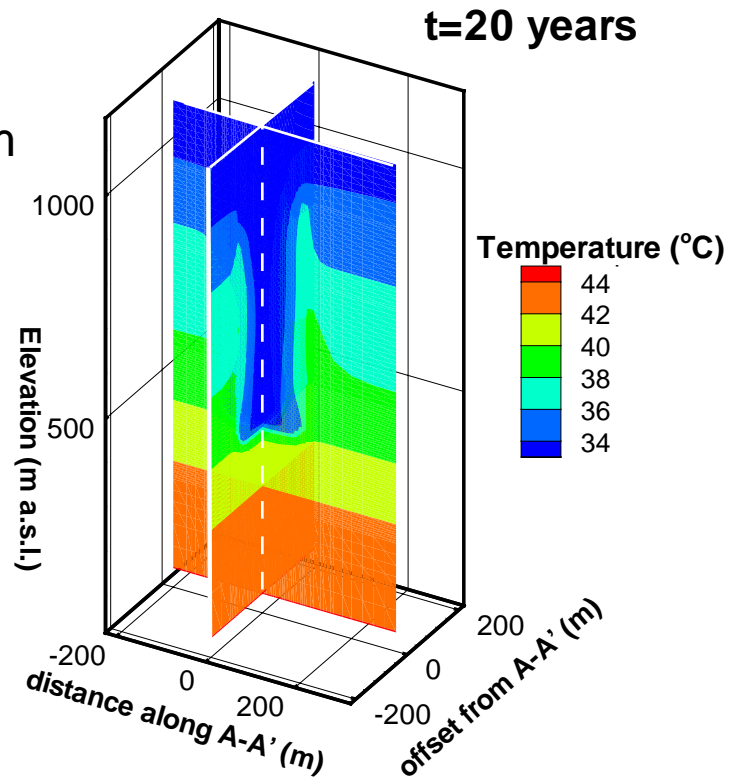


Figure 6-20. Temperature contours after 20 years of simulation under the influence of a geothermal gradient only and in the presence of high chimney permeability (CASE 3B).

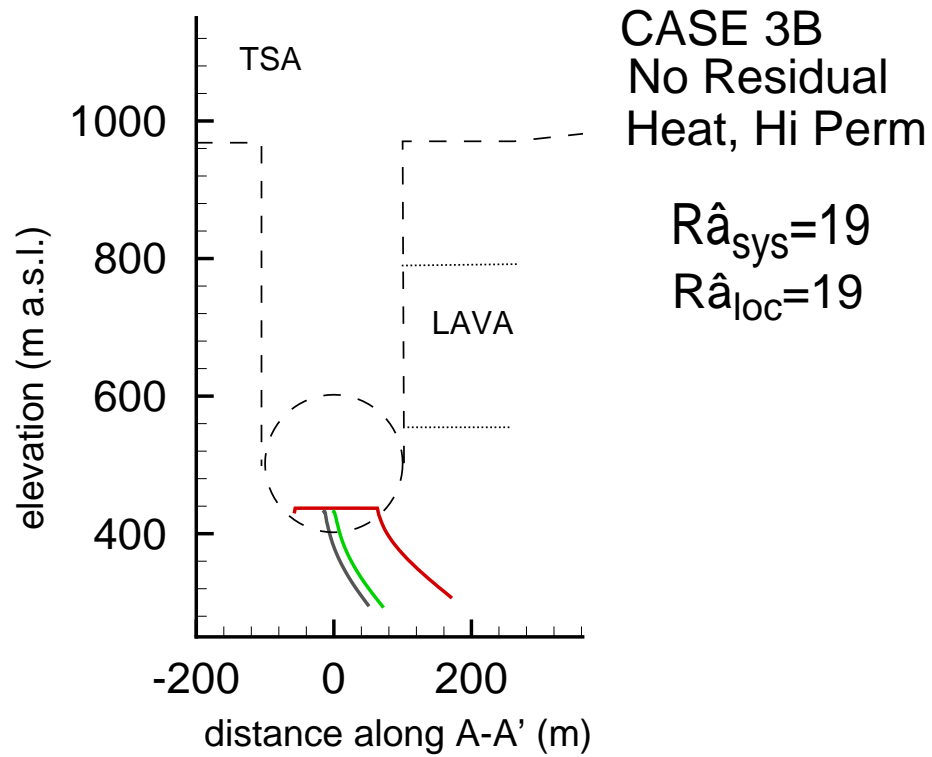


Figure 6-21. 1000-year particle pathways (projected on an x-z plane) under the influence of a geothermal gradient only and in the presence of high chimney permeability (CASE 3B). Particles do not enter TSA or LAVA aquifers in 1000 years of simulation.

6.6.5 CASE 4 Simulations: Lower Melt Glass Temperature

Maxwell et al. (2000) calibrated their source-term model of the CHESHIRE test to thermal probe data measured in a re-entry borehole at 154, 201 and 2356 days after the event. As their initial condition, they chose the 154-day MG temperature of 150°C. This temperature is probably a low estimate for the BENHAM test for two reasons: (1) This temperature is too low for a simulation that begins shortly after the cessation of multiphase processes. It also may be too low for the more shallow CHESHIRE test (150°C is much less than 270°C, which is the boiling point at CHESHIRE's working point). (2) We anticipate that the temperature-history at BENHAM may be higher and of longer duration than CHESHIRE because it was a much larger test at 1.15 Mt vs. 0.2-0.5 Mt (DOE, 2000). However, Pawloski et al. (2001) point out that the heat of vaporization at the saturated depth of the test may be too high because some cooling certainly occurs during resaturation.

To bracket a lower plausible initial temperature of the MG when transport away from the cavity begins, a simulation case with a T_0 of 150°C was run (CASE 4). The relatively high Rayleigh numbers for this case ($R\hat{a}_{sys} = 38$ and $R\hat{a}_{loc} = 158$) indicate the likelihood of vertical convection to both TSA and LAVA aquifers. Figure 6-22 shows the temperature field is much lower after 20 years than the BASE CASE as expected; however, vertical convection of heat from the MG up the chimney still occurs. Similarly, the particle-tracking plot provides evidence of this vertical convection because it exhibits particles entering the TSA at a later time than for the BASE CASE (Figure 6-23). The tabulation of RTTF particle entry to the aquifers (Tables 6-5 and 6-6) also illustrates this trend for releases from throughout the MG, showing lower concentration entering the TSA than the BASE CASE.

CASE 4
Low MG
Temperature

$$R\hat{a}_{\text{sys}}=38$$

$$R\hat{a}_{\text{loc}}=158$$

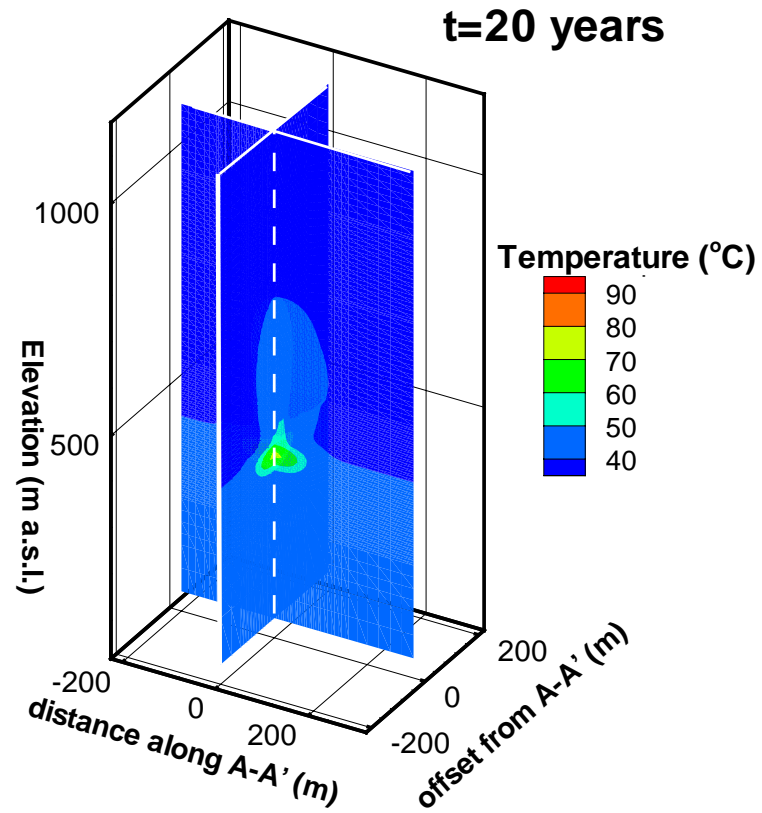


Figure 6-22. Temperature contours after 20 years of simulation for a lower MG temperature (CASE 4).

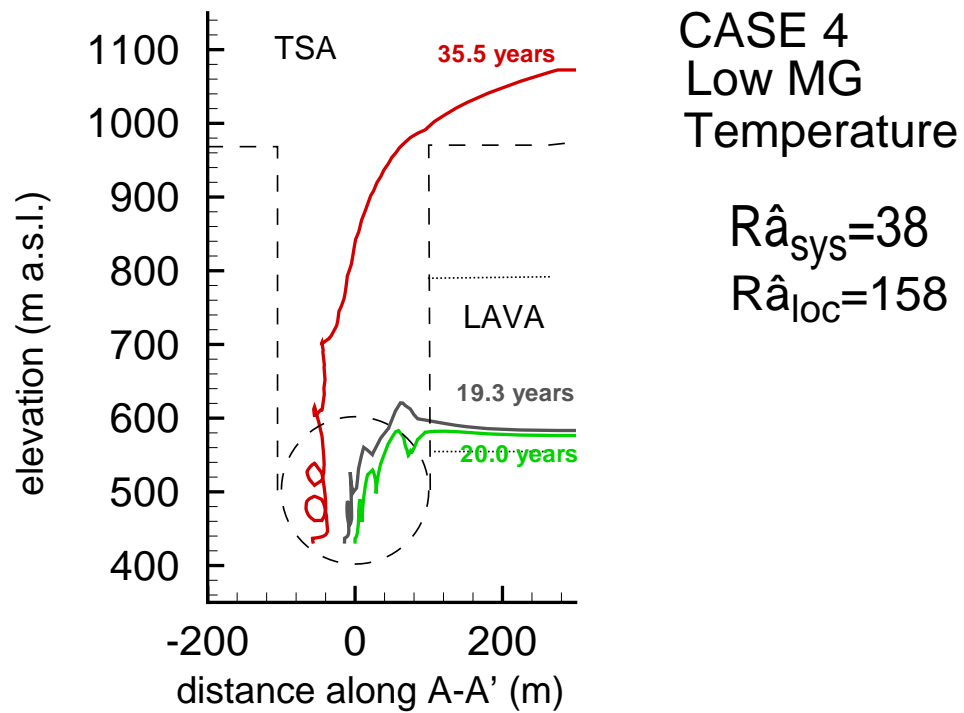


Figure 6-23. 1000-year particle pathways projected on an x-z plane for a lower MG temperature (CASE 4). Entrance times to the TSA and LAVA aquifers are noted next to each particle.

6.6.6 CASE 5 Simulations: Different Initial Melt Glass Volume or Properties

As estimated by the relation of Smith (1993), the bulk volume of MG generated by a test may vary due to uncertainty in the nature of the material collapsing and being incorporated into the MG. Further accentuating MG uncertainty is the actual mass of MG, which may range between 500 and 2700 metric tons per kiloton (Pawloski, 1999). A simulation scenario (CASE 5A) of a 2.32-times larger volume MG, a convenient value for the computational grid used, was conducted to assess the anticipated increase in vertical convection and transport that may occur in the presence of a greater energy source associated with a larger MG volume. To maintain the appropriate mass in the MG, the RN-glass stoichiometry, S_{RN} , is reduced by a factor of 2.32 (e.g., $9.57\text{e-}10$ moles Pu/moles glass). Note that the cavity/chimney density and porosity values used are those of the BASE CASE (i.e., these parameters were not re-calculated using Equation 6-9). Thus, the key difference in this case is an increase in initially hot material for these simulations and lower RN concentration per unit mass of MG.

Figures 6-24 and 6-25 illustrate the temperature field and particle pathways for this simulation. Increased MG volume decreases the convective path height, H , thereby slightly increasing the Rayleigh numbers. More critically, however, the larger MG volume increases the overall amount of energy in the system, thus increasing the duration of vertical convection.

In two other sensitivity scenarios, BASE CASE MG permeability (CASE 5B) and BASE CASE MG porosity (CASE 5C) were increased to be consistent with Pawloski et al. (2001). CASE 5B results in notably cooler chimney temperatures after a simulation of 20 years when compared to the BASE CASE (Figure 6-26), as well as significantly earlier aquifer entrance times to the TSA (Figure 6-27, Table 6-5) due to the increased flux through the MG. For the case of increased MG porosity (CASE 5C), decreased overall initial energy in the system is associated with higher voids, as well as with lower velocities in the MG. This process results in a slightly longer time duration before particles enter the aquifers and a minor decrease in the total convected mass when exiting to the aquifers (Tables 6-5 and 6-6). The difference compared to the BASE CASE is small because most transport occurs in the chimney after the particles leave the MG, regardless of the MG porosity.

CASE 5A
Larger
Volume MG

$$\hat{R}_{\text{sys}}=88$$

$$\hat{R}_{\text{loc}}=422$$

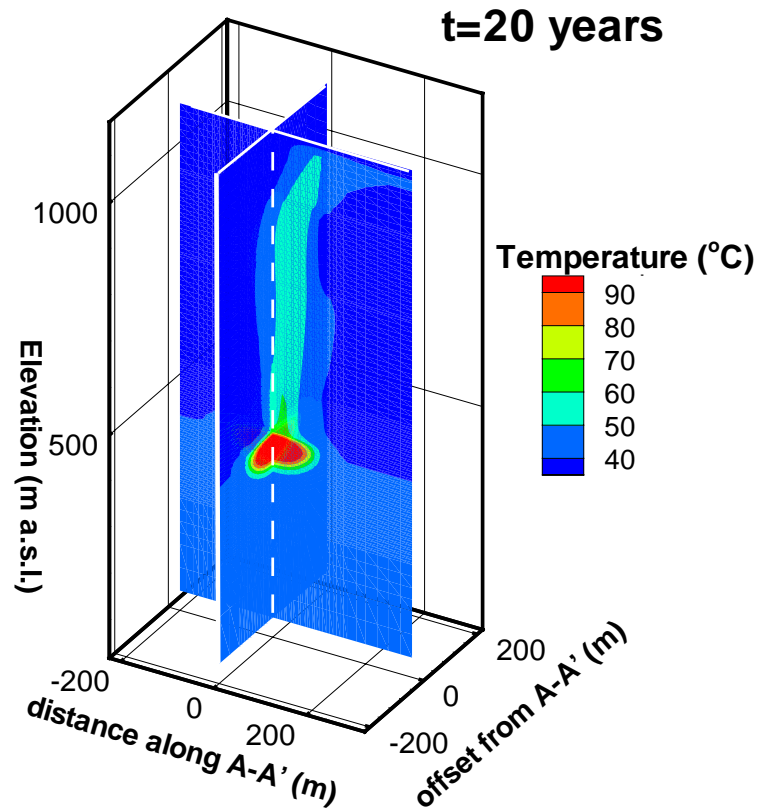


Figure 6-24. Larger MG volume case (CASE 5A) temperature contours after 20 years.

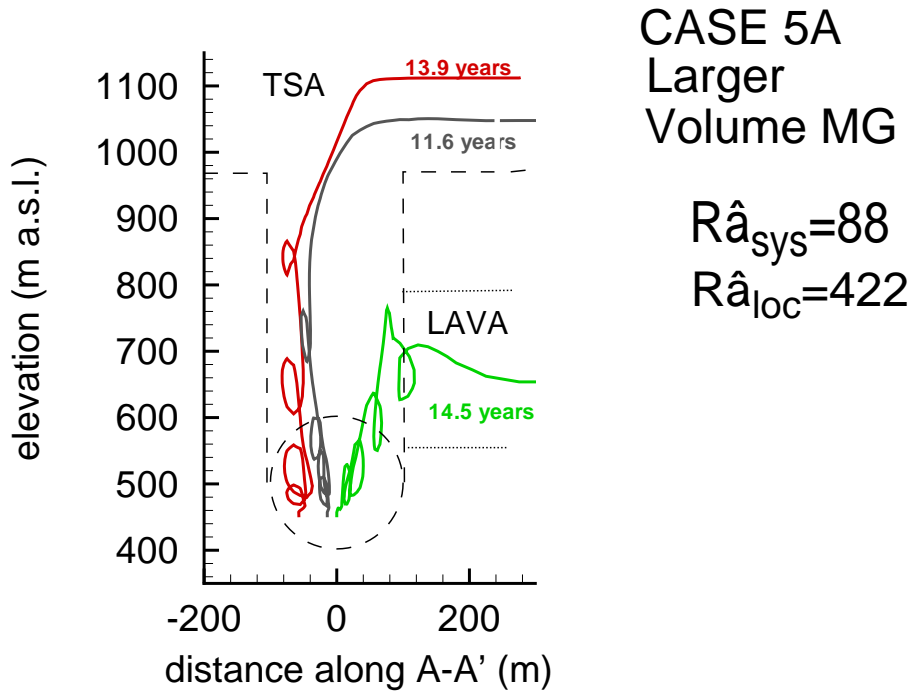


Figure 6-25. MG volume increased by 2x (CASE 5A). 1000-year particle pathways projected on an x-z plane. Entrance times to the TSA and LAVA aquifers are noted next to each particle.

CASE 5B
Higher
Perm MG

$$\hat{R}_{\text{sys}}=85$$

$$\hat{R}_{\text{loc}}=355$$

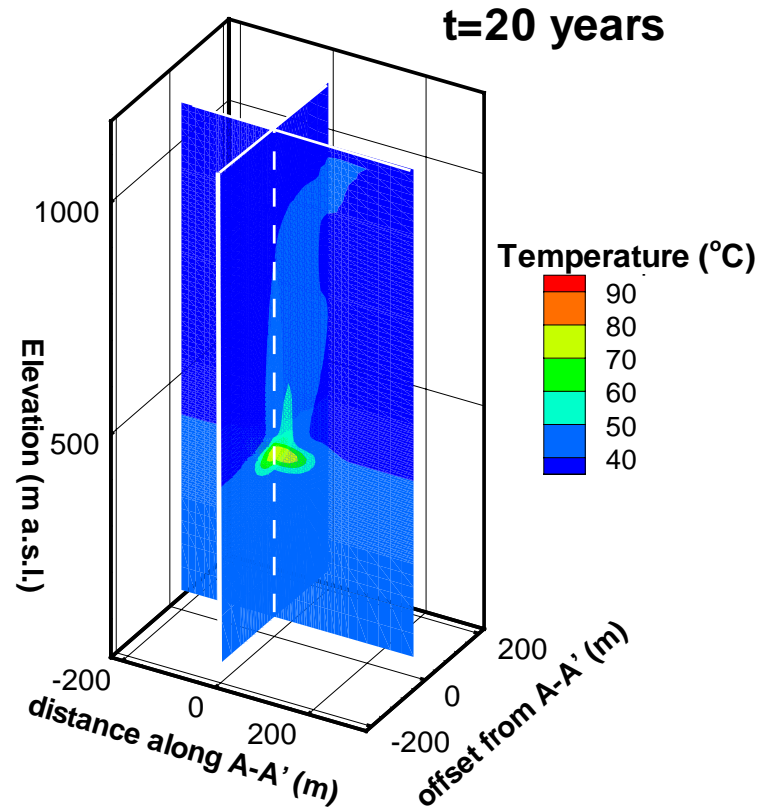


Figure 6-26. High MG permeability case (CASE 5B) temperature contours after 20 years.

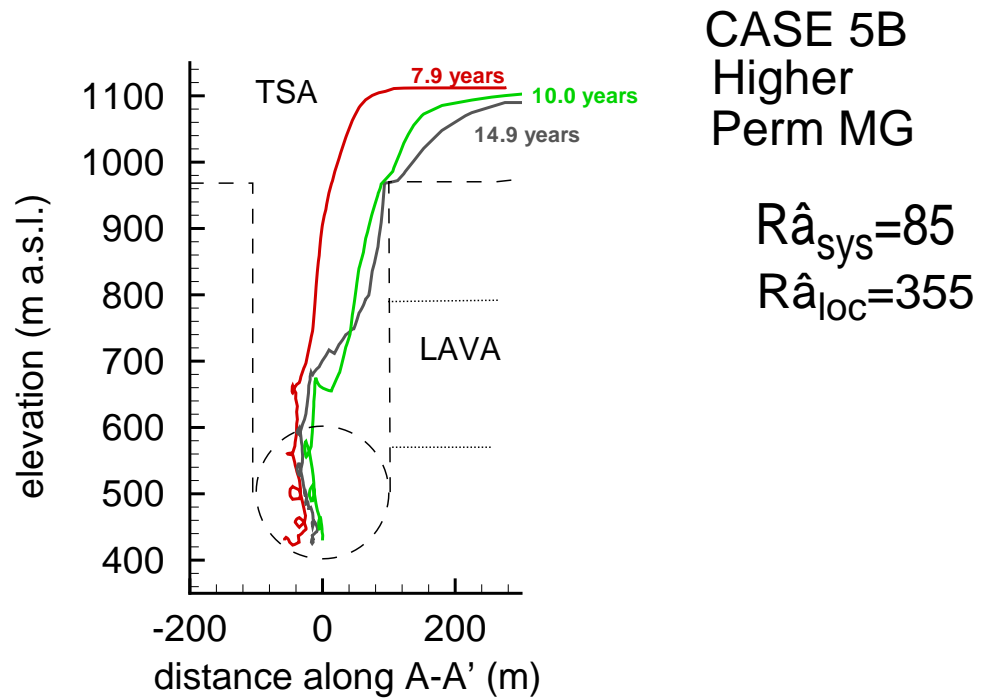


Figure 6-27. High MG permeability case (CASE 5B) with 1000-year particle pathways projected on an x-z plane. Entrance times to the TSA and LAVA aquifers are noted next to each particle.

6.6.7 CASE 6 Simulations: LAVA Permeability Variation

Analyses of lava permeabilities in the BULLION FGE (IT, 1998) suggest that permeabilities in the LAVA aquifer may be as high as $1\text{e-}10\text{ m}^2$, indicating that model sensitivity to LAVA aquifer permeability must be considered. CASES 6A, 6B, and 6C investigate the BASE CASE chimney and MG conditions with LAVA permeability values of $1\text{e-}12$, $1\text{e-}11$, and $1\text{e-}10\text{ m}^2$, respectively. Varying the LAVA permeability influences the amount of solute mass traveling to the upper TSA aquifer (Table 6-5) as it increases the amount of flow normal to the chimney. The higher the LAVA's permeability, the fewer total moles of RNs convect to the TSA. However, increased LAVA permeability for these simulations never completely precludes convection to the TSA. Interestingly, increased LAVA permeability also decreases the time of breakthrough of 0.01% of total MG-source solute into the TSA. This latter observation is caused by the increased convective mixing at the MG incurred by a larger water flux entering from the nearer LAVA aquifer. A second interesting observation is that increasing the LAVA permeability from $1\text{e-}11$ to $1\text{e-}10\text{ m}^2$ has a negligible effect on overall transport breakthrough and on total RN mass exiting to the TSA or LAVA (Tables 6-5 and 6-6). This result implies that the dominant mechanism of the cooling cavity/chimney is the buoyant convection associated with residual heat and chimney permeability rather than the hydraulic cross-flow associated with LAVA permeability.

6.7 Melt-Glass Release: Sorptive Plutonium Example

RN adsorption sensitivity can be evaluated for the BASE CASE and the comparative Rayleigh number simulation scenarios CASE 2A, CASE 2B, CASE 2C, and CASE 4. Such evaluation is only done for CASES 1 through 4 because these cases span the range of Rayleigh numbers considered in this analysis (only the most sensitive parameters, cavity/chimney permeability, and residual heat vary for these sensitivity scenarios). The effect of sorption was modeled by using a linear adsorption isotherm, Kd . The Kd values modeled, representing the RN classes in Table 6-3, are 0.1, 1.0, 5.0, 10.0, and 100.0 cc/g, having respective retardation factors of 2.04, 11.4, 52.9, 105, and 1041. Tables 6-7 and 6-8 tabulate arrival time estimates to the TSA and LAVA, respectively, along with the total percentage of mass entering the aquifer after a simulation of 1000 years. Note that only the mass originating from the MG is considered in these evaluations (the total source for MG and EV is described in Section 6.8). Generally, arrival times increase with decreasing Rayleigh numbers. Plotted in Figure 6-28 are Rayleigh numbers ($R\hat{a}_{sys}^{sorp}$ and $R\hat{a}_{loc}^{sorp}$) with aquifer arrival times (t_{ar}) for the sorptive and non-sorptive cases listed in Tables 6-7 and 6-8. A linear relation between $R\hat{a}$ and t_{ar} is exhibited for both the TSA and LAVA non-sorptive simulation results. Linear trends between $R\hat{a}^{sorp}$ and t_{ar} for the sorptive results are less apparent, especially for the LAVA, but in general they are decreasing.

When individual cases are examined, a sorptive trend is observed. Figure 6-29 plots $R\hat{a}^{sorp}$ vs. t_{ar} for the BASE CASE and CASE 2C for both the TSA and LAVA. The expected linear relation caused by sorption between $R\hat{a}^{sorp}$ and t_{ar} is observed for the LAVA. However, a linear trend is not observable for mass entrance to the TSA. Such non-linearity is due to the circuitous travel paths created by convection cells within the chimney early in the simulation (note the circular pathways

near the MG of the unretarded particles of Figure 6-30). Non-sorbing particles move farther than sorbing particles on their journey to the TSA. However, much of this increased translation is within circular convection cells (Figure 6-30). The end result is that sorbing particles show less delay relative to non-sorbing particles than would be expected for a steady linear flow-field. For example, in the TSA BASE CASE, particles with a sorption Kd of 0.1 cc/g ($R = 2.04$) have a breakthrough time only 1.15 times greater than the non-sorbing case (13.1 years vs. 11.4 years). However, for the less convective-cell-dominated travel pathway of particles to the LAVA, the arrival time to the LAVA of sorbing particles (with a retardation factor of about 2) is approximately twice the arrival time of non-sorbing particles (6.33 yrs vs. 3.29 yrs).

Table 6-7. Particle breakthrough to TSA for different sorption K_d s (in cc/g). The first number in each cell is the arrival time of 0.01% of the total MG-source mass in years; the bracketed number in each cell is the percentage of total mass entering TSA after 1000 years.

Simulation Scenario	$K_d=0.0$ $R=1.00$	$K_d=0.1$ $R=2.04$	$K_d=1.0$ $R=11.4$	$K_d=5.0$ $R=52.9$	$K_d=10.$ $R=105.$
BASE CASE (CASE 1)	11.35 yrs [13.83%]	13.06 [17.65%]	47.58 [2.641%]	n/a [0.0%]	n/a [0.0%]
CASE 2A (low chim. perm)	no arrival [0.0%]				
CASE 2B (med chim perm)	88.37 [0.3039%]	124.1 [1.567%]	no arrival [0.0%]	no arrival [0.0%]	no arrival [0.0%]
CASE 2C (high chim perm)	2.383 [21.11%]	2.566 [14.68%]	5.923 [6.440%]	446.2 [2.834%]	943.5 [4.663e-2%]
CASE 4 (low MG temp.)	27.24 [0.2747%]	32.84 [0.5863%]	no arrival [0.0%]	no arrival [0.0%]	no arrival [0.0%]

Table 6-8. Particle breakthrough to LAVA for different sorption K_d s (in cc/g). The first number in each cell is the arrival time of 0.01% of the total MG-source mass in years; the bracketed number in each cell is the percentage of total mass entering LAVA after 1000 years.

Simulation Scenario	$K_d=0.0$ $R=1.00$	$K_d=0.1$ $R=2.04$	$K_d=1.0$ $R=11.4$	$K_d=5.0$ $R=52.9$	$K_d=10.$ $R=105.$
BASE CASE (CASE 1)	3.286 yrs [9.117%]	6.328 [4.332%]	41.60 [5.196%]	451.8 [1.058%]	no arrival [0.0%]
CASE 2A (low chim. perm)	48.82 [12.00%]	126.7 [12.25%]	no arrival [0.0%]	no arrival [0.0%]	no arrival [0.0%]
CASE 2B (med chim perm)	9.50 [21.18%]	16.26 [19.47%]	124.2 [6.146%]	no arrival [0.0%]	no arrival [0.0%]
CASE 2C (high chim perm)	1.471 [14.68%]	4.080 [0.6237%]	24.36 [1.613%]	231.9 [1.672%]	472.6 [0.3039%]
CASE 4 (low MG temp.)	7.743 [1.657%]	13.28 [0.7623%]	68.41 [0.7680%]	no arrival [8.04e-3%]	no arrival [0.0%]

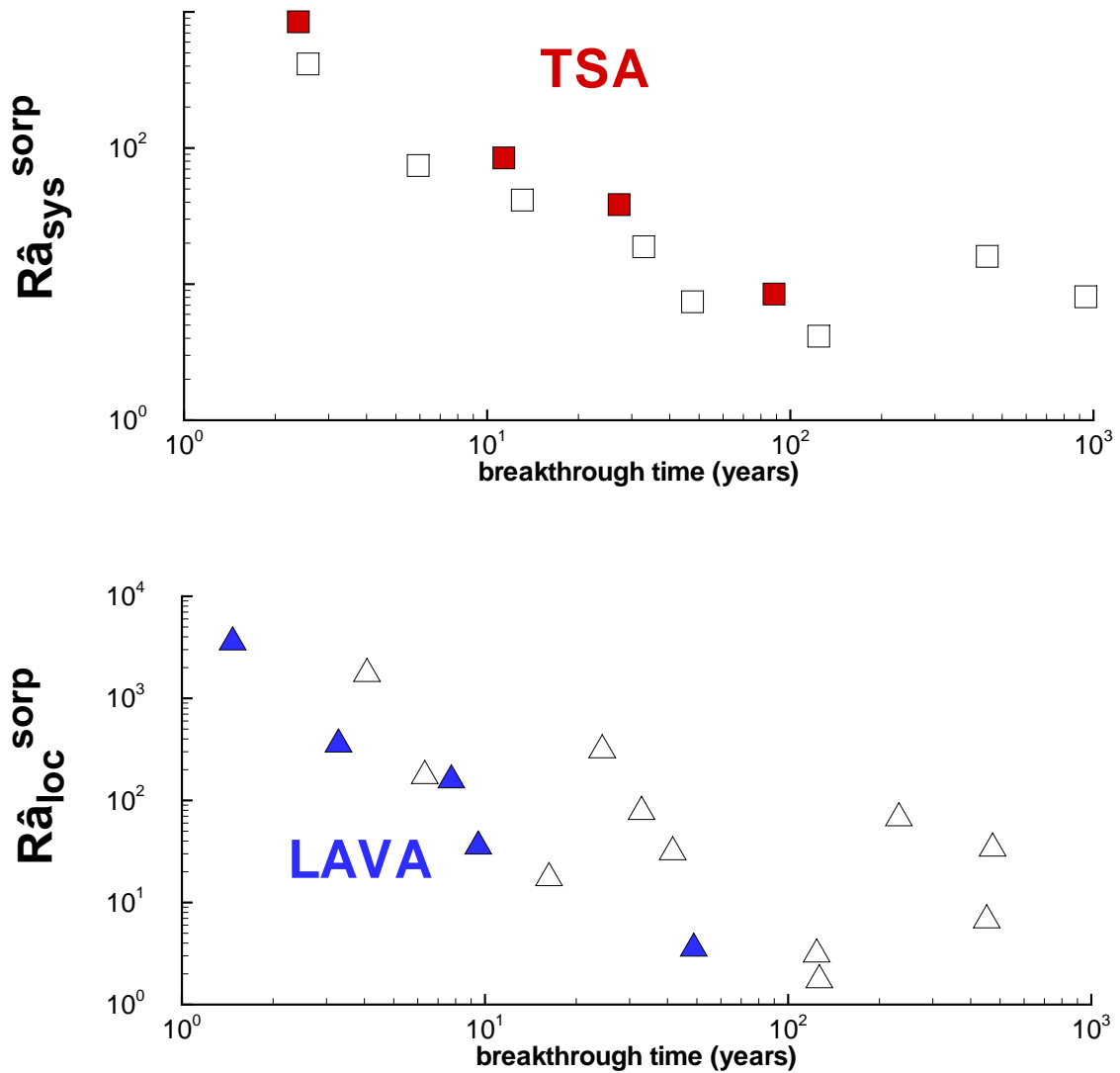


Figure 6-28. Relative Raleigh numbers vs. the breakthrough time 300 m downstream from the chimney in the TSA and LAVA for 0.01% of total mass present. Closed symbols represent non-sorbing species with a Kd of 0.0, open circles represent sorbing species with a Kd of 0.1. All flow scenarios in Cases 1 through 4 are plotted.

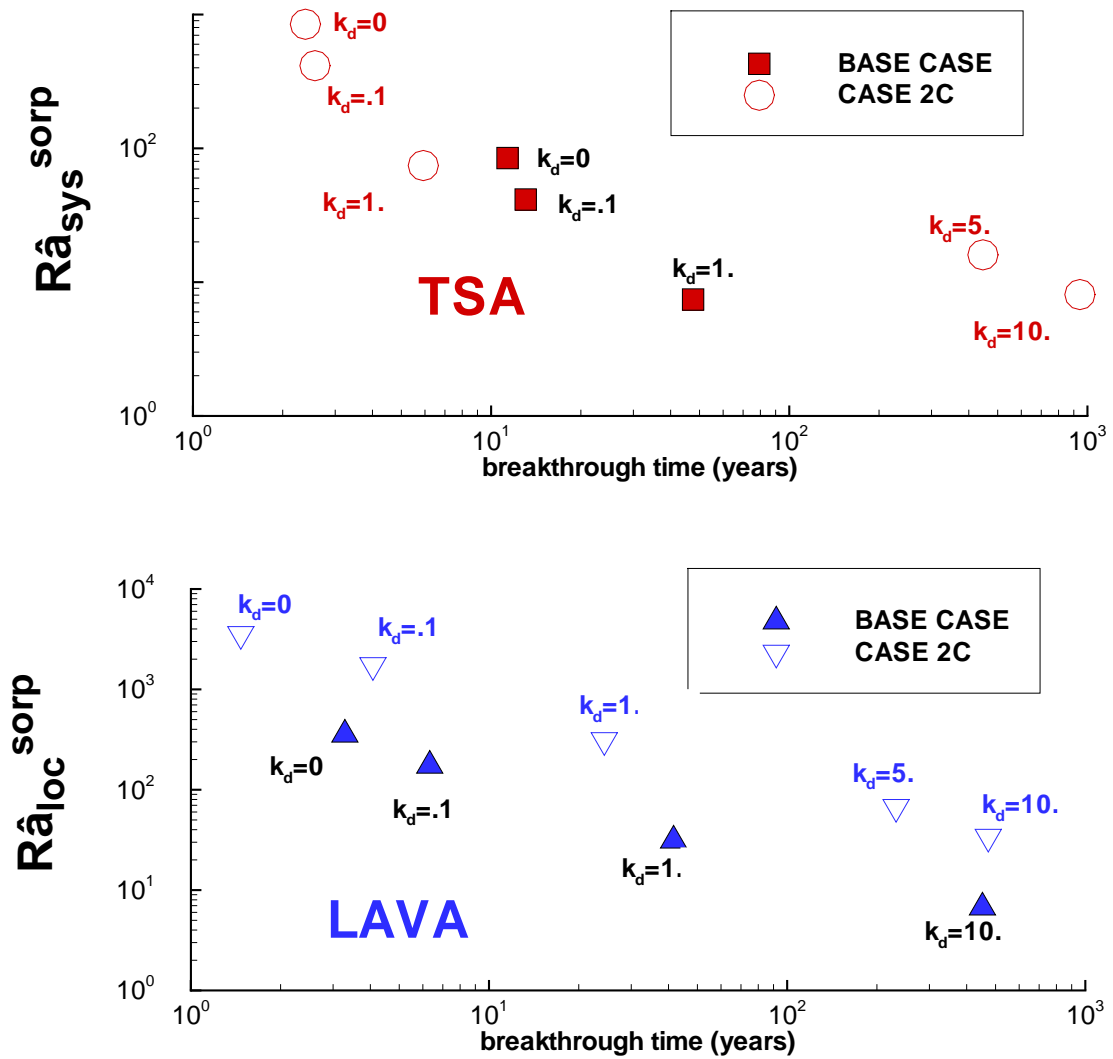


Figure 6-29. Sorptive Rayleigh numbers vs. the breakthrough time 300 m downstream from the chimney in the TSA and LAVA for 0.01% of total mass present. BASE CASE and CASE 2C scenarios are identified with multiple K_d s (cc/g) identified in this figure as k_d .

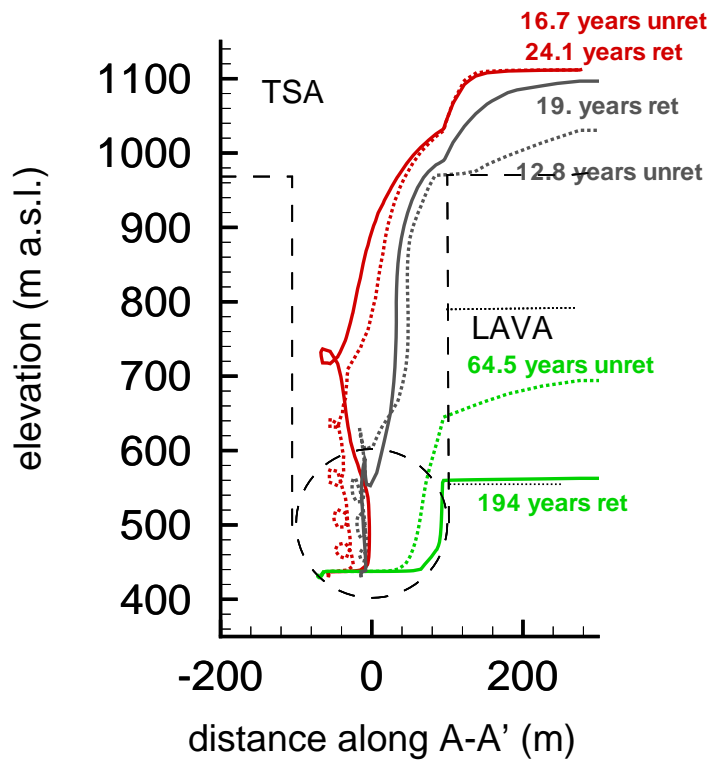


Figure 6-30. Unretarded (dotted lines) and retarded ($Kd = 0.1$ cc/g, solid lines) particle pathways for the BASE CASE. The travel times of retarded particles to the upper TSA aquifer are faster than expected (for $Kd=0.1$ cc/g, $R = 2.04$). This is due to a shorter path followed by the retarded particle (fewer and weaker convection cells at later times). Conversely, the travel time to the LAVA is longer than expected. This is due to a decrease in buoyancy at later times resulting in slower vertical transport within the cavity.

6.8 Source Term for all 16 Radionuclides

To model the mass flux of all 16 RNs (Table 6-3; a subset of those listed by Pawloski et al., 2001) and Pu-colloid entering the aquifers, the RTTF particle-tracking method is used combining both the MG and EV sources. RTTF particle simulations model 1000-year simulation periods for both MG and EV releases for each sorptive case ($Kd = 0, 0.1, 1.0, 5.0, 10.0,$ and 100.0 cc/g), thus allowing for the simulation of all RNs and the colloid class. For each RN, the number of moles per particle is scaled to the initial mass in the EV and the stoichiometry in the MG. For example, ^{99}Tc has an initial mass of 2.41 moles (see Table 6-3) distributed such that 80% is initially in the MG and 20% is initially in the EV. For the BASE CASE simulation scenario, it is calculated that $2.55\text{e}6$ particles/mole ^{99}Tc is released from the MG, whereas $4.15\text{e}6$ particles/mole ^{99}Tc is released from the EV. (Note that the unclassified masses of each RN in the inventory are taken from Smith, 2001, without decay correcting back to the test date--specific source-term calculations with actual classified inventory masses should use appropriate initial masses at the time of test.) The time-varying mass flux of each RN in Table 6-3 is simulated by superimposing appropriately scaled simulation results from the MG-source dissolution release with appropriately scaled simulation results from the instantaneous release of $2\text{e}6$ particles evenly spread throughout the EV. The breakthrough curve is then decay-corrected from time zero of the simulation. It should be noted that such a simulation neglects the initial cavity re-wetting time and thus conservatively over-predicts the mass released. Note that RNs are present as two different isotopes (i.e., Eu, U, and Pu); these are combined and given the sorptive and radioactive decay values of the mass-dominant isotope. For the colloid class, it was estimated that a very small fraction (1/10 000) of Pu irreversibly sorbs to the colloids (see Section F.5.3), and that the Pu-colloid species travels through the cavity/chimney without retardation. Further discussed in Chapter 7, this fraction is dependent upon Pu sorption and desorption rates with colloids, solute residence times in the site-scale aquifers, and sorption coefficients of immobile minerals.

From all the different cases described in Table 6-4, three are carried through this source-term analysis. The three cases, CASE1, CASE 2B, and CASE 2A (with Rayleigh Numbers of 84.6, 8.46, and 0.846), represent the range of potential convective transport in the chimney. With these three cavity/chimney property configurations, we then consider all RNs, with their unique initial distributions and Kds . In fact, for each RN, these three cases are run twice, once for the most conservative consideration with $Kd = 0$, and once for the Kd set as prescribed in Table 6-3. These results in turn are designated as SOURCES 1, 2, and 3 (A for non-sorbing and B for sorbing) for use in site-scale transport simulations in Appendix F and Chapter 7. Table 6-9 lists the parameters

for each source and its relationship to the CASEs described earlier in this chapter. Clearly, for the non-reactive Class I RNs, only the “A” conditions are considered.

Table 6-9. Modeled Source-Term Conditions.

Source Term	$R\hat{a}_{sys}$	$R\hat{a}_{loc}$	Kd (cc/g)	note
SOURCE 1A High Ra (BASE CASE)	84.6	355.	$Kd=0$	Table 6-4 CASE 1
SOURCE 1B High Ra, Chim Sorp	84.6	355.	see Table 6-3	Table 6-4 CASE 1
SOURCE 2A Med Ra	8.46	35.5	$Kd=0$	Table 6-4 CASE 2B
SOURCE 2B Med Ra, Chim Sorp	8.46	35.5	see Table 6-3	Table 6-4 CASE 2B
SOURCE 3A Low Ra	0.846	3.55	$Kd=0$	Table 6-4 CASE 2A
SOURCE 3B Low Ra, Chim Sorp	0.846	3.55	see Table 6-3	Table 6-4 CASE 2A

6.8.1 Initial Mass Source: Exchange-Volume and Melt-Glass Distribution

In this section, we discuss how variations in source-mass distribution between the EV and MG affect mass breakthrough to the aquifers. The predominant influence of variation in EV and MG mass distribution is the overall mass release. Figure 6-31 illustrates SOURCE 1 mass-flux curves of ^{99}Tc into the TSA and LAVA from both the EV and MG. As noted above, approximately 80% of the total mass of ^{99}Tc resides initially in the MG, with the other 20% distributed in the EV (see Table 6-3). As shown in Figure 6-31, approximately 50% of the mass leaving the cavity/chimney is from the EV, despite the fact that this is only 20% of the total initial mass. This distribution occurs because all (~0.5 moles) of the EV-based ^{99}Tc exits the cavity/chimney, whereas only approximately a quarter of the mass from the MG (~0.5 moles) exits (note: approximately a quarter of the MG mass dissolves in the BASE CASE scenario over the 1000-year simulations, with most of the dissolution occurring at very early time because of the then high temperatures). Mass from the EV arrives to the LAVA aquifer just before mass from the MG, simply because the EV-based mass is physically closer to the LAVA. However, it is interesting to note that the initial mass arrival to the TSA is from the MG. This early mass arrival from the MG is because water in the MG at very early times is hotter than in the EV, thus achieving greater buoyancy and increasing the potential for faster migration to the TSA prior to mixing. Note that nearly all the mass convected to both the TSA and LAVA aquifers from both MG and EV sources occurs in less than 35 years. This is because both glass dissolution and convective cells are greater at early time when the glass is hot. Thus, most non-reactive RN mass is driven from the EV and MG to the TSA and LAVA aquifers over a short-time duration early in the 1000-year simulation.

When examining sorptive RNs, a more notable difference arises in the arrival time to the aquifers of the mass released from the EV and of the mass released from the MG. Figure 6-32 illustrates the mass arrival to the aquifers for sorptive ^{239}Pu when simulating SOURCE 1B. Approximately 95% of the Pu resides in the MG, with only 5% initially residing in the EV. As with ^{99}Tc , much of the initial EV mass (~0.79 moles) exits the cavity/chimney system, whereas only a smaller amount from the MG (~0.17 moles) exits during the 1000-year simulation.

None of the sorptive RN migrates to the TSA, indicating that the convection cells die before such retarded transport can be accomplished. The pulse of Pu exiting to the LAVA from the EV represents mass closer to the LAVA than the MG, with the tail consisting of EV mass more distant from the LAVA. The MG pulse occurs later than the EV pulse because the mass released at early time still has a greater distance to travel to the LAVA. That pulse is still increasing at the end of 1000 years, indicating a favorable fluid flow pathway to the LAVA, even as the system cools. Therefore, after approximately 800 years, the mass flux to the LAVA is dominated by MG releases that occurred at early time.

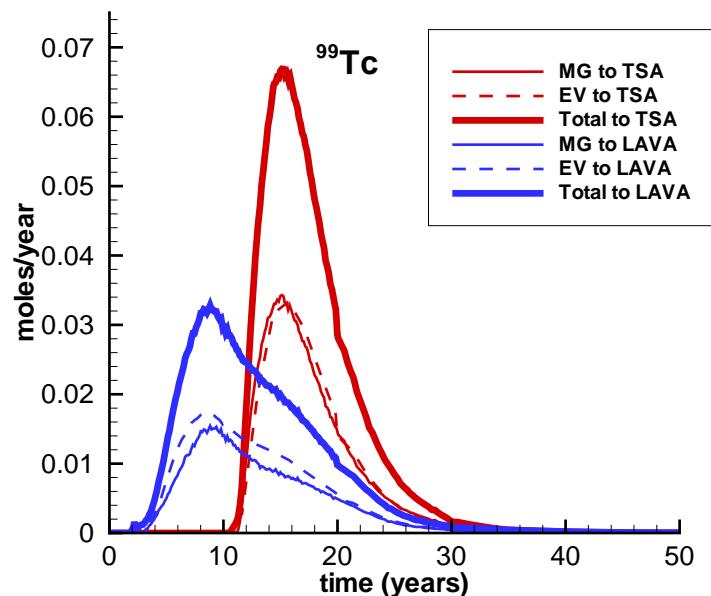


Figure 6-31. ^{99}Tc breakthrough mass fluxes to the TSA and LAVA from the MG and the EV.

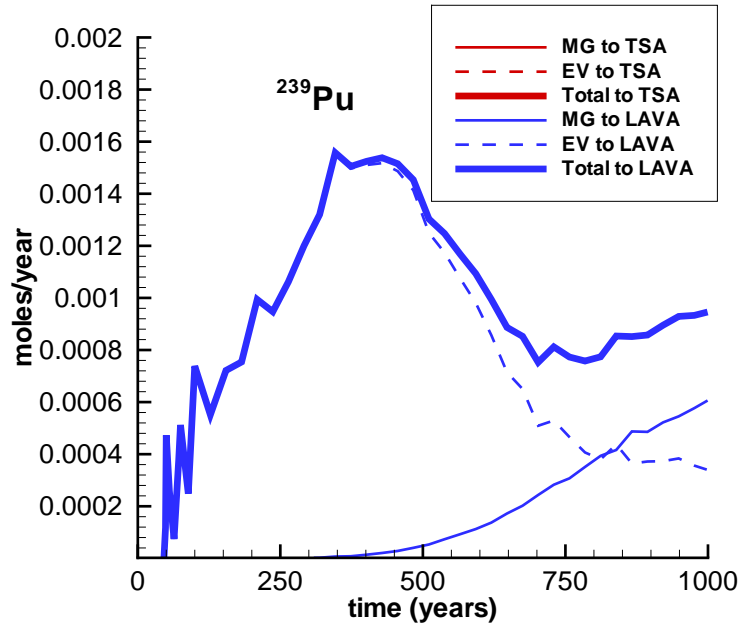


Figure 6-32. ^{239}Pu breakthrough mass fluxes to the TSA and LAVA from the MG and the EV.

6.8.2 Mass Flux Curves

SOURCE 1

Figures 6-33, 6-34, and 6-35 illustrate the mass-flux breakthrough curves into the TSA and LAVA aquifers for SOURCE 1 (Table 6-9). Figure 6-33 shows the resulting breakthrough curves for the non-sorbing species for SOURCE 1 (these are non-reactive, so no A or B distinction for Class I and VI). All Class I and VI RNs release the most mass at early times because of instantaneous EV release, high-temperature-accelerated MG dissolution, and strong vertical convection. At later times, reduced MG dissolution and temperature reductions result in less mass release (see Section 6.5.3). Note that all the curves are similar in shape at early times, especially for mass flux to the TSA, regardless of MG-EV distribution because all transport to the aquifers is associated with a thermal pulse of short duration described in Section 6.8.1. The notable exception, ^3H , has a mass flux that drops off with time relative to the other Class I RNs because ^3H has a half-life of 12.7 years.

Figure 6-34 plots the other RNs modeled conservatively (i.e., with a $Kd = 0$). The pattern here is the same as for the conservative species in Figure 6-33; namely, the mass flux release into the aquifers is scaled by the quantity of mass initially from the EV and dissolving from the MG. Mass flux curves for RNs with short half-lives (e.g., Eu) drop off with increasing time. Figure 6-35 illustrates that when Class II through V RNs are modeled as sorbing species (and using Kds from the lowest end of the range of uncertainty for each RN), only those with very low Kds (Np and U) arrive at the TSA. The more retarded species break through only to the LAVA aquifer at later times and with lower peak mass flux than when modeled conservatively.

SOURCE 2

Figures 6-36, 6-37, and 6-38 illustrate the mass flux breakthrough into the TSA and LAVA aquifers for SOURCE 2 (Table 6-9). The mass flux curves for all the different RNs at their respective sorption values are illustrated in these plots for the medium Rayleigh number ($R\hat{a}_{sys} = 8.64$). For the conservative RN releases illustrated in Figures 6-36 and 6-37 ($Kd = 0$), the peak mass flux to the TSA is approximately two orders of magnitude less than for the SOURCE 1 simulation (Figure 6-33 and 6-34), with breakthrough beginning at ~60 years rather than ~15 years. Decreases in peak mass fluxes to the LAVA are less than one order of magnitude compared to SOURCE 1, and the breakthrough time still begins in less than 5 years. When sorption is included (SOURCE 2B, Figure 6-38), only the least sorptive RN, Np, breaks through to the TSA. Significant (but delayed) breakthrough to the LAVA still occurs under sorptive conditions and the tails are actually greater than for the non-sorptive case because of the delayed release from the cavity/chimney system.

SOURCE 3

Figures 6-39, 6-40, and 6-41 illustrate the mass-flux breakthrough curves into the TSA and LAVA aquifers for SOURCE 3 (Table 6-9). Under these conditions, vertical convection is completely precluded for *all* RNs under all sorptive conditions, including $Kd = 0$, to the TSA. Breakthrough to the LAVA for all RNs is notably slower and of notably smaller peak mass flux when compared to SOURCE 1 and SOURCE 2 simulations. However, most RNs still break through even under the sorptive SOURCE 3B conditions (Figure 6-41), with the characteristic tails

associated with delayed release from the cavity/chimney system caused by retardation in the material there.

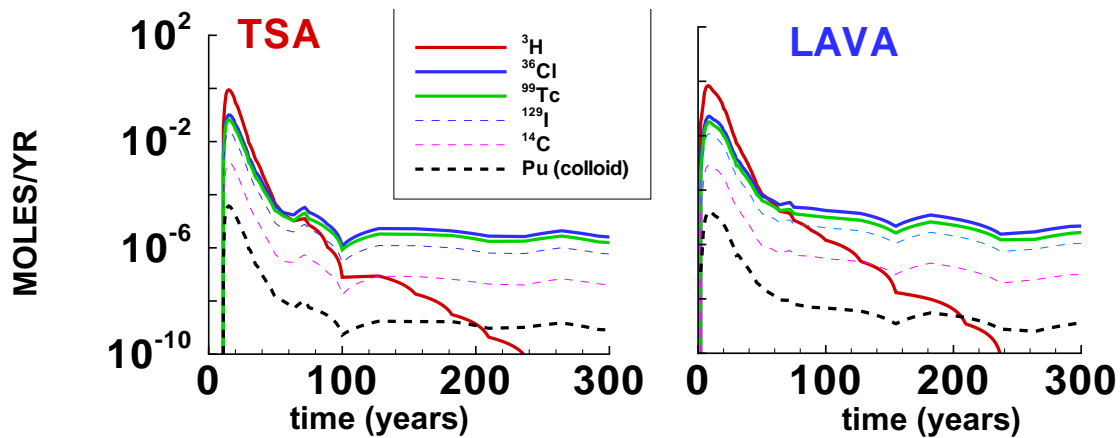


Figure 6-33. SOURCE 1 (BASE CASE $R\hat{a}_{sys}$) mass flux of conservative RNs (Class I and VI) entering the TSA and the LAVA from the cavity/chimney.

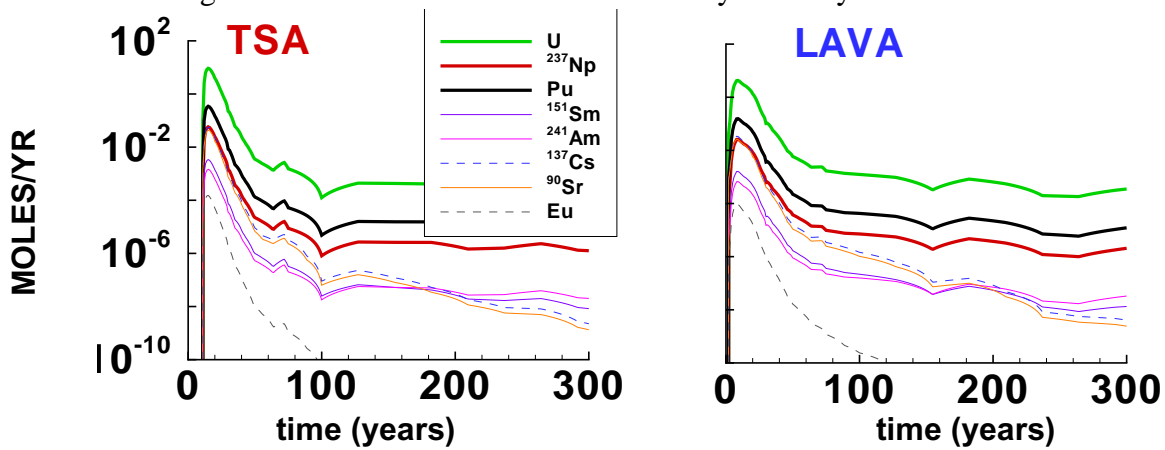


Figure 6-34. SOURCE 1A (BASE CASE $R\hat{a}_{sys}$) mass flux of Class II through VI RNs modeled without chimney sorption, entering the TSA and the LAVA from the cavity/chimney.

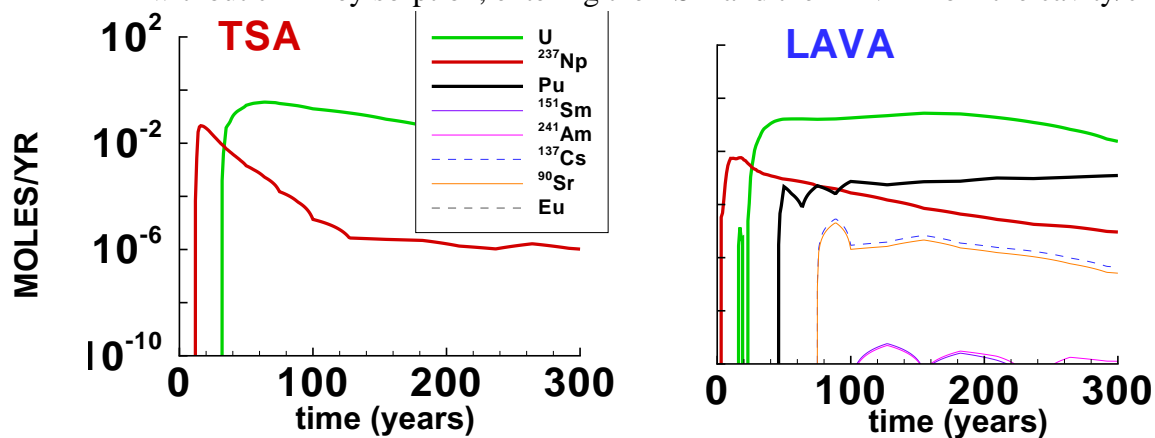


Figure 6-35. SOURCE 1B (BASE CASE $R\hat{a}_{sys}$) mass flux of Class II through VI RNs modeled with chimney sorption, entering the TSA and the LAVA from the cavity/chimney.

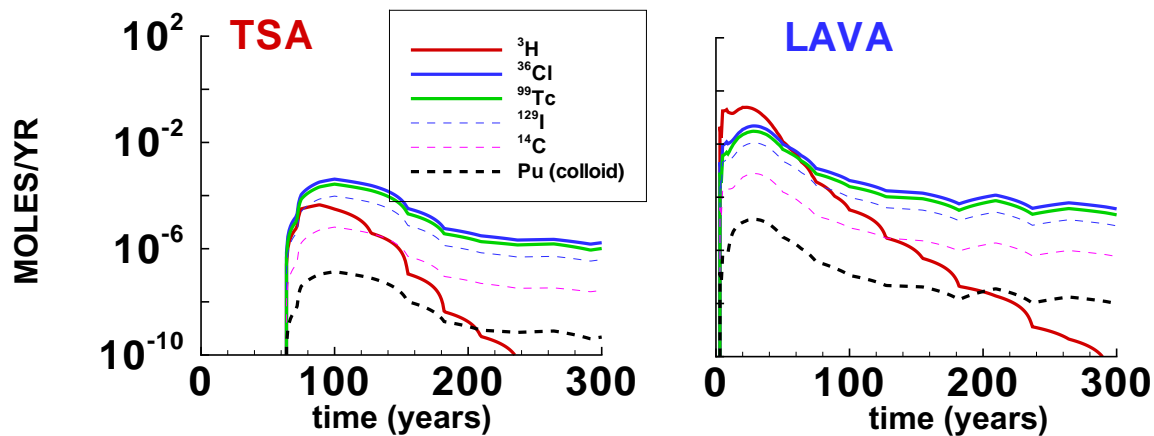


Figure 6-36. SOURCE 2 (med. $R\hat{a}_{sys}$) mass flux of conservative RNs (Class I and VI) entering the TSA and the LAVA from the cavity/chimney.

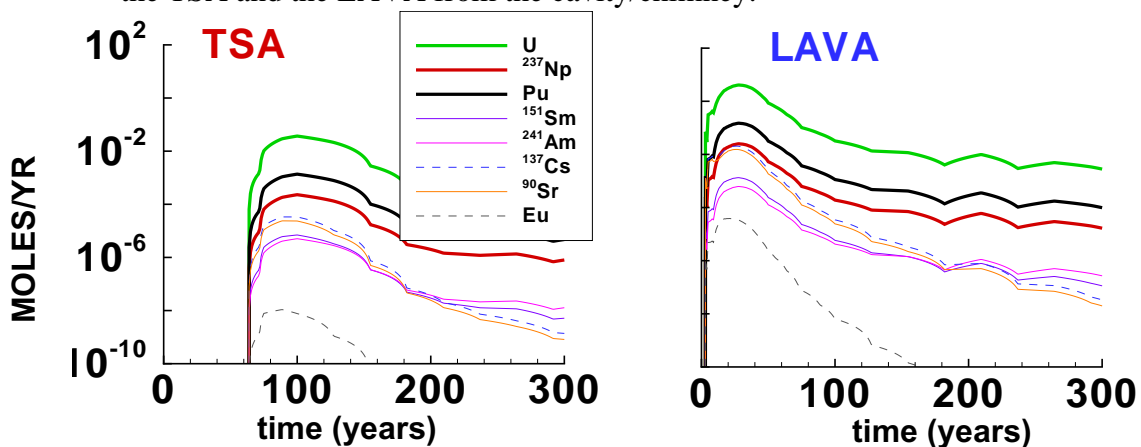


Figure 6-37. SOURCE 2A (med. $R\hat{a}_{sys}$) mass flux of Class II through VI RNs modeled without chimney sorption, entering the TSA and the LAVA from the cavity/chimney.

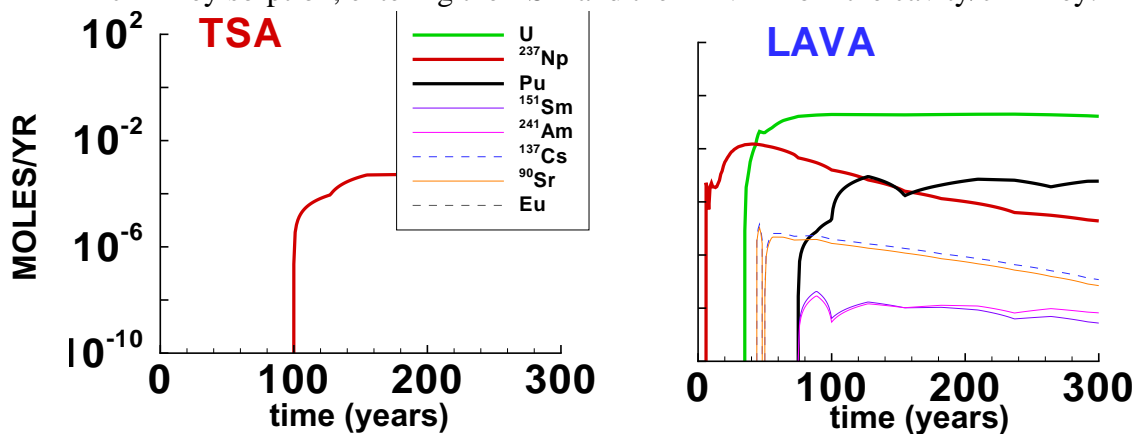


Figure 6-38. SOURCE 2B (med. $R\hat{a}_{sys}$) mass flux of remaining RNs modeled with chimney sorption, entering the TSA and the LAVA from the cavity/chimney.

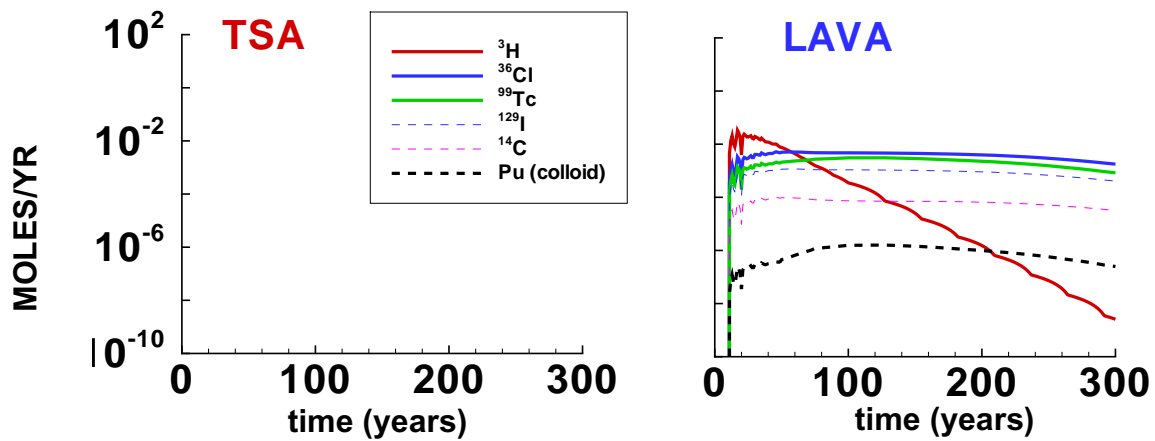


Figure 6-39. SOURCE 3 (low $R\hat{a}_{sys}$) mass flux of conservative RNs entering the TSA and the LAVA from the cavity/chimney.

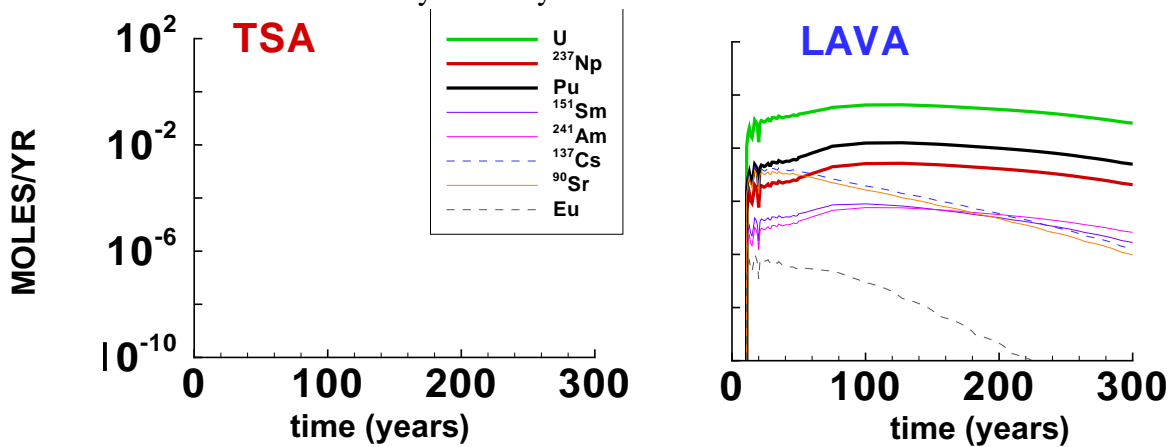


Figure 6-40. SOURCE 3A (low $R\hat{a}_{sys}$) mass flux of Class II through VI RNs modeled without chimney sorption, entering the TSA and the LAVA from the cavity/chimney.

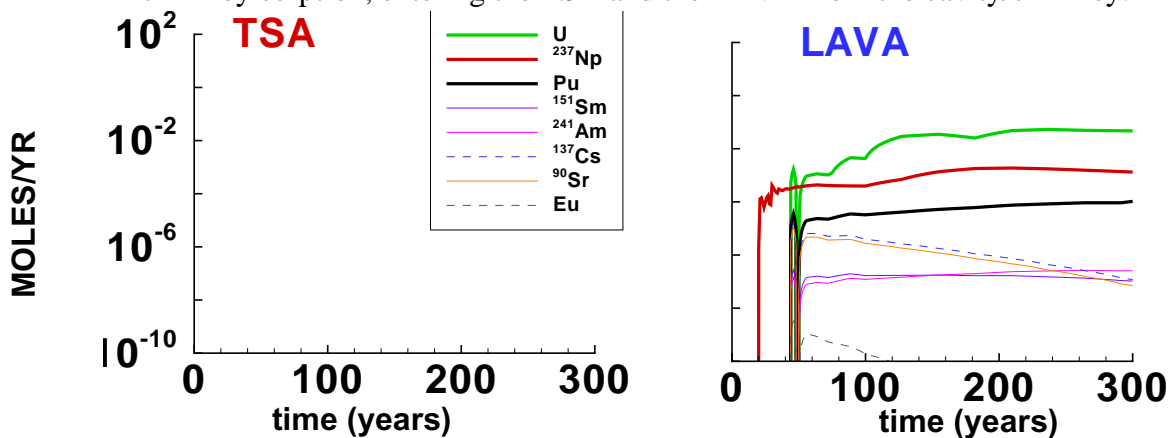


Figure 6-41. SOURCE 3B (low $R\hat{a}_{sys}$) mass flux of remaining RNs modeled with chimney sorption, entering the TSA and the LAVA from the cavity/chimney.

6.8.3 Cumulative Mass Curves

The total mass leaving the cavity/chimney to the TSA and LAVA aquifers is plotted for all six source conditions in Figures 6-42 through 6-50. These curves are simply the time integrations of the mass flux curves of Figures 6-33 to 6-41 and are used as input to site-scale models in Appendix F and Chapter 7. For the conservative conditions of SOURCE 1A (Figures 6-42 and 6-43) it is notable that while mass arrives to the TSA at a later time, a slightly larger amount of mass is convected to the TSA than to the LAVA. This is also true for the sorptive SOURCE 1B RNs (U and N_p) breaking through to the TSA, as illustrated in Figure 6-44. For the medium Rayleigh conditions of SOURCE 2, the total amount of mass for *all* RNs breaking through to the TSA is less than the total breaking through to the LAVA (Figures 6-45, 6-46, and 6-47) because the convection cells are not as strong as in SOURCE 1. Finally, for the low Rayleigh number SOURCE 3, no RN mass breakthrough occurs to the TSA at all and the cumulative mass breakthrough to the LAVA is considerably less than for the other source conditions (Figures 6-48, 6-49, and 6-50).

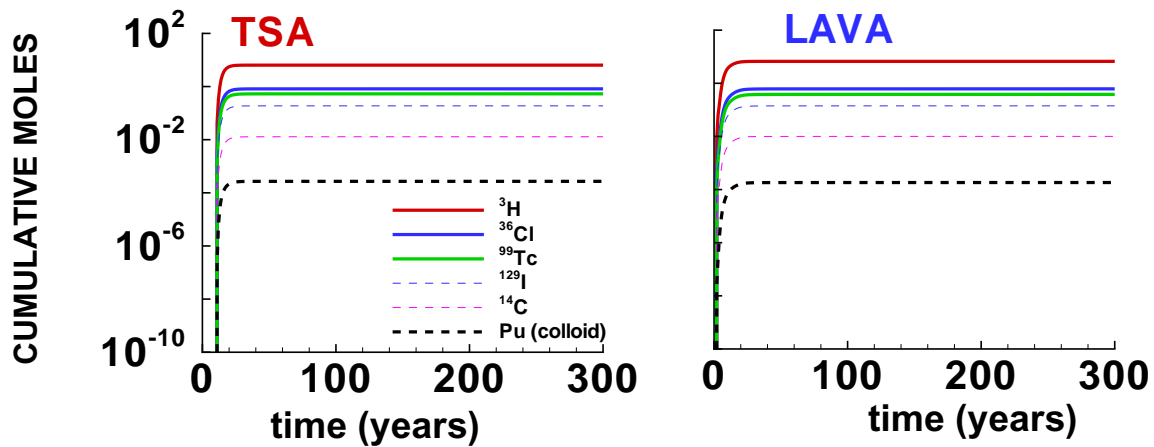


Figure 6-42. SOURCE 1 (BASE CASE $R\hat{a}_{sys}$) cumulative mass of conservative RNs (Class I and VI) entering the TSA and the LAVA from the cavity/chimney.

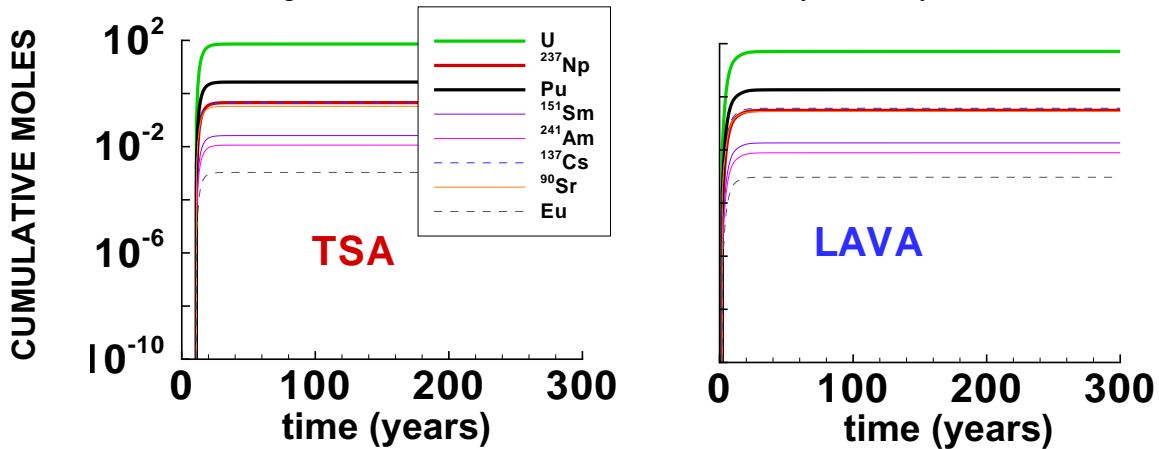


Figure 6-43. SOURCE 1A (BASE CASE $R\hat{a}_{sys}$) cumulative mass of Class II through VI RNs modeled without chimney sorption, entering the TSA and the LAVA.

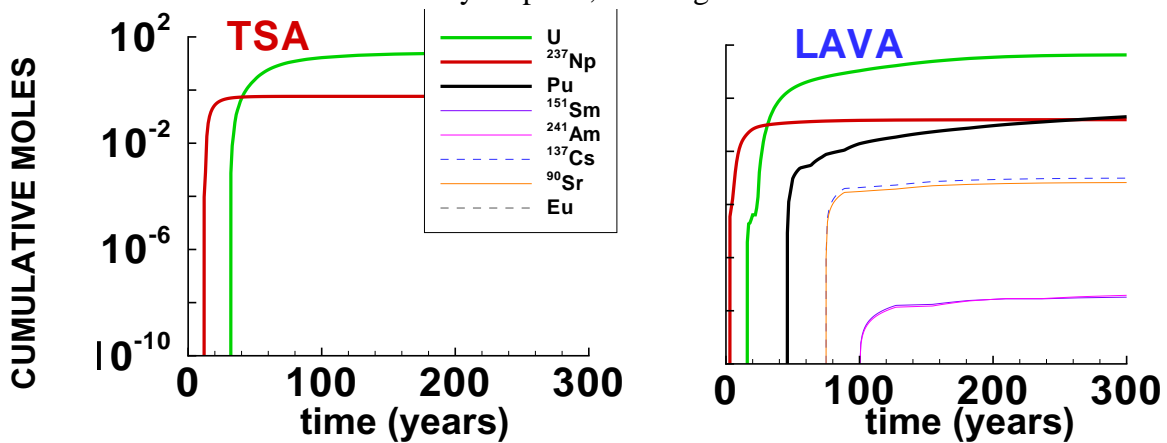


Figure 6-44. SOURCE 1B (BASE CASE $R\hat{a}_{sys}$) cumulative mass of Class II through VI RNs modeled with chimney sorption, entering the TSA and the LAVA.

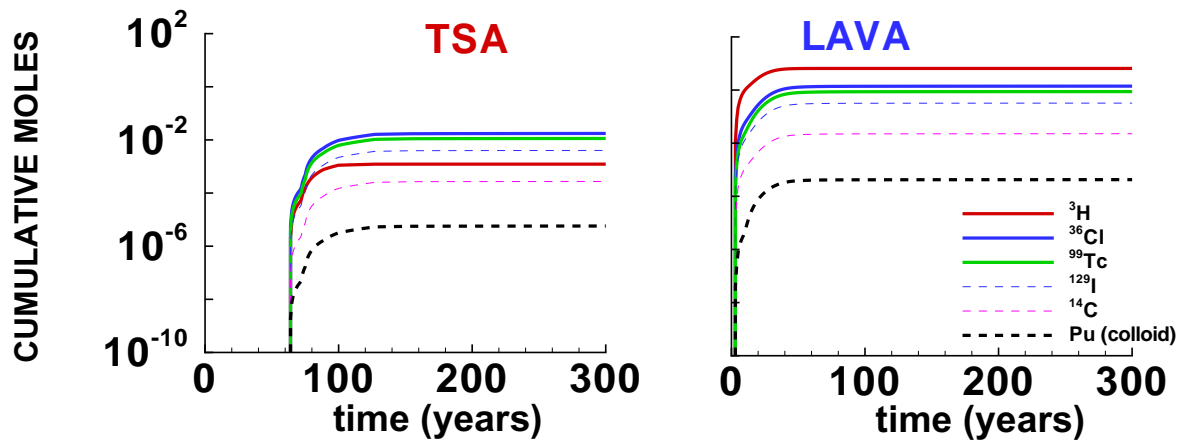


Figure 6-45. SOURCE 2 (med. $R\hat{a}_{sys}$) cumulative mass of conservative RNs (Class I and VI) entering the TSA and the LAVA from the cavity/chimney.

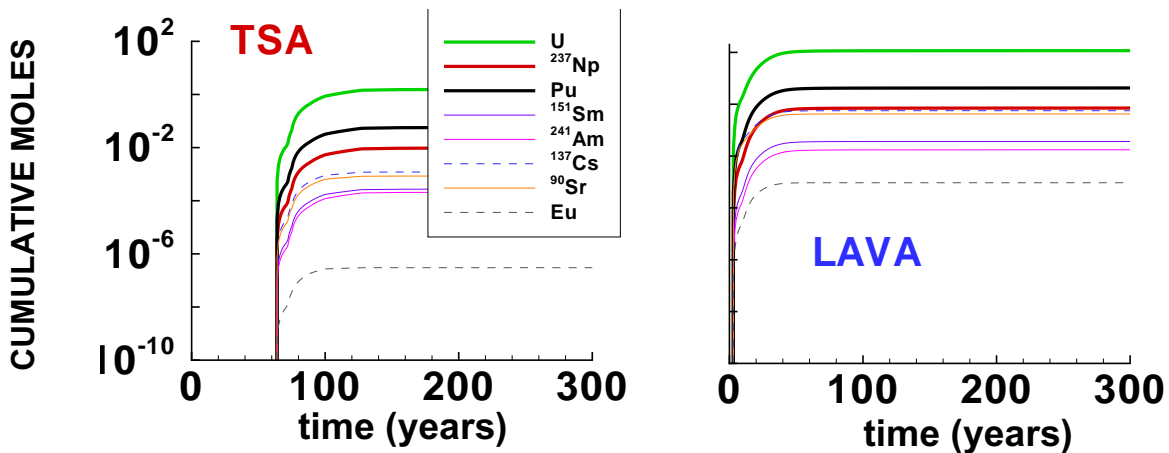


Figure 6-46. SOURCE 2A (med. $R\hat{a}_{sys}$) cumulative mass of Class II through VI RNs modeled without chimney sorption, entering the TSA and the LAVA from the cavity/chimney.

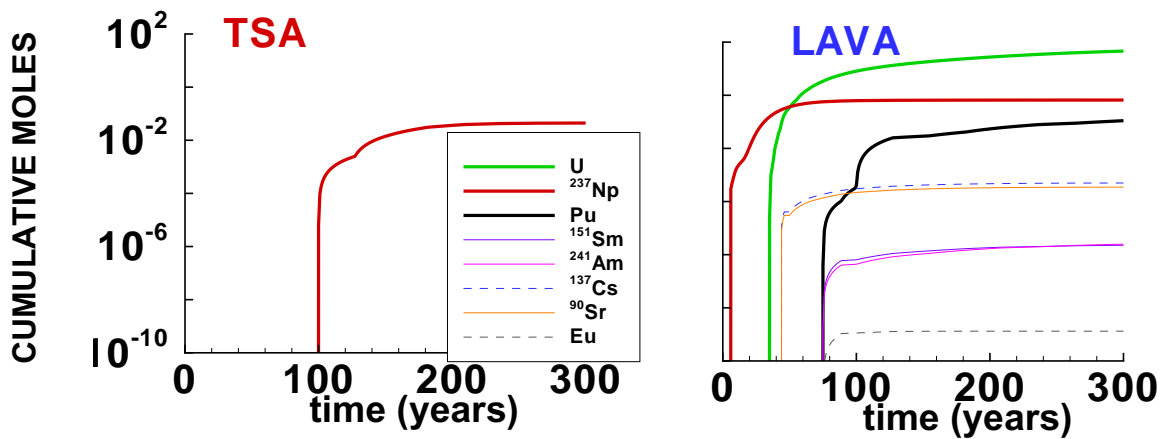


Figure 6-47. SOURCE 2B (Medium $R\hat{a}_{sys}$) cumulative mass of Class II through VI RNs modeled with chimney sorption, entering the TSA and the LAVA from the cavity/chimney.

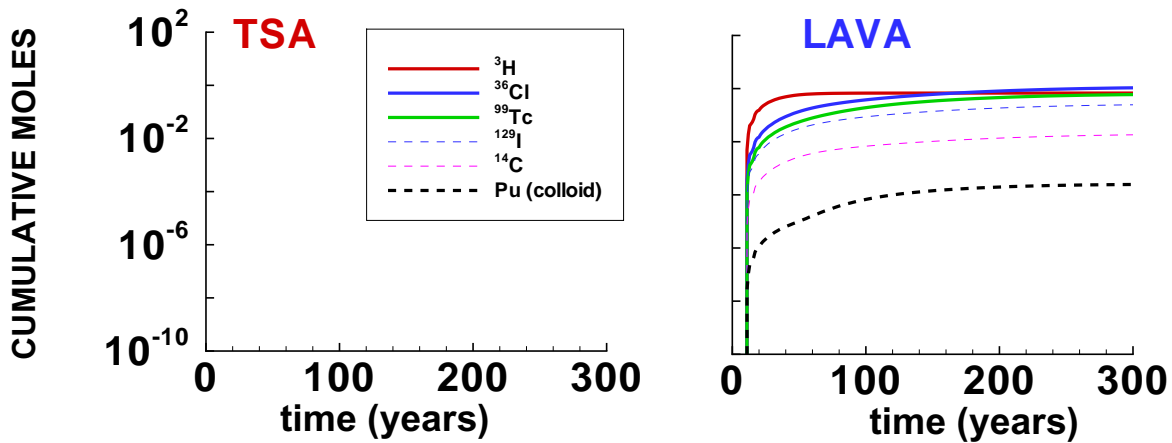


Figure 6-48. SOURCE 3 (low $R\hat{a}_{sys}$) cumulative mass of conservative RNs (Class I and VI) entering the TSA and the LAVA from the cavity/chimney.

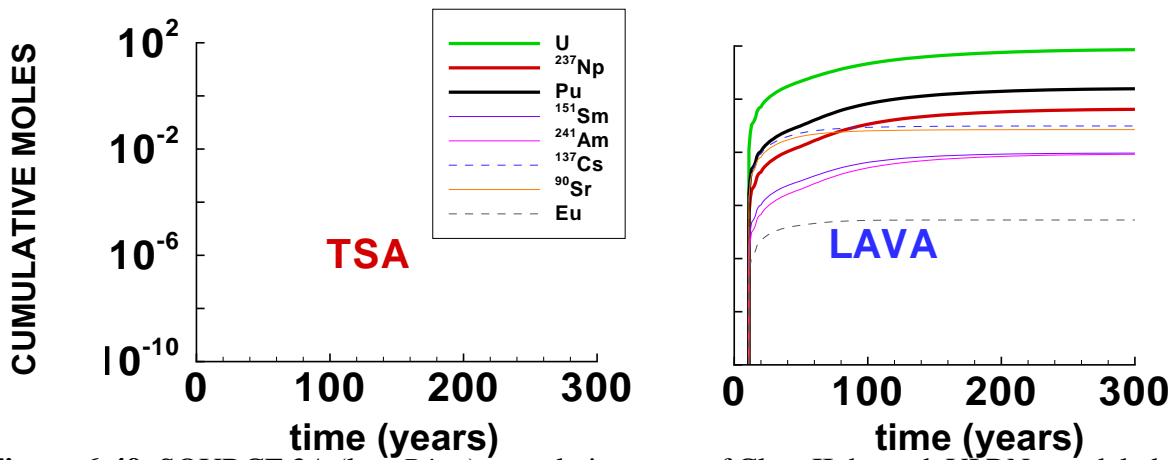


Figure 6-49. SOURCE 3A (low $R\hat{a}_{sys}$) cumulative mass of Class II through VI RNs modeled without chimney sorption, entering the TSA and the LAVA from the cavity/chimney.

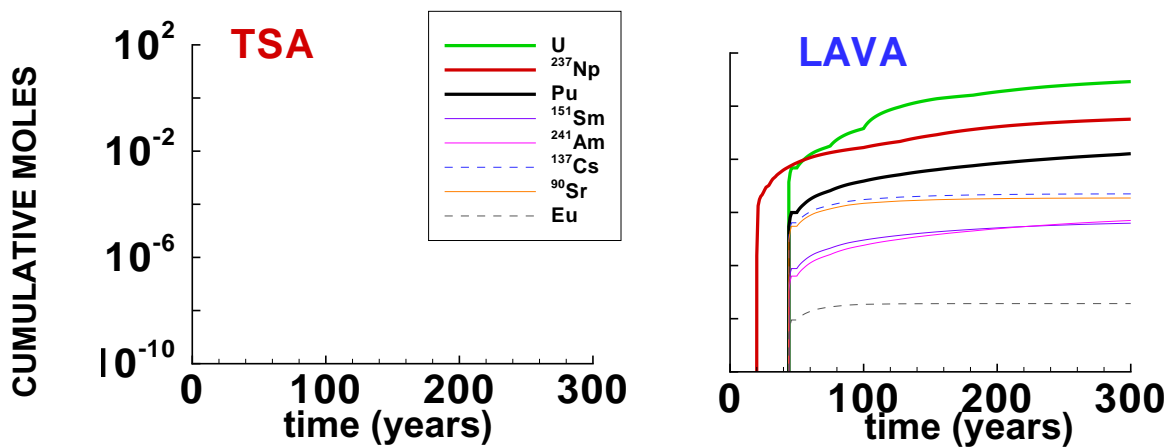


Figure 6-50. SOURCE 3B (low $R\hat{a}_{sys}$) cumulative mass of Class II through VI RNs modeled with chimney sorption, entering the TSA and the LAVA from the cavity/chimney.

6.9 Summary and Conclusions

Pu fingerprinted to the BENHAM underground nuclear test was detected 1.3 km away in the ER-20-5 observation wells. The highest concentration (0.63 pCi/l, well below the EPA drinking-water standard) was measured in an aquifer 500 m above the detonation point. Thermally driven vertical flow in the chimney and colloid-facilitated transport in the fractured tuff are possible mechanisms allowing such distant Pu migration in less than 30 years. This source-term modeling effort indicates that it is possible for the necessary vertical transport in the chimney to occur in less than 30 years for geologic, geochemical, and initial energy conditions representative of the system. Further, a Rayleigh number analysis is proposed as a generic and quick method to evaluate the likelihood of retarded and non-retarded vertical transport. A source term for all 17 RNs is obtained by the following tasks: (1) combining the particle releases from different initial mass distributions between the MG and EV, (2) modeling particle transport with Kds representing the various RNs considered, (3) stoichiometrically scaling the source to represent the mass of each RN, and (4) adjusting for radioactive decay. Further, RN transport for three different Rayleigh source conditions brackets the range of uncertainty expected from the source conditions at BENHAM. These RN source conditions are employed later for the site-scale transport studies in Appendix F and Chapter 7.

The model described in this chapter was used to conduct a non-isothermal study of the near-field release of RNs in the cavity/chimney system to the TSA and LAVA aquifers. Key assumptions are made about near-field initial conditions and post-detonation geology, thereby limiting the analysis to an evaluation of hydrologic transport and, thus, requiring bracketing of results sensitive to parameter variation. The following specific conclusions can be drawn concerning this near-field BENHAM cavity/chimney study:

- Pu breakthrough to the TSA and LAVA aquifers from BENHAM is possible due to groundwater transport under expected geologic, geochemical, and thermal conditions.
- In the absence of residual heat in the MG, the relative Rayleigh number is low and transport of solutes and particles up the chimney to the TSA is unlikely.
- If residual heat is present in the MG, transport of solutes and particles up the chimney to the TSA is possible if the relative Rayleigh number is sufficiently greater than unity and if the transport is unretarded. Simulation results imply that if the chimney collapses as a high-permeability unit, then thermally driven vertical flow through the cavity/chimney system can occur. Thermally driven upward flow through the cavity/chimney is likely precluded if the chimney collapses as unit blocks resulting in low chimney permeability.
- Uncertainty in MG volume and porosity affects the amount of RNs released from the MG. However, variation in MG parameters has a very limited effect on the general trend of vertical convection of RNs to the TSA and LAVA aquifers.
- Reduced LAVA permeability increases the amount of RN mass convecting to the TSA aquifer. However, increased LAVA permeability never completely eliminates the convection of RNs to the TSA.

- Sorption limits but does not necessarily preclude convection of RNs to the TSA and LAVA aquifers. For the BASE CASE study, transport from the MG to the TSA is precluded at Kds of 5.0 cc/g and higher, whereas transport from the MG to the LAVA is precluded at Kds of 10.0 cc/g and higher.
- System and local Rayleigh numbers can be used to bracket the likelihood of vertical convection in the chimney. There is a loose linear relationship between Rayleigh numbers and the time of entrance into the TSA and LAVA aquifers of 0.01% of a particular RN's total MG-based mass.
- Evaluation of a "Sorptive Rayleigh Number," which incorporates the effects of sorption, is useful in analyzing the likelihood of vertical convection within the cavity/chimney. An expected linear relationship between Rayleigh numbers and entrance times to the LAVA is observed for simulations at different sorption values, indicating a linear transport path from the MG to the LAVA. However, a linear relationship between Rayleigh numbers and entrance times to the TSA is not observed. Aquifer entrance times are faster than expected for a given Kd , indicating a highly non-linear transport path from the MG to the TSA caused by the large convective cells generated at early simulation times.
- The primary difference between RNs originating in the EV and RNs originating in the MG is the amount of mass breaking through to the aquifers. Nearly all mass from the EV is convected to the TSA and LAVA aquifers while only a fraction of the mass in the MG is so transported. As vertical convection occurs over a relatively short duration of ~30 years, we noted little difference in the timing and shape of the mass breakthrough curves for BASE CASE mass releases or conservative RNs. However, for mass releases of reactive RNs and for lower Rayleigh number source conditions, mass released from the MG exits into the aquifers as a tail following the initial pulse of EV mass.
- For BASE CASE simulations of conservative RNs, slightly more mass enters the TSA aquifer than the LAVA aquifer. For increasing Kd and decreasing initial Rayleigh number, less mass enters the TSA than the LAVA. This trend continues until $R\hat{a}_{sys}=0.864$, at which time all RNs regardless of sorptive condition, are prevented from entering the TSA.

Chapter 7: Site-Scale Particle-Tracking Transport Model

7.1 Introduction

A highly efficient particle-tracking model uses source functions computed in Chapter 6, the dual-porosity streamline particle-tracking method presented in Appendix C, and convolution integrals to (1) compute groundwater activities of radionuclides found in the ER-20-5 observation wells (see Tables 1-1 and 1-2) and (2) perform extensive parameter sensitivity analysis. Taken into consideration are sources from both BENHAM and TYBO, as well as multiple realizations of the heterogeneous attribute distributions. The model captures the important mechanisms affecting RN migration (such as matrix diffusion, matrix sorption, and fracture-coating sorption), represented with linear equations. The model is readily applicable to multiple different flow fields and a variety of parameter-sensitivity studies.

Appendix F discusses a more detailed process-level site-scale transport model that considers kinetic reactions between colloids and plutonium (Pu) and aqueous speciation reactions. Using a finite-volume numerical formulation to solve the full set of reactive transport equations, this process model is a site-scale extension of the detailed process model used to simulate colloid-facilitated Pu transport experiments (Appendix D). The process models provide a detailed understanding of the mechanisms affecting solute and colloid migration in the complex, fractured rock system associated with the TYBO/BENHAM site-scale domain. The understanding gained from the process models is then used to parameterize and justify simplifying assumptions in the particle-tracking model described in this chapter.

Convolution integration enables efficient site-scale transport analyses with particle-tracking simulations that incorporate complex source-release functions. The convolution integral method, which translates a transient source function to a downstream location via a unit breakthrough curve, is similar to a method often used in surface hydrology to determine downstream flow rates via convolution of a source-rainfall event with a unit (i.e., non-dimensional) hydrograph (Singh, 1988). This method has also been used for contaminant transport in the subsurface (TRW, 2000; CRWMS M&O, 2000a,b,e; Hassan et al., 1999). In this application, the convolution integral method generates downstream concentrations for different RNs at the ER-20-5 observation wells and mass fluxes at the NTS boundary. The deterministic and heterogeneous flow fields described in Chapter 5 are used in this portion of the study.

7.2 Chapter Road Map

This chapter is divided into three main components: approach and parameters, simulations on the deterministic HSU domain, and simulations on heterogeneous attribute maps.

- Sections 7.3 through 7.6 describe the method used in all simulations, including the parameters and their sources.
- Section 7.7 describes the site-scale transport simulations conducted on the deterministic HSU representation of hydrostratigraphy. In this section, we compare model results with field

observations. Also, considered are source releases from TYBO.

- Sections 7.8 and 7.9 describe the site-scale transport simulations conducted on heterogeneous attribute maps. Because not all heterogeneous attribute realizations support transport simulations consistent with field observations (migration of multiple RNs to ER-20-5 #1 and #3 by 1996), these fields are used for general transport sensitivity analysis, thereby emphasizing more the arrivals at the NTS boundary than at the observations wells.

7.3 Convolution Integral Approach

The mass flux of RNs at the ER-20-5 observation wells and the NTS boundary are simulated by performing a convolution integral of the source RN fluxes into the aquifers computed in Chapter 6 with unit source breakthrough curves at the wells and the NTS boundary. The breakthrough curves are generated with the dual-porosity, reactive, site-scale particle-tracking transport model for unit-source releases originating at BENHAM or TYBO. The code used to perform the convolution is SZ_CONVOLUTE VERSION 2.0, a fully documented and quality-assured software package (TRW, 2000; CRWMS M&O, 2000b,h). The necessary assumptions for the convolution integration are as follow: (1) the site-scale flow and transport processes are effectively independent of the source-term model; (2) site-scale transport processes are modeled with linear equations; and (3) the site-scale flow field is at steady state. We use the decoupled cavity/chimney source term described in Chapter 6 and simulate linear transport process on steady-state site-scale flow models in conjunction with the particle-tracking transport model.

Convolution integration involves a mathematical operation in which a function $h(t-t')$ does not depend on t' (the time when the input is applied), but rather only on the time difference $(t-t')$. Such a system is termed *time-invariant* (Singh, 1988). The convolution integral used to couple the time varying source term and the site-scale unit breakthrough curve is expressed as follows:

$$M_{bnry}(t) = \int_0^t (M_{src}(t-t') \exp(k_{1/2}t') f_{bnry}(t'))(dt'), \quad (\text{Eq. 7-1})$$

where $M_{bnry}(t)$ is the downstream flux, $M_{src}(t-t')$ is the time-dependent source flux, the half-life constant for radioactive decay is computed as $k_{1/2} = \ln(0.5)/t_{1/2}$, where $t_{1/2}$ is the half life and $f_{bnry}(t')$ is the residence-time distribution function obtained by integrating the non-dimensional breakthrough curve with respect to t' . For SZ_CONVOLUTE VERSION 2.0, both the time-dependent mass flux, $M_{src}(t-t')$, and the downstream concentration-time curves, $C/C_0 = \int_0^t f_{bnry}(t')(dt')$, are entered in tabular form. The subroutine then uses a trapezoidal integration scheme to approximate the integration of the source flux with a non-dimensional breakthrough curve.

Figure 7-1 illustrates an example of the convolution operation. For a rapidly decaying species (A) and a slower decaying species (B), downstream mass fluxes are calculated from source-term mass fluxes and downstream unit-source breakthrough curves corresponding to each RN. The example source functions shown in Figure 7-1 are representative of the source-release

functions in Figure 6-33. The unit-source breakthrough curves are computed with the particle-tracking model described in Appendix C. The resulting downstream flux can then be used to develop cumulative mass-arrival curves or to compute flux-averaged RN concentrations in groundwater by dividing the RN mass flux by the groundwater flow rate.

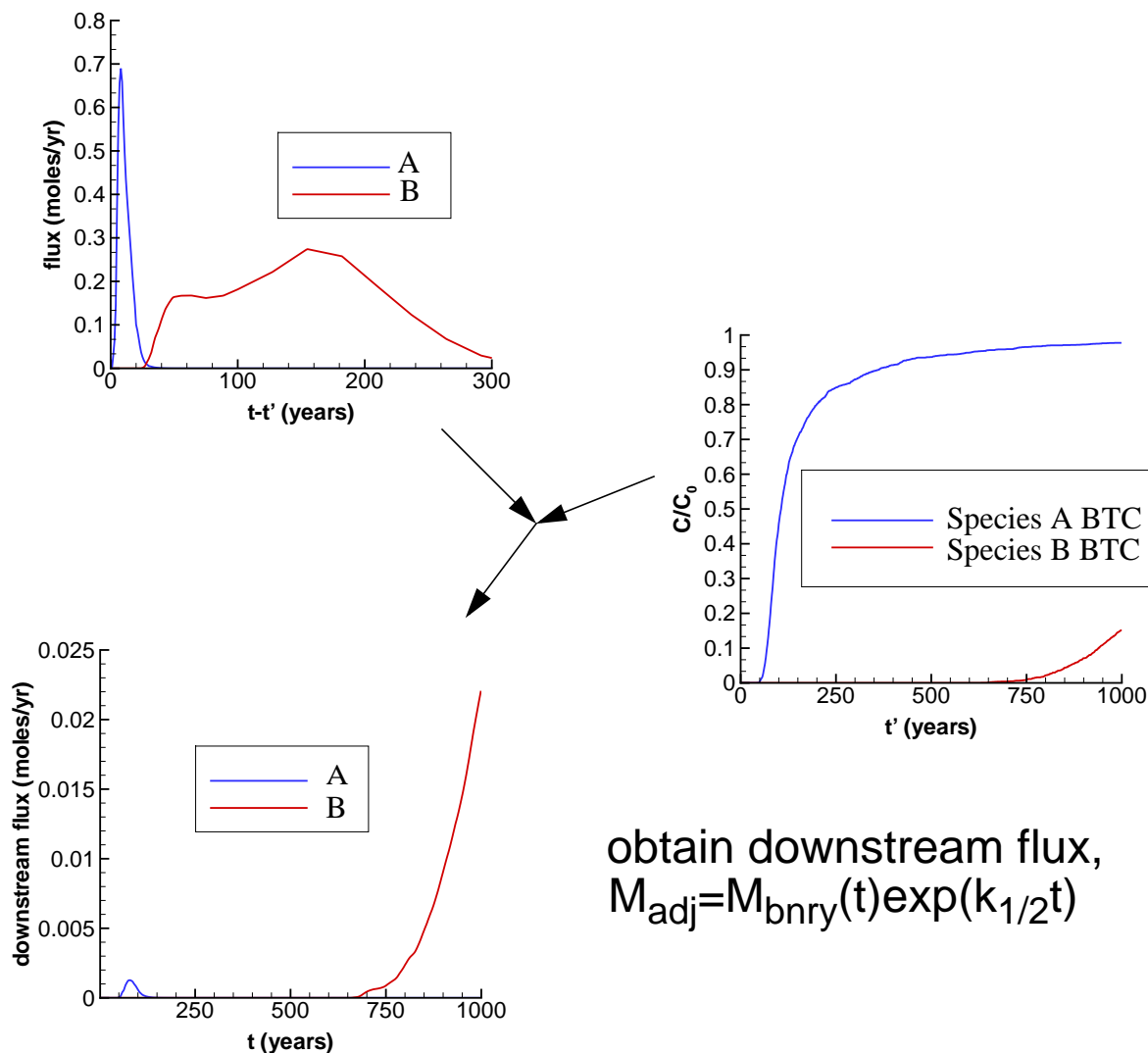


Figure 7-1. The convolution operation of the source-mass fluxes (top plot), in conjunction with the unit-source breakthrough curves (middle plot), are used to obtain downstream mass fluxes adjusted for decay (bottom plot). This illustration shows convolution for rapidly decaying, unretarded species (A) and a slow decaying, retarded species (B).

Application of SZ_CONVOLUTE to analyze RN transport from TYBO and BENHAM utilizes the time-varying source terms described in Chapter 6 and the unit source breakthrough curves at the NTS boundary and the ER-20-5 observation wells. The unit source breakthrough curves are computed for each different RN class by releasing a swarm of particles at each source

location and then tabulating at any given time the cumulative fraction of the total number of particles arriving at the wells or boundary.

A sensitivity study was conducted to determine the appropriate number of particles to use in these simulations. Figure 7-2 illustrates the convergent nature of using 625, 2500, and 10 000 particles released instantly from BENHAM for both conservative and sorbing species. These results helped establish the choice of using 2500 particles--a number sufficient for an accurate breakthrough curve (BTC) and yet small enough to be computationally efficient.

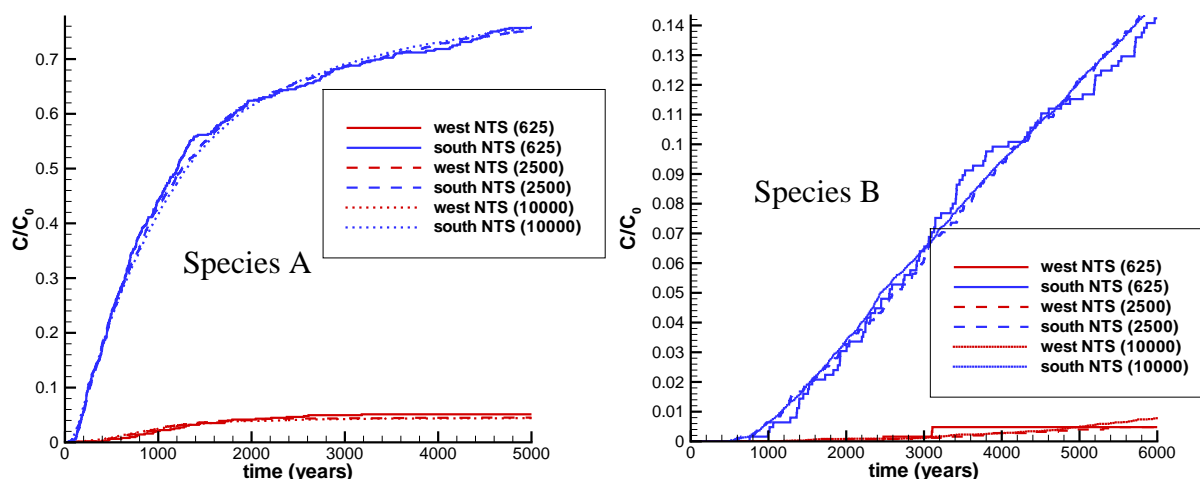


Figure 7-2. Downstream breakthrough curves for different BENHAM particle releases (625, 2500, and 10 000) for a non-retarded species (A) and a retarded species (B).

7.4 Source Term

The source model described in Chapter 6 generated the time-dependent source mass flux curves considered in all analyses. Listed in Table 6-9 and shown in Figures 6-33 through 6-50, the six source cases are the input functions $M_{src}(t-t')$ of the convolution integral in Equation 7-1. These six curves capture the range in source-term uncertainty, including reactive and non-reactive chimney properties and various thermal convective potentials in the chimney. The three different thermal convective potentials are represented with source cases 1 ($Ra_{sys} = 84.6$), 2 ($Ra_{sys} = 8.46$) and 3 ($Ra_{sys} = .846$). Additionally, for each source case listed in Table 6-9, (A) refers to conditions in which sorption is not considered in the chimney and (B) refers to conditions in which sorption of reactive species (RN classes II, III, IV, and V; Table 7-1) to chimney material is considered. Section 6.1.4 describes the TYBO source abstraction from the BENHAM source model.

7.5 Parameter Distributions

In later sections of this chapter, base-case and parameter sensitivity transport simulations are conducted and analyzed. In this section, we present the parameters used in those simulations for both the deterministic and heterogeneous attribute maps described in Chapter 5.

The RNs considered are grouped into six different classes, each with similar transport parameters. Listed in Table F-16, the matrix Kd for each RN is the primary parameter used to establish the groupings of RNs for this analysis (shown in Table 7-1). In the parameter sensitivity analysis, a breakthrough curve must be generated for each set of transport parameters for each source release location (LAVA and TSA for BENHAM). With six different RN classes, twelve breakthrough curves are needed per flow field for BENHAM, just for the base-case set of transport parameters. Twelve new breakthrough curves are needed for each modification in transport parameters.

The sensitivity study considers five different parameter sets for both the deterministic and heterogeneous attribute maps. For each parameter, perturbations from the expected value to the minimum and maximum extent of the range of uncertainty are conducted. Further, the sensitivity analysis considers a unique range of uncertainty for each different lithology (e.g., welded tuff or altered tuff) for each parameter. Tables 7-2 through 7-5 list the ranges and expected values for the parameters for each of the seven different rock types considered in the sensitivity simulations. A brief description of the model parameters associated with the sensitivity studies follows:

- **Fracture aperture.** This model parameter only affects solute diffusion between fracture and matrix material; smaller apertures lead to increased diffusion. As used in this model, aperture does not affect porosity, which is covered in the next term.
- **Fracture porosity.** This model parameter directly affects velocities in fractures. As fracture velocities increase, residence times decrease, thus also reducing the ratio of the mass that diffuses into the matrix to that which remains in the fracture. This term is estimated from geometric relationships of fracture apertures and spacing, except for the LAVA, for which results from the BULLION FGE are also used.
- **Matrix diffusion coefficient.** This model parameter has been extensively studied in laboratory experiments for a variety of solutes and rock types (e.g., Reimus et al., 2002).
- **Matrix Kd for reactive solutes.** Extensive databases for this model parameter (CRWMS, 2000g) have been developed through batch-sorption experiments on multiple rock types with various water chemical compositions for several key RNs. Other RNs are assigned Kds based on similar characteristics with those in the database.
- **Fracture Retardation Factor.** This model parameter is based on the fracture Kd terms developed in Appendix D and Appendix F. Its uncertainties are related to mineral distribution, effective reactive surface area, and thickness of the fracture coatings. In this chapter, only variations in the distribution of FeOH, AlOH, SiOH, and CA^{2+} minerals in the coatings are considered. Reactive surface area and coating thickness are held constant at their expected values. The fracture retardation factor is simply $R = 1 + Kd$

because all surface area and mineral density considerations have already been factored into the fracture Kd term (e.g., Equations F-1 and F-3). Fracture Kd is also used in the particle-tracking model to simulate retardation of Pu-colloid cause by attachment and detachment.

For each set of transport parameters, sensitivity to different source-term conditions defined by the different source-flux curves computed in Chapter 6 requires only substituting the different source term into the input file for SZ_CONVOLUTE. Computation of each BTC with SPTR is fast relative to the coupled reactive transport model, so generation of large numbers of the curves necessary for sensitivity analysis is efficient.

For all flow fields, BTCs are simulated at the two ER-20-5 observation wells and the NTS boundary for each set of sensitivity parameters. The capture zones at the observation wells are approximated with $150 \times 150 \times 150 \text{ m}^3$ boxes centered at the well locations in plan view and extending into the aquifers (LAVA and TSA) sampled by the wells. The southern and western sides of the site-scale model approximate the NTS boundary. Non-dimensional BTCs are computed by tallying particles arriving in any of the capture zones.

Table 7-1. Source Radionuclides Grouped By Class

Class	Radionuclide	Symbol	Moles in Source ¹	1/2 life
Class I	Tritium	³ H	3.13E+01	1.23E+01
	Carbon	¹⁴ C	1.17E-01	5.73E+03
	Chlorine	³⁶ Cl	2.37E+00	3.01E+05
	Krypton	⁸⁵ Kr	3.78E-02	1.07E+01
	Technetium	⁹⁹ Tc	2.41E+00	2.13E+05
	Iodine	¹²⁹ I	5.44E-01	1.57E+07
Class II	Samarium	¹⁵¹ Sm	1.89E-01	9.00E+01
	Americium	²⁴¹ Am	7.43E-02	4.33E+02
	Europium	¹⁵² Eu	1.63E-02	1.35E+01
	Europium	¹⁵⁴ Eu	4.90E-03	8.59E+00
Class III	Strontium	⁹⁰ Sr	1.28E+00	2.91E+01
	Cesium	¹³⁷ Cs	1.68E+00	3.02E+01
Class IV	Uranium (D&S)	²³⁴ U	1.26E+00	2.46E+05
	Uranium (D&S)	²³⁸ U	3.11E+03	4.47E+09
	Neptunium	²³⁷ Np	2.87E+00	2.14E+06
Class V	Plutonium	²³⁹ Pu	1.71E+01	2.41E+04
	Plutonium	²⁴⁰ Pu	1.50E+00	6.56E+03
Class VI ²	Pu-colloid			
<p>1 - Number of moles in source represents average of all tests conducted below or within 100 m of the water table on Western Pahute Mesa (Smith, 2001).</p> <p>2 - Based on simulations in Appendix F, we estimate about 1e-4 of the total Pu released from the MG and EV remain effectively irreversibly sorbed to colloids for transport of several kilometers in fractured material. This reduction factor depends on the kinetic rates of sorption and desorption, residence time in the aquifer, and competing sorption reaction coefficients for immobile material.</p>				

Table 7-2. Matrix *Kd* Sensitivity in cc/g for RN Classes (Classes I and VI have *Kd* = 0).

Rock Zone	Class II			Class III			Class IV			Class V		
	low	base	high	low	base	high	low	base	high	low	base	high
Z1-bedded	100	400	2000	10	100	1000	0	1	5	5	100	300
Z2-non-welded(nw)	100	400	2000	10	100	1000	0	1	5	5	100	300
Z3-welded	100	400	2000	10	100	1000	0	1	5	5	100	300
Z4-lava	100	400	2000	10	100	1000	0	1	5	5	100	300
Z5-altered	100	200	1000	500	1000	1000	0	7	20	50	100	400
Z6-frac nw	100	400	2000	10	100	1000	0	1	5	5	100	300
Z7-bedded-altered	100	200	1000	500	1000	1000	0	7	20	50	100	400

Note: In the deterministic flow and transport model, the TSA is a welded tuff (Z3), the LAVA is a lava (Z4), and the CHZCM is an altered tuff (Z5). Based on Table F-16, *Kd* values are derived from Yucca Mountain project database (see Appendix F).

Table 7-3. Fracture *Kd* Sensitivity in cc/g for RN Classes (Class I has *Kd* = 0).

Rock Zone	Class II			Class III			Class IV			Class V			Class VI		
	low	base	high	low	base	high	low	base	high	low	base	high	low	base	high
Z1-bedded	n/a	n/a	n/a	n/a	n/a	n/a	n/a	n/a	n/a	n/a	n/a	n/a	n/a	n/a	n/a
Z2-non-welded(nw)	n/a	n/a	n/a	n/a	n/a	n/a	n/a	n/a	n/a	n/a	n/a	n/a	n/a	n/a	n/a
Z3-welded	62	194	836	.01	.07	.23	.13	2.5	12.5	1.7	12.6	38	0	24	279
Z4-lava	162	206	230	.04	.05	.06	.35	1.7	3.9	8.2	9.3	12	0	24	279
Z5-altered	21	24	128	0.	0.	.01	.03	.43	1.5	0.	2.9	5.8	0	24	279
Z6-frac nw	191	222	264	.04	.05	.07	.43	1.7	4.5	7.4	8.6	14	0	24	279
Z7-bedded-altered	n/a	n/a	n/a	n/a	n/a	n/a	n/a	n/a	n/a	n/a	n/a	n/a	n/a	n/a	n/a

Note: particle-tracking calculations performed with fracture retardation factor $R = 1 + Kd$ for these values.
 Note: In the deterministic flow and transport model, the TSA is a welded tuff (Z3), the LAVA is a lava (Z4), and the CHZCM is an altered tuff (Z5). These values are computed from parameters in Tables F-15 and F-3 to account for carbonate complexation.

Table 7-4. Matrix Diffusion Coefficient Ranges

Rock Type	Small Molecules (Class I) (m ² /sec)			Large Molecules (Class II-V) (m ² /sec)		
	low	base	high	low	base	high
Z1-bedded	7.5e-11	1.21e-10	3.5e-10	4e-11	6.95e-11	1.3e-10
Z2-nonwelded (nw)	7.5e-11	1.21e-10	3.5e-10	4e-11	6.95e-11	1.3e-10
Z3-welded	3.5e-11	1.03e-10	3.e-10	3.2e-11	8.22e-11	2.7e-10
Z4-lava	8e-11	1.38e-10	2.3e-10	2.5e-11	8.92e-11	5e-10
Z5-altered	5.5e-11	9.02e-11	1e-10	5e-11	9.02e-11	1e-10
Z6-frac nw	7.5e-11	1.21e-10	3.5e-10	4e-11	6.95e-11	1.3e-10
Z7-bedded-altered	5.5e-11	9.02e-11	1e-10	5e-11	9.02e-11	1e-10

Note: In the deterministic flow and transport model, the TSA is a welded tuff (Z3), the LAVA is a lava (Z4), and the CHZCM is an altered tuff (Z5). These values are taken from Table F-17.

Table 7-5. Fracture Property Ranges

Rock Zone	Fracture Porosity			Fracture Aperture (m)		
	low	base	high	low	base	high
Z1-bedded	n/a	n/a	n/a	n/a	n/a	n/a
Z2-nonwelded(nw)	n/a	n/a	n/a	n/a	n/a	n/a
Z3-welded	7e-5	5e-4	3.5e-3	4e-5	2.7e-4	2.2e-3
Z4-lava	2.2e-4	2.1e-3	2e-2	5.3e-5	3.5e-4	2.1e-3
Z5-altered	1.1e-5	1.1e-4	1e-3	9e-5	2.6e-4	1.5e-3
Z6-frac nw	1.1e-5	1.1e-4	1e-3	9e-5	2.6e-4	1.5e-3
Z7-bedded-altered	n/a	n/a	n/a	n/a	n/a	n/a

Note: In the deterministic flow and transport model, the TSA is a welded tuff (Z3), the LAVA is a lava (Z4), and the CHZCM is an altered tuff (Z5). These values are taken from Tables F-19 and F-20.

7.6 Justification For Particle-Tracking Model

In the following sections, the particle-tracking model is used to simulate RN transport in both deterministic and heterogeneous representations of the hydrostratigraphy. In these sections, we compare the method with results obtained using the full reactive transport model described in Appendix F. This test problem involves comparing results for U transport in the heterogeneous flow field #3.

7.6.1 Review of the Reactive Transport Model Approach

With the reactive transport model, 225 pathlines are “excavated” from the three-dimensional flow field using non-diffusing, non-reactive particles. Preserving the flux within each tube, FEHM then simulates continuous reactive transport. Fracture-matrix interactions are solved with the Generalized Dual-Porosity Model (GDPM). The source function is modeled as a time-varying input flux to each individual stream tube. Mass flux at the exit location (the NTS boundary) is computed along each tube. The mass fluxes from each tube are added together to provide a cumulative mass flux at the NTS boundary.

7.6.2 Review of the Particle-Tracking Model Approach

With the particle-tracking approach, a swarm of 2500 particles are released instantaneously in the source region of the three-dimensional flow field. Diffusion and reactions to matrix and fracture minerals are modeled for each particle using the transfer function approach described in Appendix C. The breakthrough of all particles at the observation wells or across a control plane at the NTS boundary is tabulated and normalized to the number of particles. Such BTCs are computed for each RN class having different site-scale transport parameters. Then, the appropriate normalized BTCs are convolved with the time-varying source function for each different RN (they all have unique source curves due to unique initial mass and distribution) to generate a mass flux BTC for each RN.

7.6.3 Comparison of the Two Different Approaches.

These two site-scale modeling approaches differ significantly in how diffusion is modeled, how the time-varying source function is incorporated, and how continuity through the three-dimensional flow field is captured. However, converting the parameters used in the reactive transport model into the appropriate format for the particle-tracking algorithm leads to an excellent comparison. Although U reacts with fracture and matrix minerals as well as complexes with non-reactive species such as carbonate forms, the equilibrium chemistry can be written as effective Kds for the matrix and fracture minerals. Specifically, the effects of speciation are captured in lower Kds than were computed for the reactive cation form of U. The matrix and fracture Kds listed in Tables 7-2 and 7-3 incorporate these transformations.

Figure 7-3 illustrates the strong similarity in the results of the two different models using the same mass-flux input function. In this simulation, 2500 particles were used in the particle-tracking simulation and 225 streamlines were used in the reactive transport model. This process indicates that only 10-times more particles injected instantaneously are sufficient to capture the complexities of the dual-porosity transport processes simulated continuously along each streamline with the finite-element model.

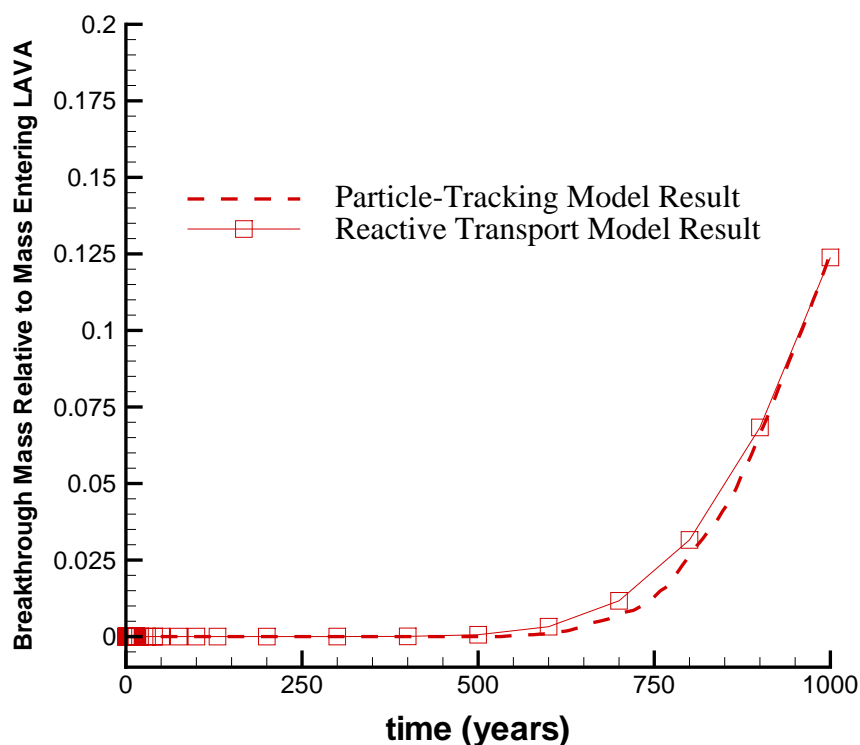


Figure 7-3. Comparison of reactive transport model with particle-tracking model. Curves show uranium breakthrough at NTS boundary using the two different approaches. Slightly more dispersion is seen in the finite-element reactive transport model as expected, but the results are extremely similar.

7.7 Transport Using the Deterministic HSU Model

7.7.1 Introduction

The calculations outlined in this section consider the deterministic hydrostratigraphy discussed in Chapter 5 (see Figure 5-3). The primary aquifers for RN migration away from BENHAM are the TSA and the LAVA unit of the CHZCM. The primary aquifer for TYBO releases is the TSA.

Using the particle-tracking model and the convolution integral for site-scale transport with transient source functions, RN migration to the ER-20-5 wells is simulated for sources at BENHAM and TYBO. The results from these simulations are compared with the field observations listed in Tables 1-1 and 1-2. Using the same method, transport sensitivity analyses are conducted for solute migration from BENHAM to the NTS boundary. The purpose of these runs is to highlight the transport parameters most sensitive to field-scale migration.

7.7.2 Base-Case Results

For a sense of particle-migration paths away from BENHAM in the deterministic flow model, Figures 5-11 and 5-12 show the particle pathways in the TSA and LAVA aquifers for unretarded transport parameters (e.g., no diffusion, dispersion, matrix Kd , or fracture retardation). Figure 7-4 shows the unit BTCs at the ER-20-5 wells for all six RN classes with base-case transport parameters originating from BENHAM with releases into the TSA and LAVA aquifers. These curves are the $f_{bnry}(t')$ terms in Equation 7-1 and are convolved with each of the different source functions to generate mass-flux curves at the wells.

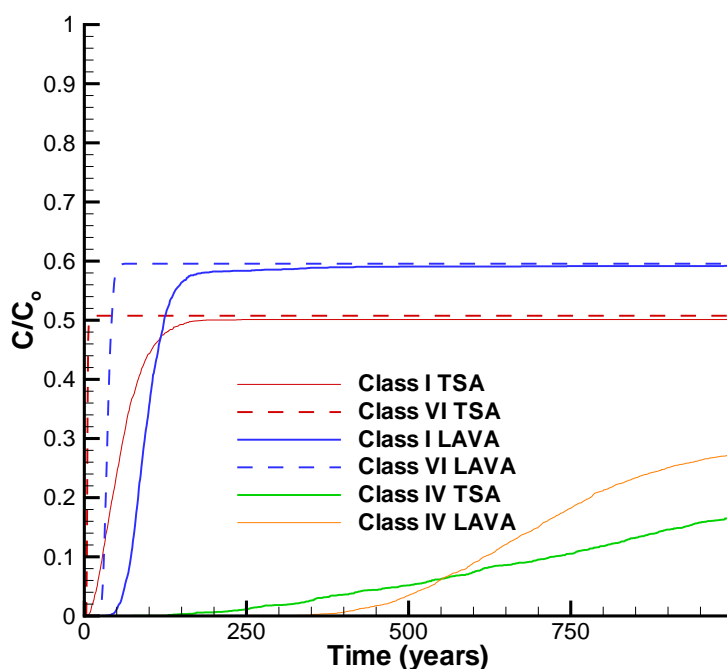


Figure 7-4. Unit breakthrough curves at the ER-20-5 wells (well #1 is in the TSA, #3 is in the LAVA) for the deterministic flow field and unit releases at BENHAM in the two aquifers. Note Class IV arrives at the wells after 50 years.

In these simulations, breakthrough occurs in the TSA earlier than in the LAVA because the TSA has higher permeability and lower fracture porosity. For base case parameters, the colloidal particles (Class VI) arrive first, retarded only by filtration (modeled here as fracture retardation). Class I solutes are slightly more retarded than Class VI solutes due to matrix diffusion. Experiencing minor sorption to fracture and matrix minerals, Class IV solutes appear later. All other classes (II, III, and V) do not appear in the ER-20-5 wells, nor do they cross the NTS boundary in either aquifer in less than 1000 years due to greater retardation.

7.7.3 Estimated Radionuclide Concentrations in Groundwater at the ER-20-5 Wells

Convolution of the unit BTCs captured at the ER-20-5 wells with the transient source functions yields mass fluxes for each RN considered (for this analysis, the BASE-CASE source from Table 6-9 is used; sensitivity to the source term is considered later). These mass fluxes are converted into groundwater concentrations by dividing the mass flux (moles/time) by the groundwater flux (l/time) to give the groundwater concentration (mole/l). To compare groundwater concentrations with the data tables in Chapter 1, the concentration for each RN considered is converted from moles per liter to picocuries per liter. In considering this flux-averaged approach for estimating groundwater concentrations, it is notable that an alternative (releasing particles at all times during the transient source release and then measuring particle concentrations in grid cells at times of interest) would not yield satisfactory results. In addition to requiring exceptionally large numbers of particles, such a process would require deciphering the resident aqueous concentration from the particles, which represent mass in fracture water, sorbed onto fracture minerals, diffused into matrix porewater, and sorbed onto matrix minerals; this process is not readily amenable to post-processing. Errors and uncertainty associated with the flux-averaged concentration estimate used here involve the size of the capture zone considered. Developed after these calculations were performed, a new method (Robinson, 2002) implements the flux-averaged concentration estimates within FEHM on a cell-by-cell basis, eliminating the need to estimate the size of the capture zone for *in situ* concentration estimates.

Pu-Colloid

The Pu-colloid species in the particle-tracking model is estimated to represent of $1e-4$ of the total Pu released from the MG and EV. The basis for this estimate comes from site-scale simulations conducted with the reactive process model (Appendix F). In these simulations, aqueous Pu is brought into contact with colloids and reactive immobile minerals. Of the initial mass entering the site-scale domain, approximately $1e-4$ of that mass migrates more than a kilometer. The rest sorbs to immobile minerals in the fracture coatings and matrix material. This fraction is a function of the sorption and desorption kinetics of Pu onto colloids, residence time in the aquifer, and sorption coefficients of the immobile minerals.

Resulting from colloid-facilitated Pu transport, Pu concentrations at both ER-20-5 wells are estimated following the particle tracking and convolution procedure (note: no Pu arrives at the wells as an aqueous species). The BENHAM source is considered first, followed by TYBO. Figure 7-5 shows the field observations compared with simulated concentrations using the BENHAM source. Because the source term is based upon unclassified information, the most important aspect in this figure is that the simulated time of transport from BENHAM to the observation wells is consistent with the data. For these simulations, only the retardation factor for the Pu-colloids was modified. Namely, the retardation in the LAVA was reduced well within the range of uncertainty (see Table 7-3) to increase the arrival times at ER-20-5 #3. It is also quite interesting that the simulated concentrations agree so well with the measurements. This implies that, within the uncertainty of the actual source inventory, these estimates involving both a non-isothermal transient source release function and site-scale transport in fractured rock provide reasonable matches with field observations.

We next consider source releases originating at TYBO. As described in Chapter 6, the TYBO transient source release to the TSA abstraction is simply equal to the sum of the simulated

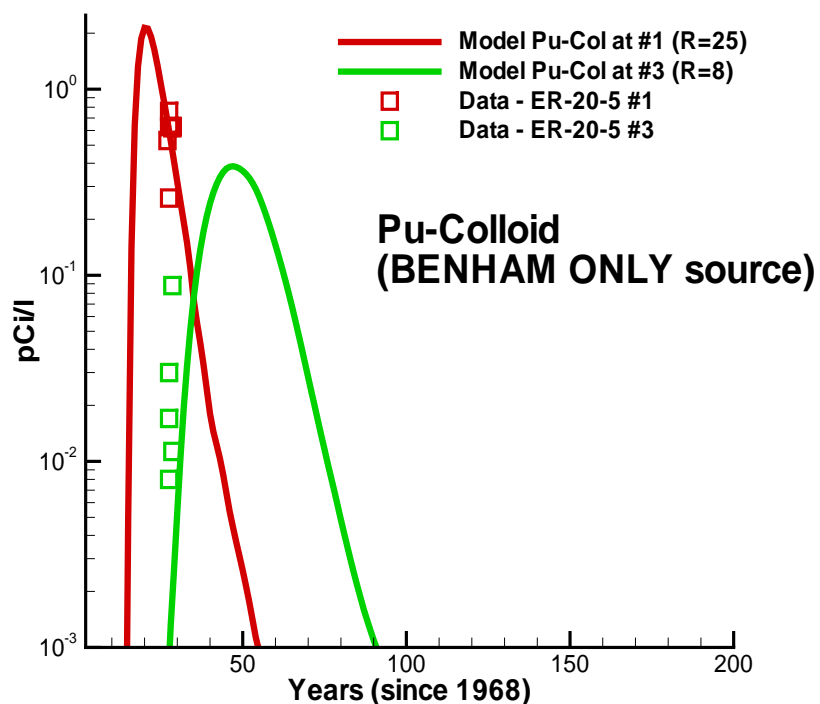


Figure 7-5. Simulated and observed Pu-colloid concentrations at ER-20-5 wells. The simulations use the BASE-CASE BENHAM source described in Chapter 6. Retardation factors for colloids in fractures are listed in parentheses. Note that no Pu arrives at the wells as an aqueous species in these simulations.

BENHAM releases to the TSA and LAVA at each time step. With no lateral dispersion on the particles leaving TYBO, the plume does not intersect the ER-20-5 #1 (See Figure 7-6). Such intersection does occur when transport from TYBO is simulated, with the dispersion described in Chapter 5 (3 m lateral dispersion) and a large capture zone at the ER-20-5 wells to account for the large volumes of water pumped during production. For such conditions, Pu-colloid mass is simulated to arrive at ER-20-5 #1, but not at ER-20-5 #3. Figure 7-7 shows the simulated Pu arrivals from TYBO, in addition to those from BENHAM for this case. With the assumptions associated with these calculations (large lateral dispersion and large capture zone for ER-20-5 wells), TYBO contributions are just as feasible as those from BENHAM in ER-20-5 #1.

Such results are inconsistent with the Pu fingerprinting of Kersting et al. (1999). Thus, TYBO could be discounted as a possible source for RN observations at ER-20-5 #1. Because migration of the other RNs discussed in the following section is governed by processes other than those for colloids, the possible contributions from TYBO for the case involving large lateral dispersion and a large capture zone at ER-20-5 #1 are presented along with the results for the BENHAM source.

Class I Radionuclides

In addition to Pu, several RNs from Classes I, II, and III were found in the ER-20-5 wells (see Tables 1-1 and 1-2). The Class I RNs migrate as non-reactive solutes that are affected by fluid

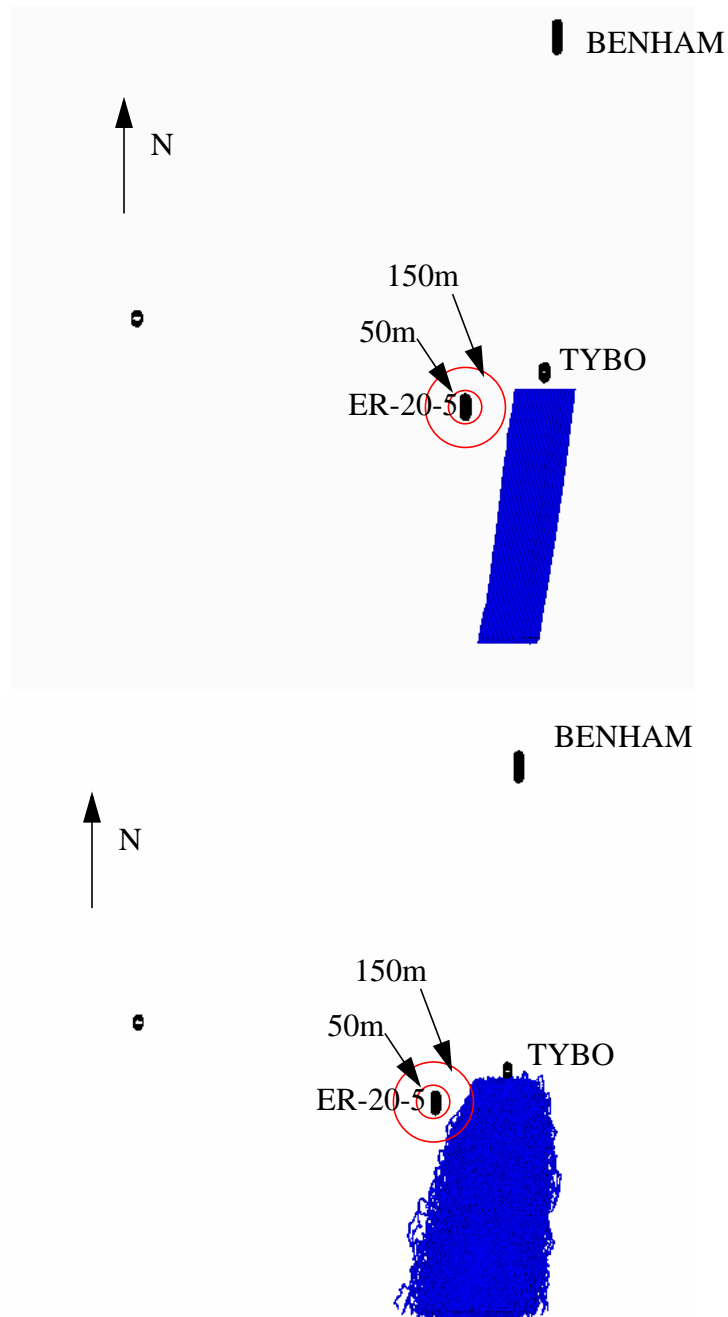


Figure 7-6. Structure of plumes originating from TYBO in the deterministic flow model. The upper plot shows plume shape for case of no dispersion. The lower plot shows same simulation, but with a lateral dispersivity of 3 m. Capture zone radii of 50 m and 150 m for ER-20-5 #1 are also shown.

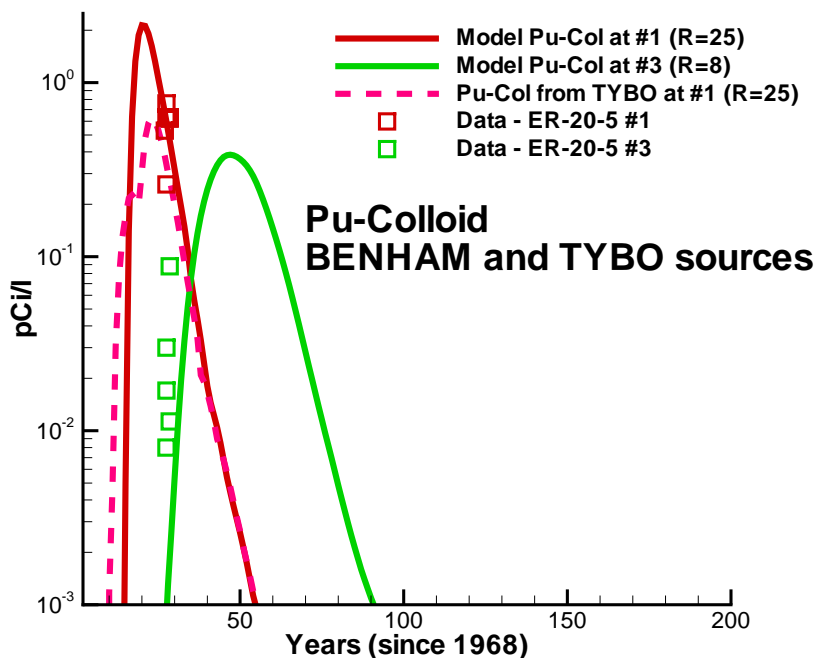


Figure 7-7. Simulated and observed **Pu-colloid** concentrations at ER-20-5 wells. The simulations use the BASE-CASE BENHAM and TYBO sources described in Chapter 6. Transport from TYBO is subject to dispersivity and capture-zone size constraints discussed in this report. Retardation factors for colloids in fractures are listed in parentheses.

velocities in the fractures and matrix diffusion. Simulations using the BASE-CASE source and the base-case site-scale transport parameters presented earlier in this chapter are compared with the field observations for ^3H , ^{14}C , ^{36}Cl , ^{99}Tc , and ^{129}I (Figures 7-8 through 7-12). First, for all five RNs, the travel times from BENHAM to the observations wells are consistent with the non-background observations in BOTH wells. This feature indicates that the site-scale flow field and transport parameters provide a reasonable representation of the governing processes in the system. Further, for each RN, the simulated and observed concentrations are remarkably close, considering that the source is for an average unclassified mass of each RN not specific to BENHAM. In some cases, the model overpredicts the observations and in some cases it underpredicts them.

For each RN, the simulated concentrations at ER-20-5 #1 (resulting from a TYBO source) are plotted with the constraints listed above. These simulations show that the travel time from TYBO is also consistent with the field data and that the concentrations are reasonable, considering that the source term is an unclassified average. If classified source models were developed for the BENHAM- and TYBO-specific RN inventories, they could be convolved readily with these site-scale transport simulations for a more detailed analysis. Such analysis may serve to shed light on the suggestion that all RNs found in ER-20-5 #1 originated exclusively at BENHAM.

Differences between simulated and observed concentrations for tritium may also be attributed to our implementation of Smith's (2001) inventory. In the source term simulations of Chapter 6, the initial masses were not decay corrected from the 1994 average values back to 1968

for BENHAM or 1975 for TYBO. Not doing so was originally justified because this unclassified source term is not specifically representative of BENHAM or TYBO. In retrospect, such correction would have led to even better concentration matches of the short-lived tritium, increasing the source mass by nearly a factor of 4. There would have been no difference for the other Class I RNs because of their long half-lives.

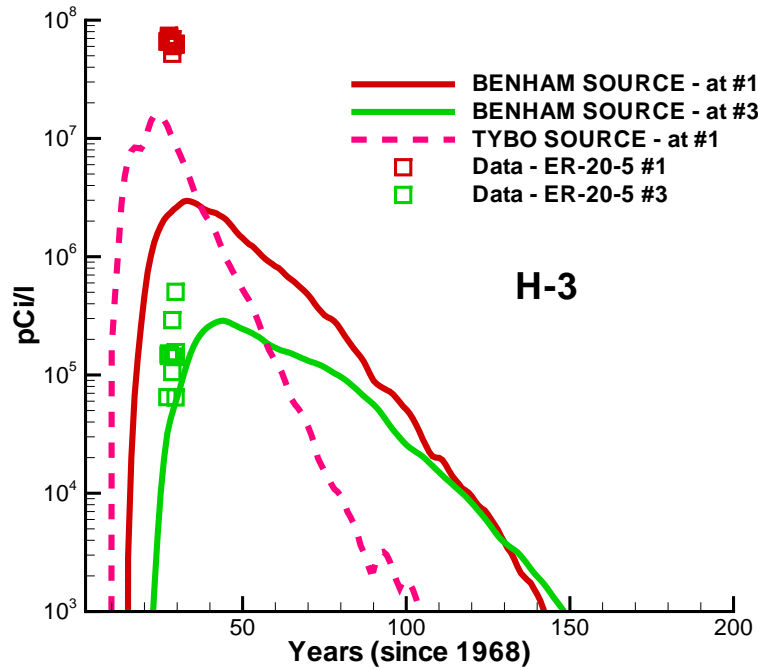


Figure 7-8. Simulated and observed **tritium** concentrations at ER-20-5 wells for BASE-CASE source and transport parameters.

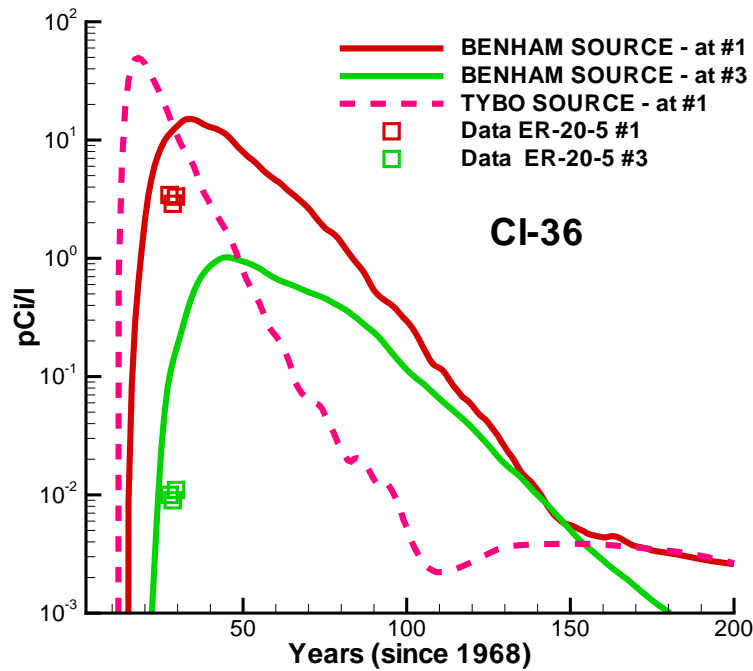


Figure 7-9. Simulated and observed **chlorine-36** concentrations at ER-20-5 wells for BASE-CASE source and transport parameters.

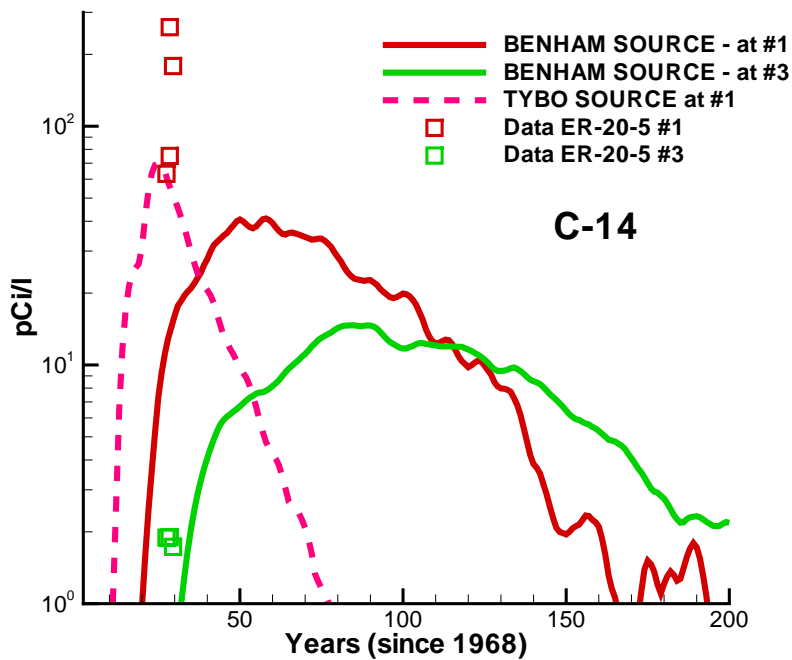


Figure 7-10. Simulated and observed **carbon-14** concentrations at ER-20-5 wells for BASE-CASE source and transport parameters.

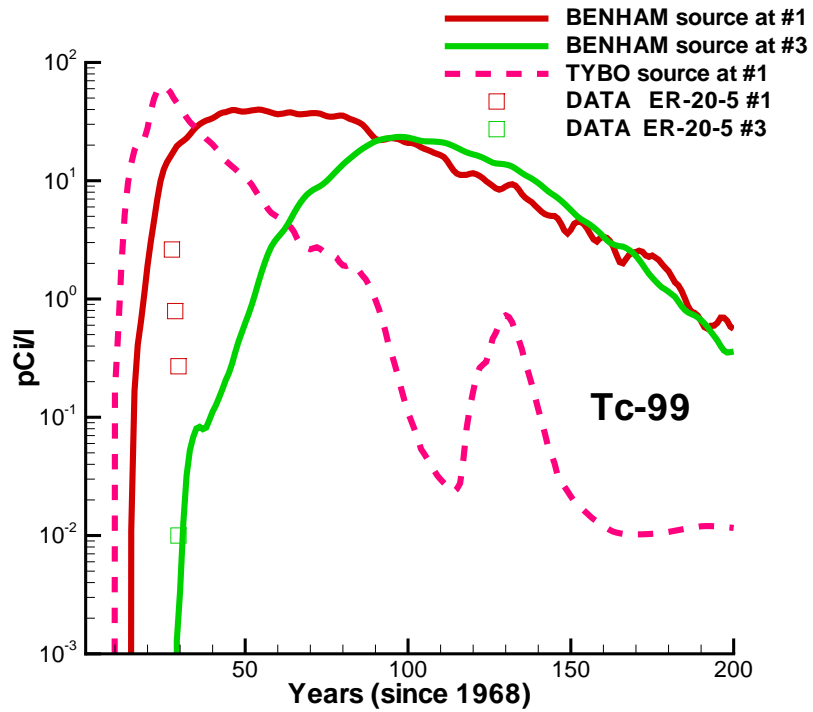


Figure 7-11. Simulated and observed **technetium-99** concentrations at ER-20-5 wells for BASE-CASE source and transport parameters.

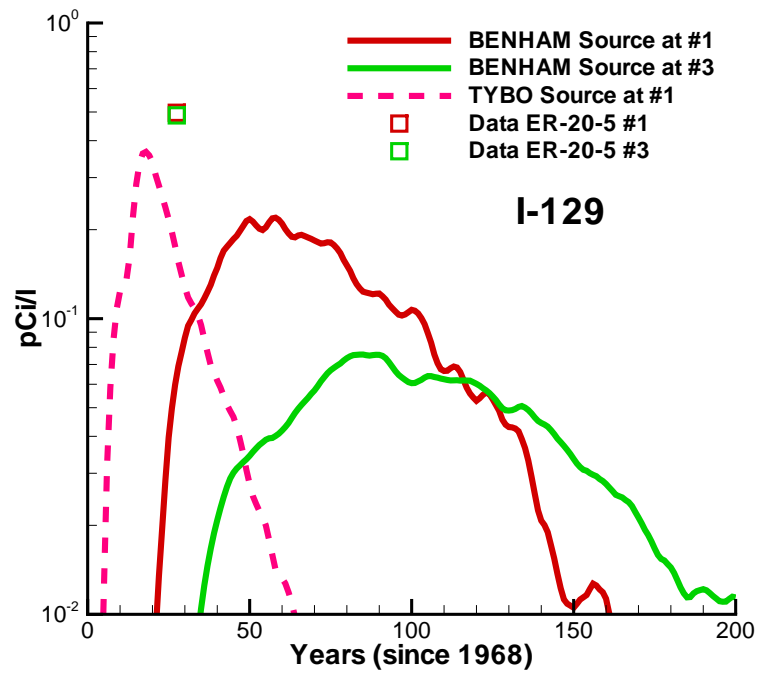


Figure 7-12. Simulated and observed **iodine-129** concentrations at ER-20-5 wells for BASE-CASE source and transport parameters. Note, data for ER-20-5 #1 from Table 1-1 is below the detection limit for that measurement. It is plotted here to show date of non-zero detect.

Class II and III Radionuclides

Class II and III RNs found in the ER-20-5 wells include Cs, Eu, and Am. In the absence of colloids, none of these species are simulated to migrate from BENHAM to the ER-20-5 wells in less than 1000 years. Of these species, Cs has the smallest matrix and fracture retardation factors and its migration as an aqueous species from TYBO to ER-20-5 #1 is simulated for the conditions of large dispersivity and a large capture zone at ER-20-5 #1, as discussed earlier. Figure 7-13 shows the aqueous species Cs concentrations at ER-20-5 #1 for the base-case matrix Kd of 100 (cc/g) and the minimum value of 10 (cc/g). For this model, the distance between the TYBO chimney and the ER-20-5 #1 capture zone is very small; such Kds do not completely preclude aqueous transport. On the other hand, Class II RNs are almost completely immobile as aqueous species because the fracture retardation factors are so large.

Because the Pu found in the ER-20-5 wells was characterized as being associated with colloidal material, Kersting et al. (1998a,b) note that the Cs and Eu found in those wells were associated with both colloids and particulates. These highly reactive species would likely sorb to colloidal material just as they sorb to immobile minerals. Because they are not simulated to migrate as aqueous species from BENHAM to the observation wells (although they were found there) further implicates colloid-facilitated transport mechanisms. Therefore, a suite of simulations were conducted in which colloid-facilitated transport of these three species is considered. For each case, the colloid unit BTCs used in the Pu simulations described earlier are convolved with modified source releases for Cs, Eu, and Am. The modification is simply a reduction factor applied to the BASE-CASE source release functions for these species (described in Chapter 6). This reduction factor, similar to the one for Pu-colloid, ranges between $1e-4$ and $1e-5$ to achieve the fits (in simulated peak height to match the data) shown in Figures 7-14 through 7-16. However, because the source function is based on an unclassified average mass, matching such concentrations is only a qualitative confirmation that the processes of flow and transport are properly represented in this model.

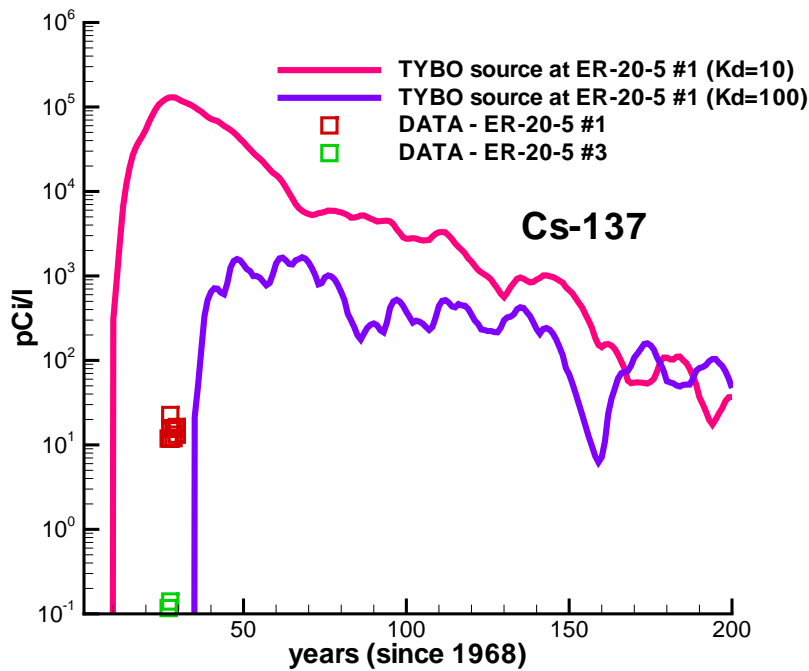


Figure 7-13. Simulated and observed **aqueous cesium-137** concentrations at ER-20-5 wells for BASE-CASE source and transport parameters. No arrivals from BENHAM simulated.

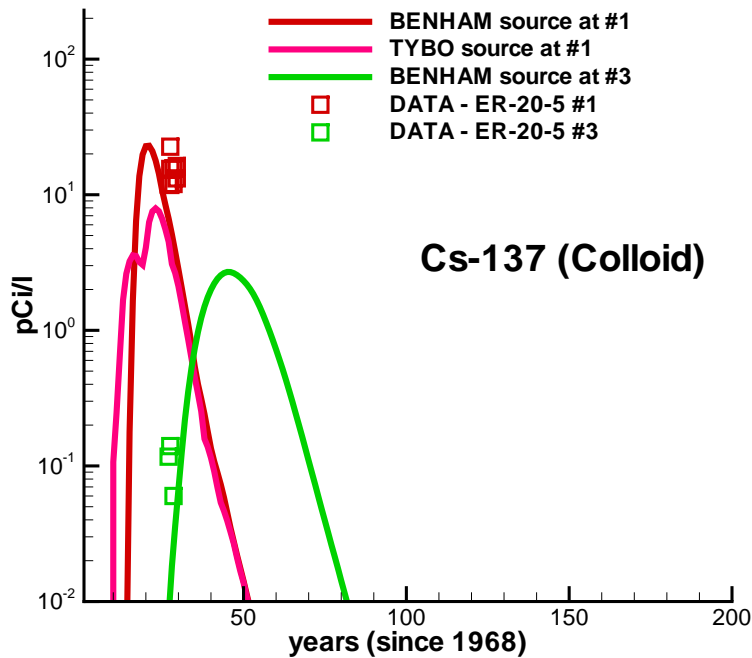


Figure 7-14. Simulated and observed **colloidal cesium-137** concentrations at ER-20-5 wells for BASE-CASE source and transport parameters (source reduction factor 1e-5).

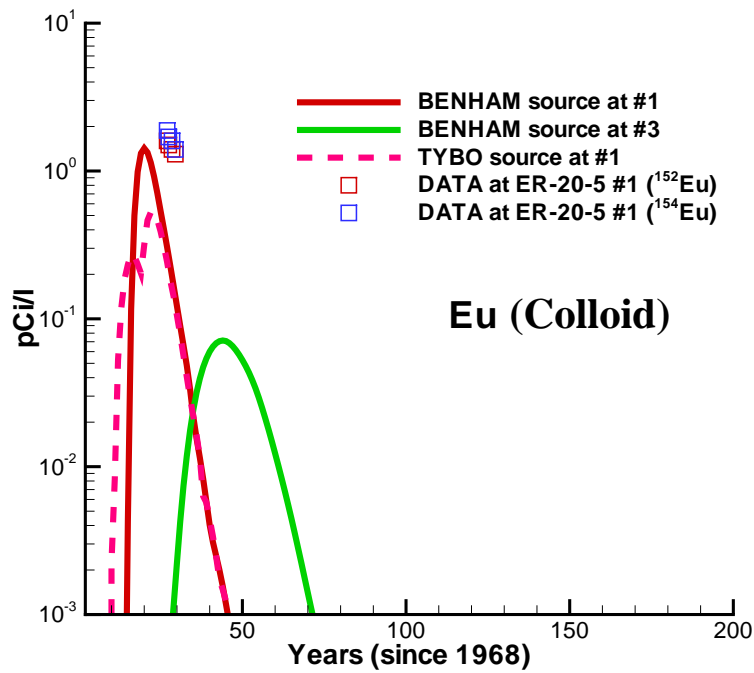


Figure 7-15. Simulated and observed **colloidal europium** concentrations at ER-20-5 wells for BASE-CASE source and transport parameters (source reduction factor 1e-4).

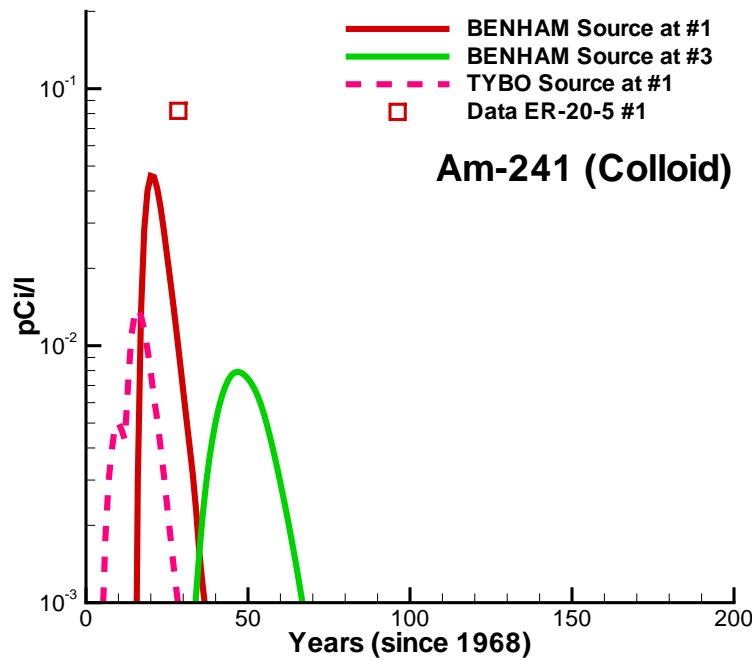


Figure 7-16. Simulated and observed **colloidal americium-241** concentrations at ER-20-5 wells for BASE-CASE source and transport parameters (source reduction factor 1e-5).

7.7.4 Parameter Sensitivity: Downstream Mass Flux Curves

The previous section examined RN migration to the ER-20-5 wells using the BASE-CASE source model and base-case site-scale transport parameters. The results show good consistency between the models and the field observations. However, the parameters are uncertain. Therefore, this section examines model sensitivity to the transport parameters. The parameter sensitivity study is conducted for simulations from BENHAM to the NTS boundary to develop a broader sense of such sensitivity and avoid issues such as those associated with the exact size of the capture zone and flow-model boundary conditions.

Computed with base-case parameters and perturbations taking each parameter in Tables 7-2 through 7-5 individually to its minimum and maximum, unit mass BTCs are convolved with the different source functions from Chapter 6 to generate cumulative mass BTCs at the NTS boundary. In the sensitivity study, the six sources described in Section 7.4 are considered with each transport parameter perturbation. Thus, a total of six different sources are considered for reactive RNs (Classes II-V) and three different sources are considered for non-reactive solutes from Class I and VI. Our BASE-CASE source involves the highest $R_{a_{sys}}$ and no chimney sorption, hence it yields the most mass to the aquifers of all sources considered.

The parameter sensitivity presented for the deterministic flow field is somewhat qualitative. In this case, figures showing the sensitivity to the various parameters are presented. In addition, a detailed quantitative assessment is saved until the next section in which multiple heterogeneous fields are considered, as well as all the source and parameter uncertainty ranges.

Class I Radionuclides

Figures 7-17 through 7-23 demonstrate the model's sensitivity to various inputs for Class I RNs. In each figure, results using the base-case transport parameters are plotted along with BTCs associated with individual parameter perturbations to the minimum and maximum value in the range of uncertainty. Figures 7-17 and 7-18 show the cumulative mass breakthrough at the NTS boundary for ^{36}Cl with the different sources in the TSA and LAVA. Although the TSA source starts approximately 10 years after the LAVA source due to convection and rising in the chimney (Figure 6-33), arrivals at the NTS boundary in the TSA are much sooner than in the LAVA due to higher velocities (see Figure 7-4). Figure 7-19 shows the combined mass breakthrough for ^{36}Cl at the NTS boundary for both sources. Similarly, Figures 7-20 and 7-21 show the cumulative mass arrival at the NTS boundary for ^3H and ^{14}C . All Class I nuclide sensitivities show that with increased aperture, arrivals are sooner because less diffusion occurs relative to the mass of solute remaining in the fracture. Similarly, arrivals are earlier when fracture porosity is decreased because velocities are larger. As was found in the data recorded in Appendix F, there is not substantial sensitivity to the diffusion coefficient for these non-reactive solutes, primarily because the range of uncertainty considered in Table 7-4 is relatively tight. The ^3H plot has a different form than the ^{36}Cl and ^{14}C due to the short half-life of tritium. For high-aperture and low-porosity cases, tritium breaks through before substantial decay has occurred. The behavior highlights the important sensitivity to fracture aperture and porosity relative to the other parameters. Decay is considered during transport, but the mass that has broken through the location of interest is not further decayed after breakthrough. This method enables a demonstration of the cumulative mass actually arriving at a location of concern.

When less convective cavity/chimney systems are considered, the relationship between the source function and the BTC at the NTS boundary is somewhat complex. The discussion for ^{36}Cl holds for all Class I RNs. The three source conditions are shown in Figures 6-42, 6-45, and 6-48, each with a decreasing Rayleigh number. Decreasing the Rayleigh number to the medium case leads to increased ^{36}Cl fluxes to the LAVA and decreased, as well as substantially delayed, fluxes to the TSA. Comparing Figures 7-22 and Figure 7-19, we determine that with a medium Rayleigh Number source, reduced convection to the TSA eliminates the very early breakthrough of ^{36}Cl at the NTS boundary, but the total mass from the LAVA is slightly higher due to the increase in mass flux at the source location. With an even lower Rayleigh number, there is no source input to the TSA and the LAVA source is decreased and delayed. Comparing Figures 7-23 and Figure 7-19, we see the delays and decreases manifested in later breakthrough times of ^{36}Cl at the NTS boundary. The general conclusions about model sensitivity to diffusion, aperture, and fracture porosity are the same, regardless of which source is considered.

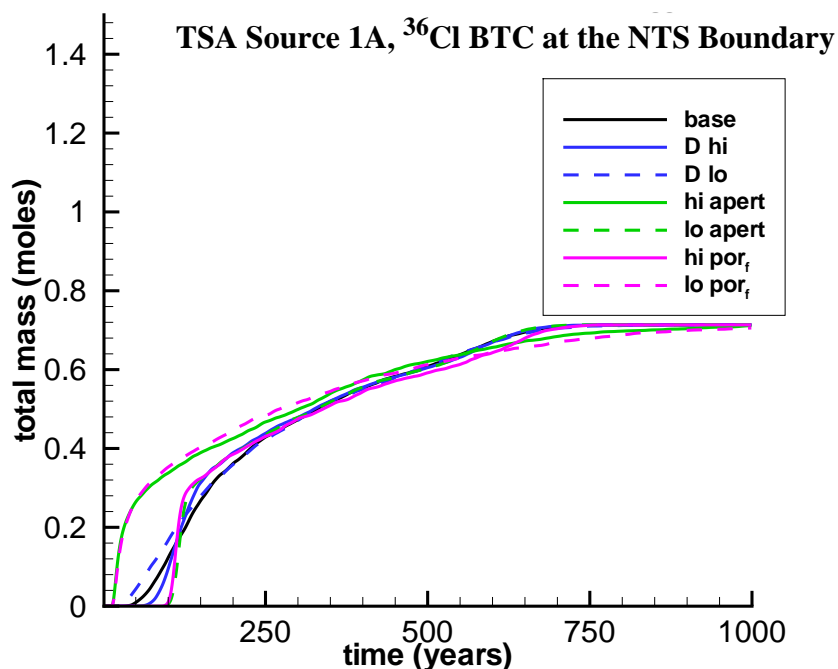


Figure 7-17. Chlorine-36 mass breakthrough at the NTS boundary for the BASE-CASE TSA source release.

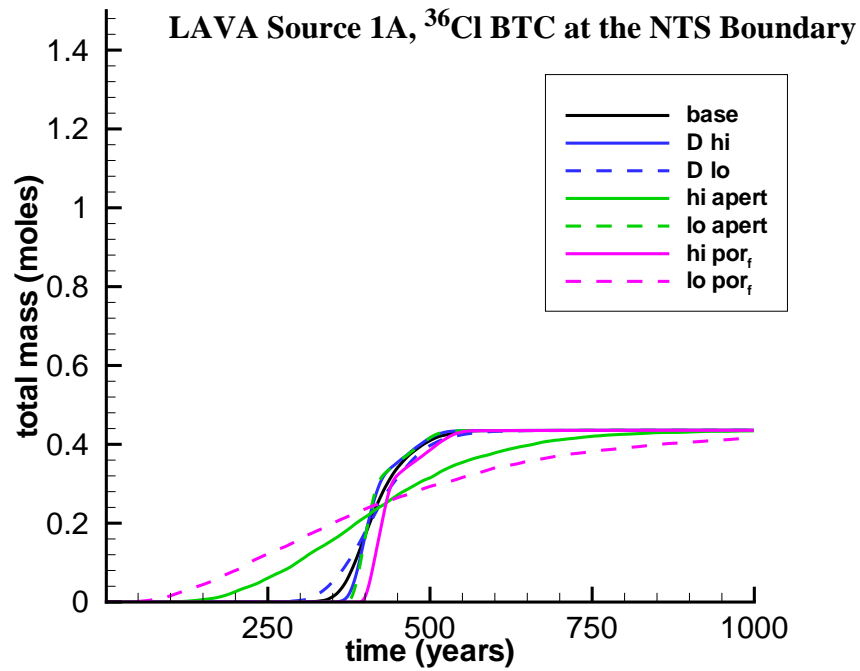


Figure 7-18. Chlorine-36 mass breakthrough at the NTS boundary for the BASE-CASE LAVA source release.

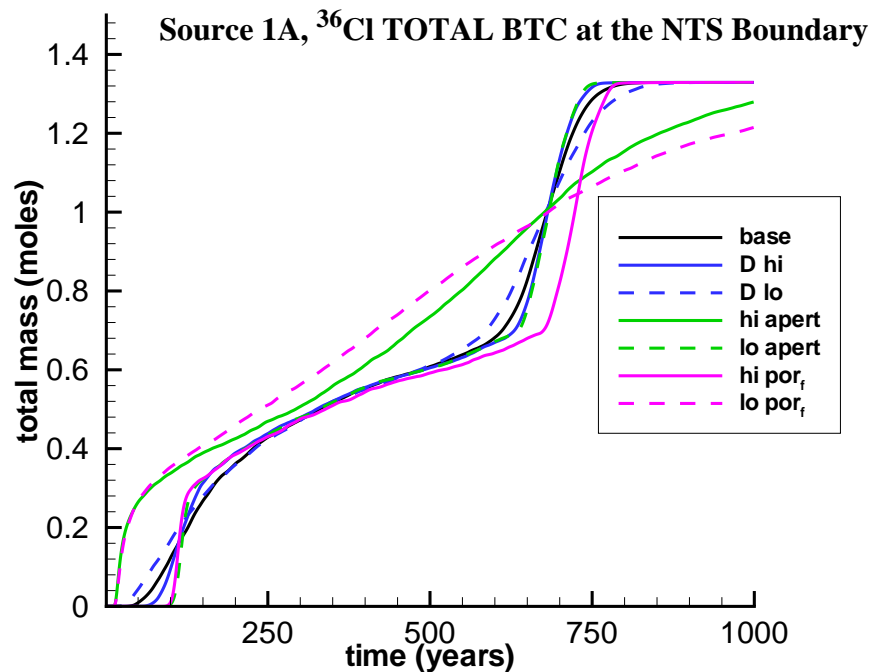


Figure 7-19. Total chlorine-36 mass breakthrough at the NTS boundary for the BASE-CASE TSA and LAVA source releases.

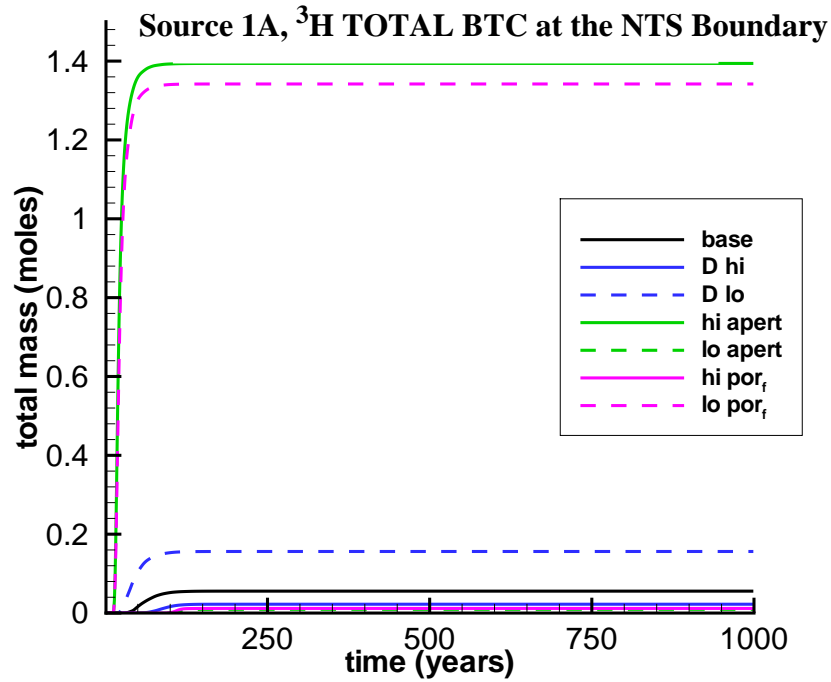


Figure 7-20. Total tritium mass breakthrough at the NTS boundary for the BASE-CASE TSA and LAVA source releases.

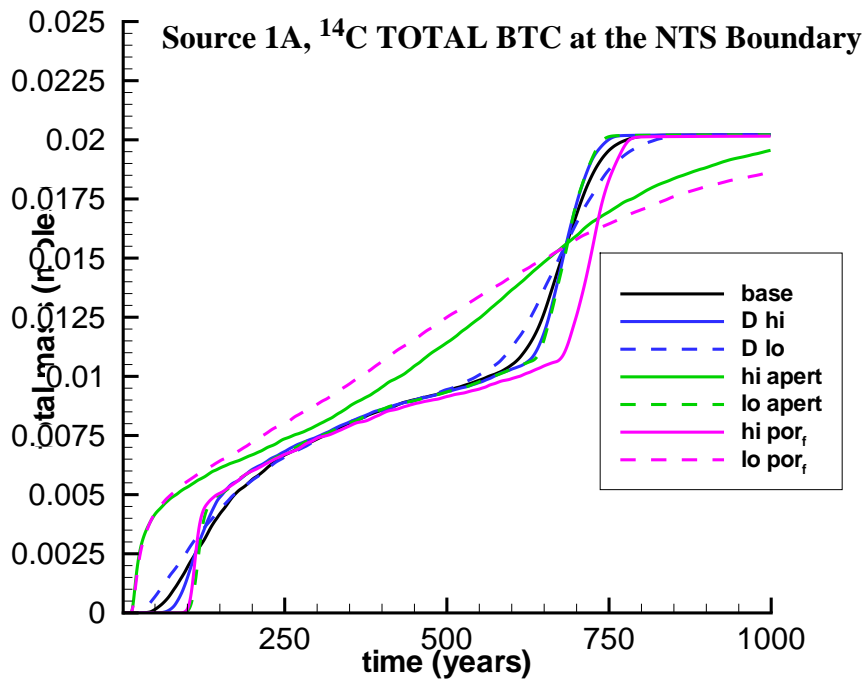


Figure 7-21. Total carbon-14 mass breakthrough at the NTS boundary for the BASE-CASE TSA and LAVA source releases.

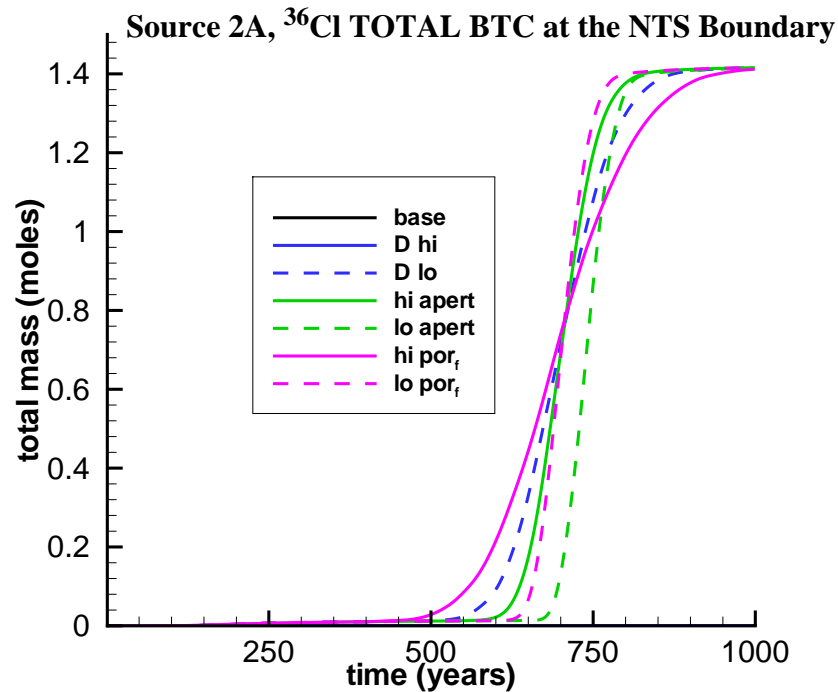


Figure 7-22. Total chlorine-36 mass breakthrough at the NTS boundary for the **medium Rayleigh** number TSA and LAVA source releases (Table 6-9: Case 2B).

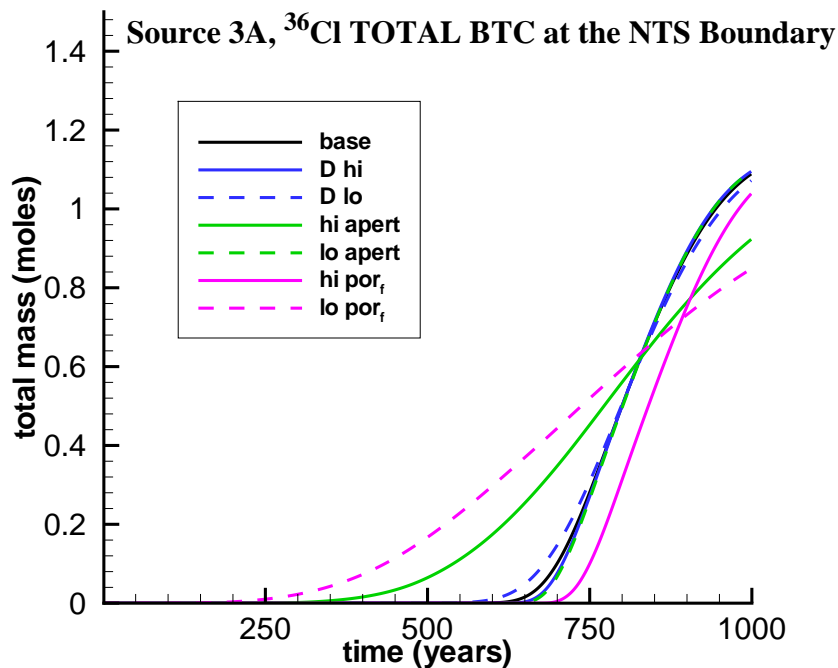


Figure 7-23. Total chlorine-36 mass breakthrough at the NTS boundary for the **low Rayleigh** number TSA and LAVA source releases (Table 6-9: Case 3A).

Class II, III, and V Radionuclides

In the absence of colloids, aqueous species of Class II and III RNs (Am, Sm, Cs, Sr, and Eu) and class V RNs (Pu) do not break through to the NTS boundary under any transport or source-term conditions considered in this study. Colloid-facilitated RN transport is considered following the discussion of Class IV RNs next.

Class IV Radionuclides

The Class IV RNs (U and Np) are the most mobile of the reactive solutes because of their low-matrix Kd and surface complexation constants for fracture minerals. For these solutes, processes considered include matrix sorption, fracture mineral sorption, and sorbing and non-sorbing chimney-source conditions, as are parameters considered for Class I nuclides, which were discussed in the previous section.

Because U and Np exhibit long half-lives and are of the same RN class (IV), they possess similar breakthrough characteristics, with the primary exception being that they have different source masses. Therefore, U is used to demonstrate the model sensitivity. Just as with ^{36}Cl , there are TSA and LAVA contributions to the mass breakthrough at the NTS boundary (as shown in Figures 7-24 and 7-25). The cumulative mass breakthrough of U and Np is shown in Figures 7-26 and 7-27. With base-case transport parameters, the retardation associated with migration in fractured media for these RNs prevents any mass arrival at the NTS boundary in the LAVA, and only a small amount arrives in the TSA. When the matrix Kd is relaxed, some mass arrives at the NTS boundary in the LAVA. Changing parameters from their base-case values, within the ranges of uncertainty specified earlier, the following items are ordered by their impact on increasing Class IV nuclide arrivals at the NTS boundary in the TSA for Source 1A:

1. reducing the matrix Kd
2. increasing the fracture aperture
3. reducing the fracture porosity
4. reducing the matrix diffusion coefficient

Thus, processes that prevent the interaction of reactive solutes with matrix minerals have the greatest impact in increasing Class IV RN mobility. Conversely, changing these parameters to increase solute-matrix interactions reduces the mobility of Class IV RNs resulting in no mass breakthrough at the NTS boundary. Note that variation in the fracture Kd is defined only by the mineralogic composition, not the reactive surface area. Appendix F addresses the great sensitivity to fracture mineral reactive surface area.

As with Class I RNs, different source functions found in Chapter 6 (Table 6-9) are considered. In addition to three different convective systems defined by their Rayleigh numbers, source releases computed with sorption and no-sorption of Class IV RNs to chimney material are considered. Reducing the BASE-CASE source from high to medium Rayleigh number leads to reduced and delayed Class IV input to the TSA aquifer (Figure 6-46). Because of this, Figure 7-28 shows that no U arrives at the NTS boundary, except for the case when matrix Kd is lowered. Figure 7-29 shows that such arrivals are reduced even more when the Rayleigh number is reduced to its lowest value.

When sorption of Class IV RNs to chimney material is considered, the total mass breakthrough to the NTS boundary is reduced. Interestingly, Figure 7-30 shows that for high Rayleigh number conditions and chimney sorption, the mass fluxes at the NTS boundary are reduced. However, sorption in the chimney alone does not eliminate mass breakthrough for any parameter sets (Figure 7-26). This is primarily due to the relatively low sorption K_d s used for Class IV RNs in the chimney (as described in Chapter 6). For lower Rayleigh numbers and chimney sorption, the trend described above is simply enhanced (as shown in Figures 7-31 and 7-32).

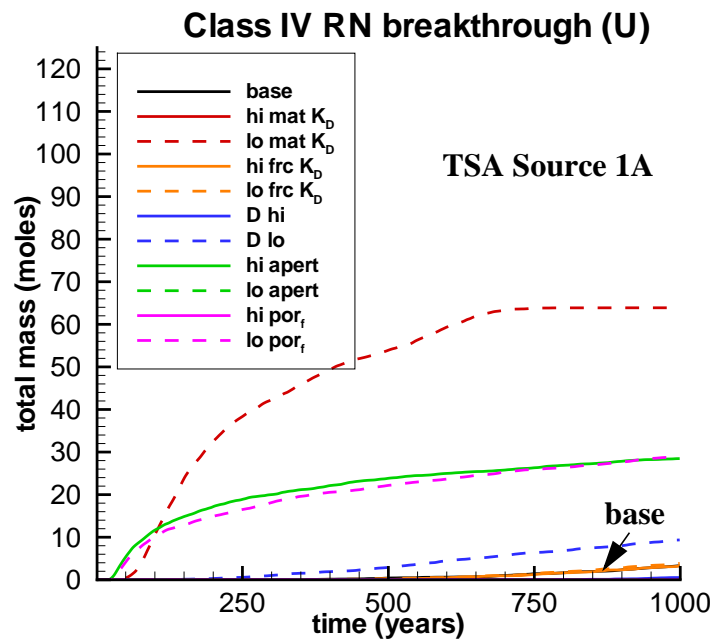


Figure 7-24. Uranium mass breakthrough at the NTS boundary for the TSA source release involving no chimney sorption and high Ra_{sys} (Case 1, no sorption; Table 6-9).

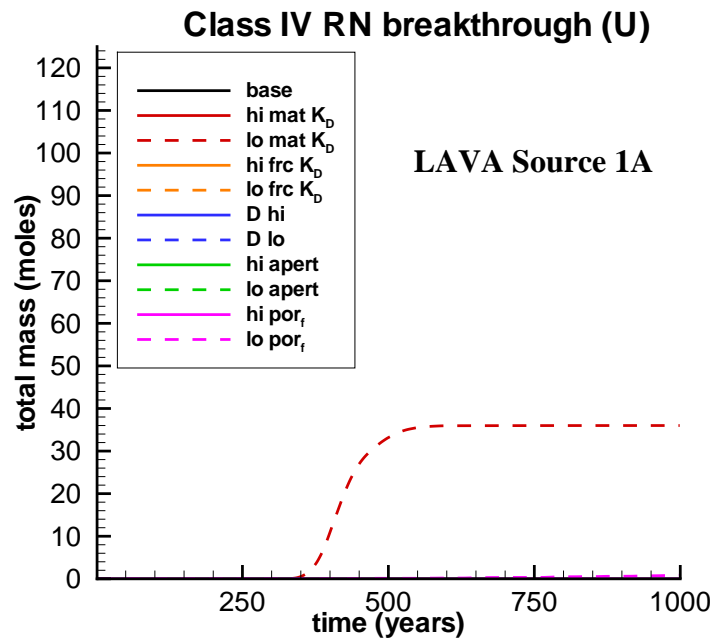


Figure 7-25. Uranium mass breakthrough at the NTS boundary for the **LAVA source** release involving no chimney sorption and high Ra_{sys} (Source 1a, no sorption; Table 6-9).

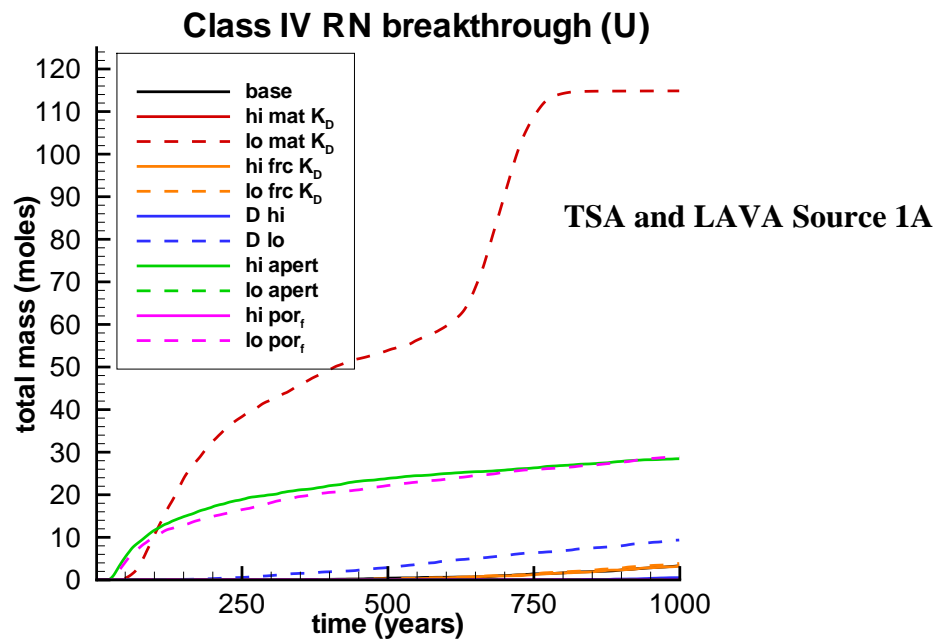


Figure 7-26. Total uranium mass breakthrough at the NTS boundary for the combined **TSA and LAVA source release** involving no chimney sorption and high Ra_{sys} (Source 1a, no sorption; Table 6-9).

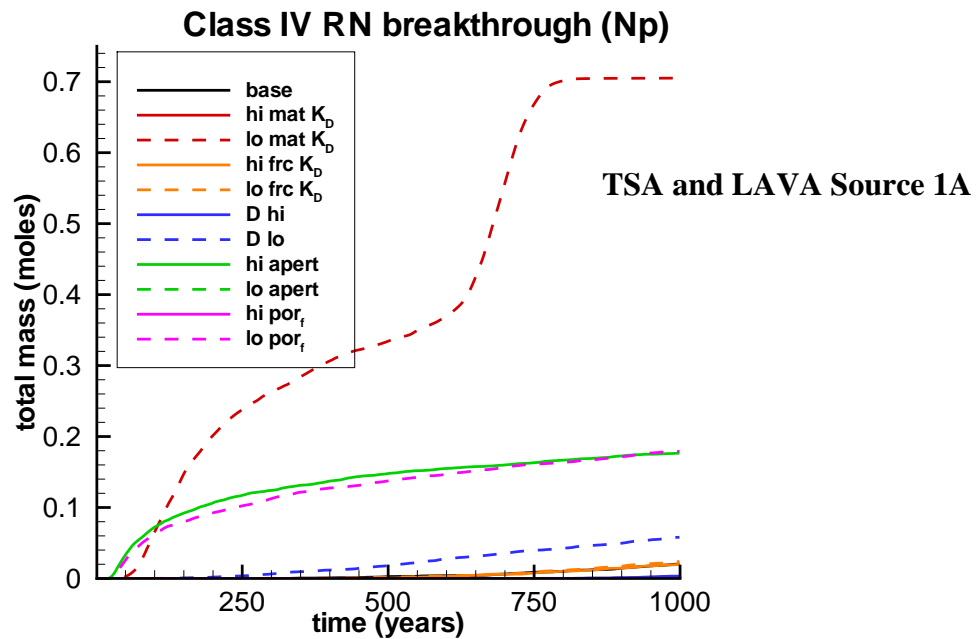


Figure 7-27. Total neptunium mass breakthrough at the NTS boundary for the combined TSA and LAVA source release involving no chimney sorption and high Ra_{sys} (Source 1a, no sorption; Table 6-9).

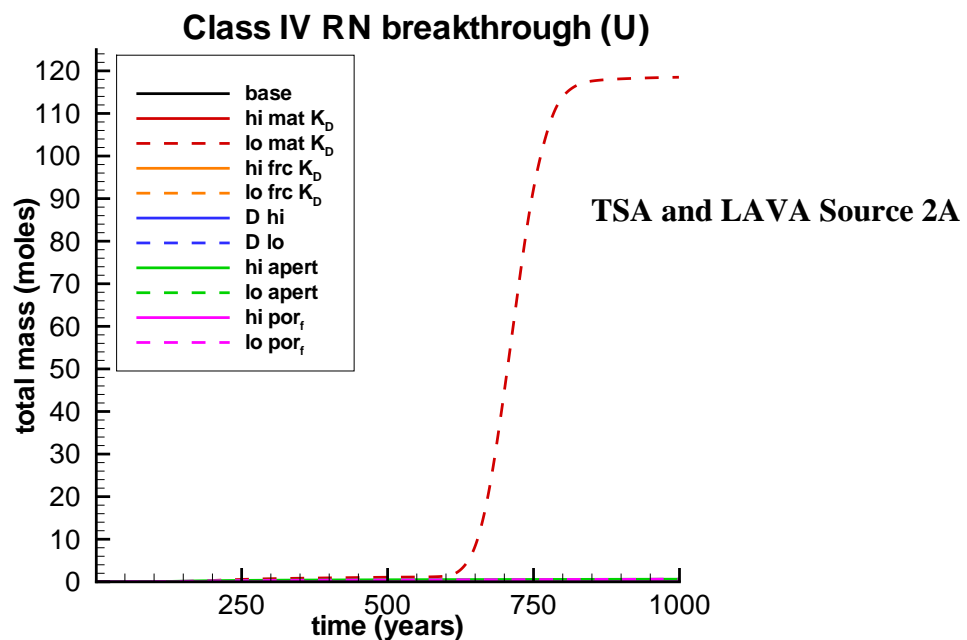


Figure 7-28. Total uranium mass breakthrough at the NTS boundary for the combined TSA and LAVA source release involving no chimney sorption and medium Ra_{sys} (Source 2a, no sorption; Table 6-9).

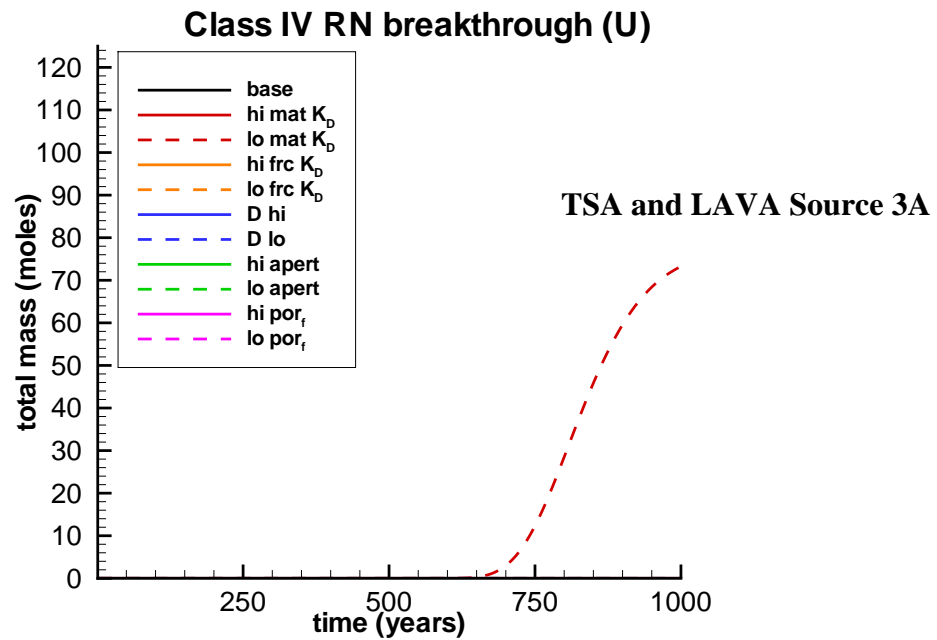


Figure 7-29. Total **uranium** mass breakthrough at the NTS boundary for the combined TSA and LAVA source release involving no chimney sorption and **low** Ra_{sys} (Source 3a, **no sorption**; Table 6-9).

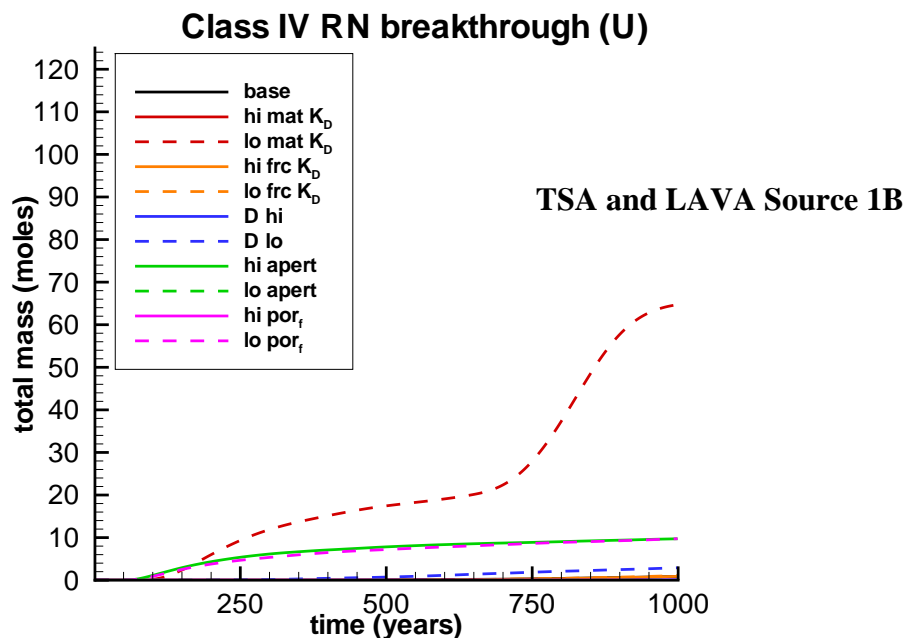


Figure 7-30. Total **uranium** mass breakthrough at the NTS boundary for the combined TSA and LAVA source release involving **chimney sorption** and **high** Ra_{sys} (Source 1b, with sorption; Table 6-9).

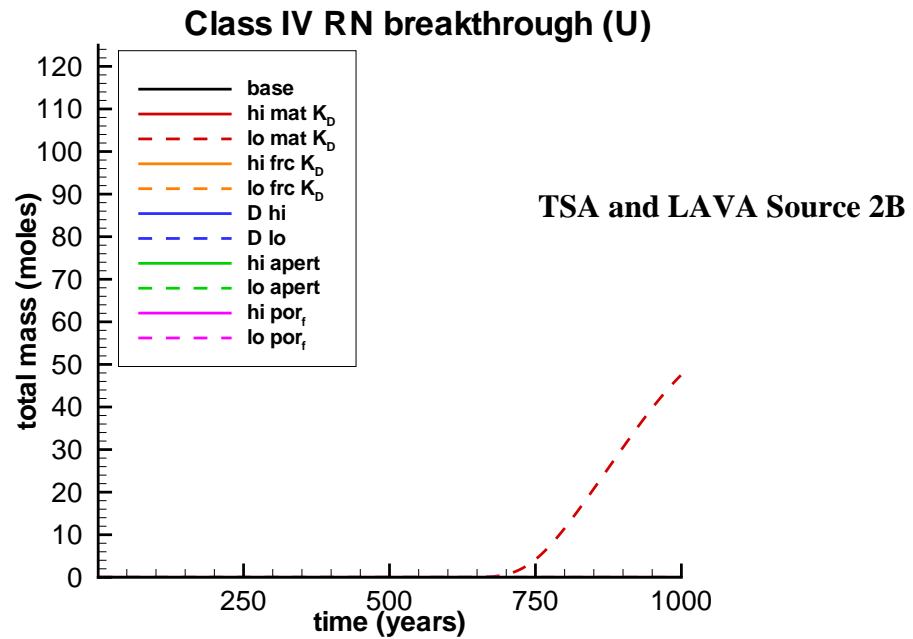


Figure 7-31. Total uranium mass breakthrough at the NTS boundary for the combined TSA and LAVA source release involving chimney sorption and medium Ra_{sys} (Source 2b, with sorption; Table 6-9).

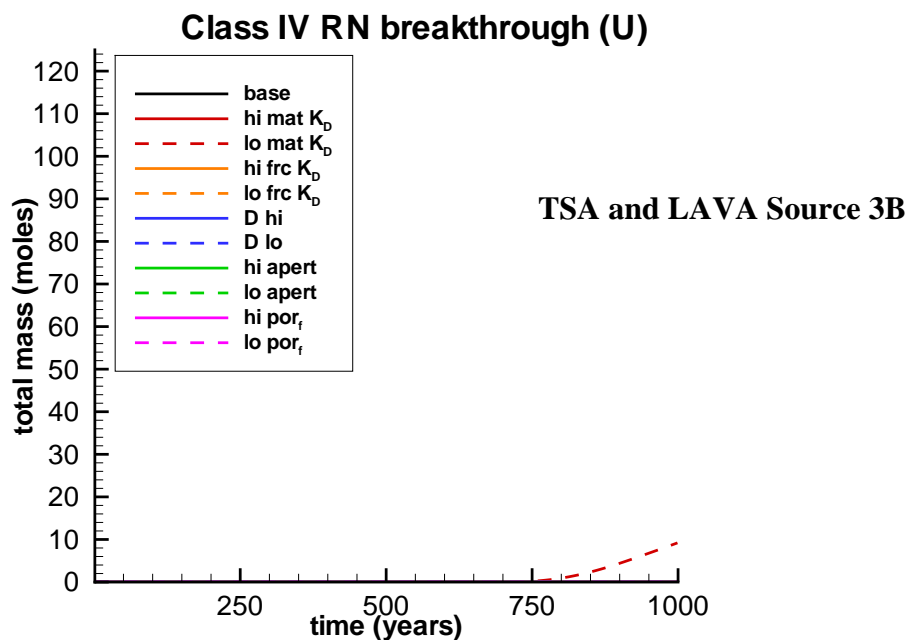


Figure 7-32. Total uranium mass breakthrough at the NTS boundary for the combined TSA and LAVA source release involving chimney sorption and low Ra_{sys} (Source 3b, with sorption; Table 6-9).

Class VI Colloids

In addition to Class I and Class IV solutes, the only other species that is predicted to migrate from the source location to the observation wells and the NTS boundary is the “colloid” abstracted solute. In this particle-tracking model, kinetic aqueous interactions between RNs and colloids are not simulated explicitly as they were in the simulations discussed in Appendix F. Rather, we approximate a portion of the total released source mass that is effectively and irreversibly sorbed onto colloids. The results (Appendix F) indicate that a reduction factor between $1e-4$ and $1e-5$ is appropriate for this system. Such a parameter that depends on RN sorption and desorption rates with colloids, residence time in the aquifer, and reactivity of fracture and matrix minerals in the aquifer. The colloid species migrates as a component experiencing only attachment and detachment from fracture walls (modeled here with a linear retardation factor); it does not experience matrix diffusion or reactions with matrix material. Thus, the only parameters affecting colloid migration are the velocity in the fractures (a function of fracture porosity) and the retardation caused by filtration processes along fracture walls.

Figures 7-33, 7-34, and 7-35 show the simulated mass arrival of the abstracted Pu-Colloid species. Comparing sensitivity simulations to the base-case parameter set, we determined that reducing the fracture porosity and/or the fracture retardation increases mobility of this species. Because the colloid species is so mobile in this model, we also observed that increasing the porosity and the fracture retardation slows migration, but it does not completely preclude movement of any mass.

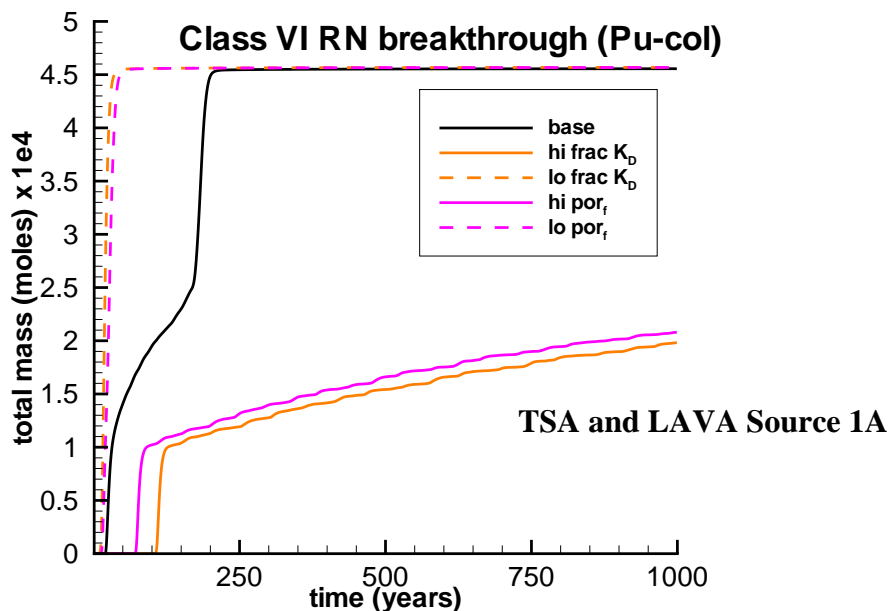


Figure 7-33. Total Pu-colloid mass breakthrough at the NTS boundary for the combined TSA and LAVA source release involving no chimney sorption and **high $R_{a,sys}$** (Source 1A, no sorption; Table 6-9). Note that the mobile mass of Pu-colloid is assumed to be 1/10 000 of aqueous Pu released from melt glass.

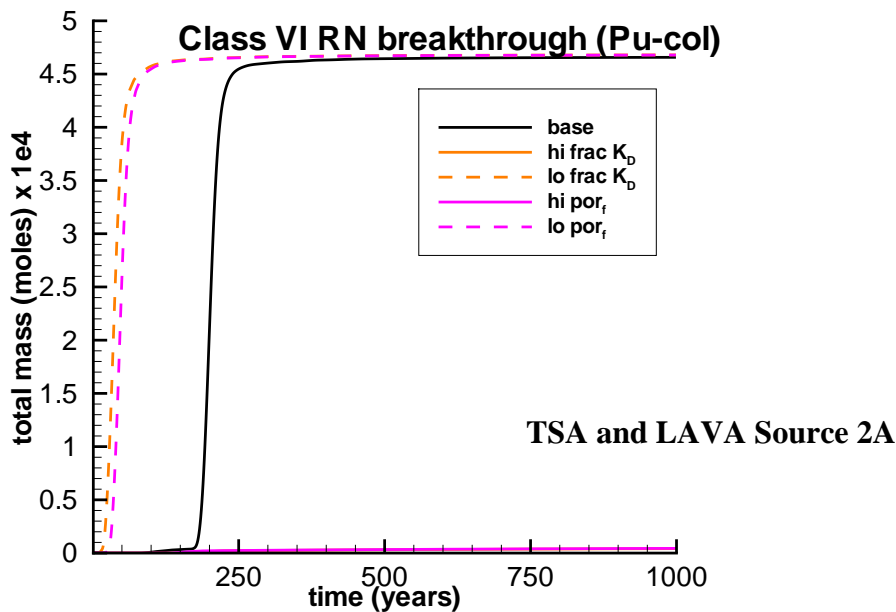


Figure 7-34. Total Pu-colloid mass breakthrough at the NTS boundary for the combined TSA and LAVA source release involving no chimney sorption and **medium** Ra_{sys} (Source 2A, no sorption; Table 6-9). Note that the mobile mass of Pu-colloid is assumed to be 1/10 000 of aqueous Pu released from melt glass.

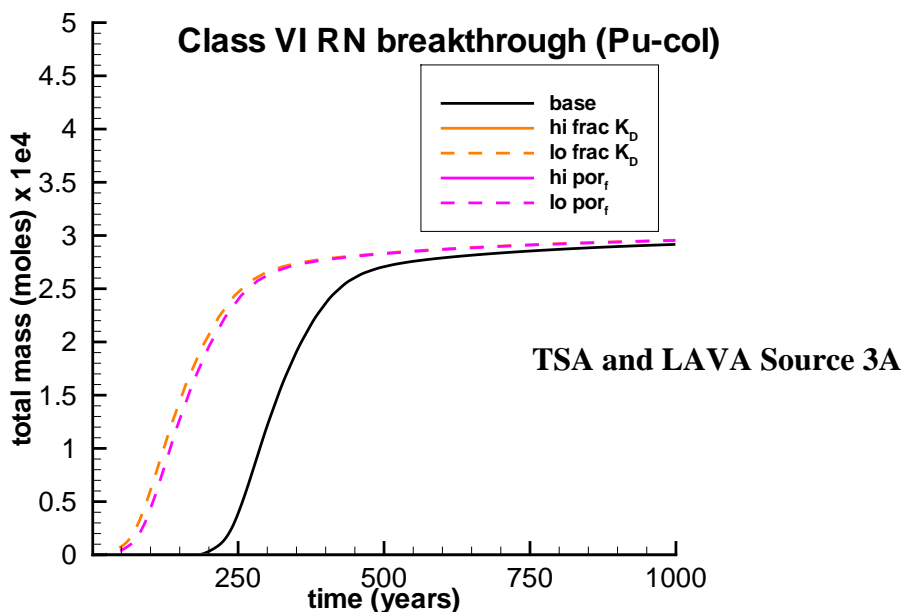


Figure 7-35. Total Pu-colloid mass breakthrough at the NTS boundary for the combined TSA and LAVA source release involving no chimney sorption and **low** Ra_{sys} (Source 3A, no sorption; Table 6-9). Note that the mobile mass of Pu-colloid is assumed to be 1/10 000 of aqueous Pu released from melt glass.

7.7.5 Summary of Transport Simulations on Deterministic Flow Field

The transport results presented in this section are as expected for solute migration in homogeneous aquifers. The source releases to the TSA remain within the TSA to the wells and the NTS boundary. Similarly, the source releases to the LAVA remain within the LAVA. Because the TSA has lower fracture porosity, travel times in that aquifer are lower than in the LAVA. However, when chimney conditions do not support vertical transport (e.g., for a low Ra_{sys} and sorption in the chimney), then BENHAM source releases exit primarily in the nearer LAVA aquifer, which becomes the dominate site-scale migration pathway. Source-term sensitivity was not considered for TYBO, but its releases would always be to the TSA.

The deterministic transport model yields results consistent with the findings of Kersting et al. (1999). With base-case parameters, this model predicts that migration from BENHAM to both ER-20-5 observation wells is feasible for all species observed in those wells in the appropriate time frame of the observations. Further, the simulated concentrations are similar to those observed, considering that the model uses an unclassified average source inventory and that the predicted concentrations result from coupling the transient source-term model (see Chapter 6) with the site-scale transport model described in this chapter, both of which are conducted with uncertainty in the model parameters. Simulations including the TYBO source demonstrate that it is feasible for TYBO releases to have arrived at ER-20-5 #1, but not at ER-20-5 #3. However, the concurrence of the simulations for BENHAM source releases with all observations in both wells (and the fact that Kersting et al. (1999) fingerprinted the Pu in both wells to have originated at BENHAM) implies that TYBO releases are not captured at ER-20-5 #1.

For the source and transport parameter ranges considered in this sensitivity study, only Class I, IV, and VI species migrate to the ER-20-5 observation wells or to the NTS boundary. The ranges of uncertainty in the transport parameters impact migration rates, and as a result, cumulative moles of source RNs migrate to the NTS boundary in less than 1000 years. For longer-lived Class I RNs, transport parameter uncertainty is not as significant as source function uncertainty. But for shorter-lived tritium, the transport parameters make all the difference as to whether migration to the NTS boundary occurs or does not occur before radioactive decay reduces mass in the system. Once solute-solid reactions are considered for Class IV RNs, the range in mobile mass increases significantly with parameter variations.

7.8 Heterogeneous Flow Fields

Flow fields computed on 30 different but equally probable parameter maps form the basis for analysis of reactive transport in heterogeneous domains (Appendix G). Whereas the simulations on the deterministic HSU model (described in the previous section) were used to predict groundwater concentrations at the ER-20-5 observations wells, multiple heterogeneous attribute fields are used to focus on transport over a larger domain. This is because only about half of the heterogeneous realizations yield BTCs in which solutes or colloids migrate from BENHAM to ER-20-5 #1 in less than 30 years. Figure 7-36 shows the BTCs at ER-20-5 #1 for BENHAM sources for the most conservative, unretarded species. This result is not surprising considering the general framework in which the geostatistical attribute maps were constructed. Summarizing the process described in Appendix G, the heterogeneous attribute maps are constructed to capture variability present in the data that are not represented in the HSU representation of materials. The trade-off is that the method does not guarantee our notion that units such as the TSA must be completely intact and of significantly higher permeability than the surrounding material (referred to as confining unit or composite material in the HSU representation). Thus, at the local scale, we have discovered that this representation does not always support simulations that predict migration with travel times completely consistent with field data. Arrivals at ER-20-5 #1 may occur after 80 or 100 years in some realizations rather than after 30 years, as required to match field data. By comparison, the LAVA was preserved as an intact unit in all heterogeneous attribute maps (by design). Thus, similar to the HSU model described in the previous section, pathlines originating in the LAVA remain in the LAVA and transport is rapid due to the fractured nature of the class.

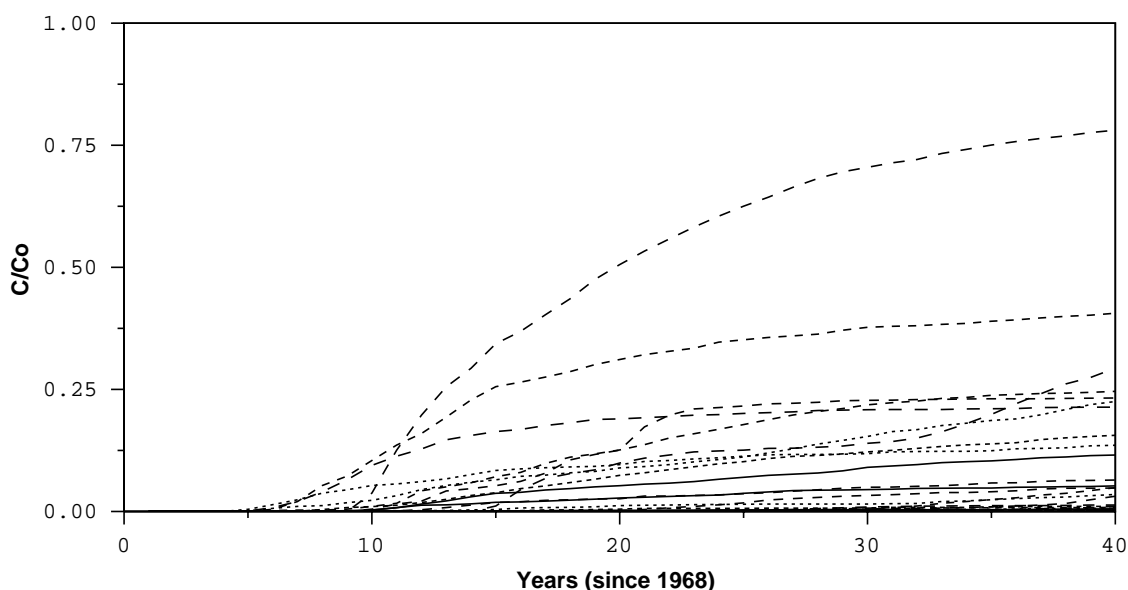


Figure 7-36. Unit breakthrough curves at ER-20-5 #1 of unretarded colloid species originating at BENHAM chimney in TSA. All 30 realizations are shown. Nontrivial breakthrough within 30 years occurs in about half of the realizations. For diffusing solutes, even fewer realizations yield arrivals within 30 years.

This method does capture variability not represented with the HSU model; units such as the TSA are generally represented, if not completely continuously (see Figure 5-5). Therefore, at larger scales (out to the NTS boundary in this case), it is more likely that all simulations contribute useful information, by integrating larger portions of the domain as will be required by CAU-transport models.

There are several approaches for addressing transport simulations on heterogeneous realizations that are not consistent with field observations. One would be to select only those realizations that can achieve consistent results. Another approach would be to modify the heterogeneous attribute properties (most likely fracture properties) to ensure that all realizations are consistent in some sense. For the purposes of this analysis, we are most interested in the overall sensitivity the “as measured” heterogeneity has on larger-scale simulations. We focus on transport from BENHAM to the NTS boundary in this section so we can avoid issues related to whether streamlines from BENHAM are captured at the upper observation well or if transport takes 60 years rather than 30 years. In doing so, we acknowledge variability in materials not captured by the HSUs but also acknowledge that data sparsity lead to a range of attribute representations, some of which do not completely support additional information, such as the measurements in ER-20-5 #1. Using the NTS boundary, where most streamlines exit the site-scale domain, enables sensitivity analyses to highlight which parameters associated with this model may have the greatest impact on CAU-transport simulations.

The process for computing mass flux at the NTS boundary and at the ER-20-5 observation wells is identical to that used for the deterministic flow fields described in this section. Unit-source-release particle BTCs are computed for the observation wells and NTS boundary; the results are convolved with the source-release functions described in Chapter 6.

7.8.1 Source Terms

The same three different thermal conditions in the cavity/chimney system described in Section 7.4 ($Ra_{sys} = 84.6, 8.46, \text{ and } 0.846$) are considered for both sorbing and non-sorbing chimney properties for 13 RNs. These source conditions are listed in Table 6-9. Figures 6-33 through 6-50 show the mass flux to the TSA and LAVA aquifers for these different source conditions at base-case parameter values. Note that the source functions were computed with a deterministic representation of the cavity/chimney system. Thus, releases are elevation dependent, but once they enter the site-scale domain, solutes encounter materials as mapped in the heterogeneous realizations.

7.8.2 Site-Scale Breakthrough Curves

Reactive, dual-porosity streamline particle tracking is used to simulate BTCs at the NTS boundary and the ER-20-5 observation wells for each flow field, RN class, and source location. Figures 5-15 and 5-16 show representative unretarded particle paths from the TSA and LAVA source-release locations for four of the 30 heterogeneous fields. The high uncertainty in heterogeneity leads to significantly varying flow paths away from BENHAM. For flow field #3, Figures 7-37 and 7-38 show the time of flight of 2500 particles released at the TSA and LAVA source locations, respectively. The figures show particle pathways and times of flight for RN classes I, IV, V, and VI with base-case site-scale transport parameters.

As in the deterministic study, BTCs of reactive dual-porosity particles are generated at each observation well and at the NTS boundary (defined as the southern and western boundary of the site-scale model). The transport parameters are defined in Section 7.7.4 and their ranges of uncertainty for the heterogeneous flow field simulations are catalogued in Tables 7-2 through 7-5. Figures 7-39 and 7-40 show the simulated unit-source BTCs of the six RN classes at the observation wells and at the NTS boundary for one heterogeneous flow field (#3 is arbitrarily chosen as a representative realization) and for base-case parameters. As with the deterministic study, breakthrough at the observation wells occurs before breakthrough at the NTS boundary. Also in agreement with the deterministic study, more mass eventually crosses the NTS boundary than is captured at the observation wells, and RN classes II, III, and V do not migrate to either boundary. In contrast to the deterministic study particles in this flow field (#3 of 30) move faster in the LAVA than in the TSA. In the geostatistical realization generation, the LAVA is kept as an intact (though heterogeneous and fractured) unit, whereas the TSA is not explicitly preserved. Thus, particles released at the TSA location in the source model enter a heterogeneous flow system in which they are unlikely to remain in fractured welded tuff all the way to the observation wells and the NTS boundary. On the other hand, LAVA release particles remain primarily in the fractured LAVA lithologic class (see Figures 5-17 and 5-18 to compare material classes particles travel in for TSA and LAVA releases).

For this flow field (#3) the flow paths are such that significantly more LAVA release particles arrive at deep observation well ER-20-5 #3 than TSA release particles arriving at the shallower observation well ER-20-5 #1. In other realizations, this is not necessarily the case. However, a small number of Class VI (Pu-Colloid) particles arrive at well ER-20-5 #1 in just over 30 years. This indicates slightly greater mobility of these particles relative to the actual Pu-colloid species (modeled in Appendix F), which did not arrive at well ER-20-5 #1, except for the most relaxed transport parameters, which arrived after 100 years. The reason for this difference is because the particle-tracking model operates on the assumption that a certain fraction of Pu released from the MG and EV is irreversibly sorbed onto colloids. This assumption depends upon Pu sorption and desorption rates onto colloids, as well as residence times in the aquifers and sorption coefficients of immobile minerals in the aquifers. As pathways between BENHAM and ER-20-5 #1 leave fractured material classes, residence times increase, as does the desorption of Pu from colloids in the process model. However, this discrepancy may be reduced in future modeling studies because recent results indicate slower desorption of Pu from zeolite colloids than was considered in Appendix F. Thus, even for slower flow rates and increased exposure to reactive immobile minerals, Pu still may behave as an irreversibly sorbed species onto colloids, just as is abstracted in the particle-tracking model.

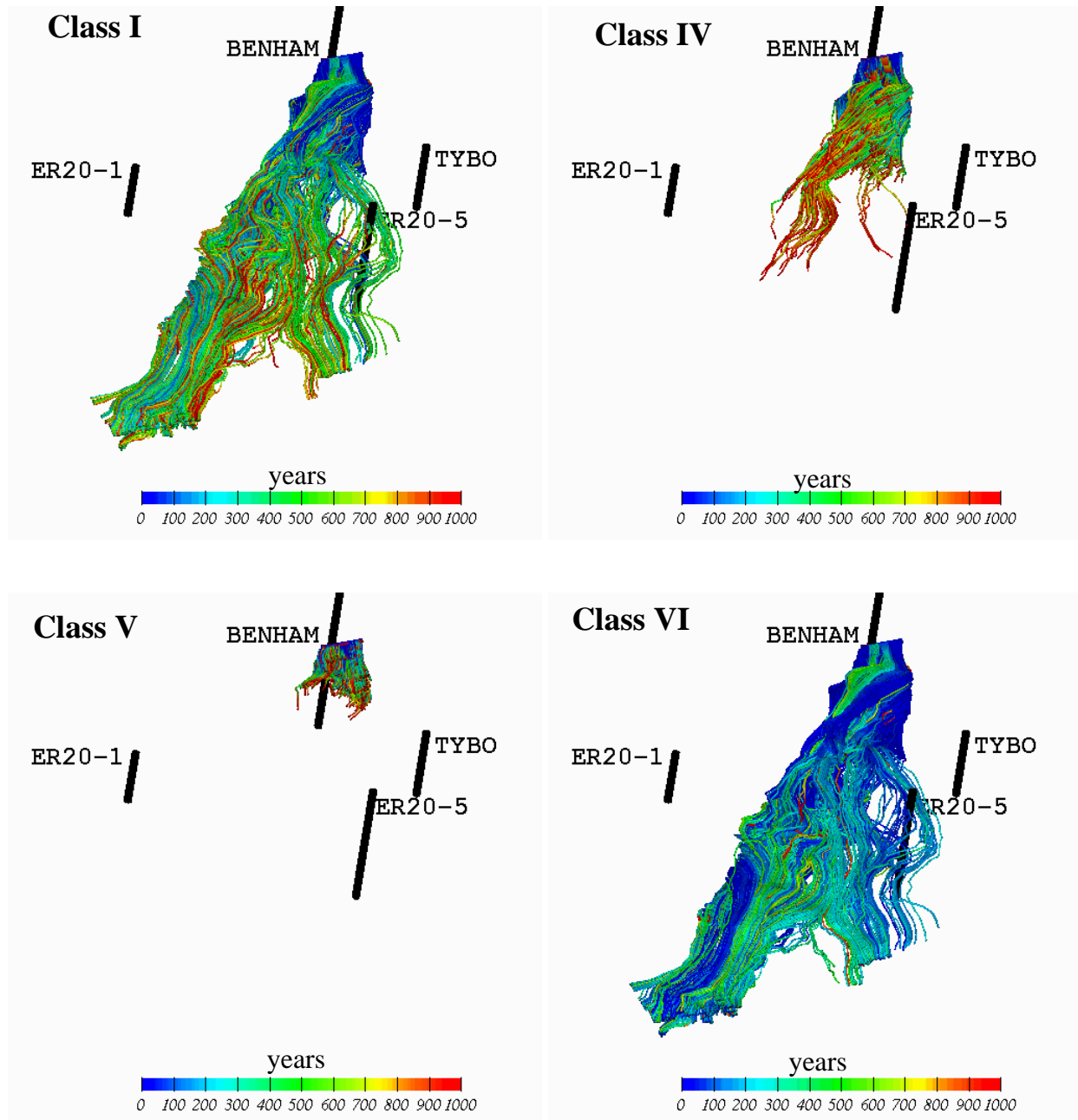


Figure 7-37. Time of flight for particles released from the **TSA source** location at BENHAM. Base-case transport parameters are assigned to each of the different radionuclide classes.

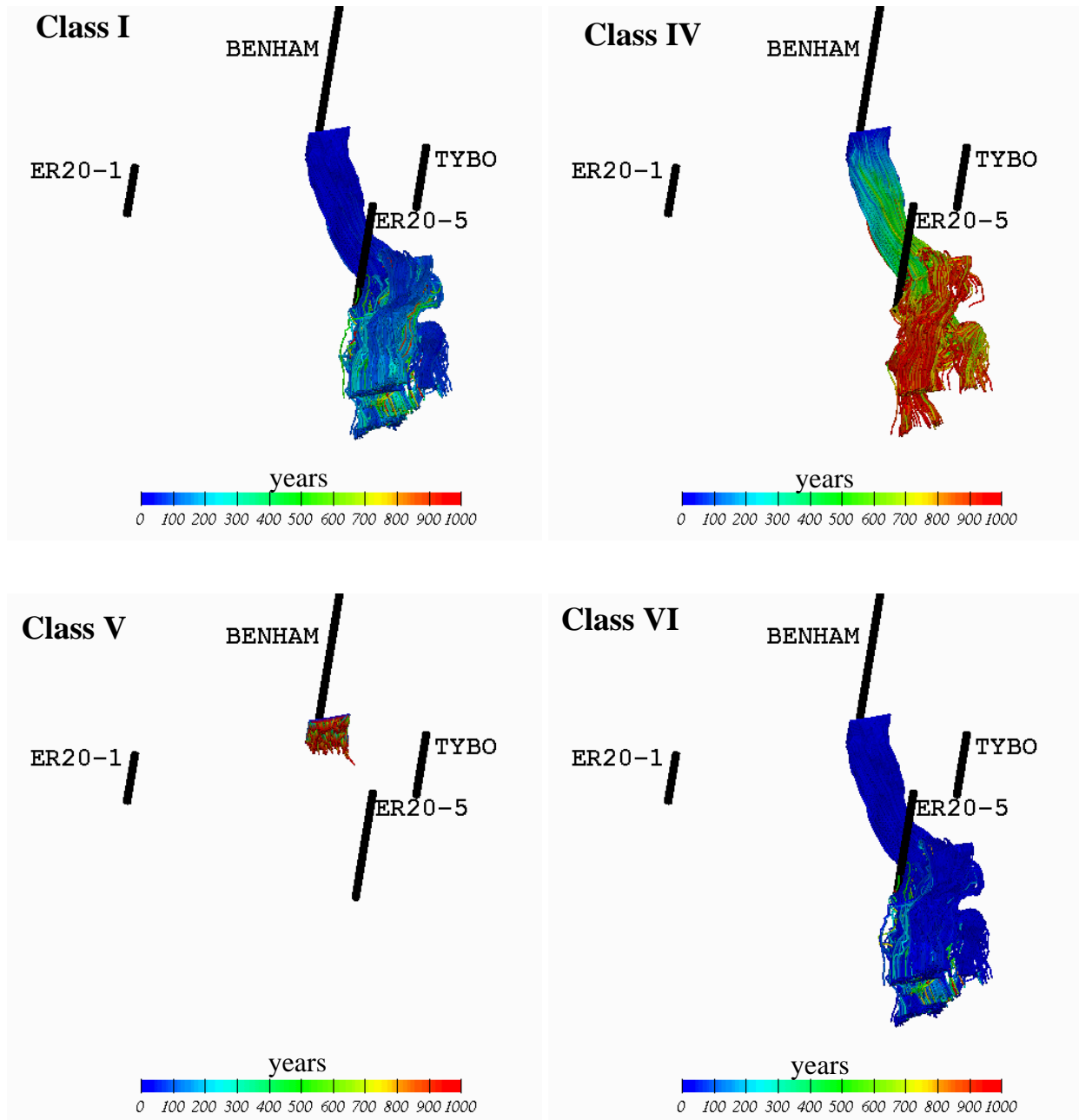


Figure 7-38. Time of flight for particles released from the **LAVA source** location at **BENHAM**. Base-case transport parameters are assigned to each of the different radionuclide classes.

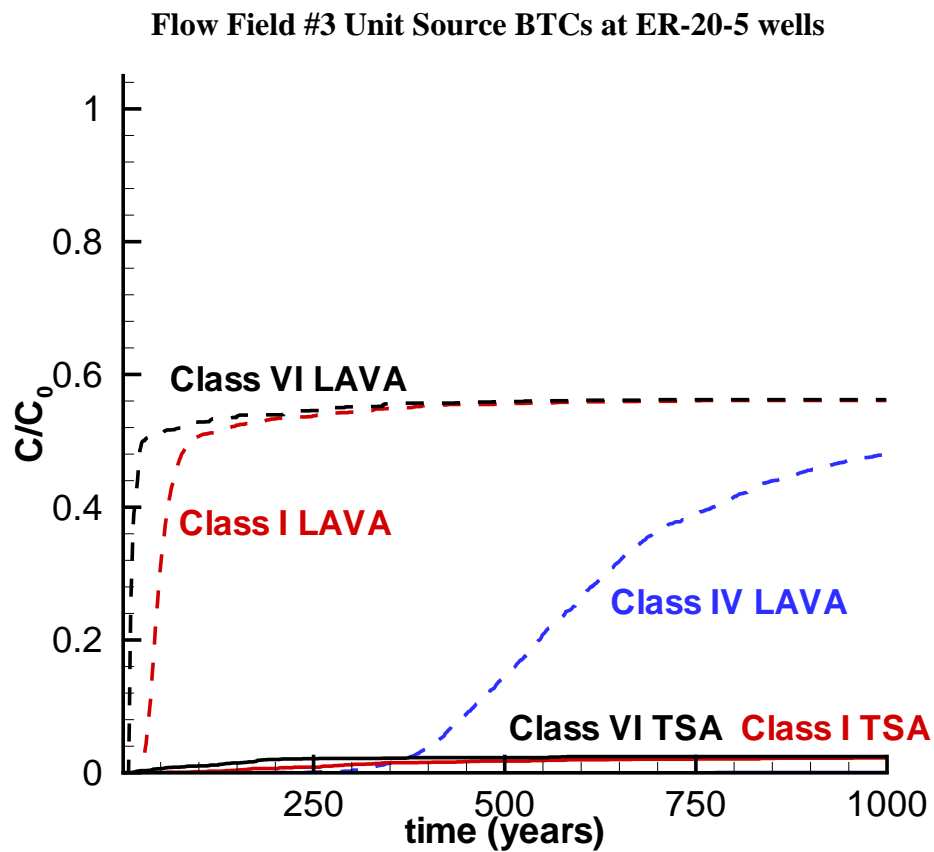


Figure 7-39. Breakthrough curves at the ER-20-5 wells for source releases in the TSA and LAVA at BENHAM using flow-field realization #3. LAVA breakthrough corresponds with ER-20-5 #3 and TSA breakthrough corresponds with ER-20-5 #1. Note that Class II, III and V never break through. Also note that some Class VI particles do arrive at well ER-20-5 #1, unlike the results using the coupled reactive transport model in Appendix F.

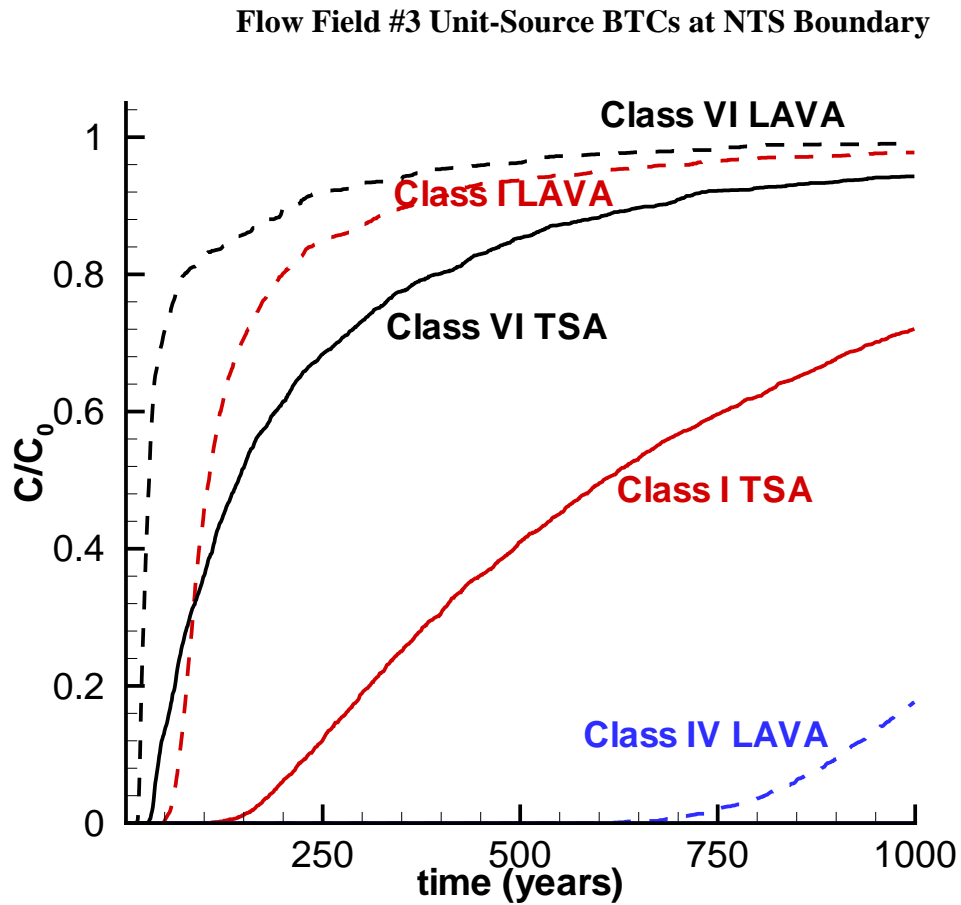


Figure 7-40. Breakthrough curves at the NTS boundary for source releases in the TSA and LAVA at BENHAM using flow-field realization #3. Note that Class II, III, and V never break through.

7.8.3 Transport on Geostatistical Flow Realization #3 with Base-Case Parameters

Geostatistical attribute realization #3 is chosen from 30 realizations to demonstrate the analysis provided for each realization. For BASE-CASE cavity/chimney thermal conditions with or without cavity/chimney sorption (sources 1A and 1B in Table 6-9), only Class I, Class IV, and Class VI (colloid) nuclides have any appreciable breakthrough to the observation wells and the NTS boundary. Figure 7-41 illustrates the computed mass flux at the source location, at the observation wells, and at the NTS boundary is for the Class I RNs ^3H and ^{36}Cl . In this example, we consider cumulative mass flux for both wells, with sources originating in both the TSA and LAVA. Both ^3H and ^{36}Cl enter the ER-20-5 wells capture zones (almost entirely in the LAVA aquifer) at approximately 20 years and cross the NTS boundary after approximately 50 simulated years. Note the reduction in ^3H mass flux at later time due to its short half-life of 12.3 years.

With base-case parameters (or with any of the sensitivity parameter sets considered), Class II, III, and V RNs do not exhibit any breakthrough at either of the observation wells or at the NTS boundary in under 1000 years. However, Class IV RNs, U and Np, do exhibit breakthrough at the wells and at the boundary in less than 1000 years. Convolving the upstream U TSA and LAVA sources with the appropriate BTCs yields the downstream mass flux of U entering the observation well capture zones after approximately 300 years and crossing the NTS boundary after 600 years of simulation (Figure 7-42).

Pu (Class V) does not cross either boundary as a sorbing species. However, the Pu-colloid species (Class VI) enters the observation well capture zone after 37 years (almost entirely in the LAVA) and crosses the NTS boundary after 70 years (Figure 7-43). The Pu-colloid species is simply a small fraction of the total Pu released during MG dissolution, which we assume sorbs irreversibly on to colloidal material or forms an intrinsic, embedded, or pseudo-colloid. We assume 1/10 000 of the total-aqueous-Pu release forms such colloids, based on analyses with the reactive transport model. However, this value may be adjusted, in which case the mass flux and total mass BTCs will simply shift up or down. The Pu-colloid species experiences retardation in the fractures due to attachment and detachment processes described earlier in this Chapter and in Appendix F. It does not diffuse into or react with matrix materials.

For all mobile species, downstream cumulative mass curves for the wells and NTS boundary are plotted in Figures 7-44 and 7-45, respectively. As expected from the evaluation of the unit-source BTCs, only Class I, IV, and VI RNs break through at the observation wells and at the NTS boundary for flow-field realization #3. Mass arrives at the observation wells before the NTS boundary, but more mass eventually arrives at the NTS boundary, with the exception of U and Np. Given an increased time interval, more of these two RNs would cross the NTS boundary.

Comparing these particle-tracking model results with the process model results in Appendix F, we note that general trends are preserved well with a few exceptions. A specific exception is that Pu-colloid arrivals at well ER-20-5 #1 are simulated with this model whereas they did not occur with the process base-case model. This indicates the Pu-colloid species modeled here (assuming that some Pu is irreversibly sorbed onto colloids) is slightly more mobile than when it is modeled as a formation product of a kinetic reaction. However, only a few particle paths leaving the TSA source are even captured by well ER-20-5 #1 in this particular flow field. The NTS boundary breakthrough provides a much better sampling of the two different models and the

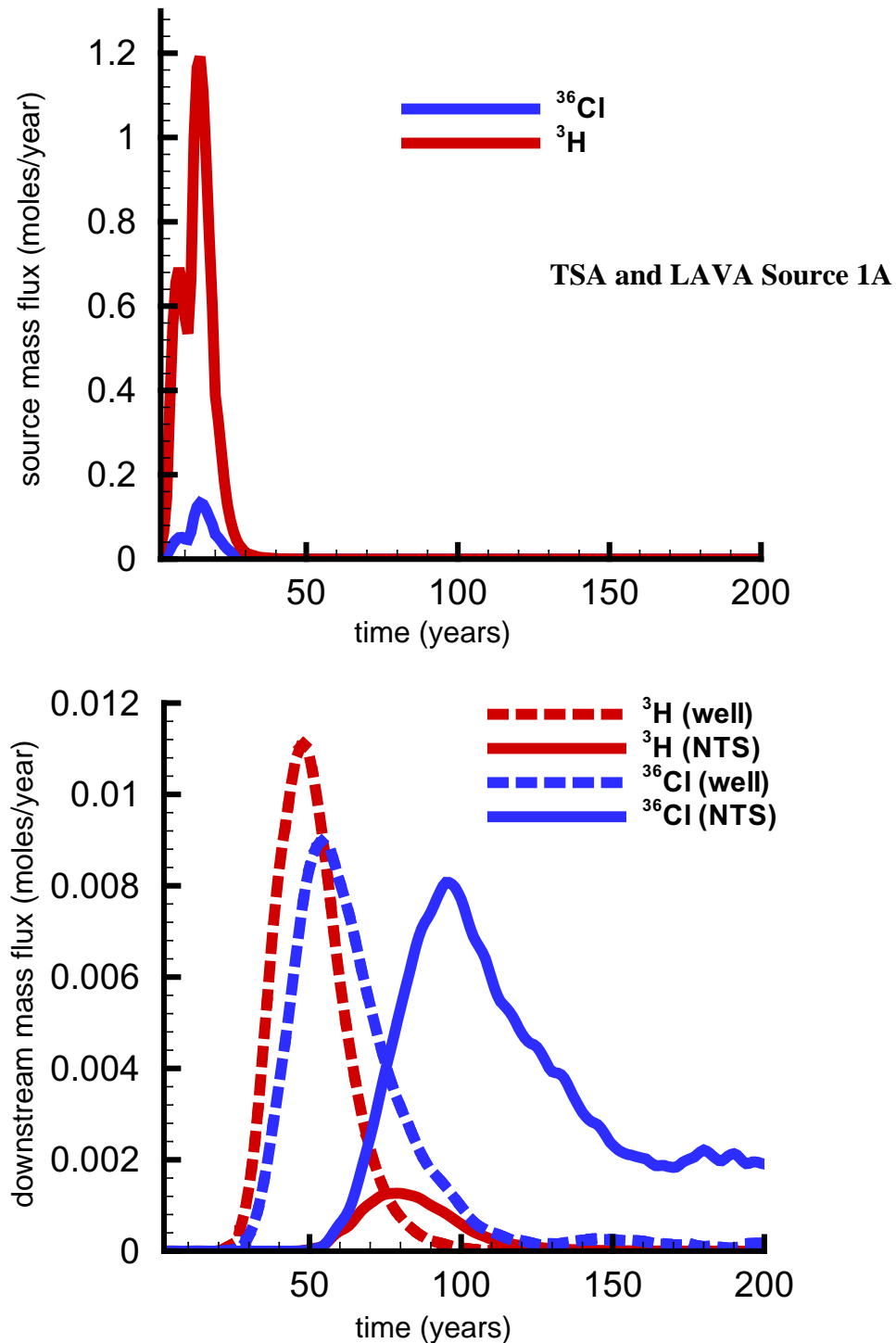


Figure 7-41. CLASS I mass flux in flow-field realization #3 with BASE-CASE source conditions and base-case transport properties. The top plot illustrates the combined TSA and LAVA source curves for Class I radionuclides ^3H and ^{36}Cl . The bottom plot illustrates the downstream mass flux curves at the ER-20-5 wells and at the NTS boundary.

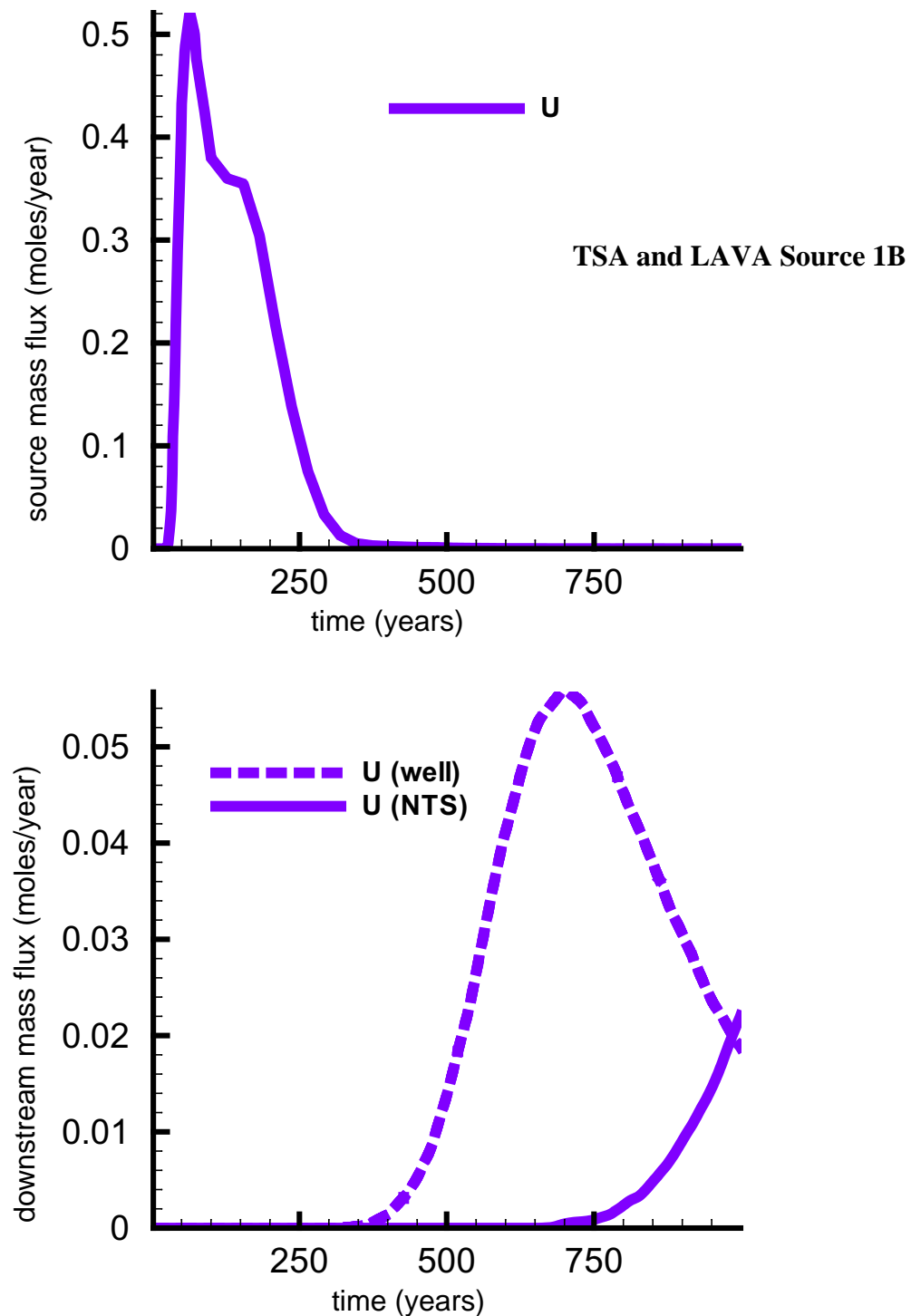


Figure 7-42. CLASS IV mass flux in flow-field realization #3 with BASE-CASE source conditions and base-case transport properties. The top plot illustrates the combined TSA and LAVA source curves for Class IV radionuclide U (reported as total U, or the sum of ^{238}U and ^{234}U). The bottom plot illustrates the downstream mass flux curves at the ER-20-5 wells and at the NTS boundary.

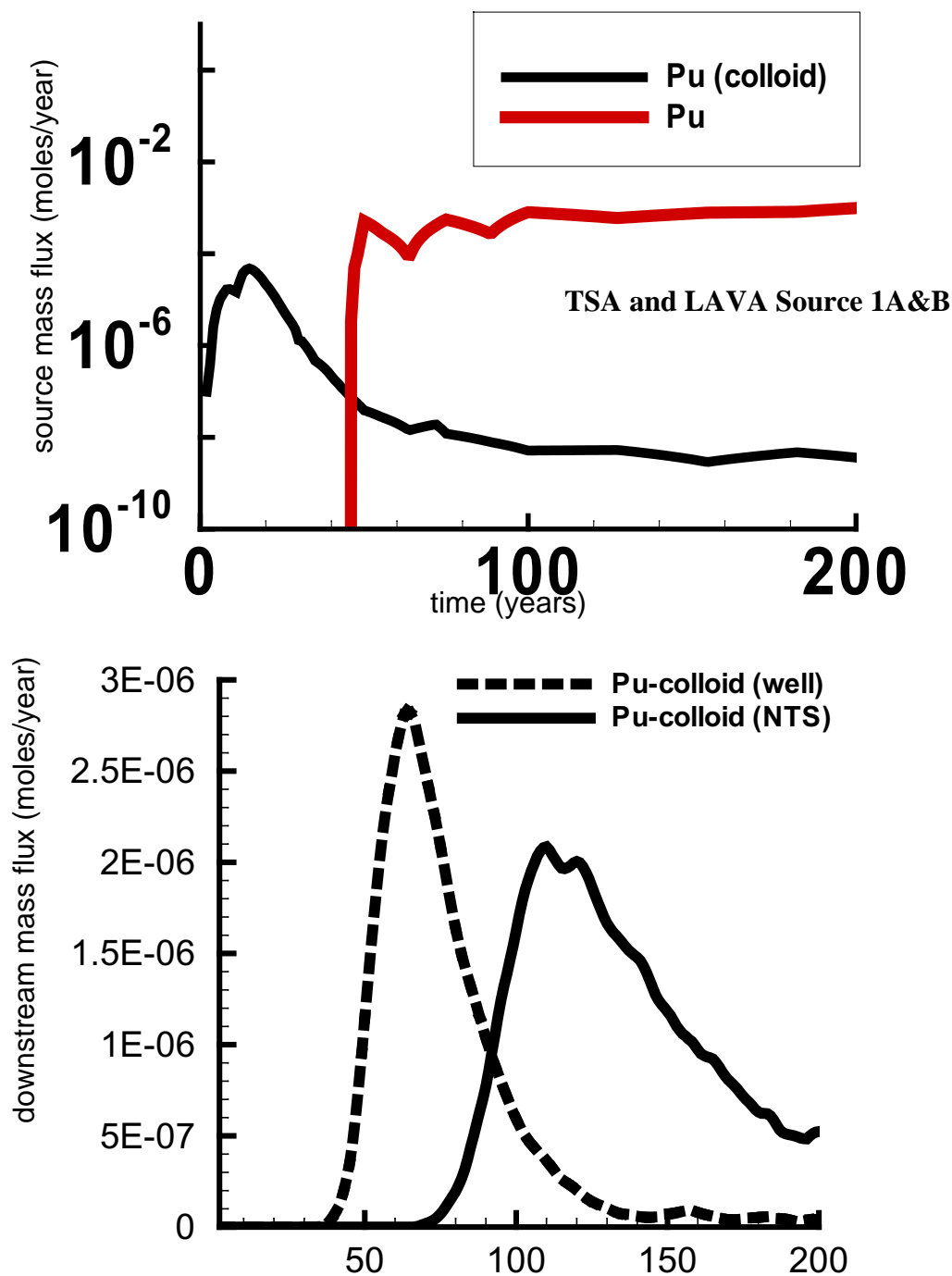


Figure 7-43. CLASS V and VI mass flux in flow-field realization #3 with BASE-CASE source conditions and base-case transport properties. The top plot illustrates the combined TSA and LAVA source curves for Class V radionuclide Pu (reported as the sum of ^{239}Pu and ^{240}Pu) and Class VI Pu-colloid (reported as 1/10 000 of total Pu source). The bottom plot illustrates the downstream mass flux curves at the ER-20-5 wells and at the NTS boundary. Note that only Pu-colloid breaks through to the wells and NTS boundary.

comparisons are much more favorable there. With the process model in Appendix F, Pu-colloids associated with both LAVA and TSA releases arrive at the NTS boundary. Similarly, with this model they arrive at the NTS boundary soon after the first arrivals at the wells. The time of arrival and the cumulative moles are very close in both studies, indicating reasonable consistency and confidence for the two different models. Thus, the results obtained in the process-model study serve to condition well the simplifications in this model, leading to the sensitivity study described in Section 7.9.

7.8.4 Estimation of Groundwater Pu-Colloid Concentrations at ER-20-5 Wells and the NTS Boundary

Applying the same approximation used in the deterministic flow field, the Pu-colloid mass flux results can be converted into groundwater concentrations (see Section 7.7.3). To estimate Pu-colloid concentrations at the ER-20-5 wells, the mass flux of a Pu-colloid (moles/yr) through the wells' capture zones is divided by the groundwater flux (liters/yr) through the same zone. At the NTS boundary, the flux-averaged concentration estimate is made by dividing Pu-colloid flux across the NTS boundary by the groundwater flux through the source region. This implies that in essence there is virtually no dilution of the plume, hence a high estimate. Using these approximations, Figure 7-46 shows the estimated Pu-colloid concentrations at the observation wells and at the NTS boundary for base-case transport parameters in heterogeneous flow field #3. As in the deterministic flow field case, the concentration pulse in the LAVA occurs at a time consistent with the findings of Kersting et al. (1999) and the concentration is reasonable, considering that the mass of Pu in the source is based on the unclassified average of Smith (2001).

The predictions of Pu-colloid concentration in the upper well, ER-20-5 #1, are not as consistent with the field observations as the deterministic model results are (as shown in Figure 7-4). As mentioned previously, the reason is because in this particular heterogeneous flow field a continuous, connected fractured pathway from BENHAM to well ER-20-5 #1 does not exist. Further, in this heterogeneous flow field, very few particles are actually captured by well ER-20-5 #1. The simulated concentrations at ER-20-5 #3 are slightly higher in this model than they are in the deterministic model because LAVA groundwater fluxes are slightly lower in this model. The concentrations estimated at the NTS boundary are based on Pu mass flux divided by groundwater mass flux (a flux averaged concentration). The rough process for doing so in these estimates does not account for mixing and dilution. If concentrations were estimated for a specific sampling location, they would likely be less than those presented.

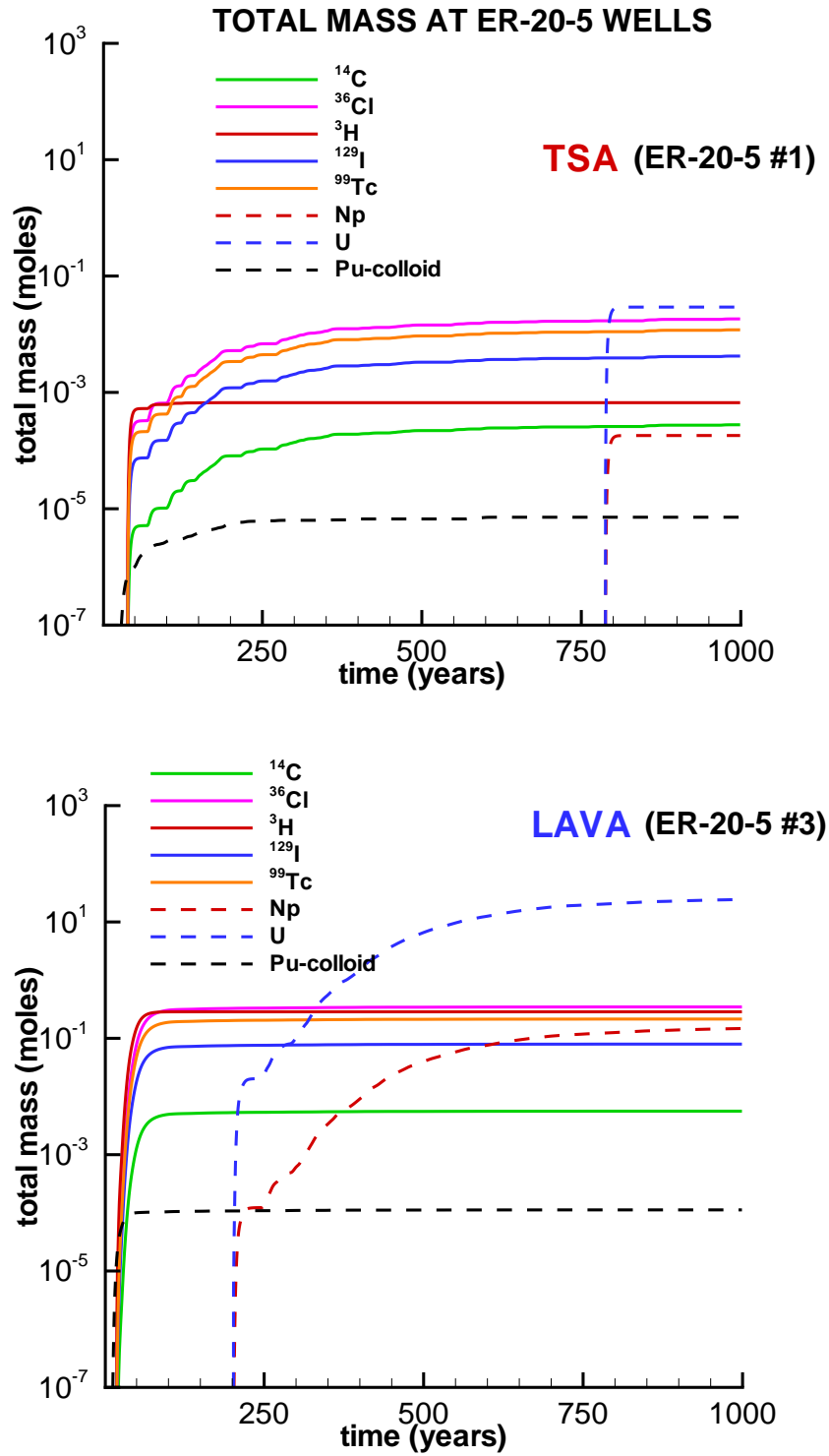


Figure 7-44. Cumulative mass at the ER-20-5 wells for flow-field realization, BASE-CASE source (Source 1a) function, and base-case transport parameters. For Pu-colloid results, it is assumed that 1/10 000 of total Pu is transported with colloidal material.

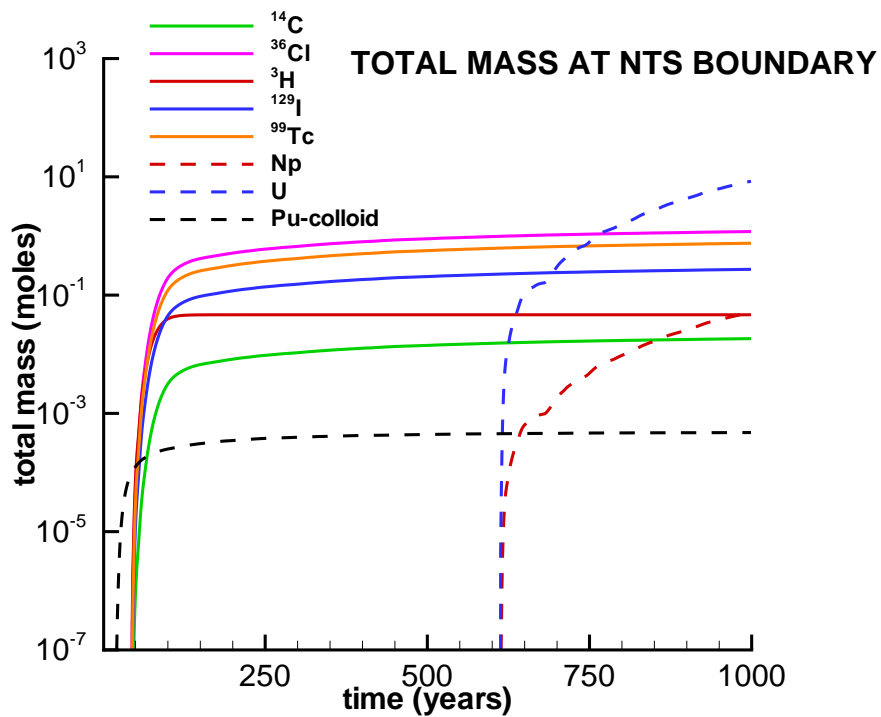


Figure 7-45. Cumulative mass at the NTS boundary for flow-field realization #3, BASE-CASE source function (Source 1a), and base-case transport parameters. For Pu-colloid results, it is assumed that 1/10 000 of total Pu is transported with colloidal material.

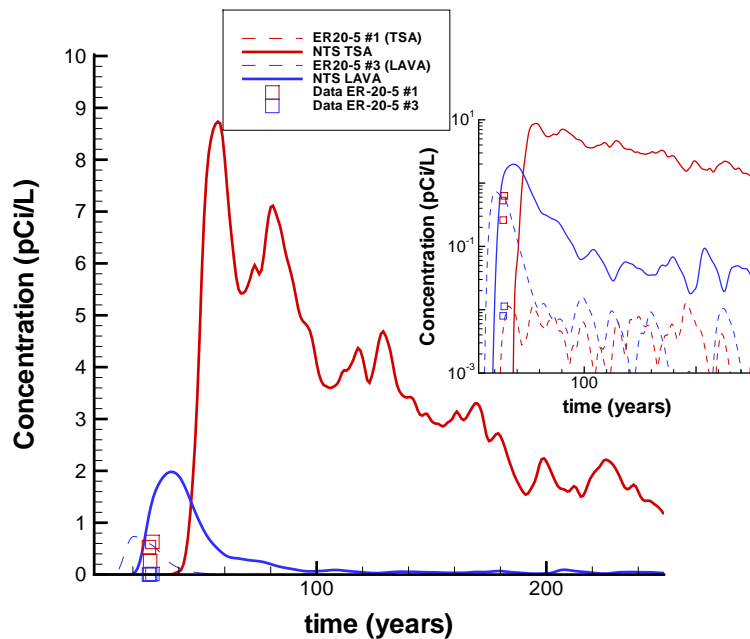


Figure 7-46. Estimated Pu-colloid concentrations in groundwater at the ER-20-5 observation wells and at the NTS boundary for flow-field realization #3, Source 1a, and base-case transport parameters. Inset shows log scale of concentration to highlight low, but non-zero, simulated concentration at ER-20-5 #1 for this realization.

7.9 Geostatistical Sensitivity Study

The same sensitivity runs considered for the deterministic model were executed for each of the 30 heterogeneous flow fields. These runs include three different cavity/chimney thermal conditions, sorbing and non-sorbing chimney properties, and 11 site-scale transport parameter sensitivity cases--these were executed for two different source locations (BENHAM only) and varying spatially with the heterogeneous attribute classes. Because of the nearly 40 000 mass BTCs at the NTS boundary created in this sensitivity study, presenting and synthesizing these results presents a challenge. Therefore, we introduce the transport parameter sensitivity first, relative to the base-case results using only the BASE-CASE, non-sorbing source term (Source 1A, Table 6-9). We then extend the sensitivity study, including the various source functions. A formal analysis of variation (ANOVA) pulls together the entire sensitivity study in the third part of this analysis.

7.9.1 Parameter Sensitivity I: BASE-CASE Source.

For BASE-CASE source-term thermal conditions and non-sorbing chimney properties (Source 1A, Table 6-9), breakthrough bars of the total mass crossing the NTS boundary at 30, 100, and 1000 years (averaged for the 30 equally probable attribute fields) are plotted for all 11 transport parameter sensitivity cases for ^3H in Figure 7-47, ^{36}Cl in Figure 7-48, U in Figure 7-49, Np in Figure 7-50, and Pu-colloid in Figure 7-51. In these figures, the low or high designation for a parameter means that all other parameters were held at base-case values while that parameter was changed to the low or high end of its uncertainty range. For example, “Kd(mat) hi” indicates that the matrix Kd was increased to its maximum value for each material class while all other parameters are held at their base-case value. Also plotted on these figures are standard deviation bars showing the range of variation across the 30 different flow field realizations. Clearly, the size of the standard deviations, often twice the mean value, indicates substantial variability in results across the 30 equally probable attribute maps. Another interpretation is that the set of 30 realizations is not nearly great enough in number to provide a statistically significant sampling of spatial variability. However, the average cumulative mass value does provide a good metric for analysis of transport and source-term sensitivity. The general trends in parameter sensitivity are the same as found in the deterministic study, as reported in Section 7.7.5.

One extension to this type of sensitivity study that could be conducted would be to discard realizations that do not lead to good matches with the field observations. However, the limitations of the geostatistical realizations discussed previously (in general, no connected welded tuff between BENHAM and ER-20-5 #1) would make such discrimination difficult. Therefore, this sensitivity is only conducted for transport to the NTS boundary (rather than to the wells) and is meant to provide a sense for which parameter the transport model is most sensitive to, rather than an indication of the quality of the model for simulating field observations. Good matches to the field observations are achieved in Section 7.7.3.

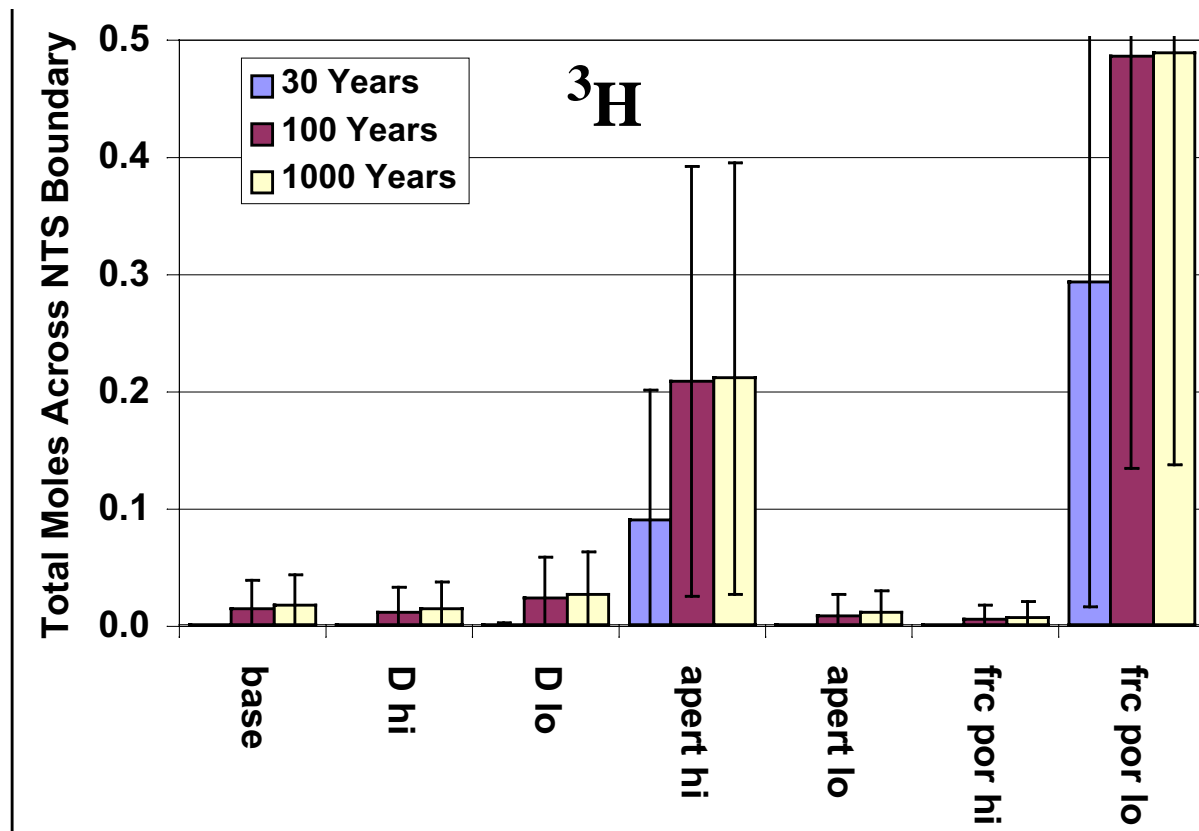


Figure 7-47. “Breakthrough bars” for 7 sensitivity cases for BASE-CASE source thermal conditions (Source 1A, Table 6-9). Each bar represents the average total amount of **tritium** crossing the NTS boundary after 30 years, 100 years, and 1000 years for all 30 flow-field realizations. Error bars represent one standard deviation for the 30 different flow fields.

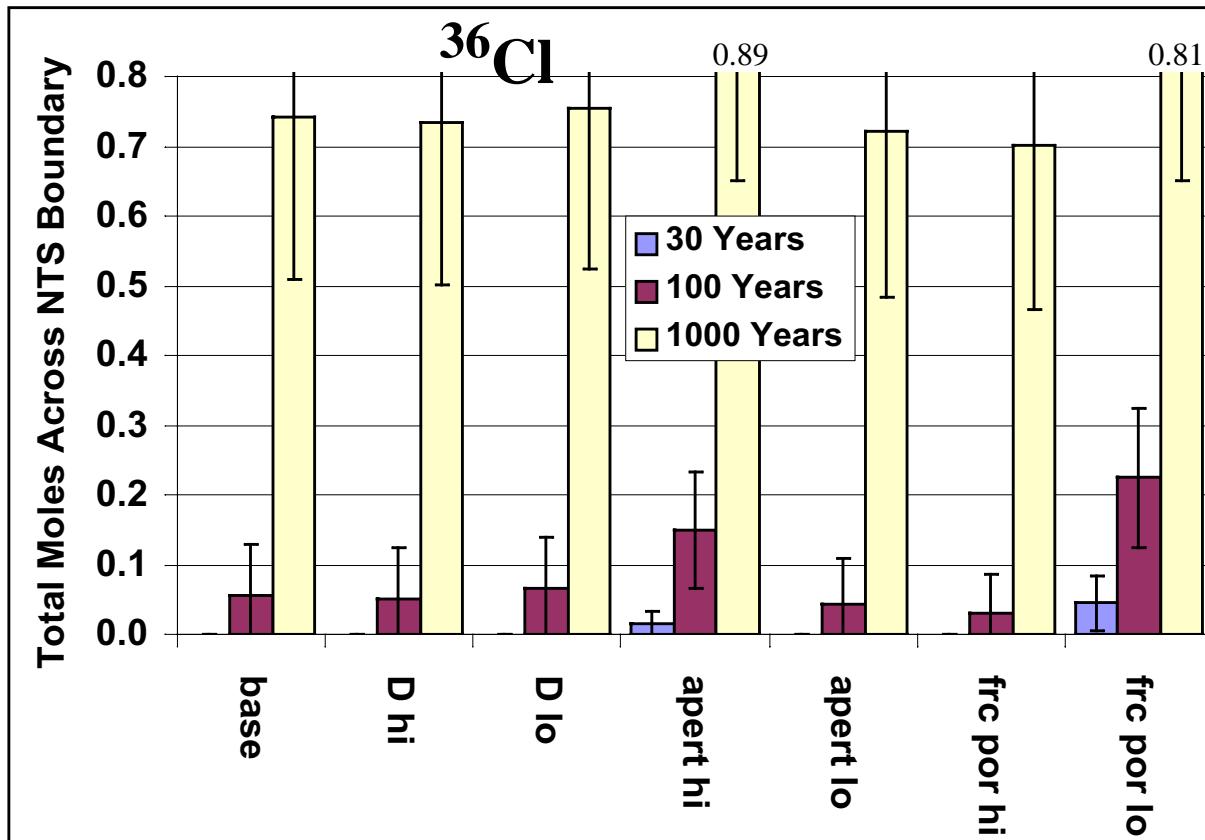


Figure 7-48. “Breakthrough bars” for 7 sensitivity cases (using Source 1A, Table 6-9). Each bar represents the average total amount of ^{36}Cl crossing the NTS boundary after 30 years, 100 years, and 1000 years for all 30 flow-field realizations. Error bars represent one standard deviation for the 30 different flow fields.

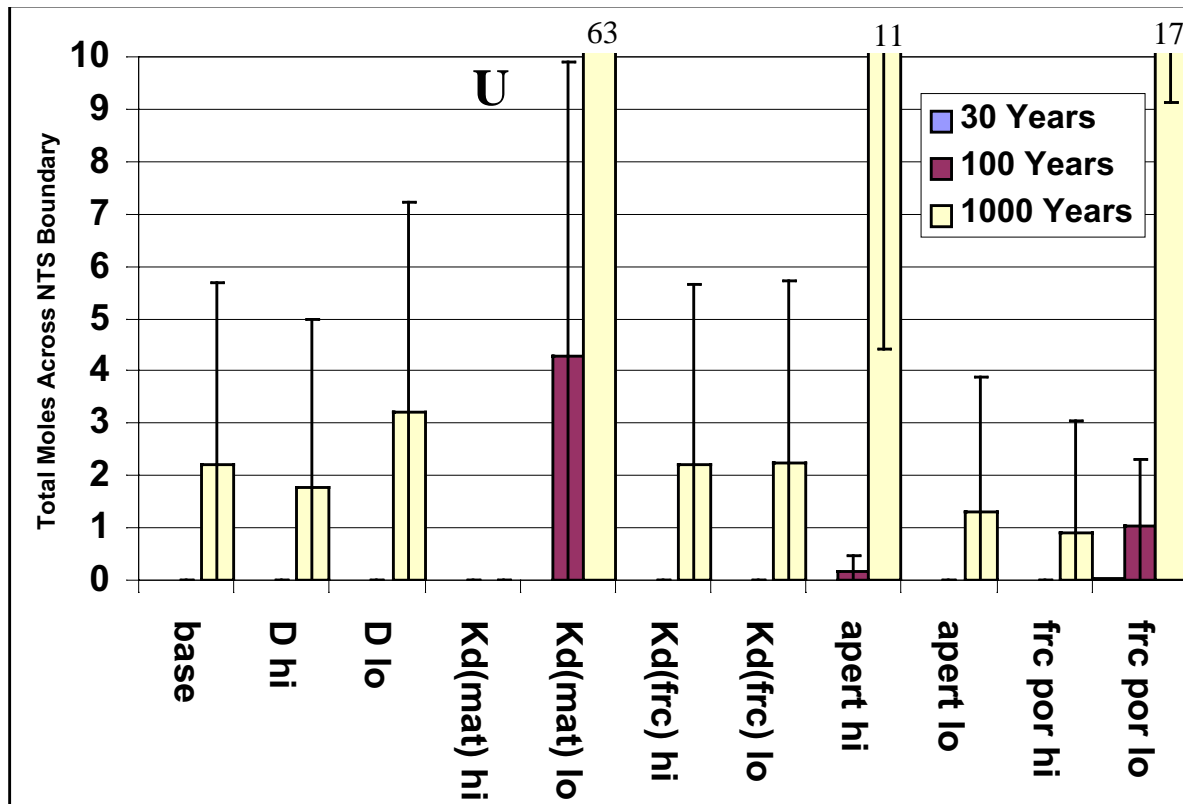


Figure 7-49. “Breakthrough bars” for all 13 sensitivity cases (using Source 1A, Table 6-9). Each bar represents the average total amount of U crossing the NTS boundary after 30 years, 100 years, and 1000 years for all 30 flow-field realizations. Error bars represent one standard deviation for the 30 different flow fields.

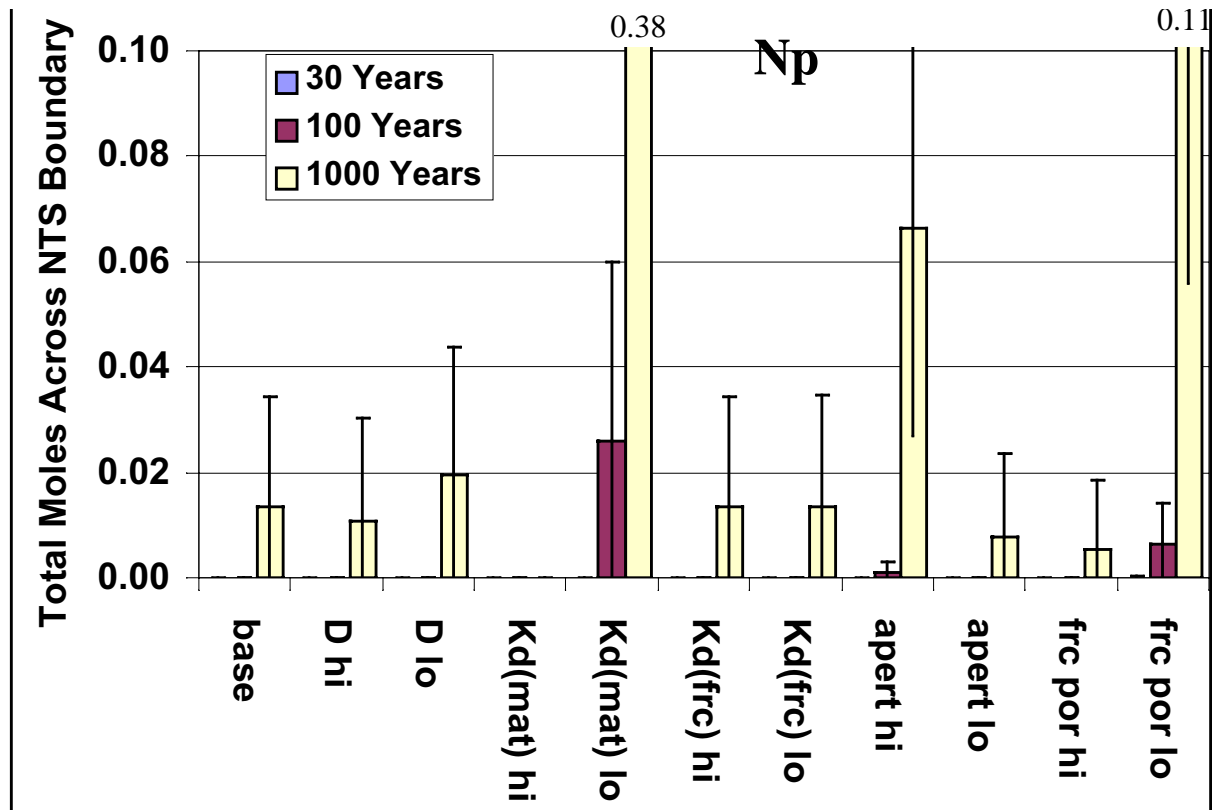


Figure 7-50. “Breakthrough bars” for all 13 sensitivity cases (using Source 1A, Table 6-9). Each bar represents the average total amount of N_p crossing the NTS boundary after 30 years, 100 years, and 1000 years for all 30 flow-field realizations. Error bars represent one standard deviation for the 30 different flow fields.

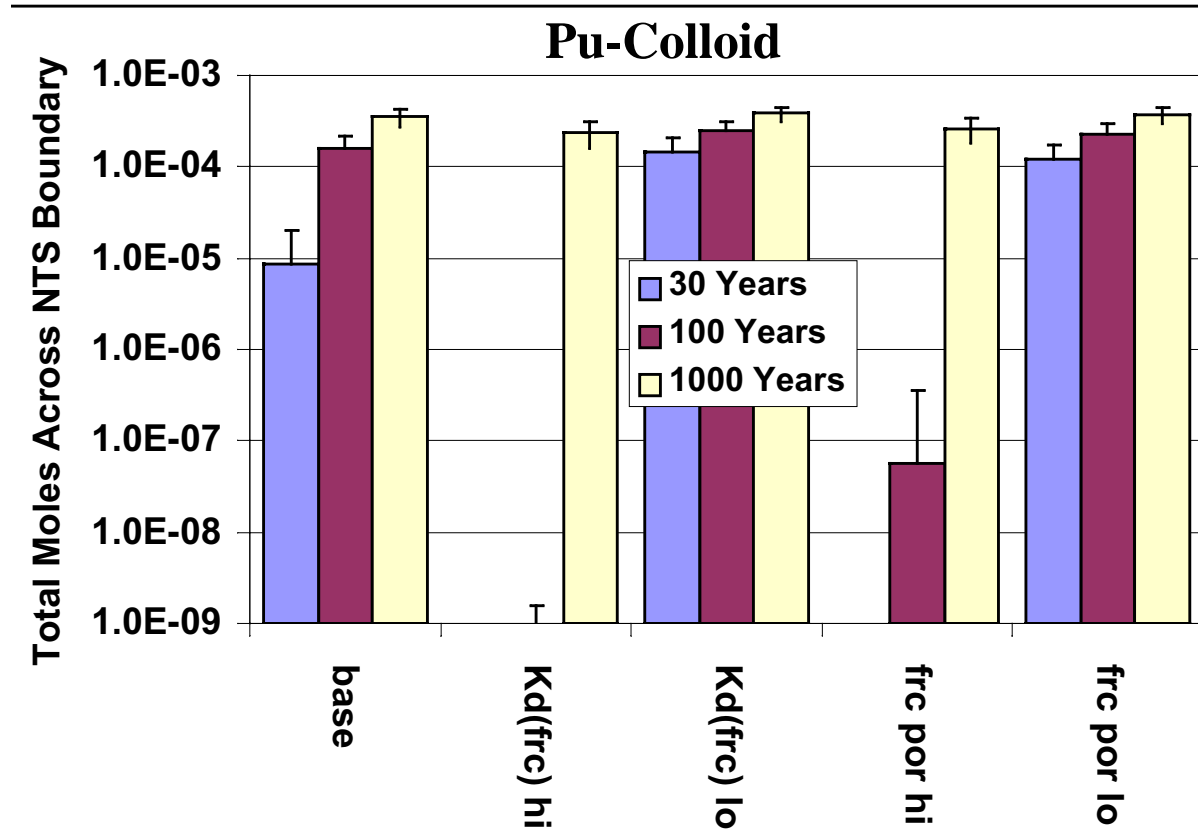


Figure 7-51. “Breakthrough bars” for all 13 sensitivity cases (using Source 1A, Table 6-9). Each bar represents the average total amount of **Pu-Colloid** crossing the NTS boundary after 30 years, 100 years, and 1000 years for all 30 flow-field realizations. Error bars represent one standard deviation for the 30 different flow fields. Note that the logarithmic scale makes standard deviation bars seem less significant. Also, Kd(frc) is the equilibrium parameter with which retardation due to filtration is approximated.

7.9.2 Parameter Sensitivity II: Impact Ratios

Section 7.9.1 began the demonstration of the sensitivity of mean mass breakthrough to variations in uncertain parameters. Although Figures 7-47 through 7-51 show the average cumulative mass arriving at the NTS boundary for different parameter sensitivity simulations, a more compact statistic is desirable to compare parameter sensitivity and source-term sensitivity. Therefore, we use an impact ratio, which is simply the ratio of the cumulative mass crossing the NTS boundary for a parameter-sensitivity simulation relative to the results with base-case parameters and BASE-CASE source term (Source 1A, Table 6-9). The impact ratio can be used to calculate the absolute mass for any simulation using the base-case mass breakthrough reported in Figures 7-47 through 7-51. Figure 7-52 shows the impact ratios for parameters affecting tritium breakthrough at the NTS boundary after 30 years. Relaxing the parameters for diffusion, fracture aperture, and fracture porosity for this non-reactive solute increases the cumulative mass breakthrough for the 30-year case. By 100 years, diffusion ceases to be as significant as the other two parameters (Figure 7-53), indicating that retardation due to diffusion with the base-case parameters is most important at smaller time scales for this particular RN (which is also significantly impacted by decay for times greater than 100 years).

It is interesting to note that as the convective potential of the source term decreases, the total mass produced decreases. Regardless of source term condition, increasing the mobility and velocity of ^3H by reducing the fracture porosity and diffusion coefficient and increasing fracture aperture (hence reducing diffusion potential) results in significant increases in solute migration. The same general trends are observed for all other Class I nuclides, as demonstrated in Figure 7-54 for ^{36}Cl at 100 years. However, the short half-life of ^3H enhances the impact of the three parameters, which in turn augment its mobility to the NTS boundary.

Class II, III, and V do not produce any mass at the NTS boundary in these simulations. The most mobile reactive solutes, Class IV, demonstrate sensitivity to additional parameters not affecting the Class I species. Figures 7-55 and 7-56 show the parameter sensitivities for U and Np at the NTS boundary after 1000 years. Matrix Kd , the diffusion coefficient, and fracture aperture all contribute to effective retardation. Because the ranges of uncertainty on matrix Kd are so large (Table 7-2), it dominates this coupled process. Also, fracture porosity plays a large role because smaller porosities lead to faster velocities, lower residence times, and reduced diffusion, thus keeping the reactive solute away from matrix minerals.

The Pu-colloid pseudo-species is affected only by fracture velocities and fracture retardation. Figure 7-57 shows that at 100 years, the cumulative mass reaching the NTS boundary is significantly impacted by the transport parameters. By 1000 years (Figure 7-58), not only has the mass leaving the source in all three source functions become more equal, but the mass reaching the NTS boundary is also closer to the same. This indicates that over long enough time, the processes impacting the migration of this species do not reduce the total mass migrating to the NTS boundary. The total mass is then completely defined by that which effectively sorbs irreversibly to colloids. Therefore, these results call for greater examination of the accuracy with which attachment and detachment processes can be effectively modeled with a retardation factor. An additional extension would be to include a filtration or retardation factor for porous media. Such a term was not built into this model because the conceptual model is that of migration in fracture media. Due to the nature of the heterogeneous fields provided by DRI, it is clear that in these

simulations particle pathways do not remain solely in fractured media, particularly for particles released in the TSA.

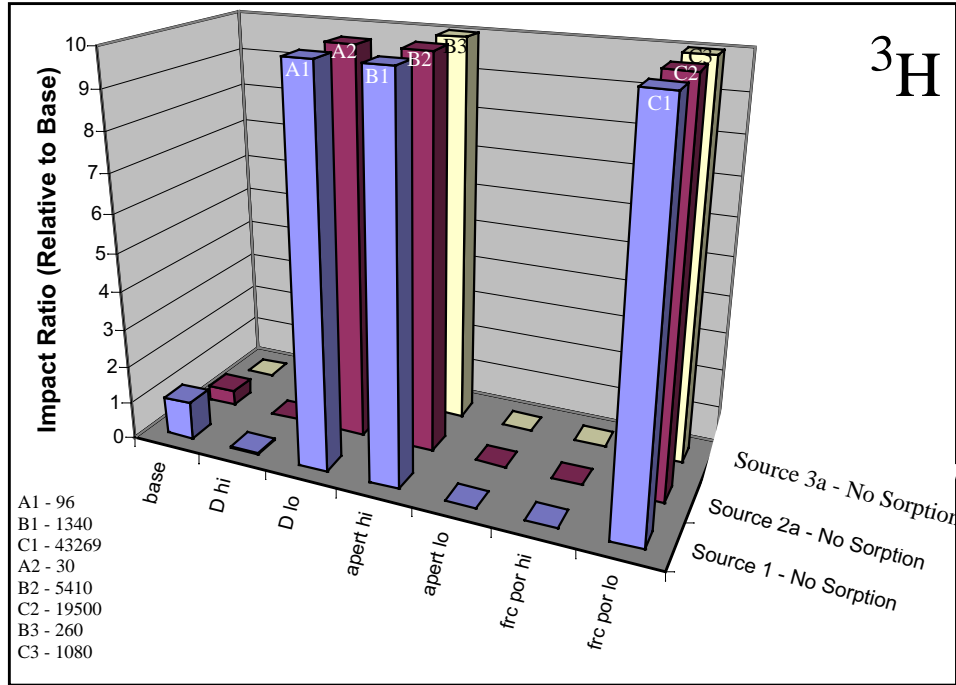


Figure 7-52. Impact ratios for tritium transport to the NTS boundary for simulations of 30 years.

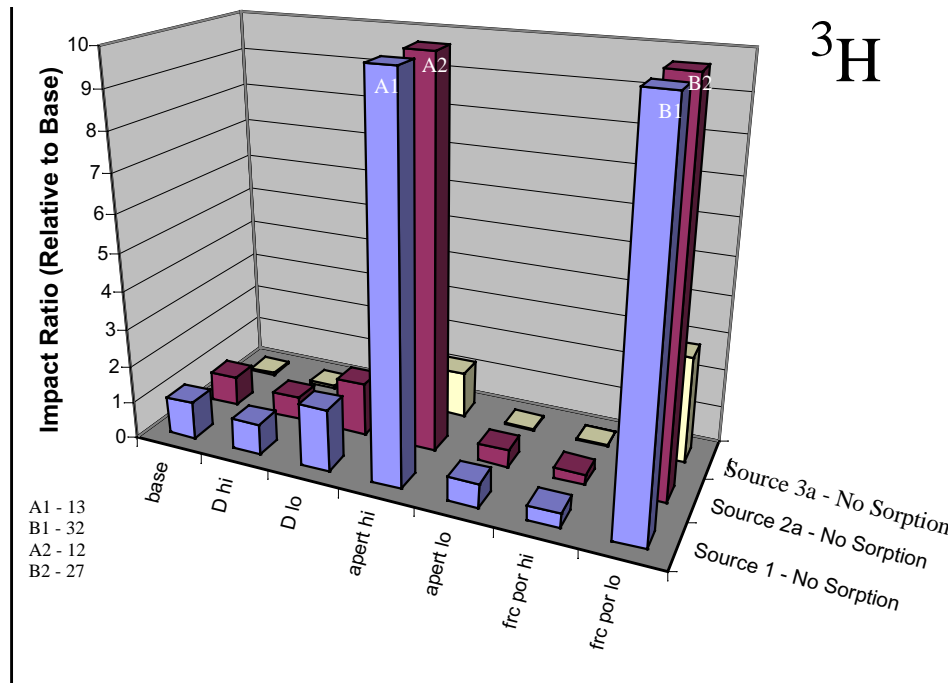


Figure 7-53. Impact ratios for **tritium** transport to the NTS boundary for simulations of 100 years.

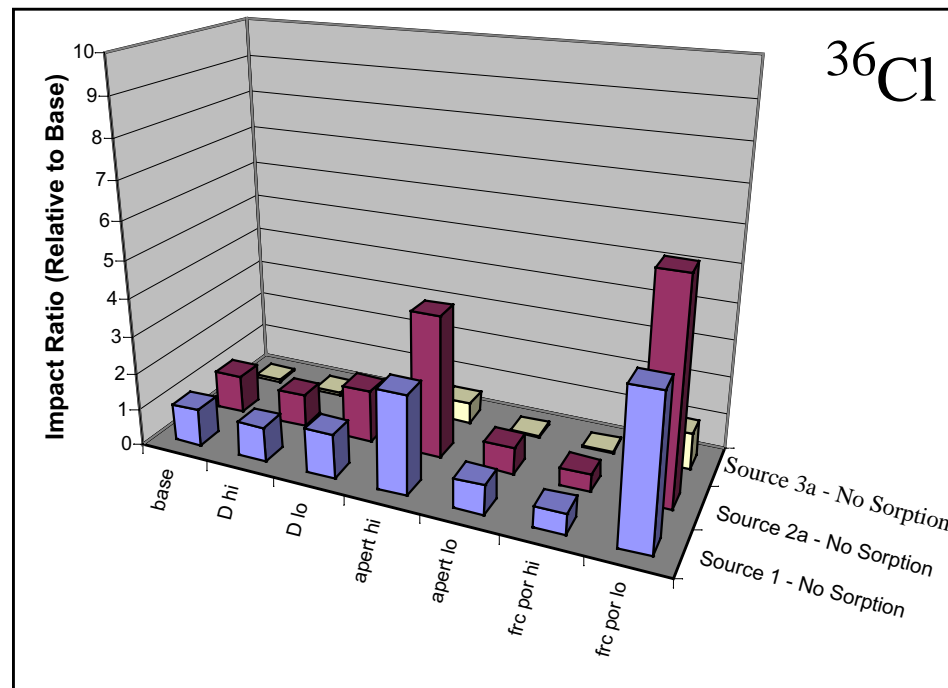


Figure 7-54. Impact ratios for **chlorine-36** transport to the NTS boundary for simulations of 100 years.

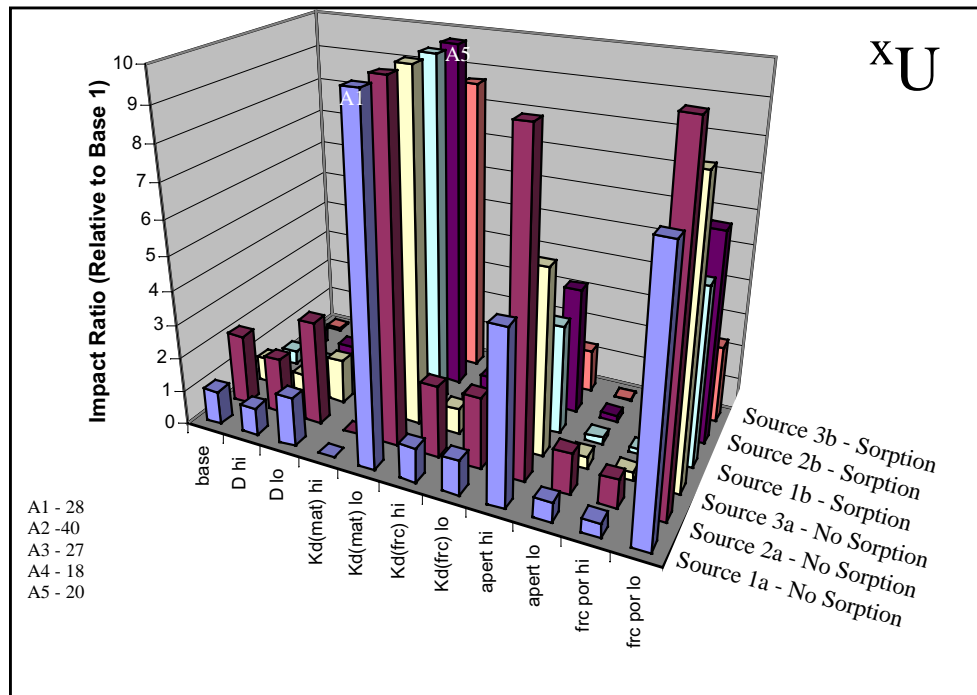


Figure 7-55. Impact ratios for **uranium** transport to the NTS boundary for simulations of 1000 years.

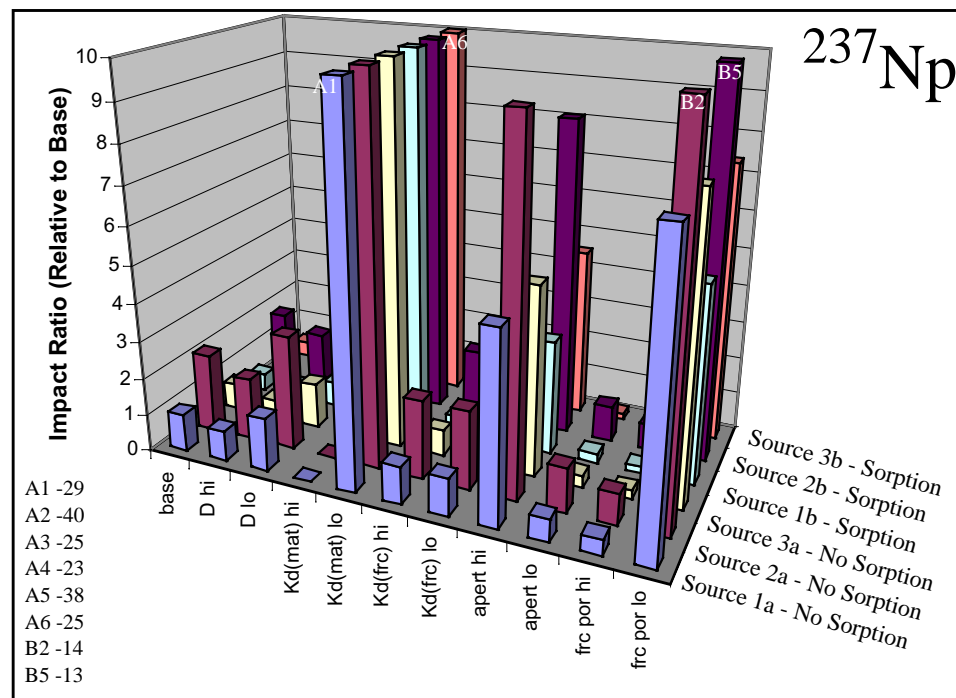


Figure 7-56. Impact ratios for **neptunium** transport to the NTS boundary for simulations of 1000 years.

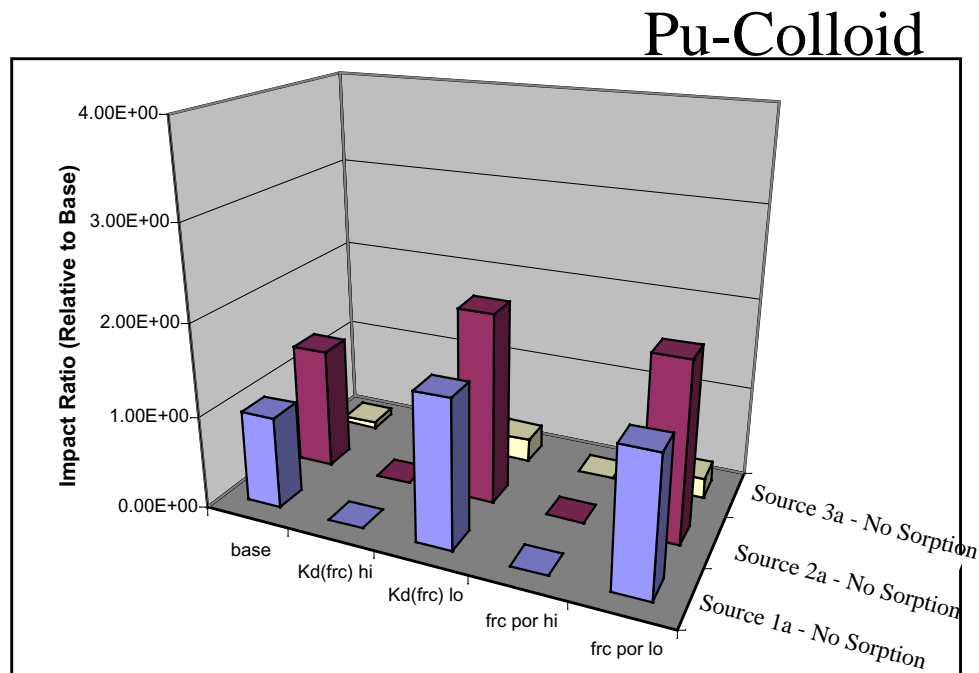


Figure 7-57. Impact ratios for **Pu-colloid** transport to the NTS boundary for simulations of 100 years.

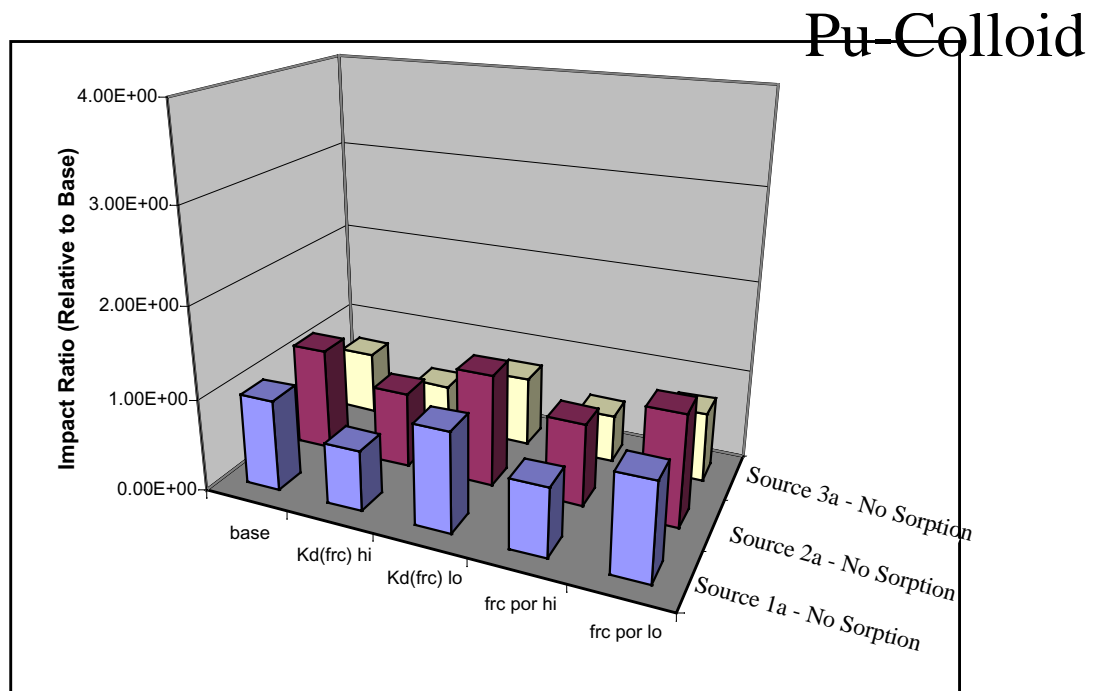


Figure 7-58. Impact ratios for **Pu-colloid** transport to the NTS boundary for simulations of 1000 years.

7.9.3 Parameter Sensitivity III: Analysis of Variation (ANOVA)

The model sensitivity study produced cumulative mass breakthrough data for 30 different geostatistical realizations using base-case parameters, high/low variations on up to five different parameters (D , R_f , Kd , b , and n), and six different source terms (Source 1A and 1B, Source 2A and 2B, and Source 3A and 3B; see Table 6-9). The Class I nuclides do not undergo sorption, so they are only analyzed for the non-sorbing source-term case. Section 7.9.1 shows figures of the average cumulative breakthrough results, as well as standard deviations considering all 30 realizations, at 30, 100, and 1000 years. Section 7.9.2 compares the average cumulative masses for each parameter and source-term variation to the base-case results with impact ratios. In this section, we present a quantitative evaluation that uses a classical statistical analysis of variation to compare the impact of variations in the different parameters and source functions on the cumulative breakthrough at the NTS boundary. ANOVA is employed to determine (1) the statistical significance of variation in all transport parameters for 30 geostatistical flow fields, (2) the statistical significance of specific transport parameter variations for 30 geostatistical flow fields, and (3) the statistical significance of source-term variation for 30 geostatistical flow fields. The level of significance chosen for this analysis is for a p-value of 0.05, meaning that we are using a confidence interval of 95% (the mean plus or minus 1.96 standard deviations).

A single-factor analysis of variation, termed ANOVA (Sokal and Rohlf, 1981), is conducted for each RN to determine statistical significance of variations of cumulative RN mass breakthrough at the NTS boundary after simulations of 30, 100, and 1000 years. The ANOVA considers the 30 heterogeneous geostatistical realizations to represent random and independent measurements on the same system. Each heterogeneous field is assumed equally probable. Hence, the variability between the means of simulations of different parameterization is a result of the changes in the parameters and does not reflect the variability between geostatistical realizations. Here, the 30 realizations for each variation in parameterization is termed a *study group*. Therefore, there are a total of 11 study groups (base case and high/low perturbations of the five sensitive parameters) for each source condition of each RN.

The statistical significance of an ANOVA is determined through a theoretical distribution called the F-ratio. The F-ratio is used to test variation for statistical significance and is simply the variance between study groups divided by the variance within study groups:

$$F = \frac{\sum (\bar{X} - \bar{\bar{X}})^2}{\sum (X - \bar{X})^2}, \quad (\text{Eq. 7-2})$$

where X is the single run value, \bar{X} is the mean of the study group, and $\bar{\bar{X}}$ is the mean of the ANOVA (the mean of all study groups). To determine statistical significance, the F-ratio, F , is compared to a critical F-ratio, F_{crit} , that is determined from the degrees of freedom for the two variances being considered. F_{crit} values are tabulated for $p = 0.05$ in Table E of Schor (1968), pp. 300-301. For a p-value of 0.05, the F-ratio will occur less than 5% of the time. In other words, the parameter variation is statistically insignificant if F is less than F_{crit} . Conversely, if F is greater than F_{crit} then the F-ratio will occur more than 5% of the time and the parameter variation is statistically significant for a 95% confidence interval.

Of the 14 RNs and species that were considered with a Model I ANOVA, 8 were found to have a statistically significant variation on a 95% confidence interval between the base case and

the high-low variable simulations for some of the source terms. These were the Class I, IV, and VI species. For the Class II, III, and V RNs, an ANOVA was not conducted because no breakthrough was observed for any of the simulations at 100 or 1000 years.

Single-Factor ANOVA for Each Source Function and all Parameter Variations

Tables 7-6 and 7-7 show the ANOVA F-ratios calculated at 100 and 1000 years, respectively, for each of the six different source functions. All results are based on cumulative mass breakthrough at the NTS boundary at the time specified for analysis (e.g., 100 years or 1000 years). Considered in the ANOVA for each source condition is the base-case study group and the 10 study groups of the five sensitive parameter variations (high and low for each parameter). The six source conditions (Source 1A through Source 3B) are defined in Table 6-9. The ANOVAs for each source demonstrate that only Class I, IV, and VI cumulative mass results warrant further paired parameter analysis to determine which parameters were most statistically sensitive. All of Class I 1000-year cumulative mass predictions are statistically insignificant except for the case of tritium. This discrepancy is explained below.

The ANOVA analysis shows that for the Class I RNs, tritium (^3H) mass accumulation is most sensitive to variations among the parameter variations and between the different source terms at both 100 years and 1000 years. The ANOVA also shows that even though there is statistical significance in parameter variation for the 100-year results of the remaining Class I nuclides, there is little or no significant difference for the 1000-year results. The explanation for the difference between tritium and the other Class I RNs lies in the short half-life of tritium. Discrepancies in cumulative mass arriving at separate times is enhanced if radioactive decay is high (i.e., the RN has a short half-life), as is the case for tritium. Cumulative mass curves are time integrations of the mass flux curves, which account for radioactive decay. Therefore, RNs exhibiting high radioactive decay (e.g., tritium) will show a marked difference in cumulative mass at late times for scenarios with different breakthrough times. Conversely, RNs exhibiting low radioactive decay (e.g., ^{36}Cl) will show little difference in cumulative mass at late times for such scenarios. To illustrate, Figure 7-59 shows both the mass flux and cumulative mass curves of tritium for the deterministic sensitivity simulations of low fracture porosity and high fracture porosity in the LAVA. Note how the low fracture porosity simulated mass arrives at the NTS boundary at an earlier time than the high fracture porosity. Also note how the mass flux of the later arrival is less as the time difference has allowed for more radioactive decay to occur. Comparing the time-integrated cumulative mass curves, we observe a large difference in cumulative mass at late times. Conversely, Figure 7-60 shows the same plots for ^{36}Cl . Because this RN does not exhibit much radioactive decay in 1000 years, the two mass flux curves are nearly identical except for their timing. Hence, at late times the cumulative mass for these two simulation scenarios is nearly identical. As a result, the difference in the tritium breakthrough at 1000 years is a reflection of its short half-life and not a reflection of parameter sensitivity. As a result, none of the Class I nuclides (including tritium) are evaluated with a paired comparison of means (as described in the next section) for 1000 years.

Table 7-6. Calculated F-ratios for ANOVA at 100 Years: Comparing Sensitivity to 6 Different Source Functions Using Base-Case Site-Scale Transport Parameters

(sources are defined in Table 6-9).

Class	Radionuclide	F_{crit}	SOURCE 1A	SOURCE 1B	SOURCE 2A	SOURCE 2B	SOURCE 3A	SOURCE 3B
Class I	Tritium	2.14	42	NBR	30	NBR	30	NBR
	Carbon	2.14	25	NBR	24	NBR	32	NBR
	Chloride	2.14	25	NBR	24	NBR	32	NBR
	Technetium	2.14	26	NBR	24	NBR	32	NBR
	Iodine	2.14	25	NBR	24	NBR	32	NBR
Class IV	Uranium	1.86	15	7	52	7	9	7
	Neptunium	1.86	15	15	11	9	9	8
Class VI	Pu-colloid	2.14	204	NBR	245	NBR	112	NBR
NBR - no breakthrough observed; No "B" source simulations conducted for Class I and Class VI radionuclides. F_{crit} is based on a $p = 0.05$.								

Table 7-7. Calculated F-ratios for ANOVA at 1000 Years: Comparing Sensitivity to 6 Different Source Functions Using Base-Case Site-Scale Transport Parameters

(sources are defined in Table 6-9).

Class	Radionuclide	F_{crit}	SOURCE 1A	SOURCE 1B	SOURCE 2A	SOURCE 2B	SOURCE 3A	SOURCE 3B
Class I	Tritium	2.14	41	NBR	30	NBR	30	NBR
	Carbon	2.14	3.4	NBR	0.32 NS	NBR	0.31 NS	NBR
	Chloride	2.14	3.3	NBR	0.29 NS	NBR	0.28 NS	NBR
	Technetium	2.14	3.4	NBR	0.29 NS	NBR	0.28 NS	NBR
	Iodine	2.14	3.3	NBR	0.29 NS	NBR	0.28 NS	NBR
Class IV	Uranium	1.86	186	133	127	147	144	133
	Neptunium	1.86	185	141	127	135	144	149
Class VI	Pu-colloid	2.14	201	NBR	193	NBR	174	NBR
NBR - no breakthrough observed; No "B" source simulations conducted for Class I and Class VI radionuclides. F_{crit} is based on a $p = 0.05$. NS - calculated F value is less then critical F value, therefore the ANOVA shows no significant variation.								

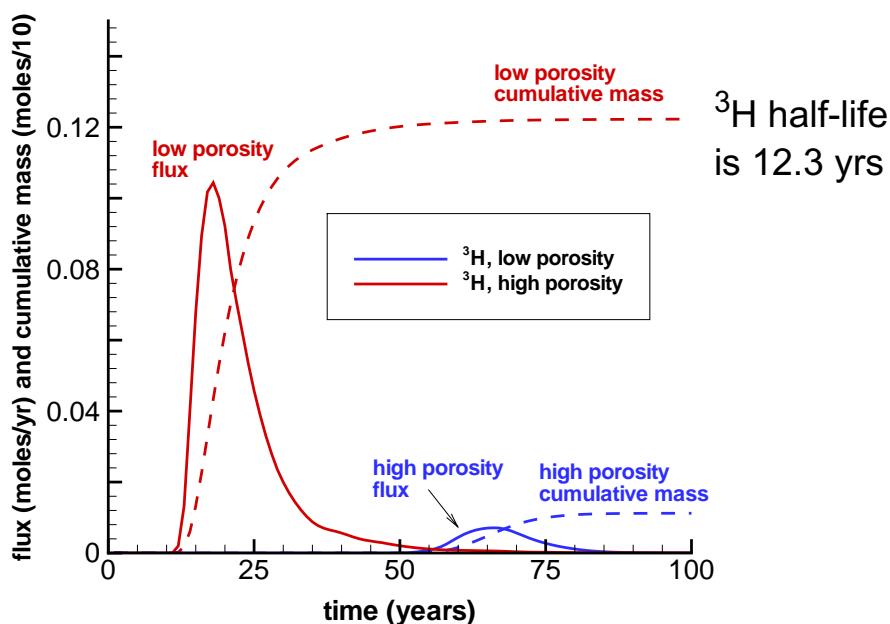


Figure 7-59. The mass flux and cumulative mass curves of tritium for the deterministic simulations of low fracture porosity and high fracture porosity in the LAVA at the NTS boundary. The late-arriving high-porosity ^3H has less mass because more radioactive decay has occurred.

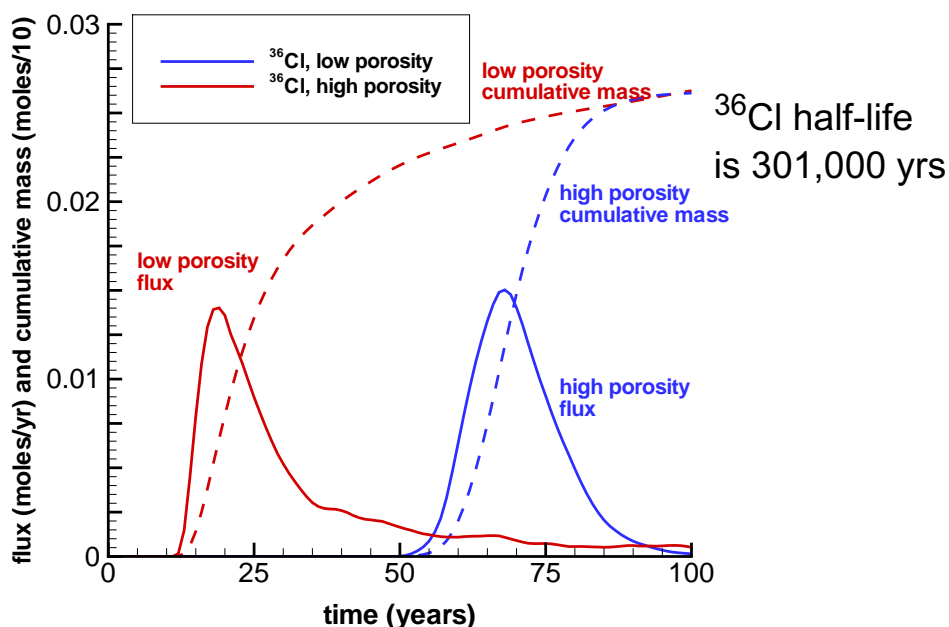


Figure 7-60. The mass flux and cumulative mass curves of ^{36}Cl for the deterministic simulations of low fracture porosity and high fracture porosity in the LAVA at the NTS boundary. The late-arriving high-porosity ^{36}Cl has comparable mass because little radioactive decay has occurred.

Statistical Significance of Transport Parameter Variation

Table 6-9 defines the six source conditions (Source 1A through Source 3B) and Figures 6-42 through 6-50 illustrate the cumulative mass curves for the BASE-CASE source conditions for all RNs. For Class IV and VI cumulative mass curves, the ANOVA calculations indicate there are statistically significant differences on a 95% confidence interval. To determine the individual sensitivities of each parameter variable, a planned comparison is conducted between the means of the study groups at base-case value, at high value, and at low value for each of the five sensitive parameter variables. This planned comparison calculates an F-value for each variable by taking the mean square between the study groups of concern and dividing by the mean square within the study groups calculated for the entire ANOVA. For example, for Source 1A U five hypotheses are tested. These hypotheses are the following: no significant difference from base-case parameter breakthrough occurs in breakthrough results using the high and low variations of the (1) diffusion coefficient, (2) fracture retardation factor, (3) matrix Kd , (4) fracture aperture, and (5) fracture porosity. If the F-ratio is less than or equal to the F critical, then the proposed null hypothesis is accepted and variation of that parameter for U breakthrough is statistically insignificant. Conversely, if the F-ratio is greater, then the alternative hypothesis is accepted and variation of that parameter for U breakthrough is statistically significant.

Tables 7-8 and 7-9 list the F-ratios for the paired comparison of study group means at 100 and 1000 years, respectively. For the simulation of Class I RN cumulative mass breakthrough at 100 years, the fracture porosity is the parameter that shows the most statistically significant variation. This means that expected variation in the fracture porosity will alter simulation results more than any of the other variables. Variations in fracture aperture are also statistically significant, but less so when compared to variations in fracture porosity. Because fracture porosity is derived as a function of fracture aperture and spacing, it is not surprising that variations in both porosity and aperture result in large uncertainty. Porosity changes affect velocity in fractures, and as a result, these changes affect the speeding up or slowing down of mass breakthrough. Therefore, for most of these simulations which have the onset of breakthrough occurring at ~100 years, cumulative mass variations that result from changes in fracture porosity are greater for the 100-year curves rather than for the 1000-year curves.

For the simulated Class IV RN cumulative mass breakthrough at 100 and 1000 years, matrix Kd is the most statistically significant parameter considered. Although fracture porosity is also statistically significant, the transport of Np and U is more affected by changes in matrix sorption in all F-ratio comparisons except for the cases of U breakthrough at 100 years for Sources 2B and 3B. It is interesting to note that for the 100-year cumulative mass curves (Table 7-8) produced by sources with chimney sorption (Source B simulations), the statistical significance of Kd goes down, whereas the statistical significance of fracture porosity goes up. Similarly, as the simulations decrease from high Ra (Source 1) to low Ra (Source 3), the statistical significance of Kd decreases, whereas the statistical significance of fracture porosity increases. This is because for chimney-sorbed or lower Ra source conditions, RN entrance is more restricted to the transport-facilitating, continuous, fractured LAVA aquifer. For the heterogeneous geostatistical simulations, the fractured LAVA aquifer is the primary aquifer of conductance due to its continuity. As the LAVA becomes the primary entry pathway for RN at lower Ra source conditions, the variation in fracture parameters become more statistically significant. The exact opposite holds for matrix parameter such as Kd (i.e., variation in Kd becomes less statistically significant for the lower Ra source conditions). For the 1000-year cumulative mass results these trends no longer hold. As

illustrated in Table 7-9, in the case of the 1000-year results, the statistical significance of variations in Kd and fracture porosity for different source conditions remains the same relative to Ra value or chimney sorption condition. This is because transport breakthrough has occurred before 1000 years for Class I, IV, and VI RNs and the cumulative mass curves are less affected by the time of entry from the source and more dependent on site-scale processes alone. For further analysis of the statistical significance of the source condition on 1000-year cumulative mass results, the BASE-CASE source conditions are directly compared by the ANOVA and paired comparison discussed below.

Statistical Significance of Source-Term Variation

An ANOVA analysis and paired comparison is conducted to investigate statistical differences in total mass crossing the NTS boundary at 100 and 1000 years. F-ratio calculations indicating the level of statistical significance can be compared between the different source conditions using base-case transport-model parameters. The hypothesis to be tested is whether the base-case parameter simulation with Source 1A produces the same cumulative mass breakthrough at the NTS boundary as with the other five source terms. If the F-ratio is higher than F critical, then the alternative hypothesis that they produce significantly different results is accepted and the difference between Source 1A and the tested source simulation is statistically significant. The six source conditions (Source 1A through Source 3B) are defined in Table 6-9, and the cumulative mass curves for the source conditions and base-case site-scale transport model parameter values are illustrated in Figures 6-42 through 6-50 for all RNs.

A source-term ANOVA that uses base-case parameter values is done for study groups of the cumulative mass of the six different sources. The ANOVA computes a statistically significant difference ($p = 0.05$) in the cumulative mass of Classes I and VI at 100 years and for Classes I, IV, and VI at 1000 years. A paired comparison between study group means is conducted for these groups. Tabulated in Table 7-10 are F-ratio values are tabulated for the paired comparison of means at a 100 and 1000 years. Note that for the cumulative mass at 100 years, only Class I and VI species are considered because all other species have no appreciable breakthrough at this time. The 100-year cumulative mass results indicate that the low Ra case source (Source 3A) results are significantly different from Source 1A. Conversely, the 100-year medium Ra case (Source 2A) results are not significantly different from Source 1A. This insignificance is because the lower Ra Source 3A release to the LAVA is significantly slower than the Source 1A release to the LAVA. The medium Ra Source 2A release to the LAVA is not significantly slower than the Source 1A release.

Interestingly, for these heterogeneous simulations the greatest mass release to the LAVA occurs for the medium Ra Source 2A. This is because more mass is convected to the LAVA for Source 2A than for Source 1A because the latter source produces a large amount of mass to the TSA. Medium Ra Source 2A releases more mass to the LAVA than lower Ra Source 3A because the latter source's mass movement is impeded by the low chimney permeability. Because the LAVA is the primary pathway of mass movement in the heterogeneous geostatistical simulations, Source 2A ultimately delivers more mass than any other source condition. This result is borne out by the statistically significant difference between Source 2A and Source 1A cumulative mass results at 1000 years for all RNs except ^3H (Table 7-10). The reason that the cumulative mass of ^3H is not statistically different has to do with tritium's relatively rapid radioactive decay (see Figures 7-59 and 7-60 and the discussion above). For the sources including chimney sorption

(Source B), cumulative mass results at 1000 years follow the same pattern as the non-sorbing chimney releases. That is, the cumulative mass result at 1000 years for the Source 2B release is significant, whereas the result for the Source 3B release is not. Summarizing, the ANOVA analyzing the variation of source conditions demonstrates that both the rate and location of RN release show significant variation.

Table 7-8. F-ratios for Each RN for Each Uncertain Transport Parameters at 100 years. The F_{crit} is 3.04 for Class I and VI and 3.03 for Class IV.

Source (see Table 6-9)	RN Species	F-ratio for Diffusion	F-ratio for Matrix Kd	F-ratio for Fracture Kd	F-ratio for Aperture	F-ratio for ϕ_f
SOURCE 1A	³ H	1.01e-02	n/a	n/a	7.47	45.2
	¹⁴ C	2.84e-02	n/a	n/a	5.36	16.9
	³⁶ Cl	2.86e-02	n/a	n/a	5.45	17.2
	¹²⁹ I	2.86e-02	n/a	n/a	5.45	17.2
	⁹⁹ Tc	2.9e-02	n/a	n/a	5.65	17.9
	U	0	29.2	0	4.61e-2	1.73
	Np	0	29.2	0	4.61e-2	1.73
	Pu-colloid	n/a	n/a	10.1	n/a	17.1
SOURCE 1B	U	0	7.69	0	7.49e-2	7.33
	Np	0	26.8	0	5.21e-2	2.42
SOURCE 2A	³ H	8.84e-3	n/a	n/a	5.68	32.7
	¹⁴ C	5.16e-2	n/a	n/a	5.86	17.3
	³⁶ Cl	5.22e-2	n/a	n/a	5.91	17.5
	¹²⁹ I	5.22e-2	n/a	n/a	6.01	17.5
	⁹⁹ Tc	5.31e-2	n/a	n/a	5.91	17.8
	U	0	19.6	0	5.18e-2	2.51
	Np	0	19.4	0	5.18e-2	2.52
	Pu-colloid	n/a	n/a	9.05	n/a	13.9
SOURCE 2B	U	0	2.72	0	8.04e-2	11.8
	Np	0	13.5	0	6.03e-2	4.08
SOURCE 3A	³ H	7.95e-3	n/a	n/a	5.64	33.0
	¹⁴ C	3.87e-2	n/a	n/a	7.88	29.2
	³⁶ Cl	3.66e-2	n/a	n/a	7.82	29.5
	¹²⁹ I	3.66e-2	n/a	n/a	7.82	29.5
	⁹⁹ Tc	3.14e-2	n/a	n/a	7.65	30.4
	U	0	14.6	0	6.56e-2	4.78
	Np	0	13.5	0	6.93e-2	5.55
	Pu-colloid	n/a	n/a	16.2	n/a	79.1
SOURCE 3B	U	0	3.08	0	7.48e-2	11.5
	Np	0	10.9	0	6.80e-2	5.58

Bold italic numbers are the largest F-ratio for that particular RN, indicating the most statistically significant variation between source conditions. The results for Sm, Am, Sr, Eu, Cs, and Pu are all at detection limits and are not significant.

Note that conservative species (³H, ¹⁴C, ³⁶Cl, ¹²⁹I, ⁹⁹Tc, and Pu-colloid) do not have Source B estimations, so the F-ratios for these are marked n/a (not applicable).

Table 7-9. F-ratios for Each RN for Each Uncertain Transport Parameters at 1000 years. The F_{crit} is 3.04 for Class I and VI and 3.03 for Class IV.

Source	RN Species	F-ratio for Diffusion	F-ratio for Matrix Kd	F-ratio for Fracture Kd	F-ratio for Aperture	F-ratio for ϕ_f
SOURCE 1A	U	2.89e-2	311	7.56e-5	5.53	16.9
	Np	2.83e-2	311	7.32e-5	5.47	16.8
	Pu-colloid	n/a	n/a	9.35	n/a	7.05
SOURCE 1B	U	1.22e-2	240	3.50e-6	4.35	15.4
	Np	9.29e-3	249	1.29e-7	2.89	10.1
SOURCE 2A	U	4.53e-2	198	3.33e-7	6.17	16.5
	Np	4.53e-2	198	2.04e-7	6.17	16.5
	Pu-colloid	n/a	n/a	5.21	n/a	3.44
SOURCE 2B	U	3.40e-2	253	8.10e-5	6.41	20.0
	Np	4.49e-2	215	4.53e-5	6.01	17.6
SOURCE 3A	U	3.84e-2	241	1.75e-4	6.85	19.7
	Np	3.85e-2	241	2.02e-4	6.89	19.8
	Pu-colloid	n/a	n/a	6.23	n/a	4.25
SOURCE 3B	U	1.22e-2	240	3.50e-6	4.35	15.4
	Np	3.32e-2	258	4.70e-5	6.82	20.4

Bold italic numbers are the largest F-ratios for that particular RN, indicating the most statistically significant variation between source conditions. The results for Sm, Am, Sr, Eu, Cs, and Pu are all at detection limits and are not significant. The results for Class I radionuclides are not included because variation at 1000 years for these RNs is not as significant as variation at 100 years.

Table 7-10. F-ratios at 100 and 1000 Years for Each RN Comparing Source 1B, 2A, 2B, 3A, and 3B Results to Source 1A Results. F Critical is 3.9.

Time of Cumulative Mass Analysis	RN Species	F-ratio for SOURCE 1B to SOURCE 1A	F-ratio for SOURCE 2A to SOURCE 1A	F-ratio for SOURCE 2B to SOURCE 1A	F-ratio for SOURCE 3A to SOURCE 1A	F-ratio for SOURCE 3B to SOURCE 1A
100 years	³ H	n/a	0.392	n/a	8.24	n/a
	¹⁴ C	n/a	0.020	n/a	8.54	n/a
	³⁶ Cl	n/a	0.015	n/a	8.89	n/a
	¹²⁹ I	n/a	0.015	n/a	8.89	n/a
	⁹⁹ Tc	n/a	0.0077	n/a	9.47	n/a
	Pu-Colloid	n/a	0.242	n/a	6.72	n/a
1000 years	³ H	n/a	0.017	n/a	8.83	n/a
	¹⁴ C	n/a	18.7	n/a	7.53	n/a
	³⁶ Cl	n/a	18.9	n/a	3.96	n/a
	¹²⁹ I	n/a	18.8	n/a	3.97	n/a
	⁹⁹ Tc	n/a	19.3	n/a	0.194	n/a
	U	1.62	6.18	1.76	0.278	4.44
	Np	1	4.19	2.07	0.290	1.09
	Pu-Colloid	n/a	19.0	n/a	1.84	n/a

Bold italic numbers are the largest F-ratio for that particular RN, indicating the most statistically significant variation between source conditions. The results for Sm, Am, Sr, Eu, Cs, and Pu are all at detection limits and are not significant.

Note that conservative species (³H, ¹⁴C, ³⁶Cl, ¹²⁹I, ⁹⁹Tc, and Pu-colloid) do not have Source B estimations, so the F-ratios for these are marked n/a (not applicable).

7.9.4 Summary of Transport Simulations on Heterogeneous Flow Fields

- Rapid transport occurs in the LAVA because it was constructed as an intact lithologic unit and is characterized as fractured media. Hence, transport results in the LAVA aquifer are most sensitive to parameters associated with fractures. Source conditions that release primarily to the LAVA (SOURCE 2A) lead to significantly more cumulative mass breakthrough after a simulation of 1000 years.
- RN transport released from the source model in the TSA region is not as rapid as in the LAVA because the welded tuff between BENHAM, well ER-20-5 #1, and the NTS boundary is not maintained as an intact lithologic unit in all heterogeneous flow fields.
- Using base-case transport properties and flow-field realization #3, estimates of groundwater concentration of Pu (on colloids) at observation well ER-20-5 #3 (sampling the LAVA) are consistent with the field observations of Kersting et al. (1999). The travel time of the elevated concentration pulse of Pu-colloid is dominated by the flux and fracture porosity term used in the model. Differences between modeled and observed concentrations are related to the fact that an unclassified average mass value for Pu was used in the source-term model and dilution at sampling wells due to pumping is only roughly approximated.
- Using base-case transport properties and flow-field realization #3, estimates of groundwater concentration of Pu (on colloids) at observation well ER-20-5 #1 (in the TSA welded tuff) are not consistent with field observations because (a) very few particle paths intersect this well and (b) migration rates of releases are too slow due to the lack of connected fracture pathways. This mismatch with field observations indicates that for the TSA aquifer, flow-field realization #3 is less probable than the deterministic model and likely other heterogeneous realizations in capturing correctly flow and transport properties.
- Sensitivity analyses show that there are significant variations in results between the 30 different heterogeneous attribute fields considered. The standard deviation is sometimes more than twice the average across the 30 fields. This indicates that there is significant model uncertainty due to lack of complete knowledge about the system heterogeneity. The attribute fields were generated assuming they are all equiprobable. Additional information regarding solute travel times to the ER-20-5 wells may be appropriate for identifying which realizations are actually more probable than others. With more than 30 realizations, it may be reasonable to use transport results at the ER-20-5 observation wells to select and discard realizations for consideration.
- The non-reactive RNs (^3H , ^{14}C , ^{36}Cl , ^{99}T , and ^{129}I) are mobile and retarded only by matrix diffusion and differences in fracture porosity. Of these Class I RNs, ^3H is the only species that experiences noticeable decay over 1000 years, causing great sensitivity to parameters that affect its migration time to the NTS boundary. Therefore, predictions of ^3H migration are sensitive to fracture porosity, fracture aperture, and diffusion coefficients. Sensitivity to the diffusion coefficient for other Class I RNs does not show up as being significant primarily because a small range of uncertainty is considered.
- Fracture porosity and fracture aperture (two correlated parameters) are the most statistically sensitive parameters for all non-sorbing RNs (Class I and VI).
- Matrix sorption Kd is the most statistically sensitive parameter for sorbing RNs. This

sensitivity is due to the large range of uncertainty used in this study for Kd .

- Mobility of the reactive RNs U and Np is statistically sensitive to fracture porosity. The fracture porosity controls the velocity of the solutes and, hence, the potential of their diffusion into the matrix and subsequent reaction with immobile minerals.
- An important uncertain parameter not considered in this sensitivity study is the oxidation/reduction potential (Eh) of the groundwater. Appendix F shows predictions are very sensitive to this parameter. Including Eh changes in this model would simply entail recalculating the effective Kd for fracture and matrix minerals and re-estimating the ratio of Pu sorbing to colloidal material.
- Another parameter not considered in this sensitivity study is the available colloid site concentration. This uncertain parameter, also examined in Appendix F, leads to substantial sensitivity in the actual mass of Pu that is mobile in these systems.
- Finally, this sensitivity study does not fully examine uncertainties associated with reactive mineral surface area as was done in Appendix F. Whereas only the distribution of different fracture minerals is examined in this chapter, how much of the fracture coating is actually accessible remains uncertain.
- Multiple different source terms were considered with respect to their implications on mass breakthrough at the NTS boundary. The different source parameters lead to different mass fluxes to the TSA and LAVA aquifers in the site-scale model. The downstream results show significant sensitivity to which source function is used, indicating CAU analyses should couple strongly to source-term uncertainty.

7.10 Summary and Conclusions

In this chapter, we discuss how a site-scale particle-tracking model was developed and applied to both deterministic and heterogeneous flow fields. Migration of multiple RNs to the ER-20-5 observation wells and the NTS boundary (approximated with the southern face of the site-scale model) are simulated. Section 7.7.5 summarizes the transport results on the deterministic model and Section 7.9.4 summarizes the transport results on the heterogeneous attribute models.

The deterministic model effectively predicts the observations of all RNs found at both ER-20-5 wells. In addition to effectively representing spatially varying attributes, the geostatistical model predicts the observations of Kersting et al. (1999) at well ER-20-5 #3 (note that of the reactive RNs observed, only Pu was considered for this comparison with the geostatistical model). These results are strongly related to the groundwater flux and fracture porosity in the pathways downstream of BENHAM. As currently simulated, the continuity required (and present in the deterministic model) does not always exist in the heterogeneous attribute models for the welded tuff sampled by ER-20-5 #1. Adjusting the heterogeneous attribute maps would require additional control to force a continuous welded tuff unit at the elevation of well ER-20-5 #1. Perhaps this could be done with a larger correlation length scale. Alternatively, the ability to match field observations with any given heterogeneous attribute map could be used as a discriminator for discarding or keeping the realization.

The site-scale particle-tracking model is particularly effective for the sensitivity study because it considers the multiple RNs for multiple source conditions, transport parameter sets, and flow fields. For all of the cases, the analysis indicates that in the absence of colloids, it is unlikely that Class II, III, and V RNs (Sm, Am, Eu, Sr, Cs, and Pu) migrate from BENHAM to either of the ER-20-5 wells or to the NTS boundary over 1000 years. However, when colloids are considered the mobility of a small amount of Pu, Eu, Am, and Cs (those reactive RNs found at the observations wells) increases substantially. The relationship between the process-level model, which was used to predict how much Pu released from the MG could be estimated to be irreversibly sorbed to colloids, and the particle-tracking model which uses that ratio to specify a Pu-colloid species is important. Linkage between the two models is necessary because the process-level model shows strong correlation between the amount of Pu sorbed onto colloids and groundwater chemistry, colloid concentration, and other competitive processes. The amount of Eu, Am, and Cs effectively bound irreversibly to colloids is treated as a fitting parameter by comparing simulations with field observations. Thus, the factors prescribing such amounts are uncertain because the models are based on an unclassified average source inventory.

Class I RNs (^3H , ^{14}C , ^{36}Cl , ^{99}Tc , and ^{129}I) showed significant mobility, affected only by diffusion and fracture porosity, both of which seem to affect mostly the exact time of arrival at the NTS boundary. Cumulative mass arrivals of Class I RNs at the NTS boundary over 1000 years are not highly sensitive to transport parameters, except ^3H which is very sensitive to any parameter that impacts residence times. With its short half-life, small increases in residence time lead to large decreases in ^3H mass arrivals at the NTS boundary.

In the absence of colloids, Class IV RNs (U and Np) are the only sorbing RN's to reach the well and boundary, but do so at late times (>150 years for the wells, >550 years for the boundary). The RNs are sensitive to processes that lead to retardation including matrix Kd and fracture retardation. However, the most important component of fracture retardation, the reactive surface area of coating minerals, was highlighted in Appendix F, not here.

From the study presented in this chapter examining the base-case conditions, the following specific conclusions can be drawn:

- Non-sorbing RNs and colloids are likely to arrive at the ER-20-5 wells and the NTS boundary in under 50 years.
- Slightly sorbing RNs (Kd less than or equal to 10 cc/g) can arrive unaided by colloids at the ER-20-5 wells and the NTS boundary, but only after migrating hundreds of years.
- The continuity of the LAVA and TSA aquifers is critical in determining the downstream breakthrough of RNs. For example, the deterministic model, with continuous LAVA and TSA aquifers, yields breakthrough of RNs at both observation wells, consistent with field data. However, the lack of a welded tuff aquifer in heterogeneous attribute study #3 yielded much less Pu-colloid at later times.
- Dilution effects at sampling wells are only roughly approximated here. Therefore, estimates of concentration in groundwater are less accurate than estimates of mass transport. Additional modeling studies could serve to link models of mass transport with well pumping and concentration estimates.
- Assuming irreversible sorption of Pu to colloids leads to mobility as Pu-colloids. Thus, the

amount of Pu that is available for transport depends on the amount assumed to sorb irreversibly to colloids, a factor determined by sorption and desorption rates, residence time, and competing reactions with immobile minerals--these factors are addressed with the process-level model. Similar arguments hold for all other reactive RNs, although far more supporting data exists for Pu.

- Integrating findings from the deterministic and heterogeneous models, we summarize that groundwater transport is a feasible mechanism to explain the 1.3 km horizontal and 0.5 km vertical migration from BENHAM to the ER-20-5 wells of all RNs listed in Tables 1-1 and 1-2 in less than 30 years, a time necessary for concurrence with field-findings of Kersting et al. (1999).

Chapter 8: Summary and Recommendations

8.1 Review of the Integrated Model

The objectives of this project were to develop a modeling framework that evaluates the processes and mechanisms by which radionuclides (RNs) migrate in Pahute Mesa groundwater. Specifically, this modeling task set out (1) to develop a methodology that can help explain the field observations of Kersting et al. (1999) and (2) to provide a defensible predictive tool for other Pahute Mesa modeling needs. To that end, a three-component approach was developed that integrates a sub-CAU flow model, source-term models, and site-scale transport models into a predictive framework. With this framework, simulations were conducted that

- provide estimates of aquifer properties and flow solutions that match head observations in 23 wells,
- predict RN releases from cavity/chimney systems incorporating processes of melt glass (MG) dissolution and thermal convection,
- predict RN concentrations consistent with field observations at both ER-20-5 wells, and
- provide sensitivity analysis for uncertain parameters.

8.1.1 Sub-CAU Flow Model

In addition to providing hydrologic control on the site-scale domain, the sub-CAU model determines aquifer, aquitard, and fault-zone permeabilities needed for the model to match head observations in boreholes. The sub-CAU flow model demonstrates the role of the Boxcar Fault by creating a steep hydrologic gradient within the study domain. Also, low-permeability aquitards are required to preserve both an upward gradient from a deep, high-pressure unit and a downward gradient in shallow units near the water table. The sub-CAU flow domain is significantly more complex than initially anticipated and, as the model sensitivity analysis indicates, is incompletely constrained by the limited data, primarily because aquifer and aquitard properties were estimated for HSUs in which no head measurements exist. To capture with greater confidence all the complexities associated with the groundwater flow system, a larger domain with more head observations in more HSUs would be required (e.g., the CAU domain). Nevertheless, the sub-CAU model effectively predicts the observations within the domain, highlights issues with fault-zone hydrologic properties, and provides reasonable boundary conditions for the site-scale flow and transport model.

8.1.2 Source-Term Models

Two source-term models complement each other in predicting source releases to the site-scale domain. A two-dimensional, fully coupled, thermal-hydrologic-chemical (THC) transport model is used first to investigate the complex relationship between MG dissolution and convective, nonisothermal flow. This model predicts how the rate of glass dissolution, and hence RN release, changes during the dynamic cooling process within the cavity/chimney system. It also highlights the importance of modeling correctly the early time processes after the chimney re-wets because dissolution rates at that early time may dominate RN releases. Because of its fully coupled

formulation, the THC model can address mixing issues in the transient flow fields associated with convective circulation cells in the cavity/chimney system that may not be adequately described by one-dimensional models along streamlines. However, extension of the THC model (developed primarily as a prototype in this study) from two to three dimensions is required for more detailed studies of the coupled phenomena in the source region.

Thermal relationships for glass dissolution rates in the non-isothermal source region are applied to a particle-release function for a three-dimensional source-term model. This model simulates the transient thermal flow and cooling processes in the cavity/chimney system and couples particle release in the MG to the temperature-dependent dissolution processes identified in the THC model. The efficiency of the three-dimensional source-term model allows for consideration of multiple sensitivity cases based on uncertainty in cavity/chimney hydrologic properties, as well as uncertainty in initial thermal conditions. For each sensitivity simulation, we compute mass fluxes of multiple RNs exiting the source region and entering the site-scale flow domain. The mass fluxes become the input functions for site-scale transport models. Additionally, the three-dimensional source-term model is used to develop and test a non-dimensional relationship, the Rayleigh number, for assessing the potential for vertical flow and RN transport in cavity/chimney systems. Comparisons of Rayleigh numbers with three-dimensional model results for a variety of scenarios confirm that, for this system, they are a reasonable indicator of flow and transport processes in the chimney. This approach may be extendable to a variety of different geologic settings as part of the source-term screening process.

8.1.3 Site-Scale Transport Models: Descriptions

Site-scale transport modeling is performed primarily with a particle-tracking model. However, a site-scale reactive-process-level model was developed to (1) provide insight into governing processes and mechanisms and (2) establish a technical basis for assumptions made in the particle-tracking model. The reactive-process model is an extension of a model developed and validated with laboratory column experiment data.

Process Model: Laboratory Column Experiment

The chemical and physical processes considered in the dual-porosity reactive transport model are (1) Pu speciation, (2) kinetic Pu–colloid reactions, (3) filtration of colloids on the fracture walls, (4) solute diffusion into the matrix, and (5) surface complexation and ion exchange of RNs with fracture minerals and matrix minerals. Because speciation and surface reactions are expected to occur fast enough for relative groundwater velocities to warrant equilibrium formulations, their representation in this model is simplified by assuming unchanging chemical conditions such as pH away from the source regions. However, successful simulation of the laboratory experiment involving Pu and clay colloids required a kinetic formulation of the Pu–colloid reaction.

Process Model: Field Scale

The process-level model is extended to the site scale by simulating reactive transport along streamtubes using the Generalized Dual-Porosity Model (GDPM) to represent fracture-matrix interactions. The GDPM method allows for heterogeneous attribute distributions including fracture aperture, spacing, and coating properties, as well as matrix K_d and porosity. With the GDPM model and hundreds of streamtubes emanating from multiple source locations, transport simulations are conducted for 14 different RNs in a three-dimensional heterogeneous site-scale

model. Multiple simulations are conducted to analyze transport parameter sensitivity with this model.

Particle-Tracking Model: Field Scale

The field-scale process model is abstracted to a more efficient simulator that uses dual-porosity reactive particle-tracking transport and convolution integrals. The particle-tracking module is used to generate unit source-term breakthrough curves at the ER-20-5 observation wells and the NTS boundary, considering the processes of matrix diffusion, retardation in fractures, and equilibrium sorption in the matrix. These breakthrough curves are then convolved with transient source-term model results to process correct mass flux curves at the observation wells and the NTS boundary. The efficiency of the field-scale particle-tracking transport model lends itself to extensive parameter sensitivity analyses.

8.1.4 Site-Scale Transport Models: Results

Process-Model Results:

The site-scale reactive-process model is applied only to a single heterogeneous domain and is used to evaluate governing mechanisms controlling transport in this groundwater system. This model demonstrates that, with expected parameter values, migration of very low quantities of Pu from BENHAM to the ER-20-5 observation wells can occur in less than 30 years if a continuous fractured aquifer exists. In the attribute model used in this study, the lava connecting BENHAM to well ER-20-5 #3 is continuous and fractured. The model simulations predict migration of Pu-colloid to that well in less than 30 years. However, the pathways from the BENHAM chimney to the upper observation well, ER-20-5 #1, encounter not only welded tuff, but non-welded tuff and bedded tuff also, both of which are classes that are not fractured. Along such pathways, rapid migration does not occur because (a) the velocities are lower in matrix-flow material and (b) retardation via matrix sorption is increased, causing Pu to desorb from the colloids and sorb onto immobile minerals when expected values for Pu-colloid desorption rates are used. The data supporting the expected values in the process model were only for clay colloids. However, recent experimental results indicate that even slower desorption of Pu from zeolitic colloids is warranted. The stronger attraction between Pu and zeolitic colloids is addressed in the parameter sensitivity study and with the site-scale particle tracking model.

The sensitivity study with the site-scale process model shows that predictions are sensitive to uncertainty in some model parameters. These include Eh, fracture-mineral reactive surface area, matrix Kd , the reaction rates for Pu-colloid formation, and colloid site concentrations associated with naturally occurring colloids (note, colloid-facilitated transport is only considered for Pu). All these parameters affect significantly the mass of Pu, U, and Np arriving at the NTS boundary in less than 1000 years. The diffusion coefficient does not generally emerge as a significant uncertain parameter because a small range in uncertainty was used. However, a small range in matrix diffusion uncertainty still impacts the transport process for U and Np migration in the upper volcanic units associated with TSA releases (upper aquifer) from the BENHAM chimney.

Particle-Tracking Model Results

The particle-tracking model simulates transport on the deterministic property field and on all 30 heterogeneous property fields. Additionally, six different source-term functions are considered for reactive RNs and three source-term functions are considered for non-reactive RNs.

Using expected values for parameters and the deterministic property model, simulated travel times and groundwater concentrations are consistent with the field observations for all RNs found in both ER-20-5 observations wells. Simulations are conducted using both BENHAM and TYBO as source locations. No simulations predict TYBO releases arriving at ER-20-5 #3 under any conditions. Allowing for a large lateral dispersion coefficient and a fairly large capture zone, the simulations do show the possibility of TYBO arrivals at ER-20-5 #1. However, because the simulations for BENHAM releases are consistent with the observations in both ER-20-5 #1 and #3, and because Kersting et al. (1999) identified the Pu found in both wells to have originated at BENHAM, not TYBO, the reasonable conclusion for reactive species is that TYBO releases are not captured in any significant quantities at ER-20-5 #1. Based on the simulations and association, the same conclusion could be drawn for non-reactive species. However, if we could prove that colloid-facilitated transport is somehow more likely from BENHAM than from TYBO (e.g., due to emplacement material), then both BENHAM and TYBO are likely contributors to the observations of non-reactive species.

Using expected values for parameters and one of 30 heterogeneous property models (#3) leads again to prolonged travel times to ER-20-5 #1 because transport pathways leaving the BENHAM chimney at the upper release location (the TSA in the source models) encounter not only welded tuff but also bedded tuff and nonwelded tuff. The particle-tracking results on field #3 are consistent with (1) the field observations of Kersting et al. (1999) in well ER-20-5 #3 in the LAVA and (2) the results from the process-level reactive-transport model, with one exception. In the particle-tracking model, Pu-colloid is predicted to arrive at ER-20-5 #1 when expected values are used for transport parameters, although this takes place well after 30 years. Although the Pu-colloid sorption and desorption reactions are modeled with kinetic rates in the process model, the particle-tracking model assumes that a small amount of the total released Pu inventory is irreversibly sorbed onto colloids. The assumption is based upon, and consistent with, the process model for rapid migration in fractured aquifers. But, when flow velocities are decreased (as in bedded tuffs), then more desorption occurs in the process model. Sensitivity simulations conducted with the process model indicate that the amount of mobile Pu depends upon the rates of that reaction. Recent results obtained for Pu and zeolitic colloids indicate that the desorption rate of the reaction is significantly less for zeolites than for clay, as was used in the process model (Kersting and Reimus, 2002). Therefore, a more irreversible formulation is warranted and would bring the process and abstraction models closer together again, even for slow-velocity systems. However, this does not resolve the issue of fast migration from BENHAM to ER-20-5 #1. These results indicate potential options for future work. Either the TSA would need to be forced to be continuous as the LAVA was or the simulation process could be used to select and discard realizations dependent upon their ability to provide matches to field observations.

A detailed set of parameter-sensitivity studies were conducted with the site-scale transport model. These studies included variation of each transport parameter for each RN class for each different source term. The results generated by these studies are numerous, all of which require statistical analysis. Therefore, a comparison of mean cumulative breakthrough mass at the NTS boundary between simulations using BASE-CASE parameters and parameter perturbations was conducted. Then, using the more elegant Analysis of Variation (ANOVA) from classical statistics, significance of result variations within parameter groups (across the 30 realizations) and between parameter groups was assessed. The parameter-sensitivity study confirms findings acquired with the site-scale process model. Namely, key uncertain parameters to which results are most sensitive

include fracture porosity and matrix Kd . The fracture porosity affects directly the solute velocity. Lower porosities lead to earlier arrivals of solutes at the NTS boundary. Matrix diffusion and matrix Kd lead to a combined retardation factor in the particle-tracking model. Because the matrix Kd has the larger range of uncertainty of the two processes, it emerges as the more dominant parameter to which results are sensitive. Finally, results are sensitive to the source-term function. If the chimney controls the release of RNs to the site-scale domain either through retardation, retention, or by lacking the convection cells to facilitate migration to the upper aquifer, then the results at the NTS boundary are ultimately impacted, thereby highlighting the importance of considering the entire plausible range of source-term processes and properties.

8.1.5 Integrating Heterogeneous Attribute Maps

In this study, independently generated maps of heterogeneous lithologic-class distributions and heterogeneous rock-permeability distributions were used in the site-scale transport simulations. These maps were generated because examination of bore-hole data indicates that significant heterogeneity exists within any HSU identified in the deterministic model. Therefore, it is expected that proper representation of the material heterogeneities will lead to more accurate assessments of dispersive transport processes. However, in executing this analysis, two very important observations were made.

First, simulating only some of the governing heterogeneous attributes but not others may lead to inconsistencies in model results. In this study, permeability maps were generated, but not corresponding maps of key transport parameters such as fracture characteristics. Therefore, assumptions were made about fracture characteristics based on lithologic class. The result is that a connected fracture pathway between the BENHAM chimney and well ER-20-5 #1 is not guaranteed. Second, simulated permeability distributions do not provide distinction between classes. Thus, simulated flow paths in the welded tuff exit readily to other classes characterized by low velocities and increased solute retardation.

8.1.6 Confidence in Results

The simulations presented in this report do not lend themselves to formal assignment of specific confidence intervals because probabilities are not attached to parameter uncertainties. Such probability distributions are currently under development for the Western Pahute Mesa Data Documentation Package. However, confidence can be discussed in qualitative terms. Most importantly, simulations using expected values for transport parameters and the simple HSU representation of aquifers and aquitards yield travel times and concentrations consistent with measured concentrations of all RNs at both ER-20-5 observation wells. With these results, we are confident that we have generally captured the complex process of source release and site-scale migration. We can not ignore that each parameter used at its expected value in those simulations is uncertain. The data tables presented throughout this report show expected, minimum, and maximum values. Therefore, studies were required to identify to which parameters model results are most sensitive. Such sensitivity studies also take into consideration heterogeneity. These results are presented in a format that may provide insight for future CAU-scale model development and applications. The simulations were not conducted in a fashion to identify which parameters precluded good matches between predicted concentrations and observations because it would have been difficult if not impossible to quantify such assessments and because the source term in these

simulations is not representative of any specific test. Thus, such considerations are reserved for classified simulations involving BENHAM- and TYBO-specific inventories.

8.2 Other Plausible Explanations

This study has focused on hydrologic transport of RNs away from underground nuclear tests. We have not considered the phenomenon of prompt injection, the hypothesized process by which RNs are transported away from a test at very early time in either a plasma or gas phase. The conceptual model for such a transport mechanism is that at early time following a test, extremely high pressures exist within the cavity created during vaporization of rock. Emanating away from the cavity, fractures open up within the host rock and provide a conduit for rapid migration. Soon thereafter, the fractures close as the stresses within the rock mass equilibrate and the temperatures and pressures drop, thereby terminating the process of prompt injection. Containment geologists were consulted early in this project to discuss the possibility of prompt injection to a distance of 1.3 km from BENHAM (because the Pu was fingerprinted to BENHAM). We were advised that it is extremely unlikely if not impossible for such a phenomenon to occur over that distance, even considering the announced yield of the BENHAM test. There are no studies or analyses we are aware of in containment science that would yield prompt injection to the distances considered here. However, that does not mean it has been proven not to be the case.

One reason for pursuing the strictly hydrologic transport pathway in this study is that if such processes can explain the observations, which we have demonstrated they can, then the inventory of RNs associated with these tests must be considered as potential sources. On the other hand, if prompt injection were the only plausible explanation, then the observations would be a curious finding, but conclusions could be drawn that the RNs in the cavity that were not promptly injected are not potential sources for groundwater transport. The results in this study show this scenario to be an unlikely conclusion.

8.3 Recommendations

The results discussed in this study highlight several areas in which additional data analysis and modeling analysis can improve our ability to predict RN migration in fractured rock aquifers at the NTS. Listed below are some notable recommendations highlighted by this effort.

8.3.1 Assessment of Transport Processes

Additional research in the following areas would serve to reduce uncertainty in model parameters.

- Assessment of available reactive surface areas in fracture coating minerals.
- *In situ* assessment of oxidation/reduction potential of groundwater in different aquifers.
- Reducing the range of uncertainty in matrix-sorption distribution coefficients.
- Characterization of fracture aperture and spacing distributions.

- Assessment of fracture porosity relative to spacing and apertures--most likely requiring a field-scale tracer test with different tracers designed to elucidate multiple transport parameters, such as diffusion coefficients, colloid filtration rates, and solute reactions with immobile minerals.
- Assessment of Pu-colloid reaction rates in flowing fractures over longer time scales.
- Scaling of laboratory-derived diffusion coefficients for field length and time scales.

8.3.2 Modeling Methods

- Better integration of geostatistical modeling approaches with field-scale transport models. Such improvements may include calibrating geostatistical attribute fields and conditioning them with sources of information other than borehole observations. Geostatistical approaches are pertinent for representing heterogeneity but also need to be constrained to capture fundamental geologic processes.
- Implementation of geostatistical modeling of significant transport attributes, such as fracture spacing, fracture porosity, and matrix Kd . Although permeability fields are created at very high resolution, correlating the appropriate parameters for transport is now a necessary step.
- Continued modeling of laboratory fracture-column experiments. The Pu and montmorillonite colloid experiments have been modeled. For future work, the Pu and silica colloid column experiments (already completed) and the Pu and zeolite colloid column experiments (when they are completed) should be modeled.
- Continuation of the development of coupled thermal-hydrological-chemical (THC) flow and transport models for source-term analysis. The two-dimensional model developed in this study may be the only one of its kind that solves dynamically the fundamental coupled chemical and thermal processes at early time in the cavity. This model addresses the complex issues associated with MG dissolution under transient flow and temperature regimes that occur during the early time frame after the cavity re-wets. Because a significant amount of dissolution likely occurs during this time frame, extension of this THC model to three-dimensions and inclusion of sorption processes in the chimney are the next steps needed to be taken.
- Consideration of two-phase flow and very early time source-term processes to reduce uncertainty in release rates when they are at their greatest.
- Improved calibration techniques. Many lessons were learned during this calibration exercise regarding model complexity relative to data quality and quantity. A new model using the CAU-scale HSU and all water wells in Areas 19 and 20 could serve as a test bed for identification of calibration issues related to data quality, data needs, and model design.
- Improved development of uncertain parameter distributions. Given the significant sensitivity of results to transport parameters demonstrated in this report, the ranges and assumptions used herein should be evaluated with respect to more recent data and with the goal of developing proper statistical distributions of uncertainty.

This Page Intentionally Left Blank

Chapter 9: References

- Bau, H.H. and K.E. Torrance, 1982. Low Rayleigh number thermal convection in a vertical cylinder filled with porous materials and heated from below, *Journal of Heat Transfer*, 104, 166-172.
- Bear, J., 1972. *Dynamics of fluids in porous media*, American Elsevier, New York.
- Bechtel, 2002. A Hydrostratigraphic Model and Alternatives for the Groundwater Flow and Contaminant Transport Model of Corrective Action Units 101 and 102: Central and Western Pahute Mesa, Nye County, Nevada, Bechtel Nevada Report DOE/NV11718--706, Las Vegas, Nevada.
- Berkowitz, B. and H. Scher, 1995. On characterization of anomalous dispersion in porous and fractured media, *Water Resource Research*, 31(6), 1461-1466.
- Berkowitz, B. and J. Zhou, 1996. Reactive solute transport in a single fracture, *Water Resources Research*, 32(4), 901-913.
- Birdsell, K.H., A.V. Wolfsberg, D. Hollis, T.A. Cherry, and K.M. Bower, 2000. Groundwater flow and radionuclide transport calculations for a performance assessment of a low-level waste site, *Journal of Contaminant Hydrology*, 46(1-2), 99-129.
- Blankennagel, R.K. and J.E. Weir, 1973. *Geohydrology of the Eastern Part of Pahute Mesa, Nevada Test Site, Nye County, Nevada*, Professional Paper 712-B, US Geological Survey, Washington, D.C.
- Brachman, A. and A.B. Kersting, 2000. Chapter 2: Characterization of groundwater colloids from the ER-20-5 well cluster and Cheshire underground nuclear test, in *Hydrologic resources management program and underground test area FY1999 progress report* (eds. D.K. Smith and G.F. Eaton), LLNL technical report UCRL-ID-139226, Livermore, CA.
- Brikowski, T., 1993. Flow between aquifers through filled cylindrical conduits: Analytical solutions and application to underground nuclear testing sites, *Journal of Hydrology* 146, 115-130.
- Burnett, R.D. and E.O. Frind, 1987. Simulation of contaminant transport in three dimensions: 2. dimensionality effects, *Water Resources Research*, 23(4), 695-705.
- Carle, S.F., 1999. TPROGS: Transition Probability Geostatistical Software, Version 2.1, Electronic copy from author. Lawrence Livermore National Laboratory.
- Cengel, Y. and M. Boles, 1989. *Thermodynamics, an Engineering Approach*. New York: McGraw-Hill.
- Contardi, J.S., D.R. Turner, and T.M. Ahn, 2001. Modeling colloid transport for performance assessment, *Journal of Contaminant Hydrology*, 47(2001), 323-333.
- CRWMS M&O, 2000a. Calibration of the site-scale, saturated zone flow model. Yucca Mountain Analysis and Model Report, ANL-NBS-HS-000011, Rev 0.0, www.ymp.gov/documents/amr/index.html (<http://www.ymp.gov/documents/amr/s0045/s0045.pdf>; accessed May 2001, confirmed July 2002).

- CRWMS M&O, 2000b. Particle tracking model and abstraction of transport processes, Yucca Mountain Analysis and Model Report, ANL-NBS-HS-000026, Rev 0.0, www.ymp.gov/documents/amr/index.html (<http://www.ymp.gov/documents/amr/u0065/u0065.pdf>; accessed May 2001, confirmed July 2002).
- CRWMS M&O, 2000c. Uncertainty distribution for stochastic parameters. Yucca Mountain Analysis and Model Report, ANL-NBS-MD-000011, Rev 0.0, www.ymp.gov/documents/amr/index.html (<http://www.ymp.gov/documents/amr/22749/22749.pdf>; accessed May 2001, confirmed July 2002).
- CRWMS M&O, 2000d. Saturated zone colloid-facilitated transport. Yucca Mountain Analysis and Model Report, ANL-NBS-HS-000031, Rev 0.0, www.ymp.gov/documents/amr/index.html (<http://www.ymp.gov/documents/amr/s0035/s0035.pdf>; accessed May 2001, confirmed July 2002).
- CRWMS M&O, 2000e. Saturated zone transport methodology and transport component integration, Yucca Mountain Analysis and Model Report, ANL-NBS-HS-000010, Rev 0.0, www.ymp.gov/documents/amr/index.html. (<http://www.ymp.gov/documents/amr/s0025/s0025.pdf>; accessed May 2001, confirmed July 2002).
- CRWMS M&O, 2000f. Probability distribution for flowing interval spacing. Yucca Mountain Analysis and Model Report, TDR-NBS-HS-000003, Rev 0.0, www.ymp.gov/documents/amr/index.html (<http://www.ymp.gov/documents/amr/22281/22281.pdf>; accessed May 2001, confirmed July 2002).
- CRWMS M&O, 2000g. Unsaturated zone and saturated zone transport parameters. Yucca Mountain Analysis and Model Report, ANL-NBS-HS-00019, Rev 0.0, www.ymp.gov/documents/amr/index.html (<http://www.ymp.gov/documents/amr/u0100/u0100.pdf>; accessed May 2001, confirmed July 2002).
- CRWMS M&O, 2000h. Saturated zone flow and transport process model report. Yucca Mountain Process Model Report, ANL-NBS-HS-00001, Rev 0.0, www.ymp.gov/documents/pmr/index.html (<http://www.ymp.gov/documents/amr/25995/25995.pdf>; accessed May 2001, confirmed July 2002).
- Daniels, W.R., F.O. Lawrence, K. Wolfsberg, V.L. Rundberg, R.S. Rundberg, and M.L. Skyes, 1982. Summary report on the geochemistry of Yucca Mountain and environs, LA-9328-MS, UC-70, Los Alamos National Laboratory, Los Alamos, NM, USA.
- Dash, Z.V., B.A. Robinson, and G.A. Zylowski, 1997. Software requirements, design, and verification and validation for the FEHM application - A finite-element heat- and mass-transfer code, Los Alamos National Laboratory Technical Report LA-13305-MS, Los Alamos National Laboratory, Los Alamos, NM.
- Dash, Z.V., 2000. Validation test report (VTR) for the FEHM application version 2.10, Yucca Mountain Project Identification Numbers SAN: LANL-1999-046; STN: 10086-2.10-00.
- Dash, Z.V., 2001. Validation test report (VTR) for the FEHM application version 2.12, Yucca Mountain Project Identification Numbers SAN: LANL-2001-133; STN: 10086-2.12-00.

- Department of Energy (DOE), 2000. United States Nuclear Tests-July 1945 through September 1992. US Department of Energy, Nevada Operations Office, Las Vegas, NV, DOE/NV-209 (Rev. 15).
- Department of Energy (DOE), 1997a. Completion report for well cluster ER-20-5, Technical Report DOE/NV-466.
- Department of Energy (DOE), 1997b. Regional groundwater flow and tritium transport modeling and risk assessment of the Underground Test Area, Nevada Test Site. Technical Report DOE/NV-477.
- Dershowitz, W. and I. Miller, 1995. Dual porosity fracture flow and transport, *Geophysical Research Letters*, 22(11): 1441-1444.
- Doherty, J., 2000. PEST, Model-Independent Parameter Estimation Users Manual. Watermark Numerical Computing. <http://members.ozemail.com.au/~wcomp/>; distributed as freeware software with documentation from SS Popadopoulos & Associates, Inc. <http://www.sspa.com/pest> (URL confirmed July, 2002).
- Drellack, S.L. and L.B. Prothro, 1997. Written communication and narrative regarding the hydrogeologic model of Western and Central Pahute Mesa Corrective Action Units. See discussion in Section 1.6.2 regarding relationship of this communication with the final Bechtel (2002) hydrostratigraphic model, Bechtel Nevada, Las Vegas, NV.
- Drellack, S.L., L.B. Prothro, K.E. Robertson, B.A. Schier, and E.H. Price, 1997. Analysis of fractures in volcanic cores from Pahute mesa, Nevada Test Site. Report to U.S. Department of Energy, Nevada Operations Office, DOE/NV/11718-160.
- Drever, J. I., 1988. *The geochemistry of natural waters*. 2nd ed. Prentice Hall, New Jersey, U.S.A.
- Fenelon, J.M., 2000. Quality assurance and Analysis of water levels in wells on Pahute Mesa and vicinity, Nevada Test Site, Nye County, Water-Resources Investigations Report 00-4014, U.S. Geological Survey, Denver Colorado.
- Flint, L.E., 1998. Characterization of matrix properties of hydrologic units at Yucca Mountain, Nevada, Water-Resources Investigations Report 97-4243, U.S. Geological Survey, Denver Colorado.
- Freeze, R.A. and J.A. Cherry, 1979. *Ground Water*, Prentice Hall, Inc. New Jersey.
- Geldon, A.L., 1996. Results and interpretations of preliminary aquifer tests in boreholes UE-25c #1, UE-25c #2, UE-25c #3, Yucca Mountain, Nye County, NV, Water-Resources Investigations Report 94-4177, U.S. Geological Survey, Denver Colorado.
- George, D.C., 1997. LaGriT Users Manual, <http://www.t12.lanl.gov/~lagrit> (URL confirmed July, 2002).
- Ginn, T.R., 2001. Stochastic-convective transport with nonlinear reactions and mixing: finite streamtube ensemble formulations for multicomponent reactions systems with intra-streamtube dispersion, *Journal of Contaminant Hydrology*, 47(2001), 1-28.

- Grasso, D.N., 2001. GIS surface effects archive of underground nuclear detonations conducted at Yucca Flat and Pahute Mesa, Nevada Test Site, Nevada, Open-File Report 01-0272, U.S. Geological Survey.
- Grisak, G. E., and J. F. Pickens, 1981. An analytical solution for solute transport through fractured media with matrix diffusion, *Journal of Hydrology*, 52, 47-57.
- Hassan, A., K. Pohlman, and J. Chapman, 1999. Modeling groundwater flow and transport of radionuclides at Amchitka Island's underground nuclear tests: Milrow, Cannikin, and Long Shot, Technical report, publication number 45172, DOE/NV/11508-51, Desert Research Institute, Las Vegas, NV.
- Hershey, R.L. and T.H. Brikowski, 1995. Continued investigations of the occurrence of water in Pahute Mesa emplacement holes. Technical report, publication number 45131, DOE/NV/10845-52, Desert Research Institute, Las Vegas, NV.
- Hill, M.C., 1998. Methods and guidelines for effective model calibration, Water Resources Investigation Report 98-405, U.S. Geological Survey, Denver, CO.
- Hochstein, M.P. and M.J. O'Sullivan, 1985. Geothermal systems created by underground nuclear testing. Proc. of the 7th NZ Geothermal Workshop.
- Hochstein, M.P. and M.J. O'Sullivan, 1988. Geothermal systems created by underground nuclear testing: implications for long-term, direct effects of underground testing. Presented at the International Scientific Symposium on a Nuclear Test Ban, January 15-16, Las Vegas, Nevada.
- IAEA (International Atomic Energy Agency), 1998. The radiological situation at the Atolls of Mururoa and Fangataufa, Technical Report, Volume 3: Inventory of radionuclides underground at the atolls, Vienna, Austria, IAEA-MFTR-3.
- IT Corporation, 1996. Underground Test Area fracture analysis report: Analysis of fractures in volcanic cores from Pahute Mesa. U.S. Department of Energy draft report.
- IT Corporation, 1998. Report and analysis of the BULLION forced gradient experiment, technical report DOE/NV/13052-042; ITLV/13052-042.
- Johns, R. A., and P. V. Roberts, 1991. A solute transport model for channelized flow in a fracture, *Water Resources Research*, 27, 1797-1808.
- Keating, E., E. Kwicklis, V. Vesselinov, A. Idar, Z. Lu, G. Zvoloski, and M. Witkowski, 2000. A regional flow and transport model for groundwater at Los Alamos National Laboratory, Earth and Environmental Sciences Division Progress Report, Los Alamos National Laboratory, Los Alamos, NM.
- Kechagia, P.E., I. Tsimpanogiannis, Y.C. Yortsos, and P.C. Lichtner. 2000. On the upscaling of reaction-transport processes in porous media with fast kinetics. Submitted for publication to *Chemical Engineering*.
- Keller, A. A., P. V. Roberts, and P.K. Kitanidis, 1995. Prediction of single phase transport parameters in a variable aperture fracture, *Geophysical Research Letters*, 22, 1425-1428.

- Kersting, A.B. and P.W. Reimus, 2002. UGTA colloid studies synthesis report. In review.
- Kersting, A.B., D.W. Efurud, D.L. Finnegan, B.A. Martinez, D.J. Rokop, D.K. Smith and J.L. Thompson, 1998a. U-20y TYBO -- U-20c BENHAM, in Laboratory and field studies related to radionuclide migration at the Nevada Test Site, October 1, 1996 -- September 30, 1997 (ed. J.L. Thompson) LANL technical report LA-13419-PR, Los Alamos National Laboratory, Los Alamos, NM.
- Kersting, A.B., D.W. Efurud, D.L. Finnegan, D.J. Rokop, D.K. Smith and J.L. Thompson, 1998b. Migration of plutonium in groundwater at the Nevada Test Site, in Hydrologic resources management program and underground test area operable unit FY1997 progress report (eds. D.K. Smith et. al.), LLNL technical report UCRL-ID-130792, Lawrence Livermore National Laboratory, Livermore, CA.
- Kersting, A.B., D.W. Efurud, D.L. Finnegan, D.J. Rokop, D.K. Smith and J.L. Thompson, 1999. Migration of plutonium in groundwater at the Nevada Test Site, *Nature*, 397.
- Kung, S., 2000. Colloid size and colloid concentration data of groundwater samples from the NTS 04/30/1998 to 10/21/1998. Yucca Mountain Project DTN: LA0002SK831352.004, Yucca Mountain Project, Las Vegas, NV.
- Landolt, H., 1982. Numerical Data and Functional Relationships in Science and Technology, Group V: Geophysics and Space Research, Volume 1, Physical Properties of Rocks. New Series Editor-in-Chief: K.H. Hellwege. Springer-Verlag, New York, 332-333.
- Laczniak, R.J., J.C. Cole, D.A. Sawyer, and D.A. Trudeau, 1996. Summary of hydrogeologic controls on ground-water flow at the Nevada Test Site, Nye County, Nevada, Water-Resources Investigation Report 96-4109, U.S. Geological Survey, Carson City, NV.
- Langmuir, D., 1997. Aqueous environmental geochemistry, Prentice hall, Upper Saddle River, New Jersey, 600p.
- Lemire, R.J., and F. Garisto., 1989. The solubility of U, Np, Pu, Th and Tc in a geological disposal vault for used nuclear fuel. Report ROE 1LO, AECL-1009. Pinawa, Manitoba: Atomic Energy of Canada Ltd., Whiteshell Nuclear Research Establishment.
- Lemire, R.J., and P.R. Tremaine, 1980. Uranium and plutonium equilibria in aqueous solutions to 200°C. *Journal of Chemical Engineering Data*, 25, 361-370.
- Lichtner, P.C., 1985. Continuum model for simultaneous chemical reactions and mass transport in hydrothermal systems, *Geochimica et Cosmochimica Acta*, 49, 779-800.
- Lichtner, P.C., 1995. Principles and practice of reactive transport modeling, *Materials Research Society Symposium Proceedings*, 353, 117-130.
- Lichtner, P.C., 1996. Continuum formulation of reactive transport. In *Reactive transport in porous media*, Reviews in Mineralogy, P.C. Lichtner, C.I. Steefel, and E.H. Oelkers, eds., Mineralogical Society of America, 34, 1-81.
- Lichtner, P.C., 2000. Critique of dual continuum formulations of multicomponent reactive transport in fractured porous media, In *Dynamics of fluids in fractured rock*, Ed. B. Faybishenko, AGU Monograph, 122, 281-298.

- Lichtner, P.C., 2001. FLOTRAN User's Manual, Report LA-UR-01-2349, Los Alamos National Laboratory, Los Alamos, NM.
- Lichtner, P.C., S. Kelkar, and B. Robinson, 2002. New form of the dispersion tensor for flow in axisymmetric media with implementation in particle tracking. *Water Resources Research* (In Press).
- LLNL-ISD, 1996. Isotopic Analyses: Monitoring Well ER-20-5, Preliminary Report, Unpublished letter report to DOE/NV, Environmental Restoration Division, 13 Nov 1996, 5 p. Isotope Sciences Division, Lawrence Livermore National Laboratory, Livermore, CA.
- LLNL-ISD, 1997. Isotopic Analyses: Monitoring Well ER-20-5, Unpublished letter report to DOE/NV, Environmental Restoration Division, 03 Oct 1997, 5 p., Isotope Sciences Division, Lawrence Livermore National Laboratory, Livermore, CA.
- LLNL-ISD, 1998. Isotopic Analyses: Monitoring Well ER-20-5, Unpublished letter report to DOE/NV, Environmental Restoration Division, 03 Dec 1998, 6 p., Isotope Sciences Division, Lawrence Livermore National Laboratory, Livermore, CA.
- Long, J. C. S. and P. A. Witherspoon, 1985. The relationship of the degree of interconnectivity to permeability in fracture networks, *Journal of Geophysical Research*, 90(B4), 3087-3097.
- Lu, G., T.P. Clement, C. Zheng, and T.H. Wiedemeier, 1999. Natural attenuation of BTEX compounds: model development and field-scale application, *Ground Water*, 37(5), 707-717.
- Lu, N.P., C.R. Cotter, H.D. Kitten, J. Bentley, & I.R. Triay, 1998. Reversibility of sorption of plutonium-239 onto hematite and goethite colloids, *Radiochimica Acta*, 83(4), 167-173.
- Maxwell, R.M., A.F.B. Thompson, J.T. Rambo, S.F. Carle, and G.A. Pawloski, 2000. Thermally induced groundwater flow resulting from an underground nuclear test. *Computational Methods in Water Resources*, vol.1, eds: L.R. Bentley, J.F. Sykes, C.A. Brebbia, W.G. Gray and G.F. Pinder. Balkema Press, Rotterdam, 45-50.
- McKay, L. D., R. W. Gillham, and J. A. Cherry, 1993. Field experiments in a fractured clay till. 2. Solute and colloid transport, *Water Resources Research*, 29(12), 3879-3890.
- Murphy, W.M., E.H. Oelkers, and P.C. Lichtner, 1989. Surface reaction versus diffusion control of mineral dissolution and growth rates in geochemical processes. *Chemical Geology*, 78, 357-380.
- National Research Council, 1996. *Rock fracture and fluid flow: contemporary understanding and applications*. National academy press, Washington, D.C.
- Neretnieks, I., T. Eriksen, and P. Tahtinen, 1982. Tracer movement in a single fissure in granitic rock: Some experimental and their interpretation, *Water Resources Research*, 18, 849-858.
- Nield, D.A. and A. Bejan, 1999. *Convection in porous media*, New York, Springer.
- Nitsche, H., K. Roberts, K. Becraft, T. Prussin, D. Keeney, S.A. Carpenter, and D. E. Hobart, 1995. Solubility and speciation results from over- and undersaturation experiments on neptunium, plutonium, and americium in water from Yucca Mountain Region Well UE-25 #1. Report LA-13017-MS, Los Alamos National Laboratory, Los Alamos, NM.

- O'Hagan, M.D. & R.J. Laczniak, 1996. Ground-water Levels Beneath Eastern Pahute Mesa and Vicinity, Nevada Test Site, Nye County, Nevada. Water-Resources Investigations Report 96-4042, U.S. Geological Survey.
- Okusu, N.M., K. Karasalai, J.C.S. Long, and G. Bodvarsson, 1989. FMMG: a program for discretizing two-dimensional fracture matrix systems. Theory, design, and user's manual. LBL-26 782, Lawrence Berkeley National Laboratory, Berkeley, CA.
- Pawloski, G., 1999. Development of Phenomenological Models of Underground Nuclear Tests on Pahute Mesa, Nevada Test Site - BENHAM and TYBO, Technical Report UCRL-ID-136003 Lawrence Livermore National Laboratory, Livermore, CA.
- Pawloski, G.A., A.F.B. Tompson, and S.F. Carle (eds.), 2001. Evaluation of the hydrologic source term from underground nuclear tests on Pahute Mesa at the Nevada Test Site: The CHESHIRE test, Technical Report UCRL-ID-147023, Lawrence Livermore National Laboratory, Livermore, CA.
- Peterson, E., K. Lie, N. Rimer, and R. Nilson, 1991. Thermodynamic evolution of nuclear cavities, in 6th Symposium on Containment of Underground Nuclear Explosions, Lawrence Livermore National Laboratory, Livermore, California, 830882, Vol.1.
- Pollock, D.W., 1988. Semianalytical computation of path lines for finite-difference models, *Ground Water*, 26, 743-750.
- Pottoroff, E.J., S.J. Erikson, and M.E. Campana, 1987. Hydrologic utility of borehole temperatures in areas 19 and 20, Pahute Mesa, Nevada Test Site. Publication number 45060. DOE/NV/10384-19.
- Press. W.H., B.P. Flannery, S.A. Teukolsky, and W.T. Vetterling, 1986. Numerical recipes: the art of scientific computing, University Press, New York, Cambridge.
- Prothro, L.B. and S.L. Drellack, 1997. Nature and extent of Lava-flow aquifers beneath Pahute Mesa, Nevada Test Site, Bechtel Nevada technical report DOE/NV/11718-156, Bechtel Nevada, NV.
- Prothro, L.B. and R.G. Warren, 2001. Geology in the vicinity of the TYBO and BENHAM underground nuclear tests, Pahute Mesa, Nevada Test Site, Bechtel Nevada Technical Report DOE/NV/11718--305, Bechtel Nevada. NV.
- Puigdomenech, I., and J. Bruno, 1991. Plutonium solubilities. Swedish Nuclear Fuel and Waste Mgmt. Co., SKB Tech. Rept. 91-04.
- Rautman, C.A., 1995. Preliminary Geostatistical Modeling of Thermal Conductivity for a Cross Section of Yucca Mountain, Nevada, SAND94-2283, Sandia National Laboratories, Albuquerque, New Mexico.
- Reimus, P.W. and M. J. Haga, 1999. Analysis of tracer responses in the BULLION forced-gradient experiment at Pahute Mesa, Nevada, LA-13615-MS, Los Alamos National Laboratory, Los Alamos, NM.

- Reimus P.W., S.D. Ware, N. Lu, A.A. Fattah, K.S. Kunk, and M.P. Neu, 1999. Progress report on colloid transport and colloid-facilitated plutonium transport in fractured rocks from Pahute Mesa, Nevada Test Site, NTS-UGTA progress report, Los Alamos National Laboratory, Los Alamos, NM.
- Reimus, P.W., A.Adams, M.J. Haga, A. Humphrey, T. Callahan, I. Anghel, and D. Counce, 1999b. Results and Interpretation of Hydraulic and Tracer Testing in the Prow Pass Tuff at the C-holes, Yucca Mountain Site Characterization Project Milestone Report SP32E7M4, Los Alamos National Laboratory, Los Alamos, NM.
- Reimus P.W., S.D. Ware, N. Lu, A.A. Fattah, K.S. Kunk, and M.P. Neu, 2001. FY2001 Progress report on colloid-facilitated plutonium transport in fractured rocks from Pahute Mesa, Nevada Test Site, NTS-UGTA progress report, Los Alamos National Laboratory, Los Alamos, NM.
- Reimus P.W., S.D. Ware, F.C. Benedict, R.G. Warren, A. Humphrey, A. Adams, B. Wilson, and D. Gonzales, 2002. Diffusive and Advective transport of ^3H , ^{14}C , and ^{99}Tc in saturated fractured volcanic rocks from Pahute Mesa, Nevada, Technical Report LA-13891-MS, Los Alamos National Laboratory, Los Alamos, NM.
- Robinson, B.A., 2002. A particle tracking transport method for the simulation of resident and flux-averaged concentration of solute plumes in groundwater models, submitted to Water Resources Research.
- Robinson, B.A., H.S. Viswanathan, and A.J. Valocchi, 1999. Efficient numerical techniques for modeling multicomponent groundwater transport based on simultaneous solution of strongly coupled subsets of chemical components. *Advances in Water Research*, 36, October issue.
- Rose, T.P., J.M Kenneally, D.K. Smith, M.L. Davisson, G.B. Hudson, and J.A.H. Rego, 1997. Chemical and Isotopic Data for Groundwater in Southern Nevada, Technical Report UCRL-ID-128000, Lawrence Livermore National Laboratory, Livermore, CA.
- Sass, J.H. and A.H. Lachenbruch., 1982. Preliminary Interpretation of Thermal Data from the Nevada Test Site. USGS-OFR-82-973, U.S. Geological Survey.
- Schor, S., 1968. *Fundamentals of Biostatistics*. G.P. Putnam and Sons, New York.
- Singh, V.P., 1988. *Hydrologic Systems, Volume 1, Rainfall-Runoff Modeling*. Prentice-Hall, Englewood Cliffs, New Jersey.
- Smith, D.K., 1993. A Review of Literature Pertaining to Leaching and Sorption of Radionuclides Associated with Nuclear Melt Glasses. Technical Report UCRL-ID-113370, Lawrence Livermore National Laboratory, Livermore, CA.
- Smith, D.K., 2001. Unclassified radiologic source term for Nevada Test Site Areas 19 and 20, Technical Report UCRL-ID-141706, Lawrence Livermore National Laboratory, Livermore, CA.
- Smith, L., and F. W. Schwartz, 1984. An analysis of the influence of fracture geometry on mass transport in fractured media, *Water Resources Research*, 20(9), 1241-1252.

- Snoeberger, D.F., C. J. Morris, and G.A. Morris, 1971. Field Measurement of Permeabilities in NTS Area 9. August 23, 1971, Radiation Lab Report UCID 15895, Lawrence Livermore National Laboratory, Livermore, CA.
- Sokal, R.R. and F.J Rohlf, 1981. Biometry, W.H. Freeman and Co., San Francisco, CA.
- Sudicky, E.A., and E.O. Frind, 1982. Contaminant transport in fractured porous media: analytical solutions for a system of parallel fractures, *Water Resources Research*, 18(3), 1634–1642.
- Sudicky, E.A., and R.G. McLaren, 1992. The laplace transform galerkin technique for large scale simulation of mass transport in discretely fractured porous formations, *Water Resources Research*, 28(2), 499-514.
- Tang, D.H., E.O. Frind, and E.A. Sudicky, 1981. Contaminant transport in fractured media: analytical solution for a single fracture. *Water Resources Research*, 17(3), 555–564.
- Thompson, J.L., D.W. Efurud, D.J. Rokop, D.L. Finnegan, M.A. Guell, A.B. Kersting, B.A. Martinez, and D.K Smith, 1997. Laboratory and field studies related to the hydrologic resources management program, October 1, 1995 -- September 30, 1996, Technical Report LA-13270-PR, Los Alamos National Laboratory, Los Alamos, NM.
- Thompson, J.L., D.L. Finnegan, K.S. Kung, and B.A. Martinez, 1999. Laboratory and field studies related to radionuclide migration at the Nevada Test Site, October 1, 1997 -- September 30, 1998, Technical Report LA-13576-PR, Los Alamos National Laboratory, Los Alamos, NM.
- Tompson, A.F.B and L.W. Gelhar, 1990. Numerical simulation of solute transport in three-dimensional, randomly heterogeneous porous medium. *Water Resources Research*, 26(10), 2541-2562.
- Tompson, A.F.B., C.J. Bruton, and G.A. Pawloski, 1999. Evaluation of the hydrologic source term from underground nuclear tests in Frenchman Flat at the Nevada Test Site: The CAMBRIC Test, Report UCRL-ID-132300, Lawrence Livermore National Laboratory, Livermore, CA.
- Travis, B.J. and K. H. Birdsell, 1991. TRACER3D: A model of flow and transport in porous media: Model description and users manual, Technical Report LA-11798-MS, Los Alamos National Laboratory, Los Alamos, NM.
- Triay, I.R., A. Meijer, J.L. Conca, K.S. Kung, R.S. Rundberg, B.A. Strietelmeier, C.D. Tait, D.L. Clark, M.P. Neu, D.E. Hobart, 1997. Summary and synthesis report on radionuclide retardation for the Yucca mountain site characterization project, LA-13262-MS, UC903 and UC-940, Los Alamos National Laboratory, Los Alamos, NM.
- TRW Environmental Safety Systems Inc., 2000. SZ_CONVOLUTE VERSION 2.0 User's Manual, 10207-UM-2.0-00. Prepared for US DOE, June 10, 2000.
- Viswanathan, H.S., 1999. Multicomponent transport in unsaturated groundwater systems, Ph.D dissertation, University of Illinois, Urbana-Champaign, IL.

- Viswanathan, H.S., B.A. Robinson, A.J. Valocchi, and I.R. Triay, 1998. A reactive transport model of neptunium migration from the potential repository at Yucca Mountain, *Journal of Hydrology*, 209, 251-280.
- Van Kampen, N.G., 1981. *Stochastic Processes in Physics and Chemistry*. Amsterdam, Netherlands: North Holland Physics Publishing.
- Warren, R., 2000. Data from southwestern Nevada volcanic field, URL location <http://queeg.ngdc.noaa.gov/seg/geochem/swnvf/> (URL confirmed July 2002).
- White, A.F, A.E. Blum, M.S. Schultz, T.D. Bullen, J.W. Harden, and M.L. Peterson, 1996. Chemical weathering rates of a soil chronosequence on granitic alluvium: I. Quantification of mineralogical and surface area changes and calculation of primary silicate reaction rates, *Geochimica Acta*, (60)4, 2533-2550.
- Winograd, I.J. and W. Thordarson, 1975. Hydrology of Nuclear Test Sites: Hydrogeologic and hydrochemical framework, South-Central Great Basin, Nevada-California, with special reference to the Nevada Test Site, Professional Paper 712-C, U.S. Geological Survey.
- Wolfsberg, A., K. Campbell, and J. Fabryka Martin, 2000. Use of chlorine-36 to evaluate fracture flow and transport models at Yucca Mountain, Nevada, in *Dynamics of Fluids in Fractured Rock*; Geophysical Monograph 122 (eds. B. Faybishenko, P. Witherspoon, and S. Benson), American Geophysical Union, Washington, DC., 349-362.
- Zheng, C. and G. D. Bennett, 1995. *Applied contaminant transport modeling, Theory and practice*. 440 pp. Van Nostrand Reinhold.
- Zimmerman, R. W., and G. S. Bodvarsson, 1996. Hydraulic conductivity of rock fractures, *Transport in Porous Media*, 23, 1-30.
- Zyvoloski, G.A., B.A. Robinson, Z.V. Dash and L.T. Trease, 1997. User's Manual for the FEHM Application, A Finite-Element Heat- and Mass-Transfer Code, LA-13306-MS, Los Alamos National Laboratory, Los Alamos, NM.

Appendix A: Sub-CAU Flow Model Grid Generation

A.1 Introduction

A three-dimensional computational mesh is constructed for the sub-CAU domain defined in Chapter 3 (the terms “mesh” and “grid” are used interchangeably in this report). The mesh-building process begins with surface files from Drellack and Prothro (1997). These surfaces define the top and bottom boundaries of each material unit and the truncating water table. From these surfaces, two computational grids are built. The first grid is at the sub-CAU scale with uniform spatial resolution, using the hydrostratigraphic model of Drellack and Prothro (1997). This second mesh represents the same domain, but is embedded with a high resolution site-scale mesh (Figure A-1). The embedded site-scale mesh provides local high resolution at the site scale of BENHAM and TYBO. However, in this study, it is only used to establish boundary conditions for heterogeneous property model occupying the same domain. Chapter 5 provides more detail on site-scale model resolution. Nevertheless, the processes of generating an embedded grid are included in this appendix because the method has applicability to other NTS projects.

A.1.1 Grid Generation Tools and Software

GEOMESH/LaGriT: LaGriT (Los Alamos Grid Toolbox; George, 1997) is a universal finite-element grid generation software package developed at Los Alamos National Laboratory. LaGriT consists of a library of user-callable tools that provide mesh generation, mesh optimization, and dynamic mesh maintenance in three dimensions for a variety of applications. For example, LaGriT is used for numerical model applications in weapons design, semiconductor development, fluid dynamics, and hydrogeology. GEOMESH is a specialized subset of LaGriT developed specifically for hydrogeologic applications.

X3DGEN is a specialized module used for OMR (Octree Mesh Refinement). This method breaks a hexahedral element into eight pieces. With each OMR refinement, all edges of a refined element are bisected and nodes are added to the centroid of each of the six faces and the centroid of the element. The octree is also balanced, which ensures that adjacent cells are only one level of refinement higher or lower.

A.2 Details of Method

The steps taken to create the three-dimensional computational mesh from the original data are listed as follows:

- Create quadrilateral surface grids for building the Mesh.
- Create boundary and refinement surface grids.
- Stack surfaces into the 3-D sub-CAU hexahedral mesh.
- Embed a high resolution site-scale mesh in the sub-CAU mesh.
- Optimize sub-CAU and embedded mesh for computations.

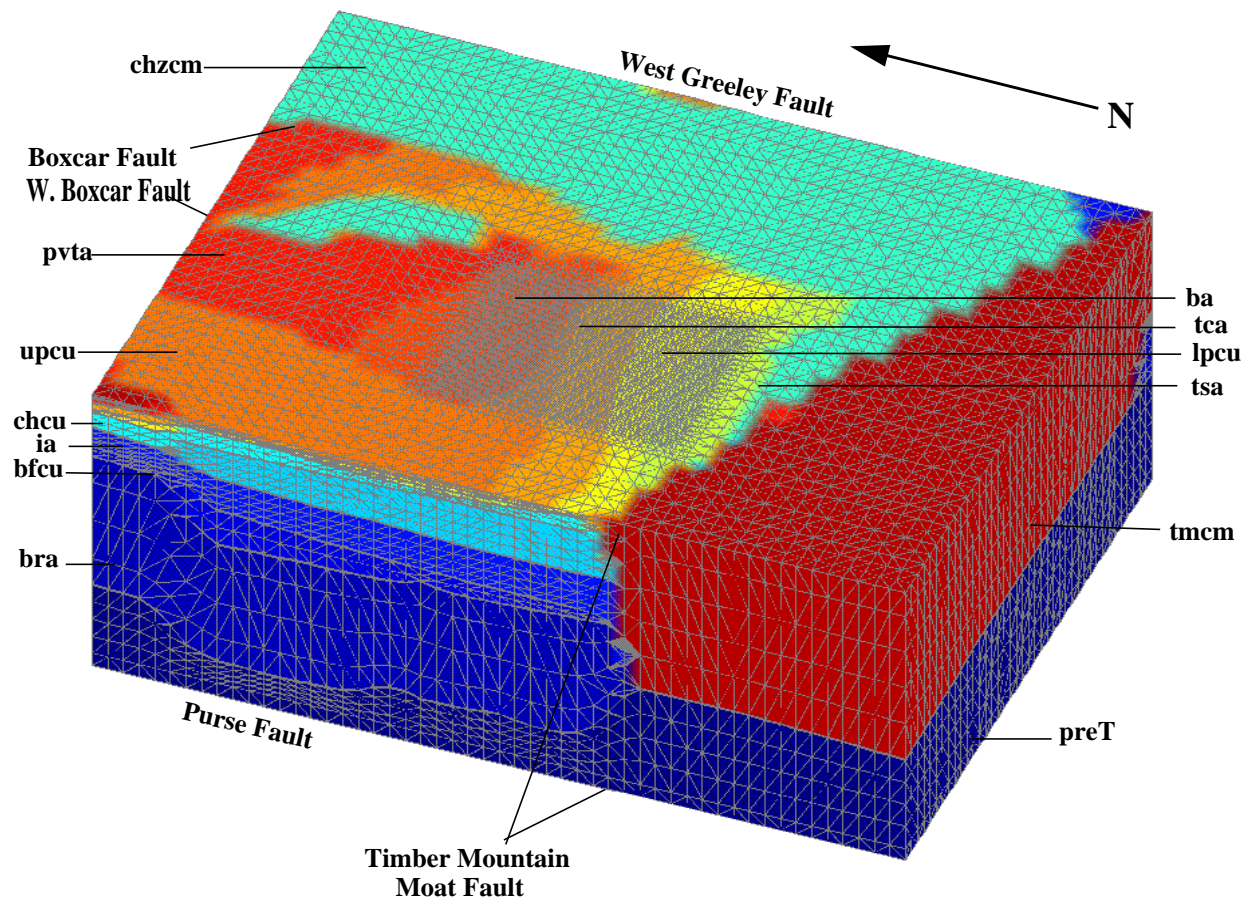


Figure A-1. The sub-CAU mesh is built from stacking the HSU surfaces from Drellack and Prothro. The point distribution has 200 m horizontal spacing. The sub-CAU mesh is used to embed a high resolution site with 50 x 50 x 10 m spacing. This image shows the final tetrahedra embedded mesh. This mesh also has values indicating elements in the Moat, Boxcar, and West Boxcar Faults.

- Assign fault and unit material identification values.
- Compute volume and area coefficients.
- Define node sets for setting initial conditions, boundary conditions and properties.
- Perform mesh quality checks.

A.2.1 Create Quadrilateral Surfaces Grids

The original data for each stratigraphic unit are converted into digital contoured surfaces of Western and Central Pahute Mesa. The data points on the surfaces are connected into quadrilateral elements, which then are converted into two triangles for each quadrilateral. Surface size is reduced

into a regular rectangular shape template covering the sub-CAU domain and the new surface is created using a ray-shooting technique. The resulting points are connected into a quadrilateral grid that becomes the new subset surface grid. Figure A-2 provides an example of a surface grid created with the ray-shooting technique. This technique is also applied to surfaces that cross faults (an example is shown in Figure A-3).

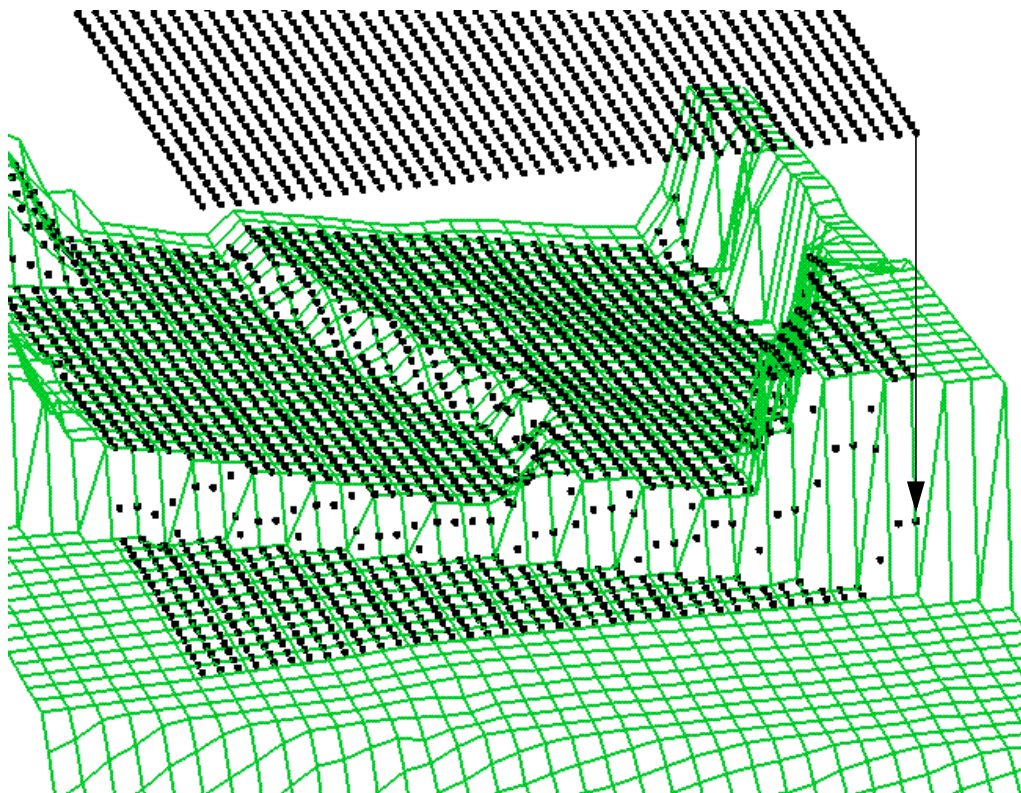


Figure A-2. Surface grids with new point distributions are created from the original surfaces with a ray-shooting technique. Surface OVCN is shown with the new point template above and the resulting point on the surface.

A.2.2 Create Boundary and Refinement Surfaces

The sub-CAU model is bounded at the top by the water table. To represent this surface, data are extracted from (Drellack and Prothro, 1997) and contoured into x, y, and z coordinates at locations corresponding to the subset quadrilateral surface grids. The water-table grid truncates all surfaces below it.

The bottom bounding surface was chosen to be an elevation of -1555.0 m because this is well below the confining unit under the area of interest for radionuclide transport. This surface grid is formed by setting all the Z-elevation values of the subset template to -1555.

Increased vertical resolution for a material unit is accomplished by adding surface grids between the top and bottom bounding unit surfaces. The refinement surfaces are derived by computing elevations at a proportional distance between the bottom and top surface. Some HSUs

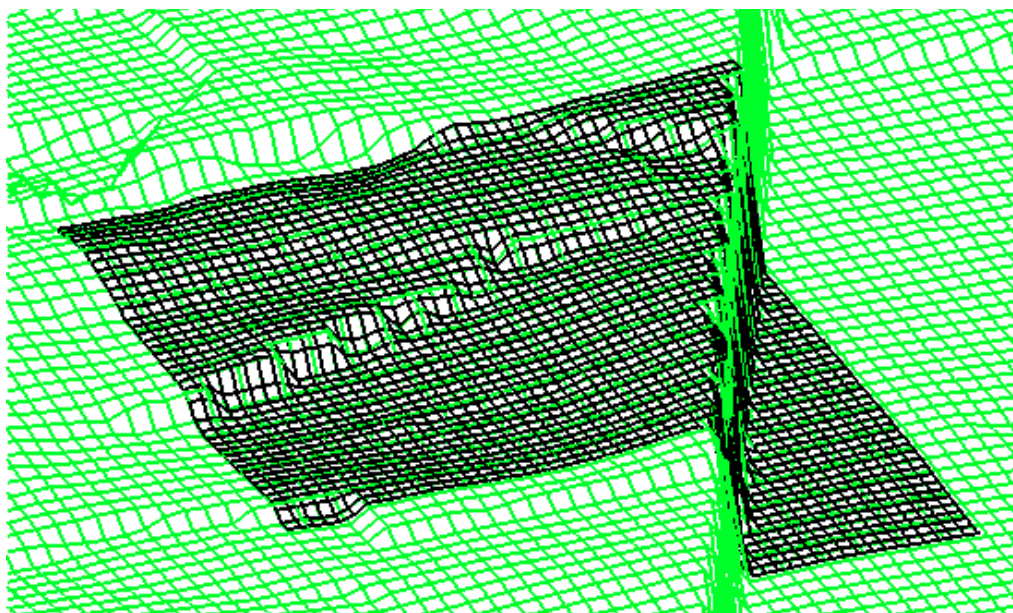


Figure A-3. Image shows original (green) and new (black) surfaces for CHZCM. View is looking east with the steep Moat Fault on the right.

are not refined or are refined just once, either because they are already very thin or because they are sufficiently distant from the expected transport pathway. There is particular interest in the CHZCM unit, so this unit is refined six times vertically, which results in elements averaging less than 100 m in height. No horizontal refinement is performed, all points remain separated by 200 m.

Interface buffers are created by adding layers 10 m below and above each material surface grid. This is done to alleviate computational difficulties at stratigraphic interfaces. Figure A-4 shows a close-up of a buffered interface. Because the computational simulations on this grid use Voronoi volumes, it is even more important to capture detail at the interfaces. The interface buffers bind the Voronoi volumes to the interface geometry. Figure A-5 shows a close-up view of the computational Voronoi cells relative to the unit interface with and without the buffer zone.

Vertical refinement to increase resolution and to buffer interfaces is conducted automatically within the LaGriT routines, enabling the mesh to be built without generating any additional surface grids.

A.2.3 Stack Surfaces into the 3-D Sub-CAU Hexahedral Mesh

The quadrilateral surfaces are stacked in order by elevation (Figure A-6) and populated with hexahedral elements (Figure A-7). If surfaces cross, the layers pinch out to zero. The approach maintains the geometry of interfaces and faults.

A.2.4 Embed a High-Resolution Site-Scale Mesh in the Sub-CAU Mesh

The site-scale mesh is embedded directly into the coarser sub-CAU model as part of the testing process to investigate whether heterogeneous attributes, generated elsewhere with geostatistical tools, can be directly embedded in a deterministic regional model. The steps in this process include the following items:

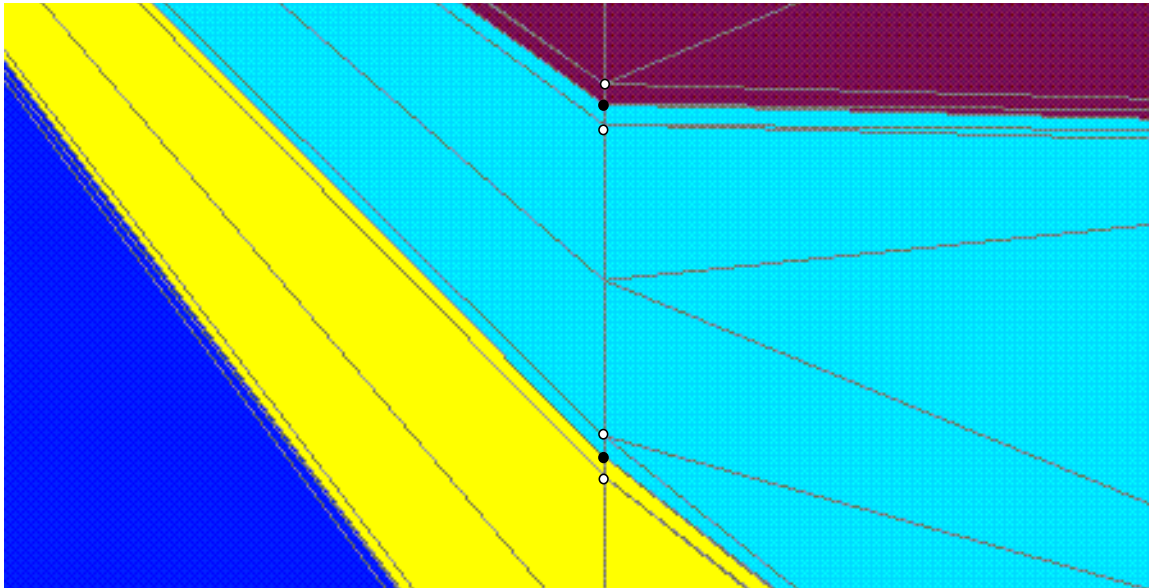


Figure A-4. Close-up of buffered layers for four materials in the tetrahedral grid. The buffer points (white dots) are created 5 m below and above each interface point (black dots).

- Create the high resolution site-scale mesh. Using the sub-CAU mesh, use OMR refinement to increase resolution in the area abutting the site grid so that 200-m-sized elements do not abut 10-m-sized elements.
- Refine vertically to reduce the number of connections from the coarse grid to a single node in the fine grid. Excavate and align the site-scale mesh in the sub-CAU mesh.
- Use reconnection to connect the entire point set into a computable mesh.

The resulting grid blocks in the embedded region are 50 x 50 x 10 m, each. The embedded region has to be buffered on all sides to reduce the large discrepancy between the sides of edges. Horizontally, the sub-CAU mesh has edges of 200 m, the buffer area has 100-m edges, and the site has 50-m edges. Figure A-8, Figure A-9, and Figure A-10 all show different characteristics of the embedded mesh and the buffer zones added around it.

A.2.5 Optimize Sub-CAU and Embedded Mesh for Computations

The sub-CAU and embedded hexahedral grids have point distributions that represent the geometry of the model, but neither is a computable mesh. They are both reconnected into Delaunay tetrahedral meshes. The reconnection module is used to optimize a grid for computations. Reconnection algorithms change the connectivity of a mesh without modifying node position or the number of nodes in the grid. Two-dimensional grids use a single reconnection algorithm that flips the shared edge of two triangles. The result is a two-triangle to two-triangle transformation that can improve the grid quality. These transformations are used in an automated reconnection algorithm to improve grid quality. For the final computational grid, points are added to create a Delaunay grid with positive coupling coefficients. This addition ensures the optimum computational mesh results.

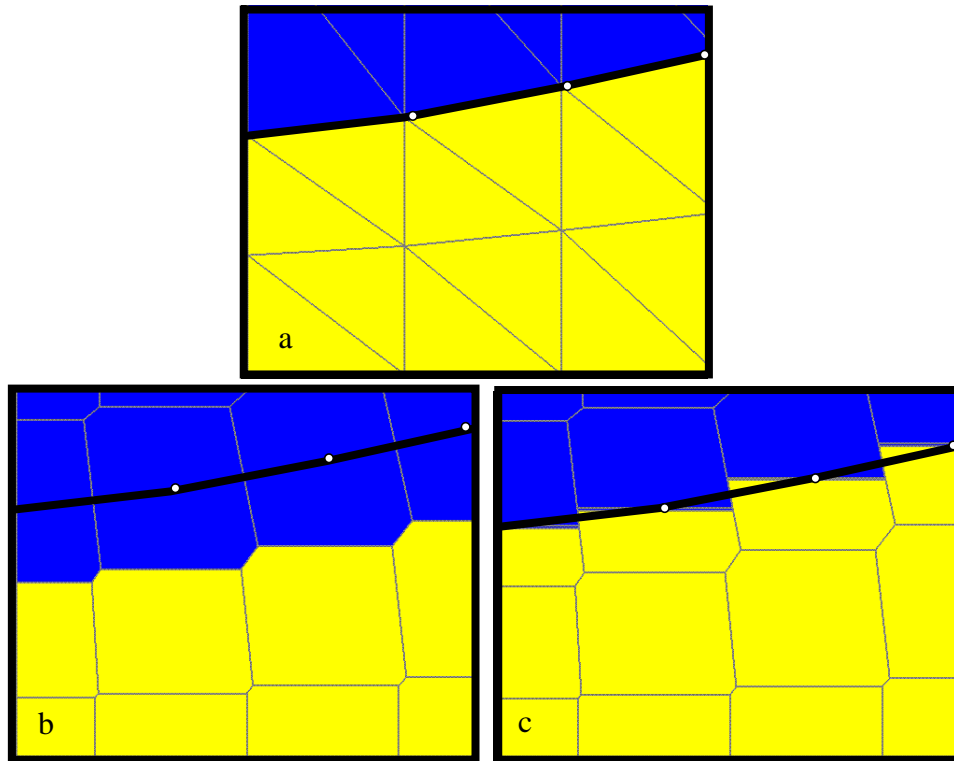


Figure A-5. The computational Voronoi cells with respect to the interface geometry formed by the TIN sheets in the TIN to TET process. Figure (a) shows the actual interface geometry, (b) shows the computational Voronoi cells formed without buffers, and (c) shows them with buffers.

A.2.6 Assign Fault and Unit Material Identification Values

Once the points have been connected into a computational mesh, they are colored with geometry surfaces used to create the hexahedral meshes. Each node of the computational mesh is located within the layer sequence and assigned a material number. For example, if a node is located between the top and bottom surface of stratigraphic unit 4, then the node would have a material number of 4. Figure A-11 is an example of the computational mesh colored by unit material.

There are three faults identified for this model: Timber Mountain Moat, Boxcar, and West Boxcar (Figures A-12 and A-13). However, hydrologic properties within a fault zone may vary vertically, depending on the material unit being faulted. LaGriT provides routines that can define a fault's various material regions. This is done by identifying which two original surfaces specific fault-zone nodes fall between. For instance, region 2 is between the surfaces representing the BRAQ layer and BFCU layer. The Moat Fault elements found in this region are tagged with an identification number representing fault Moat-region 2. These values are assigned for each of the three faults in every region. Figure A-14 shows the faults colored by their fault identification

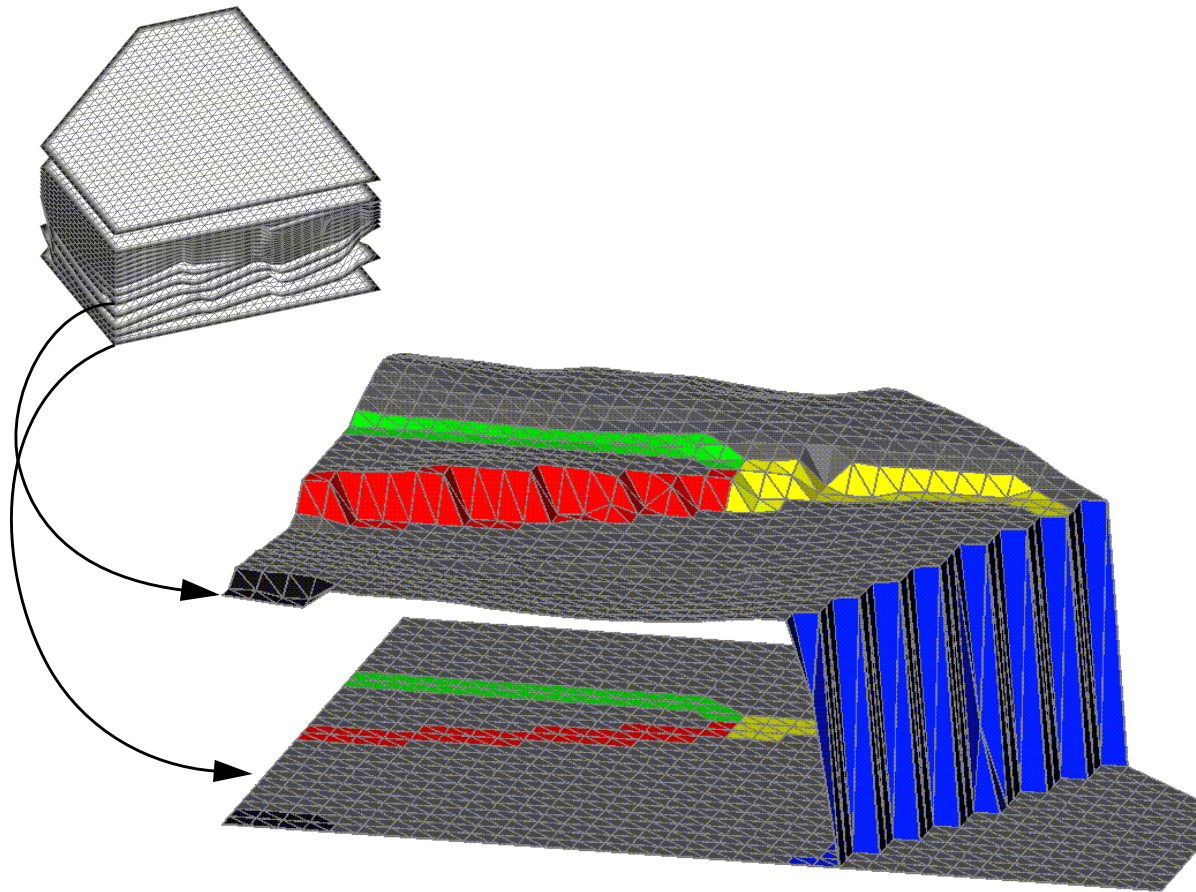


Figure A-6. The stacked grid surfaces are shown at the top, including the flat bottom layer. Shown separate from the stack are the surface grids of the CHZCM surface and the flat bottom. The Moat Fault is colored blue, West Boxcar is red, East Boxcar is green, and South Boxcar is yellow. Note the vertical tilt of the faults with respect to the surrounding stratigraphy.

number, and then by their fault-unit relationship. This procedure enables calculations to be defined for each fault in each unit.

A.2.7 Compute and Output Volume and Area Matrix Coefficients

FEHM uses finite control volumes to solve flow and transport equations. Thus, all calculations are performed on the volumes in the mesh uniquely identified to each node, the Voronoi volumes. One part of the grid generation process is to calculate the Voronoi control volumes associated with each node in the grid and the area of the polygonal faces of the Voronoi control volumes. Each node on the surface of the grid has a surface area associated with it. This area is computed and written to a file used to scale constant flux boundary conditions.

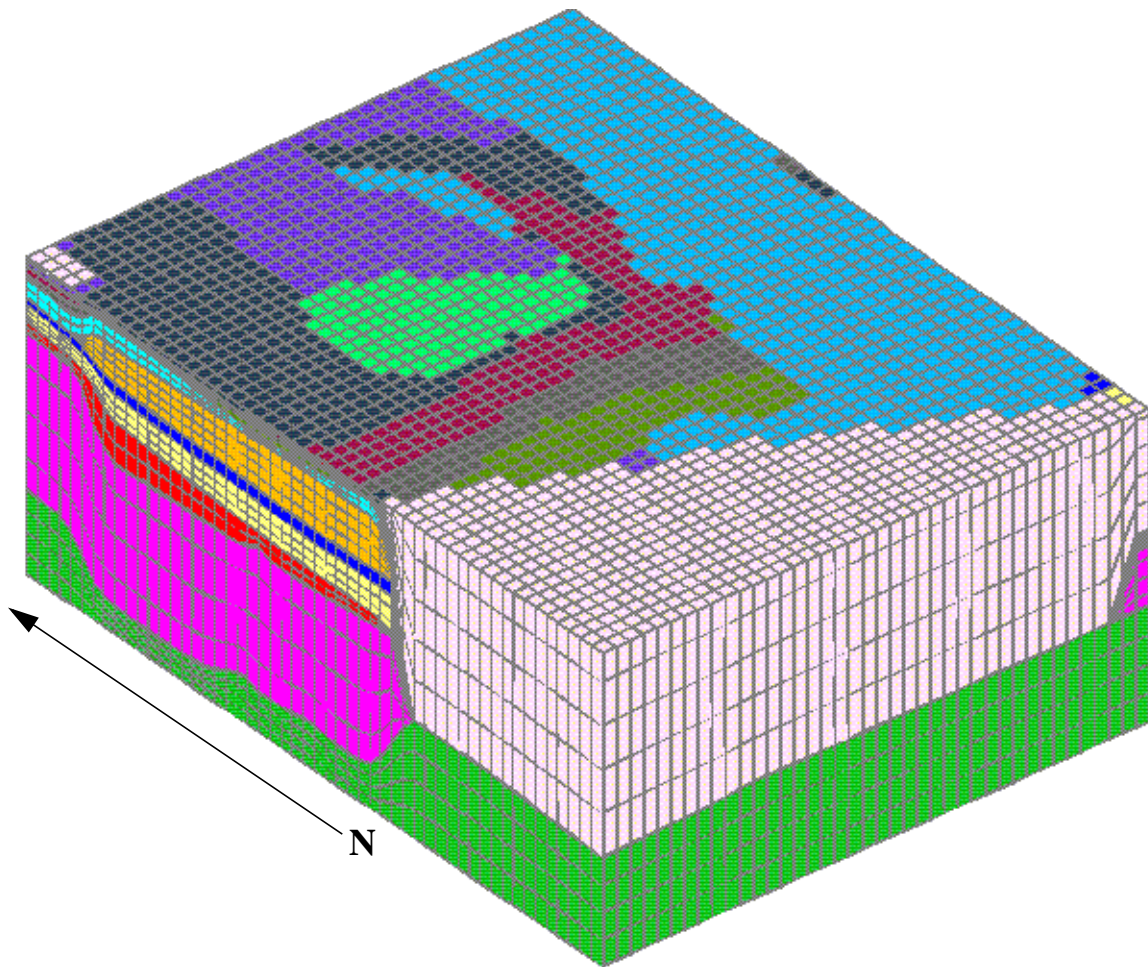


Figure A-7. Sub-CAU hexahedral mesh. The stacked surface grids are converted to a hexahedral grid. This mesh has 200 m horizontal spacing.

A.2.8 Define Node Sets for Setting Initial Conditions, Boundary Conditions and Material Properties

Lists of node sets are created and outputted for use by FEHM to set material properties and boundary conditions. The node set lists include outside, top and bottom nodes, stratigraphic unit numbers, and fault numbers. These lists also include the node identification representing the unit material, fault identification, and the fault-unit correspondence.

A.2.9 Perform Mesh Quality Checks

A number of tests are employed to ensure that the final grid meets the quality standards necessary for accurate and stable computations. These tests are as follows:

- No holes in the mesh.
- No overlapping triangles.
- All elements have positive volume/area.

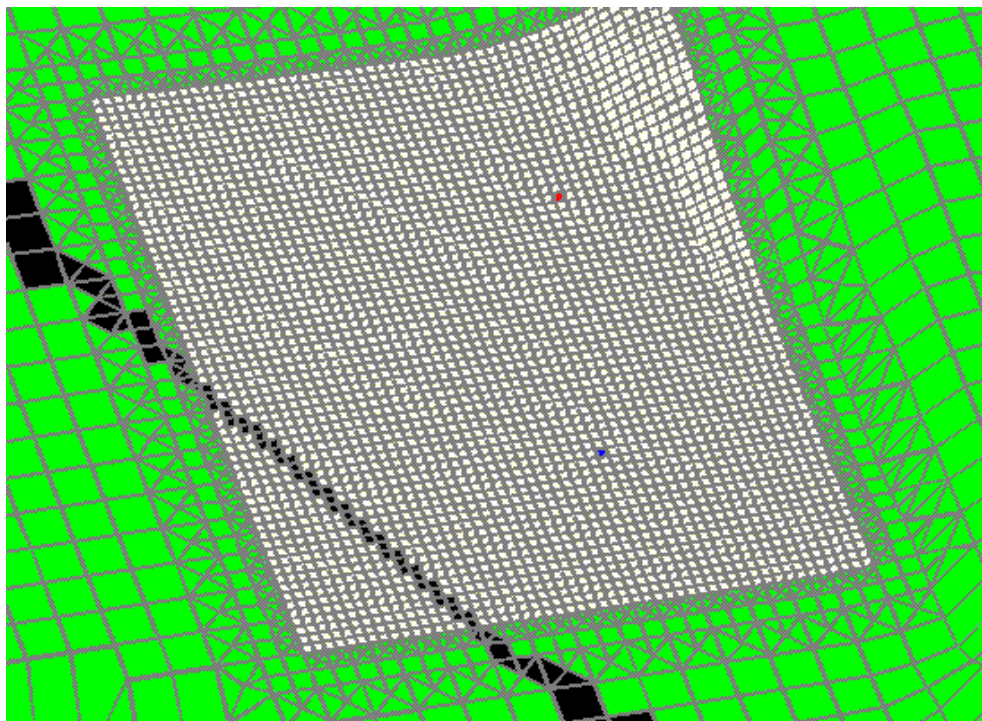


Figure A-8. Image shows a close up of final site location in white. The intersection of NTS plane with the braq surface are the black elements. The blue Well 1 is close to point (546356, 4119171) and the actual well coordinate is (546386, 4119208). The red well 2 is close to point (546606, 4120621) and the actual well coordinate is (546618, 4120648).

- All material interfaces are maintained.
- The mesh is a Delaunay triangulation.
- All geometric coupling coefficients are positive.

A.2.10 Summary

The previous sections provide a step-by-step perspective on the process of finite-element grid generation for FEHM simulations. The methods used surfaces generated elsewhere and provide grids that preserve hydrostratigraphic complexity. Faults are called out with unique properties and increased resolution is provided for regions of interest.

A.3 References

Drellack, S.L., Jr., L.B. Prothro, K.E. Robertson, B.A. Schier, E.H. Price, 1997. Analysis of fractures in volcanic cores from Pahute mesa, Nevada Test Site. Report to U.S. Department of Energy, Nevada Operations Office DOE/NV/11718-160.

George, D.C., 1997. LaGriT Users Manual, URL for publication is <http://www.t12.lanl.gov/~lagrit> (URL confirmed July, 2002).

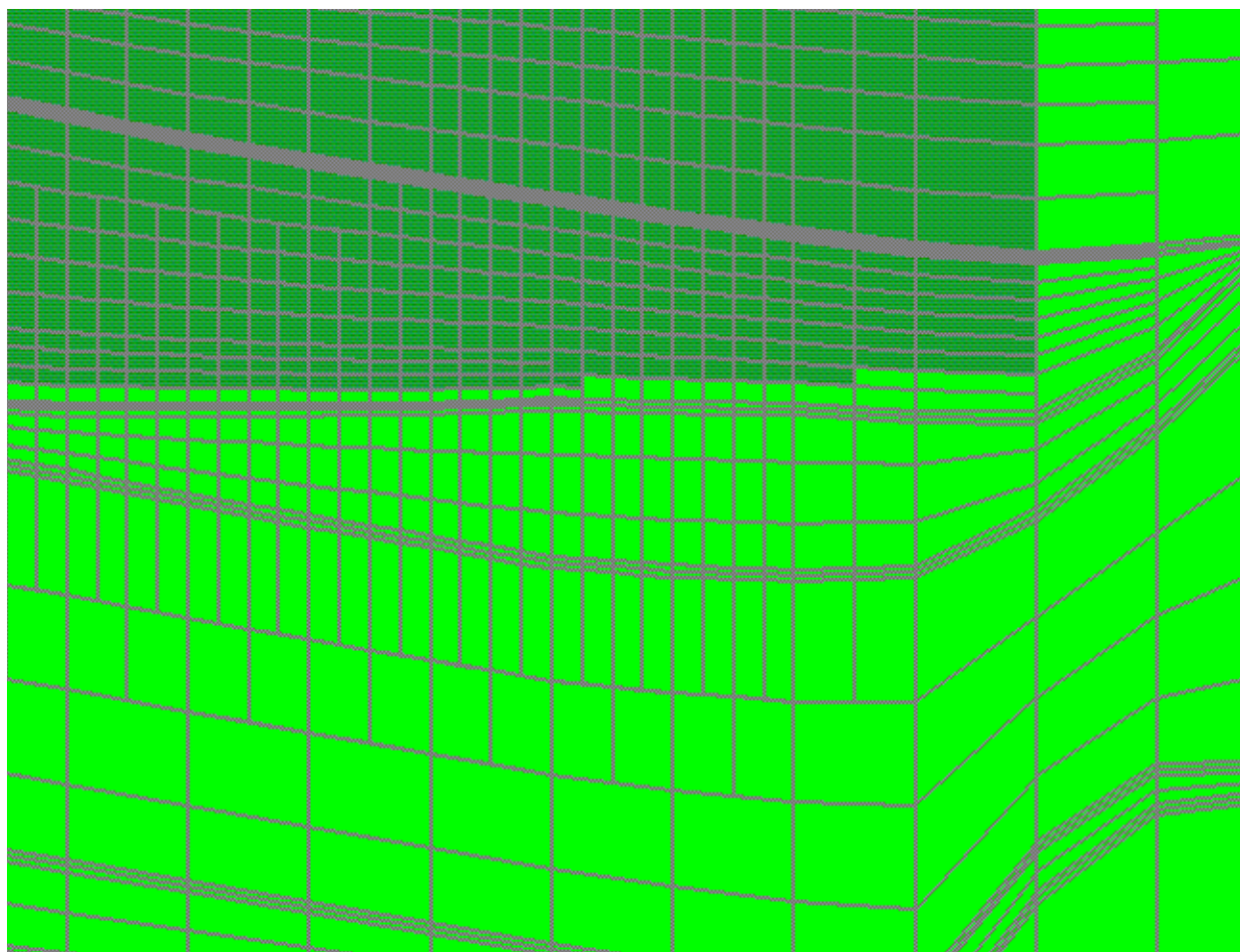


Figure A-9. Slice through the refined sub-CAU grid showing the planned location for the embedded site in dark green. The unit interfaces and their 10-m buffers can be seen as 3 lines close to each other. Under the site location, the elements have been refined with OMR three times, with the transition from large elements to smaller occurring in the thicker Bullfrog Confining Unit.

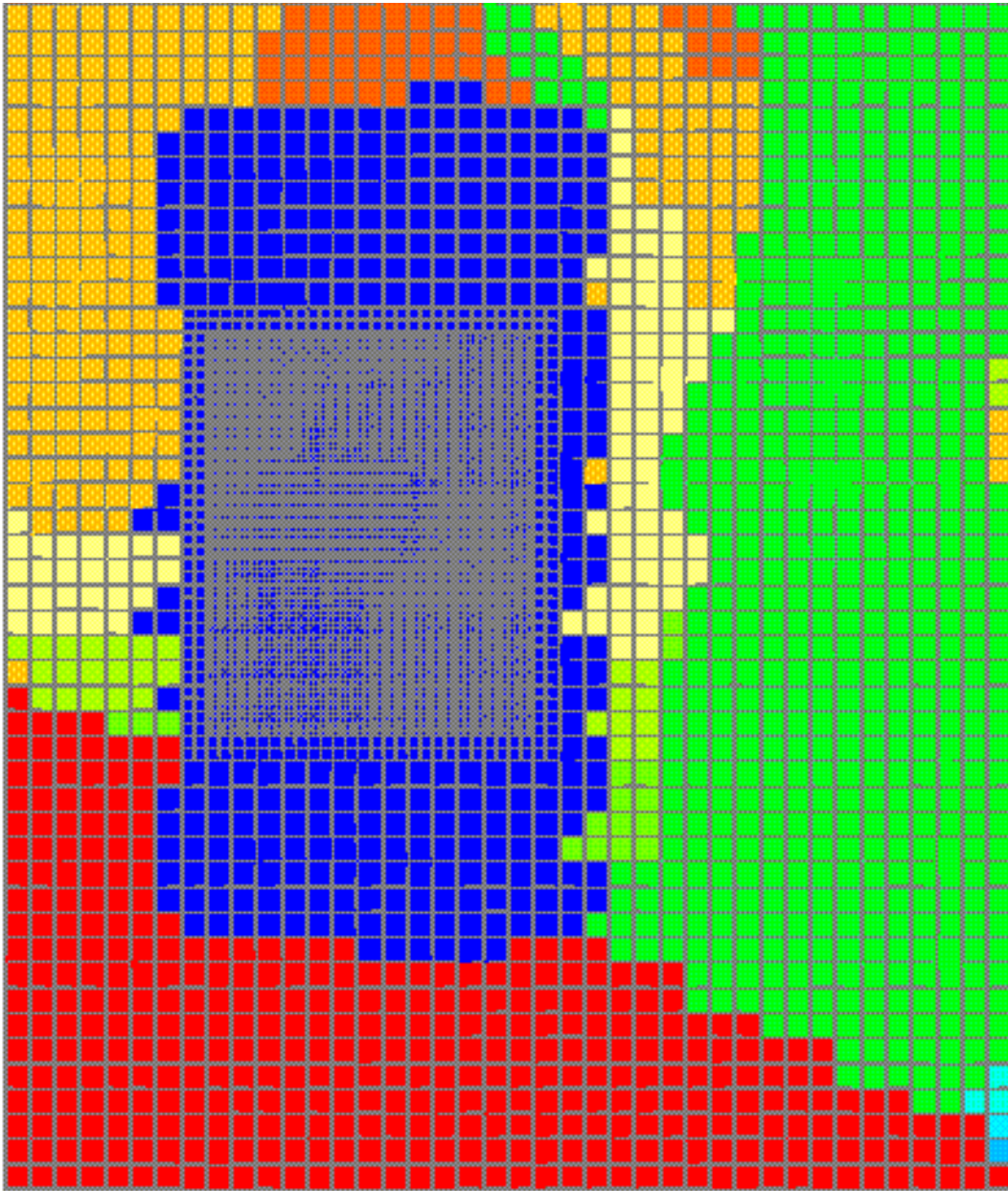


Figure A-10. View from the top shows the embedded site-scale mesh. The colors show material values, the southern unit TMCM is the red area on the bottom. The sub-CAU background mesh has horizontal spacing of 200 m. The site-scale mesh has spacing of 50 m with 10 m vertically. The site-scale mesh is buffered around its boundaries by a 100 m buffer.

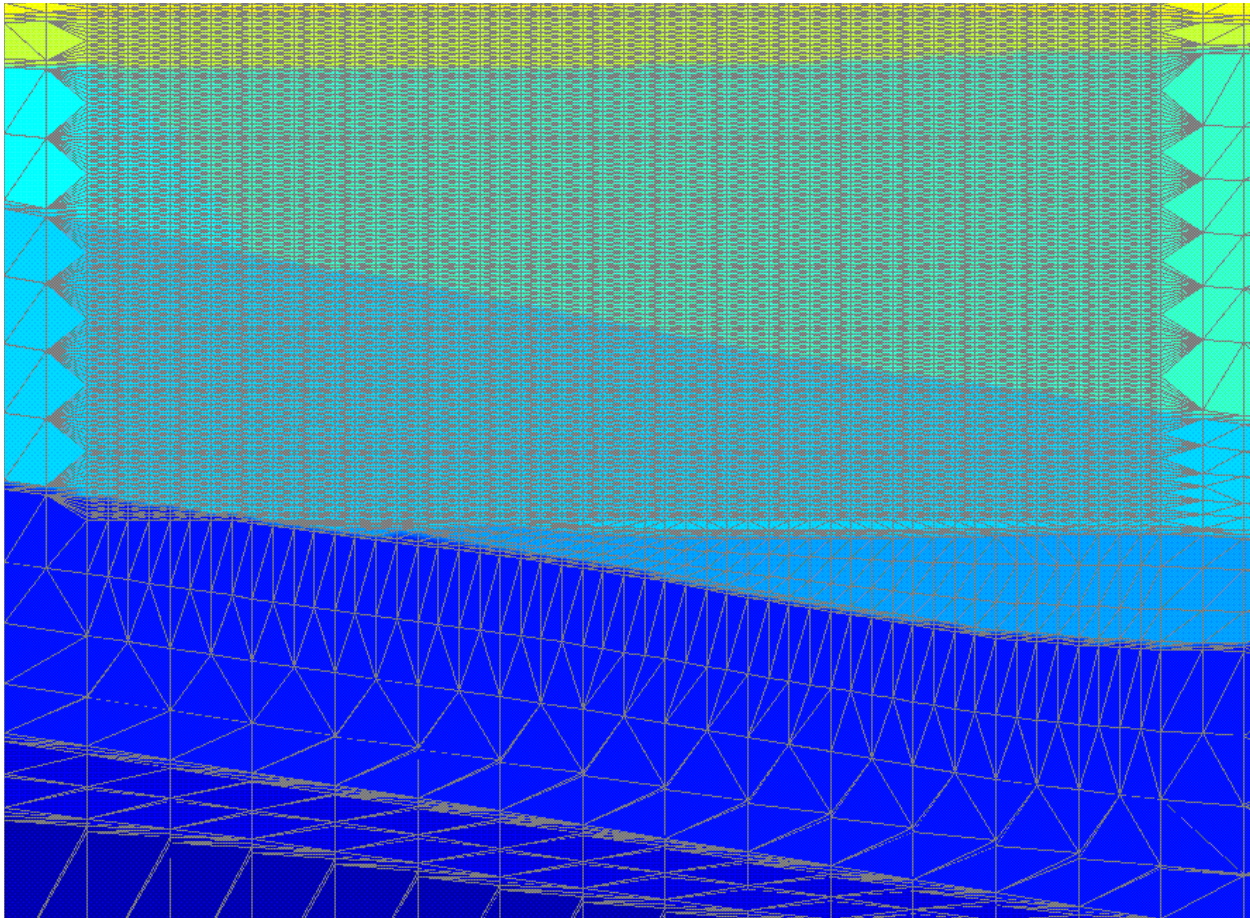


Figure A-11. Image is a slice through $y = 4\ 119\ 218$ showing the final embedded site and background mesh. The mesh has been colored with values corresponding to each unit material. Unit 1, PreTert, is at the bottom and unit 19, pvta, is at the top.

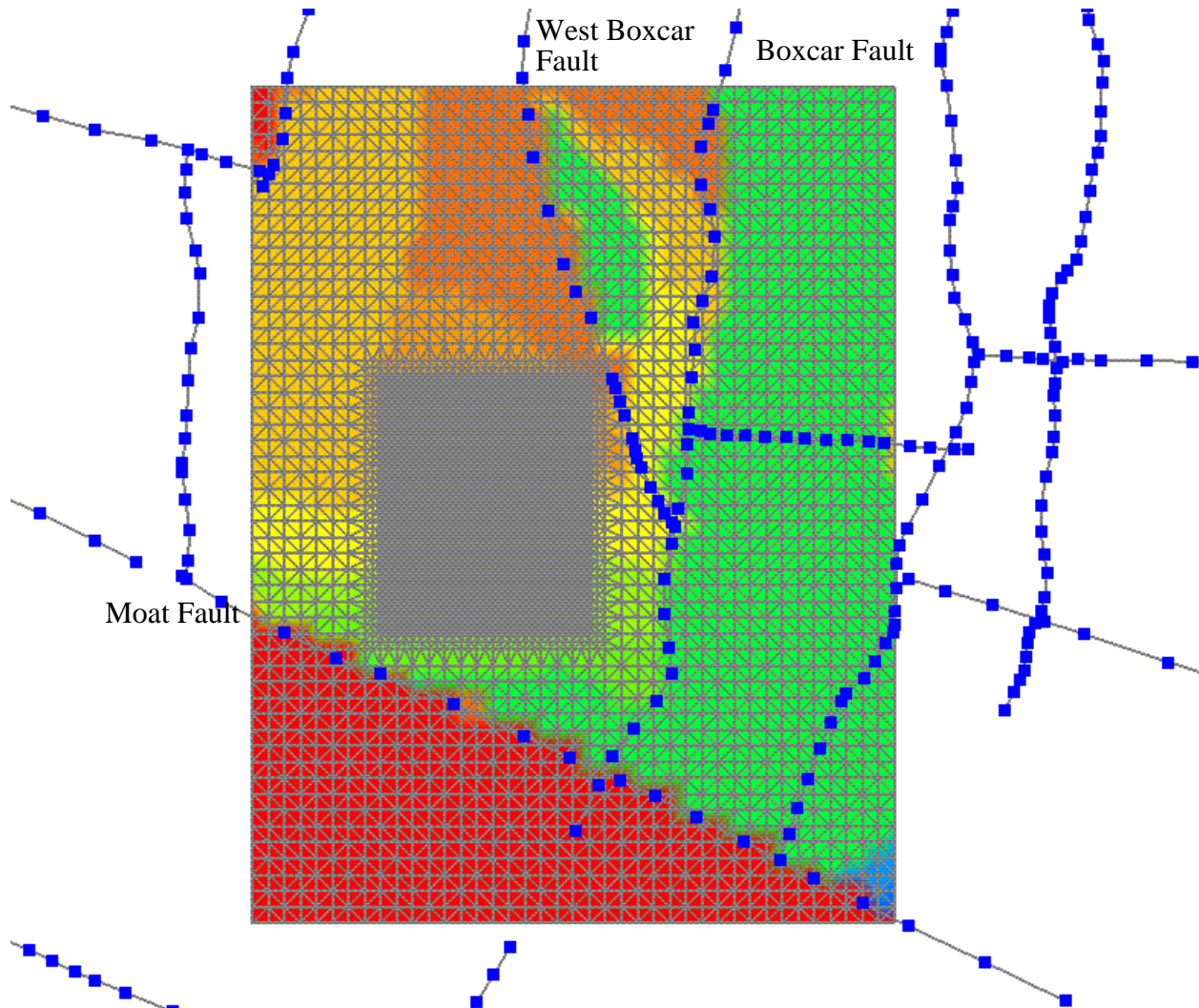


Figure A-12. Image shows the lines describing vertical faults in the model's region. Fault lines are provided by GEOTRANS. The embedded mesh is shown in the background.

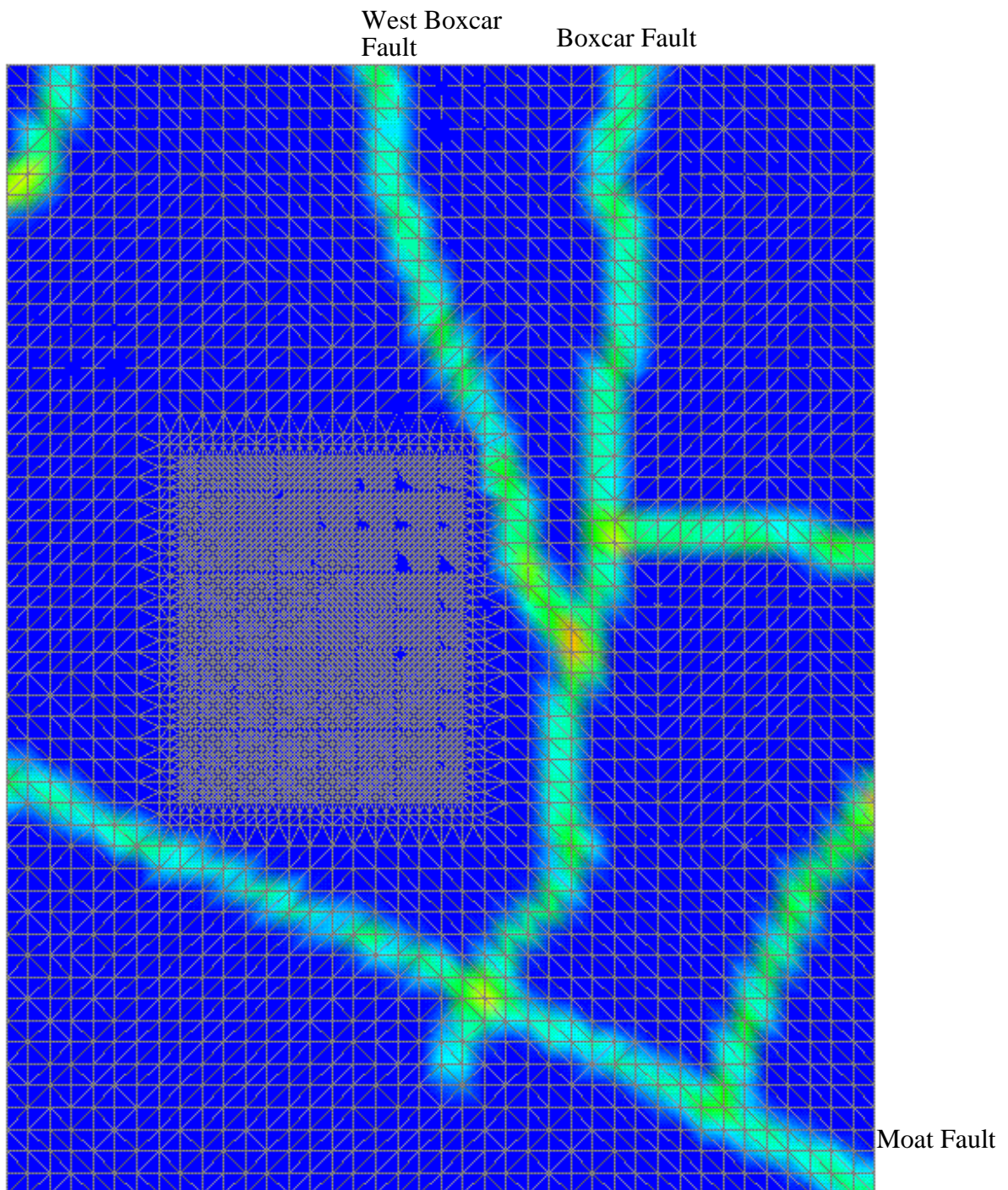


Figure A-13. View from the top of the embedded mesh colored by intersecting vertical faults. The Moat Fault is the diagonal across the southern end, bottom of image.

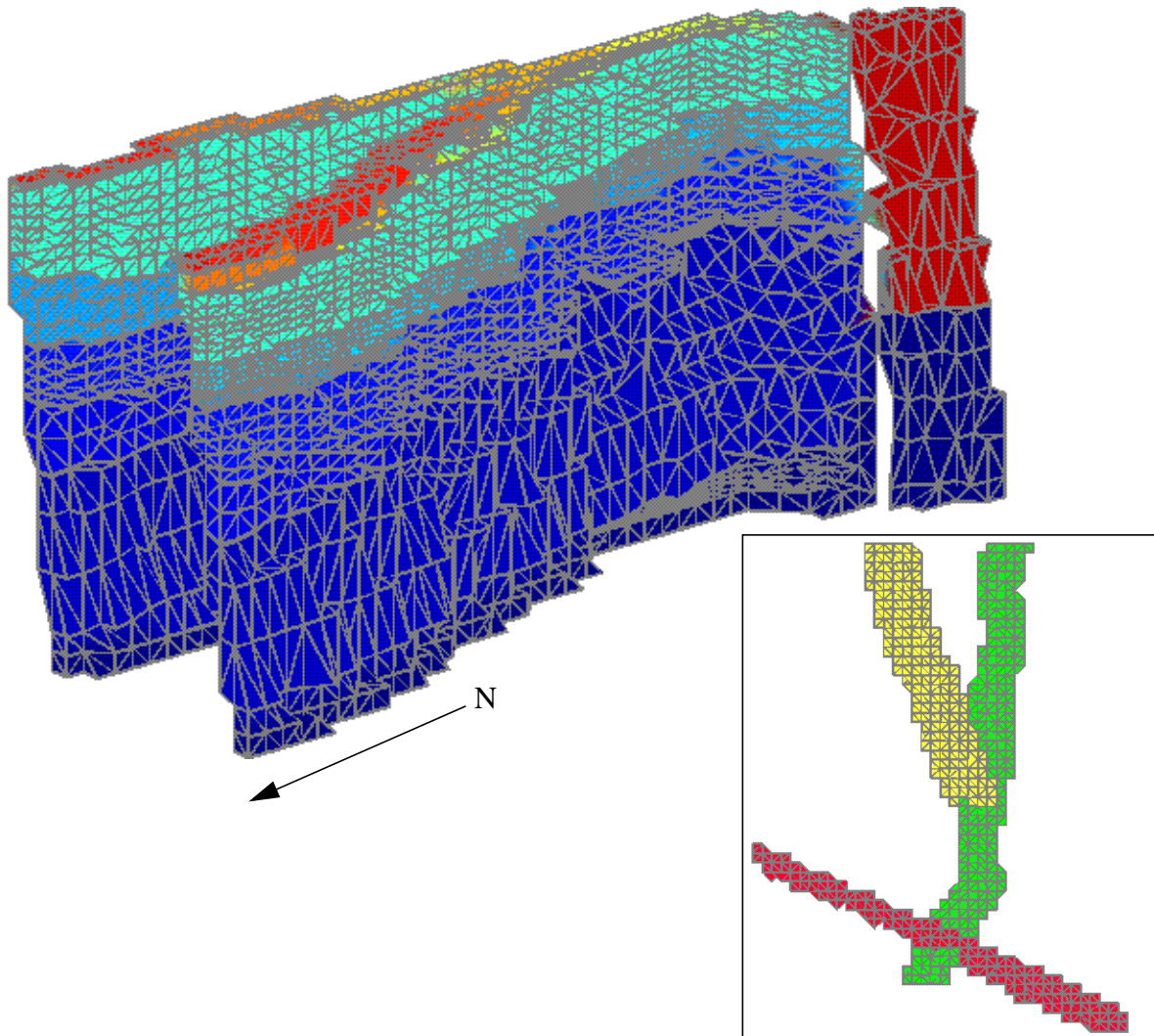


Figure A-14. Three faults were used in this model; these images show these faults extracted from the 3-D tetrahedra mesh. The bottom image is a view from above, showing the faults colored by identification color. The Moat Fault is in red and “wins” priority color over the Boxcar Fault which is in green. The West Boxcar is shown in yellow. The upper image shows the Boxcar Faults colored by their material unit identification. The West Boxcar is in front of the Boxcar Fault. The gap at the right end of the faults shows where the Moat Fault elements intersect the Boxcar Fault, and so do not appear in this image.

This Page Intentionally Left Blank

Appendix B: Coupled Thermal-Hydrologic-Chemical (THC) Source-Term Model

B.1 Introduction

A fully coupled thermal-hydrologic-chemical (THC) reactive transport model is used to investigate possible mechanisms for Pu migration from the BENHAM underground nuclear test. Pu was detected 1.3 km from the test in wells ER-20-5 #3, sampling a lava formation located near the depth of the working point (WP), and well ER-20-5 #1, sampling the TSA welded tuff aquifer located some 500 m above the detonation point (Kersting et al., 1999). In both aquifers, Pu was reported associated with colloids. The BENHAM test, with an announced official yield of 1.15 megatons (DOE, 2000), produced a spherical cavity estimated at 200 m in diameter. A cylindrical, rubblezied, chimney formed as rock above the cavity collapsed, extending from the working point of the test to above the TSA welded tuff aquifer. Forming at the bottom of the cavity was a puddle of melted rock, referred to as MG. The MG is thought to contain a large proportion of the RN inventory.

A puzzling question arises as to how Pu could have migrated from the test site to two distant wells located in aquifers that apparently do not interact with one another, except through the chimney system created by the test. To investigate this question, the computer code FLOTRAN (Lichtner, 2001), which couples transient, non-isothermal flow and reactive transport, was used to model Pu migration in the near field of the BENHAM underground test. A mechanistic model for glass dissolution is incorporated in the model to describe the release of Pu from the MG. The glass dissolution rate is dependent on temperature of the MG and solution composition within the interstitial pore spaces. FLOTRAN accounts for changes in redox state, pH, carbonate, Pu, and other species concentrations over time and distance as the ambient fluid reacts with the MG and minerals in the chimney and surrounding host rock. In addition, FLOTRAN accounts for heat released from the MG and the effects it has on the flow field and chemical reactions. The model can also account for sorption of RNs on rock surfaces and colloids, including both ion-exchange and surface complexation reactions. However, in this preliminary analysis, these processes are not considered further. Instead, a conservative analysis is presented in which Pu is modeled in the absence of retardation effects. However, the full solution chemistry of Pu is considered, including the possibility of precipitation of secondary Pu minerals. This latter effect can be important in limiting Pu concentrations under conditions of rapid dissolution of the MG.

In the development that follows, first the generic properties of a nuclear detonation are considered briefly. This is followed by a discussion of heat and mass conservation equations describing coupled THC processes in a saturated porous medium. Flow of mass and heat based on Darcy's law is coupled to reactive transport equations that account for homogeneous aqueous reactions and heterogeneous mineral precipitation and dissolution reactions. Taken into account are the effects of heat released from the MG on flow, thermodynamic properties of chemical interactions, and mineral and glass kinetic reaction rates through an Arrhenius behavior. The treatment is generally applicable to a single continuum representation of a porous medium. However, extension to dual continua incorporating fracture and matrix interaction can be carried out along the lines presented

in Lichtner (2000) and is considered elsewhere in this report. Simulations are presented for the BENHAM nuclear test to illustrate the influence of the disturbed hydrologic regime caused by heat released from the MG on the migration of Pu for a simplified layer cake stratigraphy composed of homogeneous units with a simplified mineralogy.

The THC coupled model provides a detailed assessment of MG dissolution rates and Pu release rates from the MG, a necessary input to the three-dimensional particle tracking source-term model. In this preliminary study, possible retardation of Pu by ion exchange and surface complexation reactions is ignored. This simplification provides a worst-case scenario in which Pu migrates unretarded, for example, by colloid-facilitated transport. For this to occur, however, would appear to require irreversible sorption of Pu on colloids or the formation of intrinsic Pu colloids, neither of which have been unequivocally established to date.

B.2 THC-Coupled Processes: Modeling the Aftermath of an Underground Nuclear Test

A quantitative description of RN migration following the aftermath of an underground nuclear test requires consideration of coupled THC processes produced by the detonation. A general description of modeling THC processes can be found in Lichtner (1996) and Lichtner and Seth (1996), which describe THC processes applied to the proposed Yucca Mountain high-level nuclear waste repository. In general, a variably saturated, non-isothermal system must be considered. Within a few seconds following detonation of an underground nuclear device, a cavity surrounding the epicenter of the blast is formed. The size of the cavity depends on the yield of the explosion, overburden pressure, and strength of the surrounding rock. Energy released from the blast produces temperatures as high as several million degrees centigrade that vaporize and melt the surrounding rock. The melted rock eventually falls to the bottom of the cavity, forming a puddle of MG that entraps radioactive material and rock fragments. Within minutes to hours or even days following detonation, the cavity collapses, filling with rubblized rock (Pawloski, 1999). Depending on the strength of host rock, a crater may form at the surface. The volume of rock vaporized and MG formed is proportional to the blast yield. RNs produced during the explosion are incorporated into the MG or distributed in the region of the collapse zone referred to as the exchange volume (Tompson et al., 1999). Following collapse of the cavity, re-wetting takes place as the rock and MG begin to cool. This process can take days to months before the chimney becomes fully saturated, even for a deep WP placed beneath the water table (Pawloski et al., 2001).

The geometry of the cavity-chimney-MG system has been determined empirically. The chimney radius is related to the size of the blast through the empirical relation (Smith, 1993)

$$R_C = 70.2 \frac{\mathcal{Y}^{1/3}}{(\rho_r d_{WP})^{1/4}}, \quad (\text{B-1})$$

where R_C refers to the cavity radius in meters, \mathcal{Y} denotes the yield in kilotons, ρ_r denotes the rock density in units of kg m^{-3} , and d_{WP} the depth of the detonation (working point) in meters. The height of the chimney (in meters) can be estimated from the expression

$$h_C = 0.88 R_C^{1.55}, \quad (\text{B-2})$$

and the MG volume (m^3) and mass (kg) estimated from the relations

$$V_{\text{MG}} = 280\mathcal{Y}, \quad (\text{B-3})$$

and

$$M_{\text{MG}} = 7 \times 10^5 \mathcal{Y}, \quad (\text{B-4})$$

consistent with an intrinsic MG density of 2.5 g cm^{-3} . Assuming that the MG fills the bottom of the cavity to a height h_{MG} , and assuming zero porosity, the MG height is related to its volume V_{MG} and cavity radius R_C by the expression

$$V_{\text{MG}} = \frac{\pi h_{\text{MG}}^2}{3} (3R_C - h_{\text{MG}}). \quad (\text{B-5})$$

The heat stored in the rock mass following denotation of fission device has been estimated to be on the order of $10^9 \text{ kJ/(kt yield)}$ (Hochstein and O'Sullivan, 1985 and 1988), and could be even larger for fusion devices depending upon the yield. Properties of the BENHAM test estimated by these relations are listed in Table B-1.

Table B-1: Parameters and geometry for the BENHAM underground nuclear test.

Property	Value	Units
Yield	1.15	Mt
d_{WP}	1402	m
R_C	100	m
h_C	1091	m
M_{MG}	8.05×10^8	kg
V_{MG}	3.22×10^5	m^3
h_{MG}	35	m
Heat	1.15×10^{12}	kJ

It is clear that the early time period following detonation is a highly complex multiphase problem. To simplify the analysis, only times following re-wetting of the cavity and chimney are considered. This avoids the necessity to consider single-gas and two-phase regimes. The single-gas phase regime would have no impact on MG dissolution, although volatile RNs could be released during this period. The two-phase period is relatively short compared to the single liquid-phase regime so that the effects of glass dissolution can be ignored during this period.

In the discussion that follows, the initial configuration of the system is simplified as a cylindrical collapsed chimney of rubblized material with MG at the bottom of the cavity. As the MG cools and reacts with the pore fluid, it can be expected that the glass will become chemically altered and partially replaced, for example, by clay minerals and zeolites. During the cooling process,

RNs such as Pu will be released from the glass matrix. Of interest is the fate of these RNs in the groundwater flow system. The ambient groundwater system is also expected to become altered by the heat released from the MG. For a sufficiently strong detonation resulting in a large volume of MG and stored heat, it is possible for convection cells to develop within the chimney.

From these considerations, a complicated picture evolves for the transport of RNs from the MG and cavity region to the far field. THC processes are intimately intertwined in this process. To describe the evolution of heat released from the MG as it cools, and the effect of heat on flow and transport, a fully coupled transient, non-isothermal, flow and reactive transport model FLOTRAN (Lichtner, 2001) is used to simulate Pu migration away from the BENHAM test. Because of its fully coupled formulation, FLOTRAN addresses mixing issues that may not be adequately described, for example, by a one-dimensional model along streamlines. The model is currently implemented in two spatial dimensions for homogeneous stratified rock and can be extended to three dimensions with heterogeneous media. The computer code FLOTRAN can account for changes in redox state, pH, carbonate concentration and complexes formed with Pu, and other species over time and distance as convection cells develop from the heat released from the MG. A realistic model for glass dissolution is incorporated in the model to describe the release of Pu from the MG. The dissolution rate depends on MG temperature and solution composition within the glass pores. Pu solubility is controlled by the possible formation of secondary Pu-bearing minerals.

As already noted, processes not included in the present formulation include sorption reactions and colloid-facilitated transport involving Pu. Thus the calculations are conservative in the sense that Pu is allowed to migrate unretarded. If sorption were to be included in the model, then it would also be necessary to include competing effects of colloid-facilitated transport of Pu incorporating sorption on colloids. Otherwise retardation would likely be too strong for Pu to migrate any significant distance from the cavity, contrary to observations (Kersting et al., 1999). In addition, sorption on colloids would need to be irreversible for colloids to have a significant affect on Pu retardation at their estimated loading. To avoid these complications, it was decided to model Pu migration as an unretarded tracer species to investigate the possible mechanisms for Pu to migrate the significant distances observed from the working point of the test, both vertically and laterally.

B.2.1 THC Mass and Heat Conservation Equations

THC coupled mass and heat conservation equations account for the interaction of a number of coupled processes. Heat released by the MG affects both flow through density-driven buoyancy effects and chemical interactions caused by changes in thermodynamic and kinetic parameters with temperature. In turn, disturbance of the flow field affects temperature and chemical processes. It is assumed that the chimney-cavity-MG system is emplaced instantaneously into the ambient flow system. Although the rubblization process that occurs during collapse of the chimney most likely results in the chimney being composed of large blocks of rock, for simplicity the chimney is modeled as a single porous medium with an average porosity and permeability. Likewise, the MG can be assumed to entrain blocks of rock material, resulting in a heterogeneous formation. It also is modeled as a single porous medium. Thus potentially important processes such as fracture-matrix interaction are not included in this near-field model describing the BENHAM post-test

environment.

Partial differential equations describing conservation of mass and heat are based on Darcy's law for flow in a porous medium. For a single continuum with saturated conditions, the fluid flow equations have the following form for pure water

$$\frac{\partial}{\partial t} (\phi \rho_w) + \nabla \cdot (\rho_w \mathbf{q}) = 0, \quad (\text{B-6})$$

where ϕ denotes the porosity and \mathbf{q} denotes the volumetric Darcy fluid flow velocity related to gravity and the pressure gradient by

$$\mathbf{q} = -\frac{\kappa}{\mu_w} (\nabla p - \rho_w \mathbf{g}). \quad (\text{B-7})$$

In these equations κ refers to the permeability, μ_w and ρ_w denote the viscosity and density, respectively, of pure water, both a function of fluid pressure p and temperature T , and \mathbf{g} represents the acceleration of gravity. The flow equation is coupled to the equation for heat conservation described by the equation

$$\frac{\partial}{\partial t} [\phi \rho_w U_w + (1 - \phi) C_p^r \rho_r T] + \nabla \cdot (\rho_w H_w \mathbf{q} - \kappa_C \nabla T) = 0, \quad (\text{B-8})$$

with U_w and H_w representing internal energy and enthalpy of pure water, respectively, C_p^r denotes the heat capacity and κ_C the thermal conductivity of the rock-fluid system, and ρ_r refers to the intrinsic rock density. The temperature T is assumed to be the same for both fluid and rock.

The equations for heat and mass conservation must be augmented by initial and boundary conditions that incorporate the regional hydrology and cavity-chimney system. The fluid and heat flow equations incorporate the site-scale hydrologic flow regime and the superimposed effects caused by heat released during the detonation and changes in material properties following chimney and MG formation. Both transient and liquid buoyancy effects must be included, requiring that compressibility of the fluid be taken into account. This requires an equation of state for liquid water. Fluid material properties for density and viscosity are temperature and, to a lesser extent, pressure dependent over the ranges of interest. Constitutive relations must be provided as functions of pressure and/or temperature for the density, viscosity, internal energy, and enthalpy of pure water. In FLOTRAN, this information is derived from thermodynamic properties of water obtained from the International Formulation Committee (1967).

B.2.2 Reactive Transport Equations

The dissolution rate of the MG affects how rapidly RNs can be released to the flow system. As the cooling MG reacts with the ambient groundwater, it can become altered to clay and zeolite minerals, for example, which could significantly affect its sorptive properties. Depending on the MG dissolution rate and temperature conditions, RNs may form secondary mineral phases. To account for these processes, the fluid and heat flow equations must be coupled to reactive transport equations that describe the chemical interactions taking place in the system combined with local

advective and diffusive/dispersive processes. In general, the time-evolution equations must account for transport of RNs by dissolved species and colloids, changes in fluid chemistry including pH, P_{CO_2} , oxidation-reduction reactions, reactions with minerals, and sorption. In the discussion that follows, the THC model for BENHAM is limited to aqueous speciation, reaction of the MG, and precipitation and dissolution reactions for primary and secondary minerals.

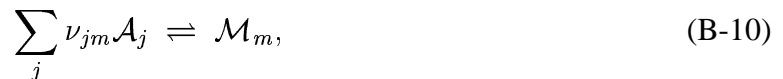
Reactive transport equations for solute species and minerals are coupled to fluid flow and heat conservation equations, Eqs. B-6 and B-8, respectively, through temperature, pressure, and velocity fields (T, p, \mathbf{v}) . In turn, the flow and heat equations may be coupled to the transport equations through changes in porosity, permeability, and heat generation caused by chemical reactions. In particular, alteration of the MG could potentially result in substantial changes in its porosity and permeability. To determine whether it is necessary to incorporate changes in porosity and permeability caused by mineral reactions, calculations are performed that first neglect these changes. If the predicted changes in porosity are significant, then the calculation must be repeated with these effects included. However, it should be noted that it is still an open question as to how best to relate permeability to changes in porosity. Very likely relations more complex than simple dependencies on porosity are needed that account for changes in mineral texture, for example. For the relatively short time period and slow dissolution rate for the MG considered in this work, it was not necessary to include effects resulting from changes in porosity and permeability.

Chemical Reactions

A simultaneous set of chemical reactions involving aqueous and mineral species is incorporated into the solute transport equations. All reactions are written in terms of a fixed set of aqueous species $\{\mathcal{A}_j\}$, referred to as primary species. The reactions taking place in the system may be classified as homogeneous or heterogeneous, depending on the number of phases involved. In the following development, rates of homogeneous reactions that take place in the aqueous phase are described through conditions of local chemical equilibrium. These reactions include ion pairing, complexing, redox, and dissociation of water. Heterogeneous reactions involving aqueous and solid phases consist of mineral precipitation/dissolution and reaction of the MG. Corresponding reaction rates are described through a kinetic rate law based on transition state theory. Homogeneous reactions can be written in the following form for aqueous species \mathcal{A}_i



with stoichiometric coefficients ν_{ji} . The species \mathcal{A}_i is referred to as a secondary species. The choice of primary and secondary species is not unique. Because of the assumption of local equilibrium for these reactions, secondary species may be swapped for primary species, provided the resulting set of reactions is linearly independent. Mineral reactions and reaction of the MG have the form



in which each reaction involves a single mineral or glass phase denoted by \mathcal{M}_m with stoichiometric coefficients ν_{jm} and reaction rate I_m . Reaction of the MG is strictly irreversible and very likely incongruent, accompanied by precipitation of various secondary phases, including clay and zeolite minerals. Solid solutions are not considered in the discussion that follows.

The stoichiometric coefficients and associated equilibrium constants, K_i and K_m , corresponding to Eqs. B-9 and B-10, respectively, depend on the choice of primary species. The equilibrium constants are functions of temperature and pressure. The temperature dependence is obtained by interpolating $\log K$ values stored at temperatures of 0.01, 25, 60, 100, 150, 200, 250, and 300°C along the saturation curve of water and interpolated at intermediate values using the Mayer-Kelly relation

$$\log K(T) = \frac{b_{-2}}{T^2} + \frac{b_{-1}}{T} + b_0 \ln T + b_1 + b_2 T, \quad (\text{B-11})$$

with expansion coefficients b_i , where T denotes the absolute temperature in degrees Kelvin. Pressure is constrained to lie along the steam saturation curve for temperatures above 100°C. Otherwise it is set at 1 bar. The discrepancy between the actual pressure in the system and the pressure at which the $\log K$ is evaluated is considered insignificant for the relatively low pressures involved.

Solute and Mineral Conservation Equations

Separate conservation equations are required for each primary species \mathcal{A}_j in addition to each kinetically reacting mineral and the MG. These equations are coupled through the kinetic rate term and local equilibrium relations for homogeneous reactions. Reactive mass transport equations for the set of primary species can be written as

$$\frac{\partial}{\partial t} (\phi \Psi_j) + \nabla \cdot \Omega_j = - \sum_m \nu_{jm} I_m. \quad (\text{B-12})$$

The quantity Ψ_j appearing in the primary species transport equations represents the total solute concentration with respect to the chosen set of primary species given by

$$\Psi_j = C_j + \sum_i \nu_{ji} C_i, \quad (\text{B-13})$$

with primary species concentration C_j . Secondary species concentrations C_i are obtained from primary species concentrations for conditions of local equilibrium using the law of mass action

$$C_i = \gamma_i^{-1} K_i \prod_j (\gamma_j C_j)^{\nu_{ji}}, \quad (\text{B-14})$$

where γ_i and γ_j refer to activity coefficients of the subscripted species. It should be kept in mind that Ψ_j can take on both positive and negative values depending on the choice of primary species (Lichtner, 1985). The total solute flux Ω_j , likewise defined relative to the chosen set of primary species, is given by

$$\Omega_j = \mathbf{J}_j + \sum_i \nu_{ji} \mathbf{J}_i, \quad (\text{B-15})$$

where the individual species flux, for primary and secondary species, is given by

$$\mathbf{J}_l = -\tau \phi D \nabla C_l + \mathbf{q} C_l, \quad (\text{B-16})$$

involving advection and diffusion/dispersion. For simplicity, the diffusion/dispersion coefficient D is assumed to be the same for all species. However, for situations involving matrix diffusion, incorporating species-dependent diffusion coefficients could be important (Lichtner, 1995).

The volume-averaged kinetic reaction rate for precipitation and dissolution of the m th mineral and dissolution of the MG is denoted by I_m . The mineral reaction rate is in general a function of temperature, pressure, solution composition, and specific mineral surface area. Section B.3.1 provides more detail on the rate expression for describing dissolution of the MG. The mass transfer equation for minerals and MG has the form

$$\frac{\partial \phi_m}{\partial t} = \bar{V}_m I_m, \quad (\text{B-17})$$

with mineral (or glass) volume fraction ϕ_m and molar volume \bar{V}_m . A typical form of the kinetic rate law for mineral precipitation/reactions involving a set of parallel reaction mechanisms labeled by the superscript σ based on transition-state theory is given by

$$I_m = -A_m \left(\sum_{\sigma} k_m^{\sigma} \prod_i a_i^{\nu_{im}^{\sigma}} \right) \left[1 - K_m \mathcal{Q}_m \right] \Theta(K_m \mathcal{Q}_m, \phi_m), \quad (\text{B-18})$$

where k_m^{σ} denotes the backward kinetic rate constant for the overall reaction given in Eq. B-10 of the m th mineral, A_m refers to the mineral surface area per unit bulk volume, ν_{im}^{σ} refers to the stoichiometric coefficient of the reaction prefactor, and the factor Θ is zero or one depending on whether the reaction can actually take place (see Eq. B-21). The different reaction mechanisms can represent dependence on pH and inhibition from other species (e.g. Al, Oelkers et al., 1994).

The specific mineral surface area A_m is proportional to the mineral volume fraction. It is related to the characteristic length scale associated with the surface, such as grain size or matrix block size b_m , surface roughness λ_m , and a geometric shape factor σ_m according to

$$A_m = \frac{\sigma_m \lambda_m}{b_m} \phi_m. \quad (\text{B-19})$$

The shape factor has the value $\sigma_m = 3$ for spherical-, and 6 for cubical-shaped grains or matrix blocks, for example. An alternative formulation of the specific surface area is based on mass rather than bulk volume as in Eq. B-19. The two forms are related by the bulk rock density:

$$A_m^M = \frac{A_m^V}{(1 - \phi) \rho_r}, \quad (\text{B-20})$$

where ρ_r denotes the intrinsic rock density with porosity ϕ .

The factor Θ is defined by

$$\Theta(K_m \mathcal{Q}_m, \phi_m) = \begin{cases} 1, & K_m \mathcal{Q}_m > f_m, \text{ or if } \phi_m > 0 \text{ and } K_m \mathcal{Q}_m < 1, \\ 0, & K_m \mathcal{Q}_m < 1 \text{ and } \phi_m = 0, \end{cases} \quad (\text{B-21})$$

where the ion-activity product \mathcal{Q}_m defined by

$$\mathcal{Q}_m = \prod_j a_j^{\nu_j^m}. \quad (\text{B-22})$$

According to this definition, a mineral is not allowed to dissolve if it is not present. Furthermore, precipitation can occur only if the nucleation kinetic barrier is exceeded by a certain amount, as determined by the saturation index f_m . Setting $f_m = 1$ presumes a kinetic barrier does not exist. In the case of MG, a very large value is taken for f_m because the glass reaction is considered strictly irreversible. This form of the rate law is based on the mineral reaction as written in Eq. B-10 with the mineral appearing on the right-hand side. The convention chosen for the sign of the rate is positive if the reaction proceeds from left to right (precipitation), and negative in the opposite direction (dissolution). Mineral stability depends on the saturation state, determined by the equilibrium constant K_m corresponding to Eq. B-10, and the ion activity product. Thus the reaction rate is positive, negative, or zero, thereby indicating precipitation, dissolution, or equilibrium, respectively, depending on the magnitude of the product $K_m Q_m$:

$$I_m = \begin{cases} > 0, & \text{if } K_m Q_m > 1, \\ = 0, & \text{if } K_m Q_m = 1, \text{ or if } K_m Q_m < 1 \text{ and } C_m = 0, \\ < 0, & \text{if } K_m Q_m < 1 \text{ and } C_m > 0, \end{cases} \quad (\text{B-23})$$

where C_m denotes the mineral concentration. Mineral concentration C_m is related to volume fraction ϕ_m by

$$C_m = \bar{V}_m^{-1} \phi_m. \quad (\text{B-24})$$

Mineral and glass surface areas are difficult to quantify in natural systems. To complicate matters, different surface areas can be involved in different processes. Thus dissolution involves the surface area of the dissolving phase, whereas precipitation of one mineral could occur on the surface of another.

Porosity is often related to mineral volume fractions by the expression

$$\phi = 1 - \sum_m \phi_m. \quad (\text{B-25})$$

However, this expression is only approximate because it does not distinguish between total and connected porosity. Nevertheless, it does provide an estimate of the extent to which mineral precipitation and dissolution affects the porosity of the porous medium.

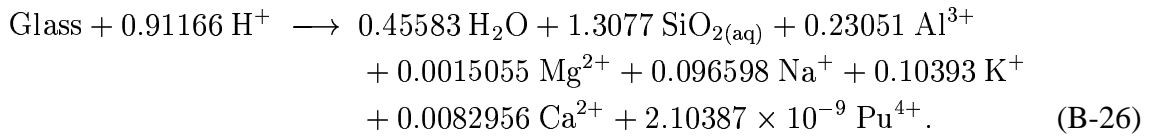
B.3 Application to the BENHAM Underground Nuclear Test

B.3.1 Melt-Glass Source Term: Composition and Dissolution Rate

Because a detailed description of the source term is classified, it is necessary to assume a generic source term in the modeling studies. The generic source term may differ from the actual source term in size of cavity, chimney volume, MG chemical composition, and RN inventory. The chimney is considered as part of the source term because it is created during the underground test and RNs could have been emplaced in the chimney during the initial detonation period. Values for

these quantities were estimated from the announced yield of the BENHAM test of 1.15 Mt. For the RN inventory, generic values are used based on unclassified average values for 76 tests near or below the water table on Pahute Mesa (Smith, 2001).

A number of processes couple chemical reactions to the flow and thermal fields. Alteration of the MG to clay and zeolite minerals can affect porosity and permeability of the glass. The glass composition is taken from Pawloski (1999), although it is modified somewhat to reduce the complexity of the glass. The only RN considered is Pu. In addition, the species iron, phosphate, titanium, chloride, and manganese were eliminated to reduce the number of primary species to describe the aqueous solution composition. Eliminating these species and adjusting the Pu stoichiometric coefficient to be consistent with 18.7 total moles of Pu, the average value of all tests conducted near or below the water table on Pahute Mesa (Smith, 2001), and modifying stoichiometric coefficients for H^+ and H_2O in the original rate expression to maintain charge balance, resulted in the following irreversible glass dissolution reaction:



The density of the glass is assumed to be 2.5 g/cm^3 , similar to quartz, the dominate component. The formula weight is 100 g/mol , which gives a molar volume of $40 \text{ cm}^3/\text{mole}$. The equilibrium constant for the reaction is taken to be the same as amorphous silica. Activation energy used for the glass is 20 kcal/mol or 83.736 kJ/mol . Although the glass dissolution reaction is written in terms of Pu^{4+} , in the calculations presented below the Pu-species PuO_2^+ is used as primary species.

The kinetic rate law for dissolution of the MG is given by transition state theory as

$$I_{MG} = -k_{MG}(\text{pH}, T) A_{MG} [1 - K_{MG} Q_{MG}], \quad (\text{B-27})$$

for $K_{MG} Q_{MG} < 0$, and $I_{MG} = 0$ otherwise. This is to ensure that MG cannot precipitate from solution if it becomes supersaturated. The MG specific surface area is denoted by A_{MG} , the glass rate constant by k_{MG} , the quantity K_{MG} refers to the glass pseudo-equilibrium constant, and Q_{MG} refers to the glass ion-activity product. The rate constant $k_{MG}(\text{pH}, T)$ is a function of temperature and pH according to the relation

$$k_{MG}(\text{pH}, T) = (k_0 + k_H a_{H^+}^a + k_{OH} a_{OH^-}^b) f_A(T), \quad (\text{B-28})$$

with rate constants $k_0 = 2.57 \times 10^{-16}$, $k_H = 3.12 \times 10^{-14}$, and $k_{OH} = 9.75 \times 10^{-13} \text{ mol cm}^{-2} \text{ s}^{-1}$, and slopes $a = 0.4566$ and $b = 0.5155$ (Pawloski, 1999). The Arrhenius factor $f_A(T)$ is given by

$$f_A(T) = \exp \left[\frac{\Delta E^\ddagger}{R} \left(\frac{1}{T_0} - \frac{1}{T} \right) \right], \quad (\text{B-29})$$

with reference temperature T_0 , gas constant R , and activation energy ΔE^\ddagger . The temperature dependence of the Arrhenius factor is shown in Fig. B-1. As can be seen from the figure, the Arrhenius factor varies over six orders of magnitude from 25°C to 300°C . The pH dependence of the rate constant is shown in Fig. B-2. The rate increases by as much or more than two orders of magnitude for low and high pH.

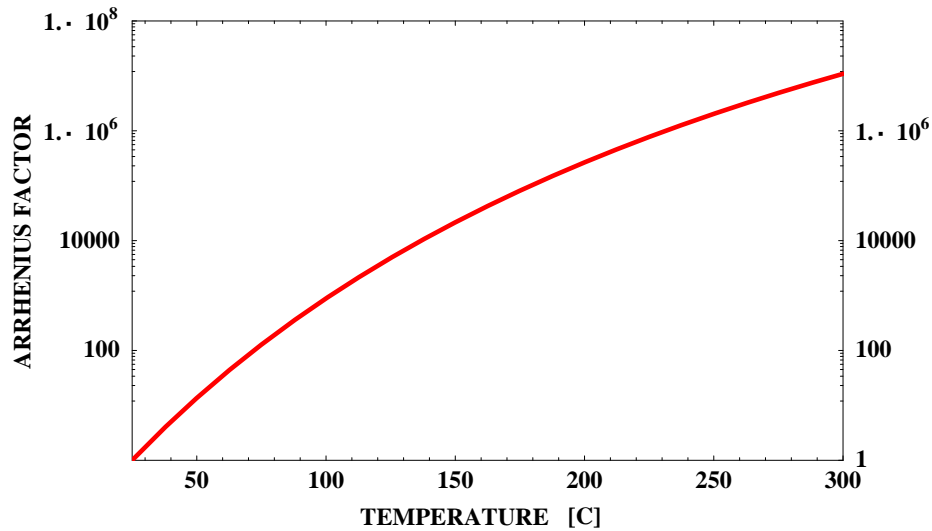


Figure B-1: Arrhenius temperature factor corresponding to an activation energy of 83.72 kJ/mol.

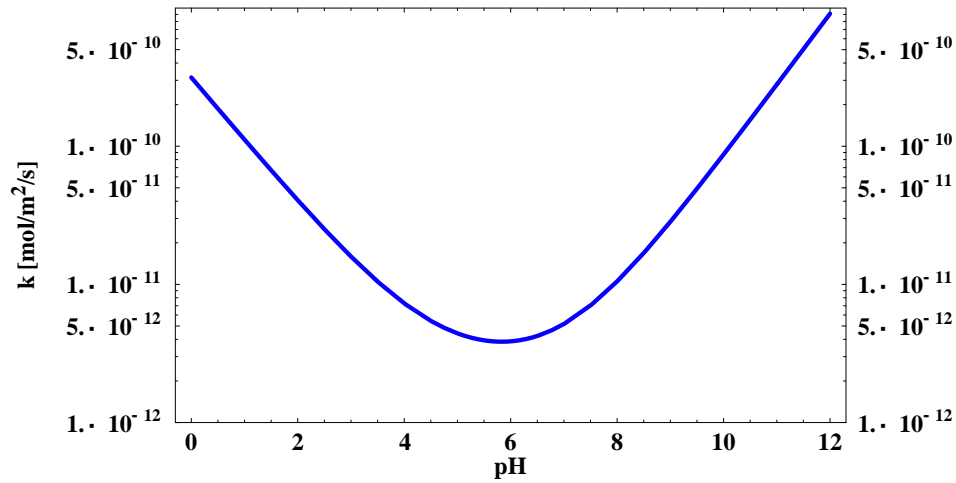


Figure B-2: The pH dependence of the melt-glass dissolution rate constant.

As the MG dissolves, its surface area changes with time. It may either increase or decrease, but eventually as the glass completely dissolves, the surface area must become zero. One possible form for the surface area is to assume a two-thirds dependence on the glass volume fraction, relating area to volume to give the relation

$$A_{\text{MG}} = \left(\frac{\phi_{\text{MG}}}{\phi_{\text{MG}}^0} \right)^{2/3} A_{\text{MG}}^0. \quad (\text{B-30})$$

To use this relation, it is necessary to estimate the initial MG surface area A_{MG}^0 . Without having much information about the physical state of the MG and properties that might be helpful for estimating its fracture density and grain size, another approach is to consider the surface area necessary for a significant change to occur in the MG volume fraction over time. From Eq. B-17,

the change in MG volume fraction with time, taking into account Eq. B-30, can be expressed as

$$\frac{\partial \phi_{\text{MG}}}{\partial t} = -\bar{V}_{\text{MG}} k_{\text{MG}} [T(t)] \left(\frac{\phi_{\text{MG}}}{\phi_{\text{MG}}^0} \right)^{2/3} A_{\text{MG}}^0, \quad (\text{B-31})$$

where the dependence of surface area on volume fraction and the dependence of the rate constant on time through the variation in temperature given by the Arrhenius expression, (Eq. B-29), has been explicitly inserted. Integrating this equation yields an expression for the fractional change in MG volume fraction given by

$$\chi_{\text{MG}}(t) = \frac{\phi_{\text{MG}}^0 - \phi_{\text{MG}}(t)}{\phi_{\text{MG}}^0} = 1 - \left[1 - \frac{1}{3} \frac{\bar{V}_{\text{MG}} A_{\text{MG}}^0}{\phi_{\text{MG}}^0} \int_0^t k_{\text{MG}} [\bar{T}_{\text{MG}}(t')] dt' \right]^3, \quad (\text{B-32})$$

which accounts for the reduction in surface area with dissolution and the change in average MG temperature \bar{T}_{MG} with time. A value of one implies all MG has dissolved. Initially, $\chi_{\text{MG}}(0) = 0$. To evaluate this relation it is necessary to obtain an estimate of the temperature of the MG $\bar{T}_{\text{MG}}(t)$ as a function of time. The MG is expected to cool primarily by convection and, furthermore, its temperature could be highly nonuniform as a result of the formation of convection cells. Nevertheless, an approximate estimate of the MG temperature can be obtained by considering the conductive cooling of a spherical mass equal to the mass of the MG. The radial temperature profile for a cooling sphere of radius a has the analytical form

$$T(r, t) = \frac{1}{2} (T_2 - T_1) \left\{ \frac{2}{r} \sqrt{\frac{\alpha t}{\pi}} \left(e^{-(a+r)^2/4\alpha t} - e^{-(a-r)^2/4\alpha t} \right) + \text{erf} \left(\frac{a-r}{2\sqrt{\alpha t}} \right) + \text{erf} \left(\frac{a+r}{2\sqrt{\alpha t}} \right) \right\} + T_1, \quad (\text{B-33})$$

where α denotes the thermal diffusivity assumed the same for MG and host rock, T_1 refers to the initial host rock temperature, and T_2 the initial temperature of the MG. Taking the average over the volume of the MG yields the desired temperature

$$\bar{T}_{\text{MG}}(t) = \frac{3}{a^3} \int_0^a T(r, t) r^2 dr. \quad (\text{B-34})$$

This temperature is used as an estimate of the MG temperature.

The average MG temperature is shown in Fig. B-3 for $a = 42.52$ m, $\alpha = 3 \times 10^{-6}$ m² s⁻¹, initial MG temperatures of 150°C and 290°C, and initial host rock temperature of 35°C. The value for the thermal diffusivity was chosen to approximate the numerically calculated temperature profile shown by the points in Fig. B-3, which accounts for advection as well as conduction. The fractional change in volume fraction of the MG is plotted in Fig. B-4a for an initial MG temperature of 150°C, and Fig. B-4b for 290°C for different surface areas as indicated in the figure. As can be seen from the figures the most of the dissolution of the MG takes place at early times when the temperature is higher. For the following simulation a value of $b_{\text{MG}} = 44$ cm for the MG block size is used, or $A_{\text{MG}} = 0.135$ cm⁻¹ with $\phi_{\text{MG}} = 0.99$, for an initial temperature of 150°C. This choice avoids significant changes in MG volume. It implies that the MG is fractured into relatively

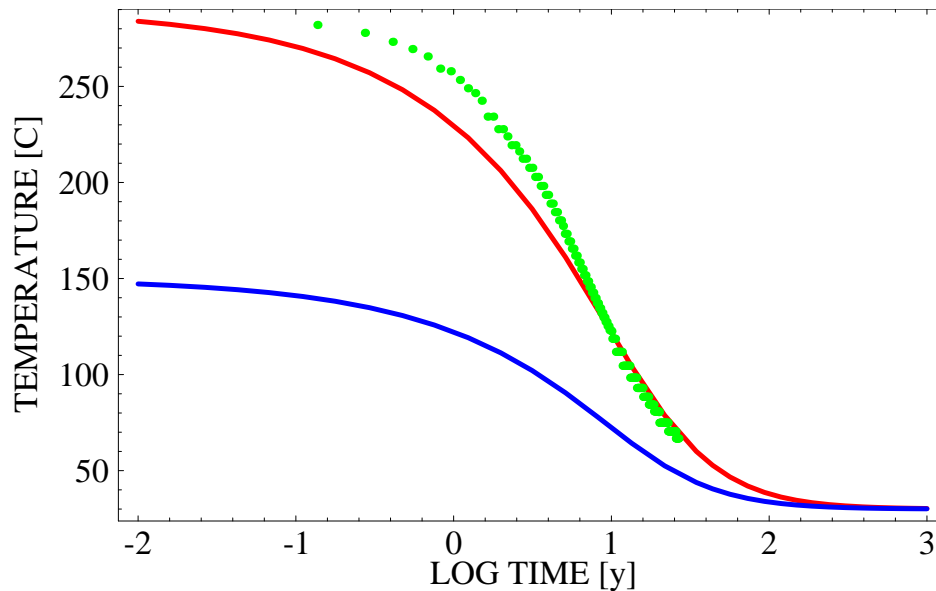


Figure B-3: Average melt-glass temperature based on a pure conduction model for cooling of a sphere with volume equal to the total MG volume for initial MG temperatures of 290°C (red curve) and 150°C (blue curve). The initial rock temperature was set to 35°C in both cases. The green dots correspond to the three-dimensional convective cooling calculation shown in Fig. 6-6

large blocks, or alternatively, that only a small fraction of the MG surface area is in contact with fluid. At the higher temperature of 290°C, and considering only heat transfer by conduction, this surface area would result in complete dissolution of the MG in a matter of years. It should be noted, however, that the pure conduction-based temperature used here probably overestimates the temperature at longer times. Further, these rates do not account for transport-limited dissolution as discussed in the next section.

B.3.2 Rate Controlling Step

At elevated temperatures, the high dissolution rate obtained for the MG could contradict the assumptions inherent for the validity of the continuum formulation of the transport equations. The continuum approach is valid provided that the concentration within a single pore space is uniform (Kechagia et al., 2002). Furthermore, the rate as predicted by the transition state rate law must not exceed the rate at which species can be transported to and from the surface where the reaction takes place. For elevated temperatures or for conditions of high supersaturation, it is possible for the rate predicted by the transition state rate law to exceed the maximum physically possible rate. In such cases the rate becomes limited by diffusive transport to the mineral surface.

To estimate the implications of the MG dissolution rate on spatial gradients in concentration, a single component system is considered in which species diffuse across a boundary layer between the bulk fluid and the MG surface. The thickness of the boundary layer is dependent on the flow

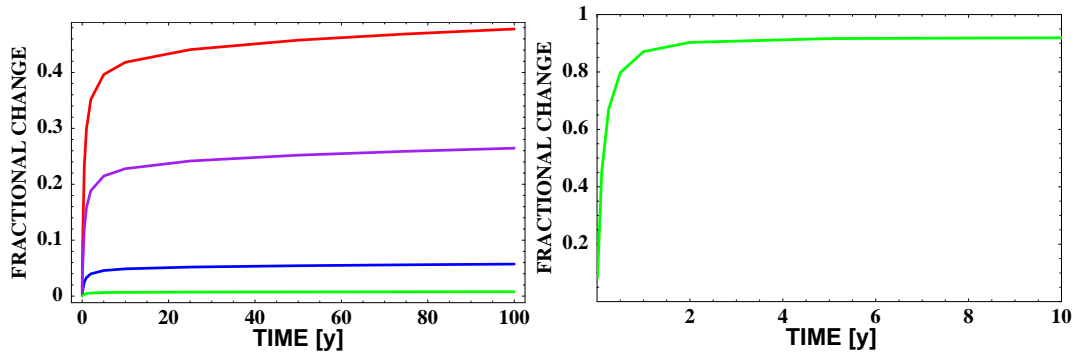


Figure B-4: Fractional change in melt-glass volume fraction plotted as a function of time taking into account changes in temperature based on a pure conduction model and melt-glass surface area. Left: initial melt-glass temperature of 150°C corresponding to surface areas of 10, 5, 1, and 0.135 cm⁻¹ in decreasing fractional change. Right: initial melt-glass temperature of 290°C corresponding to an area of 0.135 cm⁻¹.

rate. The flux J normal to the surface of the MG is equated to the reaction rate evaluated at the glass surface with area A (Murphy et al., 1989)

$$\begin{aligned} JA &= -A\phi D \frac{dC}{dl} = -A\phi D \frac{C_b - C_s}{\Delta l}, \\ &= I_s, \end{aligned} \quad (\text{B-35})$$

where Δl corresponds to the boundary layer thickness. The solute concentration at the mineral surface is denoted by C_s , and for the bulk fluid by C_b . Here I_s refers to the reaction rate at the mineral surface given by

$$I_s = kA(C_s - C_{\text{eq}}), \quad (\text{B-36})$$

where k denotes the forward rate constant. Equation (B-35) can be solved for the concentration at the surface to give

$$C_s = \frac{\phi DC_b + k\Delta l C_{\text{eq}}}{\phi D + k\Delta l}. \quad (\text{B-37})$$

With this result the rate I_s can be expressed in terms of the bulk fluid concentration appropriate to the continuum formulation. Substituting Eq. B-37 into Eq. B-36 yields

$$I_s = k_{\text{eff}} A (C_b - C_{\text{eq}}), \quad (\text{B-38})$$

where the effective rate constant k_{eff} is defined by

$$k_{\text{eff}}(T) = \frac{k(T)}{1 + \frac{k(T)\Delta l}{\phi D(T)}}, \quad (\text{B-39})$$

where the dependence on temperature is indicated. The quantity in the denominator, $\mathcal{D} = k\Delta l/\phi D$, is the Damköhler number of the second kind (Damköhler, 1936), also referred to as the Sherwood

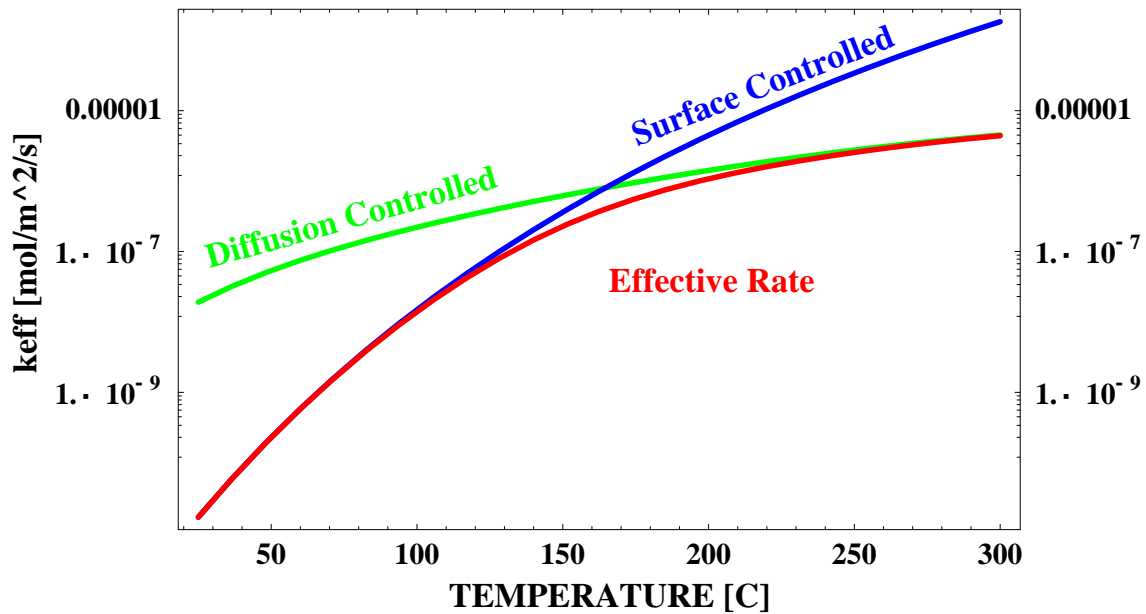


Figure B-5: Effective rate constant for dissolution of MG with a pore size of $\Delta l = 1$ mm plotted as a function of temperature. A pH of 8.5 is used in the calculation.

number (Flowler, 1997). For large values of the Damköhler number the reaction rate is diffusion controlled; whereas for small values the rate is surface controlled giving the limiting cases

$$k_{\text{eff}} = \begin{cases} k, & (\mathcal{D} \ll 1) \\ \frac{\phi D}{\Delta l}, & (\mathcal{D} \gg 1) \end{cases} \quad (\text{B-40})$$

This is demonstrated in Fig. B-5 where the effective kinetic rate constant for the MG is plotted as a function of temperature. A boundary layer thickness of $\Delta l = 1$ mm is used, which should be considered as an upper limit of the MG pore-size distribution for illustrative purposes. Smaller pore diameters shift the cross-over point between diffusion- and surface-controlled reaction to higher temperatures. More data would be needed to properly characterize this value. Generalizing the derivation of an effective rate constant to a multicomponent system involving several simultaneous reactions at the surface is much more difficult to carry out and is not attempted here. Because the resulting equations are nonlinear and must be solved numerically in most cases, it is not possible to derive an explicit expression for the effective rate constant in this case.

B.3.3 Geologic Model

A two-dimensional, vertical cross section through the center of the chimney is used to model the system. The model domain is 1050 m in depth and 500 m in length. A schematic diagram of the initial configuration showing the relationship of the chimney, cavity, and MG, to the original stratigraphy of the host rock is shown in Fig. B-6.

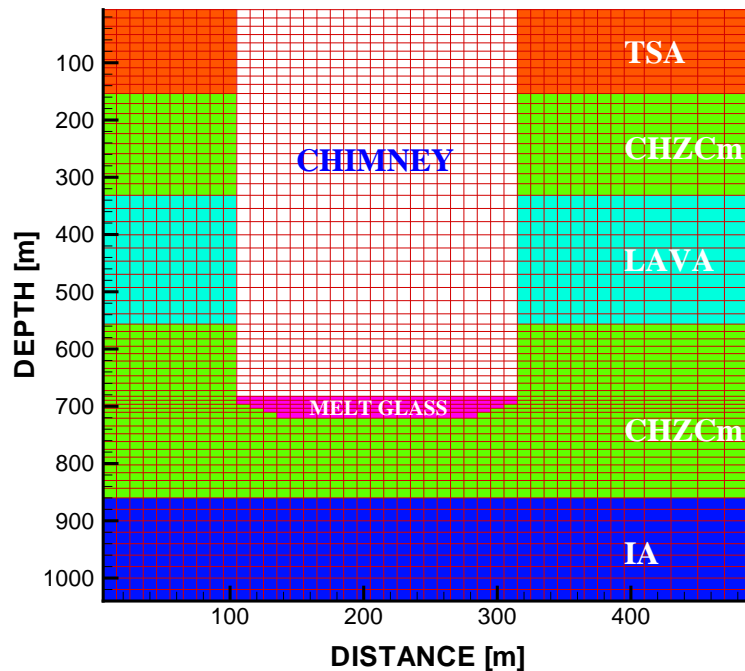


Figure B-6: Schematic showing the stratigraphic sequence at BENHAM along with emplacement of the chimney and MG following detonation of an underground test. The vertical and horizontal lines indicate placement of the grid used in the simulations. The origin corresponds to a depth of 1100 m a.s.l.

The stratigraphy at the BENHAM test consists of four distinct layers. These are designated as the Topopah Spring Aquifer (TSA), Calico Hills Zeolitic formation (CHZCm), embedded lava formation (LAVA), and Inlet Aquifer (IA), as shown in Fig. B-6. The depths and physical properties of each stratigraphic unit, including the MG and chimney, is listed in Table B-2. The chimney region is modeled as a homogeneous porous medium with uniform properties resulting from rubblization during collapse, similar to those used by Pawloski et al. (2001). An alternative approach would be to consider a stratified chimney with properties taken from the original formation at depth. However, this approach was not pursued further in this report. It should also be noted that the connected porosity used for the MG of 1% is representative of fracture porosity. A larger value, such as used by Pawloski (1999), would be more representative of the matrix of a vesicular porous media.

The host rock and MG composition and reaction rates and activation energy of primary and secondary minerals are listed in Table B-3 and B-4. The same mineralogy is assumed for each stratigraphic unit with the volume fraction for K-feldspar set to 0.4, and the volume fraction for quartz adjusted to give the assumed matrix porosity of each unit. Porosity and permeability are assumed to remain constant during the simulation and, as a consequence, the initial mineral volume fraction only affects the specific mineral surface area. Because of the slow reaction kinetics of these minerals, very little effect, if any, is expected on the final results, except perhaps within the melt region where the temperature is highest. The minerals included are based on a simplification of the

Table B-2: Stratigraphy and associated physical properties for different stratigraphic units representing the host rock surrounding the BENHAM nuclear test (see Table 6-2). Parameters used in the preliminary THC model were based on estimates from the range of Drellack and Prothro (1997). Depth to TSA, CHZCm, and IA is taken from Drellack and Prothro (1997), and depth to LAVA from Prothro and Warren (2001).

Unit Name	Depth [m]	ρ_r [kg/m ³]	C_p^r [J/(kg K)]	κ_C [J/(m s K)]	ϕ —	κ [m ²]
TSA	0–145	2500	880	1.8	0.161	3.99×10^{-11}
CHZCm	145–320	2350	1154	1.2	0.250	4.74×10^{-15}
LAVA	320–550	2270	1000	2.5	0.083	5.00×10^{-13}
CHZCm	550–850	2350	1154	1.2	0.250	4.74×10^{-15}
IA	850–1050	2270	1000	2.5	0.083	6.15×10^{-13}
Chimney	0–714	2354	1043	1.8	0.185	5.00×10^{-11}
Glass	679–714	2500	1154	2.7	0.010	5.00×10^{-13}

Table B-3: Host rock and MG properties.

Mineral	TSA	CHCZm	LAVA	IAQ	Chimney	MG
Glass	—	—	—	—	—	0.45
K-feldspar	0.400	0.400	0.400	0.400	0.400	0.14
Quartz	0.439	0.350	0.517	0.517	0.415	0.40
Porosity	0.161	0.250	0.083	0.083	0.185	0.01

whole rock composition to provide an approximation for use in this preliminary modeling study. The pH dependence of mineral rate laws is not considered in this analysis but could be added easily.

The conceptual model used for the MG is based on large fractured blocks (on the order of 1–0.1 m), consisting of entrained rock fragments surrounded by glass. Water is able to flow around the blocks, but communication with the interior of a block is considered to occur only by diffusion. There is some justification for this conceptual model from photographs of the MG taken from the RAINIER test (Wadman and Richards, 1961). The photograph shows a heterogeneous distribution of MG and rubble with entrained tuff blocks on the order of 0.3 m in length. Unfortunately, direct characterization of the MG for the BENHAM test is unavailable at present. As a first approximation only reaction with the outer surface of the blocks is taken into account. To account properly for diffusive mass transfer and reaction within each block interior would require a dual continuum approach, which lies beyond the scope of the present study.

Table B-4: Mineral kinetic rate parameters used in this study.

Mineral	k_m [mol cm ⁻² s ⁻¹]	A_m [cm ⁻¹]	ΔE^\ddagger [kJ mol ⁻¹]
Glass	(see text: Eq. B-28)	0.135	83.736
K-feldspar	3.02×10^{-16}	1.	35
Quartz	3.16×10^{-18}	1.	35
Muscovite	1×10^{-14}	1.	35
Calcite	1×10^{-12}	1.	35
Gibbsite	1×10^{-14}	1.	35
Kaolinite	1×10^{-14}	1.	35
Analcime	1×10^{-14}	1.	35

Table B-5: Comparison of kinetic rate parameters used to model the CHESHIRE (Pawloski, 1999) and BENHAM (this study) tests.

Property	Test	
	CHESHIRE	BENHAM
A_{MG}^0	10 [cm ² /g] (25 [cm ⁻¹])	0.12 [cm ² /g] (0.1325 [cm ⁻¹])
l_{MG}	0.24 cm	50 cm
ϕ_{MG}^0	1	0.45
$\Delta\phi_{MG}/\phi_{MG}$	25%	~5%

Very different MG surface areas were used in the CHESHIRE study (Pawloski, 1999) and the BENHAM study (this contribution) resulting in different dissolution rates. Shown in Table B-5 for comparison are the surface area and derived block size l_{MG} used in the two studies. Also presented is the percent change in average MG volume fraction $\Delta\phi_{MG}/\phi_{MG}$ over a time span of 50 years. The kinetic rate constants, including pH dependence, were the same in the two studies. As can be seen from the values listed in the table, the value for the effective rate constant (rate constant times surface area) is approximately 190 times larger in the CHESHIRE (Pawloski et al., 2001) study compared to that used in the BENHAM study. Using the porous medium conceptual model presented in Chapter 6 with greater effective surface area leads to dissolution of approximately 25% of the MG, which is similar to the CHESHIRE model (Pawloski et al., 2001).

B.3.4 Initial and Boundary Conditions

The initial conditions imposed on the simulation are based on an approximate treatment of the post-detonation environment. The precise initial temperature of the MG is difficult to determine, because it depends on the transfer of heat from the denotation to the surrounding rock and the rate of re-wetting of the cavity and MG. In addition, entrainment of relatively “cold” rock fragments into the MG could lower its temperature substantially. A lower initial MG temperature than the maximum possible is used to avoid the complications resulting from two-phase conditions and hydrothermal temperature regimes which can greatly complicate the numerical and conceptual analysis of mineral reaction rates and which require appropriate thermodynamic data for mineral, aqueous, and gaseous species. Ideally, the volume of rock heated by the detonation should be determined such that the correct total heat input is maintained regardless of the initial temperature assumed.

The temperature along the saturation curve of pure water for a saturation pressure corresponding to the WP depth of the detonation is shown in Fig. B-7. For the BENHAM test with a WP of 800 m, saturation corresponds to a temperature of the MG of approximately 293°C (see Fig. B-7). The initial MG temperature is arbitrarily set to 150°C, slightly higher than half the saturation temperature at the WP depth (see Fig. B-7). This value is in agreement with that used by Maxwell et al. (2000) for the CHESHIRE test which, however, had a lower yield compared to BENHAM. The calculations in Chapter 6 use the maximum possible single-phase temperature for this system because the amount of cooling that would occur is uncertain. However, cooler initial temperatures are used in the sensitivity study.

Simulations are carried out over a time span of 50 years. The chimney-cavity-MG configuration resulting from the detonation is presumed to be emplaced instantaneously in the ambient groundwater flow system. The initial ambient groundwater system is assumed to be at a steady state with a geothermal gradient of 0.01069 °C/m and a lateral pressure gradient of 2 m/km. Zero flux boundary conditions are imposed at the top and bottom of the flow domain.

The initial fluid composition for host rock, chimney, and MG is determined by assuming equilibrium with minerals k-feldspar, calcite, muscovite, and quartz. This fixes the concentrations of species K^+ , Ca^{2+} , Al^{3+} , and $SiO_{2(aq)}$. Feldspars were chosen to result in undersaturation of other aluminosilicate minerals such as kaolinite and albite. The pH is fixed at 8.5 and pCO_2 at 3.5 outside the MG region. The redox state is set to an oxygen fugacity of pO_2 of 10. Chloride is fixed by charge balance. Species Na^+ and Mg^{2+} are set to 2×10^{-2} and 2×10^{-5} mol/L, respectively. The initial Pu concentration is set to a small value of 10^{-25} mol/L. The fluid composition varies spatially due to variation of the ambient temperature with depth. In addition, within the MG region the fluid composition is equilibrated with the MG at its initial temperature of 150°C by adjusting the concentration of aqueous silica. The pH was set to 7.92 at temperature within the MG region to avoid supersaturation with respect to albite and analcime. The set of chemical reactions included in the simulations are listed in Table B-6.

The choice of initial concentration of Pu within the MG region is also somewhat uncertain. One choice is to assume that during rewetting, the glass has dissolved sufficiently fast resulting in a significant release of Pu to come to equilibrium with a Pu-bearing mineral such as $PuO_2(OH)_2$.

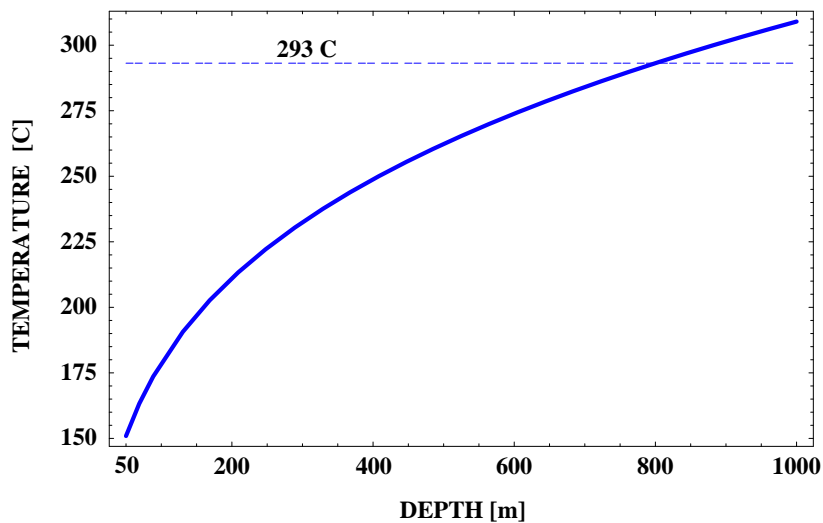


Figure B-7: Temperature corresponding to two-phase conditions plotted as a function of depth (solid curve). The horizontal dotted line designates a temperature of 293°C that corresponds to two-phase conditions at a depth of 800 m which coincides with the BENHAM test WP.

This assumption would certainly be consistent with the the rapid dissolution obtained at high temperatures, even with a relatively small MG specific surface area. Alternatively, one could take the initial concentration of Pu to be zero and assume that all Pu came from reaction of the MG at later times. The former approach leads to a higher release of Pu compared to the latter approach which is used here.

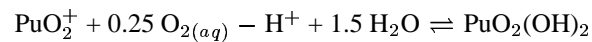
Although both the TSA and LAVA layers are dominated by fracture flow with typical porosities of 0.001 and 0.01, respectively, in this study they were both modeled using matrix porosities. This leads to much slower transport in these units compared to fracture dominated transport. However, because the primary objective of this study was to determine if it was possible for Pu released from the MG to reach the TSA and LAVA aquifers, the use of fracture porosities for transport is not essential. Matrix flow is assumed to take place in the CHZCm layers. Likewise the chimney and MG are treated as porous media with matrix flow.

Table B-6: The set of aqueous and mineral reactions included in the THC-coupled processes simulations. Equilibrium constants for a temperature range of 0–300°C are taken from the EQ3/6 database (Wolery, 1983) modified for use with FLOTRAN.

Aqueous Reactions	
Primary Species	Secondary Species
	$\text{H}_2\text{O} - \text{H}^+ \rightleftharpoons \text{OH}^-$
	$\text{H}^+ + \text{HCO}_3^- - \text{H}_2\text{O} \rightleftharpoons \text{CO}_{2(\text{aq})}$
	$\text{HCO}_3^- - \text{H}^+ \rightleftharpoons \text{CO}_3^{2-}$
	$\text{Al}^{3+} + \text{H}_2\text{O} - \text{H}^+ \rightleftharpoons \text{AlOH}^{2+}$
	$\text{Al}^{3+} + 2\text{H}_2\text{O} - 2\text{H}^+ \rightleftharpoons \text{Al}(\text{OH})_2^+$
	$\text{Al}^{3+} + 2\text{H}_2\text{O} - 3\text{H}^+ \rightleftharpoons \text{HAlO}_2(\text{aq})$
	$\text{Al}^{3+} + 2\text{H}_2\text{O} - 4\text{H}^+ \rightleftharpoons \text{AlO}_2^-$
	$\text{Ca}^{2+} + \text{HCO}_3^- - \text{H}^+ \rightleftharpoons \text{CaCO}_{3(\text{aq})}$
	$\text{Ca}^{2+} + \text{HCO}_3^- \rightleftharpoons \text{CaHCO}_3^+$
	$\text{HCO}_3^- + \text{Mg}^{2+} - \text{H}^+ \rightleftharpoons \text{MgCO}_{3(\text{aq})}$
	$\text{Cl}^- + \text{Mg}^{2+} \rightleftharpoons \text{MgCl}^+$
	$\text{HCO}_3^- + \text{Mg}^{2+} \rightleftharpoons \text{MgHCO}_3^+$
	$\text{H}_2\text{O} + \text{SiO}_{2(\text{aq})} - \text{H}^+ \rightleftharpoons \text{HSiO}_3^-$
	$3 \text{H}^+ + \text{PuO}_2^+ - 0.25 \text{O}_{2(\text{aq})} - 1.5 \text{H}_2\text{O} \rightleftharpoons \text{Pu}^{4+}$
	$2 \text{H}^+ + \text{PuO}_2^+ - 0.5 \text{O}_{2(\text{aq})} - \text{H}_2\text{O} \rightleftharpoons \text{Pu}^{3+}$
	$\text{H}^+ + \text{PuO}_2^+ + 0.25 \text{O}_{2(\text{aq})} - 0.5 \text{H}_2\text{O} \rightleftharpoons \text{PuO}_2^{2+}$
	$2 \text{HCO}_3^- + \text{PuO}_2^+ + 0.25 \text{O}_{2(\text{aq})} - \text{H}^+ - 0.5 \text{H}_2\text{O} \rightleftharpoons \text{PuO}_2(\text{CO}_3)_2^{2-}$
	$\text{PuO}_2^+ + 0.25 \text{O}_{2(\text{aq})} + 0.5 \text{H}_2\text{O} \rightleftharpoons \text{PuO}_2\text{OH}^+$
	$\text{H}^+ + \text{PuO}_2^+ - 0.5 \text{O}_{2(\text{aq})} \rightleftharpoons \text{PuOH}^{2+}$
	$2 \text{H}^+ + \text{PuO}_2^+ - 0.250 \text{O}_{2(\text{aq})} - 0.5 \text{H}_2\text{O} \rightleftharpoons \text{PuOH}^{3+}$

Table B-6 Continued

Mineral Reactions	
	$9.6598\text{E-}2 \text{Na}^+ + 0.1039 \text{K}^+ + 8.2956\text{E-}3 \text{Ca}^{2+}$
	$+ 1.5055\text{E-}3 \text{Mg}^{2+} + 0.2305 \text{Al}^{3+} - 0.9117 \text{H}^+ + 1.308 \text{SiO}_{2(\text{aq})}$
	$+ 2.1039\text{E-}09 \text{PuO}_2^+ - 5.2597\text{E-}10 \text{O}_{2(\text{aq})} + 0.4558 \text{H}_2\text{O} \rightleftharpoons \text{Glass}$
	$\text{Ca}^{2+} - \text{H}^+ + \text{HCO}_3^- \rightleftharpoons \text{Calcite}$
	$\text{SiO}_{2(\text{aq})} \rightleftharpoons \text{Chalcedony}$
	$2 \text{Al}^{3+} - 6 \text{H}^+ + 2 \text{SiO}_{2(\text{aq})} + 5 \text{H}_2\text{O} \rightleftharpoons \text{Kaolinite}$
	$\text{K}^+ + \text{Al}^{3+} - 4 \text{H}^+ + 3 \text{SiO}_{2(\text{aq})} + 2 \text{H}_2\text{O} \rightleftharpoons \text{K-Feldspar}$
	$\text{K}^+ + 3 \text{Al}^{3+} - 10 \text{H}^+ + 3 \text{SiO}_{2(\text{aq})} + 6 \text{H}_2\text{O} \rightleftharpoons \text{Muscovite}$
	$0.96 \text{Na}^+ + 0.96 \text{Al}^{3+} - 3.84 \text{H}^+ + 2.04 \text{SiO}_{2(\text{aq})} + 2.92 \text{H}_2\text{O} \rightleftharpoons \text{Analcime}$
	$\text{SiO}_{2(\text{aq})} \rightleftharpoons \text{Quartz}$
	$\text{SiO}_{2(\text{aq})} \rightleftharpoons \text{SiO}_{2(\text{am})}$



B.3.5 THC-Modeling Results

The resulting temperature field for times of 10 and 30 years superimposed on the corresponding flow field is shown in Figs. B-8 and B-9. As can be seen from the figures, convection cells are formed that carry packets of fluid through the MG and upwards through the chimney to the TSA aquifer. With time the MG cools sufficiently to collapse the convection cells and the system returns to approximate ambient conditions.

The distribution of dissolved Pu is shown in Figs. B-10 and B-11 for times of 10 and 30 years, respectively. A pulse of Pu is released from the MG as it dissolves. It rapidly advances through the chimney and into the TSA aquifer. The Pu pulse advances somewhat more slowly in the LAVA aquifer because of its lower permeability.

It appears that this result can provide a plausible mechanism for release of Pu from the MG to the upper TSA as well as the lower LAVA aquifers. Vigorous convection caused by heat released from the MG enables flow to occur vertically through the chimney and into the overlying aquifer. However, vertical flow can only be maintained over a relatively short time span during which the temperature of the MG is sufficiently high. The minimum temperature to sustain vertical flow depends crucially on the permeability of the chimney region. A Raleigh number analysis for the relation between chimney temperature and permeability is presented in Chapter 6.

To follow the migration of Pu from the MG, the breakthrough curves for Pu in the TSA and LAVA aquifers are shown in Fig. B-12 at a distance of 300 m from the center of the chimney. The breakthrough concentrations are computed by averaging the flux over each layer weighted by the cross sectional area perpendicular to the direction of flow according to the expression

$$\langle \Psi_j \rangle = \frac{\sum_n A_n v_n \Psi_{jn}}{\sum_{n'} A_{n'} v_{n'}}, \quad (\text{B-41})$$

where Ψ_{jn} represents the total concentration (see Eq. B-13) evaluated at the n th node, and v_n and A_n denote the fluid velocity and nodal area perpendicular to the flow, respectively, at the n th node. According to the figure, a pulse of Pu is released from the MG to both the TSA and LAVA aquifers. The double peak in concentration obtained for the TSA aquifer is presumably a result of the complex flow field resulting from the formation of convection cells which grow and collapse over time. At latter times as the flow field becomes more stable, these effects are no longer present as evidenced in the LAVA breakthrough curve.

The pulse release is related to the lifetime of the convection cells and the enhanced dissolution rate of the MG at elevated temperatures. As the MG cools, its dissolution rate decreases exponentially reaching some steady state value after the system returns to ambient conditions. RNs are

still released as the glass dissolves, but at a much slower rate. In addition, they travel laterally in the absence of upward buoyant convection, rather than vertically through the chimney as at earlier times when the MG is hotter. It should be noted that the relative breakthrough times of the pulse release of Pu in the two aquifers is an artifact of the use of matrix porosities. If fracture porosities had been used the breakthrough curves for the LAVA and TSA aquifers would have been much earlier and very likely reversed in their first appearance from the results presented in Fig. B-12.

The pH is shown in Figs. B-13 and B-14 for times of 10 and 30 years. A relatively high pH pulse of approximately 10 rapidly advances up the chimney and into the TSA aquifer. The pulse can still be seen in the LAVA aquifer after 30 years have elapsed, but has disappeared after 10 years in the TSA aquifer.

The dissolution rate of the MG is shown in Figs. B-15 and B-16 for times of 10 and 30 years. The dissolution rate is highly nonuniform as a result of the convection cells which develop around the melt region.

B.4 Discussion

From these results it becomes apparent that there exists a relatively narrow window in time for RNs released from the MG to escape from the cavity-chimney system into the upper-lying aquifers. The duration of the window is controlled by the effect of heat released from the MG on both the perturbation of the flow field and the dissolution rate of the MG. Elevated temperatures result in the formation of convection cells which eventually decay with time as the MG cools. Likewise, the MG dissolution rate is many orders of magnitude larger compared to ambient conditions. The pulse release is a combination of these two effects.

Reaction of the MG results in strong changes in pH which in turn may influence sorption properties involving surface complexation. Under such circumstances using a K_D approach may not be valid. Unfortunately, detailed site-specific data for mineral concentrations and their associated surface areas is unavailable for the BENHAM site. In addition, it must be recognized that often minerals in trace quantities, such as iron and manganese oxides, can contribute more to retardation than major host rock minerals with high concentrations. Such information could help greatly in constraining the possibilities of model predictions. Ideally, mineral abundances and surface areas should be treated as stochastic variables. However, at the present time there do not exist models with such capabilities to handle reactive flows and their inherent nonlinearity.

B.5 Conclusion

Two-dimensional calculations predict strong coupling between thermal, hydrologic, and chemical processes at the BENHAM test. The thermal perturbation produced by the explosion and subsequent cooling of the MG results in the formation of convection cells within the chimney. As convection becomes more vigorous, fluid flows vertically driven by buoyancy forces into the overlying tuff aquifer. As the MG cools, the convection cells collapse, resulting in a pulse release of conservatively transported RNs contained in the MG to both the upper and lower aquifers.

According to the calculations presented in this report, the far field is strongly coupled to the BENHAM cavity-chimney system source term due to the formation of convection cells that grow and decay over time, resulting in a pulse release of Pu to the upper TSA and lower fractured LAVA aquifers. The question arises as to what extent this interpretation applies to other underground tests at the NTS. However, it must be cautioned that the stratigraphy may be very different for different tests as well as the physical properties of the tests themselves including yield and WP depth. It would seem prudent to investigate a suite of representative tests before any general conclusions are drawn.

Future studies should include the following:

- three-dimensional THC simulations incorporating multicomponent chemistry,
- sorption and colloid-facilitated transport of Pu with irreversible sorption reactions,
- sensitivity of results to higher initial MG temperature and the immediate surrounding host rock and chimney,
- more general mineral and glass kinetic rate laws, including e.g. Al-inhibition factors, and
- heterogeneous fractured porous media based on a THC-DCM (Dual Continuum Model) approach accounting for fracture-matrix interaction.

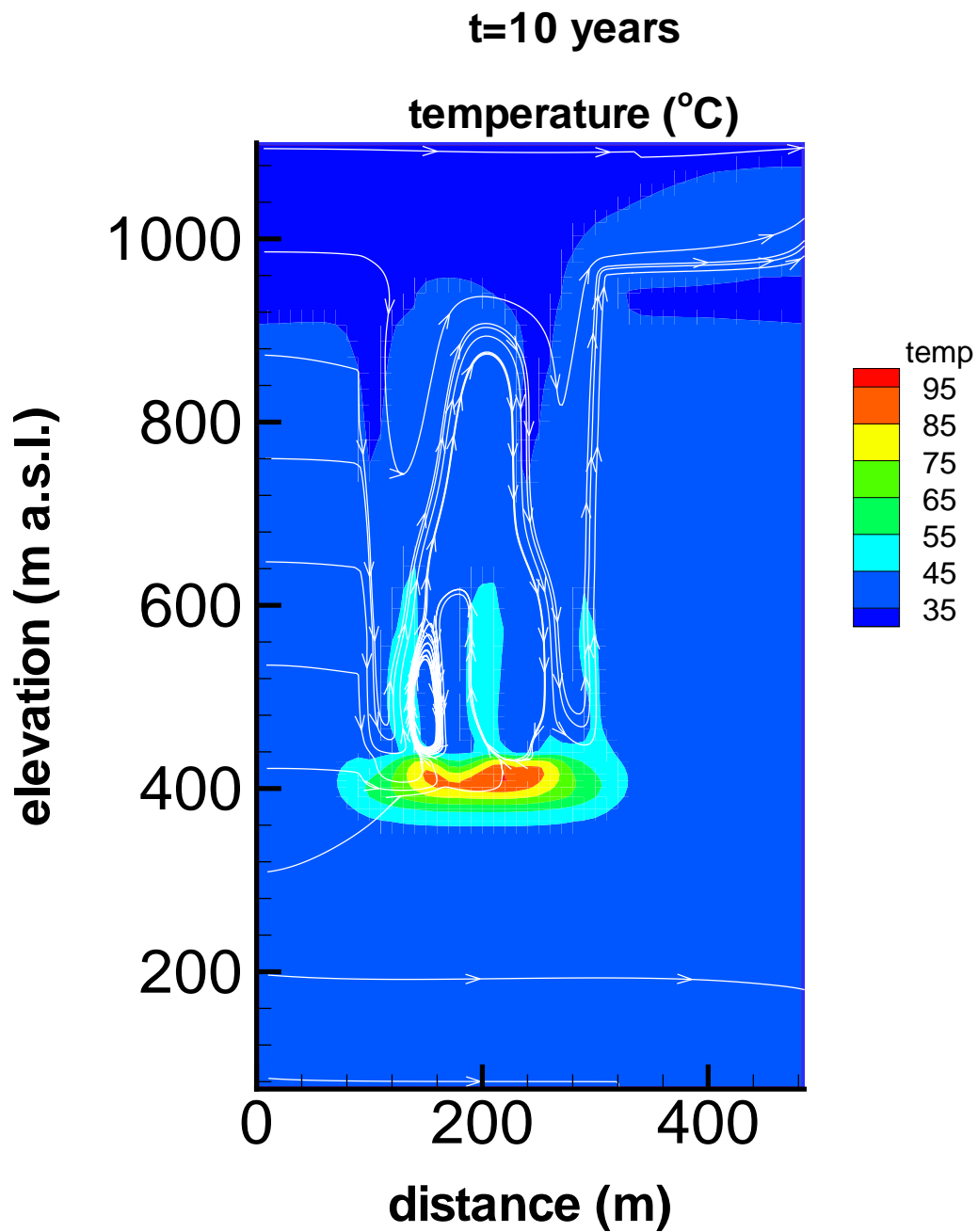


Figure B-8: Temperature distribution after an elapsed time of 10 years. The lines with arrows indicate instantaneous streamlines.

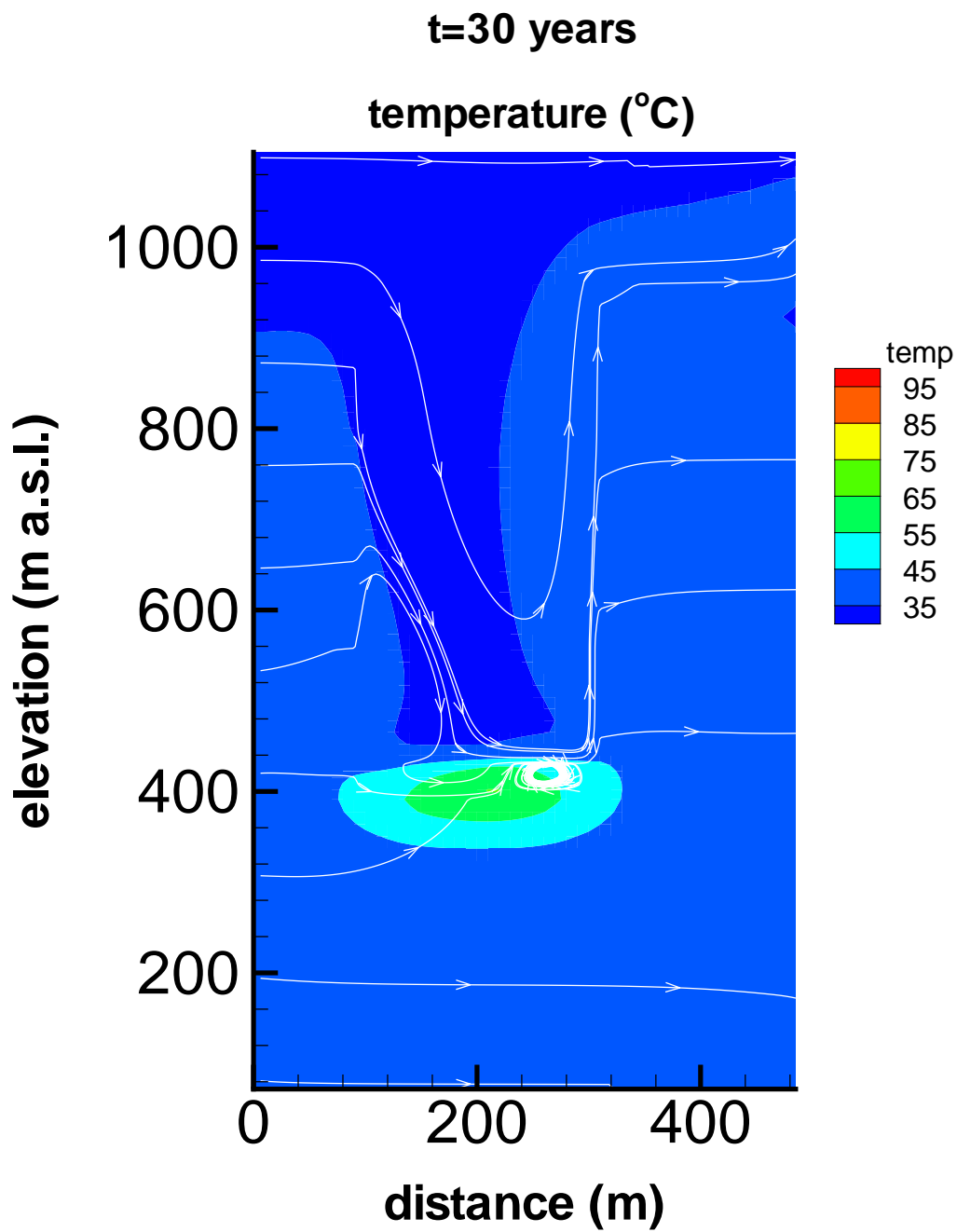


Figure B-9: Temperature distribution after an elapsed time of 30 years. The lines with arrows indicate instantaneous streamlines.

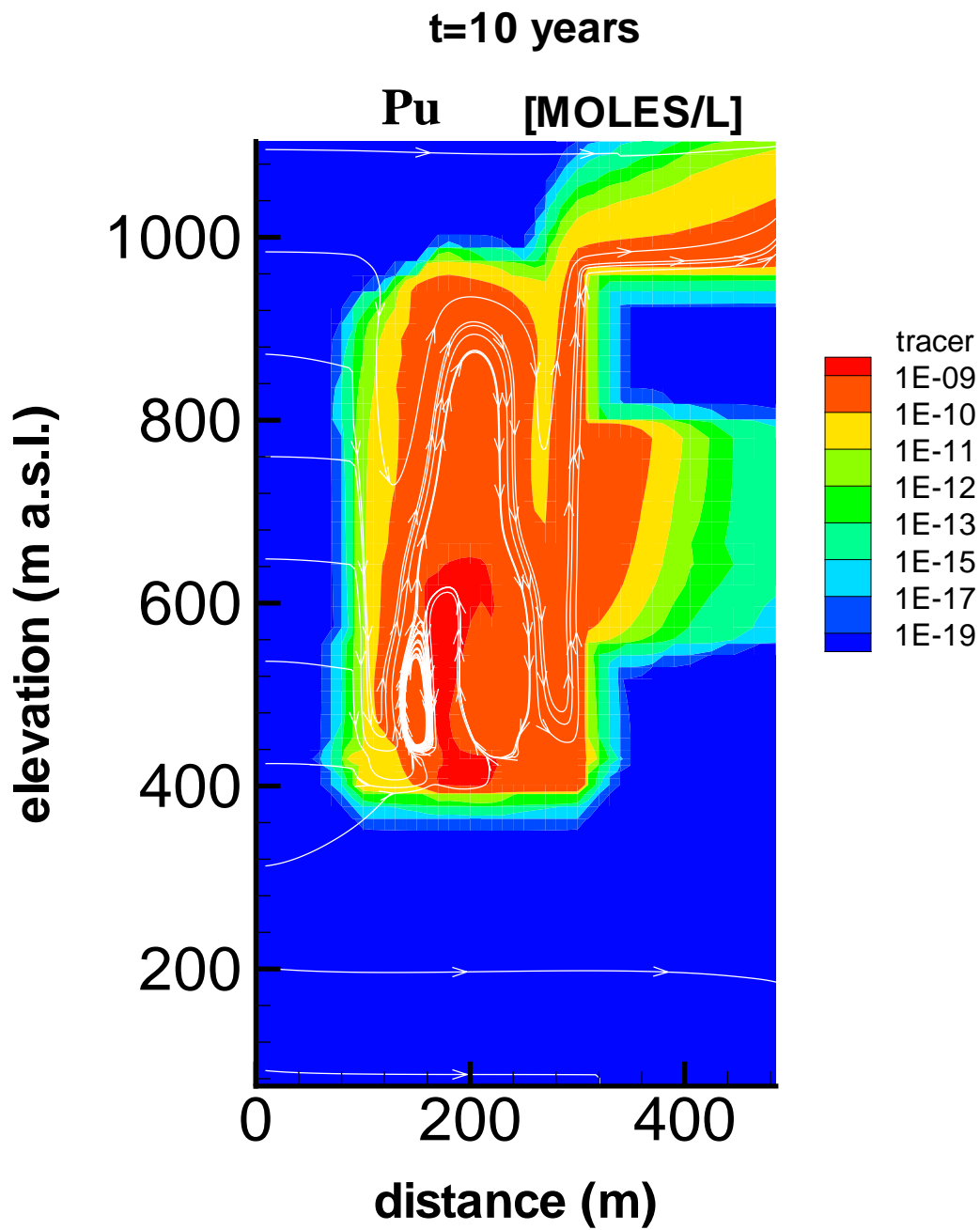


Figure B-10: The distribution of Pu in the absence of sorption after an elapsed time of 10 years. The lines with arrows indicate instantaneous streamlines.

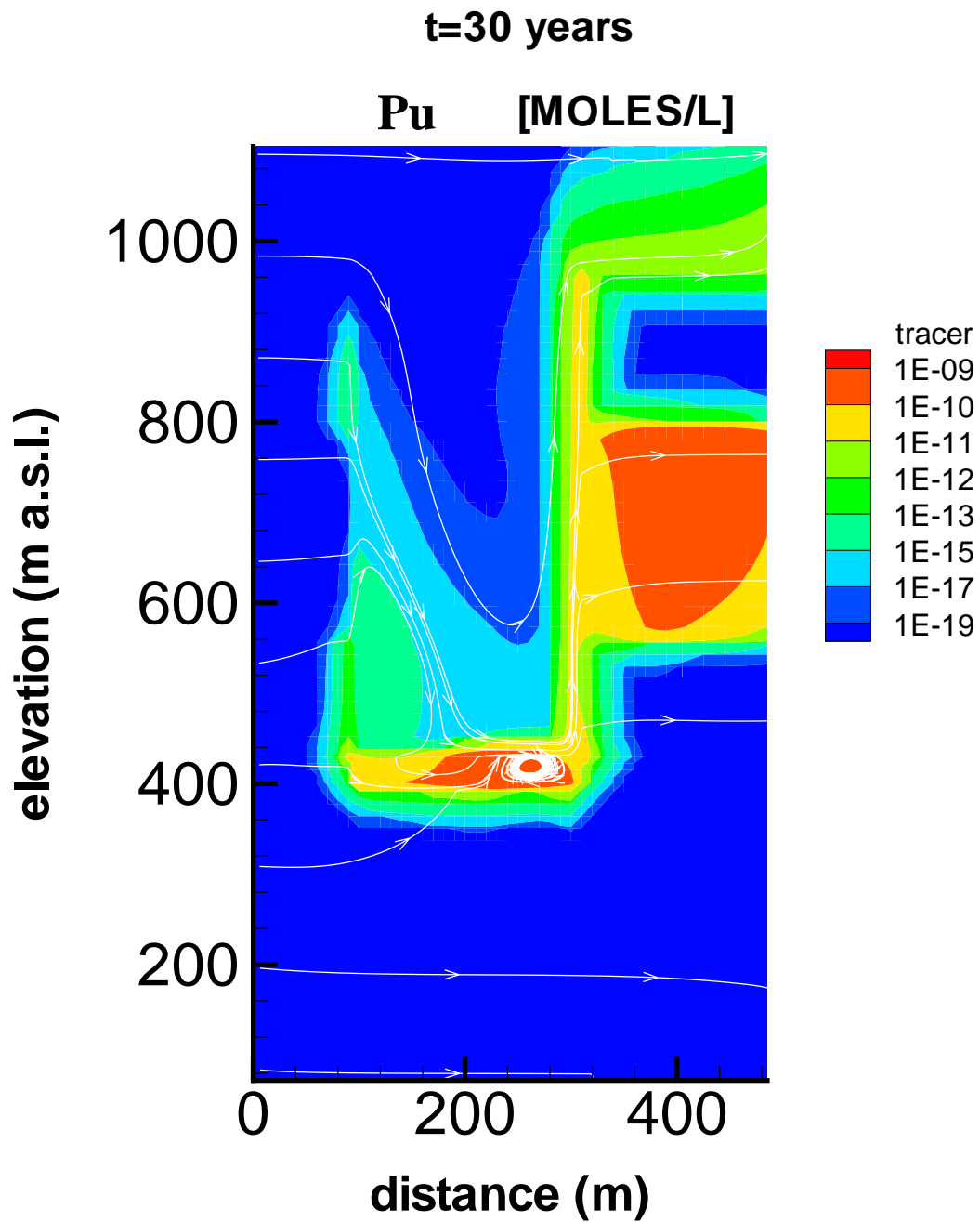


Figure B-11: The distribution of Pu in the absence of sorption after an elapsed time of 30 years. The lines with arrows indicate instantaneous streamlines.

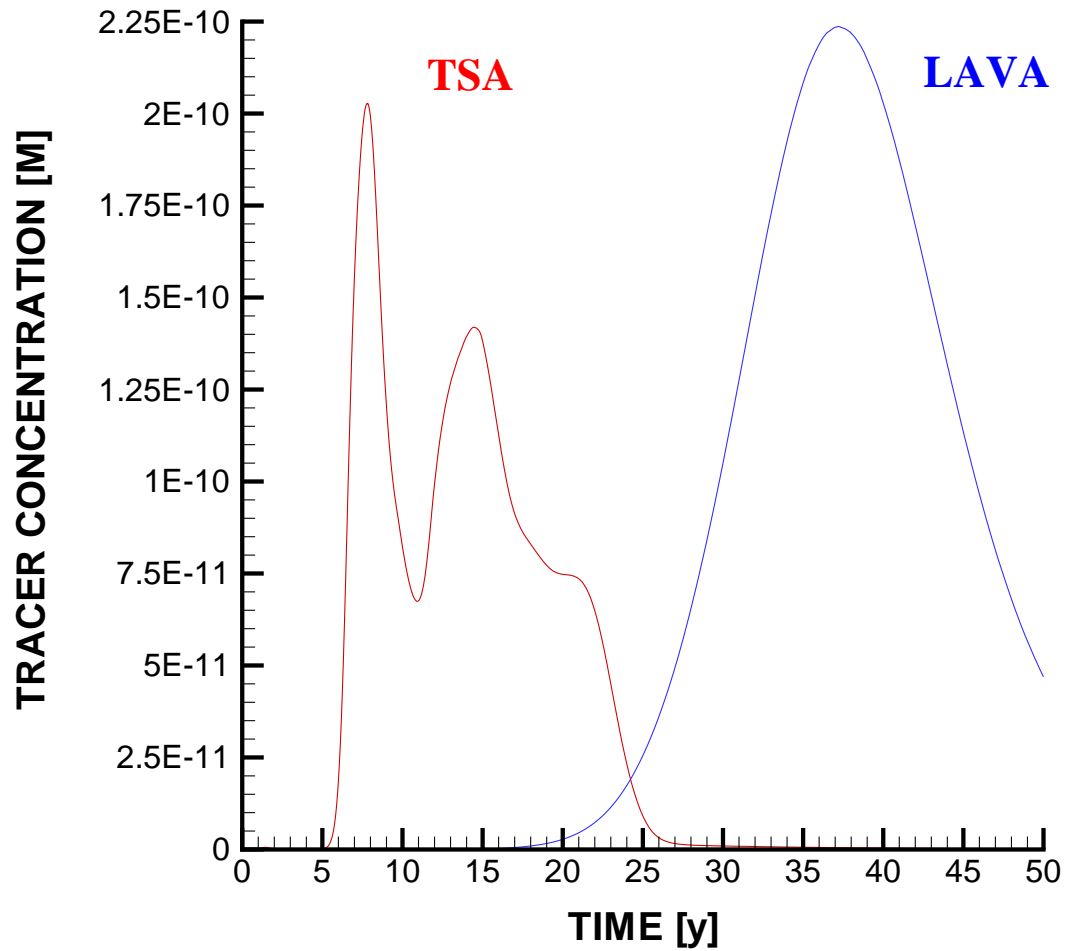


Figure B-12: Breakthrough curves for Pu at a distance of 300 m from the center of the chimney in the indicated stratigraphic units plotted against time.

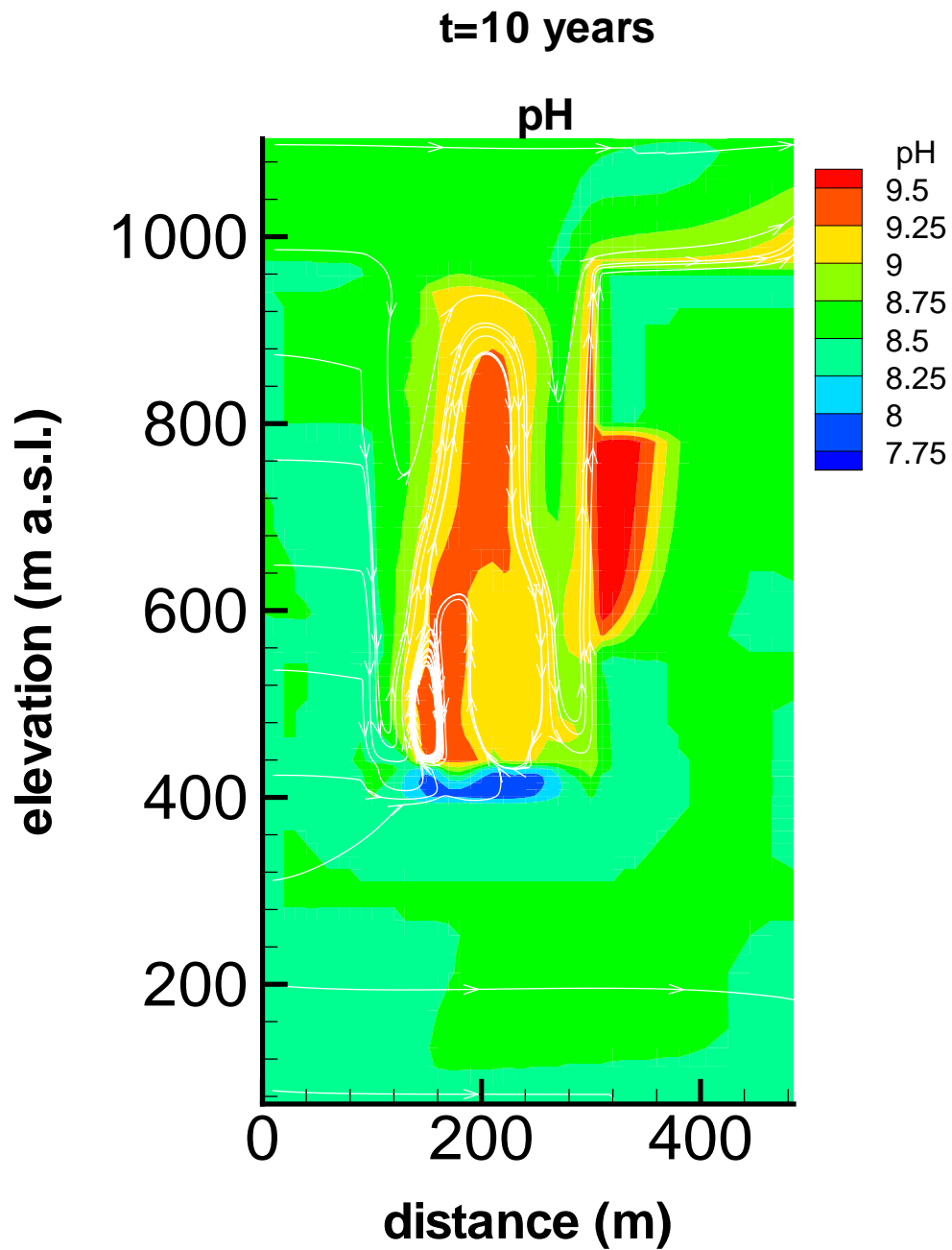


Figure B-13: The pH distribution after an elapsed time of 10 years. The lines with arrows indicate instantaneous streamlines.

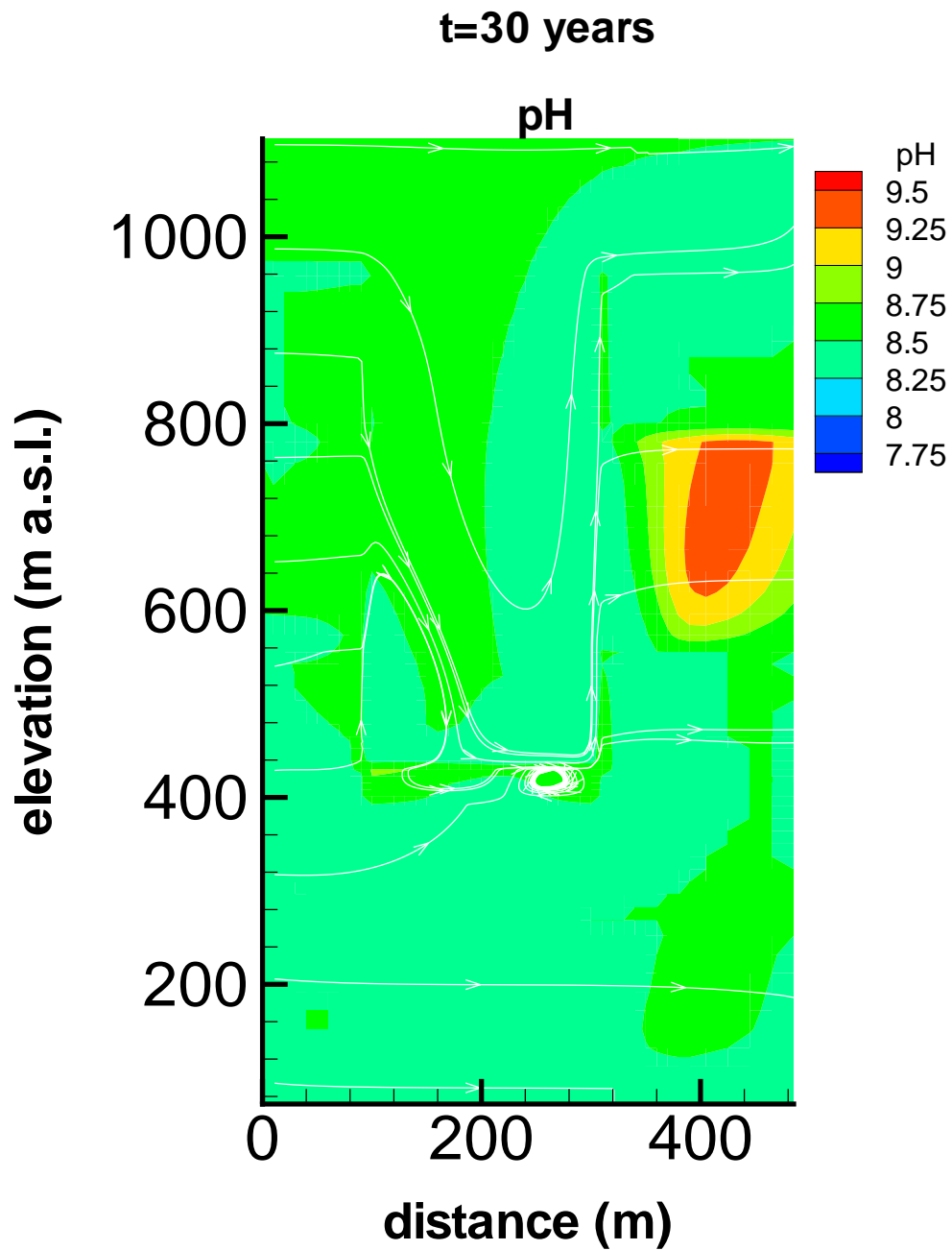


Figure B-14: The pH distribution after an elapsed time of 30 years. The lines with arrows indicate instantaneous streamlines.

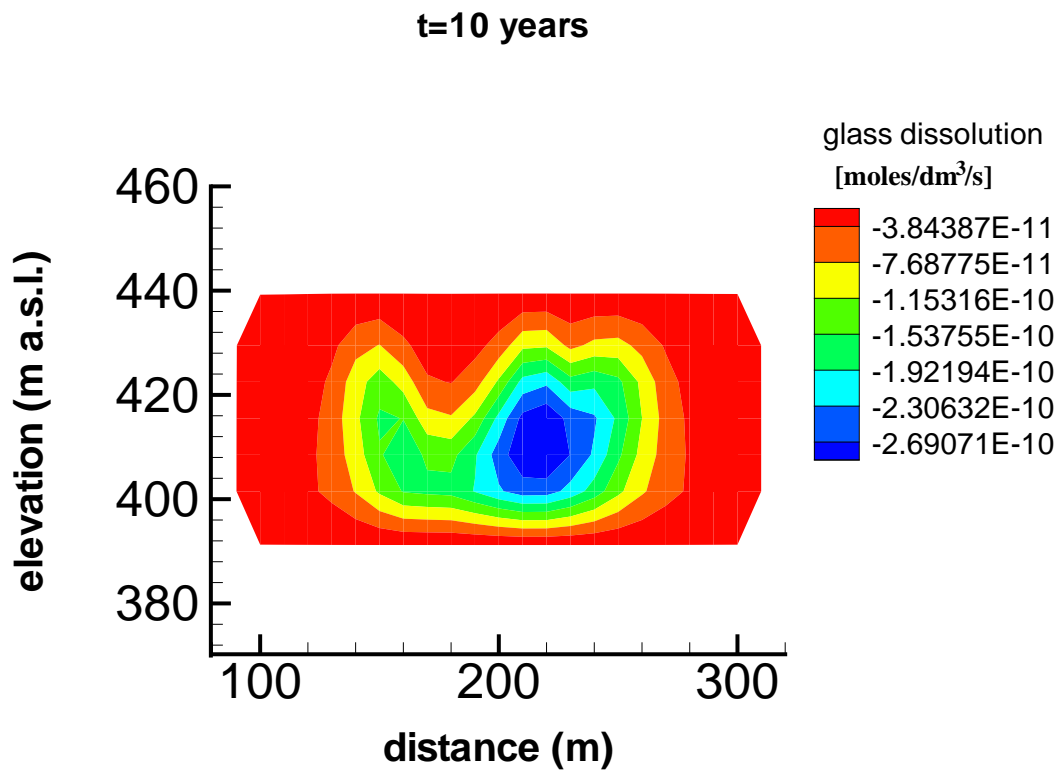


Figure B-15: Glass dissolution rate after an elapsed time of 10 years.

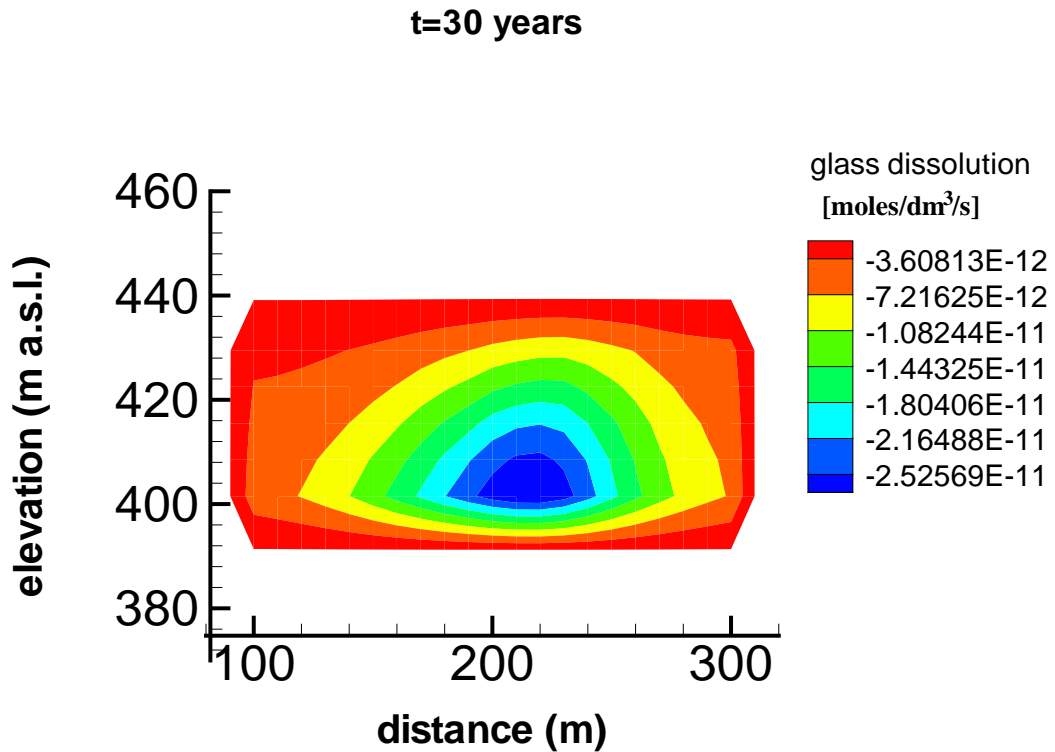


Figure B-16: Glass dissolution rate after an elapsed time of 30 years.

B.6 List of Symbols

a	Radius of sphere equal in volume to the MG
a_i	Activity of i th secondary species [—]
a_j	Activity of j th primary species [—]
A	Surface area [m^2]
A_m	Specific surface area of m th mineral [cm^{-1}]
A_{MG}	MG specific surface area [cm^{-1}]
b_i	Meyer-Kelly expansion coefficients [C^{-i}]
b_{MG}	MG block size [cm].
C_b	Bulk fluid concentration [mol L^{-1}]
C_{eq}	Equilibrium concentration [mol L^{-1}]
C_i	Concentration of i th secondary species [mole L^{-1}]
C_j	Concentration of j th primary species [mole L^{-1}]
C_m	Concentration of m th mineral [mol dm^{-3}]
C_p^r	Specific heat [$\text{J kg}^{-1} \text{K}^{-1}$]
C_s	Fluid concentration at mineral surface [mol L^{-1}]
d_{WP}	Depth of working point of underground test [m]
D	Diffusion/dispersion coefficient [$\text{m}^2 \text{s}^{-1}$]
$f_A(T)$	Arrhenius factor [—]
f_m	Saturation index for the m th mineral [—]
g	Acceleration of gravity [m s^{-2}]
h_C	Height of chimney [m]
H_w	Specific internal enthalpy of pure water [kJ mol^{-1}]
ΔE^\ddagger	Activation energy [kJ/mol]
I_m	Mineral kinetic reaction rate [$\text{mol dm}^{-3} \text{s}^{-1}$]
I_{MG}	Kinetic rate for MG [$\text{mol dm}^{-3} \text{s}^{-1}$]

I_s	Reaction rate at mineral surface [mol s^{-1}]
J	Flux [$\text{mol m}^{-2} \text{s}^{-1}$]
J_i	Flux of i th secondary species [$\text{mol m}^{-2} \text{s}^{-1}$]
J_j	Flux of j th primary species [$\text{mol m}^{-2} \text{s}^{-1}$]
k	Kinetic rate constant [m s^{-1}]
k_{eff}	Effective kinetic rate constant [m s^{-1}]
k_m^σ	Kinetic rate constant associated with m th mineral for the σ th parallel reaction [$\text{mol cm}^{-2} \text{s}^{-1}$]
k_{MG}	Kinetic rate constant for MG [$\text{mol cm}^{-2} \text{s}^{-1}$]
k_0	Neutral pH kinetic rate constant for MG [$\text{mol cm}^{-2} \text{s}^{-1}$]
k_{H}	Acid pH kinetic rate constant for MG [$\text{mol cm}^{-2} \text{s}^{-1}$]
k_{OH}	Basic pH kinetic rate constant for MG [$\text{mol cm}^{-2} \text{s}^{-1}$]
K_i	Secondary species reaction equilibrium constant [—]
K_m	Mineral reaction equilibrium constant [—]
l_{MG}	Characteristic length of MG blocks [m]
M_{MG}	Mass of MG [kg]
p	Pressure [Pa]
\mathbf{q}	Darcy flux [m s^{-1}]
Q_m	Ion-activity product associated with the m th mineral
Q_{MG}	MG ion activity product []
r	radial coordinate [m]
R	Gas constant [$\text{J K}^{-1} \text{mol}^{-1}$]
R_C	Chimney radius [m]
t	Time [s]
T	Temperature [C]
T_0	Reference temperature [C]
T_1	Initial host rock temperature [C]

T_2	Initial MG temperature [C]
\bar{T}_{MG}	Average MG temperature [C]
U_w	Specific internal energy of pure water [kJ mol ⁻¹]
\mathbf{v}	Velocity field [m s ⁻¹]
V_{MG}	Volume of MG [m ³]
V_m	Molar volume of m th mineral [cm ³ mol ⁻¹]

Greek Symbols

α	Thermal diffusivity [m ² s ⁻¹]
γ_i	Activity coefficient of i th secondary species [—]
γ_j	Activity coefficient of j th primary species [—]
Δl	Boundary layer thickness [m]
$\Delta\phi_{MG}/\phi_{MG}$	Fractional change in MG volume fraction [—]
Θ	Reaction factor with values zero or one [—]
κ	Permeability [m ²]
$\kappa_0(\mathbf{r})$	Initial permeability at position vector \mathbf{r} [m ²]
κ_C	Thermal conductivity [J m ⁻¹ s ⁻¹ K ⁻¹]
μ_w	Viscosity of pure water [Pa s]
ν_{ji}	Stoichiometric coefficient matrix for homogeneous reactions [—]
ν_{jm}	Stoichiometric coefficient matrix for mineral reactions [—]
ϕ	Porosity [—]
$\phi_0(\mathbf{r})$	Initial porosity at position vector \mathbf{r} [—]
ϕ_m	Volume fraction of m th mineral [—]
ρ_r	Rock density [kg m ⁻³]
τ	Tortuosity [—]
Ψ_j	Total concentration of j th primary species [mol L ⁻¹]
Ω_j	Total flux of j th primary species [mol m ⁻² s ⁻¹]
χ_{MG}	Fractional change in MG volume fraction [—]

Other

A_i	Designation for i th secondary species [—]
A_j	Designation for j th primary species [—]
D	Damköhler number [—]
M_m	Designation for m th mineral [—]
\mathcal{Y}	Yield of nuclear explosion [kiloton]

B.7 References

- Damköhler, von G. 1936. Einflüsse der strömung, diffusion und des wärmeüberganges auf die leistung von reactionsöfen. *Zeitschrift Elektrochem.* 42: 846–862.
- Department of Energy. 2000. United States Nuclear Tests-July 1945 through September 1992. US Department of Energy, Nevada Operations Office, Las Vegas, NV, DOE/NV-209 (Rev. 15).
- Drellack, S.L. and L.B. Prothro. 1997. Descriptive Narrative for the Hydrogeologic Model of Western and Central Pahute Mesa Corrective Action Units. Bechtel Nevada, Las Vegas, NV.
- Hochstein, M.P., M.J. O’Sullivan. 1985. Geothermal systems created by underground nuclear testing. *Proc. of the 7th NZ Geothermal Workshop.*
- Hochstein, M.P., M.J. O’Sullivan. 1988. Geothermal systems created by underground nuclear testing: implications for long-term, direct effects of underground testing. Presented at the International Scientific Symposium on a Nuclear Test Ban, January 15-16, Las Vegas, Nevada.
- International Formulation Committee. 1967. A Formulation of the Thermodynamic Properties of Ordinary Water Substance. IFC Secretariat, Dusseldorf, Germany.
- Kechagia, P.E., I. Tsimpanogiannis, Y.C. Yortsos, and P.C. Lichtner. 2002. On the upscaling of reaction-transport processes in porous media with fast or finite kinetics, *Chemical Engineering Science* 57: 2565–2577.
- Kersting, A.B., D.W. Efurud, D.L. Finnegan, D.J. Rokop, D.K. Smith, and J.L. Thompson. 1999. Migration of plutonium in groundwater at the Nevada Test Site, *Nature* 397: 56–59.
- Lichtner, P.C., S., Kelkar, and B. Robinson. 2002. New Form of dispersion tensor for axisymmetric porous media with implementation in particle tracking, *Water Resources Res.*, in press.
- Lichtner, P.C. 2001. FLOTRAN User’s Manual. Los Alamos National Laboratory report, Los Alamos, NM, LA-UR-01-2349.
- Lichtner, P.C. 2000. Critique of dual continuum formulations of multicomponent reactive transport in fractured porous media, In *Dynamics of Fluids in Fractured Rock*, Ed. B. Faybishenko, AGU Monograph, 122: 281–298.
- Lichtner, P.C. 1996. Continuum formulation of reactive transport. In *Reactive Transport in Porous Media*. Reviews in Mineralogy P.C. Lichtner, C.I. Steefel, and E.H. Oelkers, eds. Mineralogical Society of America 34: 1–81.
- Lichtner, P.C. 1995. Principles and practice of reactive transport modeling, *Mat. Res. Soc. Symp. Proc.* 353: 117–130.
- Lichtner P.C. 1985. Continuum model for simultaneous chemical reactions and mass transport in hydrothermal systems, *Geochimica et Cosmochimica Acta*, 49: 779–800.

- Lichtner, P.C. and Seth M.S. 1996. Multiphase-Multicomponent Nonisothermal Reactive Transport in Partially Saturated Porous Media: Application to the Proposed Yucca Mountain HLW Repository, Proceedings International Conference on Deep Geologic Disposal of Radioactive Waste. Canadian Nuclear Society, September 16-19, Winnipeg, Manitoba, Canada, 3-133-3-142.
- Maxwell, RM, AFB Tompson, JT Rambo, SF Carle, and GA Pawloski. 2000. Thermally induced groundwater flow resulting from an underground nuclear test. IN: Computational Methods in Water Resources, Volume 1, Eds: LR Bentley, JF Sykes, CA Brebbia, WG Gray, and GF Pinder, A.A. Balkema Publishers, Rotterdam, pp. 51-58.
- Murphy, W.M., E.H. Oelkers, and P.C. Lichtner. 1989. Surface reaction versus diffusion control of mineral dissolution and growth rates in geochemical processes. *Chemical Geology* 78: 357-380.
- Oelkers, E.H., J. Schott, and J.L. Devidal. 1994. The effect of aluminum, pH, and chemical affinity on the rates of aluminosilicate dissolution reactions. *Geochem. Cosmochim. Acta* 58: 2011-2024.
- Pawloski, G.A. 1999. Development of phenomenological models of underground nuclear tests on Pahute Mesa, Nevada Test Site-BENHAM and TYBO, Lawrence Livermore National Laboratory, UCRL-ID-136003.
- Pawloski, G.A., A.F.B. Tompson, and S.F. Carle (eds.). 2001. Evaluation of the hydrologic source term from underground nuclear tests on Pahute Mesa at the Nevada Test Site: The Cheshire test, Lawrence Livermore National Laboratory, UCRL-ID-147023.
- Prothro, L.B. and R.G. Warren. 2001. Geology in the vicinity of the TYBO and BENHAM underground nuclear tests, Pahute Mesa, Nevada Test Site, Bechtel Technical Report DOE/NV/11718-305.
- Smith, D.K. 1993. A review of literature pertaining to leaching and sorption of radionuclides associated with nuclear melt glasses, Lawrence Livermore National Laboratory technical report UCRL-ID-113370, 26 p.
- Tompson, A.F.B., C.J. Bruton, and G.A. Pawloski. 1999. Evaluation of the hydrologic source term from underground nuclear tests in Frenchman Flat at the Nevada Test Site: The CAM-BRIC test, Lawrence Livermore National Laboratory technical report UCRL-ID-132300.
- Wadman, R.E. and D. Richards. 1961. Posthot geologic studies of excavations below RAINIER Ground Zero, Lawrence Livermore National Laboratory, Livermore, CA, UCRL 6586.
- Wolery, T. 1983. EQ3NR, A computer program for geochemical aqueous speciation-solubility calculations: Users guide and documentation, Lawrence Livermore National Laboratory, Livermore, CA, UCRL-53414, 191 p.

Appendix C: Field-Scale Transport in Fractured Rock: Reactive Dual-Porosity Particle Tracking

C.1 Introduction

In this study, particle tracking is used for several purposes. In Chapter 5, it is used to visualize flow patterns in complex three-dimensional flow fields. In Appendix F, particle tracking is used to prescribe multiple pathlines through a three-dimensional heterogeneous flow field, along which coupled reactive transport is simulated with the finite-volume method. In Chapter 7, particle tracking is used to conduct a large number of simulations necessary for the parameter sensitivity study. For all these applications, the streamline particle tracking (SPTR) capability in FEHM is used.

Whereas the simple ability to map out pathlines is employed in Chapters 5 and Appendix F, the full suite of transport capabilities in FEHM's streamline particle tracking is used in Chapter 7. Streamline particle tracking provides an efficient method for modeling large-scale transport of solutes in three-dimensional heterogeneous flow fields. By contrast, finite-element or finite-difference continuum approaches generally suffer from numerical dispersion associated with the large grid blocks required to represent large three-dimensional systems. With streamline particle tracking, plumes can be simulated at scales smaller than the grid block size and source zones can be smaller than the grid resolution. Dispersion can be added with the random walk algorithm, or by not invoking the random walk component, dispersive effects strictly related to prescribed heterogeneity can be evaluated.

Streamline particle tracking can be used as a method strictly for mapping out pathlines, along which complex processes such as diffusion and reactions can be studied with high-resolution models. Matrix diffusion also can be simulated directly. Further, the reactive processes of matrix sorption and fracture retardation can be included. Thus, for fully three-dimensional fractured rock systems, all processes except those involving kinetics and solute-solute interactions can be effectively and efficiently simulated with streamline particle tracking.

One significant limitation associated with particle-tracking methods is that they are most efficient when all particles can be started at or about the same time. That is, generally a large number of particles are required to resolve complex three-dimensional effects, so it is best to add them all at once. Resolving a complex, transient input function with actual particle releases could require an impractically large number of particles. In Chapter 7 we demonstrate a method for integrating unit releases of particles with time-varying input functions to provide time-varying breakthrough curves and appropriate solute breakthrough curves at locations of interest. For this method to be valid, all transport processes must be linear. To date, this method had not been extended to provide simulations of concentration contours at all locations in three-dimensional domain at all times of interest. However, the methods described in Chapter 7 may be extendable to provide results in such a format. The method is currently best suited to provide breakthrough curves at a limited number of locations or zones of interest.

The reactive, dual-porosity particle-tracking method used in this study is described in detail in CRWMS M&O (2000e). In that document the mathematical formulation of the method is

provided, along with verification and validation documentation. Therefore, only a summary of the method is provided here.

C.2 Advective and Dispersive Components

Transport with streamline particle tracking is decomposed into the advective component, the dispersive component, and the physiochemical component involving diffusion out of fractures and reactions with immobile minerals. The advective component is based directly on that of Pollock (1988). With this method, particle pathways are computed with a semi-analytical solution that computes the exit time and location of a particle entering a grid cell. Thus, each particle is marched through the system entering and exiting cells, with each computation using interpolations of flow velocities computed with the flow model.

The dispersive component is calculated using a random walk method (Tompson and Gelhar, 1990), which is based on an analogy between the mass transport equation and the Fokker-Plank equation of statistical physics (Van Kampen, 1981). Using uniform random numbers, the dispersive displacement of each particle is computed based on the dispersivity tensor and the flow velocity at the particle's location. Although a detailed description of the derivation of the dispersivity tensor defined by Burnett and Frind (1987) is provided in CRWMS M&O (2000e) and Lichtner et al. (2002), we provide no additional details in this report because in nearly all calculations presented herein that use particle tracking, random walk dispersion is turned off and dispersive effects are generated by the incorporation of heterogeneity. Random walk dispersion is used in Chapter 7 when the plume from TYBO is considered with and without dispersion.

C.3 Dual-Porosity Reactive Streamline Particle Tracking in FEHM

Using a residence-time transfer function, adjustments to the velocity of particles moving in fractures are made to account for physiochemical processes, such as diffusion into the matrix, reaction with fracture minerals, and reaction with matrix minerals. The travel time of each particle moving along a streamline is governed by a transfer function that describes the probability of the particle spending a given length of time in each portion of its path. The residence time of any particle in any segment of its path is determined by sampling randomly from a cumulative probability density function of particle residence times that is a function of both solute and aquifer material. Thus, if a large enough number of particles encounter this portion of the domain, the cumulative residence time distribution of the particles will reproduce the shape of the transfer function. The transfer function is derived from analytical or numerical solutions that capture such processes of diffusion in matrix material with finite spacing between fractures, as well as linear chemical sorption processes.

Figure C-1 provides a schematic with which to discuss the transfer functions; The primary parameters are:

- $2b$ - the fracture aperture,
- $2B$ - the spacing between fractures,
- v - the velocity in the fracture,

- θ - the porosity in the matrix,
- Kd - the distribution coefficient for the matrix material and a given solute,
- R - the retardation factor for the solute in the fracture (computed with a Kd as well),
- and D' - the matrix diffusion coefficient.

A transfer function defined in Sudicky and Frind (1982) and described in CRWMS M&O (2000g) utilizes the primary parameters to compute the transfer function that provides a delay in a particle's velocity relative to an unretarded, non-diffusing particle. Efficient implementation of the model in FEHM is achieved with a series of type curves generated to represent the transfer functions. Then, for a given set of transport parameters specific to a solute's location, properties, and the material it is in, FEHM performs a linear interpolation between the nearest type curves to obtain a result. This approach is much more efficient than computing the transfer functions (requiring numerical integration) at run time.

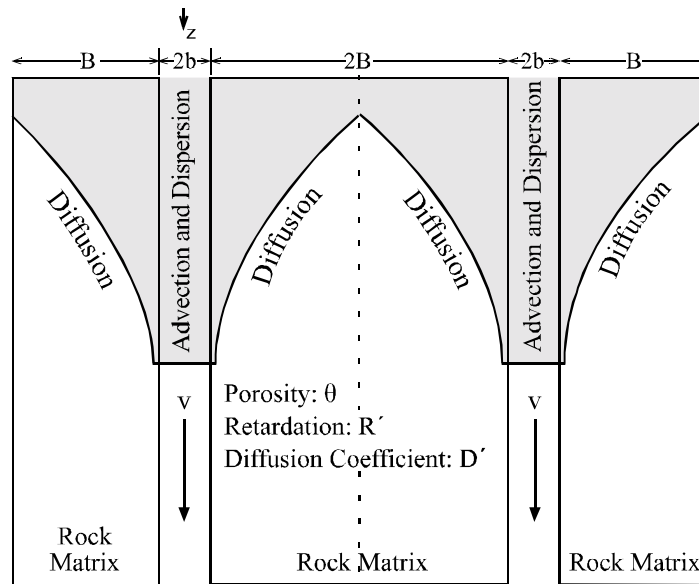


Figure C-1. Matrix diffusion schematic taken from CRWMS M&O (2000g).

C.4 References

- Burnett, R.D., and Frind, E.O. 1987. "Simulation of Contaminant Transport in Three Dimensions: 2. Dimensionality Effects." *Water Resources Research*, 23(4), 695–705.
- CRWMS M&O, 2000g. Unsaturated zone and saturated zone transport parameters. Yucca Mountain Analysis and Model Report, ANL-NBS-HS-00019, Rev 0.0, www.ymp.gov/documents/amr/index.html (<http://www.ymp.gov/documents/amr/u0100/u0100.pdf>; accessed May 2001, confirmed July 2002).
- CRWMS M&O, 2000e. Saturated zone transport methodology and transport component integration, Yucca Mountain Analysis and Model Report, ANL-NBS-HS-00010, Rev 0.0, www.ymp.gov/documents/amr/index.html. (<http://www.ymp.gov/documents/amr/s0025/s0025.pdf>; accessed May 2001, confirmed July 2002).
- Lichtner, P.C., S. Kelkar, and B. Robinson, 2002. New form of the dispersion tensor for flow in axisymmetric media with implementation in particle tracking. *Water Resources Research* (In Press).
- Pollock, D.W. 1988. "Semianalytical Computation of Path Lines for Finite-Difference Models." *Ground Water*, 26 (6, November-December), 743-750. TIC:226464.
- Sudicky, E.A., and R.G. McLaren. 1992. The Laplace transform Galerkin technique for large scale simulation of mass transport in discretely fractured porous formations. *Water Resources Research*, 28(2): 499-514.
- Tompson, A.F.B & L.W. Gelhar. 1990. Numerical simulation of solute transport in three-dimensional, randomly heterogeneous porous medium. *Water Resources Research*, 26(10):2541-2562.
- Van Kampen, N.G. 1981. *Stochastic Processes in Physics and Chemistry*. Amsterdam, Netherlands: North Holland Physics Publishing. TBD.

Appendix D: Reactive, Colloid-Facilitated Plutonium Transport Model: Development and Testing

D.1 Overview

To study the Pu transport under natural conditions in fractured, porous media, a dual-porosity transport model was developed incorporating plutonium speciation, reactions with other solutes, reactions with immobile minerals, reactions with colloids, and colloid filtration. In this appendix, the governing equations and assumptions are presented followed, by a series of model verification and sensitivity simulations to match laboratory experimental observations. Because of the homogeneity of the columns considered in the verification simulations, the models are built with a simple discrete fracture formulation. In Appendix F, the model is extended to the site-scale domain and utilizes the Generalized Dual-Porosity Method (GDPM) to account for heterogeneous material properties.

D.2 Background for Dual-Porosity Fracture Transport Model

Groundwater flow and solute transport in fractured media have been investigated by several studies (Grisak and Pickens, 1981; Neretnieks et al., 1982; Johns and Roberts, 1991; Keller et al., 1995; Berkowitz and Scher, 1995; Berkowitz and Zhou, 1996; and Zimmerman and Bodvarsson, 1996). For many problems involving transport of solutes in fractured rock, the permeability of the aquifer is high and the time scale of the modeling is long enough that diffusive mass transfer becomes a factor in determining large-scale solute transport patterns (National Research Council, 1996, pages 346-347). McKay et al. (1993) simulated tracer tests at an experimental site in a fractured clay till by applying an analytical model to describe advective/diffusive transport with evenly spaced, parallel fractures. Sudicky and McLaren (1992) used a Laplace transform in conjunction with a finite-element model to (1) overcome numerical problems of different time scales involved for transport along fracture and in the matrix and (2) to represent the sharp concentration gradients at the fracture-matrix interface. Dershowitz and Miller (1995) implemented a discrete fracture model to simulate matrix diffusion using a probabilistic particle-tracking technique. To support flow and transport simulations, Okusu et al. (1989) created a mesh generator to discretize the matrix for any two-dimensional fracture network.

Although impractical at large field scales, discrete network models incorporate explicitly information concerning dominating fracture features and processes associated with fracture-matrix interactions. Discrete network models are valuable tools for concept evaluation or model-based process studies (Long and Witherspoon, 1985, and Smith and Schwartz, 1984), which proved useful in examining requirements for the characterization of a fracture network as an equivalent porous medium or dual-porosity media and for studying the scale dependence of dispersion processes (National Research Council, 1996). Therefore, in this study a discrete fracture model is used first to test the reactive transport formulation against a controlled laboratory experiment. And second, the method is extended to the Generalized Dual-Porosity Method (GDPM) for practical application in heterogeneous material at the field scale.

D.3 Mathematical Model

D.3.1 Introduction

With the exception of the non-isothermal transient flow and transport simulations in Chapter 6, all reactive transport simulations are conducted in steady-state flow environments. Beginning with a steady-state flow regime, the following governing set of transport equations describing the fate and migration of a mobile species is solved with the Finite Element Heat and Mass Transport code, FEHM (Zyvoloski et al., 1997):

$$\frac{\partial[C]}{\partial t} = \frac{\partial}{\partial x_i} \left[D_i \frac{\partial[C]}{\partial x_i} \right] - \frac{\partial(v \cdot [C])}{\partial x_i} + \frac{q_s}{\phi} [C]_s + \sum_{k=1}^N r_k, \quad (\text{Eq. D-1})$$

where $\sum_{k=1}^N r_k$ is the chemical sink/source term representing the rate of change in solute mass of a particular species due to N chemical reactions, D_{ij} is the dispersion tensor, v_i is the transport velocity, q_s is the fluid sink/source term, and ϕ is porosity. $[C]$ is the concentration of the mobile species of interest, such as PuO_2^+ , $\text{PuO}_2(\text{CO}_3)^-$, or Pu-Colloid (plutonium-colloid). Viswanathan et al. (1998) and Robinson et al., (1999) describe in detail how FEHM solves the reactive transport equations by using a technique that involves solving the mixed equilibrium-kinetic transport problem in large, two- and three-dimensional domains. Although somewhat benign looking, Equation D-1 captures multiple complex processes. In the following sections, the processes are introduced and the mathematical formulations for each are presented.

The chemical and physical processes considered in this model are (1) Pu speciation, (2) Pu-colloid reactions to form Pu-colloid, (3) filtration of colloids on the fracture walls, (4) solute diffusion into the matrix, and (5) surface complexation and ion exchange of Pu with fracture minerals and matrix minerals. A schematic diagram for the processes and reactions are illustrated in Figure D-1.

D.3.2 Chemical Speciation Network

Aqueous speciation calculations in this study use Gibbs free-energy data cited in Langmuir (1997). The Langmuir compilation mainly uses the sources of Puigdomenech and Bruno (1991), Lemire and Tremaine (1980), Lemire and Garisto (1989), and Nitsche et al. (1995). In this model, chemical speciation reactions (including oxidation/reduction, hydration, and carbonate complexation) are considered and are listed in Section D.5. Using the equations in Section D.5, the speciation results for a total Pu concentration of 10^{-10} mol/l (somewhat arbitrarily chosen based on Pu solubility and estimated groundwater flux near the source) at Eh = 550 mVolts and temperature = 25°C are shown in Figure D-2. The dominant species are $\text{PuO}_2(\text{CO}_3)^-$, $\text{Pu}(\text{OH})_4$, and PuO_2^+ . PuO_2^+ is the only dominant positively charged species. Under the field-measured conditions of pH = 8.6, the majority of the colloid and mineral surfaces in the fractures and matrix will be negatively charged. Thus, we assume that surface complexation reactions involve only PuO_2^+ and these

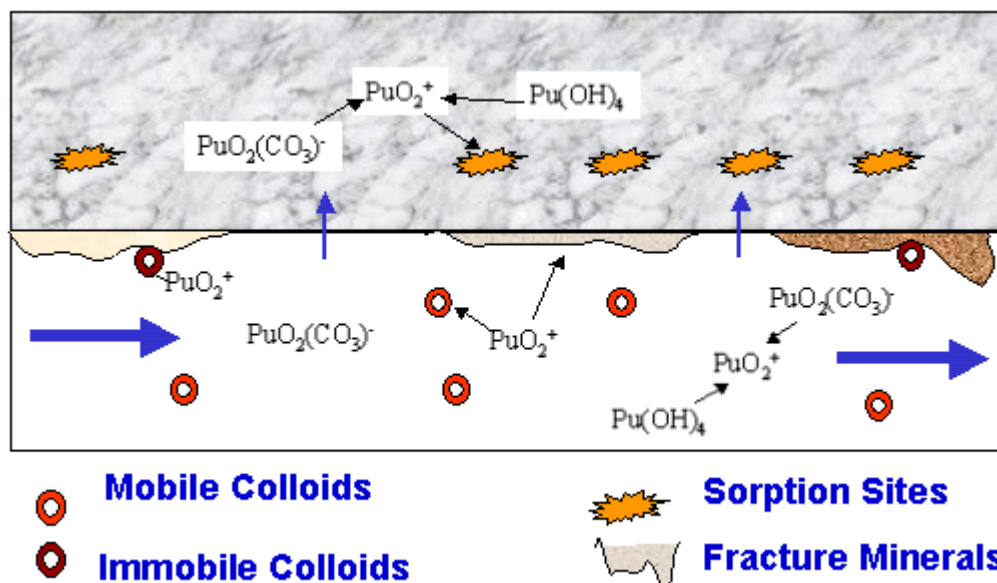


Figure D-1. Schematic of processes and reactions associated with Pu and colloid-facilitated Pu transport in fractures.

negative sites. Although it has been suggested that Pu(IV) may sorb strongly to various minerals, the Pu surface complexation data developed for this project (Pawloski et al., 2001) provide only for PuO_2^+ and Pu^{4+} (see Section D.5). Under the conditions considered in generating Figure D-2, Pu(OH)_4 is the dominant Pu(IV) species and Pu^{4+} concentrations are essentially zero. Thus, aqueous concentrations and sorption of Pu^{4+} are not considered for these calculations. We note that Pu speciation and sorption are actively studied at both LLNL and LANL. Future findings may lead to modifications in the present assumptions. Nevertheless, PuO_2^+ sorption is a strong process (as will be shown in the next section), providing an appropriate mechanism for removal of Pu from aqueous solutions.

The concentrations of $\text{PuO}_2(\text{CO}_3)^-$ and Pu(OH)_4 under equilibrium will be 4.1 and 1.3 times the concentration of PuO_2^+ , respectively, as indicated in Figure D-2 if the pH, Eh, and carbonate concentrations in the water remain unchanged. This approach for relating PuO_2^+ and other Pu species can be invoked for any Eh and pH when equilibrium speciation is assumed. For these conditions, a pseudo equilibrium constant is defined by

$$K^{sp} = \frac{C^{sp}}{C} = 5.4, \quad (\text{Eq. D-2})$$

where C^{sp} is the combined concentration of non-sorbing $\text{PuO}_2(\text{CO}_3)^-$, Pu(OH)_4 and other species that can be used to compute the equilibrium concentration relationship between the reactive Pu cation and all other significant species, assuming fixed pH and Eh.

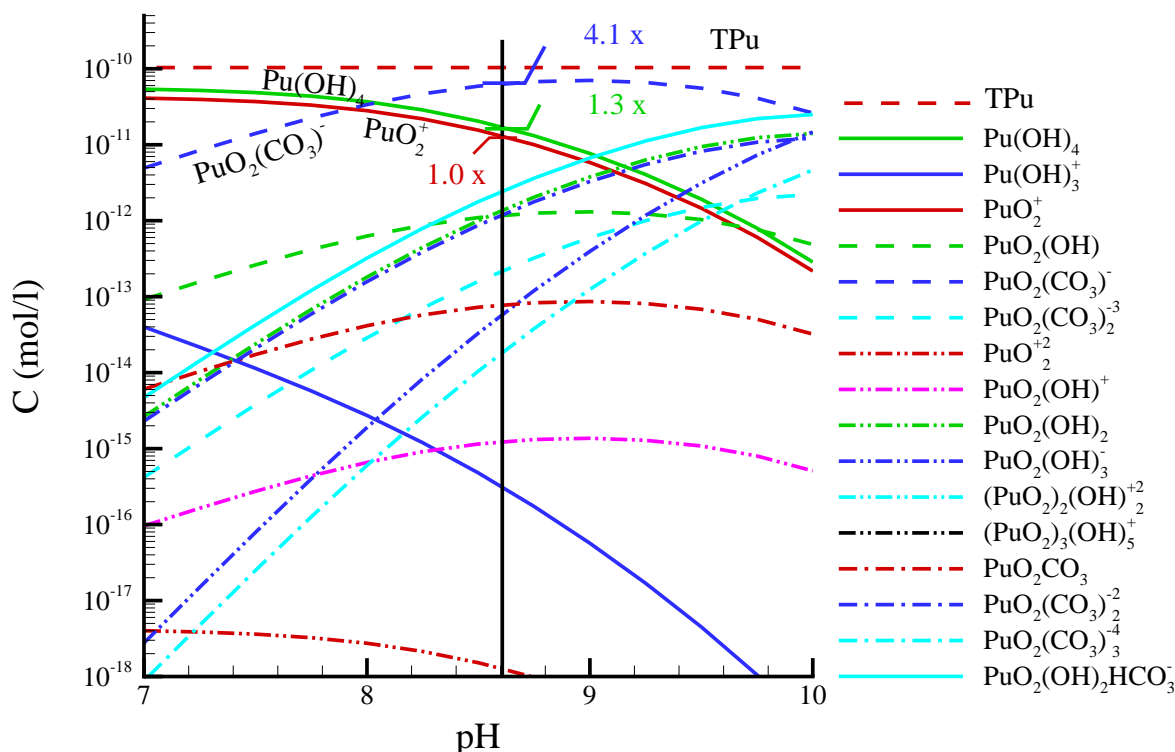


Figure D-2. Speciation of 10^{-10} M Pu at Eh = 550mV, $[\text{HCO}_3^-] = 2.27\text{e-}3$, and 25 °C.

D.3.3 Plutonium–Colloid Reactions

In this model we assume any significant colloidal form of Pu will occur due as a result of sorption reactions between aqueous PuO_2^+ and naturally occurring colloids. Certainly, other intrinsic Pu colloids could form due to molecular aggregation or due to Pu being embedded in colloidal glass particles during the dissolution and weathering of the cavity melt glass (MG). However, no studies to date have indicated a significant Pu-Colloid form created as a result of MG dissolution. By comparison to waste form releases studied by the Yucca Mountain Project (YMP), the process of Pu release from the MG is different from the corrosion process of canisters in the unsaturated zone. Although iron may be abundant in the canister-corrosion process YMP is interested in, it is expected to be very small (less than 1%) in MG following an underground nuclear test. Further, naturally occurring colloids onto which Pu may sorb in the saturated zone are in abundance (Kung 2000). Assuming that Pu-colloids result primarily from sorption reactions, this model is consistent with the process in which Pu-colloid solutions are created for the laboratory experiments the model is verified with. Namely, aqueous Pu is brought into contact with clay (montmorillonite) colloids (Reimus et al., 1999) and, more recently, silica and zeolite colloids (Reimus et al., 2001) and allowed to sorb onto those colloids to generate the feed solution for the column experiments described later in this appendix.

A simplification in this model design is that colloids are not actually considered as mobile entities. Rather, the sorptive sites on the colloids are modeled as an aqueous species that does not diffuse out of fractures in matrix material. Thus, aggregation, buoyancy, and other issues

associated with the actual size and shape of individual colloids is not considered. Only the concentration of available reactive sites on colloids are considered. This approximation is warranted for this study due to the very low aqueous concentrations of Pu under consideration. If larger Pu concentrations were considered, then issues of increased utilization of available colloid sites would need to be addressed. As more and more sites on colloids are taken by Pu molecules, then the rate at which sorption to the remaining sites decreases. In this case, the available sites on natural colloids exceed the aqueous concentration of reactive Pu, thereby minimizing our concern about needing a more complex representation of available colloid site concentration. Kung (2000) reports that the colloids in groundwater from observation wells ER-20-5 #1 and ER-20-5 #3 have an average diameter of 90.0 nm and 80.8 nm, respectively, and average standard errors of 4.61 and 4.28, also respectively. On average, there are 3.02×10^{10} and 7.86×10^{10} particles/ml for ER-20-5 #1 and ER-20-5 #3, respectively (Brachmann and Kersting, 2000, Table 2). The colloid site concentration C_{col} (moles sites/l) can be defined by

$$C_{col} = n_c \text{ (particles/l)} \cdot 4\pi r^2 \text{ (nm}^2\text{/particle)} \cdot x_n \text{ (sites/nm}^2\text{)} / A_v \text{ (sites/mole)}, \quad (\text{Eq. D-3})$$

where n_c is the colloid particle concentration (particles/l), r is the particle radius (nm), x_n is the sorption sites per nm^2 (2.31 sites/ nm^2 of goethite was used for the calculation), and A_v is Avogadro's number, 6.022×10^{23} sites/mole sites.

The number of colloids per liter and the colloid sizes vary within a range, as shown in Table D-1. The colloid site concentrations are 2.9×10^{-9} and 6.0×10^{-9} moles sites/l for wells ER-20-5 #1 and #3, respectively, computed using Equation D-3 for average colloid sizes and concentrations. These values of colloid-site concentrations are more than an order of magnitude greater than conservatively estimated maximum aqueous Pu concentrations (e.g. 1×10^{-10} M).

Under Western Pahute Mesa field conditions, the pH is approximately 8.6. Thus, the colloids are predominantly negatively charged, favoring reaction with PuO_2^+ in the following form:



where $>XO_{(col)}$ represents an aqueous colloid hydroxide site. However, recent experiments indicate that reactions between Pu and colloids may be better represented with a kinetic formulation, thus allowing for irreversible and semi-irreversible adsorption of Pu onto colloids.

Reimus et al. (2001) conducted experiments on Pu sorption to both clay (montmorillonite) and silica colloids. These data were collected to capture the rate-limited process of Pu sorption onto the colloids and then, by removing Pu's aqueous phase, the desorption rate as well. Fitting kinetic parameters to the Pu-colloid sorption and desorption curves was accomplished through a coupling of TRACRN V1.0 (Travis and Birdsell, 1991) with a widely used Levenberg-Marquardt (LM) algorithm (Press et al. 1986). The LM package finds parameter values that minimize the sum of squared differences (SSD) between a set of observations (the concentration of sorbed Pu versus time) and the rate constants calculated by the code. The TRACRN code solves a set of partial differential equations using appropriate boundary and initial conditions that approximate the sorbing and desorbing experiments.

The parameters used for matching the data are the forward and reverse sorption rates. An initial estimate of each was specified at the beginning of the fitting process. Through a series of TRACRN simulations with perturbed parameter values that provide derivatives of the simulation results with respect to the various parameters, the LM package searches until the sum of the square differences (SSD) no longer is reduced in value with further parameter changes. Coupling the LM algorithm with a simulated annealing process (Press et al. 1986) provides an approximate global SSD minimum to the objective function.

A kinetic sorption model is used for the preliminary analysis of Pu(V) sorption and desorption onto the clay and silica colloids. In TRACRN, the exchange of Pu between the aqueous and solid phases is governed by (Travis and Birdsell 1991)

$$\frac{\partial S}{\partial t} = k_f C \left(1 - \frac{S}{S_{max}}\right) - k_r \left(1 - \frac{C}{C_0}\right) S, \quad (\text{Eq. D-5})$$

where

k_f = forward reaction rate ($M_{water}/M_{colloid}/t$),

k_r = reverse reaction rate ($1/t$),

S = sorbed concentration ($M_{solute}/M_{colloid}$),

S_{max} = maximum sorbing capacity of the colloid ($M_{solute}/M_{colloid}$),

C = aqueous phase concentration (M_{solute}/M_{water}),

C_0 = the solubility limit (M_{solute}/M_{water}),

M denotes mass, and t denotes time

Equation D-5 describes the kinetic balance between sorption and desorption processes. Under equilibrium conditions $\frac{\partial S}{\partial t} = 0$ and it reduces to the Langmuir form:

$$S = G(C) = \frac{K_d C}{1 + K_L C}, \quad (\text{Eq. D-6})$$

where

$G(C)$ = symbolizes the relation between S and C ,

$K_L = K_d/S_{max}$, and

$K_d = k_f/k_r$.

Table D-2 shows the results from fitting data from Reimus et al.'s (1999) experiments.

Table D-1. Colloid Measurement Data

From Brachman and Kersting, 2000

		Number of Samples	Average	Std. Dev.
Colloid Sizes (nm)	Well ER-20-5 #1	15	90.90	4.61
	Well ER-20-5 #3	19	80.8	4.28
Colloid Particles (particles/ml)	Well ER-20-5 #1	20	3.02e+10	4.33e+8
	Well ER-20-5 #3	19	7.86e+10	1.07e+9

Table D-2. Forward and Reverse Rate Fits to Experimental Pu-Colloid Sorption Data

Colloid Type	kf (g/g/hr)	kr (1/hr)
Ca-Montmorillonite	8.06E+01	5.98E-03
Silica	2.36E+02	8.56E-04
Note: Recent preliminary experiments indicate that Pu sorbs nearly irreversibly onto zeolite colloids, with over six orders of magnitude between the forward and reverse rates.		

D.3.4 Colloid Filtration

Colloids attach and detach to/from the fracture wall during filtration. The filtration reactions for colloids and Pu-colloids can be expressed as follows:



The processes and mechanisms associated with colloid filtration in fractures are not fully understood. However, both UGTA and YMP have supported studies seeking to quantify parameters associated with colloid filtration processes. Most relevant are the recent studies of Reimus et al. (2001), in which filtration parameters are fit for multiple, different, natural colloid types in fractured core experiments in the laboratory. These are presented later in this appendix when we discuss modeling laboratory experiments. LANL has also conducted experiments directed toward assessing attachment and detachment rates of colloids onto fracture walls using synthetic microspheres in field tests.

Summarizing several different field experiments, Table D-3 lists estimated attachment and detachment rates of colloids to fracture surfaces, as well as retardation factors that would be

associated with the attachment and detachment rates if the time scales are large enough to assume local equilibrium conditions. The retardation factors are based on

$$R = 1 + \frac{k_f}{bk_r}, \quad (\text{Eq. D-9})$$

where b is the fracture aperture. As described in CRWMS M&O (2000d), for each experiment multiple different pathways were identified, each having unique attachment and detachment rates. The probabilities of the attachment and detachment rates associated with each pathway are weighted by the mass fraction of colloids traveling in each pathway. Thus, for each pathway, a unique pair of forward and reverse rates and their probabilities are determined. Then, similar rates are binned into cumulative distributions. When retardation factors are computed, the coupled pairs are used in Equation D-9 and the associated probability of that pair is reported. The experiments indicate that retardation due to filtration of colloids can range from nearly negligible values to values that lead to significant retardation in predicted colloid migration rates. CRWMS M&O (2000d) provides further discussion and analyses of these parameters. For the purposes of the current study, colloid filtration rates are considered as a fitting parameters for the laboratory data presented later in this appendix. In Appendix F and Chapter 7, sensitivity to colloid filtration, modeled as a retardation factor, is considered in site-scale transport models. Table D-3 is used to define ranges of uncertainty.

Table D-3. Colloid Filtration
(From CRWMS M&O 2000d)

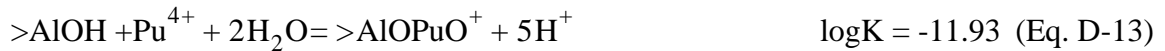
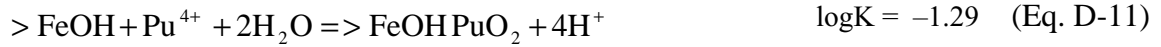
Attachment Only		Detachment Only		Retardation Factors with Coupled Rates Distribution			
k_{filt} , 1/hr	Probability	bk_{res} , 1/hr	Probability	R	k_{filt}	bk_{res}	Probability
0.04	0.25	0.000154	0.25	1.06	0.2	3.33	0.0105
0.043	0.5	0.00025	0.7395	1.1	0.04	0.4	0.039
0.07	0.75	0.000404	0.91875	6	0.04	0.008	0.08125
0.2	1	0.008	0.961	100	0.04	0.0004	0.2605
		0.4	0.9895	280	0.07	0.000251	0.5102
		3.33	1	280	0.043	0.000154	0.7605
				800	0.2	0.00025	1.0

D.3.5 Surface Complexation of Plutonium with Fracture and Matrix Minerals

In the model simulations described later in this appendix, fracture and matrix Kd values are estimated for the columns considered. However, in this section we provide a method that estimates the Kd , starting with mechanistic complexation reactions and developing simplifications that ultimately lead to such Kd values. This approach is used in Appendix F, where fracture Kds must be estimated rather than fit to experimental data.

Plutonium species are expected to complex or undergo exchange with secondary fracture lining minerals. These reactions include the interactions with $>Ca^{2+}$, $>FeOH$, $>MnOH$, $>SiOH$,

and $>AlOH$, where “ $>$ ” indicates a site on an immobile mineral. Pawloski et al. (2001) list equilibrium coefficients for the following surface complexation reactions:



The concentration of Pu^{4+} , at $pH = 8.6$, $Eh = -550$ mV, and bicarbonate concentration of 2.27×10^{-3} is estimated to be more than 20 orders of magnitude lower than the concentration of PuO_2^+ . It does not even show up in Figure D-2. Therefore, although its concentration can be written in terms of PuO_2^+ (reactions D-10 and D-11 can be rewritten in the form of either reaction D-15 or D-16 with the appropriate relationship from Section D.5), it is not considered in these calculations. Thus, in this study the surface complexation of Pu to these minerals is only described with reactions D-15 through D-20.

Due to the low Pu concentration anticipated for this study, the concentration of stationary mineral sites and pH are assumed to remain constant. Eh and bicarbonate concentration are also assumed to remain constant. With these assumptions, the surface complexation reactions are simplified and modeled using a lumped K. For reaction (D-15),

$$K^{r1} = \frac{C^{r1}}{[>FeOH]C} \quad (\text{Eq. D-21})$$

$$K_{lump}^{r1} = K^{r1} [>FeOH] = \frac{C^{r1}}{C}, \quad (\text{Eq. D-22})$$

where C^{r1} is the concentration of $>FeOHPuO_2^+$ and C is the concentration of PuO_2^+ . Similar equilibrium constant K and lumped K values can be written for the remaining reactions as

$$K^{r2} = \frac{C^{r2} 10^{-2pH}}{[>FeOH]C} \quad (\text{Eq. D-23})$$

$$K_{lump}^{r2} = K^{r2} [>FeOH] 10^{2pH} = \frac{C^{r2}}{C} \quad (\text{Eq. D-24})$$

$$K^{r3} = \frac{C^{r3} [Ca^{+2}]}{[>Ca^{+2}]C} \quad (\text{Eq. D-25})$$

$$K_{lump}^{r3} = \frac{K^{r3} [>Ca^{+2}]}{[Ca^{+2}]} = \frac{C^{r3}}{C} \quad (\text{Eq. D-26})$$

$$K^{r4} = \frac{C^{r4} 10^{-1pH}}{[>AlOH]C} \quad (\text{Eq. D-27})$$

$$K_{lump}^{r4} = K^{r4} [>AlOH] 10^{1pH} = \frac{C^{r4}}{C} \quad (\text{Eq. D-28})$$

$$K^{r5} = \frac{C^{r5} 10^{-1pH}}{[>SiOH]C} \quad (\text{Eq. D-29})$$

$$K_{lump}^{r5} = K^{r5} [>SiOH] 10^{1pH} = \frac{C^{r5}}{C} \quad (\text{Eq. D-30})$$

$$K^{r6} = \frac{C^{r6} 10^{-2pH}}{[>SiOH]C} \quad (\text{Eq. D-31})$$

$$K_{lump}^{r6} = K^{r6} [>SiOH] 10^{2pH} = \frac{C^{r6}}{C}, \quad (\text{Eq. D-32})$$

where C^{r2} , C^{r3} , C^{r4} , C^{r5} , and C^{r6} are the concentrations of $>FeOHPuO_3^-$, $>PuO_2^+$, $>AlOPuO_2$, $>SiOPuO_2$ and $>SiOPuO_3H^-$, respectively. Because we assume that the aqueous Pu concentrations are low enough that the available surface reaction sites are not depleted during the course of a simulation, Equations D-22, D-24, D-26, D-28, and D-30 can be combined into one effective lumped K to describe all sorbed Pu species on fracture minerals

$$K_{lump}^e = K_{lump}^{r1} + K_{lump}^{r2} + K_{lump}^{r3} + K_{lump}^{r4} + K_{lump}^{r5} + K_{lump}^{r6} \quad (\text{Eq. D-33})$$

$$K_{lump}^e = \frac{C^{r1} + C^{r2} + C^{r3} + C^{r4} + C^{r5} + C^{r6}}{C} \quad (\text{Eq. D-34})$$

Equation D-34 provides a simplified method for estimating the ratio of sorbed to nonsorbed species for the case when surface site concentrations of the reactive minerals can be assumed to be unchanging. However, there is still great uncertainty in the actual concentration of fracture mineral surface sites available to react with solutes flowing in the fracture.

The sorption sites, ω_m (mole sites/l), on the fracture mineral surfaces are related to the specific surface site density η [sites/nm²] of the medium by the relation

$$\omega_m = (\eta A_s \rho / A_v) F_i, \quad (\text{Eq. D-35})$$

where A_s (m²/kg) is the specific sorptive surface area of fracture-lining minerals, ρ is the mineral density [g/dm³], F_i is the mineral volume fraction of mineral i (e.g., >FeOH), and A_v is Avogadro's number, 6.022×10^{23} sites/mole site. The specific sorptive surface area for the various minerals (represented here by their actual reactive site species) will vary depending on the structure of the mineral coating. Because of uncertainty in this term and even greater uncertainty in other terms, a value of 1 m²/g is used for all fracture coatings. This value is representative of those measured by White et al. (1996) on a variety of soil and mineral components. For these calculations, η is assumed to be 2.31 sites/nm² (note: 1 nm = 10⁻⁹ m), $A_s = 1$ m²/g, $\rho = 2650$ g/dm³. The resulting sorption sites $\omega_m = 0.01 F_i$. The available reactive mineral in the fracture (mineral volume fraction of mineral i) can be approximated by the following equation:

$$F_i = P_{\text{exp}}\% \times P_{\text{cov}}\% \times P_{\text{min}}\% \times (d/b/2), \quad (\text{Eq. D-36})$$

where $d/b/2$ is the ratio of the thickness of the secondary fracture-lining mineral to the aperture, $P_{\text{exp}}\%$ is the percentage of the mineral mass exposed to the aqueous phase, $P_{\text{cov}}\%$ is the percentage of the fracture surface covered by mineral lining, and $P_{\text{min}}\%$ is the proportion of a mineral (i) in the coating. Estimates regarding the concentration of sorption sites in fractures are highly uncertain because the following characteristics have not been measured in detail: the coating mineral's exposure to the fluid, the fracture wall's coverage by the coating mineral, and each specific mineral's percentage. However, in Appendix F relevant observations from field studies are incorporated into sensitivity studies of these parameters (e.g., Tables F-4 to F-15). For this initial testing of the transport model, the Kd for Pu sorption to fracture minerals is treated as a lumped parameter and the individual components are not derived. However, when the coatings for these particular experimental cores are analyzed, the more and less certain components of Equation D-36 can be extracted.

In the simulations conducted with this reactive transport model, sorption to matrix minerals is represented with Kd parameters. These are either fit, as is done later in this appendix, or derived from laboratory batch studies for the site-scale transport model. The following general-purpose surface complexation reaction is assumed take place in the matrix.



where >OX is the matrix reaction site. As with fracture sorption, assuming a constant pH and unchanging available site concentration, a lumped Kd can be written for the complexation in the matrix

$$K^{rma} = \frac{C^{rma}}{[>OX]C} \quad (\text{Eq. D-38})$$

$$K_{lump}^{rma} = K^{rma} [> OX] = \frac{C^{rma}}{C}, \quad (\text{Eq. D-39})$$

where C^{rma} is the concentration of total sorbed Pu in the matrix. The lumped $\log(K)$ values for matrix sorption are obtained from YMP sorption studies (CRWMS M&O 2000g - see Table F-16) with a range between 5 and 300 cc/g for Pu on a variety of devitrified and altered tuffs.

Using the method described above for estimating Kds for sorption to fracture minerals, matrix Kds can be derived that fit approximately in the range of 5 to 300 cc/g. The sorption experiments by Triay et al. (1997) give surface areas of tuffs between 3 to 5 m²/g and Daniels et al. (1982) report Fe content in Yucca Mountain tuffs as less than 0.1%. Thus, assuming that $>FeOH$ and $>Ca^{2+}$ represent a volume fraction in the matrix material of between 0.1% to 1.0%, the site concentration for these two minerals ranges between 3.1e-8 to 5.1e-7 mole sites/l, which leads to a K_{lump}^{matrix} between 1.1 and 180 for pH = 8.6.

D.4 Pu-Colloid Transport in Fractured Column Experiments

D.4.1 Overview of Column Experiments

A series of colloid-facilitated Pu(V) transport experiments in naturally fractured rock cores was conducted by Reimus et al. (1999). In these experiments, soluble Pu(V) was sorbed onto inorganic colloids (Ca-montmorillonite) and then some of the Pu-colloid solution was injected into saturated, fractured rock cores, through which steady water flow had been established. Also, tritiated water was injected with the Pu-colloid solution, thus providing a non-reactive tracer for comparison. Figure D-3 is a schematic of the experiments and resulting data.

Two separate cores with fractures from the Topopah Spring Tuff unit in well UE-20c were used in the experiments. The fractured cores were cut perpendicular to their axes such that the fracture bisected the length of the resulting core section. The final dimensions of the cut cores are listed in Table D-4. After assembly, the cores were saturated under water by replacing oxygen and nitrogen with CO₂ and subsequent evacuation of the CO₂ using a vacuum. Detailed steps are (1) evacuating the cores under vacuum, (2) introducing CO₂ gas to displace oxygen and nitrogen, (3) evacuating the CO₂ using vacuum, (4) slowly introducing degassed water while still maintaining vacuum, and (5) keeping the cores under vacuum and under water until they no longer evolved gas bubbles. This procedure takes advantage of the fact that CO₂ dissolves in water more readily than oxygen or nitrogen.

For each fracture, transport experiments were conducted with a low flow rate (approximately 0.5 ml/hr) and a high flow rate (approximately 1.5 ml/hr), yielding a total of four sets of results. For each experiment, artificial groundwater water was prepared in the laboratory to replicate the composition of major cations and anions found in water from U-20WW (water well

20) on Pahute Mesa. In the artificial water, sodium was used in place of calcium to minimize colloid aggregation induced by multivalent cations.

The montmorillonite-colloidal solution was prepared by dispersing Ca-montmorillonite powder in nanopure deionized water. The dispersed suspension was allowed to stand for 5 hours at room temperature for larger particles to settle. Thereafter, the supernatant solution was carefully collected as a stock colloidal solution. The mass of the colloidal particles in the solution was determined by the difference in the weight before and after vaporizing and oven-drying (105°C) a given amount of solution. The working solution was obtained by diluting a measured amount of stock solution into a liter of artificial water. The average particle size of the colloidal solution was 90.4 nm and the pH of the working solution was 8.5, almost identical to Pahute Mesa groundwater conditions.

The experimental parameters for these column experiments are listed in Table D-4 and the results are shown in Figures D-5 through D-8, along with the simulation results.

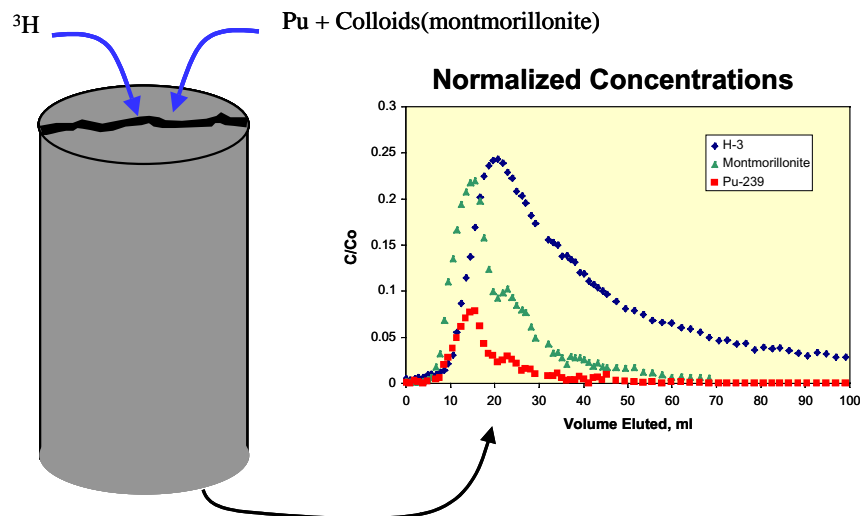


Figure D-3. Experimental design for fractured column experiments.

D.4.2 Column Simulations

We conceptualize the column experiment with a discrete fractured-media model for colloid-facilitated Pu transport using FEHM (Zyvoloski et al., 1997). This model (Figure D-4) uses a computational grid normal to the fracture to capture both the fracture and the matrix and all chemical and physical processes described in the previous sections. Affecting Pu migration in the fractures are advective transport, speciation, sorption onto colloids, sorption onto fracture minerals, and colloid filtration on fracture walls. In the matrix, the dominant processes are diffusion of the ions and molecules, speciation, and sorption of the cation PuO_2^+ onto matrix minerals. Because the fracture-coating minerals have not yet been characterized, only a lumped K_d is used for the complexation and ion exchange of Pu(V) with fracture minerals in these simulations.

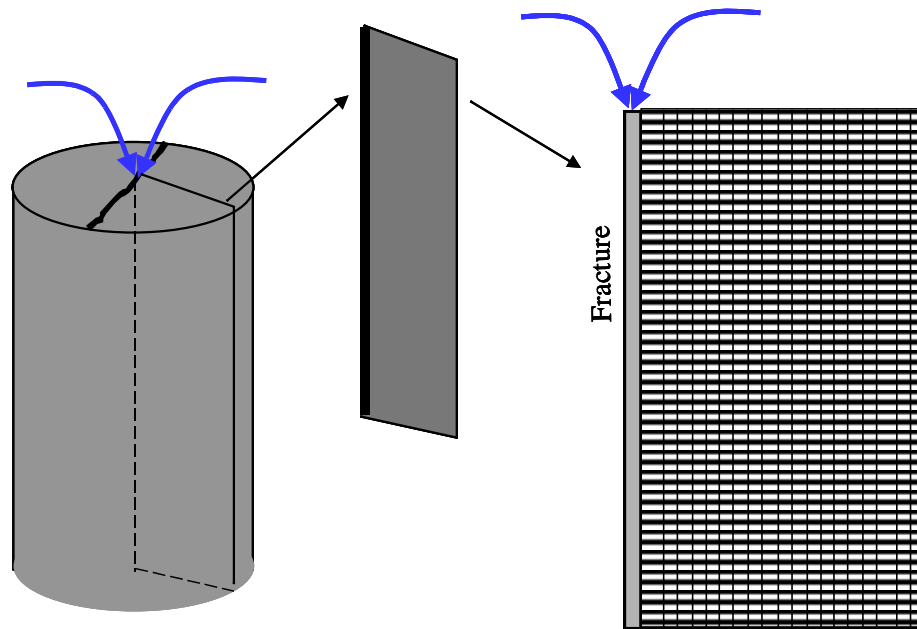


Figure D-4. Schematic of model grid for column experiments. Note the computational grid is actually not uniformly discretized as shown in this schematic.

The column experiments are modeled using a two-dimensional x-, y-grid of 400 rows and 20 columns. The first column represents the fracture and its width is set to the fracture aperture. The next five rows into the matrix are spaced at 0.5 mm. Then, the spacing of the remaining rows increases geometrically, with the final row residing at outer wall of the core. Along the length of the core, the grid is evenly discretized with 400 intervals. The third-dimension of the model, perpendicular to the longitudinal cross section of the column, is scaled to unit length. The injection flow rate and concentrations are also scaled correspondingly.

To represent conditions in the experiments, 75% of the total Pu in the feed solution is in the form of Pu-colloid, and the remaining 25% is distributed between the positive charged PuO_2^+ and the other species [$\text{PuO}_2(\text{CO}_3)^-$, $\text{Pu}(\text{OH})_4$, etc.] by ratio of 1:5.4 (as per Figure D-2). The flow fields were modeled as steady state using the injection flow rates of the experiments (see Table D-4).

In the transport model, the diffusion coefficient and dispersivity of the conservative tracer ^3H was adjusted to yield a breakthrough curve that closely matched the experimental data (Table D-5). Then, reactive transport parameters were systematically varied to match the experimental results. The best-fit parameters for all processes for each of the four experiments are reported in Table D-5 and fall well within reasonable bounds derived from independent estimates. Figures D-5 through D-8 show the simulation results for the four columns compared to laboratory measurements.

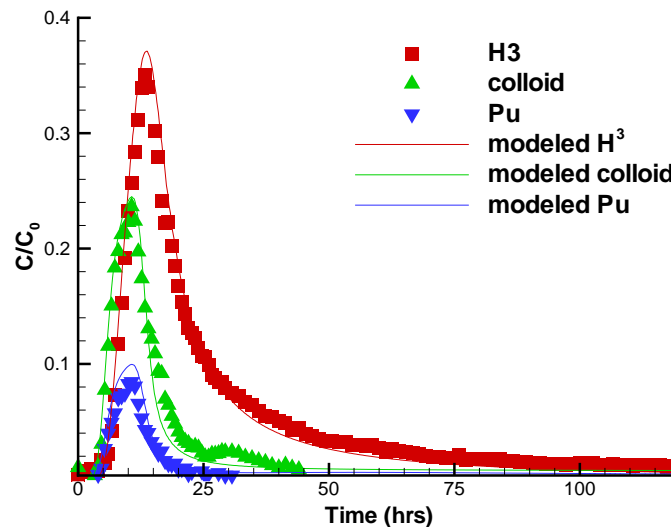
D.4.3 Sensitivity Analysis

A systematic sensitivity analysis was conducted to evaluate how the model parameters affect the Pu migration in the column. The sensitivity coefficient with respect to a particular

parameter can be approximated by making a small perturbation in the parameter value while keeping all other parameters constant, and dividing the change in the dependent variable (the peak breakthrough concentrations for Pu-colloid here) by the change in the parameter. This can be expressed by the formula (Zheng and Bennett, 1995, Lu et al., 1999):

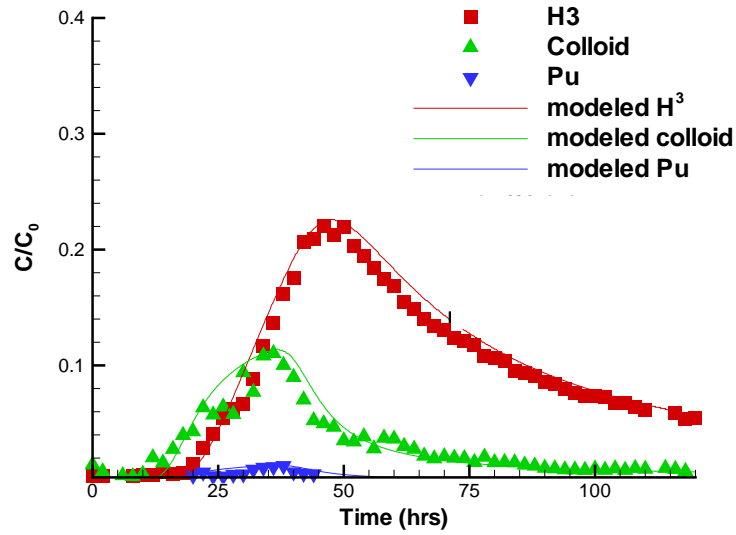
$$X_k = \frac{\partial y/y}{\partial a_k/a_k} \approx \frac{[y(a_k + \Delta a_k) - y(a_k)]/y(a_k)}{\Delta a_k/a_k}, \quad (\text{Eq. D-40})$$

where X_k is the sensitivity coefficient of the model dependent variable, y , with respect to the k^{th} parameter. Further, $y(a_k)$ and $y(a_k + \Delta a_k)$ are the values of the dependent variable obtained for the base case and for the perturbed-parameter case, respectively. In this case, the calibrated parameters for Column 1 (Table D-5) are the base case, and each parameter was perturbed to 50% above its base-case value. Table D-6 summarizes the results of the sensitivity analysis. The Pu-colloid reverse reaction rate and Pu-colloid filtration rate have negative sensitivity coefficients. This indicates that increases of their values will yield lower peak concentrations. Conversely, mineral surface complexation (in the fracture), diffusion coefficient, and longitudinal dispersivity have positive sensitivity coefficients. For this study, the matrix Kd , the filtration detachment rate, and forward rate of Pu-colloid formation show no sensitivity at all. Of the parameters examined, Pu-colloid filtration is the most sensitive of the parameters.



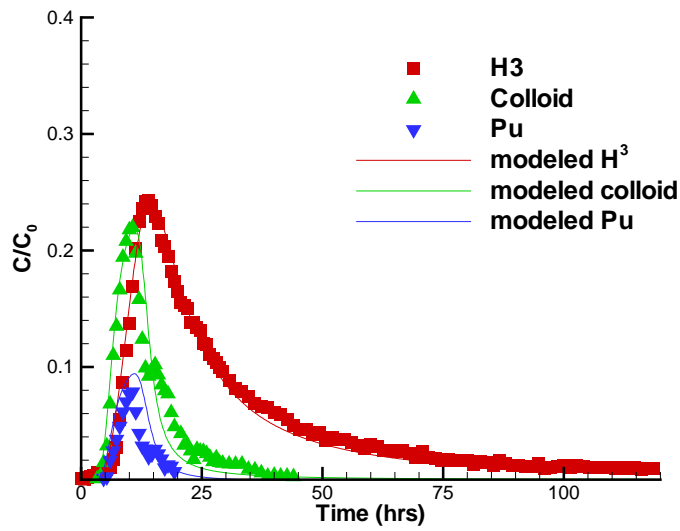
Column 1 with high flow rate

Figure D-5. Experimental data and modeled results for Column 1 - high flow rate.



Column 1 with low flow rate

Figure D-6. Experimental data and modeled results for Column 1 - low flow rate.



Column 2 with high flow rate

Figure D-7. Experimental data and modeled results for Column 2 - high flow rate.

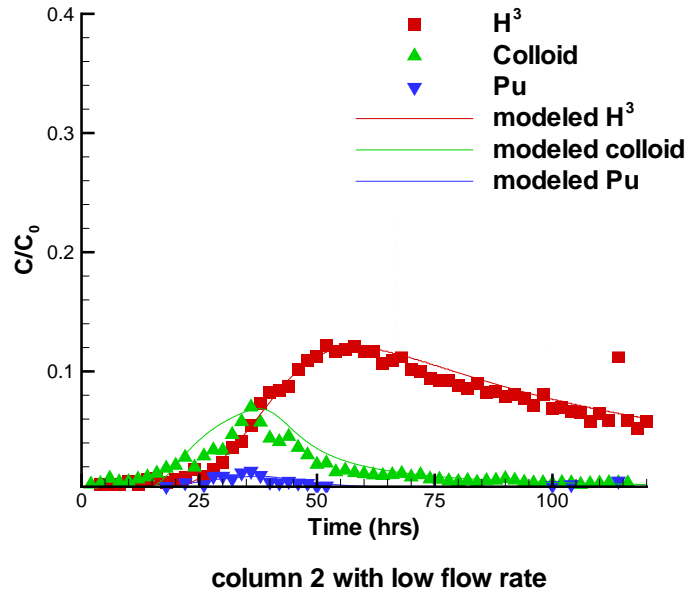


Figure D-8. Experimental data and modeled results for Column 2 - low flow rate.

Table D-4. Physical Description of Column Experiments

Core No.		Core 1		Core 2	
Core sample depth		2851 ft. at well UE-20c		2858 ft. at well UE-20c	
Experiment No		1	2	3	4
Core Geometry	Length (cm)	16.7		21.90	
	Diameter (cm)	8.7		8.7	
	Average fracture aperture (cm)	0.058		0.057	
Flow Rate (ml/hr)		1.55	0.575	1.53	0.587
Injection Duration (hr)		7.73	24.4	7.52	23.4
Injection Concentration	^3H (mol/l)	1.65e-11	1.66e-11	1.65e-11	1.01e-11
	^{239}Pu (mol/l)	9.08e-9	1.4e-8	9.08e-9	1.21e-8
	Colloids (1/ml)	3.95e9	1.99e9	3.95e9	2.25e9
	Colloid sites ¹ (mol/l)	3.89e-10	1.98e-10	3.89e-10	2.22e-10
1 - The average size of montmorillonite colloid is 90 nm, the sorption site density on colloids is assumed to be 2.31 sites/nm ² .					

Table D-5. Column Simulation Parameters

Experiment No		1	2	3	4
Core No.		Core 1		Core 2	
Flow rate (ml/hr)		1.55	0.575	1.53	0.587
^3H matrix diffusion coefficient (m^2/s) ¹		2.0e-10	2.2e-10	2.1e-10	2.7e-10
<i>^3H matrix diffusion coefficient (m^2/s) Estimated by Reimus et al. (1999)</i>		2.0e-10	2.2e-10	2.1e-10	2.7e-10
Colloid and Pu-Colloid diffusion coefficient (m^2/s) Into stagnant zone of fracture ²		0.075e-10	0.28e-10	0.07e-10	0.30e-10
Longitudinal dispersivity (cm)		0.1	0.1	0.1	0.1
Rxn 1: Pu-colloid reaction > $\text{XOH}_{(\text{col})} + \text{PuO}_2^+ \Rightarrow \text{XOHPuO}_{2(\text{col})}^+$	k_f^b	$k_f \geq 10^1$	$k_f \geq 10^1$	$k_f \geq 10^1$	$k_f \geq 10^1$
	k_r^b	$k_r \leq 10^{-2}$	$k_r \leq 10^{-2}$	$k_r \leq 10^{-2}$	$k_r \leq 10^{-2}$
Rxn 2: colloid filtration > $\text{XOH}_{(\text{col})} \Rightarrow \text{XOH}_{(s)}$	k_f	3.15e-1	2.30e-1	2.85e-1	2.3e-1
	k_r	5.05e-3	7.0e-4	2.3e-3	3e-4
<i>colloid filtration Estimated by Reimus et al. (1999)</i>	k_f	2.9e-1	1.8e-1	3.1e-1	2.4e-1
	k_r	5.0e-3	1.0e-3	5.0e-3	1.0e-3
Rxn 3: Pu-colloid filtration > $\text{XOPuO}_{2(\text{col})} \Rightarrow \text{XOHPuO}_{2(s)}$	k_f	3.15e-1	2.30e-1	2.85e-1	2.3e-1
	k_r	5.05e-3	7.0e-4	2.3e-3	3e-4
Rxn 4: surface complexation in the matrix > $\text{XOH} + \text{PuO}_2^+ \Rightarrow \text{XOHPuO}_2^+$	Kd	>10	>10	>10	>10
Rxns 5-7: composite surface complexation on fracture minerals > $\text{XOH} + \text{PuO}_2^+ \Rightarrow \text{XOHPuO}_2^+$	Kd	>6	>6	>6	>6
<p>1 - Used Reimus et al.'s diffusion coefficient estimates and achieved good fit for Tritium.</p> <p>2 - This term was added to fit model tail results where first-order kinetic processes do not lead to a good match.</p> <p>a - Assumed aqueous complexation ratio of $\text{PuO}_2^+(\text{aq})$ to $\text{PuO}_2(\text{CO}_3)$-& other species(aq) = 4.5.</p> <p>b - Combination of k_f and k_r produces same breakthrough curves.</p>					

Table D-6. Sensitivity Coefficients for Column 1 Simulation

Parameter	Peak Pu- Colloid Concentration	Sensitivity Coefficient
Base	0.0933	0
Diffusion Coefficient (D)	0.0982	0.105
Dispersivity	0.0943	0.021
Pu-colloid formation rate (k_f)	0.0933	0.0
Pu-colloid reverse formation rate (k_r)	0.091	-0.049
Pu-colloid filtration: attachment rate (k_f)	0.0358	-1.233
Pu-Colloid filtration: detachment rate (k_r)	0.0955	0.047
Matrix Kd	0.0933	0.0
Fracture lumped Kd	0.0954	0.043
Carbonate speciation constant	0.0933	-0.001

D.5 Pu Speciation Reactions

In the aqueous speciation calculation, Pu redox between the states 3+ to 6+, pH, and carbonate complexation were considered. Gibbs free-energy data used were cited from Langmuir (1997), who references mainly from Puigdomenech and Bruno (1991), Lemire and Tremaine (1980), Lemire and Garisto (1989), and Nitsche et al. (1995). The equilibrium constants were derived in terms of the standard Gibbs free energy of the reaction ΔG° (J/mol):

$$\log K = \frac{-\Delta G^\circ}{2.303RT} \quad (\text{Eq. D-41})$$

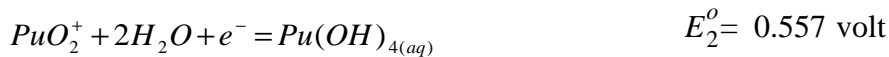
$$pK = -\log K \quad (\text{Eq. D-42})$$

where K is the standard equilibrium constant, T is the temperature on the Kelvin scale (K), and R is the gas constant ($8.3143 \text{ J mol}^{-1} \text{ K}^{-1}$) (Langmuir, 1997; Drever, 1988).

The redox reactions

$$Eh = E_1^0 + \frac{2.303RT}{F} \log \frac{[Pu(OH)_{4(aq)}^0]}{[Pu^{3+}][OH^-]^4}, \quad (\text{Eq. D-43})$$

where F is Faraday's constant.



$$Eh = E_2^0 + \frac{2.303RT}{F} \log \frac{[PuO_2^+]}{[Pu(OH)_{4(aq)}]} \quad (\text{Eq. D-44})$$

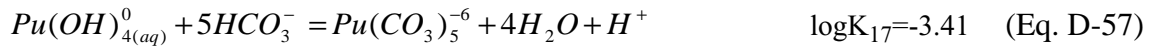
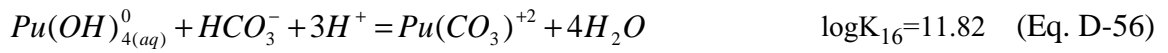


$$Eh = E_3^0 + \frac{2.303RT}{F} \log \frac{[PuO_2^{+2}]}{[PuO_2^+]} \quad (\text{Eq. D-45})$$

The hydration reactions



Chemical complexation reactions with carbonate



The mass balance for Pu is

$$TPu = TPu^{3+} + TPu^{4+} + TPu^{5+} + TPu^{6+} \quad (\text{Eq. D-64})$$

where TPu is the total concentration of Pu, TPu^{3+} , TPu^{4+} , TPu^{5+} , and TPu^{6+} are total concentrations of Pu of the corresponding redox state. Their values in terms of PuO_2^+ are

$$\begin{aligned} TPu^{3+} &= [Pu^{3+}] = Pu(OH)_{4(aq)}^0 10^{(-Eh-1.77)/0.0592 + 4pOH} \\ &= [PuO_{2(aq)}^+] 10^{(-Eh+0.557)/0.0592 + (-Eh-1.77)/0.0592 + 4pOH} \end{aligned}$$

$$\begin{aligned}
TPu^{4+} &= [Pu^{4+}] + [Pu(OH)_{4(aq)}^0] + [Pu(OH)_{3(aq)}^+] + [Pu(OH)_{2(aq)}^{+2}] + [Pu(OH)_{(aq)}^{+3}] \\
&+ Pu(CO_3)^{+2} + Pu(CO_3)_5^{-6} \\
&= [Pu(OH)_{4(aq)}^0] 10^{pk4+4pOH} + [Pu(OH)_{4(aq)}^0] (1 + 10^{-pk7+pk4+pOH} + 10^{-pk8+pk4+2pOH} + 10^{-pk9+pk4+} \\
&+ [Pu(OH)_{4(aq)}^0] (10^{-pk16-3pH} [HCO_3^-] + 10^{-pk17+pH} [HCO_3^-]^5) \\
&= [PuO_{2(aq)}^+] 10^{(-Eh+0.557)/0.0592+pk4+4pOH} + [PuO_{2(aq)}^+] 10^{(-Eh+0.557)/0.0592} (1 + 10^{-pk7+pOH} \\
&+ 10^{-pk8+pk4+2pOH} + 10^{-pk9+pk4+3pOH}) \\
&+ [PuO_{2(aq)}^+] 10^{(-Eh+0.557)/0.0592} (10^{-pk16-3pH} [HCO_3^-] + 10^{-pk17+pH} [HCO_3^-]^5)
\end{aligned}$$

$$\begin{aligned}
TPu^{6+} &= [PuO_{2(aq)}^{+2}] + [PuO_2(OH)_{(aq)}^+] + [PuO_2(OH)_{2(aq)}^0] + [PuO_2(OH)_{3(aq)}^-] \\
&+ [(PuO_2)_2(OH)_{2(aq)}^{+2}] + [(PuO_2)_3(OH)_{5(aq)}^+] \\
&+ [PuO_2CO_{3(aq)}] + [PuO_2(CO_3)_{2(aq)}^{-2}] + [PuO_2(CO_3)_{3(aq)}^{-4}] + [PuO_2(OH)_2HCO_{3(aq)}^-] \\
&= [PuO_{2(aq)}^{+2}] \{1 + 10^{-pk11-pOH} + 10^{-pk12-2pOH} + 10^{-pk13-3pOH} \\
&+ 10^{-pk14-2pOH} [PuO_{2(aq)}^{+2}] + 10^{-pk15-5pOH} [PuO_{2(aq)}^{+2}]^3 \\
&+ 10^{-pk20+pH} [HCO_3^-] + 10^{-pk21+2pH} [HCO_3^-]^2 + 10^{-pk22+3pH} [HCO_3^-]^3 + 10^{-pk23-2pOH} [HCO_3^-] \} \\
&= [PuO_{2(aq)}^+] 10^{(Eh-0.956)/0.0592} \{1 + 10^{-pk11-pOH} + 10^{-pk12-2pOH} + 10^{-pk13-3pOH} \\
&+ 10^{-pk14-2pOH} [PuO_{2(aq)}^{+2}] + 10^{-pk15-5pOH} [PuO_{2(aq)}^{+2}]^3 \\
&+ 10^{-pk20+pH} [HCO_3^-] + 10^{-pk21+2pH} [HCO_3^-]^2 + 10^{-pk22+3pH} [HCO_3^-]^3 + 10^{-pk23-2pOH} [HCO_3^-] \}
\end{aligned}$$

D.6 Summary

Following these simulations, a few general observations are as follows:

- The model results are reasonably sensitive to the diffusion coefficient. This is because the diffusion coefficient helps control the rate at which PuO_2^+ is exposed to matrix minerals to which the positive molecule sorbs.
- A kinetic model of Pu-colloid formation is necessary to match the data. The forward rate must be fast enough to create appropriate amounts of Pu-colloids and the reverse rate must be slow enough to keep the Pu on the colloids. The forward and reverse rates used are extremely close to those rates estimated from the batch sorption/desorption experiments. The model is more sensitive to the reverse rate than the forward rate because, in laboratory experiments, the colloids are effectively “doped” with Pu before injection into the fracture. No free-ion Pu was observed in the effluent solution. Hence, the reverse rate controls how much Pu remains on the colloids. The field-scale implication of this parameter sensitivity is that the reverse rate controls how the Pu remains on the colloids for large time and space scales. The site-scale transport model results presented in Appendix F show that this parameter does, in fact, have a governing role in determining whether Pu transport is facilitated by colloids over the distance between BENHAM and ER-20-5 #1 and #3.
- At the short time and space scales associated with these experiments, it is necessary to model with kinetic rates the attachment and detachment of colloids and Pu-colloids to the fracture surfaces.
- A very small colloid diffusion coefficient (more than an order of magnitude smaller than the solute diffusion coefficient) was needed to match the curvature of the tails of the breakthrough curves. The detachment rate of colloids from the fracture surface captured the decreasing slope in the tails, but not the change in curvature. The physical and chemical effects this parameter could be capturing include diffusion into a low-velocity boundary film of water near the fracture surface, second-order kinetic attachment/detachment processes not captured in the first-order equation, and actual diffusion of colloids into large matrix pores.
- Matrix Kds and fracture Kds must be large enough to retain (e.g., retard) the Pu that desorbs from the colloids. All Pu in the effluent was reported to be on colloids. Thus, PuO_2^+ cannot travel as a free ion in this system.

D.7 References

- Berkowitz, B. and H. Scher, 1995. On characterization of anomalous dispersion in porous and fractured media, *Water Resource Research*, 31(6), 1461-1466.
- Berkowitz, B. and J. Zhou, 1996. Reactive solute transport in a single fracture, *Water Resources Research*, 32(4), 901-913.
- Dershowitz, W. and I. Miller, 1995. Dual porosity fracture flow and transport, *Geophysical Research Letters*, 22(11): 1441-1444.
- Grisak, G. E., and J. F. Pickens, 1981. An analytical solution for solute transport through fractured media with matrix diffusion, *Journal of Hydrology*, 52, 47-57.
- Johns, R. A., and P. V. Roberts, 1991. A solute transport model for channelized flow in a fracture, *Water Resources Research*, 27, 1797-1808.
- Keller, A. A., P. V. Roberts, and P.K. Kitanidis, 1995. Prediction of single phase transport parameters in a variable aperture fracture, *Geophysical Research Letters*, 22, 1425-1428.
- Kersting, A.B. and A. Brachmann, 1998. Progress report FY98: Characterization of groundwater colloids from the ER-20-5 well cluster, Isotope Sciences Division, Lawrence Livermore National Laboratory, Livermore, CA.
- Kung, S., 2000. Colloid size and colloid concentration data of groundwater samples from the NTS 04/30/1998 to 10/21/1998. Yucca Mountain Project DTN: LA0002SK831352.004, Yucca Mountain Project, Las Vegas, NV.
- Landolt, H., 1982. Numerical Data and Functional Relationships in Science and Technology, Group V: Geophysics and Space Research, Volume 1, Physical Properties of Rocks. New Series Editor-in-Chief: K.H. Hellwege. Springer-Verlag, New York, 332-333.
- Langmuir, D., 1997. Aqueous environmental geochemistry, Prentice hall, Upper Saddle River, New Jersey, 600p.
- Lemire, R.J., and F. Garisto., 1989. The solubility of U, Np, Pu, Th and Tc in a geological disposal vault for used nuclear fuel. Report ROE 1LO, AECL-1009. Pinawa, Manitoba: Atomic Energy of Canada Ltd., Whiteshell Nuclear Research Establishment.
- Lemire, R.J., and P.R. Tremaine, 1980. Uranium and plutonium equilibria in aqueous solutions to 200°C. *Journal of Chemical Engineering Data*, 25, 361-370.
- Long, J. C. S. and P. A. Witherspoon, 1985. The relationship of the degree of interconnectivity to permeability in fracture networks, *Journal of Geophysical Research*, 90(B4), 3087-3097.
- Lu, G., T.P. Clement, C. Zheng, and T.H. Wiedemeier, 1999. Natural attenuation of BTEX compounds: model development and field-scale application, *Ground Water*, 37(5), 707-717.
- National Research Council, 1996. Rock fracture and fluid flow: contemporary understanding and applications. National academy press, Washington, D.C.

- McKay, L. D., R. W. Gillham, and J. A. Cherry, 1993. Field experiments in a fractured clay till. 2.Solute and colloid transport, *Water Resources Research*, 29(12), 3879-3890.
- Neretnieks, I., T. Eriksen, and P. Tahtinen, 1982. Tracer movement in a single fissure in granitic rock: Some experimental and their interpretation, *Water Resources Research*, 18, 849-858.
- Nitsche, H., K. Roberts, K. Becraft, T. Prussin, D. Keeney, S.A. Carpenter, and D. E. Hobart, 1995. Solubility and speciation results from over- and undersaturation experiments on neptunium, plutonium, and americium in water from Yucca Mountain Region Well UE-25 #1. Report LA-13017-MS, Los Alamos National Laboratory, Los Alamos, NM.
- Okusu, N.M., K. Karasalai, J.C.S. Long, and G. Bodvarsson, 1989. FMMG: a program for discretizing two-dimensional fracture matrix systems. Theory, design, and user's manual. LBL-26 782, Lawrence Berkeley National Laboratory, Berkeley, CA.
- Pawloski, G.A., A.F.B. Tompson, and S.F. Carle (eds.), 2001. Evaluation of the hydrologic source term from underground nuclear tests on Pahute Mesa at the Nevada Test Site: The CHESHIRE test, Technical Report UCRL-ID-147023, Lawrence Livermore National Laboratory, Livermore, CA.
- Press. W.H., B.P. Flannery, S.A. Teukolsky, and W.T. Vetterling, 1986. Numerical recipes: the art of scientific computing, University Press, New York, Cambridge.
- Puigdomenech, I., and J. Bruno, 1991. Plutonium solubilities. Swedish Nuclear Fuel and Waste Mgmt. Co., SKB Tech. Rept. 91-04.
- Reimus P.W., S.D. Ware, N. Lu, A.A. Fattah, K.S. Kunk, and M.P. Neu, 1999. Progress report on colloid transport and colloid-facilitated plutonium transport in fractured rocks from Pahute Mesa, Nevada Test Site, NTS-UGTA progress report, Los Alamos National Laboratory, Los Alamos, NM.
- Reimus P.W., S.D. Ware, N. Lu, A.A. Fattah, K.S. Kunk, and M.P. Neu, 2001. FY2001 Progress report on colloid-facilitated plutonium transport in fractured rocks from Pahute Mesa, Nevada Test Site, NTS-UGTA progress report, Los Alamos National Laboratory, Los Alamos, NM.
- Robinson, B.A., H.S. Viswanathan, and A.J. Valocchi, 1999. Efficient numerical techniques for modeling multicomponent groundwater transport based on simultaneous solution of strongly coupled subsets of chemical components. *Advances in Water Research*, 36, October issue.
- Smith, L., and F. W. Schwartz, 1984. An analysis of the influence of fracture geometry on mass transport in fractured media, *Water Resources Research*, 20(9), 1241-1252.
- Sudicky, E.A., and R.G. McLaren, 1992. The laplace transform galerkin technique for large scale simulation of mass transport in discretely fractured porous formations, *Water Resources Research*, 28(2), 499-514.
- Travis, B.J. and K. H. Birdsell, 1991. TRACER3D: A model of flow and transport in porous media: Model description and users manual, Technical Report LA-11798-MS, Los Alamos National Laboratory, Los Alamos, NM.

Viswanathan, H.S., B.A. Robinson, A.J. Valocchi, and I.R. Triay, 1998. A reactive transport model of neptunium migration from the potential repository at Yucca Mountain, *Journal of Hydrology*, 209, 251-280.

Zheng, C. and G. D. Bennett, 1995. *Applied contaminant transport modeling, Theory and practice*. 440 pp. Van Nostrand Reinhold.

Zimmerman, R. W., and G. S. Bodvarsson, 1996. Hydraulic conductivity of rock fractures, *Transport in Porous Media*, 23, 1-30.

Zyvoloski, G.A., B.A. Robinson, Z.V. Dash and L.T. Trease, 1997. *User's Manual for the FEHM Application, A Finite-Element Heat- and Mass-Transfer Code*, LA-13306-MS, Los Alamos National Laboratory, Los Alamos, NM.

This Page Intentionally Left Blank

Appendix E: Field-Scale Transport in Fractured Rock: The Generalized Dual-Porosity Model (GDPM)

E.1 Generalized Dual-Porosity Model Description

Figure E-1 shows several computational methods designed to handle fracture matrix interactions. A discrete fracture model (DFM), as used in Appendix D allows the fracture and matrix to be explicitly discretized, allowing for user-specified grid resolution in the matrix. This method is accurate and requires that the flow and transport equations be solved for each node, which can be computationally restricting for large problems and impractical for field-scale simulation of flow and transport in fracture networks. In addition, it does not readily extend to represent heterogeneous systems involving flow paths through fractured rock and porous, unfractured material.

Another method is the dual-continuum model, in which the fracture and matrix media are discretized on the same numerical grid via a one-to-one pairing of grid points for each medium. Flow may occur in each continuum, and a coupling term allows transport to occur between the media. Although this method extends readily to heterogeneous two- and three-dimensional problems, sharp concentration or pressure gradients in the matrix cannot be resolved because it is only represented with one node. This is a prohibitive issue for solute transport in fractured systems, in which diffusion into the matrix and perhaps sorption on the bulk rock are important. Furthermore, in saturated, fractured media in which fracture permeabilities are much larger than the matrix permeability, it is not really necessary to compute flow over field-scale distances within the matrix medium because the majority of the flow probably occurs within the fractures.

An efficient alternative to the dual continuum approach is to decouple the matrix nodes from each other, following the assumption that little flow occurs in the matrix relative the fractures. The numerical solution for this system is efficient because the equation set can be decomposed into a series of small one-dimensional systems for the matrix connected to the fracture continuum. However, the resolution in the matrix domain away from the fractures still dominates the accuracy of the method in correctly resolving concentration.

To address some of these problems, we have developed a flexible approach called the Generalized Dual-Porosity Model (GDPM). GDPM is a modular capability invoked within the FEHM flow and transport model. To use GDPM, a numerical grid for FEHM is generated for the system to capture the spatial variability of attributes such as permeability. Each node in the grid represents a segment of the domain that is either fracture or matrix dominated. If the node is fracture dominated, then GDPM matrix nodes of user-specified number and resolution are set. The user may specify different fracture spacing, matrix porosity, and fracture porosity at each node location in the domain or for zones defined by similar properties such as lithology. In the site-scale transport model for BENHAM, welded tuff, lava, fractured zeolitic tuff, and fracture nonwelded tuff are modeled as dual-porosity media in which flow occurs in fractures and diffusion occurs into the matrix within which sorption may also occur. The bedded tuff, nonwelded tuff, and unfractured altered tuff are modeled as matrix-flow-dominated single continua.

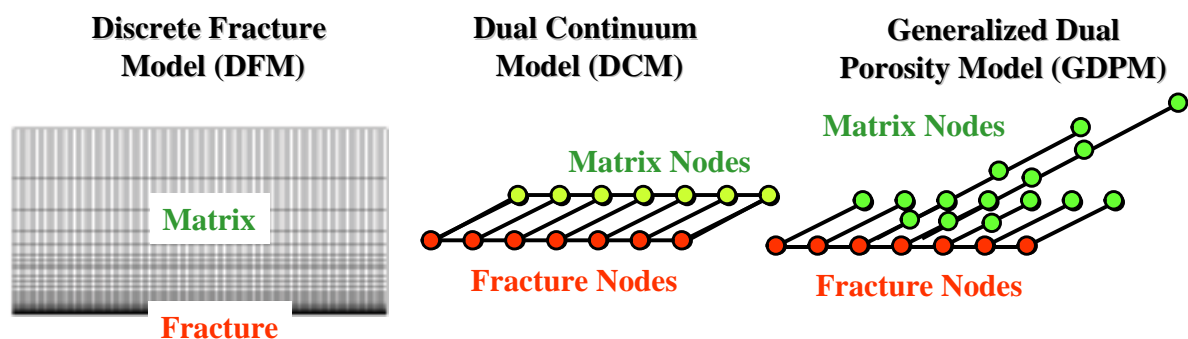


Figure E-1. Schematic representation of a discrete fracture model, a dual-continuum model, and the generalized dual-porosity model.

E.2 Verifying GDPM

E.2.1 One-Dimensional Tests: Diffusion and Reactive Transport

GDPM verification for the present study involves several different test cases in which breakthrough curves are simulated for transport through a one-dimensional, 5000-m-long domain that has a fracture half spacing of 5 m. The steady-state flow rate through the fracture is 0.68 l/day. The fracture volume fraction in the model is 0.0001, the matrix porosity is 0.05, and the diffusion coefficient is $1.5 \times 10^{-12} \text{ m}^2/\text{sec}$. The first problem compares GDPM results in the homogeneous model domain with the analytical solution of Tang et al. (1981) for a nondiffusing tracer, a diffusing tracer, and a diffusing tracer with matrix sorption. The results from the three sets of simulations, shown in Figure E-2, demonstrate that the GDPM solution and the analytical solution for a homogeneous model match almost exactly.

Using the same model, the next set of tests use components A, B, and C to examine some generic simple reactions. The primary reaction tested is $A + B \rightleftharpoons C$. In this reaction, the forward rate, k_f , is 1.0×10^4 (1/hr) and the reverse rate, k_r , is 2.0×10^{-1} (1/hr). A and B are introduced in the column feed solution in equal concentration and C, set initially everywhere at a concentration of 0, is formed in the reaction. In the first case, the reaction is only allowed to occur in the fracture and component A is allowed to diffuse, but components B and C do not diffuse. This test problem is meant to mimic a chemical system of interest in the present study, namely fracture transport with sorption of a diffusing aqueous component (A) to a nondiffusing aqueous colloidal component (B). Because there are no analytical solutions for this problem with reactions, GDPM is compared to a high-resolution discrete fracture simulation. Figure E-3 shows that there is good agreement between the two sets of simulations. In the second reactive transport test, a matrix-sorption reaction is added for component A, where $A(\text{aq}) \rightleftharpoons A(\text{s})$ in the matrix only. Figure E-4 shows nearly identical solutions for GDPM and the discrete fracture model again. In the final test of reactive transport on this system, all three components are involved in sorption reactions in the matrix.

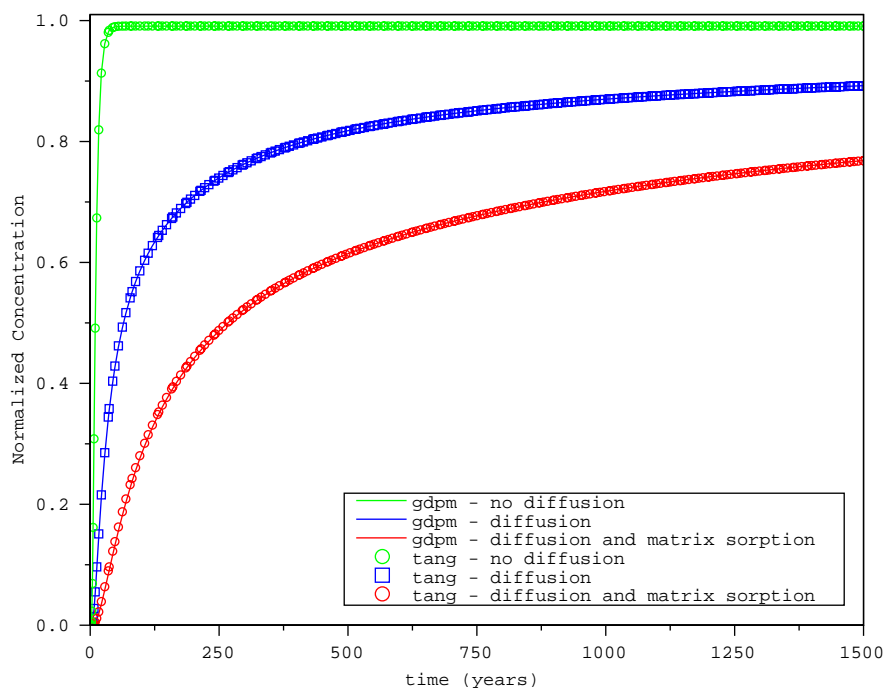


Figure E-2. Test of GDPM method against the analytical solution of Tang et al. (1981)

Figure E-5 shows that the solution between the GDPM and DFM models match very well with this increased complexity. This is not an exhaustive test of different possible reactions. However, this benchmarking analysis does provide confidence by testing the basics before investigating more complex systems with GDPM.

E.2.2 Applying GDPM Along Streamtubes in Three-Dimensional Flow Fields

For the TYBO/BENHAM site-scale transport study, streamtubes generated by the streamline particle-tracking algorithm in FEHM are extracted for reactive transport simulations conducted with GDPM. This process consists of first transforming the streamtubes into one-dimensional grids for simulation with GDPM. And second, the transformed domain is parameterized for simulation with the GDPM option in FEHM. This parameterization involves specifying, for each lithology through which the streamline passes, fracture porosity, matrix porosity, fracture spacing, and all transport parameters related to reactions with fracture and matrix minerals. Figure E-6 provides a schematic of the steps to create one-dimensional GDPM simulations using pathlines in three-dimensional flow fields.

A three-dimensional test block that is $1000 \times 1000 \times 1000 \text{ m}^3$ is used to generate streamtubes to test the GDPM algorithm in homogeneous and heterogeneous media. The first 3-D test involves a homogeneous block with uniform properties. The second 3-D test is a sandwich model in which the center 200 m (normal to flow) has a reduced permeability, and the third 3-D test is a cube model where a $200 \times 200 \times 200 \text{ m}^3$ block on the side of the model has a very low permeability, thereby creating a deviation of flow around the embedded cube.

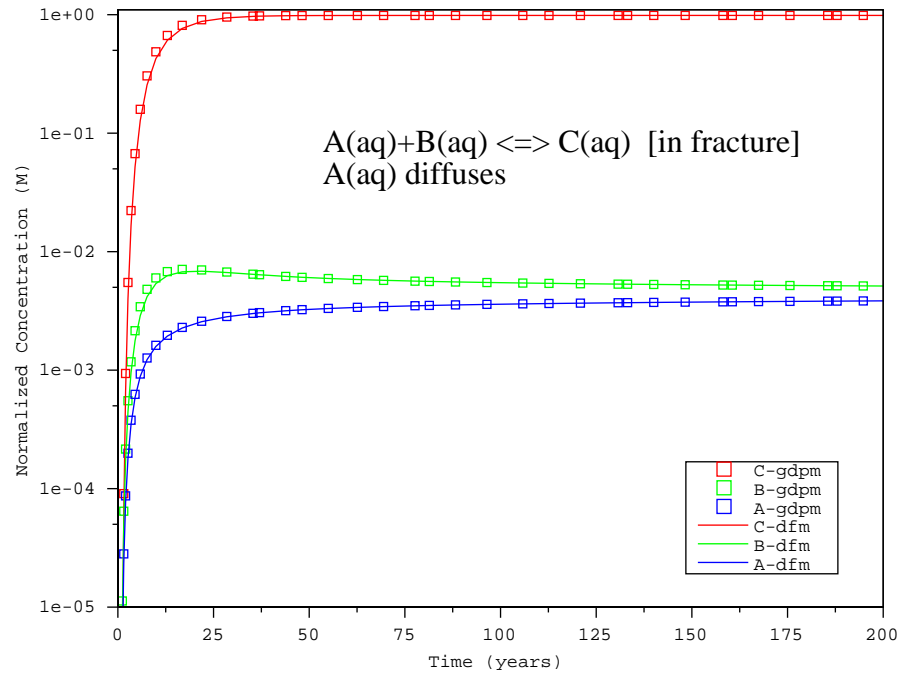


Figure E-3. Comparison of GDPM with a discrete fracture model with a simple reaction in the fracture only. A also diffuses.

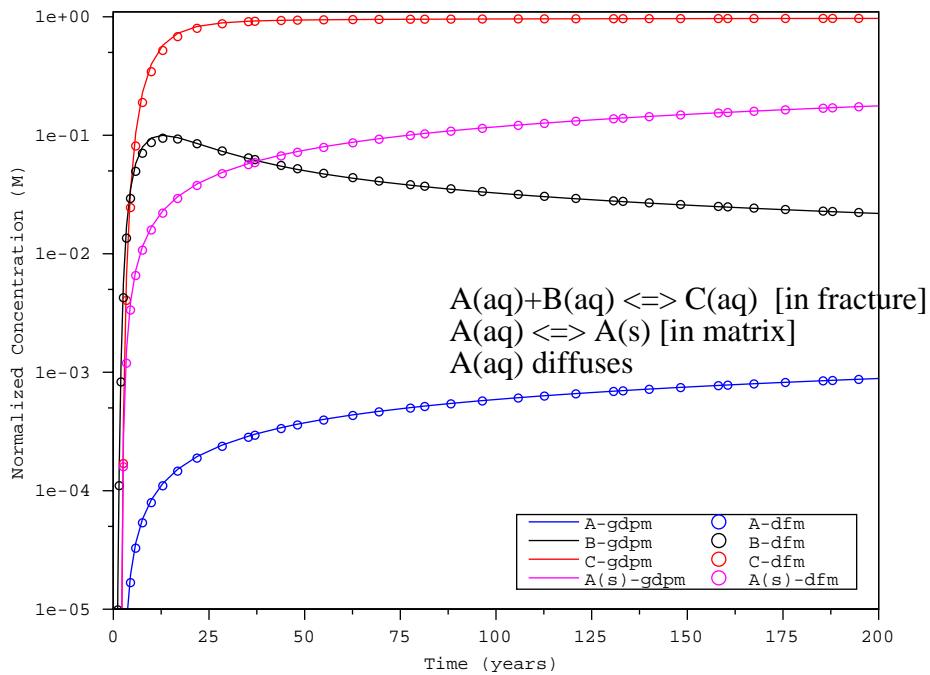


Figure E-4. Comparison of the GDPM model to a discrete fracture model for a test in which only species A diffuses into the matrix and reacts with matrix minerals. B and C do not diffuse or react with immobile minerals.

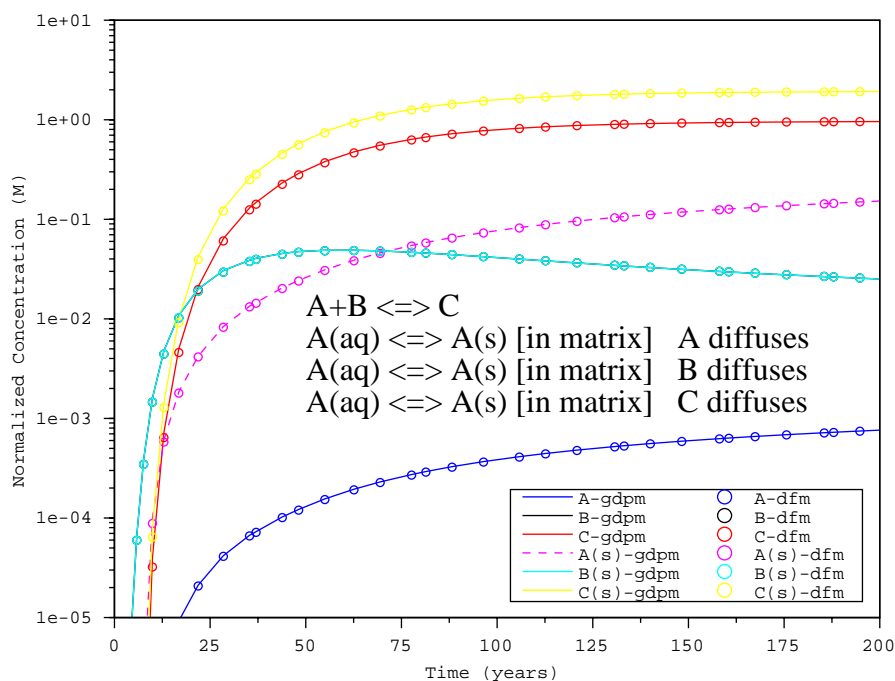


Figure E-5. Comparison of the GDPM model to a discrete fracture model for a test in which all species diffuse into the matrix and react with matrix minerals.

In the first test, a streamtube is created with a single particle in the homogeneous domain. Transport results for a nondiffusing, nonreacting solute computed with GDPM are compared to a single-continuum finite-volume simulation in the three-dimensional flow field with a point source release. Figure E-7 shows that the 50% breakthrough of the single continuum model (SCM) and the one-dimensional GDPM solution match well the travel time of the unretarded particle (denoted as a single point).

For a diffusing tracer, the GDPM results are compared to a semi-analytical solution obtained by releasing 8000 particles for which FEHM simulates diffusion with transfer functions based on the analytical solution of Tang et al. (1981). In the homogenous domain, the GDPM model matches the semi-analytical solution fairly well (Figure E-8). There is a slightly earlier breakthrough with the semi-analytical result because there is less numerical diffusion associated with the particles than with GDPM, but the overall shape and time scales match within 5-10%. These results indicate that the process used for transforming a streamtube into a one-dimensional grid for GDPM analysis works properly for this simple case.

The next case tests the “sandwich model” in which the flow path passes through a low-permeability zone in the center of the model. Figure E-9 shows that the 50% breakthrough points of the single-continuum model (computed in the three-dimensional flow field) and GDPM (computed along a single transformed one-dimensional grid) match the particle travel time reasonably well for a case with no diffusion and no dispersion. The particle breakthrough occurs slightly later than either of the other simulations due to minor interpolation effects at the interfaces between the two different materials in the domain. Increasing the resolution of the grid transformed from the streamtube can reduce this slight error, which highlights a balance between computational

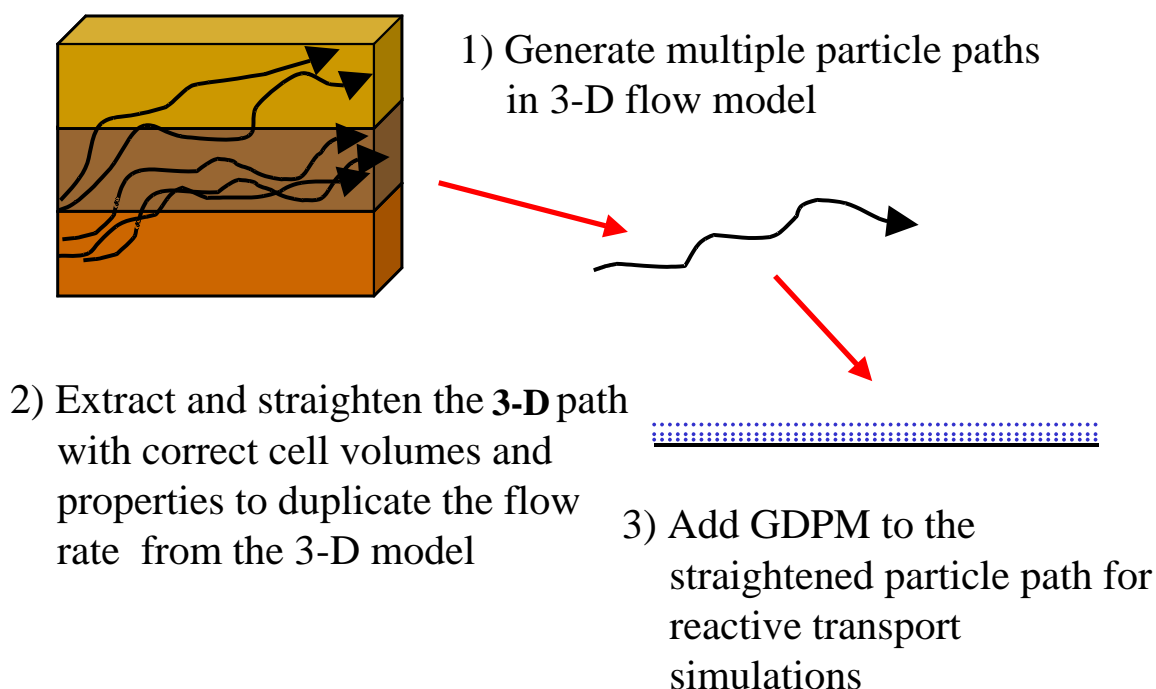


Figure E-6. Schematic of transforming streamtubes in three-dimensional flow field to one-dimensional grids for GDPM simulation.

efficiency and sufficient grid resolution to reduce such interpolation errors. However, the results show that acceptable agreement can be obtained. With matrix diffusion invoked, the GDPM solution and the 8000-diffusing-particle simulation compare well (Figure E-10), indicating that the slight heterogeneity does not adversely impact the model's accuracy.

The final model tested includes a low-permeability cube in the model that forces the flow path to go around the cube. Figure E-11 shows the results for the case with no diffusion. In this case, the particle arrival is slightly earlier than the 50% GDPM breakthrough. However the difference is less than 2%, indicating that issues associated with three-dimensional paths that curve through the flow field are resolved well through the grid transformation process and GDPM simulation.

For the test cases considered, the results comparing dual-porosity particle-tracking simulations, analytical solutions, and discrete fracture simulations with GDPM simulations compare well. In cases for which there are slight discrepancies, the error is always less than 10% and generally less than 5%. These results provide confidence that the streamtube extraction process works well and that GDPM is fully appropriate for simulating complex processes involving fracture-matrix interactions and reactive processes.

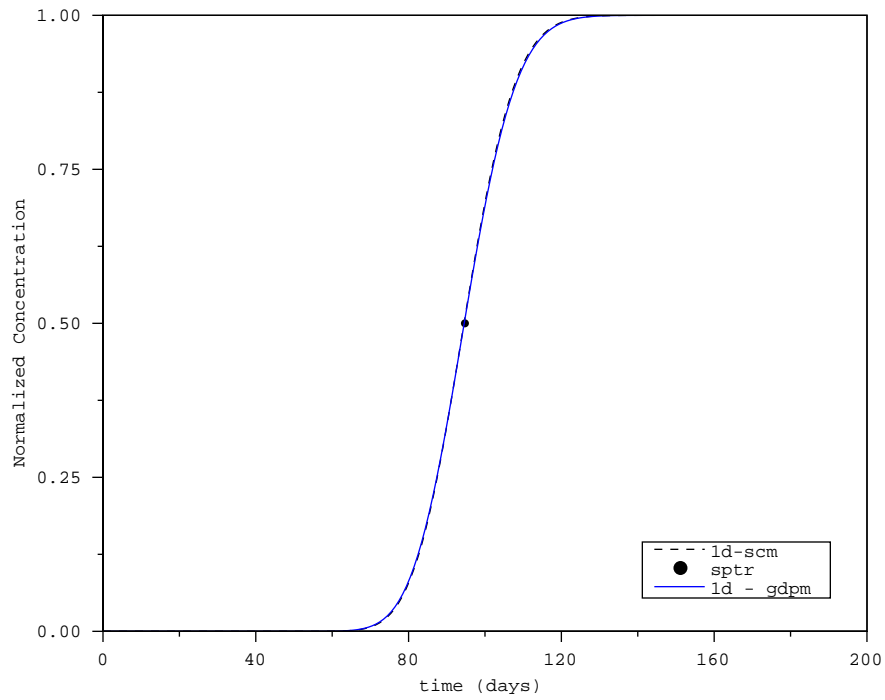


Figure E-7. Comparison of GDPM with the travel time of the particle used to map the GDPM grid (sptr) and a three-dimensional single-continuum model (SCM).

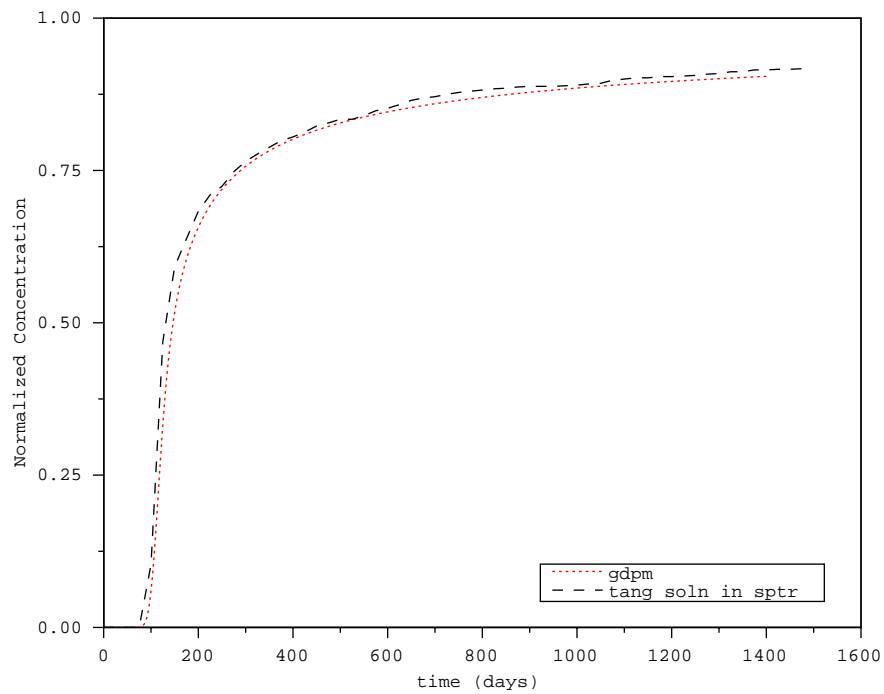


Figure E-8. Comparison of the GDPM solution and the semi-analytical solution obtained using 8000 particles for a homogeneous block with diffusion.

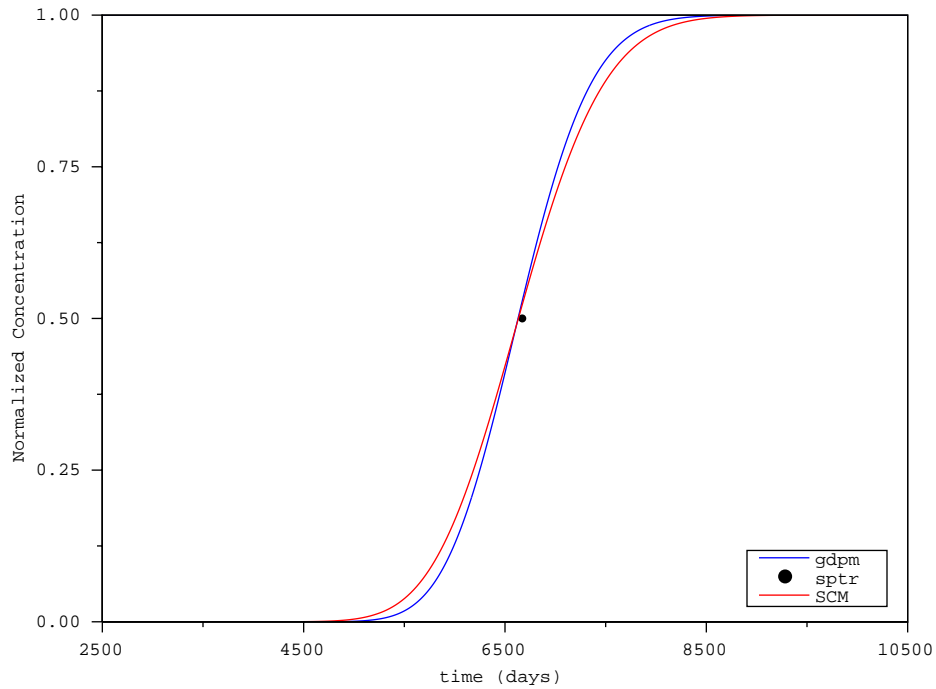


Figure E-9. Comparison of the GDPM solution and the semi-analytical solution obtained using 8000 particles for the sandwich model with no diffusion and no dispersion.

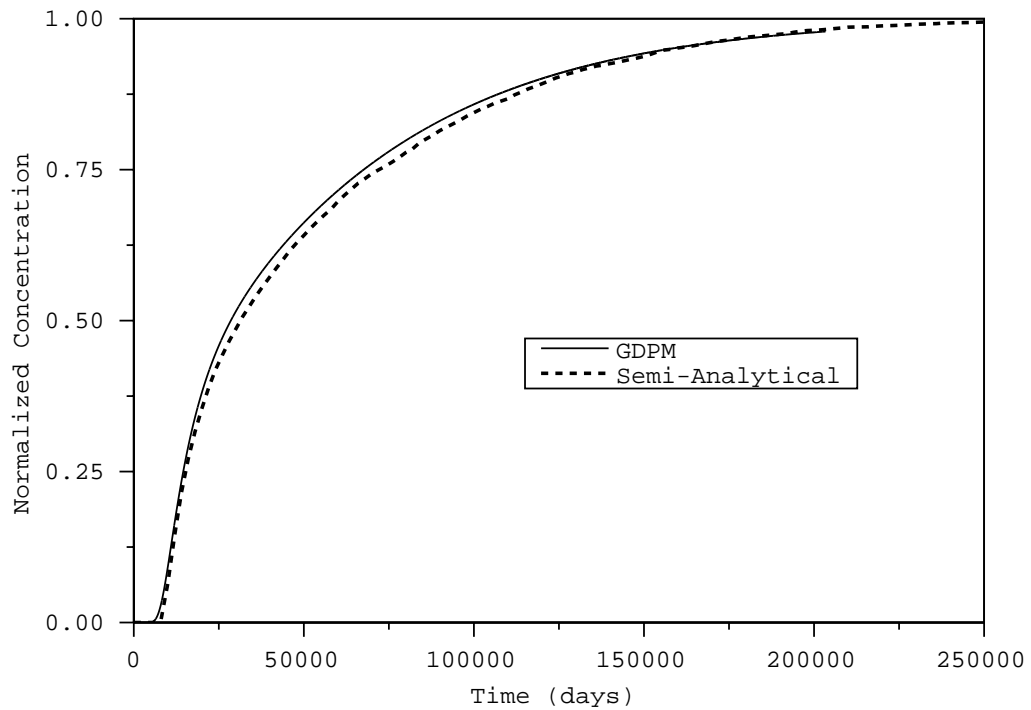


Figure E-10. Comparison of GDPM solution with diffusion in the sandwich model to a semi-analytical solution (Sudicky and Frind, 1982) obtained using 8000 particles.

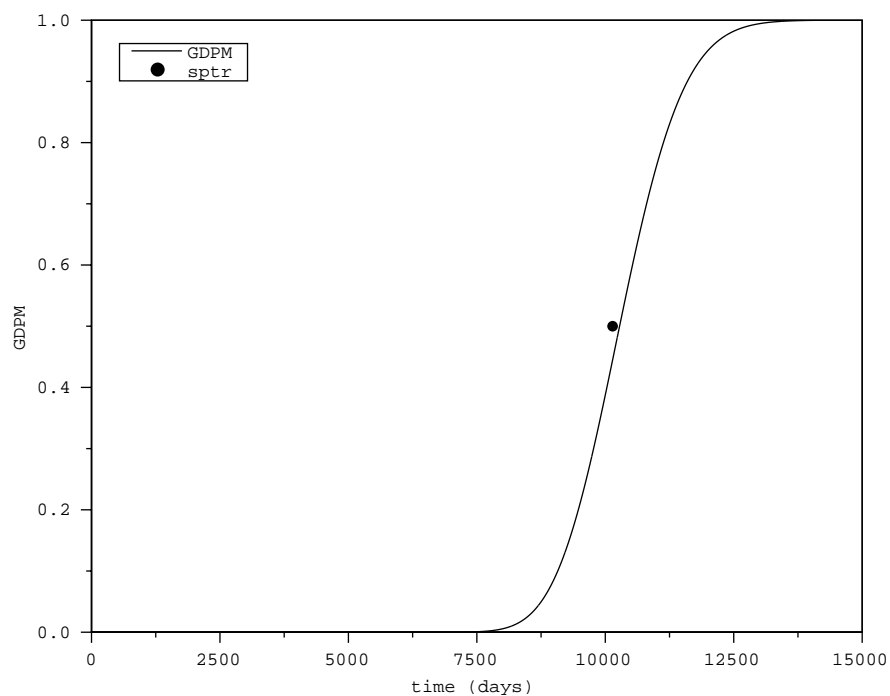


Figure E-11. Comparison of GDPM solution and Tang solution in SPTR for a cube block with no diffusion.

E.3 References

Tang, D.H., Frind, E.O., and Sudicky, E.A., 1981. Contaminant Transport in Fractured Media: Analytical Solution for a Single Fracture, *Water Resources Research*, 17(3), 555–564.

This Page Intentionally Left Blank

Appendix F: Site-Scale Transport Model - Reactive Transport Along Streamlines

F.1 Introduction

In this appendix, the reactive transport model described in Appendix D is extended for application to the three-dimensional site-scale flow and transport domain. The four primary components of the extension are as follows:

- Application along streamtubes within a heterogeneous three-dimensional site-scale flow field.
- Use of the Generalized Dual Porosity Model (GDPM, described in Appendix E) to simulate reactive transport in fractured media.
- Consideration of multiple solutes in addition to the plutonium and colloids considered in Appendix D.
- Use of the time-varying source functions described in Chapter 6.

These extensions are implemented for analysis of contaminant migration from BENHAM to the ER-20-5 observation wells and NTS boundary. Releases from TYBO are considered with the particle-tracking model in Chapter 7. A stepwise procedure for conducting these simulations is described as follows:

1. Develop steady-state flow field on a heterogeneous attribute map.
2. Release a swarm of particles from the source location and map the time of flight along the pathway of each non-reactive, non-diffusing particle until it leaves the simulation domain.
3. Convert each particle pathway through the three-dimensional domain into a high-resolution, one-dimensional, finite-element grid.
4. Simulate reactive, dual-porosity transport for each solute of interest by using GDPM to model fracture-matrix interactions and the source functions from Chapter 6 to model the time-varying source functions from the BENHAM cavity/chimney system in the TSA and LAVA aquifers.
5. Analyze results through examination of mass fluxes across the model boundary and at the observation wells.

F.2 Reactive Transport in Fractured Rock

F.2.1 Generalized Dual-Porosity Model

Reactive transport in fractured rock is simulated along one-dimensional streamtubes using GDPM and FEHM's reactive multispecies transport capabilities. Described in greater detail in Appendix E, GDPM provides an efficient mechanism for capturing diffusion and pressure transients between fracture and matrix material. Conceptually, for every node in a domain representing the fracture continuum, GDPM provides a user-specified number of nodes into the matrix at a user-specified resolution that need not be uniform. Although the discrete fracture model in Appendix D requires two spatial dimensions to represent an experiment with flow in only one-dimension, GDPM provides the capability for one-, two-, and three-dimensional flow systems. Further, even though discrete fracture models are not well equipped to handle heterogeneity in fracture and matrix properties (e.g., varying aperture, coating thickness, mineralogy), GDPM was designed to readily incorporate such variations. This is possible because any node in the model can be populated with unique fracture properties, as can the corresponding matrix nodes associated with that particular fracture node.

F.2.2 Solutes of Interest and Reactive Processes

Because spatial attribute variability must be considered at the site scale. GDPM is used instead of a discrete fracture model to simulate the fundamental processes described in Appendix D. We now also consider tritium (^3H), and isotopes of carbon (^{14}C), chlorine (^{36}Cl), krypton (^{85}Kr), technetium (^{99}Tc), iodine (^{129}I), samarium (^{151}Sm), americium (^{241}Am), strontium (^{90}Sr), cesium (^{137}Cs), uranium ($^{234,235,238}\text{U}$), neptunium (^{237}Np), europium ($^{152, 154}\text{Eu}$), and plutonium ($^{239, 240}\text{Pu}$). This list is a subset of those reported by Pawloski et al. (2001). For these solutes, the following processes are considered when appropriate:

- carbonate speciation,
- complexation and ion exchange with different fracture minerals,
- diffusion between fractures and matrix material,
- sorption to matrix minerals, and
- radioactive decay.

However, certain simplifications and assumptions regarding the list of source RNs must be noted. The separate isotopes of U, Eu, and Pu are not considered individually. Because migration of all isotopes of any element are expected to be controlled by the same physical and chemical processes, only differences in source inventory and radioactive decay rates lead to differences in mass breakthrough at locations of interest. For the purposes of this study, we assume that all U isotopes behave like ^{238}U and lump them together. ^{238}U has the longest half-life of the three device-related U isotopes and accounts for nearly 90% of the U in the radiologic source term (using the unclassified average value for all tests conducted below or within 100 m of the water table in Areas 19 and 20; Smith, 2001). Thus, this assumption leads to slightly conservative estimates in total U mass, although the half-lives of ^{234}U and ^{235}U are also extremely long relative to the 1000-year simulation times used in this study.

To assess actual dose, these isotopes would need to be considered as a post-processing calculation in the ^{238}U BTCs. This assumption also leads to the omission of daughter products caused by U decay, although with the long half-lives of the U isotopes, little decay will occur. On the other hand, ^{241}Pu will decay through ^{241}Am to ^{237}Np , which is far more mobile (quite similar to ^{238}U). However, with less than 0.05 moles of ^{241}Pu in the average source inventory and 2.87 moles of ^{237}Np , the maximum increase in the ^{237}Np would be less than 2%. Therefore, this process is ignored for now. This omission leads to a minor reduction in the modeled Np inventory and a minor increase in conservatism with regard to Pu migration by not considering the process of colloid-facilitated transport of Pu followed by decay to Np. ^{154}Eu is lumped together with ^{152}Eu because they both have short half-lives, they have very small source-term inventories, and they are highly sorptive.

In addition to the expanded list of RNs and their unique transport properties, Pu reactions with colloids and colloid filtration to fracture surfaces are considered. Although colloid reactions with other RNs are likely, only Pu is considered in this study for two reasons. First, the data at the ER-20-5 observation wells indicate that the Pu was measured in the filtered portion of the samples in the presence of colloids, not as an aqueous species. Such association between colloids and the other RNs has not yet been made. And second, following the field observations at ER-20-5, the UGTA Project has conducted substantial laboratory characterization of the colloid-facilitated Pu transport process, thus providing data support for this model. Colloid-facilitated transport of the other RNs found in the ER-20-5 observation wells is treated in Chapter 7 as a fitting process to determine what percent of the released inventory must attach to colloids to yield simulations consistent with the field observations.

F.3 Transport Parameters for Site-Scale Calculations

F.3.1 Data Sources

Several different data sources are integrated in this appendix to develop appropriate transport parameters. Table F-1 lists the types and some of the sources of field and laboratory data.

F.3.2 Process Model Parameter Road Map

The remaining subsections in F.3 describe the various chemical processes considered in this reactive transport model. A summary of these processes is as follows:

- The extension of the model developed in Appendix D requires site-scale simulations in heterogeneous media. The use of GDPM and spatially variable parameters are incorporated into this model - Section F.3.3
- Carbonate speciation for six RNs is considered because the carbonate complexes of these RNs tend to compete with the sorption processes. Carbonate speciation complexity is reduced to a relationship between free-ion and carbonate species concentrations by invoking assumptions of constant pH, eH, and bicarbonate concentrations - Section F.3.4.

Table F-1. Data Sources For Transport Parameters

Type of Data	Study	Reference
Matrix sorption of RNs onto volcanic rocks	YMP	Triay et al. (1997), CRWMS M&O (2000g)
Complexation of RNs with fracture minerals (Mn, Fe, Al/Si, Ca)	UGTA ¹	Pawloski et al. (2001)
Matrix diffusion of RNs	UGTA, YMP	Reimus et al. (2002)
Pu-colloid reaction rates	UGTA, YMP	CRWMS M&O (2000g), Reimus et al. (2001), This study
Colloid filtration	UGTA, YMP	CRWMS M&O (2000g), Reimus et al. (2001)
Colloid size distributions and concentrations	UGTA, YMP	Kung (2000)
Groundwater chemistry (pH, Eh, pCO ₂ , etc.)	UGTA	IT Data Base (IT, 2002)
RN source mass and concentration	UGTA	Smith (2001), This Study ²
Fracture apertures	UGTA	Drellack et al. (1997)
Fracture spacing	UGTA YMP	Drellack et al. (1997) CRWMS M&O (2000f, c)
Fracture coating minerals	UGTA	Reimus et al. (2002) [Appendix A by Benedict and Warren]
<p>Notes:</p> <p>1 - Derivation of equilibrium complexation constants based on field and lab studies from UGTA, YMP, and other projects.</p> <p>2 - Source masses from Smith (2001). This study computes dissolution and mass flux into aquifers (Chapter 6).</p>		

- RN sorption to fracture minerals is considered. These reactions are simplified by assuming constant pH and unvarying surface site concentrations due to the low concentrations of RNs in solution. However, spatially varying mineral surface concentrations are considered for each reactive mineral for each different fractured rock class - Sections F.3.5 and F.3.6.

- Matrix sorption of RNs is primarily based on existing databases in which Kds were determined in batch experiment. Because these experiments were conducted in the presence of carbonate species, we apply a simple correction to simulate only the sorption of the free ion, thereby allowing the inclusion of the carbonate speciation reactions - Section F.3.7.
- Diffusion values are based on a recent UGTA laboratory study (Reimus et al., 2002). The ranges of uncertainty in that study are not very large, relative to some references in the literature - Section F.3.8.
- Fracture properties (including aperture, porosity, and spacing) affect the velocity and diffusion potential of solutes. Little field data exists in which all of these properties are measured explicitly. Therefore, geometric arguments and relationships between the three properties are used to specify model parameters and ranges of uncertainty - Section F.3.9.
- Pu-colloid reactions, already described Appendix D, are modeled with a kinetic formulation. In addition to UGTA data and our model fit to column data, additional studies from YMP are included in the development of rate ranges - Section F.3.10.

F.3.3 Transport Parameters in Heterogeneous Domains

Many transport parameters discussed in the next several sections vary spatially and depend on the lithologic rock class. Chapter 5 introduced the attributes associated with the heterogeneous flow systems used for these site-scale transport simulations. Distributed heterogeneously throughout the domain are seven different lithologic classes, including (1) bedded tuff, (2) nonwelded tuff, (3) fractured welded tuff, (4) fractured lava, (5) fractured altered tuff, (6) non-fractured altered tuff, and (7) fractured non-welded tuff. We assign different transport parameters to each different lithologic class. Therefore, in many of the parameter tables, ranges of uncertainty are presented for each different lithologic class. During the simulations, these parameters are distributed appropriately among the different lithologic classes. At present, heterogeneity in transport parameters within the lithologic classes is not specified due to lack of information from which such spatial variability could be modeled. However, significant heterogeneity in transport parameters is represented in these models due to the heterogeneity in the lithologic class maps that were generated by DRI.

F.3.4 Aqueous System Chemistry: Carbonate Speciation

Reactions and Speciation Diagrams

Six of the RNs considered in this study are susceptible to carbonate speciation reactions. These are particularly significant processes because the carbonate species of the RNs do not tend to participate in sorption reactions with surface minerals, with the exception of those involving surface calcium sites, $>Ca^{2+}$. Therefore, carbonate speciation serves as a competitive process that keeps RNs mobile, acting against the retarding processes of sorption with surface minerals in the fractures and in the matrix.

Pu speciation is discussed in Appendix D. Table F-2 presents the carbonate speciation reactions considered for the remaining RNs affected by this process. Figures F-1 through F-6 show speciation diagrams for the RNs under redox conditions of $eH = 550$ mV. Note that Figure F-7 shows the impact that variation in redox condition plays on carbonate speciation, thus significantly affecting the distribution between sorptive and nonsorptive aqueous species for the RN.

Based on limited data, it is believed that the upper aquifer in the Pahute Mesa area has an oxidized eH approximately 550 mV. Although there are no reported *in situ* water measurements indicating lower Eh values, thin section analyses from Warren (2000) identified pyrite, a reduced form of iron, in the matrix at depths similar to the deeper observation well, ER-20-5 #3. This indicates that the lower aquifer has experienced reduced conditions in the past, which in turn could indicate that relative to the upper aquifer the water is more reduced, but this has not been verified. For comparison, in their CHESHIRE study Pawloski et al. (2001) assume an oxygen fugacity of 10^{-7} , equivalent to an Eh of approximately 615 mV. Their slightly more oxidizing conditions may be reflective of the shallower groundwater system at CHESHIRE compared to BENHAM. However, this parameter remains uncertain until direct measurements are made, a process currently underway in the UGTA project.

Simplifying Assumptions

A complete hydrochemical transport model of RN migration would include each of the reactions in Table F-2, as well as all of the sorption reactions discussed later in this appendix. However, certain simplifications are available when considering which processes govern RN mobility and reactivity and which parameters remain constant for the simulation scale under consideration.

The first assumption is that pH remains constant. Away from the source region there are no data to suggest that pH varies along the flow paths under consideration caused by natural geochemical processes. Therefore, the only mechanisms to cause pH variations are associated with source releases. These mechanisms include thermal effects and reactions between source release solutes and surface minerals. Although there is a thermal pulse associated with the source regions (Appendix B and Chapter 6), our simulations indicate that this thermal pulse does not persist a significant distance into the aquifers in which site-scale transport will occur. Likewise, there are no data to indicate such a thermal plume either, other than the one-degree anomaly in UE-20n #1 near CHESHIRE reported by Pawloski et al. (2001). pH changes caused by reactions between source-release RNs and surface minerals are also expected to be minor because of the low RN concentrations.

The second assumption is that the redox conditions remain constant. If temporal or spatial variations in Eh were to occur, then the distribution between free-ion and neutral species could be significantly affected, impacting sorption parameters (e.g., Figure F-7). As part of the sensitivity study presented later, an Eh of 350 mV is considered in the lava due to indications of reducing conditions at a depth based on observations of Warren (2000). Finally, the bicarbonate concentration in groundwater is assumed to remain constant.

With these assumptions, the unknowns in Table F-2 reduce down to the free-ion concentrations and the other species (primarily carbonate species) concentrations. Using the equations and the assumptions stated above (or simply using Figures F-1 through F-6), the ratio of free ion to all other species can be computed for $pH = 8.6$. This ratio constitutes a pseudo speciation

coefficient that can be used to calculate the free-ion and other species concentrations during a dynamic transport simulation. Table F-3 shows these coefficients for each RN that undergoes carbonate speciation. Also shown is the coefficient for Pu when more reducing conditions are prevalent.

Table F-2. Carbonate Speciation

Reaction	Log K
$\text{Sm}^{3+} + 2\text{HCO}_3^- = \text{Sm}(\text{CO}_3)_2^- + 2\text{H}^+$	log K = 7.8576
$\text{Sm}^{3+} + \text{HCO}_3^- = \text{SmCO}_3^+ + \text{H}^+$	log K = 2.4790
$\text{Am}^{3+} + 2\text{HCO}_3^- = \text{Am}(\text{CO}_3)_2^- + 2\text{H}^+$	log K = 8.3868
$\text{Am}^{3+} + \text{HCO}_3^- = \text{AmCO}_3^+ + \text{H}^+$	log K = 2.5434
$\text{Am}^{3+} + 2\text{H}_2\text{O} = \text{Am}(\text{OH})_2^+ + 2\text{H}^+$	log K = 14.1145
$\text{Am}^{3+} + \text{H}_2\text{O} = \text{AmOH}^{2+} + \text{H}^+$	log K = 6.4072
$\text{Eu}^{3+} + 2\text{HCO}_3^- = \text{Eu}(\text{CO}_3)_2^- + 2\text{H}^+$	log K = 7.6676
$\text{Eu}^{3+} + \text{HCO}_3^- = \text{EuCO}_3^+ + \text{H}^+$	log K = 2.3688
$\text{Eu}^{3+} + 2\text{H}_2\text{O} = \text{Eu}(\text{OH})_2^+ + 2\text{H}^+$	log K = 14.8609
$\text{NpO}_2^+ + \text{HCO}_3^- = \text{NpO}_2\text{CO}_3^- + \text{H}^+$	log K = 5.7288
$\text{NpO}_2^+ + \text{H}_2\text{O} = \text{NpO}_2\text{OH}_{(\text{aq})} + \text{H}^+$	log K = 8.9000
$\text{UO}_2^{+2} + 2\text{HCO}_3^- = \text{UO}_2(\text{CO}_3)_2^{-2} + 2\text{H}^+$	log K = 3.7577
$\text{UO}_2^{+2} + 3\text{HCO}_3^- = \text{UO}_2(\text{CO}_3)_3^{-4} + 3\text{H}^+$	log K = 9.4411
$\text{UO}_2^{+2} + \text{H}_2\text{O} = \text{UO}_{3(\text{aq})} + 2\text{H}^+$	log K = 10.3117

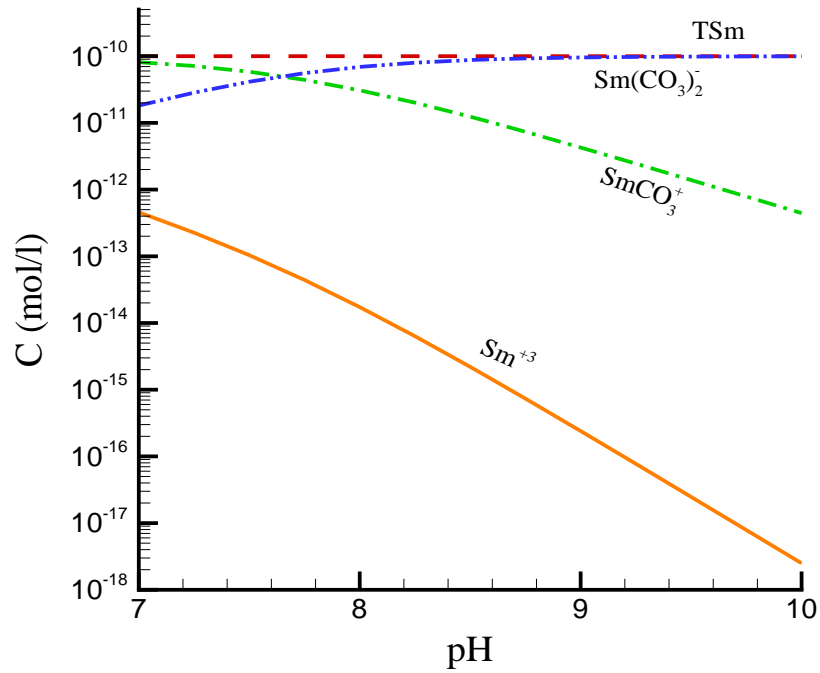


Figure F-1. Samarium speciation diagram for $E_h = 550$ mV and $[\text{HCO}_3^-] = 2.27\text{e-}3$

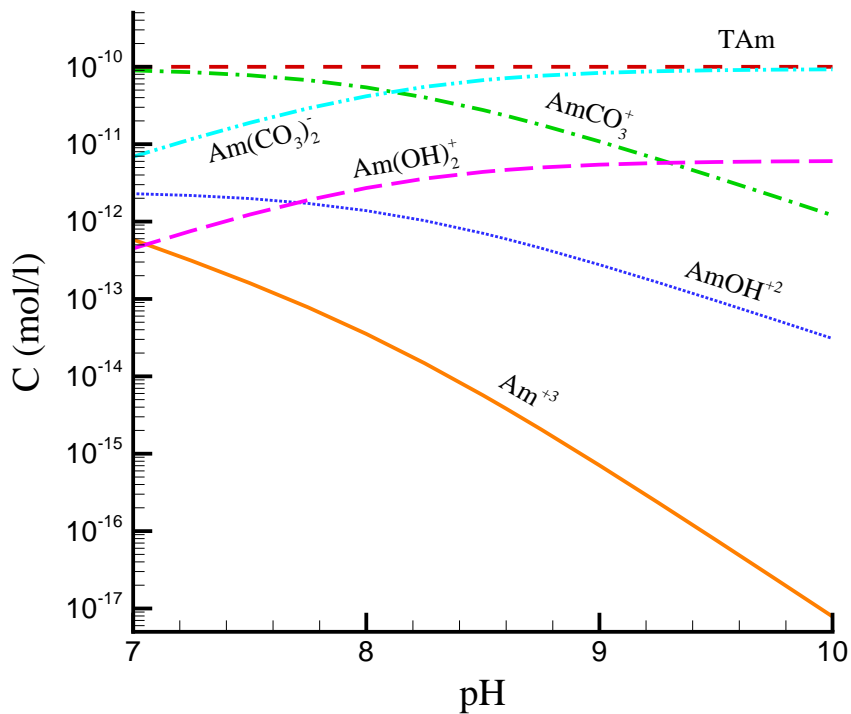


Figure F-2. Americium speciation diagram for $E_h = 550$ mV and $[\text{HCO}_3^-] = 2.27\text{e-}3$.

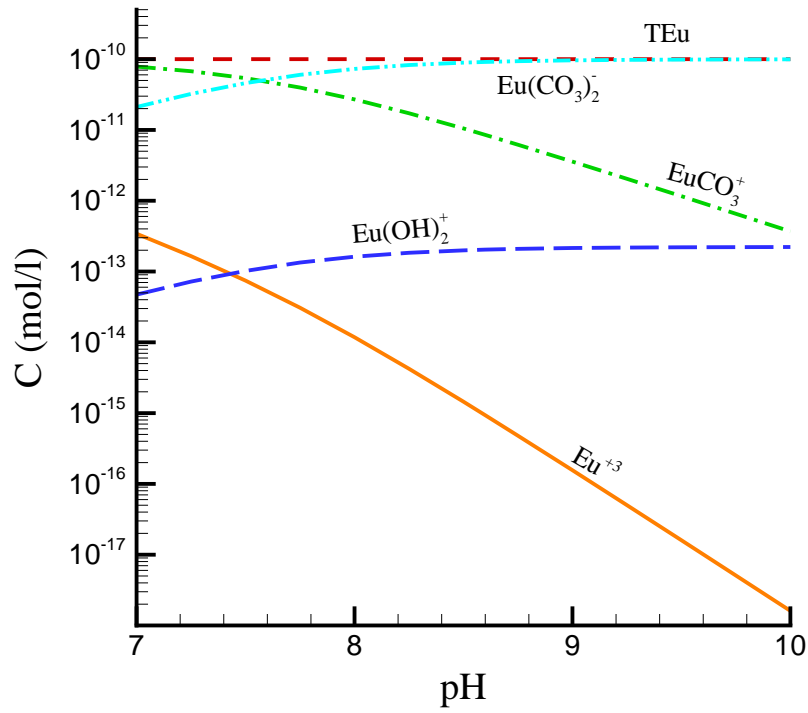


Figure F-3. Europium speciation diagram for Eh = 550 mV and $[\text{HCO}_3^-] = 2.27\text{e-}3$.

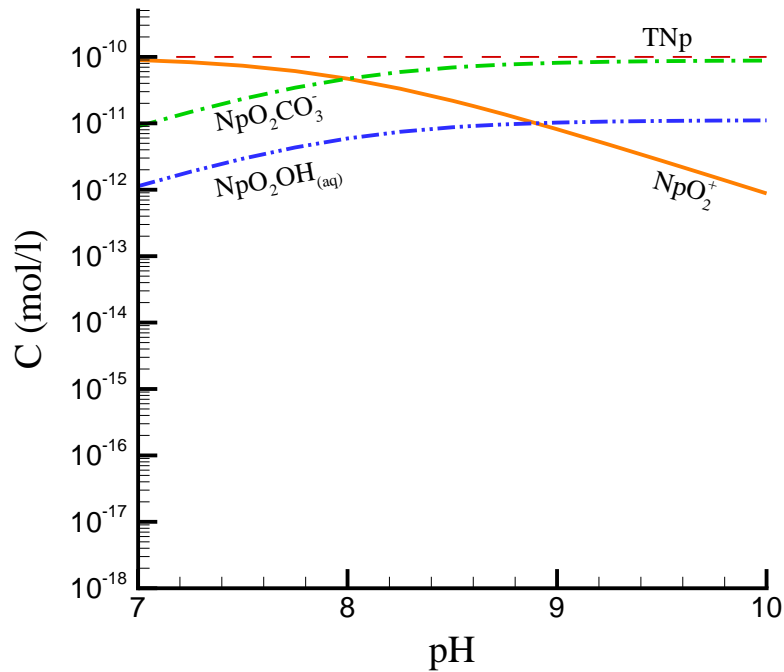


Figure F-4. Neptunium speciation diagram for Eh = 550 mV and $[\text{HCO}_3^-] = 2.27\text{e-}3$.

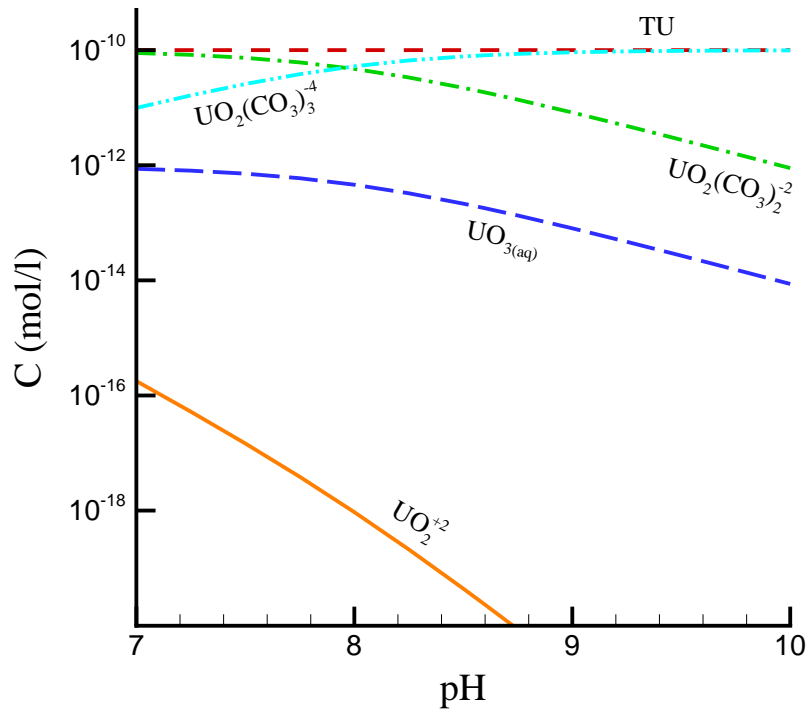


Figure F-5. Uranium speciation diagram for $Eh = 550$ mV and $[HCO_3^-] = 2.27 \times 10^{-3}$.

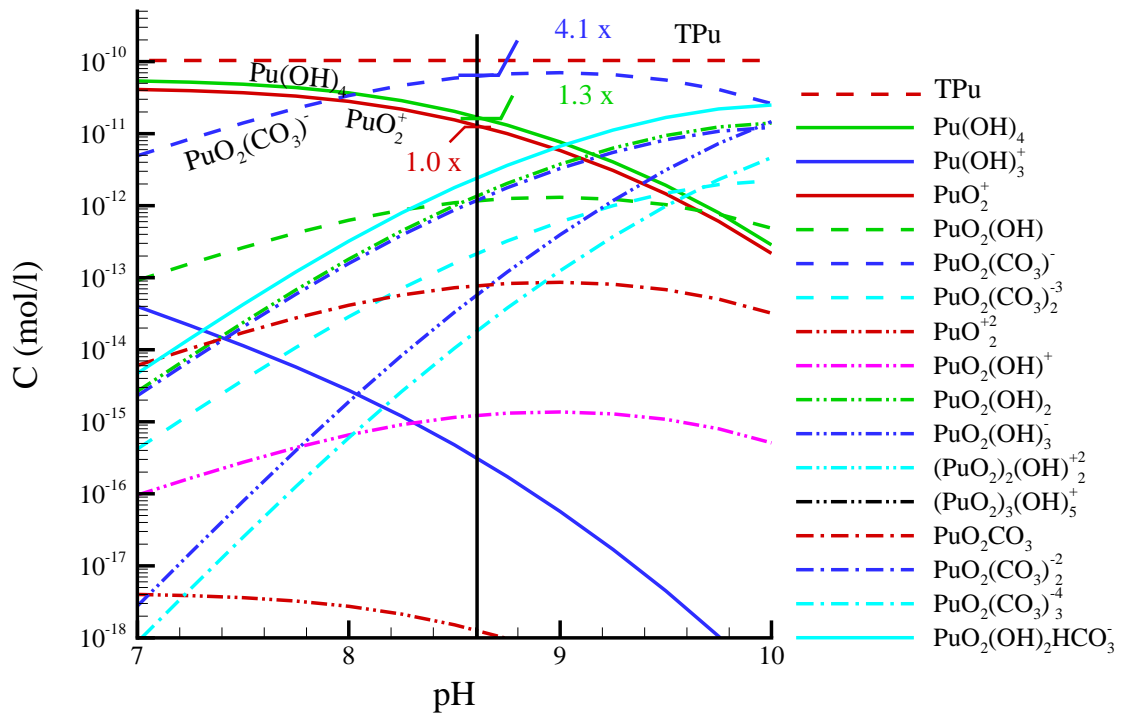


Figure F-6. Plutonium speciation diagram for $Eh = 550$ mV and $[HCO_3^-] = 2.27 \times 10^{-3}$.

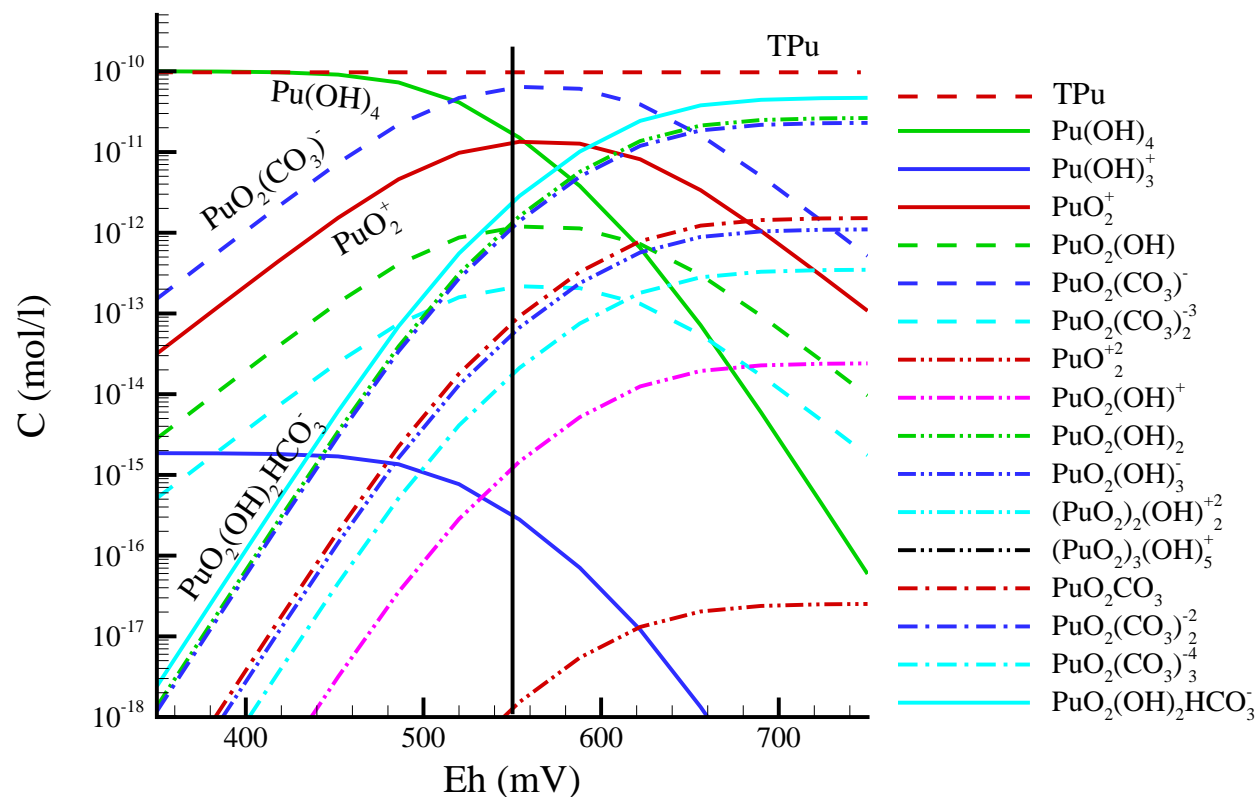


Figure F-7. Plutonium speciation diagram for pH = 8.6 and $[\text{HCO}_3^-] = 2.27\text{e-}3$.

Table F-3. Pseudo Carbonate Speciation Coefficients

pH=8.6, Eh=550 mV, and $[\text{HCO}_3^-] = 2.27\text{e-}3$

Element	Pseudo Speciation Coefficient ([all neutral species]/[free ion])
Sm	7.03e+4
Am	2.48e+4
Eu	1.07e+5
Sr	NA
U	4.33e+9
Np	3.99
Pu ¹	5.44
1 - Note: at Eh = 350mV, the pseudo speciation coefficient for Pu becomes 3144.	

F.3.5 Sorption in Fractures

For each RN, surface complexation with reactive sites in fracture minerals (including $>FeOH$, $>Ca^{2+}$, $>AlOH$, $>SiOH$, and $>MnOx$) may serve to retard migration as well as inhibit diffusion into the matrix material. In Section D.3.5, the model parameters for Pu reactions with fracture mineral sites were developed. In this section, they are extended to all reactive RNs of interest. Moreover, uncertainty in the parameters used to compute the equilibrium constants is considered.

For each RN, we assume that the cation form is the reactive species for complexation with fracture-coating minerals. Pawloski et al. (2001) provided tables of equilibrium coefficients for surface complexation of many RNs of interest with specific fracture mineral sites. Pawloski et al. (2001) also provide ion-exchange coefficients for Sr^{2+} , Cs^+ , and UO_2^{2+} . No data are available for reactions with manganese oxides ($MnOx$) so these mineral sites are lumped with iron hydroxides, yielding a class of mineral sites, $>FeOH/MnOx$, referred to from here on as $>FeOH$.

Estimation of fracture-mineral sorption-site concentration

Although the equilibrium coefficients for the individual reactions enable detailed representation of the sorption process, the uncertainty in fracture mineral composition, distributions, abundance, and accessibility to solutes flowing in fractures dominates the variability in calculations of this nature. At each location in the model domain, the concentration of available surface complexation sites is necessary to simulate these reactions. In Section D.3, we developed a model to calculate the concentration of each type of fracture mineral site. The following paragraph repeats the derivation of Equation D-36 for continuity with the remainder of this section.

This model estimates the surface mineral sorption sites, ω_m (mole sites/l), on the fracture mineral surfaces as related to the specific surface site density η [sites/nm²] of the medium by the relation:

$$\omega_m = (\eta A_s \rho / A_v) F_i, \quad (\text{Eq. F-1})$$

where A_s (m²/kg) is the specific sorptive surface area of fracture-lining minerals, ρ is the mineral density [g/dm³], F_i is the volume fraction of mineral i (e.g., $>FeOH$), and A_v is Avogadro's number, 6.022×10^{23} sites/mole sites, and η is the reactive site density. In these calculations, $A_s = 1$ m²/g (see Section D.3.5, White et al., 1996) and $\rho = 2650$ g/dm³. For $\eta = 2.31$ sites/nm² (a parameter that varies for fracture mineral site types), the resulting sorption site concentration $\omega_m = 0.01 F_i$. And, the available reactive site concentration (i) in the fracture can be approximated by the following equation:

$$F_i = P_{exp}\% \times P_{cov}\% \times P_{min}\% (d \times l) / (l \times b/2), \quad (\text{Eq. F-2})$$

which simplifies to

$$F_i = P_{exp}\% \times P_{cov}\% \times P_{min}\% \times 2(d/b), \quad (\text{Eq. F-3})$$

where d is the thickness of the secondary fracture-lining mineral, $b/2$ is half fracture aperture, l is the unit length of the fracture, $P_{exp}\%$ is the percentage of the mineral mass exposed to the aqueous phase, $P_{cov}\%$ is the percentage of the fracture surface covered by mineral lining, and $P_{min}\%$ is the

proportion of mineral i in the coating. The simplification in Equation F-3 is noted because the ratio of the mineral thickness (d) to the aperture (b) is considered as a single parameter affecting the mineral volume fraction.

Each term in Equation F-3 introduces uncertainty into the estimate of reactive sorption site concentrations. Further, for each different rock class in the heterogeneous domain, the distributions of the minerals are expected to be different. One of the uncertainties in estimating these sorption site concentrations is the mineralogic makeup of the fracture coatings. Therefore Tables F-4 to F-7 show the parameters used to compute the surface site concentrations for the four different fracture mineral site types considered in the four different fractured rock classes considered (the other three classes are treated as unfractured porous media). The fundamental distinguishing difference between welded tuff, lava, altered tuff, and fractured non-welded tuff in this portion of the analysis is the mineralogic composition of the fracture coatings. The differences, as derived from Reimus et al. (2002), are highlighted in column 4 of tables that follow. In addition to the base-case parameters, a “high” set and a “low” set are provided. The high and low terms are representative of the uncertainty in mineralogic composition of the fracture coatings. Although the base-case parameters are the expected values, the high set favors the more reactive $>FeOH$ and $>MnOx$ minerals, whereas the low set favors the aluminosilicates. Although these compositions ($P_{min}\%$) are not absolute, they demonstrate the impact uncertainty in mineralogic composition has on surface site concentration estimates.

The other uncertain parameters that are held constant provide significant additional uncertainty in estimates of ω_m . There are currently no available data with which to bound the percent exposed parameter $P_{exp}\%$ or the percent coverage parameter $P_{cov}\%$. However, as ω_m is a linear function of both of them, uncertainty in either can be dealt with as a lumped parameter. Namely, changes in the product of the two represents uncertainty in either parameter. Similarly, there are very little data correlating mineral coating thickness with aperture (affecting the term, $d/(b/2)$ in Equation F-3). However, following the sensitivity analysis that deals primarily with uncertainty in mineral composition, a study is presented in Section F.3.6 that examines the sensitivity to less constrained $P_{exp}\%$ and $P_{cov}\%$ parameters.

Table F-4. Surface Mineral Sorption Sites: Welded Tuff

Fracture Mineral	P _{exp} %	P _{cov} %	P _{min} %	d (mm)	b/2 (mm)	F _i	ω _{base}	η	As	ω _m
Welded Tuff Base										
>FeOH	0.1	0.5	0.22	0.01	0.1	2.2E-3	2.2E-5	13.5	1.8	2.31E-05
>Ca	0.1	0.5	0	0.01	0.1	0.0E+0	0.0E+0	2.31	10	0.0E+00
>SiOH	0.1	0.5	0.7	0.01	0.1	7.0E-3	7.0E-5	7.8	0.14	3.31E-06
>AlOH	0.1	0.5	0.07	0.01	0.1	7.0E-4	7.0E-6	2.35	10	7.12E-06
Welded Tuff High										
>FeOH	0.1	0.5	0.65	0.01	0.1	6.5E-3	6.5E-5	13.5	1.8	6.84E-05
>Ca	0.1	0.5	0.12	0.01	0.1	1.2E-3	1.2E-5	2.31	10	1.20E-05
>SiOH	0.1	0.5	0.08	0.01	0.1	8.0E-4	8.0E-6	7.8	0.14	3.78E-07
>AlOH	0.1	0.5	0.15	0.01	0.1	1.5E-3	1.5E-5	2.35	10	1.53E-05
Welded Tuff Low										
>FeOH	0.1	0.5	0.03	0.01	0.1	3.0E-4	3.0E-6	13.5	1.8	3.16E-06
>Ca	0.1	0.5	0	0.01	0.1	0.0E+0	0.0E+0	2.31	10	0.0E+00
>SiOH	0.1	0.5	0.9	0.01	0.1	9.0E-3	9.0E-5	7.8	0.14	4.25E-06
>AlOH	0.1	0.5	0.07	0.01	0.1	7.0E-4	7.0E-6	2.35	10	7.12E-06
Mineral sorption site percentages derived from Reimus et al. (2002). Other parameters are estimated as described in text.										

Table F-5. Surface Mineral Sorption Sites: Nonwelded Tuff

Fracture Mineral	P _{exp} %	P _{cov} %	P _{min} %	d	b/2	Fi	ω _{base}	η	As	ω _m
Nonwelded Tuff Base										
>FeOH	0.1	0.5	0.14	0.01	0.1	1.4E-3	1.4E-5	13.5	1.8	1.47E-05
>Ca	0.1	0.5	0.09	0.01	0.1	9.0E-4	9.0E-6	2.31	10	9.00E-06
>SiOH	0.1	0.5	0.37	0.01	0.1	3.7E-3	3.7E-5	7.8	0.14	1.75E-06
>AlOH	0.1	0.5	0.4	0.01	0.1	4.0E-3	4.0E-5	2.35	10	4.07E-05
Nonwelded Tuff High										
>FeOH	0.1	0.5	0.2	0.01	0.1	2.0E-3	2.0E-5	13.5	1.8	2.10E-05
>Ca	0.1	0.5	0.48	0.01	0.1	4.8E-3	4.8E-5	2.31	10	4.80E-05
>SiOH	0.1	0.5	0.24	0.01	0.1	2.4E-3	2.4E-5	7.8	0.14	1.13E-06
>AlOH	0.1	0.5	0.08	0.01	0.1	8.0E-4	8.0E-6	2.35	10	8.14E-06
Nonwelded Tuff Low										
>FeOH	0.1	0.5	0.12	0.01	0.1	1.2E-3	1.2E-5	13.5	1.8	1.26E-05
>Ca	0.1	0.5	0.09	0.01	0.1	9.0E-4	9.0E-6	2.31	10	9.00E-06
>SiOH	0.1	0.5	0.37	0.01	0.1	3.7E-3	3.7E-5	7.8	0.14	1.75E-06
>AlOH	0.1	0.5	0.42	0.01	0.1	4.2E-3	4.2E-5	2.35	10	4.27E-05
Mineral sorption site percentages derived from Reimus et al. (2002). Other parameters are estimated as described in text.										

Table F-6. Surface Mineral Sorption Sites: Lava

Fracture Mineral	P _{exp} %	P _{cov} %	P _{min} %	d	b/2	Fi	ω _{base}	η	As	ω _m
				Lava Base						
>FeOH	0.1	0.5	0.12	0.01	0.1	1.2E-3	1.2E-5	13.5	1.8	1.26E-05
>Ca	0.1	0.5	0.42	0.01	0.1	4.2E-3	4.2E-5	2.31	10	4.20E-05
>SiOH	0.1	0.5	0	0.01	0.1	0.0E+0	0.0E+0	7.8	0.14	0.0E+00
>AlOH	0.1	0.5	0.45	0.01	0.1	4.5E-3	4.5E-5	2.35	10	4.58E-05
				Lava High						
>FeOH	0.1	0.5	0.17	0.01	0.1	1.7E-3	1.7E-5	13.5	1.8	1.79E-05
>Ca	0.1	0.5	0.38	0.01	0.1	3.8E-3	3.8E-5	2.31	10	3.80E-05
>SiOH	0.1	0.5	0.35	0.01	0.1	3.5E-3	3.5E-5	7.8	0.14	1.65E-06
>AlOH	0.1	0.5	0.1	0.01	0.1	1.0E-3	1.0E-5	2.35	10	1.02E-05
				Lava Low						
>FeOH	0.1	0.5	0.1	0.01	0.1	1.0E-3	1.0E-5	13.5	1.8	1.05E-05
>Ca	0.1	0.5	0.42	0.01	0.1	4.2E-3	4.2E-5	2.31	10	4.20E-05
>SiOH	0.1	0.5	0	0.01	0.1	0.0E+0	0.0E+0	7.8	0.14	0.0E+00
>AlOH	0.1	0.5	0.48	0.01	0.1	4.8E-3	4.8E-5	2.35	10	4.88E-05

Mineral sorption site percentages derived from Reimus et al. (2002). Other parameters are estimated as described in text.

Table F-7. Surface Mineral Sorption Sites: Zeolite

Fracture Mineral	P _{exp} %	P _{cov} %	P _{min} %	d	b/2	F _i	ω _{base}	η	As	ω _m
Zeolite Base										
>FeOH	0.1	0.5	0	0.01	0.1	0.0E+0	0.0E+0	13.5	1.8	0.0E+00
>Ca	0.1	0.5	0.5	0.01	0.1	5.0E-3	5.0E-5	2.31	10	5.00E-05
>SiOH	0.1	0.5	0.5	0.01	0.1	5.0E-3	5.0E-5	7.8	0.14	2.36E-06
>AlOH	0.1	0.5	0	0.01	0.1	0.0E+0	0.0E+0	2.35	10	0.0E+00
Zeolite High										
>FeOH	0.1	0.5	0	0.01	0.1	0.0E+0	0.0E+0	13.5	1.8	0.0E+00
>Ca	0.1	0.5	1	0.01	0.1	1.0E-2	1.0E-4	2.31	10	1.00E-04
>SiOH	0.1	0.5	0	0.01	0.1	0.0E+0	0.0E+0	7.8	0.14	0.0E+00
>AlOH	0.1	0.5	0	0.01	0.1	0.0E+0	0.0E+0	2.35	10	0.0E+00
Zeolite Low										
>FeOH	0.1	0.5	0	0.01	0.1	0.0E+0	0.0E+0	13.5	1.8	0.0E+00
>Ca	0.1	0.5	0	0.01	0.1	0.0E+0	0.0E+0	2.31	10	0.0E+00
>SiOH	0.1	0.5	1	0.01	0.1	1.0E-2	1.0E-4	7.8	0.14	4.73E-06
>AlOH	0.1	0.5	0	0.01	0.1	0.0E+0	0.0E+0	2.35	10	0.0E+00
Mineral sorption site percentages derived from Reimus et al. (2002). Other parameters are estimated as described in text.										

Derivation of sorption coefficients for each radionuclide

Once ω_m is estimated for each of the fracture-mineral-site types in each of the rock classes, sorption coefficients are derived for each of the RNs of interest. The derivation uses the surface complexation coefficients provided by Pawloski et al. (2001). Lumped fracture sorption coefficients are derived, as described in Appendix D, based on the assumptions that (1) the concentration of surface sorption sites in fracture coatings far exceeds the aqueous concentrations of the trace RNs, (2) the groundwater chemical composition remains invariant, and (3) that the reactions occur fast enough to be described with equilibrium formulations. Tables F-8 to F-14 show the surface complexation reactions and the corresponding lumped sorption coefficients. Any term that appears in the K_{lump} value, such as pH and the sorption site concentrations for the various fracture minerals, is assumed to be constant. With these lumped equilibrium coefficients, the surface sorption site concentrations (e.g., >FeOH, >Ca, >AlOH, and >SiOH) computed in Tables F-4 to F-7 impact the aqueous concentration of the free and sorbed ions. The Pu reactions and lumped equilibrium coefficients were presented in Section D.3.5.

Table F-8. Plutonium Fracture Mineral Sorption Coefficients

Reaction	Log K	K_{lump}
$> \text{FeOH} + \text{PuO}_2^+ = > \text{FeOHPuO}_2^+$	$\log K = 4.79$	$K_{lump} = K[> \text{FeOH}]$
$> \text{FeOH} + \text{PuO}_2^+ + \text{H}_2\text{O} = > \text{FeOHPuO}_3^- + 2\text{H}^+$	$\log K = -10.66$	$K_{lump} = \frac{K[> \text{FeOH}]}{[\text{H}^+]^2}$
$> \text{Ca}^{+2} + \text{PuO}_2^+ = > \text{PuO}_2^+ + \text{Ca}^{+2}$	$\log K = 1.85$	$K_{lump} = \frac{K[> \text{Ca}^{+2}]}{[\text{Ca}^{+2}]}$
$> \text{AlOH} + \text{PuO}_2^+ = > \text{AlOPuO}_2 + \text{H}^+$	$\log K = -3.09$	$K_{lump} = \frac{K[> \text{AlOH}]}{[\text{H}^+]}$
$> \text{SiOH} + \text{PuO}_2^+ = > \text{SiOPuO}_2 + \text{H}^+$	$\log K = -6.43$	$K_{lump} = \frac{K[> \text{SiOH}]}{[\text{H}^+]}$
$> \text{SiOH} + \text{PuO}_2^+ + \text{H}_2\text{O} = > \text{SiOPuO}_3\text{H}^- + 2\text{H}^+$	$\log K = -14.80$	$K_{lump} = \frac{K[> \text{SiOH}]}{[\text{H}^+]^2}$

Table F-9. Samarium Fracture Mineral Sorption Coefficients

Reaction	Log K	K_{lump}
$> \text{Ca}^{+2} + \text{SmCO}_3^+ = > \text{SmCO}_3^+ + \text{Ca}^{+2}$	$\log K = 2.53$	$K_{lump} = \frac{K[> \text{Ca}^{+2}]}{[\text{Ca}^{+2}]}$

Table F-10. Americium Fracture Mineral Sorption Coefficients

Reaction	Log K	K_{lump}
$> \text{Ca}^{+2} + \text{AmCO}_3^+ = > \text{AmCO}_3^+ + \text{Ca}^{+2}$	$\log K = 4.13$	$K_{\text{lump}} = \frac{K [> \text{Ca}^{+2}]}{[\text{Ca}^{+2}]}$
$> \text{AlOH} + \text{Am}^{+3} = > \text{AlOAm}^{2+} + \text{H}^+$	$\log K = 2.49$	$K_{\text{lump}} = \frac{K [> \text{AlOH}]}{[\text{H}^+]}$
$> \text{SiOH} + \text{Am}^{+3} = > \text{SiOAm}^{2+} + \text{H}^+$	$\log K = 0.7$	$K_{\text{lump}} = \frac{K [> \text{SiOH}]}{[\text{H}^+]}$
$> \text{SiOH} + \text{Am}^{+3} + \text{H}_2\text{O} = > \text{SiOAmO} + 3\text{H}^+$	$\log K = 14.2$	$K_{\text{lump}} = \frac{K [> \text{SiOH}]}{[\text{H}^+]^3}$

Table F-11. Europium Fracture Mineral Sorption Coefficients

Reaction	Log K	K_{lump}
$> \text{FeOH} + \text{Eu}^{+3} = > \text{FeOEu}^{+2} + \text{H}^+$	$\log K = 1.89 \pm 0.69$	$K_{\text{lump}} = \frac{K [> \text{FeOH}]}{[\text{H}^+]}$
$> \text{FeOH} + \text{Eu}^{+3} + \text{H}_2\text{O} = > \text{FeOEuO} + 3\text{H}^+$	$\log K = -13.7$	$K_{\text{lump}} = \frac{K [> \text{FeOH}]}{[\text{H}^+]^3}$
$> \text{Ca}^{+2} + \text{EuCO}_3^+ = > \text{EuCO}_3^+ + \text{Ca}^{+2}$	$\log K = 3.75$	$K_{\text{lump}} = \frac{K [> \text{Ca}^{+2}]}{[\text{Ca}^{+2}]}$
$> \text{AlOH} + \text{Eu}^{+3} = > \text{AlOEu}^{+2} + \text{H}^+$	$\log K = 2.29$	$K_{\text{lump}} = \frac{K [> \text{AlOH}]}{[\text{H}^+]}$
$> \text{SiOH} + \text{Eu}^{+3} = > \text{SiOEu}^{+2} + \text{H}^+$	$\log K = -0.63$	$K_{\text{lump}} = \frac{K [> \text{SiOH}]}{[\text{H}^+]}$
$> \text{SiOH} + \text{Eu}^{+3} + \text{H}_2\text{O} = > \text{SiOEuO} + 3\text{H}^+$	$\log K = -14.13$	$K_{\text{lump}} = \frac{K [> \text{SiOH}]}{[\text{H}^+]^3}$

Table F-12. Neptunium Fracture Mineral Sorption Coefficients

Reaction	Log K	K_{lump}
$> \text{FeOH} + \text{NpO}_2^+ = > \text{FeOHNpO}_2^+$	$\log K = 4.32$	$K_{\text{lump}} = K[> \text{FeOH}]$
$> \text{FeOH} + \text{NpO}_2^+ + \text{H}_2\text{O} = > \text{FeOHNpO}_3^- + 2\text{H}^+$	$\log K = -11.46$	$K_{\text{lump}} = \frac{K[> \text{FeOH}]}{[\text{H}^+]^2}$
$> \text{Ca}^{+2} + \text{NpO}_2^+ = > \text{NpO}_2^+ + \text{Ca}^{+2}$	$\log K = 2.35$	$K_{\text{lump}} = \frac{K[> \text{Ca}^{+2}]}{[\text{Ca}^{+2}]}$
$> \text{AlOH} + \text{NpO}_2^+ = > \text{AlONpO}_2 + \text{H}^+$	$\log K = -4.67$	$K_{\text{lump}} = \frac{K[> \text{AlOH}]}{[\text{H}^+]}$
$> \text{AlOH} + \text{NpO}_2^+ + \text{H}_2\text{O} = > \text{AlONpO}_3\text{H}^- + 2\text{H}^+$	$\log K = -14.26$	$K_{\text{lump}} = \frac{K[> \text{AlOH}]}{[\text{H}^+]^2}$
$> \text{SiOH} + \text{NpO}_2^+ = > \text{SiONpO}_2 + \text{H}^+$	$\log K = -3.72$	$K_{\text{lump}} = \frac{K[> \text{SiOH}]}{[\text{H}^+]}$
$> \text{SiOH} + \text{NpO}_2^+ + \text{H}_2\text{O} = > \text{SiONpO}_3\text{H}^- + 2\text{H}^+$	$\log K = -12.16$	$K_{\text{lump}} = \frac{K[> \text{SiOH}]}{[\text{H}^+]^3}$

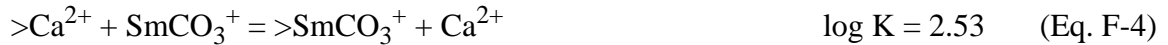
Table F-13. Uranium Fracture Mineral Sorption Coefficients

Reaction	Log K	K_{lump}
$> \text{FeOH} + \text{UO}_2^{+2} = > \text{FeOHUO}_2^{+2}$	$\log K = 6.63$	$K_{\text{lump}} = K[> \text{FeOH}]$
$> \text{FeOH} + \text{UO}_2^{+2} + \text{H}_2\text{O} = > \text{FeOHUO}_3 + 2\text{H}^+$	$\log K = -3.05$	$K_{\text{lump}} = \frac{K[> \text{FeOH}]}{[\text{H}^+]^2}$
$> \text{Ca}^{+2} + \text{UO}_2^{+2} = > \text{UO}_2^{+2} + \text{Ca}^{+2}$	$\log K = 5.12$	$K_{\text{lump}} = \frac{K[> \text{Ca}^{+2}]}{[\text{Ca}^{+2}]}$
$> \text{AlOH} + \text{UO}_2^{+2} = > \text{AlOUO}_2^+ + \text{H}^+$	$\log K = 3.13$	$K_{\text{lump}} = \frac{K[> \text{AlOH}]}{[\text{H}^+]}$
$> \text{SiOH} + \text{UO}_2^{+2} + \text{H}_2\text{O} = > \text{SiOUO}_3\text{H} + 2\text{H}^+$	$\log K = -5.18$	$K_{\text{lump}} = \frac{K[> \text{SiOH}]}{[\text{H}^+]^2}$
$> \text{SiOH} + \text{UO}_2^{+2} + \text{H}_2\text{O} = > \text{SiOUO}_3^- + 3\text{H}^+$	$\log K = -12.35$	$K_{\text{lump}} = \frac{K[> \text{SiOH}]}{[\text{H}^+]^2}$

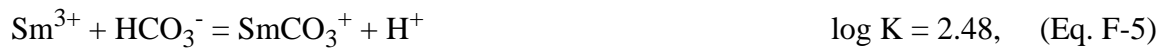
Table F-14. Strontium Fracture Mineral Sorption Coefficients

Reaction	Log K	K_{lump}
$> \text{FeOH} + \text{Sr}^{+2} = > \text{FeOHSr}^{+2}$	$\log K = 2.22$	$K_{\text{lump}} = K[> \text{FeOH}]$
$> \text{FeOH} + \text{Sr}^{+2} = > \text{FeOSr}^+ + \text{H}^+$	$\log K = -5.30$	$K_{\text{lump}} = \frac{K[> \text{FeOH}]}{[\text{H}^+]}$
$> \text{FeOH} + \text{Sr}^{+2} + \text{H}_2\text{O} = > \text{FeOSrOH} + 2\text{H}^+$	$\log K = -5.30$	$K_{\text{lump}} = \frac{K[> \text{FeOH}]}{[\text{H}^+]^2}$
$> \text{Ca}^{+2} + \text{Sr}^{+2} = > \text{Sr}^{+2} + \text{Ca}^{+2}$	$\log K = -1.75$	$K_{\text{lump}} = \frac{K[> \text{Ca}^{+2}]}{[\text{Ca}^{+2}]}$

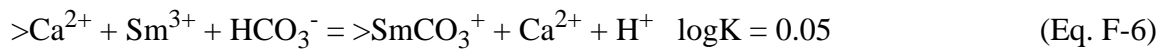
For most RNs, the free ion participates in the sorption reactions with the fracture minerals. An exception, however, are the surface complexation reactions with $>Ca^{2+}$ for Sm, Am, and Eu. For these RNs, the carbonate species reacts with the surface site. As part of the simplification of the chemical model in this section, these three reactions are rewritten in terms of the free ion, using the equilibrium speciation partitioning described above. Thus, the three reactions between Sm, Am, and Eu with $>Ca^{2+}$ shown in the previous tables can be converted to represent the free ion. For Sm, we start with the carbonate species sorption reaction



and the carbonate speciation reaction

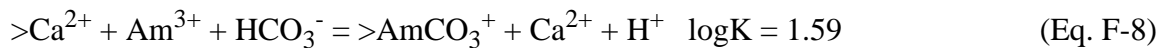


both of which can be combined to yield the following reaction for the sorption of the free ion:

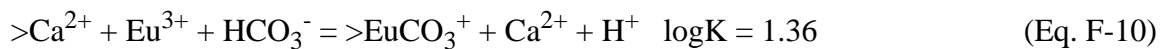


$$K_{\text{lump}} = K[>Ca^{2+}][HCO_3^-]/[H^+][Ca^{2+}] \quad (\text{Eq. F-7})$$

Similarly, surface complexation with calcium for Am and Eu can be written as



$$K_{\text{lump}} = K[>Ca^{2+}][HCO_3^-]/[H^+][Ca^{2+}] \quad (\text{Eq. F-9})$$



$$K_{\text{lump}} = K[>Ca^{2+}][HCO_3^-]/[H^+][Ca^{2+}] \quad (\text{Eq. F-11})$$

These three equations are substituted for the carbonate species reactions shown in the tables.

The final reduction in complexity of reaction parameters involves grouping all the K_{lump} terms for each RN into a single effective coefficient, K_{lump}^e . This term represents the partitioning between the aqueous phase and the sorption on fracture minerals for the free ion of each RN. For each RN, the K_{lump} terms are added together to give a single effective lumped K, K_{lump}^e . This reduces the number of equations that need be solved for the carbonate speciation reactions described previously and the free-ion sorption reaction described in this section. However, because the mineral-coating composition varies between all rock classes, different K_{lump}^e terms must be considered for each different material. Table F-15 summarizes the K_{lump}^e terms used for free-ion sorption to fracture mineral sites in the different rock classes and the different sensitivity sets outlined in Tables F-4 through F-7. Thus, in the fractures, the transport model explicitly simulates competition for free ions by sorption reactions using the parameters in Table F-15 and mobile non-reactive species using the coefficients in Table F-3.

Table F-15. K^e_{lump} (cc/g) for Free-Ion Sorption to Fracture Minerals in Four Different Rock Classes

Actinide	Rock Class	Low	Base ¹	High ²
Class II (Sm)	Welded	2.60e+6	2.20e+6	4.28e+6
	Lava	1.39e+7	1.35e+7	9.04e+6
	Zeolitic	1.89e+6	1.03e+7	1.88e+7
	Nonwelded ³	7.65e+6	7.40e+6	1.05e+7
Class II (Am)	Welded	2.60e+6	2.20e+6	4.28e+6
	Lava	1.39e+7	1.35e+7	9.04e+6
	Zeolitic	1.89e+6	1.03e+7	1.88e+7
	Nonwelded	7.65e+6	7.40e+6	1.05e+7
Class II (Eu)	Welded	6.62e+6	3.20e+7	8.96e+7
	Lava	2.21e+7	2.45e+7	2.89e+7
	Zeolitic	2.21e+6	6.69e+6	1.12e+7
	Nonwelded	2.14e+7	2.40e+7	3.37e+7
Class III (Sr)	Welded	0.01	0.08	0.23
	Lava	0.04	0.05	0.06
	Zeolitic	0	0.005	0.01
	Nonwelded	0.04	0.05	0.07
Class IV (U)	Welded	5.74e+8	3.37e+9	9.68e+9
	Lava	1.51e+9	1.81e+9	2.58e+9
	Zeolitic	1.38e+8	6.91e+7	6.91e+4
	Nonwelded	1.86e+9	2.15e+9	3.01e+9
Class IV (Np)	Welded	3.67	21.32	62.10
	Lava	12.98	14.82	19.19
	Zeolitic	0.88	4.17	7.46
	Nonwelded	12.66	14.51	22.6
Class V (Pu)	Welded	11.14	81.68	245.8
	Lava	52.72	60.14	77.22
	Zeolitic	0.001	18.56	37.11
	Nonwelded	47.89	55.32	92.07

1 - Low refers to iron content in fracture mineral distribution. It usually leads to low K, but not always.
2 - High refers to iron content in fracture mineral distribution. It usually leads to high K, but not always.
3 - In these simulations, one of the seven rock classes considered is fractured nonwelded tuff.

F.3.6 Additional Fracture K^e_{lump} Uncertainty

The column-experiment models described in Appendix D indicate that K^e_{lump} terms for Pu in welded tuff must be greater than approximately 10 cc/g. The short time and distance scales of such experiments do not provide upper bounds. The experiments also do not provide parameters for other tuffs or other RNs, hence the theoretical analysis in the previous sections. In the previous section, fracture Kd uncertainty ranges were developed for variations in the mineralogic composition of specified coating geometry. This means that although the specific mineral volume fractions were changed, the coating thickness and its accessibility to solutes in fracture fluid was held constant at our expected value. In fact, we know very little about how accessible fracture

minerals are to solutes flowing in the fracture fluid. In this model, only those reactive surface sites that are immediately available are of significance. If the solute must diffuse into the fracture coating, then the retardation associated with that process is captured by the matrix-sorption component.

The two uncertain parameters in Equation F-3 that were not varied in the previous section are $P_{\text{exp}}\%$ and $P_{\text{cov}}\%$, the percent of the fracture coating that is accessible to solutes in the fracture fluid and the percent of the fracture surface that is coated at all, respectively. In the previous section, these two terms were set at 10% and 50%, so their product is 0.05. If we allow $P_{\text{exp}}\%$ to vary from 1% to 50% and if we allow $P_{\text{cov}}\%$ to vary between 10% and 100%, then the range on the product of the two terms is between 0.001 and 0.5. Thus, the quantity ($P_{\text{exp}}\% * P_{\text{cov}}\%$) that was held constant in Equation F-3 as 0.5 may vary by almost 3 orders of magnitude. In the sensitivity studies in Section F.7, this increased uncertainty is factored into the fracture Kd uncertainty presented in the previous section as a secondary analysis.

Ion exchange has not been considered in the development of fracture sorption parameters. It is possible that some radionuclides such as Pu(IV) species other than Pu^{+4} may sorb to fracture minerals by this process. Pawloski et al. (2001) provide ion-exchange coefficients for Sr^{2+} , Cs^+ , and UO_2^{2+} . Presently, however, coefficients are not available to markedly reduce uncertainty in the fracture coating sorption process for the other radionuclides. In the next section, we note that surface complexation and ion-exchange process are lumped together for matrix material sorption coefficients.

F.3.7 Matrix Sorption

In addition to competitive chemical reactions modeled in the fractures, sorption with matrix minerals is also considered for solutes which diffuse into the matrix. The parameters used to bound the sensitivity simulations for matrix sorption come primarily from the YMP analysis and modeling report (CRWMS M&O 2000g) that contain the best qualified data from the project. Whereas theoretical estimates were required for fracture-coating sorption coefficients due to lack of data, laboratory measurements are used to bound the matrix-material sorption coefficients. The YMP data for the Kd parameter are applicable for Western Pahute Mesa aquifer material because the rock material used for the experiments is of the same origin as the units under consideration on Western Pahute Mesa. In this study, we are interested primarily in the Calico Hills and Topopah Spring lithologic units. These units extend south of Western Pahute Mesa to Yucca Mountain and have been extensively studied. Aqueous-solid matrix sorption data were available for most of the RNs of interest on vitric, devitrified, and zeolitic tuffs, classifications that can be used represent bedded, non-welded, welded, and zeolitic tuffs at both Yucca Mountain and Western Pahute Mesa. In fact, the only differences for sorbing RNs to any of these rock types are whether they are zeolitized or not (Table F-16). Lava material has not been studied by the YMP and to date Kd data have not been measured for Pahute Mesa lavas. Therefore, for the purposes of this study, the lavas are assumed to sorb reactive RNs similarly to welded vitric tuffs.

To help simplify the modeling and account for species with limited data, RNs and actinides with similar sorption properties were grouped into five classes. These classes were then used to represent the behavior of RNs in which specific data were not available and to provide the maximum range of parameters for sensitivity analysis. For the species considered, Eu was the only

one not published in CRWMS M&O (2000g). However, Triay et al. (1997) report that the sorption behavior of Eu is similar to Am and Sm. Therefore, the parameters from those species were used in the model. When available, the expected value determined by the YMP was used as the base case for each RN. However, an expected Kd value was not available from the YMP for Sr, U, and Cs. Therefore, the expected value for another species in their respective classes was used. Also, the highest and lowest values from experimental measurements of all RNs in each class were used to set the range of uncertainty for the sensitivity simulations.

The batch experiments on which matrix Kds are based were conducted in carbonate solutions. Thus, they represent the ratio of sorbed species to aqueous species in which the carbonate reactions are already competing for free ions. Because we model the free ions and the carbonate species separately and explicitly simulate those competitive reactions, the measured Kds are corrected for our system. Simply, the measured Kds are multiplied by the pseudo carbonate speciation coefficients in Table F-3 to yield a free-ion-only Kd . The bulk solution Kds and the resulting free-ion Kds are shown in Table F-16.

Table F-16. Matrix *K*_ds for Seven Rock Classes

Actinide	Rock Class	Bulk <i>K</i> _d (cc/g)			Free-Ion <i>K</i> _d (cc/g)		
		Base	Low	High	Base	Low	High
Class II (Sm)	Bedded	400	100	2000	2.81e+7	7.03e+6	1.41e+8
	Nonwelded	400	100	2000	2.81e+7	7.03e+6	1.41e+8
	Welded(f) ¹	400	100	2000	2.81e+7	7.03e+6	1.41e+8
	Lava(f)	400	100	2000	2.81e+7	7.03e+6	1.41e+8
	Zeolitic(f)	200	100	1000	1.41e+7	7.03e+6	7.03e+7
	Nonwelded(f)	400	100	2000	2.81e+7	7.03e+6	1.41e+8
	Zeolitic ¹	200	100	1000	1.41e+7	7.03e+6	7.03e+7
Class II (Am)	Bedded	400	100	2000	9.92e+6	2.48e+6	4.96e+7
	Nonwelded	400	100	2000	9.92e+6	2.48e+6	4.96e+7
	Welded(f)	400	100	2000	9.92e+6	2.48e+6	4.96e+7
	Lava(f)	400	100	2000	9.92e+6	2.48e+6	4.96e+7
	Zeolitic(f)	200	100	1000	4.96e+6	2.48e+6	2.48e+7
	Nonwelded(f)	400	100	2000	9.92e+6	2.48e+6	4.96e+7
	Zeolitic	200	100	1000	4.96e+6	2.48e+6	2.48e+7
Class II (Eu)	Bedded	400	100	2000	2.81e+7	7.03e+6	1.41e+8
	Nonwelded	400	100	2000	2.81e+7	7.03e+6	1.41e+8
	Welded(f)	400	100	2000	2.81e+7	7.03e+6	1.41e+8
	Lava(f)	400	100	2000	2.81e+7	7.03e+6	1.41e+8
	Zeolitic(f)	200	100	1000	1.41e+7	7.03e+6	7.03e+7
	Nonwelded(f)	400	100	2000	2.81e+7	7.03e+6	1.41e+8
	Zeolitic	200	100	1000	1.41e+7	7.03e+6	7.03e+7
Class III (Sr)	Bedded	100	10	1000	100	10	1000
	Nonwelded	100	10	1000	100	10	1000
	Welded(f)	100	10	1000	100	10	1000
	Lava(f)	100	10	1000	100	10	1000
	Zeolitic(f)	1000	500	5000	1000	500	5000
	Nonwelded(f)	100	10	1000	100	10	1000
	Zeolitic	1000	500	5000	1000	500	5000
Class IV (U)	Bedded	1	0	5	4.33e+09	0	2.17e+10
	Nonwelded	1	0	5	4.33e+09	0	2.17e+10
	Welded(f)	1	0	5	4.33e+09	0	2.17e+10
	Lava(f)	1	0	5	4.33e+09	0	2.17e+10
	Zeolitic(f)	7	0	20	3.03e+10	0	8.66e+10
	Nonwelded(f)	1	0	5	4.33e+09	0	2.17e+10
	Zeolitic	7	0	20	3.03e+10	0	8.66e+10
Class IV (Np)	Bedded	1	0	5	4.98	0	24.9
	Nonwelded	1	0	5	4.98	0	24.9
	Welded(f)	1	0	5	4.98	0	24.9
	Lava(f)	1	0	5	4.98	0	24.9
	Zeolitic(f)	7	0	20	34.9	0	99.7
	Nonwelded(f)	1	0	5	49.8	0	24.9
	Zeolitic	7	0	20	34.9	0	99.7
Class V (Pu)	Bedded	100	5	300	644	32.2	1.93e+03
	Nonwelded	100	5	300	644	32.2	1.93e+03
	Welded(f)	100	5	300	644	32.2	1.93e+03
	Lava(f)	100	5	300	644	32.2	1.93e+03
	Zeolitic(f)	100	50	400	644	322	2.57e+03
	Nonwelded(f)	100	5	300	644	32.2	1.93e+03
	Zeolitic	100	50	400	644	322	2.57e+03

Based on CRWMS M&O (2000g)

F.3.8 Matrix Diffusion

Diffusion of solutes out of fractures and into matrix material retards their migration by removing them from the flowing fractures and by bringing them into contact with reactive matrix minerals. Two sets of experimental data from diffusion cell experiments conducted at LANL (Reimus et al., 2002) were used to determine the diffusion coefficients and their ranges of uncertainty. These experiments provide data for diffusion of tritium (^3H) and technetium (Tc) on samples of welded tuff, non-welded zeolitic tuff, non-welded tuff, and lava, respectively. For each unit, the high and low value was selected to bound a range for examination and the base-case value was calculated by taking the log average of all available samples, except for the non-welded zeolitic tuff in which only a single sample was available. For this case, the value measured was used as the low value, the high value was selected to be a factor of 2 higher, and the base case was calculated from the linear relationship developed in Reimus et al. (2002) for ^3H diffusion as a function of porosity and permeability.

Reimus' data set provides a range of diffusion coefficients for small molecules with the ^3H data and larger molecules with the Tc data. Table F-17 shows the data derived from Reimus' study. In this application, the ^3H data are applied to ^3H , ^{14}C , and ^{36}Cl . The Tc data are applied to all other nuclides in Table F-16.

The ranges of diffusion coefficients in Table F-17 may seem narrow relative to some other studies for Pahute Mesa and Yucca Mountain. For example, Reimus et al. (1999b) estimate diffusion coefficients for iodide and PFBA in field experiments conducted in poor to moderately welded tuff and densely welded tuff (also described in CRWMS M&O, 2000g). The range on iodide is between $1.1\text{e-}6$ and $17.5\text{e-}6$ cm^2/s , thus exceeding the maximum value considered here. However, the large values in that study (above $3.3\text{e-}6$ cm^2/s) were calculated based on the assumption that the aperture in the experiment was a constant 0.2 cm. Neglecting such estimates brings the maximum value closer to those used in this study. Similarly, the PFBA diffusion range is between $4.4\text{e-}7$ and $7\text{e-}6$ cm^2/s , providing a slightly higher range for large molecules. Again, the larger PFBA diffusion coefficients (above $1.3\text{e-}6$ cm^2/s) are estimated assuming a constant experimental aperture of 0.2 cm. By using the data in Table F-17, the results are perhaps slightly conservative because the largest possible values *estimated* in other studies are not used. More importantly, however, sensitivity coefficients to the diffusion parameter are computed in Section F.7, providing a quantitative assessment of this parameter relative to the other parameters in the reactive dual-porosity transport model.

Table F-17. Diffusion Coefficients for Rock Classes (cm²/sec)

Rock Class	Tritium				Technetium			
	Low	Base	High	# of samples	Low	Base	High	# of samples
Zone I - Bedded	7.50E-07	1.21E-06	3.50E-06		4.00E-07	6.95E-07	1.30E-06	
Zone II - Nonwelded	7.50E-07	1.21E-06	3.50E-06	8	4.00E-07	6.95E-07	1.30E-06	8
Zone III - Welded	3.50E-07	1.03E-06	3.00E-06	8	3.20E-07	8.22E-07	2.70E-06	14
Zone IV - Lava	8.00E-07	1.38E-06	2.30E-06	6	2.50E-07	8.92E-07	5.00E-06	6
Zone V - Altered	5.50E-07	9.02E-07	1.00E-06	1	5.00E-07	9.02E-07	1.00E-06	1
Zone VI - Fractured non-welded	7.50E-07	1.21E-06	3.50E-06		4.00E-07	6.95E-07	1.30E-06	
Zone VII - Bedded - altered	5.50E-07	9.02E-07	1.00E-06		5.00E-07	9.02E-07	1.00E-06	
Data reported in Reimus et al. (2002)								

F.3.9 Fracture Properties d , b , ϕ_f

The fracture properties (half-spacing, aperture, and porosity) for modeling are related through the equation

$$b/d = \phi_f, \quad (\text{Eq. F-12})$$

where b is the aperture, d is the fracture spacing, and ϕ_f is the fracture porosity. Information on spacing of open fractures in the saturated zone was obtained from Drellack et al. (1997). Drellack's report provides information on the fracture density for several different boreholes on Pahute Mesa and Area 18 for welded tuff aquifers (WTA), lava flow aquifers (LFA), and tuff confining units (TCU). It classifies the fracture angles into high (60-90), medium (30-60), and low (0-30) categories, and then reports the percent of fractures within each group. The fracture frequency is corrected by the measured angles using

$$\text{Corrected fracture density} = \text{fracture density} * \cos \alpha. \quad (\text{Eq. F-13})$$

Because the fracture angle is reported as categories, the average for each category is used in the correction. For example, an angle of 75 is used for all fractures in the high-angle category. The corrected fracture density for each category is summed, correcting for the percentage in each category to determine a single fracture density for each data set. Inverting the fracture density results in fracture spacing. Table F-18 shows the high and low values of fracture spacing in meters for the three

different HSUs.

Table F-18. Low and High Values of Fracture Spacing (m)

Range	Welded	Lava	Altered/ Non-welded
Low (m)	0.57	2.42	7.95
High (m)	1.86	6.73	73.30

These values represent fractures that were observed in the core and do not distinguish between flowing and non-flowing fractures. We are unaware of any correlated data of borehole flow meters and core samples for multiple HSUs in Western Pahute Mesa. Limited data of this form are available from the YMP. However, CRWMS M&O (2000f) found that there were not enough YMP data to provide a flowing fracture spacing analysis for individual HSUs, so for this analysis the data was lumped for all HSUs. The results indicate that the fracture spacing for flowing and nonflowing fractures is 1 to 100 m, which is consistent with Table F-18. A correction was applied to distinguish the fractures that are flowing, with the range increasing to 8 to 500 m. A comparison is not available for the Pahute Mesa HSUs, but the YMP analysis indicates that a sensitivity analysis with a larger range of fracture spacing than obtained based on the above analysis should be included.

Data on the fracture aperture was available from seven boreholes examined in the same report as was used to determine fracture spacing (Drellack et al., 1997). A base, high, and low value of fracture aperture were derived from the data. The base case was determined by taking the log average of the values available, which assumes that the distribution of fracture apertures is log-normal distributed. The high and low value for each unit were used for the extremes. Table F-19 shows the range determined in this analysis. For the Lava, the high end is skewed by data from Area 18.

Table F-19. Fracture Apertures

	Welded	Lava	Altered/ Non-welded
Base (m)	2.65E-4	3.46E-4	2.55E-4
Low (m)	4.00E-5	5.30E-4	9.00E-5
High (m)	2.19E-3	2.09E-3	1.51E-3

The fracture porosity (fracture volume fraction) data are limited, and are therefore derived from fracture aperture and density data assuming parallel plates. In general, the angle corrected fracture density is multiplied by the fracture aperture to estimate the fracture porosity. If the fractures occur in three dimensions, a factor of three is multiplied to the value to account for the effects of dimensionality (CRWMS M&O, 2000f). However, not including the correction is more conservative because it leads to a smaller fracture porosity.

Using the fracture aperture and spacing data from Drellack et al. (1997), the fracture porosity was calculated for the three different units. The low values of porosity were based on the parallel plate equation that does not account for the fracture being three dimensional, which provides the smallest porosity. The high value was determined using the equation that did account for the three-dimensional nature of the fracture, which produced the largest porosity possible. The base case for the porosity was determined by taking the log averages of the high and low case. The ranges calculated for the lava aquifer had very low porosities, but based on the experimental results from the BULLION tracer experiment (IT, 1998), the fracture porosity was expected to be higher. Therefore, for the lava aquifer, the high value was extended to allow for the high porosities observed in the field. Porosity values used are listed in Table F-20.

Table F-20. Fracture Porosities

	Welded	Lava	Altered/ Nonwelded
Base	4.98E-4	2.09E-3	1.06E-4
Low	7.00E-5	2.19E-4	1.13E-5
High	3.54E-3	2.00E-2	1.00E-3

These values compare well to the range available from YMP analysis on wells G-1, G-4, GU-3, and UE25a#1e of 8.0E-5 to 1.0E-3 (CRWMS M&O, 2000f). An analysis by IT (1996) reports a variation in fracture porosity of 6.1E-6 to 2.1E-4. Both the range reported in Table F-20 and the values from Yucca Mountain are not as small as those reported by IT (1996). Hence, IT (1996) values are used as a lower bound, whereas the other sources are used for the upper bound.

Although fracture porosity is a derived parameter, in these studies it is treated as a sensitivity parameter because velocity directly depends upon it. Also, in the FEHM transport model, porosity and aperture are primary variables and fracture spacing is computed from them based on Equation F-12.

F.3.10 Plutonium-Colloid Reactions

Forward and Reverse Kinetics

The kinetics of Pu-colloid formation were discussed in Section D.3.3. In summary, a set of experiments was conducted and analyzed that yielded estimates of the forward and reverse rates of reaction over a relatively short time frame for Pu and montmorillonite colloids. Simulations of montmorillonite colloid-facilitated Pu migration in the column experiments yielded results that were consistent with the fits to laboratory data. However, the simulations also indicated that to match the column experiments, it was most important that the forward rate be large enough and that the reverse rate be small enough, but that there were no bounds on how large or how small. This finding is due to the short spatial and temporal scales associated with the experiments. An additional concern is that silica and zeolite colloids are present in NTS groundwater. Preliminary findings in ongoing NTS studies indicate that zeolite colloids sorb Pu much more strongly than

clay or silica colloids (Kersting and Reimus, 2002). Therefore, to help develop ranges of uncertainty for the field-scale kinetic rates of Pu-colloid formation, additional data are considered. Forward and reverse rates of Pu sorption onto colloids were fit to data in CRWMS M&O (2000g) using the same technique described in Section D.3.3. Table F-21 lists the forward and reverse rates fit-to-existing-data sets. Additionally, recent analyses indicate that desorption rates in flowing fractures are different than those measured in batch experiments (Kersting and Reimus, 2002), possibly due to collisions with fracture surfaces that do not occur in batch experiments.

The values used in the sensitivity (Table F-22) span a large range with respect to the potential for forming Pu-colloids onto which the Pu will remain long enough to migrate a significant distance. The base case uses the maximum k_f and minimum (approximately) k_r for the data sets that do not include zeolite colloids. The minimum set of k_r and k_f simply reduce k_r from the base-case value by one order of magnitude (as may be appropriate for zeolites) to provide for even more irreversible behavior of the Pu-colloid. The maximum case seeks to decrease k_f and increase k_r , reducing the likelihood of retention of Pu onto colloids. Thus, the model parameters are informed by the batch data and other recent analyses, but do not draw explicitly from any one data set.

Table F-21. Forward and Reverse Rate Fits to Experimental Pu-Colloid Sorption Data

Experiment	k_f (g/g/hr)	k_r (1/hr)
Pu(V) on Ca-Montmorillonite ¹	8.06E+01	5.98E-03
Pu(V) on Ca-Montmorillonite - Model ²	>1E+01	<1E-02
Pu(V) on Silica ¹	2.36E+02	8.56E-04
Pu(IV)- J13 ³	6.48E+03	5.62E-02
Pu(IV)- Syn ³	4.01E+05	3.00E-02
Pu(V)- J13 ³	5.4E+03	1.58E-01
Pu(V)- Syn ³	1.62E+03	1.61E-01
Sources of Data: 1 - Reimus et al. (2001)--UGTA studies. 2 - Results from Appendix D, this study--simulating Reimus column experiment. 3 - Yucca Mountain Study CRWMS M&O (2000g)--studies conducted with J-13 water and synthetic J-13 water.		

Table F-22. Forward and Reverse Rates Used in This Sensitivity Study

Base-Case		Minimum-Case		Maximum-Case	
k_f (1/hr)	k_r (g/g/hr)	k_f (g/g/hr)	k_r (1/hr)	k_f (g/g/hr)	k_r (1/hr)
4E+05	1E-03	4E+05	1E-04	1.6E+03	5E-02

Colloid Site Concentration

Kung (2000) has analyzed samples for colloid size distributions in 21 wells at the NTS. Using his size distributions, we compute the total colloid site concentration in each sample with

$$C_{col} = (4\pi x_n / Av) \sum_i r(i)^2 n_c(i) , \quad (\text{Eq. F-14})$$

where i is the bin number in the size distribution, $r(i)$ is the particle radius (nm) in the bin, $n_c(i)$ is the colloid particle concentration (particles/l) in each bin of the size distribution, x_n is the sorption sites per nm^2 (2.31 sites/ nm^2 of goethite was used for the calculation), and Av is Avogadro's number, 6.02×10^{23} sites/mole sites. Taking the average of the logs of the resulting site concentrations for all samples yields a colloid site concentration of 6.29×10^{-9} moles/l. In most calculations, this value is held constant. However, due to the range in the measurements, a sensitivity study looks at the maximum value calculated using Equation F-14 for any single sample, 6.2×10^{-6} moles/l of reactive sites.

F.4 Reactive Transport Along Heterogeneous Pathlines

A variety of methods can model transport in the three-dimensional flow fields presented in Chapter 5. Full three-dimensional finite-element calculations could be performed using GDPM, but the simulation times would be substantial and the numerical dispersion may be significant, even at the increased resolution of the site-scale domain. Another approach would be to abstract the process to a single one-dimensional representation at the risk of oversimplifying significant impacts of three-dimensional flow and spatial heterogeneity. In this study, we applied a method developed by Viswanathan (1999) in which multiple streamtubes map out pathlines and attribute distributions through the three-dimensional domain which are then transformed into one-dimensional grids for transport simulations. Whereas Viswanathan (1999) solved reactive multi-solute transport in his study, we extend his approach to include the GDPM to simulate reactive transport with fracture-matrix interactions at the site scale along pathlines mapped with individual streamtubes in our heterogeneous flow field. Although using GDPM for reactive transport is novel for this study, the transforming of pathlines in three-dimensional flow fields to multiple one-dimensional grids for transport simulations is often used to minimize numerical dispersion and increase efficiency (e.g., Ginn, 2001; Tompson et al., 1999). In the present application, dispersion is only considered along the streamtube. Transverse dispersion between streamtubes is not captured by this model. However, the heterogeneous attribute maps on which the flow and transport simulations are conducted provide the primary dispersive component for this study.

Each tube may encounter up to seven different materials (see Table 5-1), each of which has different physical and chemical attributes. For example, the bedded and non-welded tuff classes are modeled as matrix-only materials in which all flow and transport occurs only in porous matrix material. However, when a streamtube leaves a nonwelded tuff and enters a welded tuff, then all the fracture-matrix interaction processes described above must be considered. As described in Section F.3.3, the physical (aperture, porosity, and fracture spacing) and chemical (fracture Kd , diffusion coefficient, and matrix Kd) properties vary spatially, with the seven heterogeneous

lithologies for each of the sensitivity simulations described in the next section. The process of modeling reactive transport along these pathlines is as follows:

- A swarm of non-diffusing, non-reactive particles are released in the heterogeneous flow field for which the effective porosity is specified as the fracture volume fraction in fracture materials (Rock types 3, 4, 5, and 6) and the matrix porosity in matrix flow only units (Rock types 1, 2, and 7). Figures 5-15 and 5-16 show examples of the pathlines.
- The pathline of each particle is transformed into a one-dimensional finite-element grid.
- Physical and chemical transport parameters are transformed from the three-dimensional attribute field to the one-dimensional grids, thereby preserving the heterogeneous properties encountered along the streamtubes. Tables F-15 through F-20 provide the parameters for each of the encountered heterogeneous lithologic groups.
- The fluid flux along each pathline is preserved; to confirm that the one-dimensional pathline reproduces the transport behavior of the original streamtube, finite-element simulations of non-diffusing conservative tracers are tested to ensure they have the same mean travel time as the particle that mapped the pathline.
- Reactive and non-reactive solute transport with fracture-matrix interactions is simulated along each pathline using the GDPM methodology described in Appendix E.
- The flux rates and cumulative mass fluxes of RNs at the ER-20-5 observation wells and the NTS boundary are computed by integrating results from the individual streamtubes.

F.5 Site-Scale Application

F.5.1 Overview

Using the source-release functions to the TSA and LAVA aquifers described in Chapter 6, reactive transport is simulated along 225 streamtubes originating in the BENHAM cavity/chimney system at both aquifers. The following analysis examines the mass arrivals of RNs at the NTS boundary and at the ER-20-5 observations wells for base case, maximum retardation, and minimum retardation conditions. The maximum and the minimum cases use the parameters for all processes described previously in this appendix for the most and least favorable retardation conditions, with two exceptions. First, Eh is not varied from 550 mV. And second, the colloid site concentration remains constant at $6.29\text{e-}09$ moles/l. Sensitivity to these two parameters is studied separately. For each RN set, we examine independently source originations at the TSA and LAVA aquifer locations (as defined by the deterministic model). This approach provides additional insight regarding impacts from releases in the two different zones of interest. However, we acknowledge a discrepancy between release locations defined by the deterministic model for a heterogeneous site-scale model.

For this set of analyses, a single heterogeneous domain is used for the detailed evaluations. The full set of 30 equally likely realizations described in Chapter 5 are then examined in Chapter 7 in our evaluation of the significance of heterogeneity. Figures 5-15a and 5-16a show the

streamtubes generated with the three-dimensional flow field (flow-field realization #3). The streamtubes are used in the reactive transport simulations.

F.5.2 Source Term

The SOURCE 1A mass flux curves computed in Chapter 6 (Table 6-9 and Figures 6-33 and 6-34) are converted into time-varying source terms for each of the streamtubes originating in the TSA and LAVA source locations. Sensitivity to other source functions is examined in Chapter 7. The total mass flux into each aquifer is divided by the number of streamtubes associated with the transport model, in this case 225 at each source release location in this case. Then, that fraction is applied uniformly to each streamtube. Although this process represents a normalization in distributing the source flux once it reaches the aquifer of interest, it is reasonable because (a) the source term was computed using a stratigraphic representation of the geology and this site-scale model is a heterogeneous representation, (b) the approach is representative of the process that would need to be implemented for CAU simulations for reasons of expediency, and (c) these mass-flux curves out of the source region are of the same format as have been developed in Frenchman Flat (Tompson et al., 1999).

Because reactive transport is simulated on each streamtube, these calculations yield a large number of results that need to be integrated to represent the three-dimensional, site-scale transport behavior. One of the key distinguishing characteristics of the results is whether the source function is associated with TSA or LAVA releases. It is instructive to see which source contributes to mass fluxes at the ER-20-5 wells and the NTS boundary, so the results from each source release are presented separately. Because the results are presented as cumulative mass arrivals, results from each of the two sources can be simply combined for, say, total mass arrival at the NTS boundary.

F.5.3 Plutonium Base, Minimum, and Maximum Cases

The first set of results reported are the colloid-facilitated Pu transport simulations for heterogeneous flow-field realization #3. The base-case parameters indicate our expected value for each of the transport parameters discussed earlier in this appendix. The maximum case favors retardation in each parameter by choosing the most retarding value from the range of uncertainty for each parameter. It also favors desorption of Pu from colloids and large colloid retardation due to filtration. The minimum case favors solute and colloid mobility by choosing the least retarding value from each parameter's range of uncertainty. It favors retention of Pu on colloids with small desorption rates.

Figures F-8 through F-10 show the cumulative mass BTCs at the NTS boundary and at the ER-20-5 wells for Pu leaving the source domain in the TSA aquifer. Figures F-11 through F-13 show the cumulative mass BTCs at the NTS boundary and at the ER-20-5 wells for Pu leaving the source domain in the LAVA aquifer. For this particular flow field (one of thirty equally likely fields described in Appendix G), there are no Pu arrivals at the observation wells or the NTS boundary when the maximum case parameters are used.

When Pu breakthrough does occur, the figures show that the total Pu breakthrough is dominated by the Pu-colloid contribution. In fact, the other species present in the BTCs are due to the desorption of PuO_2^+ from the colloids and then equilibrium speciation; they are not due to independent migration of those aqueous species. In the absence of colloids, Pu does not migrate in these simulations. Under base-case conditions, there are no Pu arrivals at the ER-20-5 wells for

releases into the location of the TSA aquifer, but there are arrivals at the NTS boundary. This model result indicates that the pathways most conducive to transport (e.g., least amount of bedded non-fractured tuff) are not captured by the observation wells for this flow-field realization. In fact, Figure 5-15a shows that for this flow-field realization (number 3), very few streamtubes leaving BENHAM in the TSA zone come near the observation well. Closer inspection of Figure 5-15a reveals that the pathlines that do come near well ER-20-5 #1 must encounter significant matrix-flow-only regimes, as indicated by their late time of flight.

By comparison, a substantial number of streamtubes leaving BENHAM in the LAVA zone intersect the capture zone for the observation well ER-20-5 #3. Considering the continuity of fractured media in the LAVA (see Figure 5-18), it is not surprising that there are arrivals at the well ER-20-5 #3 for base-case parameters (Figure F-11). As with the TSA source releases, Pu migration associated with early arrivals in the LAVA is dependent upon Pu-colloid reactions. Starting with the minimum-case simulations (Figure F-13) we see that Pu-colloid arrivals dominate the total Pu mass breakthrough curve in the LAVA at the NTS boundary.

As stated above, the aqueous species arrivals at the NTS boundary are due to desorption from colloids, not from aqueous species mobility. Moving from minimum-case parameters to base-case parameters (Figure F-11) sorption coefficients are increased as are desorption rates for Pu from colloids. Thus the total aqueous mass arrival is less than in the minimum case, but it is also closer to that of the Pu-colloid mass arrival. Again, this is due to desorption from colloids, not aqueous species transport. Moving to the maximum case (Figure F-12), desorption rates are highest (yet still less than the forward sorption rates), leading to no arrivals of Pu associated with colloids. In this case, the aqueous species arrive with extremely low contributions and at times much greater than would be necessary to match field observations. Whereas desorption rates measured in the laboratory for clay colloids are less than sorption rates (Reimus et al., 2001), but still larger than those used in the minimum-case study, recent UGTA studies examining other colloidal material indicate that desorption rates for Pu from zeolites are likely much smaller (Kersting and Reimus, 2002). Transport modeling studies using the new parameters should provide additional insight regarding the role of kinetics in colloid-facilitated solute-transport.

Examination of the cumulative mass arrivals at the NTS boundary for base-case parameters compared with source Pu releases (Figure 6-43) shows that approximately $1e-5$ of the total Pu released from the MG to the LAVA (the input to these models) arrives at the NTS boundary. This comparison provides the basis for estimating the amount of Pu that can be approximated to be irreversibly sorbed to colloids for the particle-tracking model discussed in Chapter 7. This fraction depends on the desorption rate (see Appendix D) and the residence time. Thus, we use the results for the LAVA to make this estimate because the travel times are consistent with the field observations of Kersting et al. (1999). In these simulations of heterogeneous field #3, residence times in the TSA are much greater than in the LAVA, and as a result more desorption occurs. A factor of $1e-6$ represents the fraction of Pu in the source released to the TSA that arrives at the NTS boundary. As discussed in other sections, this particular heterogeneous realization does not provide for a fractured aquifer pathway in the upper welded tuff, leading to results inconsistent with the field observations. Therefore, if we posit that a fractured welded tuff aquifer actually is involved in migration to ER-20-5 #1, then the $1e-5$ factor is likely more appropriate and is therefore used in the particle-tracking model abstraction.

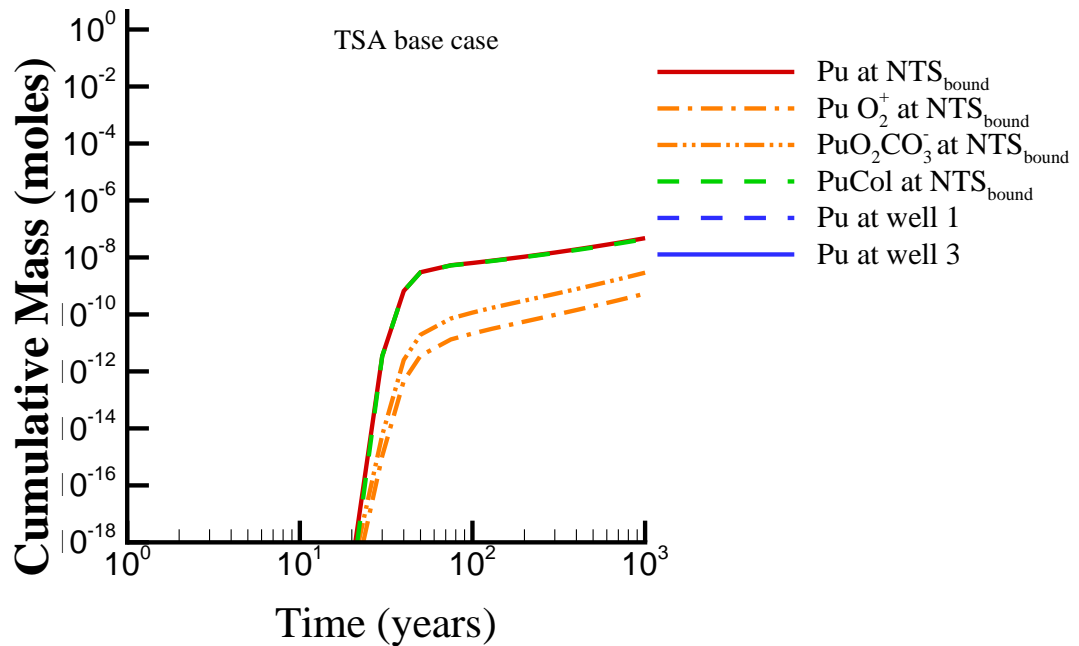


Figure F-8. Plutonium transport simulation results using **base-case** transport parameters for **TSA** source release. Cumulative mass arrivals at NTS boundary ($\text{NTS}_{\text{bound}}$) are shown for total plutonium as well as for significant species. In this simulation, there are no plutonium arrivals at the ER-20-5 observation wells 1 and 3.

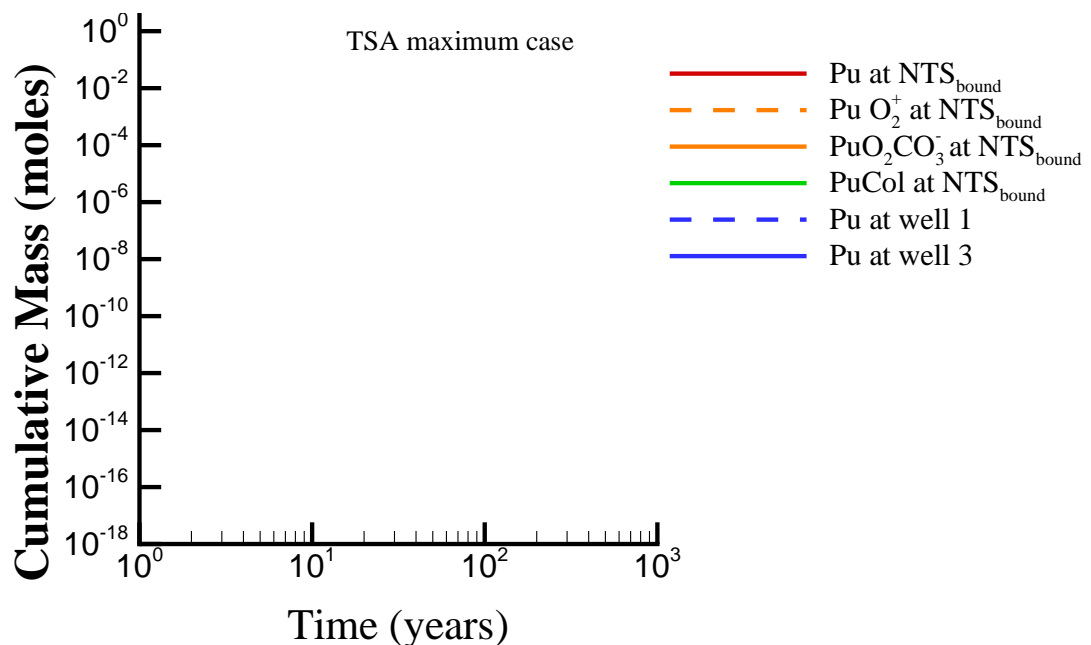


Figure F-9. Plutonium transport simulation results using **maximum-case (most retarding)** transport parameters for **TSA** source release. There are no mass arrivals at NTS boundary or at the ER-20-5 observation wells 1 and 3.

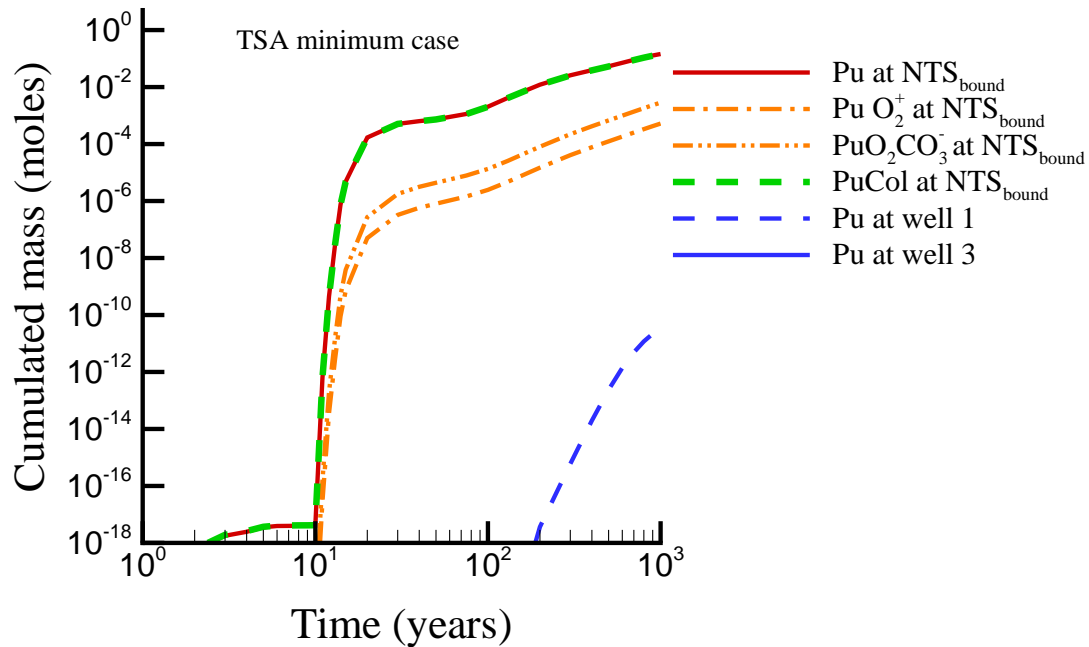


Figure F-10. Plutonium transport simulation results using **minimum-case (least retarding)** transport parameters for **TSA** source release. Cumulative mass arrivals at NTS boundary ($\text{NTS}_{\text{bound}}$) are shown for total plutonium as well as for significant species. Also shown are predicted total plutonium arrivals at the ER-20-5 observation wells.

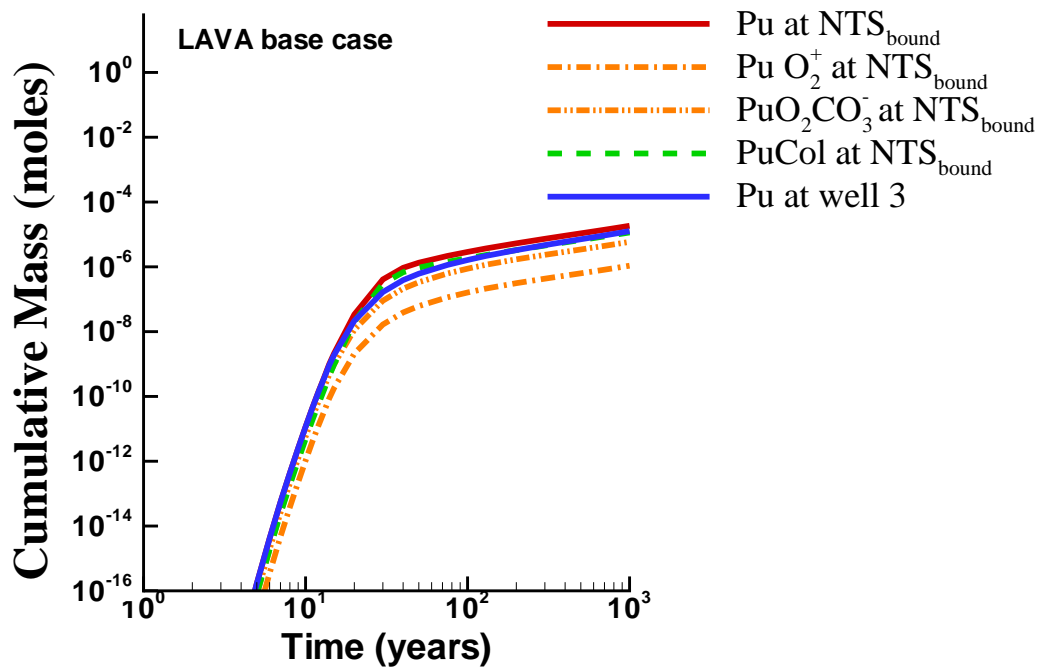


Figure F-11. Plutonium transport simulation results using **base-case** transport parameters for the **LAVA** source release. Cumulative mass arrivals at the NTS boundary ($\text{NTS}_{\text{bound}}$) are shown for total plutonium as well as for significant species. Also shown are total plutonium arrivals at the ER-20-5 #3 observation well.

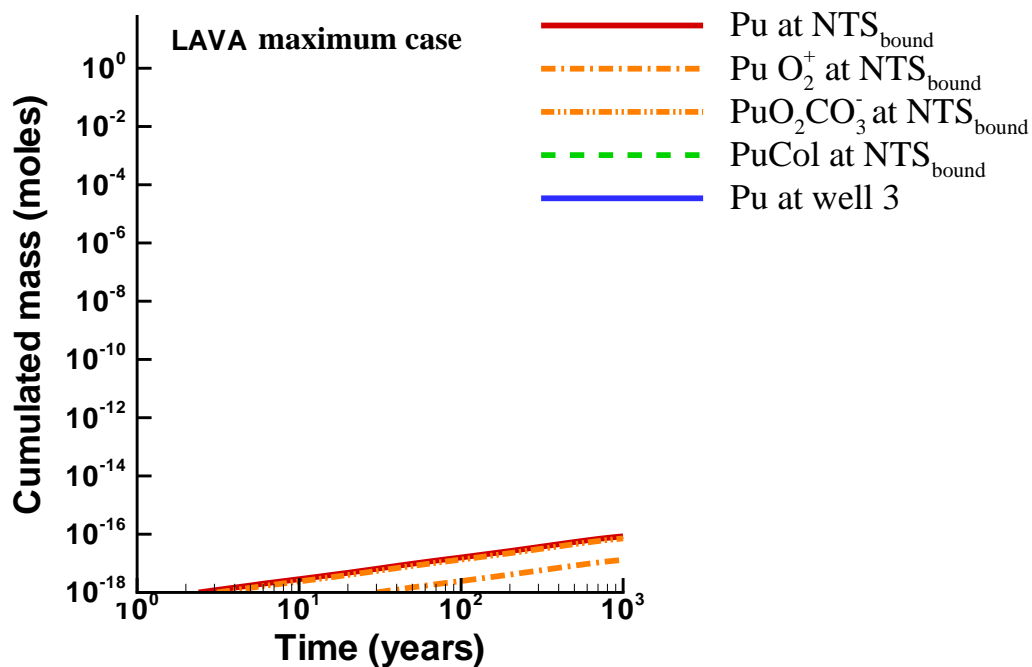


Figure F-12. Plutonium transport simulation results using the **maximum-case (most retarding)** transport parameters for the **LAVA** source release. Essentially no mass arrives at the NTS boundary or at the ER-20-5 #3 observation well.

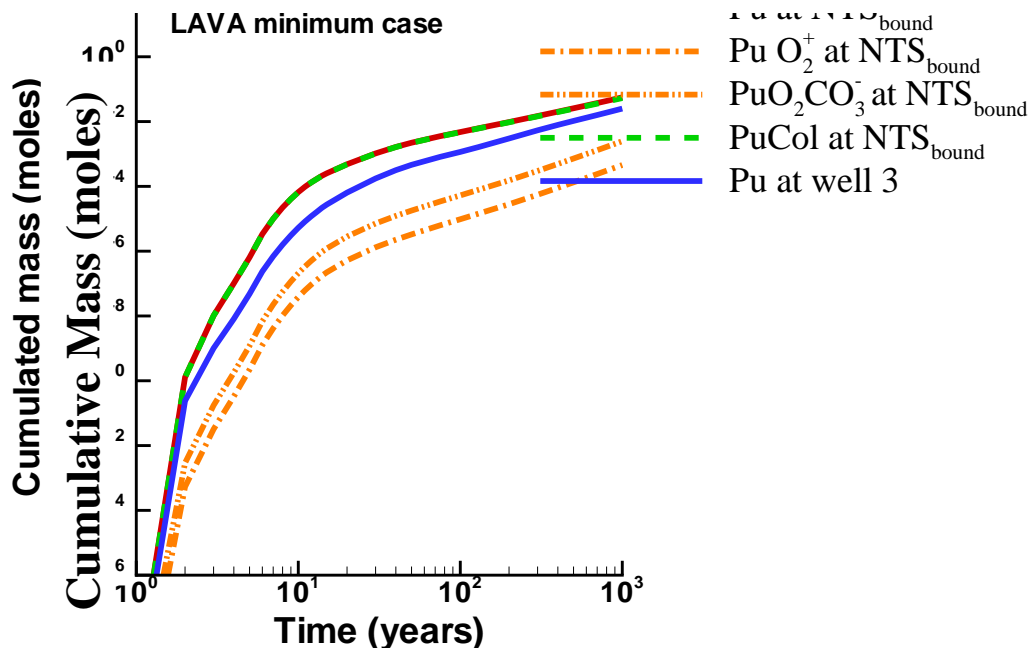


Figure F-13. Plutonium transport simulation results using the **minimum-case (least retarding)** transport parameters for the **LAVA** source release. Cumulative mass arrivals at the NTS boundary (NTS_{bound}) are shown for total plutonium as well as for significant species. Also shown are predicted total plutonium arrivals at the ER-20-5 #3 observation well.

F.5.4 Uranium, Neptunium and Strontium

Results for U, Np, and Sr BTCs at the NTS boundary and the ER-20-5 wells are shown in Figures F-14 through F-19. These figures show the results for both TSA and LAVA source releases for base, maximum, and minimum transport parameters. The minimum and maximum parameter sets represent all of the most and least favorable parameter values for RN mobility. Thus, the minimum set includes, from the ranges of parameter uncertainty, the lowest matrix Kds , the lowest fracture Kds , and the lowest diffusion coefficients. U and Np have very similar transport properties, so the differences in their BTCs are primarily due to differences in source inventory. Because the BTCs are plotted in log space, U often appears to have significantly early arrivals. However, the differences are actually just shifts caused by the significantly greater U inventory (see Chapter 6).

Sr differs from U and Np in that it has larger matrix Kds and undergoes no carbonate complexation. Both of these factors reduce its mobility. Therefore, Sr breakthrough at well ER-20-5 #3 and the NTS boundary are only simulated with the minimum transport parameter set in the sensitivity study. It never arrives at the upper well, ER-20-5 #1, in these simulations. No other RNs exhibit any breakthrough at the observation wells or the NTS boundary with the parameters considered in this study.

F.5.5 Colloid Transport of Other Radionuclides

It is worth restating that in these simulations, reactions between RNs other than Pu with colloids are not considered. However, the process of doing so, just as with Pu, is straightforward and requires only expected values and ranges for the rates of sorption and desorption of the actinides onto colloidal material. Others have made estimates of the potential for colloid-facilitated transport of other RNs using site-specific chemistry and colloid concentrations (Contardi et al., 2001). Using equilibrium chemical relationships, they compute reduced retardation factors caused by competition colloid sorption sites present to RNs that would otherwise sorb to immobile material. They conclude that weakly sorbing RNs such as U and Np are affected minimally by colloids, but that strongly sorbing RNs such as Am may be substantially affected.

F.6 Non-reactive Class I Species

Of the Class I RNs, ^3H , ^{14}C , ^{36}Cl , ^{99}Tc , and ^{129}I are considered here. ^{85}Kr is not considered because its source distribution is primarily in the gas phase (Pawloski et al., 2001). The source functions for these species differ from each other because of source-term inventory (Smith, 2001) and distribution between MG and cavity water. In Chapter 6, the source fluxes to the TSA and LAVA aquifers was computed for each of these RNs (Figures 6-33). Once these solutes enter the site-scale model domain, they only experience matrix diffusion and radioactive decay. Their transport is not tied to any of the reactive process discussed earlier for Pu, U, Np, and the immobile species. Thus, for all Class I RNs other than ^3H , the BTCs at downstream locations mirror the mass flux curves entering the system.

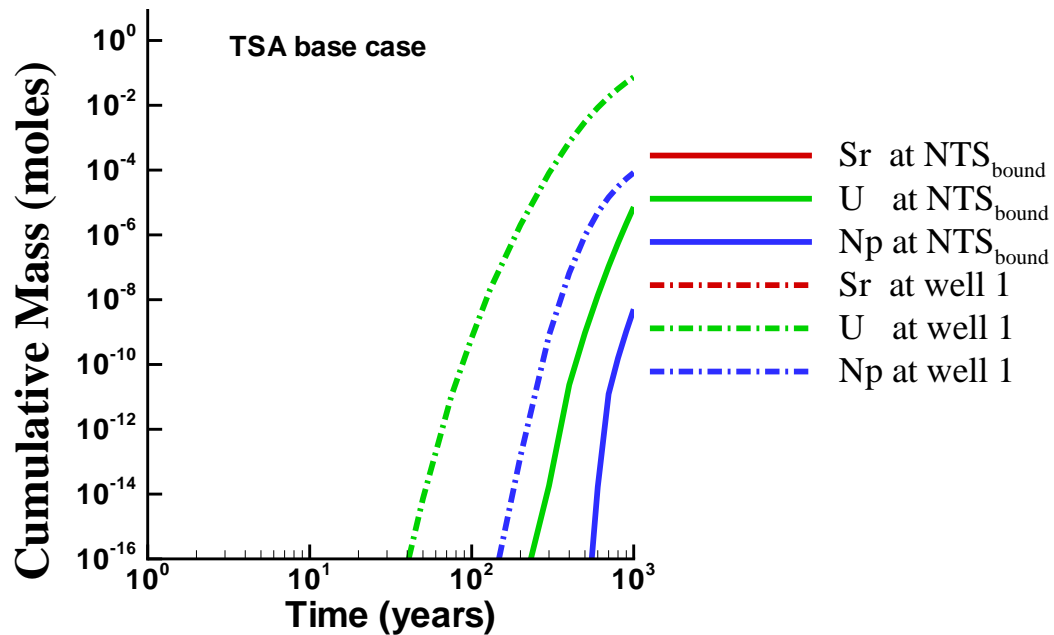


Figure F-14. U, Np, and Sr transport simulation results using **base-case** transport parameters for **TSA** source release. Cumulative total species mass arrivals at the NTS boundary (NTS_{bound}) and ER-20-5 #1 well are shown.

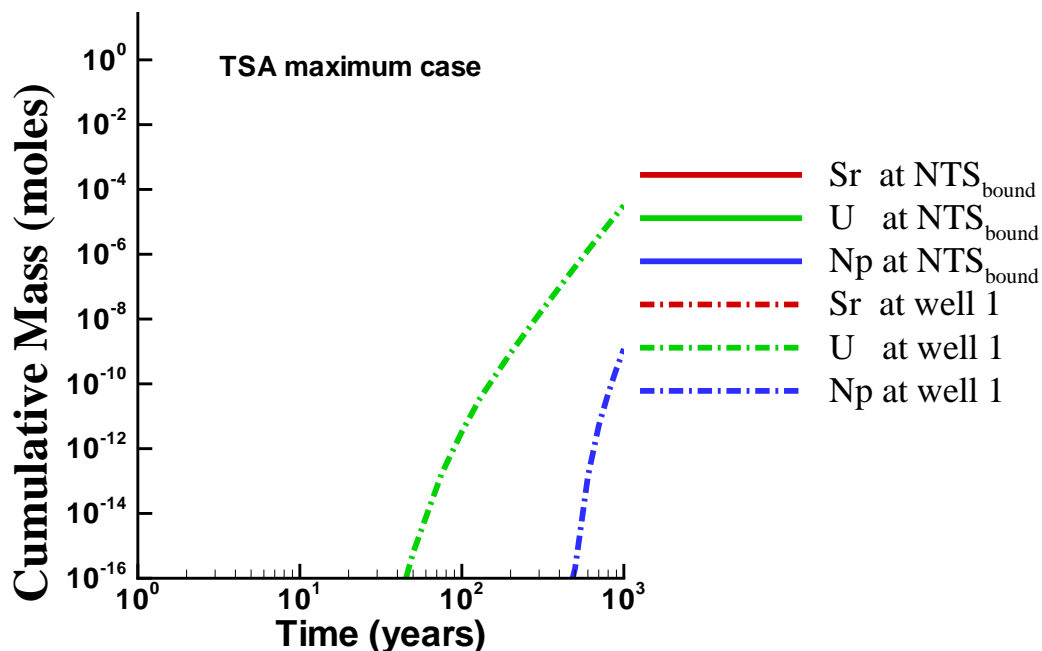


Figure F-15. U, Np, and Sr transport simulation results using **maximum-case (most retarding)** transport parameters for **TSA** source release. Shown are the cumulative total species mass arrivals at the NTS boundary (NTS_{bound}) and ER-20-5 #1 well.

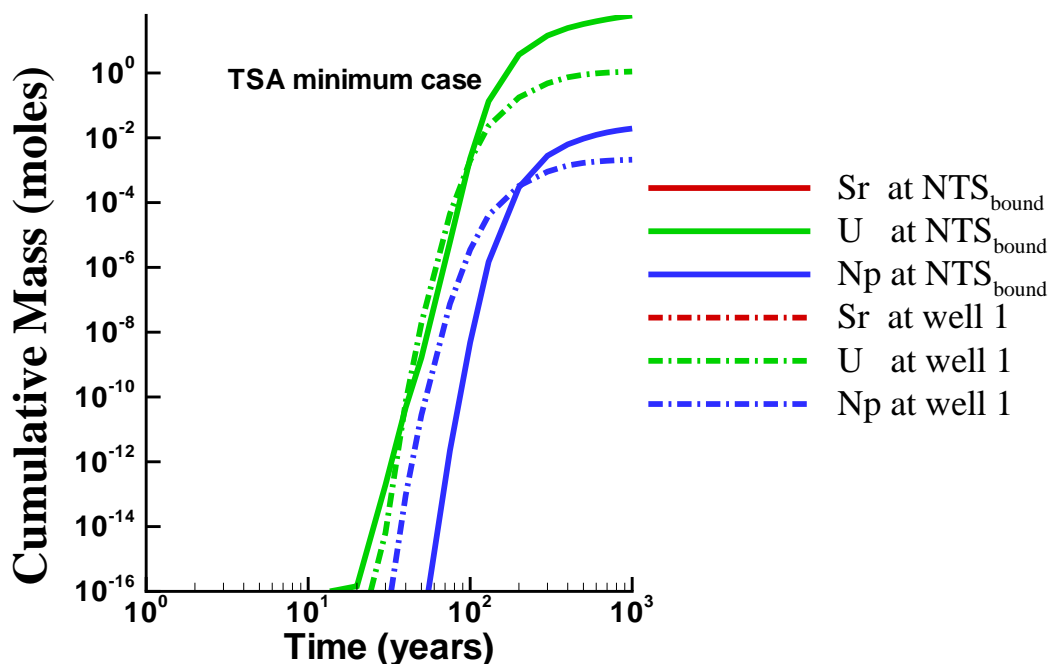


Figure F-16. U, Np, and Sr transport simulation results using **minimum-case (most retarding)** transport parameters for **TSA** source release. Shown are the cumulative total species mass arrivals at the NTS boundary (NTS_{bound}) and ER-20-5 #1 well.

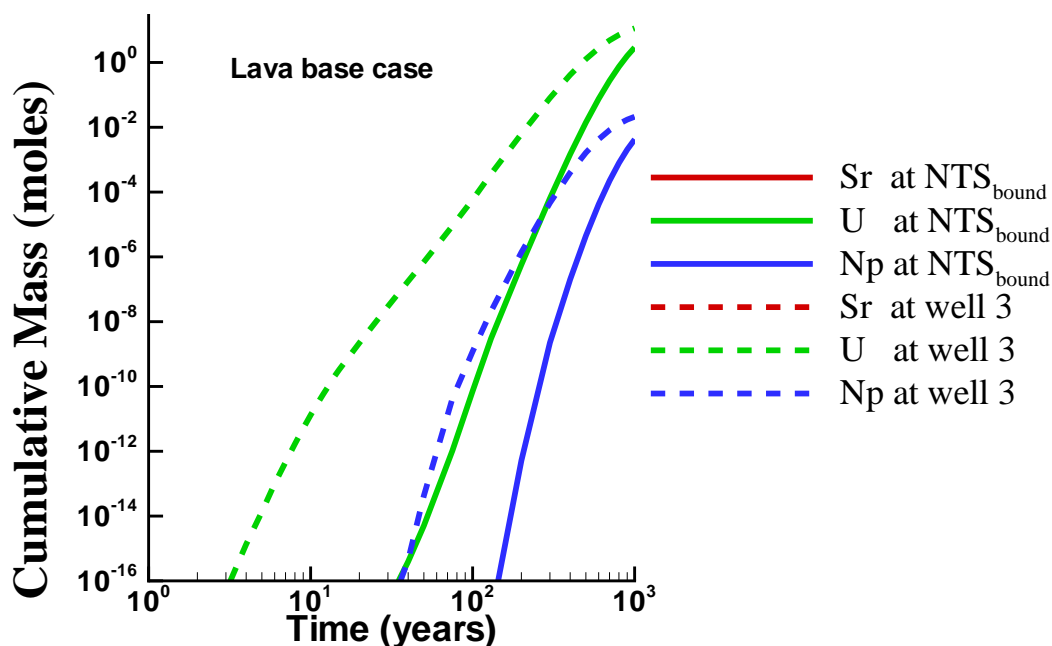


Figure F-17. U, Np, and Sr transport simulation results using **base-case** transport parameters for **LAVA** source release. Shown are the cumulative total species mass arrivals at the NTS boundary (NTS_{bound}) and ER-20-5 #3 well.

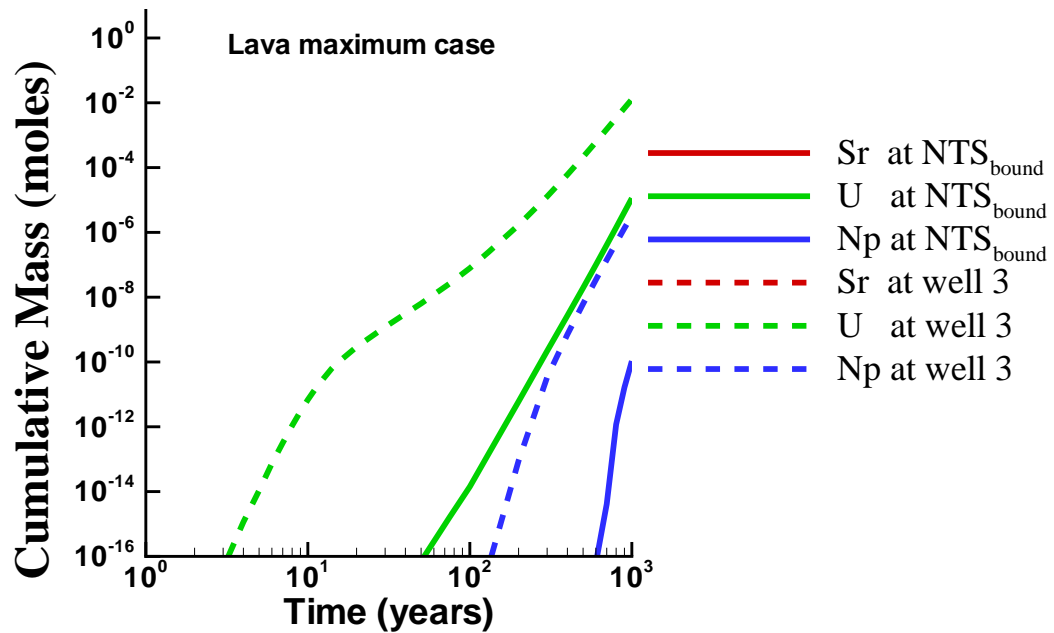


Figure F-18. U, Np, and Sr transport simulation results using **maximum-case (most retarding)** transport parameters for **LAVA** source release. Shown are the cumulative total species mass arrivals at the NTS boundary (NTS_{bound}) and ER-20-5 #3 well.

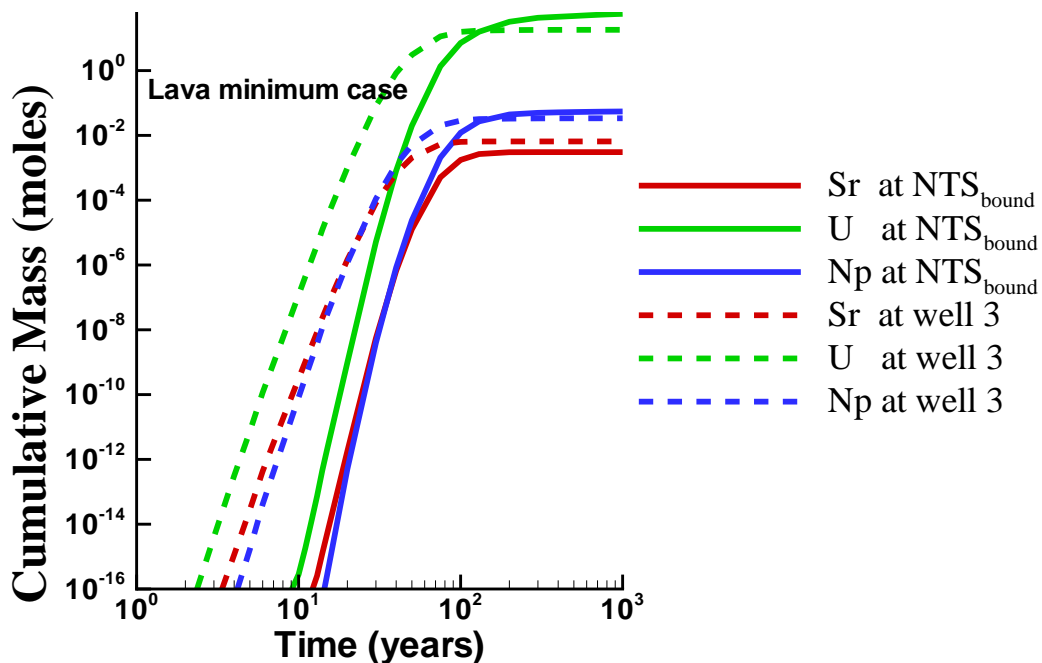


Figure F-19. U, Np, and Sr transport simulation results using **minimum-case (least retarding)** transport parameters for **LAVA** source release. Shown are the cumulative total species mass arrivals at the NTS boundary (NTS_{bound}) and ER-20-5 #3 well.

Figure F-20 shows the Class I RN BTCs at the NTS boundary for the TSA source release. In this calculation, base-case source term and transport parameters are applied. Although ^3H has the highest mass flux into the TSA aquifer (Figure 6-33), decay during transport in the site-scale model from BENHAM to the NTS boundary leads to significant mass reductions in this short-lived species. Figure F-21 shows the similar Class I RN BTCs at the NTS boundary for the LAVA source release. Due to a fracture-dominated path from the LAVA release, travel times to the NTS boundary are less, so arrival occurs more quickly. For this reason, less tritium decay occurs for these releases. However, tritium still emerges as the lowest cumulative mass contributor. Figure F-22 sums up the LAVA and TSA contributions to breakthrough at the NTS, showing that for these simulations, the LAVA is the predominant contributor.

Figure F-23 shows that there is very little sensitivity to the range of diffusion coefficients used in these simulations for ^{36}Cl . Due to the simplicity of the transport processes associated with Class I RNs, the results are nearly the same as those achieved with the particle-tracking model described in Chapter 7. Therefore, the remainder of the sensitivity study (which includes other sources) is presented in Chapter 7.

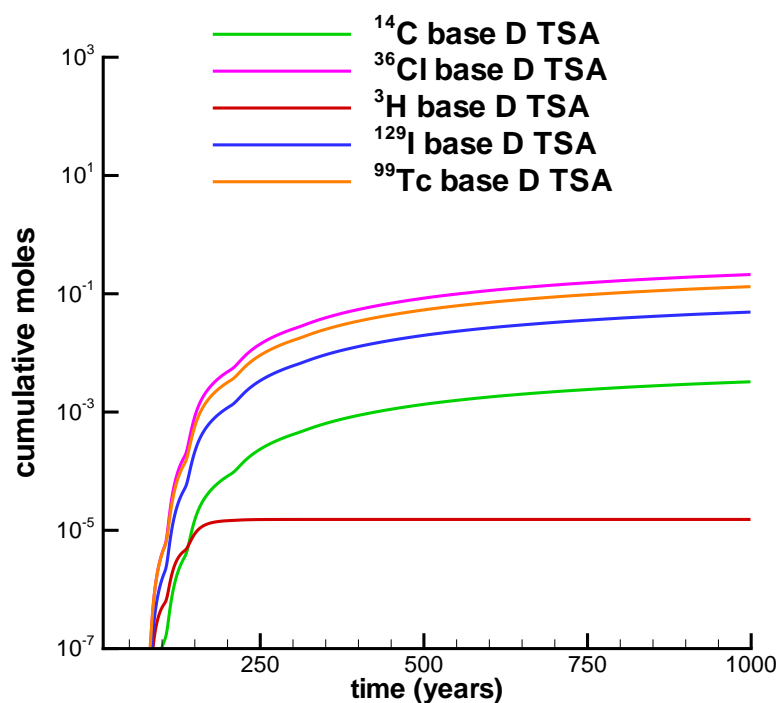


Figure F-20. Class I radionuclide breakthrough at the NTS boundary from the TSA source using base-case transport parameters.

F.7 Sensitivity Analysis

In the previous section, the figures highlight the resulting differences when transport parameters, within the range of uncertainty, favor retardation or maximum mobility of the RNs of

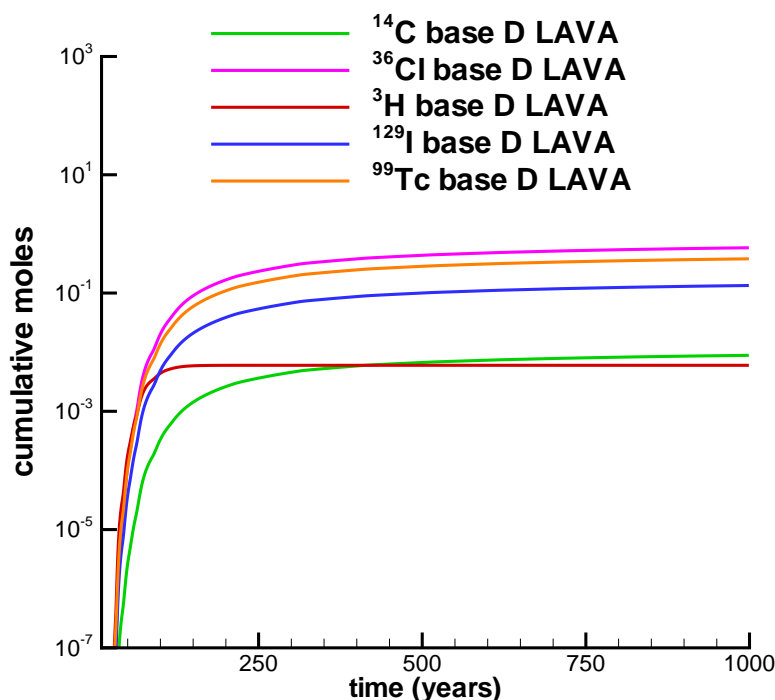


Figure F-21. Class I radionuclide breakthrough at the NTS boundary from the LAVA source using base-case transport parameters.

interest. However, a more detailed analysis presented here examines the sensitivity to several of the individual parameters, thus providing information that may serve to direct future data-collection activities. Starting with the base-case parameter values, each parameter was varied individually to its maximum and minimum value within the range of uncertainty presented earlier in this appendix. Transport simulations were conducted for each case and mass breakthrough at the ER-20-5 wells and NTS boundary were compiled. Each sensitivity transport simulation simulates the entire suite of source RNs along every pathline mapped out of the three-dimensional flow field. Thus, even for a single flow-field realization, these results constitute a large number of transport calculations.

Several different quantifiers can be used to assess the relative significance of each parameter change, two of which include the cumulative mass at a particular time and the actual time at which a specified cumulative mass has reached the boundary of interest. We present in this section results focusing on the cumulative mass at the NTS boundary at 1000 years (in Chapter 7, sensitivity analyses also consider other quantifiers). In the following discussion, the impact of uncertainty is presented as the cumulative number of moles reaching the NTS boundary for a given sensitivity simulation normalized to the result with base-case transport parameters. Thus, this ratio is known as an “impact ratio.”

For Pu transport, the parameters that were varied, the resulting cumulative mass at the NTS boundary, and the impact ratios are presented in Table F-23 for LAVA source releases and Table F-26 for TSA source releases. The numeric values of the parameter variations (min, base, and max) are given in the tables earlier in this appendix. The following points can be made about the sensitivity to the various parameters:

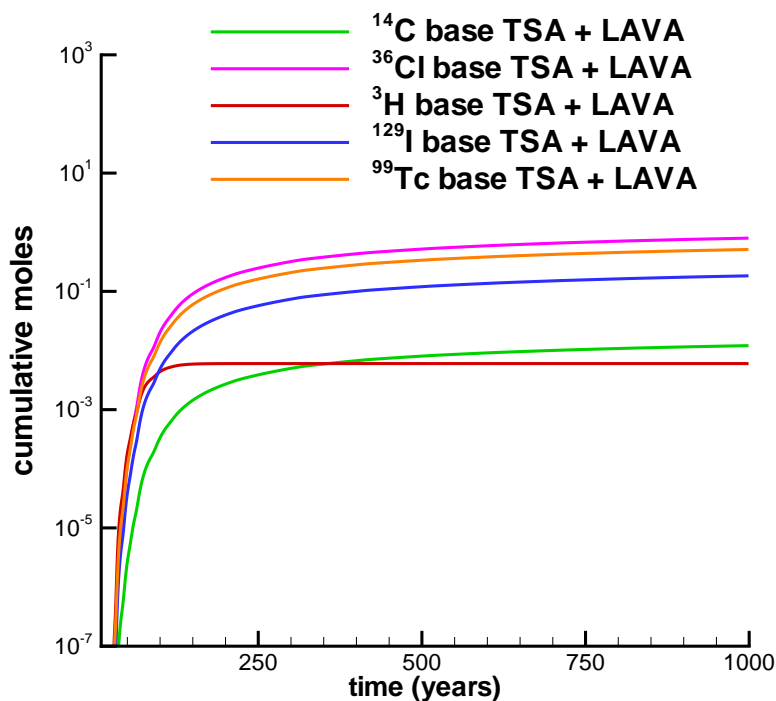


Figure F-22. Cumulative Class I radionuclide breakthrough at the NTS boundary from both LAVA and TSA sources using base-case transport parameters.

- Oxidation/reduction potential of the groundwater: For this sensitivity analysis, the pseudo equilibrium coefficient for PuO_2^+ and nonreactive Pu species was simply changed (from 5.4 at Eh = 550, Table F-3) to 3144 for Eh = 350 mV for the LAVA source release only because it is deeper (Table F-23). With this simple test, we did not allow the composition of reactive surface minerals or colloid species to change. Thus, this change resulted in significantly more non-reactive Pu species relative to the cation form. Although less colloid-facilitated transport occurs with this change, the only retarding mechanism operating on the non-reactive Pu species is diffusion, which does not prevent significantly more mass traveling to the NTS boundary in 1000 years.
- Colloid site concentration: Most calculations involving colloids in this appendix used a colloid site concentration of 6.29e-09 moles/l, the log average based on all samples. Due to the variability in measurements on field samples, we increase this value to the maximum site concentration computed on any sample to 6.2e-06 moles/l of reactive sites, based upon 7.86e10 colloids per ml, the maximum reported by Kung (2000). With this increase, significantly greater quantities of Pu are predicted to migrate to the NTS boundary in less than 1000 years.
- Reactive surface area of the fracture-coating minerals (reflected in fracture mineral K_d): A highly uncertain parameter, the surface area prescribes how many fracture coating minerals sites are actually accessible to solutes in the fluid. Significantly increasing this value effectively immobilizes the migration of Pu; significantly reducing it leads to large increases in the migration mass of Pu.

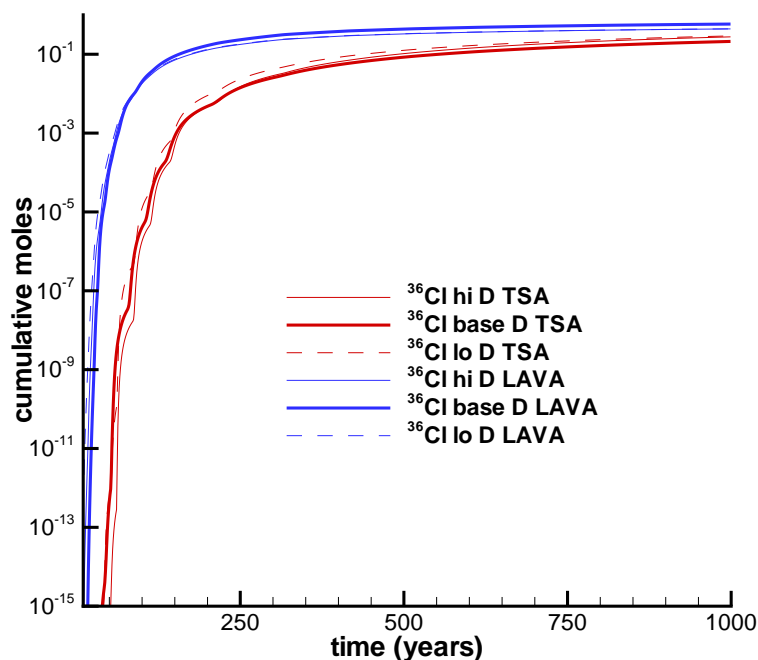


Figure F-23. Sensitivity of ^{36}Cl breakthrough at the NTS boundary to high- and low-diffusion coefficient.

- **Kinetic rates of sorption/desorption of Pu onto colloids:** A fairly large range of values for the kinetic rates associated with this reaction are used in the sensitivity study. This parameter is particularly important because rates measured in laboratory batch experiments (relatively short time scale) lead to very little Pu migration. However, model matches to flowing column experimental data indicate only the minimum k_f rate and the maximum k_r rate. Most important in these field-scale predictions is the minimum k_r . Additionally, recent preliminary results (Kersting and Reimus, 2002) indicate lower k_r values for Pu and zeolite colloids than those reported in this chapter for clay and silica colloids.
- **Matrix K_d :** Although the YMP has compiled an extensive database of matrix K_d values for various RNs on various rock types, the range in uncertainty still significantly impacts predictions such as this.
- **Diffusion coefficient:** For 1000-year simulations, this parameter does not appear to be as significant of a parameter as the others in this study. One reason for this low impact is that the the range of diffusion uncertainty considered is small. If higher and lower diffusion coefficients were included, which are cited in studies other than the one that was used here (Reimus et al., 2002), then impact ratios would go up.
- **Fracture mineral composition:** Changing the distribution of $>\text{FeOH}$, $>\text{Ca}^{2+}$, $>\text{AlOH}$, and $>\text{SiOH}$ (as outlined in Tables F-4 through F-7) has very little impact on Pu migration. The differences in the effective retardation factors associated with different distributions of

minerals is very small relative to the impacts of other uncertain parameters.

The impact ratios reported here must be considered with respect to the ranges in parameter uncertainty utilized. For example, the range in our uncertainty on fracture mineral reactive surface area leads to enormous impact ratios. However, we have very little basis with which to bound the range in uncertainty. Measurements on fracture mineral coatings have tended to focus more on the distribution of minerals in the coating rather than the exposure of those minerals to fluid flowing in the fracture. This analysis shows very little sensitivity to the distribution of the different minerals in the coating ensemble.

U and Np parameter sensitivities are considered in much the same fashion as the Pu parameters, with the exception that colloid-facilitated transport is not considered for these actinides. Tables F-24 and F-25 show the parameters that were varied and results for LAVA releases and Tables F-27 and F-28 show the parameters that were varied and results for TSA releases. Fracture mineral reactive surface area (affecting fracture Kd) and matrix Kd top the list of parameters for which the range of uncertainty leads to large variations in the total mass of RN transported to the NTS boundary. The diffusion coefficient again has a minor impact and the fracture mineral speciation (also affecting fracture Kd) again has little impact.

A second look at diffusion

The sensitivity to diffusion coefficients appears to be quite small for 1000 year simulations. However, the diffusion coefficient does impact the migration rate of the plume moving away from BENHAM. A second look at this parameter sheds some light on its impact. Table F-29 shows the impact ratios to the diffusion coefficient at 30 years and 100 years. These results show that the diffusion coefficient significantly affects how early U and Np arrives at the NTS boundary in the LAVA. Therefore, for shorter time considerations, as also shown in the column experiment model in Appendix D, diffusion is in fact a significant parameter in uncertainty assessments.

Table F-23. Plutonium Transport Parameter Sensitivity for Lava Source Release

Sensitivity based on cumulative moles crossing NTS boundary after 1000 years

	Plutonium (Minimum Parameter)		Plutonium (Maximum Parameter)	
	Cumulative Moles	Impact Ratio (Normalized to Base Case)	Cumulative Moles	Impact Ratio (Normalized to Base Case)
Base Case	1.63E-05	1.00	1.63E-05	1.00
Colloid Filtration Rate	1.74E-05	1.07	1.35E-05	0.82
Pu-Col Filtration Rate	1.77E-05	1.09	7.86E-06	0.48
Pu-Col Sorption Rate	1.98E-03	121.15	2.22E-19	0.000
Diffusion Coefficient	3.57E-05	2.19	8.83E-06	0.54
Fracture Mineral Composition ¹	1.63E-05	1.00	1.57E-05	0.96
Fracture Mineral Kd ²	7.45E-02	4569.75	1.04E-16	0.00
Matrix Kd	5.60E-04	34.35	9.40E-06	0.58
Colloid Concentration ³	6.33E-01	38808.34	NA	NA
Eh Reduction to 350 mV ⁴	5.38E-01	32985.90	NA	NA
<p>1 - Varying only the distributions of >FeOH, >Ca²⁺, >SiOH, and >AlOH; Pcov%*Pexp% = 0.5</p> <p>2 - Varying Pcov%*Pexp% (min = 0.001, max = 0.5)</p> <p>3 - Increased for 7.86e10 particles/ml--the maximum measured by Kung (2000)</p> <p>4 - Only reduced from 550 mV to 350 to examine impacts of more reducing conditions</p>				

Table F-24. Uranium Transport Parameter Sensitivity for Lava Source Release
Sensitivity based on cumulative moles crossing NTS boundary after 1000 years

	Uranium (Minimum Parameter)		Uranium (Maximum Parameter)	
	Cumulative Moles	Impact Ratio (Normalized to Base Case)	Cumulative Moles	Impact Ratio (Normalized to Base Case)
Base Case	2.92	1.00	2.92	1.000
Diffusion Coefficient	3.15	1.08	0.46	.16
Fracture Mineral Speciation ¹	2.93	1.00	0.52	0.18
Fracture Mineral K_d ²	29.40	10.01	1.11E-05	0.00
Matrix K_d	6.30	2.15	1.06E-05	0.00
1 - Varying only the distributions of >FeOH, >Ca ²⁺ , >SiOH, and >AlOH; Pcov%*Pexp% = 0.5				
2 - Varying Pcov%*Pexp% (min = 0.001, max = 0.5)				

Table F-25. Neptunium Transport Parameter Sensitivity for Lava Source Release
Sensitivity based on cumulative moles crossing NTS boundary after 1000 years

	Neptunium (Minimum Parameter)		Neptunium (Maximum Parameter)	
	Cumulative Moles	Impact Ratio (Normalized to Base Case)	Cumulative Moles	Impact Ratio (Normalized to Base Case)
Base Case	4.26E-03	1.00	4.26E-03	1.000
Diffusion Coefficient	4.66E-03	1.09	3.71E-03	0.871
Fracture Mineral Speciation ¹	4.27E-03	1.00	4.25E-03	0.998
Fracture Mineral K_d ²	5.49E-02	12.90	8.87E-11	0.000
Matrix K_d	1.06E-02	2.49	8.12E-10	0.000
1 - Varying only the distributions of >FeOH, >Ca ²⁺ , >SiOH, and >AlOH; Pcov%*Pexp% = 0.5				
2 - Varying Pcov%*Pexp% (min = 0.001, max = 0.5)				

Table F-26. Plutonium Transport Parameter Sensitivity for TSA Source Release

Sensitivity based on cumulative moles crossing NTS boundary after 1000 years

	Plutonium (Minimum Parameter)		Plutonium (Maximum Parameter)	
	Cumulative Moles	Impact Ratio (Normalized to Base Case)	Cumulative Moles	Impact Ratio (Normalized to Base Case)
Base Case	4.53E-08	1.00	4.53E-08	1.00
Colloid Filtration Rate	4.63E-08	1.02	4.25E-08	0.94
PuCol Filtration Rate	4.79E-08	1.06	4.39E-08	0.97
Pu-Col Sorption Rate	1.16E-03	25519.34	2.80E-21	0.000
Diffusion Coefficient	7.34E-07	16.18	2.48E-08	0.55
Fracture Mineral Speciation ¹	4.55E-08	1.00	4.51E-08	1.00
Fracture Mineral K_d ²	1.41E-01	3109717.37	1.04E-16	0.00
Matrix K_d	6.65E-07	14.67	1.51E-08	0.33
Colloid Concentration ³	1.11	2.45E+07	NA	NA
<p>1 - Varying only the distributions of >FeOH, >Ca²⁺, >SiOH, and >AlOH; Pcov%*Pexp% = 0.5</p> <p>2 - Varying Pcov%*Pexp% (min = 0.001, max = 0.5)</p> <p>3 - Increased for 7.86e110 particles/ml--the maximum measured by Kung (2000)</p>				

Table F-27. Uranium Transport Parameter Sensitivity for TSA Source Release

Sensitivity based on cumulative moles crossing NTS boundary after 1000 years

	Uranium (Minimum Parameter)		Uranium (Maximum Parameter)x	
	Cumulative Moles	Impact Ratio (Normalized to Base Case)	Cumulative Moles	Impact Ratio (Normalized to Base Case)
Base Case	7.25E-06	1.00	7.25E-06	1.00
Diffusion Coefficient	1.50E-03	206.99	1.92E-10	0.00
Fracture Mineral Speciation ¹	7.26E-06	1.00	7.2E-06	1.00
Fracture Mineral K_d ²	5.93E+01	8187685.38	4.26E-18	0.00
Matrix K_d	4.15E-01	57271.82	3.55E-13	0.00
<p>1 - Varying only the distributions of >FeOH, >Ca²⁺, >SiOH, and >AlOH; Pcov%*Pexp% = 0.5</p> <p>2 - Varying Pcov%*Pexp% (min = 0.001, max = 0.5)</p>				

Table F-28. Neptunium Transport Parameter Sensitivity for TSA Source Release

Sensitivity based on cumulative moles crossing NTS boundary after 1000 years

	Neptunium (Minimum Parameter)		Neptunium (Maximum Parameter)	
	Cumulative Moles	Impact Ratio (Normalized to Base Case)	Cumulative Moles	Impact Ratio (Normalized to Base Case)
Base Case	5.06E-09	1.00	5.06E-09	1.00
Diffusion Coefficient	2.30E-06	454.10	4.84E-22	0.00
Fracture Mineral Speciation ¹	5.14E-09	1.02	4.90E-09	0.97
Fracture Mineral K_d ²	1.94E-02	3828703.91	3.46E-20	0.00
Matrix K_d	5.72E-04	113017.83	5.51E-22	0.00
1 - Varying only the distributions of >FeOH, >Ca ²⁺ , >SiOH, and >AlOH; Pcov%*Pexp% = 0.5				
2 - Varying Pcov%*Pexp% (min = 0.001, max = 0.5)				

Table F-29. Sensitivity to Diffusion at 30 and 100 Years

NBT stands for no breakthrough at this time

Time (years)	Radionuclide and Source Location	Cumulative Moles - Base Parameters	Diffusion (Minimum Parameter)		Diffusion (Maximum Parameter)	
			Cumulative Moles	Impact Ratio (Normalized to Base Case)	Cumulative Moles	Impact Ratio (Normalized to Base Case)
LAVA						
30	Pu: LAVA	4.09E-07	5.16E-07	1.26	3.20E-07	0.78
30	U: LAVA	NBT	1.59E-13	HUGE	NBT	NA
30	NP: LAVA	NBT	1.13E-11	HUGE	NBT	NA
100	Pu: LAVA	2.88E-06	4.55E-06	1.54	1.91E-06	0.66
100	U: LAVA	4.06E-10	6.30E-06	15488.92	1.36E-16	0.00
100	NP: LAVA	NBT	5.11E-06	HUGE	8.16E-26	NA
TSA						
30	Pu: TSA	3.40E-12	8.35E-12	2.45	2.77E-12	0.81
30	U: TSA	NBT	NBT	NA	NBT	NA
30	NP: TSA	NBT	NBT	NA	NBT	NA
100	Pu: TSA	6.38E-09	2.23E-08	3.49	5.27E-09	0.83
100	U: TSA	NBT	NBT	NA	NBT	NA
100	NP: TSA	NBT	NBT	NA	NBT	NA

F.8 Summary

In this appendix, we discussed how a reactive, dual-porosity transport model for RN migration in fractured and unfractured rock was developed and applied at the site scale of BENHAM and TYBO. Building upon the colloid-facilitated Pu transport model developed and tested in Appendix D, additional RNs were incorporated and the model was applied to a complex three-dimensional heterogeneous flow field. Preparation of the model involved developing uncertain ranges for physical and chemical transport parameters. These parameter ranges were systematically analyzed in a detailed sensitivity analysis. The importance of the sensitivity analysis is highlighted in the differences in simulation results as parameters are varied throughout their ranges of uncertainty. Thus, it is extremely important to note that although expected values exist for some of the parameters, the ranges of uncertainty do not indicate substantial decreasing probability. In other words, we have no basis upon which to rule out the results obtained with parameters extended to their upper and lower ranges of uncertainty. The implications of the sensitivity analysis are more important than any single predictive simulation. From the sensitivity analysis, we draw the following conclusions:

- With base-case transport parameters, predictive results for heterogeneous flow-field realization #3 are consistent with field observations in the LAVA. Namely, colloid-facilitated Pu migration to observation well ER-20-5 #3 is feasible in less than 30 years. However, such migration to well ER-20-5 #1 was not simulated for two reasons. First, the heterogeneous flow field (#3) on which these calculations were conducted yields very few streamtubes to the capture zone of well ER-20-5 #1. Second, even though the LAVA is maintained as an intact lithologic unit in the heterogeneous attribute maps, the TSA is not. Therefore, any streamtube leaving the TSA source location of the BENHAM chimney does not stay in welded tuff. Most pathlines move into either bedded tuff or non-welded tuff, both of which have slow velocities (matrix flow only) and high retardation.
- With changes in transport parameter values to favor mobility of reactive solutes, some Pu arrives at well ER-20-5 #1, but more than 50 years later. As described above, the pathways away from the TSA source in this heterogeneous flow field are not supported in fractured welded tuff, as would be expected in the deterministic model (examined in greater detail in Chapter 7).
- The sensitivity study shows substantial variation in results to uncertainty in parameters. The most significant are the Eh of the groundwater, the colloid site concentration, and the reactive surface area of fracture minerals.
- The kinetic rates of sorption and desorption of Pu onto colloids are significant. However, the sensitivity to this parameter is due, in part, to a specified large range. If ongoing experiments measuring such rates continue and field studies are conducted to determine scaling parameters between the lab and field, then a much tighter bound can be established on this currently large range. If the exact values derived from a single experiment are used, with no consideration for scaling between the laboratory and the field, then no significant Pu migration would be predicted with this model.
- Large ranges in matrix Kd lead to large impacts in the sensitivity analysis. In this study, minimum, maximum, and expected values of Kd for the different rock types and RNs were used. If the existing Kd databases will support such analysis, development of probability distribution functions for Kds and implementing them into the predictive modeling may help reduce the large impact on the sensitivity analysis associated with this parameter. This may also suggest that more sophisticated geochemical characterization and modeling are warranted to link matrix material reactivity to mineralogic characterization and spatial distributions. However, such models require information (such as mineralogic composition) that often is not available with Kds as historically measured.
- For simulation of cumulative mass arrivals at the NTS boundary over 1000 years, there was no significant sensitivity to the diffusion coefficient. An UGTA database with relatively small differences between maximum and minimum values was used to define the range for this modeling effort. However, investigation of sensitivity to diffusion coefficients at earlier times indicates that it does play a significant role in controlling the travel time of reactive solutes.

- This study presented in this appendix did not consider multiple heterogeneous flow fields nor the deterministic flow field. Such sensitivities are addressed in Chapter 7. Chapter 7 analyses indicate that of the 30 realizations 10 may support rapid migration to ER-20-5 #1 from BENHAM. Therefore, the conclusions drawn in this appendix are not representative of each realization.

F.9 References

- Contardi, J.S., D.R. Turner, and T.M. Ahn, 2001. Modeling colloid transport for performance assessment, *Journal of Contaminant Hydrology*, 47(2001), 323-333.
- CRWMS M&O, 2000c. Uncertainty distribution for stochastic parameters. Yucca Mountain Analysis and Model Report, ANL-NBS-MD-000011, Rev 0.0, www.ymp.gov/documents/amr/index.html (<http://www.ymp.gov/documents/amr/22749/22749.pdf>; accessed May 2001, confirmed July 2002).
- CRWMS M&O, 2000f. Probability distribution for flowing interval spacing. Yucca Mountain Analysis and Model Report, TDR-NBS-HS-000003, Rev 0.0, www.ymp.gov/documents/amr/index.html (<http://www.ymp.gov/documents/amr/22281/22281.pdf>; accessed May 2001, confirmed July 2002).
- CRWMS M&O, 2000g. Unsaturated zone and saturated zone transport parameters. Yucca Mountain Analysis and Model Report, ANL-NBS-HS-00019, Rev 0.0, www.ymp.gov/documents/amr/index.html (<http://www.ymp.gov/documents/amr/u0100/u0100.pdf>; accessed May 2001, confirmed July 2002).
- Drellack, S.L., L.B. Prothro, K.E. Robertson, B.A. Schier, and E.H. Price, 1997. Analysis of fractures in volcanic cores from Pahute mesa, Nevada Test Site. Report to U.S. Department of Energy, Nevada Operations Office, DOE/NV/11718-160.
- Ginn, T.R., 2001. Stochastic-convective transport with nonlinear reactions and mixing: finite streamtube ensemble formulations for multicomponent reactions systems with intra-streamtube dispersion, *Journal of Contaminant Hydrology*, 47(2001), 1-28.
- IT Corporation, 1996. Underground Test Area fracture analysis report: Analysis of fractures in volcanic cores from Pahute Mesa. U.S. Department of Energy draft report.
- IT Corporation, 1998. Report and analysis of the BULLION forced gradient experiment, technical report DOE/NV/13052-042; ITLV/13052-042.
- Kersting, A.B., D.W. Efurud, D.L. Finnegan, D.J. Rokop, D.K. Smith and J.L. Thompson, 1999. Migration of plutonium in groundwater at the Nevada Test Site, *Nature*, 397.
- Kung, S., 2000. Colloid size and colloid concentration data of groundwater samples from the NTS 04/30/1998 to 10/21/1998. Yucca Mountain Project DTN: LA0002SK831352.004, Yucca Mountain Project, Las Vegas, NV.

- Pawloski, G.A., A.F.B. Tompson, and S.F. Carle (eds.), 2001. Evaluation of the hydrologic source term from underground nuclear tests on Pahute Mesa at the Nevada Test Site: The CHESHIRE test, Technical Report UCRL-ID-147023, Lawrence Livermore National Laboratory, Livermore, CA.
- Reimus, P.W., A. Adams, M.J. Haga, A. Humphrey, T. Callahan, I. Anghel, and D. Counce, 1999b. Results and Interpretation of Hydraulic and Tracer Testing in the Prow Pass Tuff at the C-holes, Yucca Mountain Site Characterization Project Milestone Report SP32E7M4, Los Alamos National Laboratory, Los Alamos, NM.
- Reimus P.W., S.D. Ware, N. Lu, A.A. Fattah, K.S. Kunk, and M.P. Neu, 2001. FY2001 Progress report on colloid-facilitated plutonium transport in fractured rocks from Pahute Mesa, Nevada Test Site, NTS-UGTA progress report, Los Alamos National Laboratory, Los Alamos, NM.
- Reimus P.W., S.D. Ware, F.C. Benedict, R.G. Warren, A. Humphrey, A. Adams, B. Wilson, and D. Gonzales, 2002. Diffusive and Advective transport of ^3H , ^{14}C , and ^{99}Tc in saturated fractured volcanic rocks from Pahute Mesa, Nevada, Technical Report LA-13891-MS, Los Alamos National Laboratory, Los Alamos, NM.
- Smith, D.K., 2001. Unclassified radiologic source term for Nevada Test Site Areas 19 and 20, Technical Report UCRL-ID-141706, Lawrence Livermore National Laboratory, Livermore, CA.
- Tompson, A.F.B., C.J. Bruton, and G.A. Pawloski, 1999. Evaluation of the hydrologic source term from underground nuclear tests in Frenchman Flat at the Nevada Test Site: The CAMBRIC Test, Report UCRL-ID-132300, Lawrence Livermore National Laboratory, Livermore, CA.
- Triay, I.R., A. Meijer, J.L. Conca, K.S. Kung, R.S. Rundberg, B.A. Strietelmeier, C.D. Tait, D.L. Clark, M.P. Neu, D.E. Hobart, 1997. Summary and synthesis report on radionuclide retardation for the Yucca mountain site characterization project, LA-13262-MS, UC903 and UC-940, Los Alamos National Laboratory, Los Alamos, NM.
- Viswanathan, H.S., 1999. Multicomponent transport in unsaturated groundwater systems, Ph.D dissertation, University of Illinois, Urbana-Champaign, IL.
- Viswanathan, H.S., B.A. Robinson, A.J. Valocchi, and I.R. Triay, 1998. A reactive transport model of neptunium migration from the potential repository at Yucca Mountain, *Journal of Hydrology*, 209, 251-280.
- Warren, R., 2000. Data from southwestern Nevada volcanic field, URL location <http://queeg.ngdc.noaa.gov/seg/geochem/swnvf/> (URL confirmed July 2002).

Appendix G: Personal Communication Regarding Development of Geostatistical Attribute Maps at DRI

Craig Shirley - DRI

G.1 Introduction

This project by the Desert Research Institute entails estimating the distribution in three-dimensional space of properties or attributes important to modeling groundwater flow and radionuclide transport. The study area as shown in Figure 1 and Figure 2 is a rectangle 2600 meters east to west by 3200 meters north to south. The study domain covered the vertical distance from 2 meters to 1332 meters above sea level. The five attributes initially considered for estimation were hydraulic conductivity, porosity, clay abundance, zeolite abundance and iron oxide abundance. The distributions were to be estimated using existing measurements, information about the general geologic setting and secondary information such as geophysical logs. No sampling specifically in support of this characterization was undertaken. Iron oxide was dropped from the project due to the extreme paucity of measurements. The maps produced were dimensioned to allow use in a larger flow and transport study being undertaken by Los Alamos National Laboratory.

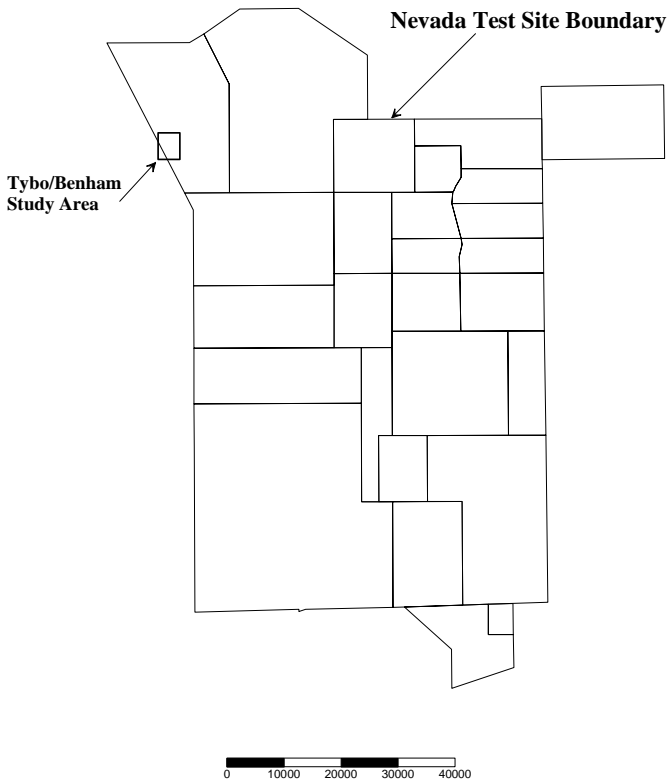


Figure 1. Location map

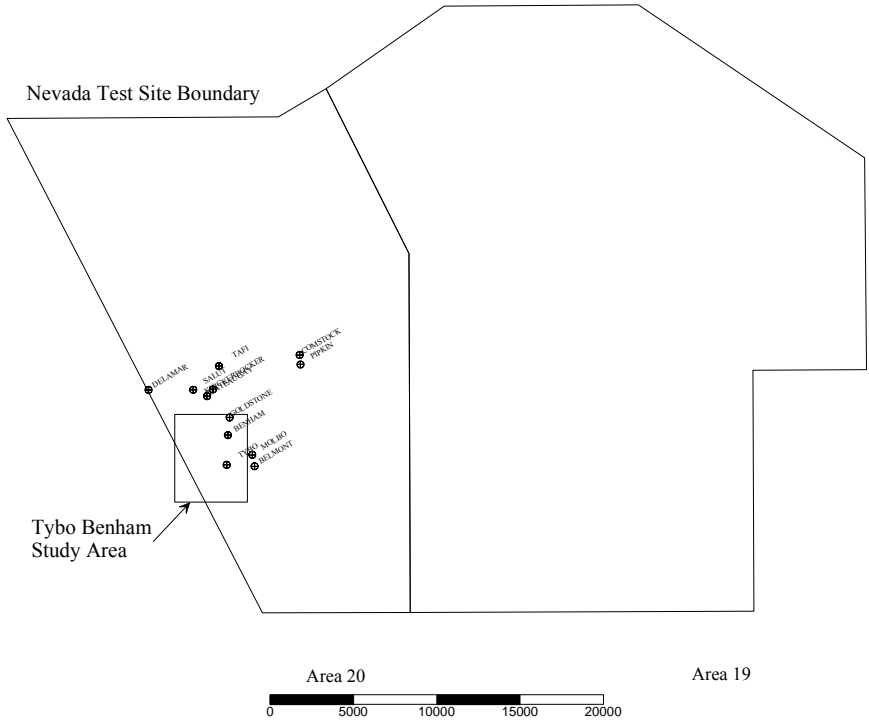


Figure 2. Study area and proximate tests.

G.2 Background Information

As listed in Table 1 and shown in Figure 3, twelve underground tests have been conducted between 1963 and 1984 within 5 kilometers of the TYBO/BENHAM study area. Most of these tests have been near or below the published static water level.

Table 1 Nuclear Tests with a 5-kilometer distance of the TYBO/BENHAM Study area

Test	East UTM (meters)	North UTM (meters)	Elevation at surface	Elevation at test	Depth of Burial	Static Water Level
BELMONT	547684.52	4119430.94	1897.68	1292.68	605.00	613.0
BENHAM	546618.29	4120674.84	1914.45	512.36	1402.08	641.0
CHATEAUGAY	545785.96	4122227.15	1903.47	1296.24	607.23	632.0
COMSTOCK	549482.20	4123870.62	1987.29	1366.99	620.30	626.0
DELAMAR	543453.51	4122478.01	1901.95	1357.85	544.10	617.5
GOLDSTONE	546687.61	4121377.26	1913.53	1364.53	549.00	596.0
KNICKERBOCKER	546022.25	4122498.18	1905.61	1274.98	630.63	632.0
MOLBO	547591.74	4119887.29	1900.12	1262.12	638.00	614.0
PIPKIN	549514.34	4123491.31	1991.56	1367.94	623.62	640.0
SALUT	545234.88	4122484.00	1900.43	1292.43	608.00	622.0
TAFI	546263.17	4123429.23	1886.10	1206.10	680.00	607.0
TYBO	546571.06	4119488.03	1906.83	1141.83	765.00	630.0

Both the TYBO and BENHAM, as shown in Figure 3, were more deeply buried and at a lower elevation than many of the other tests which took place in western Pahute Mesa.

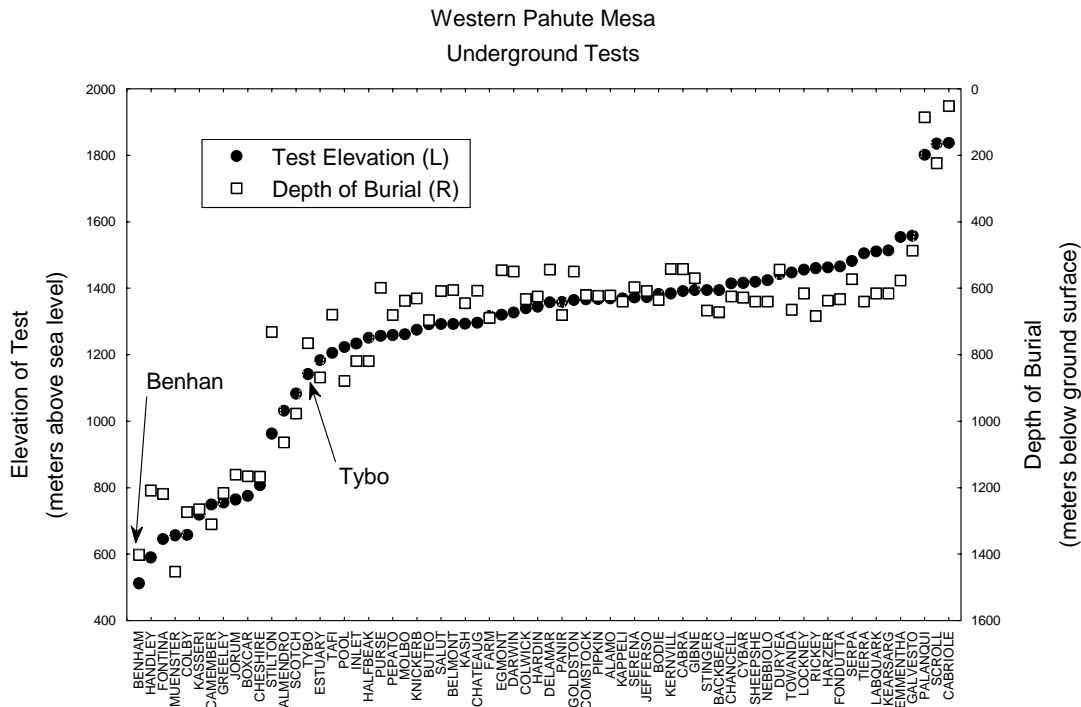


Figure 3. Underground tests at Pahute Mesa

The geology of the TYBO/BENHAM area is characterized by numerous air fall and ash flow tuffs, lava flows, breccias and alteration products of these volcanic materials. A detailed description of the study area geology can be found in Prothro and Warren, 1999. These materials occur in thin beds ranging from centimeters to hundreds of meters in thickness. Traditional efforts at inter-borehole correlation based upon field observable characteristics have generally proven unsatisfactory. Lithostratigraphic units have been identified but are commonly comprised of numerous textural classes which may profoundly affect flow and transport. Identification by means of chemical composition has shed considerable light upon the origin of these volcanic materials. The geologic description in Prothro and Warren, 1999 was used in conjunction with Drellack and Prothro, 1997 and computer files of the hydrogeologic model (Sully, 1999) as the deterministic zoned model in this study.

G.2.1 Approaches to Modeling

There are two basic approaches to the development of geologic and hydrogeologic models, the traditional deterministic model consisting of layers and the geostatistical or stochastic approach, which treats the distribution of material properties as random fields. Applicability, weakness, and benefits of these two basic approaches remain active topics

of discussion in the research literature as shown by the two following quotes from a recent journal.

“Zonation has been, and we think will continue to be, a very useful tool in some circumstances, especially when distinct geologic contacts exist, dominate the subsurface hydrology, and are characterized.” (Cooley and Hill, 2000)

If a zone could be identified with a lithology, this [grouping of hydraulic conductivities into 9 zones] might have been a defensible approach, but given the arbitrary uniform mesh discretization that was used, a “zone” is a complex assemblage of different lithologies of the very complex Yucca Mountain system. When the role of faults, the variability of facies, the depth of each layer is so variable, this arbitrary calibration constraint by zoning does not have any physical sense. (RamaRao *et al.*, 2000)

In a complex geologic setting, such as the TYBO/BENHAM study area, where there was substantial preexisting topographic relief, multiple eruptive events and sources, contemporaneous erosion activity, faulting, both during and subsequent to deposition, and alteration both during and subsequent to deposition, it is highly unlikely that homogeneous, continuous layers are adequate to accurate characterization of the hydrogeology.

The term deterministic zonation will be used in this paper to mean traditional, lithostratigraphically based layered models where discrete layers are defined by fixed surfaces and homogeneity of attribute values within the layers. Geostatistical fields are produced using a space-filling simulation that adheres to a statistical description of the attribute. The maps produced in this project use a combination of these two approaches to yield zoned geostatistical simulations of the spatial distribution of attributes.

G.2.2 Deterministic Zonation

Description

The traditional approach builds a layered model with each layer having known upper and lower boundaries and assigned a value for the attribute of interest. Sources of information that can be included in this type of model include borehole contacts, data from both surface and borehole geophysical surveys, surface geologic mapping and fault identification from aerial photos. Many of the techniques developed by geologists and hydrologists can and are used in developing models in this fashion.

Benefits

The benefits of this method include incorporation of expert opinion and knowledge, and accurate characterization of abrupt discontinuities such as faults. Where the geometry of lithostratigraphic layers is distinct and is known to be, or can be strongly inferred to be

critical to control of flow and transport, then this method may be preferred. In areas where relevant measurements are missing, sparse or biased, reliance on expert knowledge of the region and its geologic and hydrologic peculiarities may be the only means to develop a model.

Weaknesses

The disadvantages of this method include a false sense of certainty regarding the location of contacts and a tendency to lump dissimilar facies together to produce a horizontally continuous layer or zone, i.e., unrealistic assumption of homogeneity. Additionally in a volcanic setting such as the TYBO/BENHAM study area, the layers maybe made coincident with lithostratigraphic units, resulting in a tendency to separate texturally similar materials, if these are from differing eruptive sources.

This approach fails to address uncertainty in the spatial distribution of attributes in two ways, the contacts between layers are fixed at all points in the model, not just where data exist, and there is no spatial correlation of attributes within layers. The assumption that the location of the boundary dividing significantly different media is known equally well at boreholes and at great distances from those boreholes is difficult to support.

G.2.3 Geostatistical Fields

Description

In the geostatistical approach, the distribution in space of attributes such as permeability and porosity are considered to be random fields. These fields are generally described by a limited number of parameters, such as, mean, variance and correlation length. At those locations where the value of an attribute is known, geostatistical simulation techniques will reproduce that measured value. At locations where the value of the attribute is unknown, simulated values are produced. The complete field of attribute values reproduces the statistics describing the random field.

Benefits

Geostatistical fields honor known data, allow the inclusion of some types of soft data, and are equiprobable. Within the constraints of available computing resources, any desired number of fields can be generated, all of which are equally likely. Equiprobability allows for the quantitative treatment of uncertainty arising from the practical constraints of limited site data. The variance found in the complete set of maps of an attribute is the uncertainty of that attribute.

Weaknesses

Geostatistical methods are not particularly good at reproducing sudden, abrupt changes in attributes such as would be produced by faults. Unless substantial sampling immediately adjacent to such discontinuous features had been done, the feature would not be reproduced in the multiple realizations produced by geostatistical methods. Because these methods rely upon relative simple mathematical functions to describe the variation of attributes in space, the random fields produced tend to be excessively smooth to accurately represent faulted terrain.

Attribute sampling correctly located in space and at an appropriate scale is rarely available to rigorously estimate the both the vertical and horizontal correlation lengths. Scaling adjustments required by measurements taken at various scales, often quite different from the scale of the model, introduce significant uncertainty into the resulting estimate. It cannot be overstated that an adequate number of properly spaced, correctly scaled, unbiased samples are a requisite if these methods are to deliver the promised statistical rigor. When used with lesser quality data and more assumptions, the methods can provide useful models, but the rigor will be lost.

G.3 Methods/Approach

G.3.1 Zoned Geostatistical Simulation; a hybrid approach

Lithologically based model classes and the flow and transport attributes in this study are treated as a random variables. Model classes representing an exhaustive, mutually exclusive categorizations of the lithology are simulated. The zoned deterministic model is used as soft data to supplement borehole data to provide spatially distributed estimates of conditional probability for each class. A transition probability simulation (Carle, 1999) was used to simulate the spatial distribution of the model classes. This method has the advantage of reproducing the juxtapositional tendencies of the lithologic classes found in volcanic settings characterized by multiple cooling units (Figure 4).

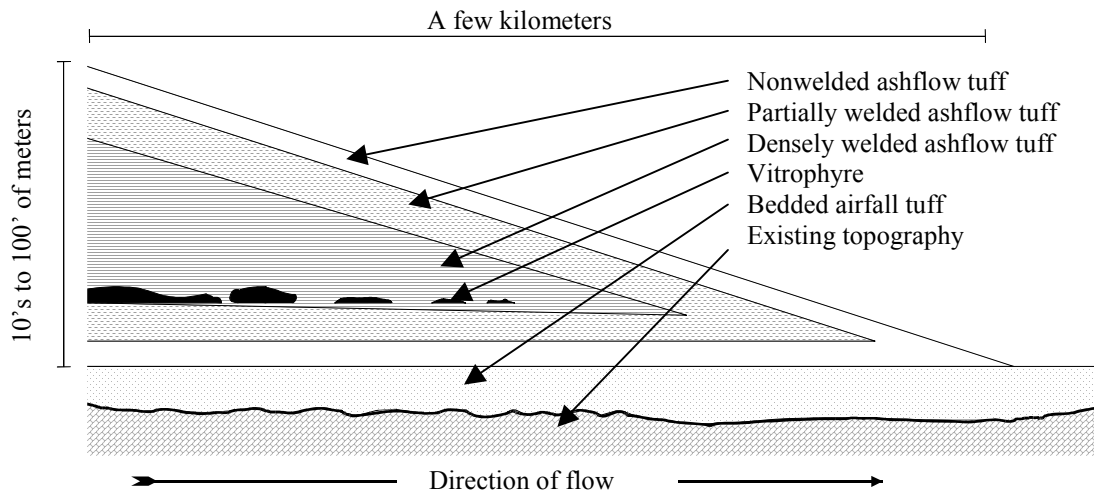


Figure 4. Simple cooling units

Within each model class, attributes are treated as random variables. Attribute variability within each model class is simulated as a spatially correlated random field. A composite attribute field is constructed by superpositioning the attribute value from the field corresponding to the model class at that location (Figure 5). The superpositioning process requires the existence of a field of categorical classes. This field may be a zoned deterministic model, or as in this study, a geostatistically simulated field. At each element of the model, the class is known. Random attribute fields of the same dimensions as the entire domain are generated for each class. The attribute value is chosen from the appropriate, i.e., corresponding to the class at that location, random field. The composite attribute field thus demonstrates spatial structure due to the size, shape, abundance and juxtaposition of the classes, and the inherent variation within class.

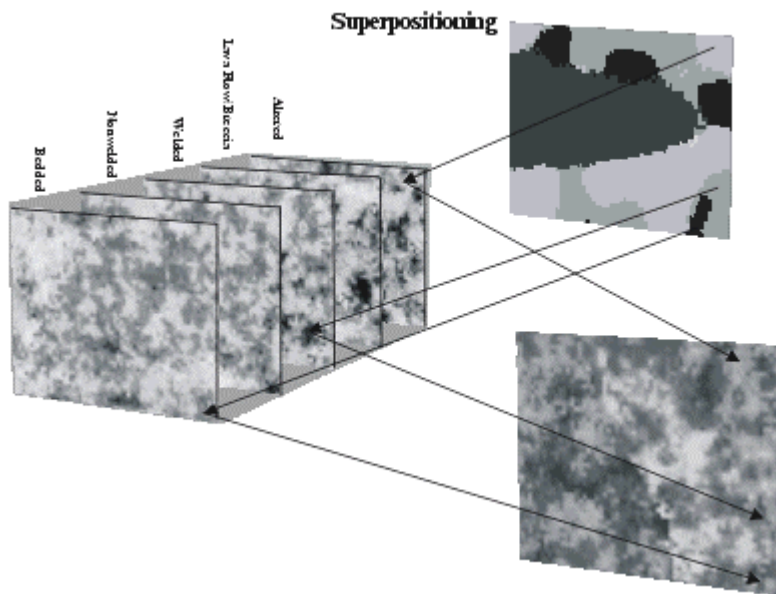


Figure 5. Superpositioning process

The composite attribute field reproduces the variability due to large scale, more deterministic spatial features such as faulting and bed pinch-out, as well as the smaller scale, more stochastic, and more sparsely sampled variability found within each class. In portions of the study domain where great confidence exists in the zoned deterministic model, it is possible to force the model to reproduce exactly the tabular arrangement of the deterministic model.

At present, there exists no rigorous way to determine how much soft conditioning data should be used from zoned deterministic model. In the event that the zoned deterministic model is believed to be perfectly accurate, then the transition probability class model becomes superfluous. When uncertainty on the location of contacts exists, then the frequency of conditioning represents an expression of how accurately large and small details are captured by the zoned deterministic model. If the zoned deterministic model is believed to accurately represent general geometric relationships, but uncertain in the exact location of specific contacts, then the transition probability simulation should be conditioned to the extent that difference observed between individual simulations is consistent with the users degree of belief and uncertainty. The deterministic zoned model contacts are boundaries where the probabilities of occurrence of models classes change.

G.3.2 Approach

The selection of model classes was driven by the requirements of observability and geologic plausibility. The requirement of observability is a consequence of the type of

data available. If sufficient number and location of appropriately sized measurements of the attributes existed, then traditional geostatistical methods would allow for direct estimation. However, the attribute measurements available for this study are sparse, far from optimally located and of wildly varying scales. Therefore, an approach exploiting the available attribute measurements, strongly supplemented by geologic observations and an evolving deterministic zoned model was adopted. Once it became apparent that the direct measurements of the attributes were insufficient to simply use traditional geostatistical simulation, the requirement of geologic plausibility comes into play. The transition probability method chosen requires that the classes to be simulated be categorical, i.e., mutually exclusive and exhaustive (Carle, 1999). The purpose of generating maps of classes was to subdivide the attribute continuum into the most meaningful and distinctly different populations. Ideally, each class would be separated in attribute parameter space (see Figure 7) from every other class. The large amount of data necessary to quantitatively subdivide the attribute continuum is virtually never available, necessitating a pragmatic, qualitative subdivision. However, it is worth keeping the ideal of optimal separation in attribute parameter space in mind when choosing the categorical classes.

There are three steps in creating attribute fields (permeability, porosity, clay or zeolite abundance). These are:

- Construction of the observable model class field
- Construction of spatially correlated attribute fields with the distribution of the attribute reproducing the specified distribution (means, variances and correlation lengths) of that attribute as specified for each class.
- Construction of a composite attribute field by superpositioning attribute values from the various class specific fields according to the class designation at each grid location.

The horizontal correlation length is the most difficult parameter for which to develop an estimate. The horizontal spacing of boreholes constrains the lag distances available for use in developing a semivariogram. Figure 6 illustrates the distribution of separation distances between boreholes at western Pahute Mesa.

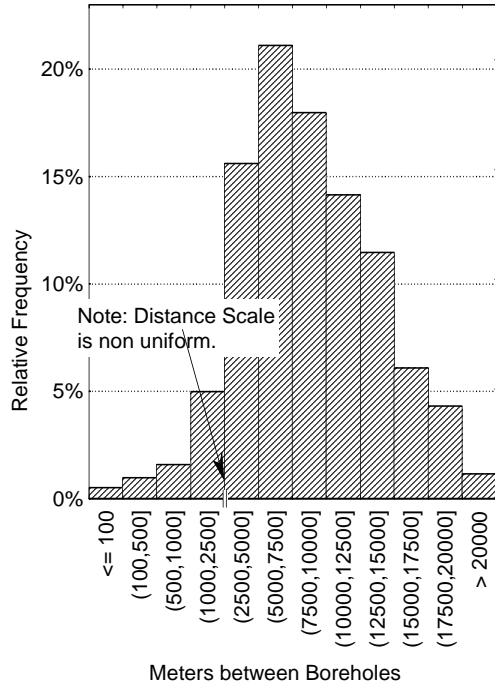


Figure 6. Distribution of horizontal separation distance between boreholes.

Spatially correlated, zero mean, unit variance random fields identical in size to the model domain are generated for each attribute and for each class. For each attribute these fields are differ only in the correlation lengths specified for each class. A single composite field is constructed by interrogating the class field at each location and choosing the zero mean, unit variance random value corresponding to that class. This zero mean, unit variance value is transformed to the correct value using a lookup table specific to that class. The lookup table is created from the available measured data and specifying how values at the tails of the distribution should be truncated. This method creates conductivity fields, which reproduce the CDF of the measurements and conform to the specified spatial statistics.

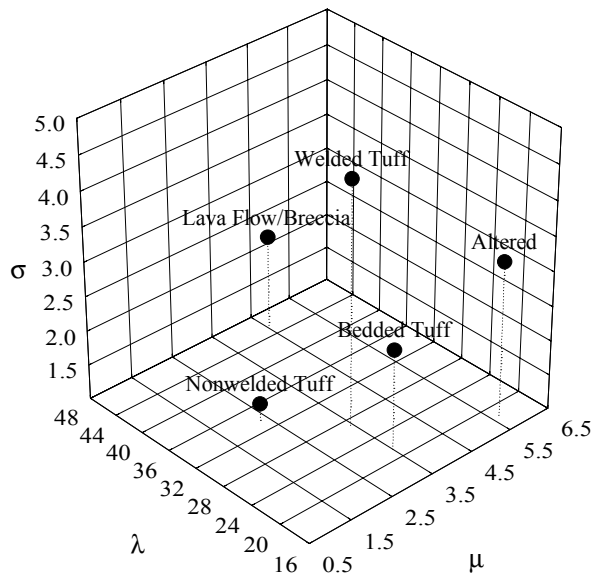


Figure 7. Idealized model class location in attribute parameter space

Because two of the attributes being estimated, hydraulic conductivity and porosity are part of the defining characteristics of hydrostratigraphic units, “A hydrostratigraphic unit is a body of rock distinguished and characterized by its porosity and permeability.” (Seaber, 1992), the classes can be considered as informal hydrostratigraphic units, or hydrofacies. However, because the distribution of the attributes is being treated as a random field, “... random-function-based stochastic simulations tend to bypass the actual genetic process and rely on global statistics that are deemed representative of the end phenomenon actually observed.” (Deutsch and Journel, 1992), consideration of both

population and spatial statistics needs to be added to the existing description of hydrostratigraphic units.

The lithologically observable classes are characterized by the geometry of occurrence in space and the likelihood of occurring adjacent to another class. This arrangement in space needs to meet the test of geologic plasticity, that is, a geologist familiar with the area should be able to conclude that any equiprobable class maps is a reasonable approximation to reality.

Virtually all modeling involves subdividing the spatial domain in some fashion. This process of subdivision raises the problem of scaling of attributes. If the entire domain is thought of as a single block, then it is obvious that the variance is zero and the correlation is infinite (relative to the domain). If the domain is subdivided into infinitesimal points, then the variance is at its maximum and the correlation length is at a minimum. However, there is no evidence that either the variance decreases linearly or that correlation length increases linearly with the scale of support. It is likely that each attribute will have its own distinctive relationship between support scale, variance and correlation length. Samples of increasing size and correct location would make it possible to experimentally determine how the variance and correlation length change with scale, but this type of data is not available for this study.

The same evaluation was performed for each of the attributes; data was collected, a population distribution was estimated taking into account the size of samples and any known biases, and the correlation lengths were estimated. Point samples were useful for helping to establish ranges, although for some attributes there were reasons to believe that the smallest scale samples failed to accurately represent the extreme values.

Hydraulic Conductivity

Measures of hydraulic conductivity range in scale from sub-core plugs to aquifer tests. The advantage of the smallest scale tests is the certainty that only a specific lithologic class is being sampled. The drawback is that the sampling is biased toward the least conductive end of the distribution. The highest conductivity in most of these materials was where the material is strongly fractured. If the fracture is large enough, then a sub-core plug would be smaller than the fracture, and simply never be sampled. Thus the very smallest, but most specific samples are from a biased population. The extent of this bias is unquantifiable. Borehole scale samples suffer from a similar bias. It is more difficult to recover intact fractured core for testing than it is to recover unfractured core. So again, the population is biased toward the lower end of the conductivity distribution. Packer tests offer an improvement between specificity of lithology tested and a bias toward an unfractured population. However, even these tests must be sited to avoid fractures at packer locations if a good seal is to be achieved. Additionally, this method is unable to accurately measure extremely low permeability. So data from packer testing is often

censored on both the upper and lower ends of the distribution. There is no way to determine if the censoring is symmetric, thus the mean as well as the variance may be in error. If the packed intervals are large, then the likelihood of isolating a single lithologic class is diminished. Aquifer tests and tracer tests suffer from the problem of sampling a volume larger than the model discretization. Thus the estimates of hydraulic conductivity are smoothed over several grid blocks. Additionally, the likelihood of sampling multiple lithologic classes increases with the volume sampled in the test.

The population distribution of hydraulic conductivity was estimated for this report from a series of tests conducted at the Nevada Test Site. The IT CORPORATION has collected the results of these tests. The results were grouped so that the lithologies sampled most closely resemble the observable lithologic classes. The resulting distributions are shown in Figure 8.

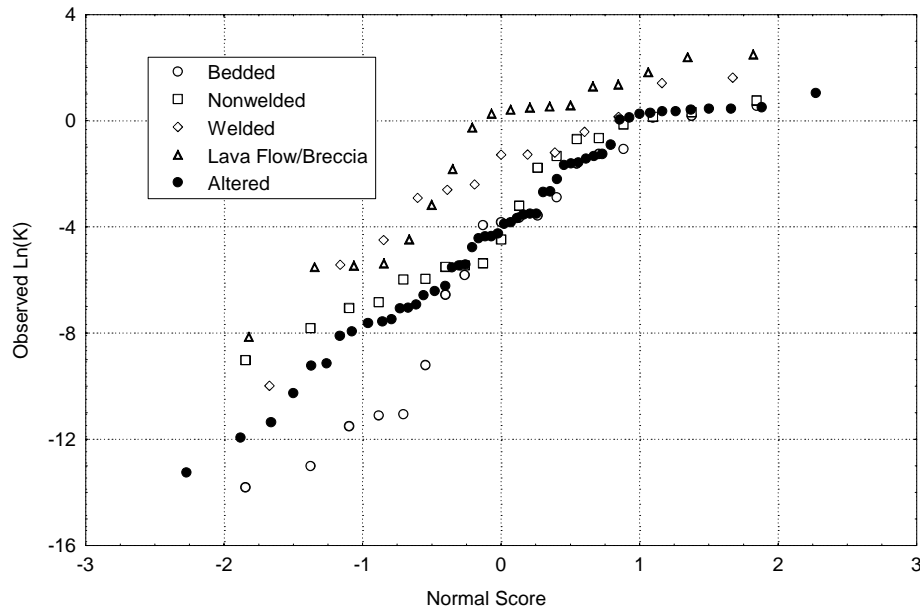


Figure 8. Ln(K) distribution by observable model class.

These distributions somewhat understate the variability because of the scale of support of the measurements, and because the tests are unlikely to be sampling only individual lithologic units. However, this represents the best available data at the time when the estimates were made. If additional data becomes available to refine the distributions, then additional, more accurate maps may be made.

The correlation lengths of hydraulic conductivity were and remain the most difficult and problematic parameters to estimate. Packer tests, covering intervals equivalent to model

grid blocks, isolated in single observable lithologies and separated vertically and horizontally by multiples of the model grid blocks would be needed to rigorously estimate the spatial correlation of this attribute. The data available does not even faintly approximate this ideal, thus the estimates of correlation length must be considered the most uncertain parameter in this study. However, some information useful for bounding and ordering the correlation lengths may be gained from secondary sources. The average thickness and length of the observable classes has been obtained from borehole observations and geologic maps. It is unlikely that the hydraulic conductivity within a class would be spatially correlated for a greater distance than the class itself. Thus the correlation lengths of hydraulic conductivity were set to be less than the average length of the class used in the transition probability simulation. The ordering of correlation, i.e., which class is correlated for the longest distance and which is correlated for the least has been set to be consistent with the geometry of the observable classes. For example the bedded air fall tuffs are found in thin continuous layers, consistent the nature of original deposition. By contrast, the lava flow/breccias are found in thicker, more massive deposits. Thus the bedded tuffs are simulated with a high vertical to horizontal anisotropy, and are horizontally correlated to a greater degree than the lava flow/breccias.

Table 2 Horizontal and vertical correlation lengths of hydraulic conductivity

Observable Model Class	Horizontal Correlation Length (m) (Short, Medium, Long cases)	Vertical Correlation Length (m) (Short, Medium, Long cases)
Bedded Air fall Tuff	300, 500, 900	10, 20, 50
Nonwelded Tuff	200, 250, 500	30, 45, 90
Welded Tuff	250, 500, 900	15, 30, 35
Lava Flow/Breccia	125, 250, 500	50, 100, 250
Altered	250, 750, 900	50, 125, 250

In the absence of either dynamic flow data in the study area, strongly correlated geophysical data or additional, appropriately spaced and scaled sampling, estimates of the correlation lengths of hydraulic conductivity must be considered highly uncertain. Similar rationale that was employed for bounding correlation lengths of hydraulic conductivity was used in establishing correlation lengths for bulk porosity, clay and zeolite abundance.

Bulk Porosity

The porosity estimated in this report is bulk porosity, not effective porosity. The available data consisted of core and sub-core samples, geophysical logs and calculated porosity from aquifer tests. The most useful data were the estimates of bulk porosity from geophysical logs.

$$\phi = 1 - \frac{\rho_b}{\rho_g}(1 - Z)$$

Where ρ_b is bulk density estimated from a gamma-gamma density log, ρ_g is grain density is a mean value for that observable lithologic class, and Z is the water content estimated from coincident epithermal neutron logs. The scale of these measurements is less than that of the model grids, but porosity is an attribute that may be upscaled by arithmetically averaging, unlike hydraulic conductivity. The variance must be reduced to reflect the upscaling and the correlation length increased. The porosity distributions used in this project are shown in Figure 9.

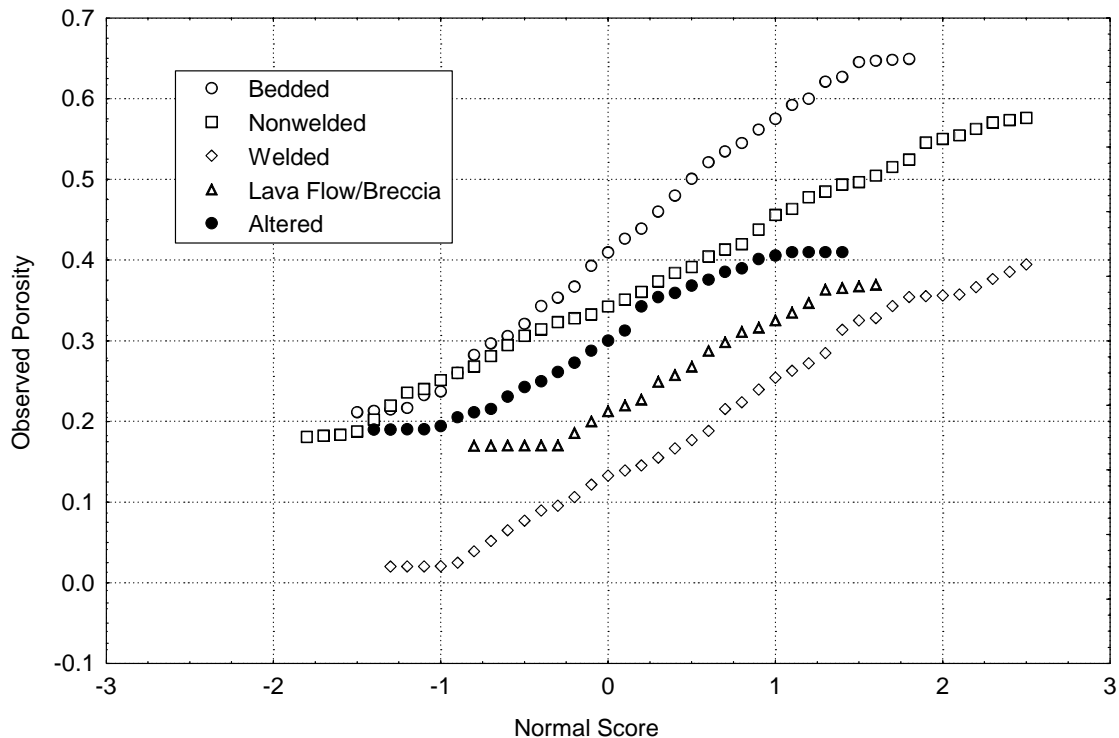


Figure 9. Bulk porosity by observable model class.

Clay and Zeolites

The data available for estimating the distribution of clay and zeolites consists of x-ray diffraction analysis (XRD) performed on samples taken from borehole sidewall samples and sub-core plugs. The sample volume is extremely small, less than 1 cc, so the scaling problem is acute. Exacerbating the scaling problem, the samples were not located in space so that an arithmetic average could be calculated. Therefore the affine transform variance reducing procedure was used in developing the estimated distribution. The affine transform or correction as defined by Isaaks and Srivastava, 1989 is

$$q' = \sqrt{f} * (q - m) + m$$

where q is a quantile in the original distribution, q' is the quantile in the transformed or corrected distribution, m is the mean of both distributions and f is a variance adjustment factor. The effect of changing the variance adjustment factor is illustrated in Figure 10. The extreme values were set to be consistent with geologic expert opinion and the shape of the distributions controlled by the point samples. The distributions are shown in Figure 11 and Figure 12.

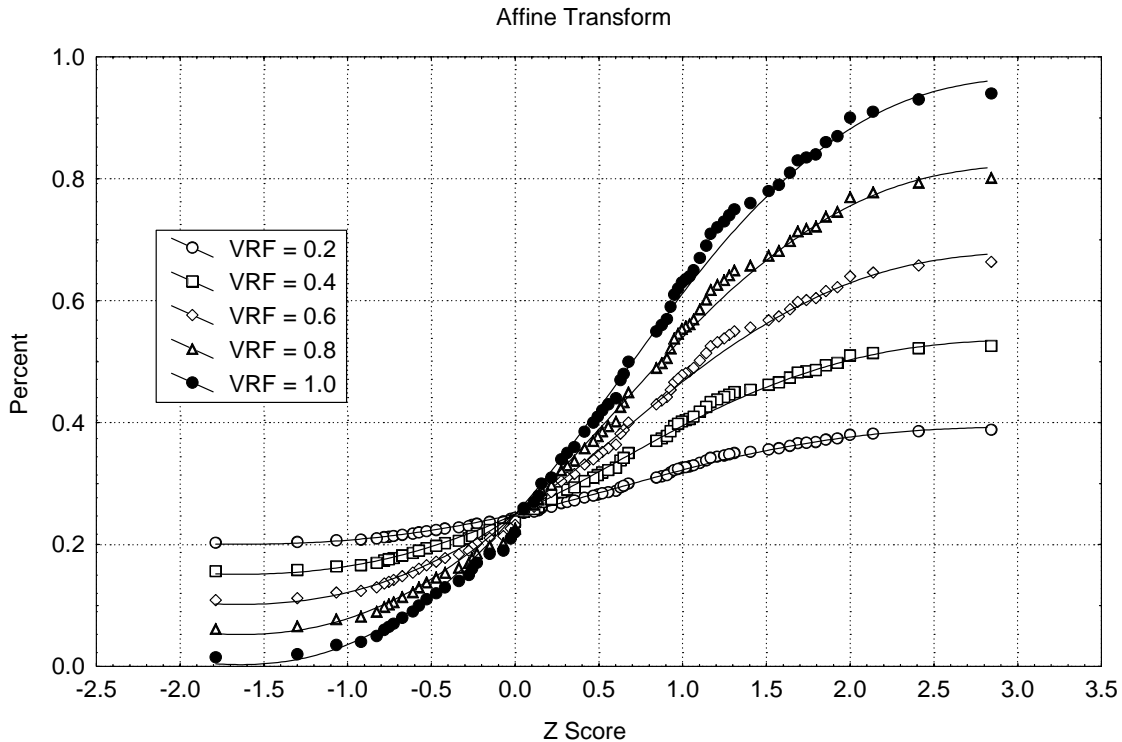


Figure 10. Affine transform

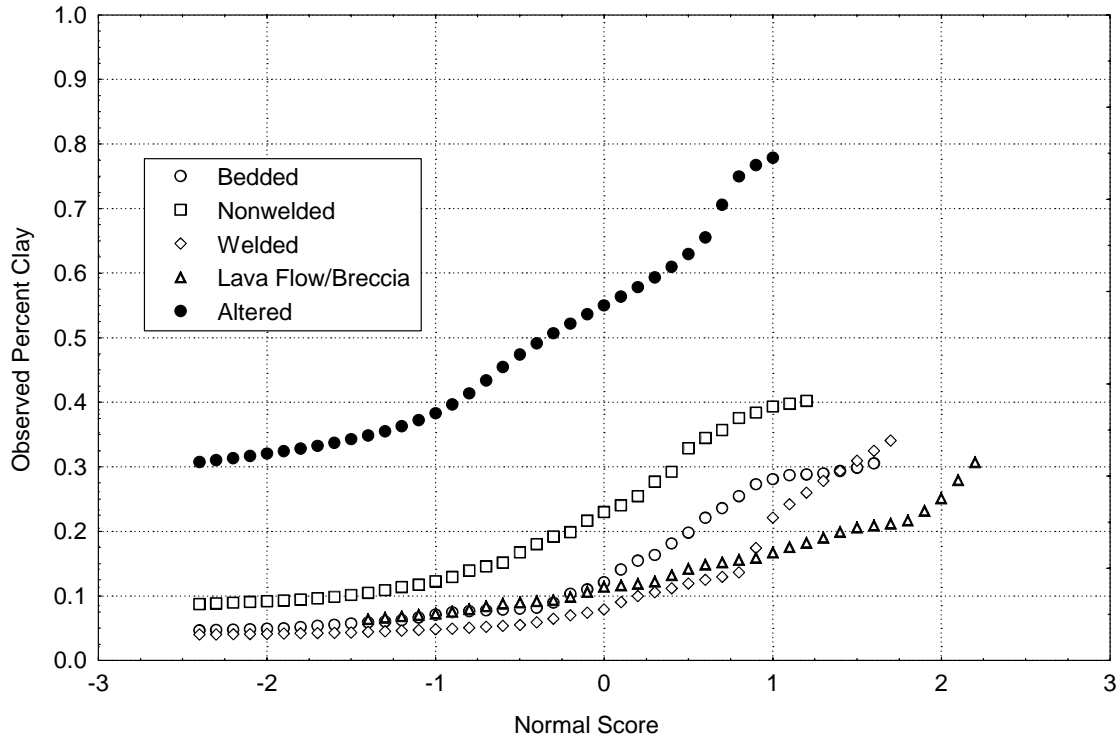


Figure 11. Clay distribution by observable model class.

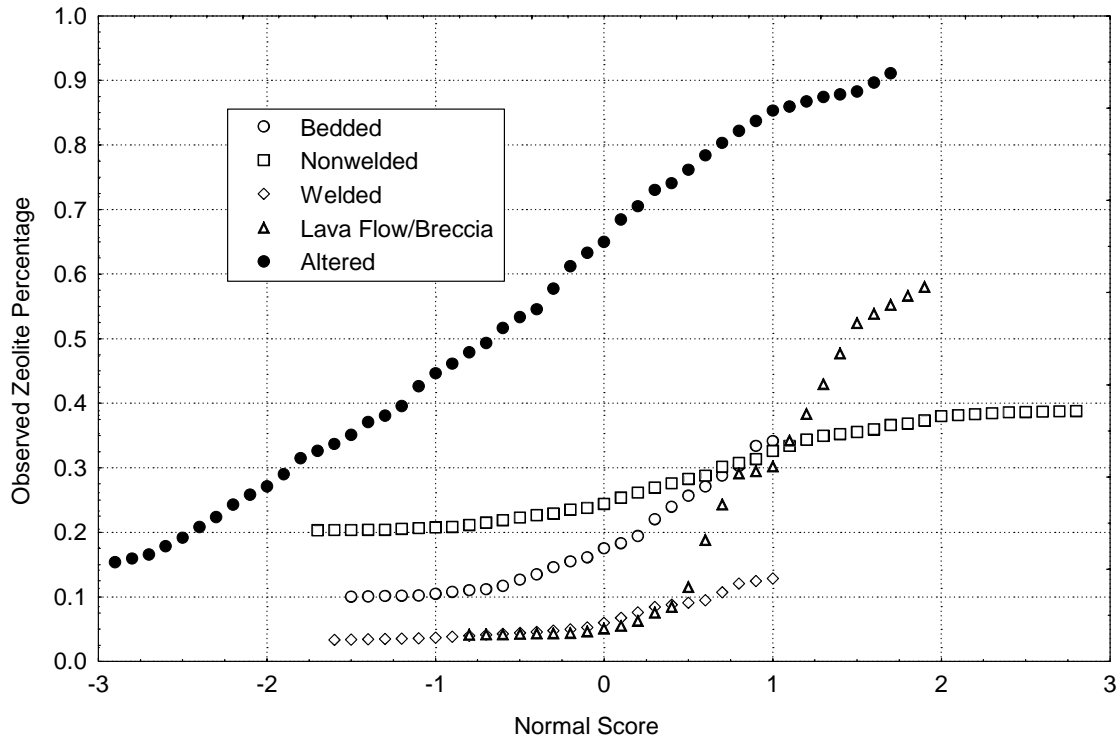


Figure 12. Zeolite distribution by observable model class

The correlation lengths used in generating the composite clay and zeolite attribute fields are listed in Table 3.

Table 3 Clay and zeolite correlation lengths.

Clay	Horizontal Correlation Length	Vertical Correlation Length
Bedded	300	10
Nonwelded	200	30
Welded	250	30
Lava Flow/Breccia	250	100
Altered	750	125
Zeolites		
Bedded	300	20
Nonwelded	250	30
Welded	450	30
Lava Flow/Breccia	250	100
Altered	750	125

G.4 Results and Discussion

G.4.1 Simulated Attribute Maps

Zoned geostatistical simulation is a systematic method of subdividing the attribute continuum exploiting quantitative measurements of attributes, spatially registered contacts between observable lithologic units and qualitative knowledge of the nature of occurrence of these lithologic units. The variation between the equiprobable class maps represents the uncertainty of the exact spatial distribution of lithologic classes. The variation between the equiprobable composite attribute maps represents the joint uncertainty of both the spatial distribution of lithologic classes and of the attribute within each lithologic class. If the classes are well selected, the classes should display minimal attribute variability within class and maximum attribute variability between classes. The geometry of each class within the study domain should be distinctly different.

The relationship between observable lithologic units and flow and transport attribute distributions could be better established if sampling at appropriate locations and scales were conducted. However, given that the purpose of this study was to develop estimates of the spatial distribution of specific flow and transport attributes using only previously collected data, simplifying assumptions regarding the representativeness of the available data were necessary.

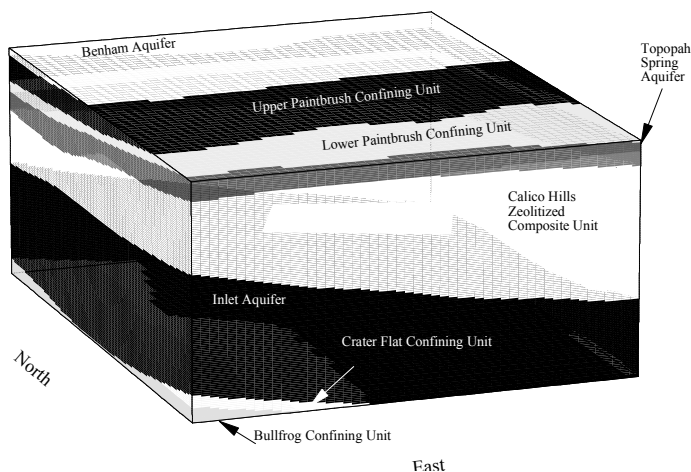


Figure 13. Deterministic model in study domain

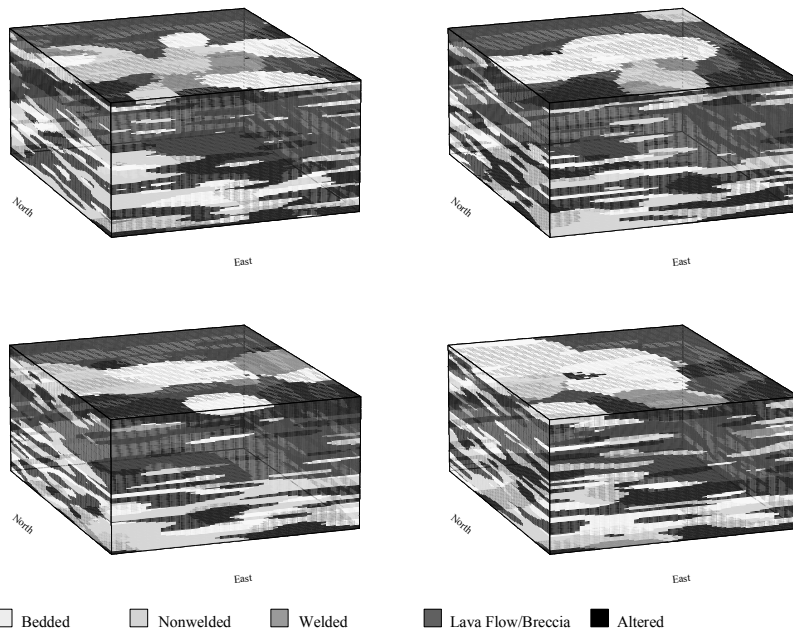


Figure 14. Equiprobable maps of observable model classes.

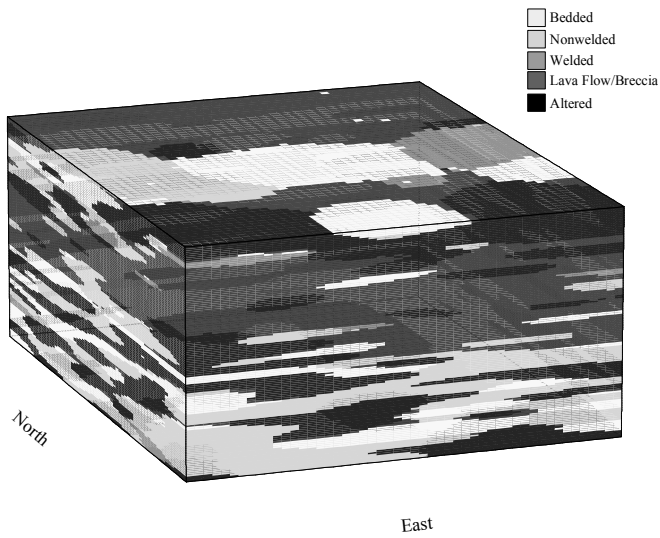


Figure 15. Transition probability simulation of model classes

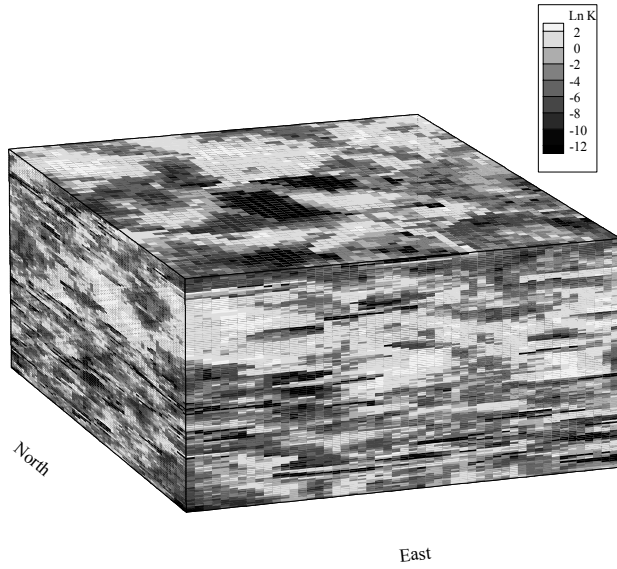


Figure 16. Ln(K) Long correlation lengths

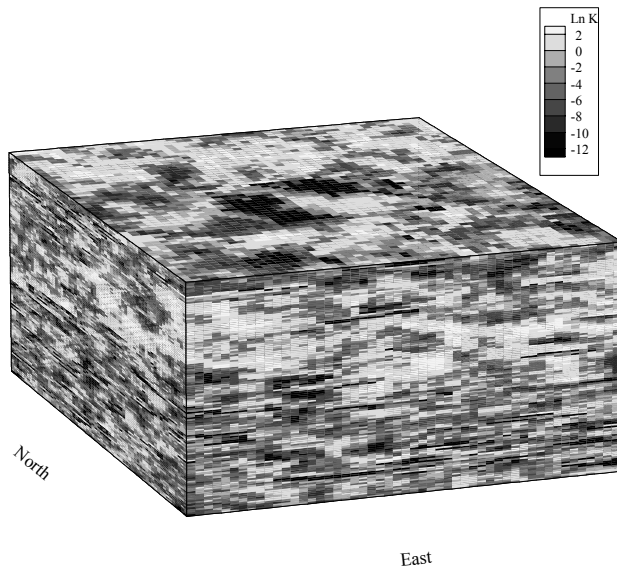


Figure 17. Ln(K) Medium correlation lengths

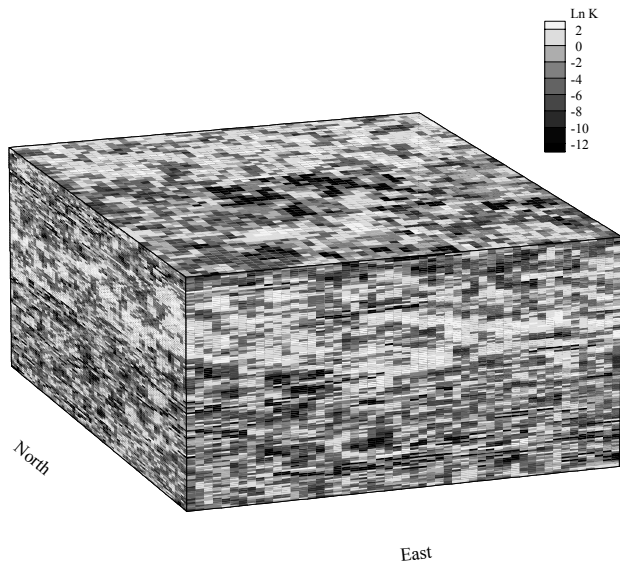


Figure 18. Ln(K) Short Correlation Lengths

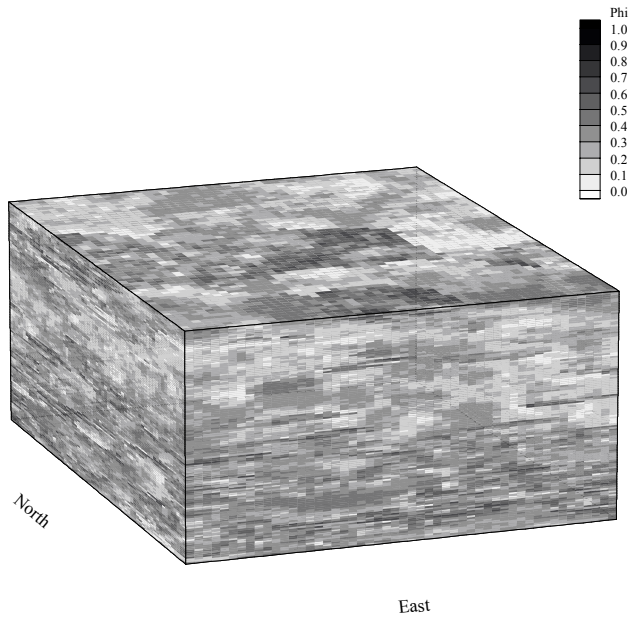


Figure 19. Porosity Map

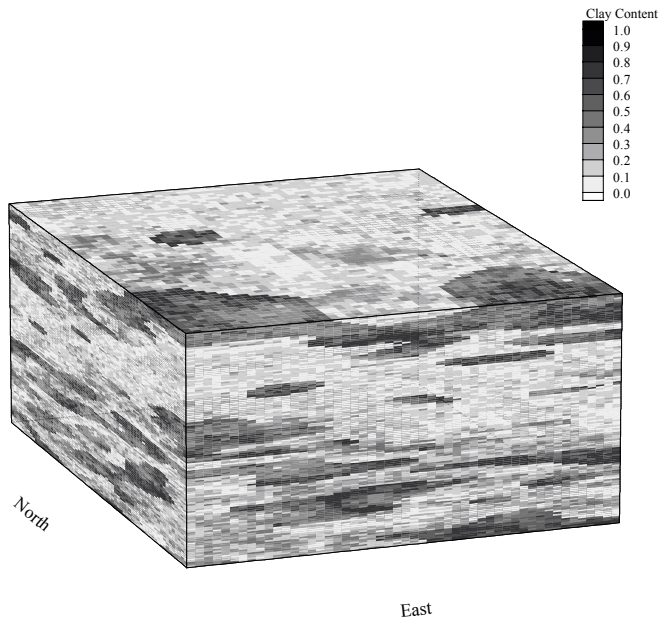


Figure 20. Clay Map

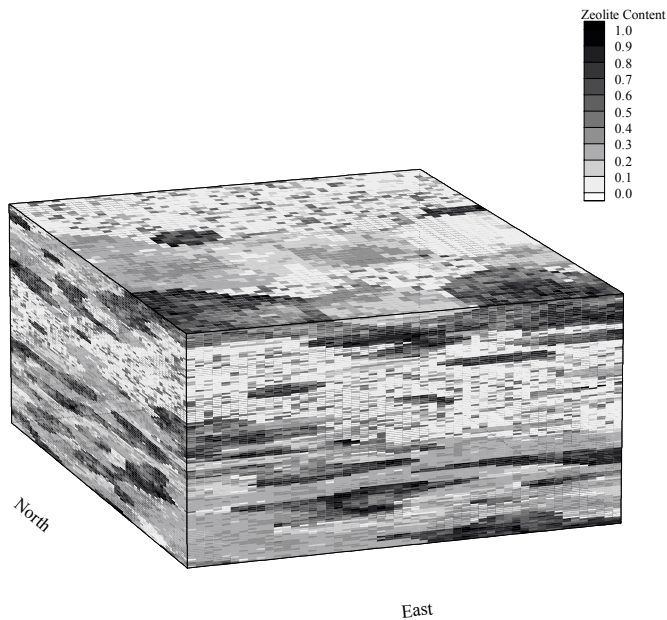


Figure 21. Zeolite Map

Faults are known to occur in the study area. Large faults are mapped and included in the zoned deterministic model. Smaller faults are likely to exist, but are not likely to be included in the zoned deterministic model. Additionally, it is unknown if buried faults and the deeper portions of faults expressed at the surface are a series of smaller faults or single large faults. The methods used to identify faulting (gravity and seismic surveys) do

not have the ability to resolve features at the scale of the model discretization. The transition probability simulation uses an average length for each observable lithologic class. The effect of non-deterministic faulting and textural pinch out is simulated by reducing the average length of a class to less than the infinite (i.e., as large as the domain) length of layers of the zoned deterministic model.

G.4.2 Rescaling, Variance, and Correlation Lengths

“This problem of the discrepancy between the support of our samples and the intended support of our estimates is one of the most difficult we face in estimation” (Isaaks and Srivastava, 1989).

The affine transfer is a variance reduction method that does not affect the mean but rather proportionally reduces extreme values. When applied to attribute its such as porosity or clay content which may be arithmetically averaged it serves acceptably to upscale point measurements. However, when the attribute in question does not average arithmetically the affine transfer is not applicable. Hydraulic conductivity is example of an attribute that may not be rescaled using the affine transfer.

While the affine transfer was used in this study due to the great difference in scale between the measurements and the model grid blocks, it should not be considered anything but a pragmatic approach. The problem of rescaling attributes remains an open area of research as noted by Cressie, 1993, “From a statistical point of view, current solutions to the change-of-support problems are unsatisfactory; I believe that further progress will have to be model based.” and Isaaks and Srivastava, 1989, “There are a variety of mathematical methods for adjusting a distribution so that its variance will be reduced while its mean remains unchanged. Unfortunately, all of these depend on unverifiable assumptions about how the distribution changes as the support increases; the also require knowledge of certain parameters that are very difficult to estimate precisely.”

The attributes of porosity clay content and the zeolite content have all been measured at the point scale, specifically very small samples used for X-ray diffraction (X R D). The upscaling process from thumbnail size samples to 50 m blocks inevitably introduces a great uncertainty. Compounding the uncertainty due to scaling, there are a number of sources of bias that may affect the accuracy of the data. It is unknown if a specific selection process or set of criteria were used in choosing which cores to sample and which samples from a core to analyze in detail. Thus it is impossible to determine if the samples represent a biased or unbiased estimate of the attributes. Because of this uncertainty, the resulting estimates should be considered more as relative measures than absolute. If a rigorous estimate of the absolute clay, zeolite or iron oxide content is critical, then a sampling program designed with both the model scale and the need for absolute measures will have to be undertaken.

Differences in the mean value and variance as well as extreme values were noted when specific analysts were considered and when the date of analysis was considered. It is not possible to distinguish between biases introduced by specific analytical methods from improvements in detection limits some resulting from more recent equipment. These unquantified sources of bias coupled with the uncertainty introduced by the extreme upscaling process mean that the distributions should be treated more as a qualitative estimate rather than a rigorous quantitative estimate.

The measurements of attributes, i.e., existing samples, were not comparable in size to the model grid. When sample are made of differing size or support, some type of adjustment must be made to render the data comparable. However all of the methods available for rescaling data have undesirable effects. As Noel Cressie noted in 1993, "From a statistical point of view, current solutions to the change-of-support problems are unsatisfactory; I believe that further progress will have to be model based."

While efforts have been made to be consistent with both the sparse measurements and expert opinion, the relationship between observable lithologic classes and some flow and transport attributes remains open to question. Until statistically significant numbers of attribute measurements, appropriately located for the scale of modeling to be done, are available, the spatial distribution of those attributes must be considered uncertain.

G.5 Conclusions

The zoned geostatistical method is a hybrid method that seeks to exploit the strengths of both the zoned deterministic method and the pure geostatistical approach. The method employed in this study of using borehole observations and deterministic model surfaces, to generate equiprobable maps of observable classes allows for the expert knowledge encoded in the deterministic zoned model to be blended with uncertainty which must exist between points of observation. The simulation of flow and transport attributes as random variables within these observable model classes allows for variation and uncertainty characteristic of the lithologies upon which the units are based.

The most serious weakness of the zoned geostatistical method is the need for correctly sized and located sampling. This is particularly acute for the estimation of horizontal correlation lengths. Hydraulic conductivity is probably the parameter most sensitive to the rescaling required by diverse testing methods. The use of dynamic data may be a means to improve estimation of this critical parameter.

G.6 Recommendations

Estimating the spatial distribution of any attribute in the absence of exhaustive sampling is always an exercise in division and aggregation, i.e., a set of decisions of what to lump

together and what to split apart. The zoned geostatistical approach is a two-step process, 1) estimate the spatial distribution of observable classes which have distinct populations of the attribute of interest, and; 2) estimate the spatial distribution of the attribute within each observable class. The current set of classes was used for all attributes. The accuracy could be improved by selecting observable classes specifically for each attribute to be estimated. For example, instead of using a single class for altered volcanics, multiple classes could have been used for each type and degree of alteration. This finer resolution would improve the accuracy of the estimate, if supported by adequate sampling. However, the sampling required for this approach is more demanding than for a coarser subdivision of the attribute continuum. Additionally this approach would make the inclusion of the maps into larger models more difficult because each attribute map would be independent of other attribute maps.

The inclusion of dynamic data such as aquifer and tracer tests could dramatically improve the quality of the attribute estimates. Numerous authors (Gomez-Hernandez *et al.*, 1997, Capilla *et al.*, 1997, Capilla *et al.*, 1998, Wen *et al.*, 1999) have demonstrated that the inclusion of flow data can dramatically improve the estimation of the spatial distribution of transmissivity and hydraulic conductivity. If the dynamic data is obtained within the study area, then the estimate can be directly conditioned. If the data is not from the study area, but is from a comparable setting, then the estimates of difficult to obtain parameters such as correlation length can be improved. This improvement is subject to the degree of comparability. If the amount of dynamic data is limited, and is being reserved for calibration purposes, then this method of improving the attribute estimates is foreclosed.

Sampling of attributes needs to be designed with the size and resolution of the model in mind. Samples, which are taken at scales smaller than the model grid blocks, need to be selected so that a meaningful aggregation can be done. Samples, which encompass volumes greater than the model grid blocks, need to be carefully considered. The number of samples for spatially correlated attributes needs to be carefully considered for any specific degree of certainty (Barnes, 1988). In this study, the spatial distribution of iron oxides could not be modeled in any meaningful way because of the absence of adequate sample data. If dynamic data acquisition such as flow and tracer tests are to be conducted, the specific attributes being estimated needs to be considered.

G.7 References

- Barnes, R.J., 1988, Bounding the Required Sample Size for Geologic Site Characterization, *Mathematical Geology*, 20(5):477-490
- Capilla, J.E., J.J. Gomez-Hernandez and A. Sahuquillo and, 1997, Stochastic simulation of transmissivity fields conditional to both transmissivity and piezometric data. 2. Demonstration in a synthetic data case., *Journal of Hydrology*, 203(1-4), 175-188
- Capilla, J.E., J.J. Gomez-Hernandez and A. Sahuquillo and, 1998, Stochastic simulation of transmissivity fields conditional to both transmissivity and piezometric data. 3. Application to the Waste Isolation Pilot Plan in New Mexico (USA)., *Journal of Hydrology*, 207(3-4), 254-269
- Carle, S.F., 1999, *TPROGS: Transition Probability Geostatistical Software, Version 2.1*, Electronic copy from author.
- Cooley, R.L., and M.C.Hill, 2000, Comment on *RamaRao et al.* [1995] and *LaVenue et al.* [1995], *Water Resour. Res.*, 36(9):2795-2797.
- Cressie, N.A.C, 1993. *Statistics for Spatial Data*. John Wiley & Sons, Inc.
- Deutsch, C.V., and A.G. Journel, 1998, *GSLIB Geostatistical Software Library and User's Guide*, 2nd edition, Oxford University Press.
- Drellack, S.L., and L.B. Prothro, 1997, Descriptive Narrative for the Hydrogeologic Model of Western and Central Pahute Mesa Corrective Action Units, Bechtel Nevada , Report under contract DE-AC08-96NV11718.
- Gomez-Hernandez, J.J., A. Sahuquillo and J.E. Capilla, 1997, Stochastic simulation of transmissivity fields conditional to both transmissivity and piezometric data. 1. The theory., *Journal of Hydrology*, 203(1-4),162-174
- Isaaks, E.H., and R.M. Srivastava, 1989, *An introduction to applied geostatistics*. Oxford University Press.
- Prothro, L.B., and R.G. Warren, 1999, Geology in the Vicinity of the TYBO and Benhan Underground Nuclear Tests, Pahute Mesa, Nevada Test Site, Bechtel Nevada Report, DOE/VN/11718—305.
- RamaRao, B.S., A.M. LaVenue, G. de Marsily and M.G. Marietta, 2000, Reply to Comment on *RamaRao et al.* [1995] and *LaVenue et al.* [1995], *Water Resour. Res.*, 36(9):2799-280
- Seaber, P.R., 1992, Proposed addition to the North American Code of Stratigraphic Nomenclature (Draft)
- Sully, M., 1999, Computer files of hydrogeologic model surfaces, personal communication.
- Wen, X.H., J.E. Capilla, C.V. Deutsch, J.J. Gomez-Hernandez and A.S. Cullick, 1999 A program to create permeability fields that honor single phase flow rate and pressure data, *Computers & Geosciences*, 25(3), 217-230

THIS PAGE INTENTIONALL LEFT BLANK

This report has been reproduced directly from the best available copy. It is available electronically on the Web (<http://www.doe.gov/bridge>).

Copies are available for sale to U.S. Department of Energy employees and contractors from:

Office of Scientific and Technical Information
P.O. Box 62
Oak Ridge, TN 37831
(865) 576-8401

Copies are available for sale to the public from:

National Technical Information Service
U.S. Department of Commerce
5285 Port Royal Road
Springfield, VA 22616
(800) 553-6847



Los Alamos NM 87545